Activity-guided isolation of natural products with immunosuppressive activity

Inauguraldissertation

zur

Erlangung der Würde eines Doktors der Philosophie

Vorgelegt der

Philosophisch-Naturwissenschaftlichen Fakultät

der Universität Basel

von

Jakob Klaus Reinhardt

2020

Originaldokument gespeichert auf dem Dokumentenserver der Universität Basel
edoc.unibas.ch

Dieses Werk ist unter dem Vertrag «Creative Commons Namensnennung-Keine kommerzielle Nutzung-Keine Bearbeitung 4.0 International» lizenziert. Die vollständige Lizenz kann unter
creativecommons.org/licenses/by-nc-nd/4.0/
eingesehen werden.

Genehmigt von der Philosophisch-Naturwissenschaftlichen Fakultät

auf Antrag von

Prof. Dr. Matthias Hamburger
PD Dr. Martin Smieško
Prof. Dr. Till Opatz

Basel, den 13.10.2020

Prof. Dr. Martin Spiess
Dekan

Attribution-NonCommercial-NoDerivatives 4.0 International

(CC BY-NC-ND 4.0)

You are free to share – to copy, distribute and transmit the work

Under the following conditions:

Attribution – You must give appropriate credit, provide a link to the license, and indicate if changes were made. You may do so in any reasonable manner, but not in any way that suggests the licensor endorses you or your use.

Noncommercial – You may not use the material for commercial purposes.

No Derivative Works – If you remix, transform, or build upon the material, you may not distribute the modified material.

Attribution – You must give appropriate credit, provide a link to the license, and indicate if changes were made. You may do so in any reasonable manner, but not in any way that suggests the licensor endorses you or your use.

With the understanding that:

Waiver – Any of the above conditions can be **waived**, if you get permission from the copyrightholder.

Public Domain – Where the work or any of its elements is in the **public domain** under applicable law, that status is in no way affected by this license.

Other Rights – In no way are the following rights affected by this license:

Your fairdealing or **fairuse** rights, or other applicable copyright exceptions and limitations;

The author’s **moral** rights;

Rights other persons may have either in the work itself or in how the work is used, such as publicity or **privacy** rights.

Notice – For any reuse or distribution, you must make clear to others the license terms of this work. The best way to do this is with a link to this webpage:

https://creativecommons.org/licenses/by-nc-nd/4.0/ Date: October 23, 2020

For my family - Blood and Otherwise

We have learned that nothing is simple and rational
Except for what we ourselves have invented;
That God thinks in terms neither of Euclid nor Riemann;
That science has "explained" nothing;
That the more we know the more fantastic the world becomes;
And the profounder the surrounding darkness.

From: **Along the Road** *– Aldous Huxley*

Table of contents

ACKNOWLEDGEMENTS

The time of working towards my PhD here in the Department of Pharmaceutical Biology in Basel was one of the most fulfilling and educating experiences in my life. These past years were not always easy, neither for me nor the rest of the world, but I could not imagine to have spent this time in a more kind, helpful, and enjoyable environment. Thus, I want to acknowledge all the people, who contributed to this work.

First and foremost, I want to thank Professor Dr. Matthias Hamburger, who gave me the opportunity to come to Basel for my PhD. His valuable experience, supervision, and encouragement enabled me to do this work as it is now. This allowed me to explore many different ideas in the pursuit of my work. And although only some of those led to solutions, each of them was an insight into becoming a better scientist.

Secondly, I owe many thanks to Professor Dr. Carsten Gründemann for the work together and for building the enjoyable and prolific collaboration between Freiburg and Basel on which this work was build.

Next, I want to express my gratitude to PD Dr. Martin Smieško for not only agreeing to be my second supervisor, but for actively taking on this role for himself throughout my PhD. Without his consultation and guidance, the computational aspects of this work would not be as it is.

I cannot express enough thanks to Dr. Amy Zimmermann-Klemd, who was a cornerstone during the work. Without her extraordinary efforts and curiosity, many biological aspects would have stayed unexplored.

I want to thank Prof. Dr. Thomas Bürgi for introducing me to VCD, for the measurement of many of my samples in his lab in Geneva, and for his patient explanations on the evaluation of VCD spectra.

Also, I must thank Prof. Dr. Olivier Potterat for his valuable advices over the years and many helpful discussions.

Big thanks to Dr. Eliane Garo for her efforts enabling me to solve NMR spectra on long train rides to Germany.

I want to thank Dr. Timothy Sharpe from the biophysics facility for enabling and securing the possibility to measuring ECD spectra.

I owe deep gratitude to Dr. Ombeline Danton as a colleague, as a friend, and for being a great sparring partner for the discussion of difficult structural questions.

I want to acknowledge Orlando Fertig for his valuable technical support as well as for his composure and knowledge when troubleshooting various instruments.

I want to thank Dr. Thanasan Nilsu for his commitment, his conscientious way of working, and the exchange of experience during his time in Basel.

I would also like to thank all co-authors for their help, contributions, and advice for the publications that emerged from this project and that are presented in this work.

I also owe deep gratitude to Dr. Maria-Teresa Faleschini, who introduced me to many of the instruments, when I started and with whom it was always a pleasure to exchange ideas.

In general, I want to thank all the former and current members of this lab for the outstanding work atmosphere, the support, and the many adventures we had together, both inside and outside of the lab.

Also, on the other side of the “work-life balance”, I have to thank my family, which was always there when I needed them, and my flatmates, who distracted me once in a while from this work to show me the beauty of Switzerland and its rocks. Here, I also want to appreciate all the great people I met during this time inside and outside the great city of Basel, along or in the Rhine, while cycling, swimming, paddling, bouldering, or hiking in the beautiful mountains of Switzerland. Your support and friendship helped me get through all the ups and downs of my doctoral studies, which are now coming to an end.

Thank you!

List of Abbreviations

AC	Absolute configuration
ADAP	Adhesion- and degranulation-promoting adapter Protein
AP-1	Activator protein 1
ATC	Anatomical Therapeutic Chemical classification system
AG	Antigen
APC	Antigen presenting cell
AIRE	Autoimmune regulator
BCR	B cell receptor
BCL-10	B-cell lymphoma protein 10
B3LYP	Becke, 3-parameter Lee-Young-Parr
CRAC	Calcium release-activated channels
CFSE	Carboxyfluorescein diacetate succinimidyl ester
CARMA1	Caspase-recruitment domain membrane associated guanylate kinase
CE	Cotton effect
CPC	Centrifugal partition chromatography
CAR	Chimeric antigen receptor
CD	Circular dichroism
CD#	Cluster of differentiation # (i.e. CD8)
CBM complex	Complex from CARMA1, BCL-10, and MALT1
COSY	Correlation spectroscopy
CRD	Crohn's disease
cAMP	Cyclic adenosine monophosphate
DAMP	Damage-associated molecular pattern
DC	Dendritic cells
DFT	Density functional theory
DNA	Deoxyribonucleic acid
DAG	Diacylglycerol
Elk-1	E26 transformation-specific like protein 1
ECD	Electronic circular dichroism
ER	Endoplasmatic reticulum
EtOH	Ethanol
EtOAc	Ethyl acetate
Eu(hfc)$_3$	Europium tris[3-(heptafluoropropylhydroxymethylene)-(+)-camphorate]
ERK	Extracellular signal-regulated kinase
FACS	Fluorescence-activated cell sorting
FOXP3	Forkhead box P3
GCMS	Gas chromatography-mass spectrometry
GvHD	Graft versus host disease
GDP	Guanosine diphosphate
GTP	Guanosine triphosphate
HMBC	Heteronuclear multiple-bond correlation spectroscopy

HSQC	Heteronuclear single-quantum correlation spectroscopy
HPLC	High performance liquid chromatography
IPEX	Immunodysregulation polyendocrinopathy enteropathy X-linked
IG	Immunoglobulins
ITAM	Immunoreceptor tyrosine based activation motif
IR	Infrared
IκB	Inhibitor of NF-κB
IKK	Inhibitor of NF-κB kinase
IP$_3$	Inositol 1,4,5-trisphosphate
IP$_3$R	Inositol 1,4,5-trisphosphate receptor
IL	Interleukin
JAK	Janus kinases
JNK	Jun kinase
KSR	Kinase Suppressor of Ras
LAT	Linker for activation of T cells
LPS	Lipopolysaccharide
LPS	Lipopolysaccharide
Lck	Lymphocyte specific protein tyrosine kinase
MHC	Major histocompatibility complex
mTOR	Mammalian target for rapamycin
MEK1	MAPK/ERK kinase 1
MeOH	Methanol
MAPK	Mitogen activated protein kinase
MAPKK	Mitogen activated protein kinase kinase
MAPKKK	Mitogen activated protein kinase kinase kinase
MO	Molecular orbital
MALT1	Mucosa-associated lymphoid tissue protein 1
MS	Multple sclerosis
NK cells	Natural killer cells
NEMO	NF-κB essential modulator
NO	Nitric oxide
NSAID	Non-steroidal anti-inflammatory drug
NF-κB	Nuclear factor kappa-light-chain-enhancer of activated B cells
NFAT	Nuclear factor of activated T-cells
NMR	Nuclear magnetic resonance
NOE	Nuclear Overhauser effect
NOESY	Nuclear Overhauser effect spectroscopy
OR	Optical rotation
ORD	Optical rotation dispersion
PAMP	Pathogen-associated molecular pattern
PRR	Patterns recognition receptors
PIP$_3$	Phosphatidylinositol 3,4,5-triphosphate
PIP$_2$	Phosphatidylinositol 4,5-biphosphate

PDE4	Phosphodiesterase 4
PI$_3$ kinase	Phosphoinositide 3-kinase
PLC-γ	Phospholipase C-γ
PLT	Primary lymphoid tissue
PKC-θ	Protein kinase C-θ
RasGRP	Protein Ras-guanyl-releasing protein
RC	Relative configuration
ROA	Raman optical activity
RA	Rheumatoid arthritis
ROESY	Rotating frame nuclear Overhauser effect spectroscopy
SLP-76	SH2 domain containing leukocyte protein of 76kda
STIM1	Stromal interaction molecule 1
SLE	Systemic lupus erythematosus
TCR	T cell receptor
TDDFT	Time-dependent density functional theory
TLR	Toll-like receptor
TCM	Traditional Chinese medicine
TGF	Transforming growth factor
TNF	Tumor necrosis factor
TRAF-6	Tumor necrosis factor receptor-associated factor 6
TRAIL-DR5	TNF-related apoptosis-inducing ligand-death receptor 5
T1D	Type 1 diabetes
UV/Vis	Ultraviolet/visible
VCD	Vibrational circular dichroism
VOA	Vibrational optical activity
VTCD	Vibrational transition current density
WHO	World Health Organization
WHOCC	WHO Collaborating Centre for Drug Statistics Methodology

Summary

The worldwide incidence of autoimmune diseases is rising, especially in industrialized countries. Apart from alleviating symptoms, the aim of any treatment is to regain a balance between tolerance and immunity. As T cells play a central role in both processes, the pathways leading to their activation are attractive targets for immunosuppressant drugs. The search for new inhibitors in recent years, however, was mostly focused on biologicals like monoclonal antibodies or fusion proteins. This improved the treatment of autoimmune conditions significantly, but administration and immunogenicity limit their application. Thus, there is a need for new small molecule immunosuppressant drugs with new modes of action.

To pursue new lead compounds, we mined the chemical space contained in a library of extracts from plants used in Traditional Chinese Medicine (TCM). This pre-selection was done to focus on plants used over a long period of time with some evidence for bioactivities. To identify extracts and compounds that inhibit the proliferation of activated primary T lymphocytes isolated from human blood, we used an *in vitro* assay. Through FACS analysis, the assay also allowed for the direct identification of cytotoxic or necrosis inducing effects.

We screened 435 extracts from plants used in TCM at a concentration of 30 µg/mL. From these, around 40 extracts showed T cell proliferation inhibition and 6 plants in total were selected for further investigations based on the absence of cytotoxicity, availability, batch to batch reproducibility, and a literature survey. Seven extracts from these plants were subjected to HPLC activity profiling, which allowed the identification of regions of activity in four of the extracts. The compounds in these active regions were the focus of subsequent isolation of compounds from these plant extracts. The work on two plants, *Artemisia argyi* and *Toddalia asiatica*, resulted in the publication of three peer reviewed publications. The work on two other extracts is still ongoing.

The first extract was an ethyl acetate extract from the aerial parts of *A. argyi*. From this extract, 18 compounds, including 5 new sesquiterpene lactones were isolated. A series of four isomeric sesquiterpene lactones, two diastereomeric *seco*-tanapartholides and two diastereomers of canin, showed activity at micromolar concentrations (IC_{50} values between 1.0 and 3.7 µM). Published data on the series of canin-diastereomers gave only unsatisfactory information on their identities and absolute configurations. Thus, their absolute configurations were determined independently using ECD and VCD. The relative configurations of *seco*-tanapartholides A and B were only known in part and interestingly, ECD gave almost enantiomeric spectra. Therefore, the absolute configuration was solved by VCD. Visual and computational methods were used for evaluation of the spectra. The knowledge of their absolute configurations can now be used as the basis for possible development as immunosuppressant lead compounds. These results are published in the Journal of Natural Products (Vol. 82, 2019).

Next, we investigated the mode of action of the isolated compounds and the ethyl acetate extract from *A. argyi*. To identify the affected transcription factors, reporter cell lines for AP-1, NFAT, and NF-κB were used. The target of the *A. argyi* extract and the tested sesquiterpene lactones was thereby found to be located upstream of NFAT and NF-κB. We further investigated the effects of both, the extract and the sesquiterpene lactones, on calcium signaling involved in the NFAT pathway. Although some of the compounds had an effect on calcium signaling, none of them, nor a combination of all, inhibited calcium influx into the cell or from the ER as effectively as the extract itself. These results were published in Frontiers in Pharmacology (Vol. 11, 2020).

The second extract we investigated in the course of this work was the MeOH extract from the roots of *T. asiatica*. Here, the alkaloid nitidine was identified as a highly active constituent with an IC_{50} value of 0.37 µM. Another, less active (IC_{50} 6.72 µM), alkaloid was identified along with other inactive alkaloids, lignans and coumarins, some of them glycosylated. A combination of ECD, OR, GCMS analysis of hydrolyzed sugars, enantioselective HPLC analysis of hydrolyzed aglycones

and NMR in the presence of the chiral shift reagent $Eu(hbc)_3$ was used to identify the absolute configurations of these compounds. Three of the compounds were new natural products. The results are published in the Journal of Natural Products (Vol. 83, 2020).

From identifying several compounds with significant activity in inhibiting T cell proliferation, we found the CFSE assay to be useful for the identification of new lead compounds with relevant activities. As many of the natural products found did not have well described absolute configurations, we used a broad array of methods to fill this gap and publish the results for use by future researchers. The combination of ECD (as a sensitive method) with complementary techniques like VCD, chromatography of hydrolyzed compounds, or the use of shift reagents in NMR proved to be very effective. It enabled us to solve challenging cases like *seco*-tanapartholides A and B from *A. argyi* and the glycosylated coumarins from *T. asiatica*.

Zusammenfassung

Die weltweite Inzidenz von Autoimmunerkrankungen hat in den letzten Jahren, vor allem in Industrieländern, zugenommen. Für die Behandlung ist es wichtig, abgesehen von der Symptommilderung, die Balance zwischen Toleranz und Immunität wiederherzustellen. Da T Zellen in beiden Prozessen eine zentrale Rolle spielen, sind die T Zell aktivierenden Signalwege über AP-1, NFAT und NF-κB attraktive Ziele für immunsuppressive Medikamente. Die Entwicklung von neuen Inhibitoren ist aktuell primär auf Biopharmazeutika wie monoklonale Antikörper oder Fusionsproteine fokussiert. Das hat zwar die Therapie von Autoimmunerkrankungen deutlich verbessert, allerdings ist deren Anwendung durch Darreichungsform und Immunogenizität limitiert. Dadurch entsteht in der Therapie ein Bedarf für neue kleine Moleküle mit neuen Wirkmechanismen.

Um neue Leitstrukturen zu finden, nutzten wir die chemische Diversität in einer Bibliothek von Extrakten aus Pflanzen, die in der traditionellen Chinesischen Medizin (TCM) Verwendung finden. Diese Auswahl sollte den Fokus auf Pflanzen lenken, die bereits über lange Zeit genutzt werden und damit zumindest über eine begrenzte Evidenz für biologische Aktivität verfügen. Für die Identifizierung von Extrakten oder Stoffen, die die Proliferation von primären, aus menschlichem Blut isolierten T Zellen hemmen, wurde ein *in vitro* Test verwendet. Durch die Analyse mit Fluoreszenz aktivierter Zellsortierung (FACS) wurden dabei auch zytotoxische oder nekroseinduzierende Effekte identifiziert.

Wir testeten 435 Extrakte von Pflanzen aus der TCM bei einer Konzentration von 30 µg/mL. Bei etwa 40 Extrakten stellten wir eine Hemmung der T Zell Proliferation fest. Insgesamt sechs Pflanzen wurden, basierend auf Zytotoxizität, Verfügbarkeit, Reproduzierbarkeit und bekannter Literatur, für weitere Untersuchungen ausgewählt. Für sieben Extrakte dieser Pflanzen wurde ein HPLC Aktivitätsprofil erstellt, welches in vier Extrakten aktive Regionen aufzeigte. Die Stoffe in den aktiven Regionen standen demnach im Fokus der Isolierung. Die Arbeit an zwei der Pflanzen, *Artemisia argyi* und *Toddalia asiatica*, führte zu drei im Peer-Review Verfahren begutachteten Publikationen. Die Arbeit an zwei anderen Extrakten ist noch im Gange.

Der erste Extrakt war ein Ethylacetatextrakt der überirdischen Teile von *A. argyi*. Aus diesem Extrakt wurden 18 Stoffe isoliert, darunter fünf neue Sesquiterpenlaktone. Eine Reihe von isomeren Sesquiterpenlaktonen, zwei Diastereomere *seco*-Tanapartholide und zwei Diastereomere von Canin, zeigten Aktivität bei mikromolaren Konzentrationen (IC_{50} Werte zwischen 1.0 und 3.7 µM). Die Daten in der Literatur zu Identität und absoluter Konfiguration reichten nicht für eine eindeutige Identifizierung dieser Stoffe. Daher wurden die absoluten Konfigurationen unabhängig mit ECD und VCD bestimmt. Die relativen Konfigurationen der *seco*-Tanapartholide A und B waren nur zum Teil bekannt und im ECD wurden quasi-enantiomere Spektren gemessen. Daher wurden die absolute Konfiguration final mit VCD bestimmt. Für die Auswertung der Spektren wurden sowohl visuelle als auch rechnerische Methoden verwendet. Die jetzt bestätigten absoluten Konfigurationen der isolierten Stoffe können nun als Basis für eine mögliche weitere Entwicklung als immunsuppressive Leitstruktur dienen. Die Ergebnisse wurden im Journal of Natural Products veröffentlicht (Vol. 82, 2019).

Als nächstes haben wir die Wirkmechanismen des *A. argyi* Extrakts sowie die der isolierten Stoffe untersucht. Um die inhibierten Transkriptionsfaktoren zu identifizieren wurden Reporterzelllinien für AP-1, NFAT und NF-κB verwendet. Die Angriffsziele von sowohl Extrakts als auch der isolierten Sesquiterpenlaktone wurden dadurch in der Signaltransduktion oberhalb von NFAT und NF-κB lokalisiert. Der Einfluss des Extrakts sowie den Sesquiterpenlaktonen auf die Kalziumsignaltransduktion im NFAT Signalweg wurde im Detail untersucht. Dabei wurde sowohl der Einfluss auf den Kalziumeinstrom in die Zelle als auch aus dem ER ins Zytosol gemessen. In beidem haben weder die einzelnen isolierten Sesquiterpenlaktone noch eine Mischung aus Allen

eine annähernd starke inhibierende Wirkung auf den Kalziumfluss gezeigt wie der *A. argyi* Extrakt. Die Ergebnisse wurden in Frontiers of Pharmacology publiziert (Vol. 11, 2020).

Der zweite Extrakt, den wir untersuchten, war ein Methanolextrakt der Wurzeln von *T. asiatica*. Darin wurde das Alkaloid Nitidin mit einem IC_{50} Wert von 0.37 µM als hochaktiver Bestandteil identifiziert. Ein weniger aktives Alkaloid (IC_{50} 6.72 µM) wurde zusammen mit einer Reihe von inaktiven, zum Teil glykosylierten, Alkaloiden, Lignanen und Coumarinen isoliert. Eine Kombination aus ECD, OR, GCMS Analyse der hydrolysierten Zucker, enantioselektiver HPLC der hydrolysierten Aglykone und NMR in Gegenwart des Shift-Reagenzes $Eu(hbc)_3$ wurde zur Identifizierung der absoluten Konfigurationen der isolierten Stoffe verwendet. Zwei der isolierten Stoffe waren neu und ein Stoff wurde als erstes überzeugend beschrieben. Die Ergebnisse wurden im Journal of Natural Products veröffentlicht (Vol. 83, 2020).

Die Isolierung von mehreren Stoffen mit signifikanter T Zell Inhibition zeigt den Nutzen des CFSE Assays für die Identifizierung von neuen Leitstrukturen mit relevanter Aktivität. Für viele der isolierten Stoffe waren keine gut beschriebenen absoluten Konfigurationen publiziert. Daher haben wir ein breites Spektrum an Methoden verwendet, um diese Lücke zu füllen und die Ergebnisse für zukünftige Forschung zu publizieren. Die Kombination von ECD (als sensitiver Methode) mit komplementären Techniken wie VCD, Chromatografie der hydrolysierten Stoffe und der Verwendung von Shift-Reagenzien im NMR hat sich dabei als effektiv erwiesen. So wurden auch anspruchsvolle Fälle wie die *seco*-Tanapartholide A und B aus *A. argyi* und die glykosylierten Coumarine aus *T. asiatica* gelöst.

1. Aim of the Work

Autoimmune diseases are a rising burden in industrialized countries. Regardless of the cause for this increase, the development of therapeutics is focused almost exclusively on biologics like antibodies and fusion proteins. As these are limited in their application by their possible immunogenicity and dosage forms, there is an increasing need for new small molecule drugs to treat this diverse group of diseases. None of the small molecule immunosuppressant drugs of natural product origin on the market originate, so far, from plants. Due to diversity and complexity of secondary metabolites present in plants, this lack was identified as a potential lead to address the need for new small molecule therapeutics. Thus, the aim of this work is the identification of new immunosuppressant lead structures from plant extracts. For this, an assay measuring the proliferation inhibition of human primary T lymphocytes *in vitro* is used to identify plant extracts and compounds with immunosuppressant properties. This assay mimics physiological activation of T cells, which is relevant to many autoimmune diseases, where a constant activation of autoreactive T cells leads to their proliferation and subsequent attack on healthy tissues. As this assay is done in a medium throughput format, only a focused library of plant extracts can be screened with a reasonable effort. To prioritize extracts, the application of plants as traditional medicines, for example in traditional Chinese medicine (TCM), can be used. These culminate the experience of practical applications over thousands of years, which could increase the chance of finding pharmacologically active ones. Additionally, our library of extracts from plants used in TCM contains a broad spectrum of plant genera among the 435 extracts. This corresponds to the presence of a variety of scaffolds, which is an ideal prerequisite for finding new ones. Hit extracts are subjected to HPLC activity profiling, thereby guiding the isolation of possibly active compounds. Furthermore, the isolation of close derivatives can give hints at possible structure activity relationships. To this end, however, the absolute configurations need to be known. Thus, we aim to do an extensive characterization of the isolated compounds. This is done by the use of available technologies like microprobe NMR, ECD, VCD, OR, as well as advanced chemical and chromatographic methods. Once structures are sufficiently characterized, the biological data obtained from their testing can be used to reliably assess their prospect for further development. This enables the meaningful characterization of the mechanism of action for the isolated compounds and, for the extracts itself. In the end, the characterization of absolute configuration of natural products is valuable for this project in itself, but also for the use by future researchers.

2. Introduction

2.1. Autoimmune diseases

The definition of an autoimmune disease can be given as "a clinical syndrome caused by the activation of T cells or B cells, or both, in the absence of an ongoing infection or other discernible cause".[1] As the immune responses of T cells, B cells, and other immune cells are highly interconnected, their understanding is essential to bringing new treatment options into the clinic.

2.1.1. The immune response

The primary protection of the human body from foreign structures is the skin and other epithelial tissues. These form strict physical and chemical barriers around it and as soon as the surface of the skin is breached by a pathogen, it is recognized by cells of the **immune system** residing in the skin. The following reaction is usually divided in two branches, the "inherited" (or innate) and the "acquired" (or adaptive) immune system. In a more modern view, this corresponds to a static (or inherited) set of receptors recognizing general signs of a pathogen and a flexible (or adaptive) repertoire of receptors responding to any other unknown structure.[2]

The innate immune system

The innate immune system is the first response to any pathogen. It acts fast (minutes to hours) but unspecific, and uses, among other cell types, macrophages, dendritic cells, and natural killer (NK) cells. Its cells employ a range of pattern recognition receptors (PRRs) that recognize pathogen- and damage-associated molecular patterns (PAMPs and DAMPs). Bacterial lipopolysaccharides (LPS), for example, are recognized through Toll-like receptors (TLRs).[3] This prompts the expression of antimicrobial proteins and pro-inflammatory cytokines.[2] Cytokines are a class of proteins used for the signaling between cells. They form expression patterns that influence the reaction of immune cells by signaling either pro- or anti-inflammatory conditions. This influences, whether an immune response is started, or tolerance against an antigen is induced. The second important group of signal molecules are chemokines, which are chemoattractants to guide necessary immune cells to a site of inflammation.[4]

Practically, when PRRs are activated in a tissue, a local inflammation reaction starts. This is characterized by pro-inflammatory cytokine patterns activating immune cells close by. They, in turn, emit chemokines, which attract macrophages and other supporting immune cells to get rid of the source of inflammation. Inflammation is clinically characterized by swelling, redness and increased temperature of the effected tissue. In many cases, this response already leads to the clearance of the pathogen, which is phagocytized by macrophages. Parts from these phagocytized pathogens are then presented on the cell surface as antigens. The recognition of presented antigens and future memory of this antigen is part of the adaptive immune response.

The adaptive immune system

The **adaptive** immune system uses highly variable receptors on B and T cells to recognize unknown threats. Both, B and T cells, are derived from hematopoietic stem cells in the bone marrow. But, while B cells also mature in the bone marrow itself, T cells migrate into the thymus for maturation, hence the names. For this reason, both the bone marrow and the thymus are considered **primary lymphoid tissues (PLT)**.[5] The development of B and T cells each generates a diverse population of naïve cells with an individual receptor specificity of each individual cell. This repertoire of receptors differs between individuals.

B cells recognize antigens directly through their **B cell receptor (BCR)** expressed on the cell. This receptor can also be expressed by B cells in a soluble form as antibodies (also called immunoglobulins or IG).[6] After maturation, not yet activated B cells, also called naïve B cells, are found in secondary lymphoid tissues (SLT) including lymph nodes, the spleen, and gut-associated lymphoid tissues (Peyer's patches).[7]

T cells express a **T cell receptor (TCR)**, which only recognizes antigens presented by the Major Histocompatibility Complex (MHC) on Antigen Presenting Cells (APC).[8] Mature naïve T cells circulate between the blood and different SLTs, in which they sample as many antigens presented as possible. When the TCR on a T cell recognizes its antigen on a MHC molecule, the T cell can in principle become activated. This leads to the excretion of interleukin 2 (IL-2), which stimulates T cell proliferation. Mature T cells can be defined by clusters of differentiation (CD) on their surface. Whether a T cell is CD8-positive ($CD8^+$ T cell) or CD4 positive ($CD4^+$ T cell) determines the class of MHC molecule, by which it is activated.

The binding of **MHC class I** molecules to the TCR is mediated by CD8. Therefore, they are only recognized by **$CD8^+$ T cells**.[9] Induced by the presence of interferons (IFN α, β, and γ) during inflammation, MHC class I molecules can be expressed by any nucleated cell to present antigens from inside of the cell.[10] This identifies cells with, for example, intracellular viruses to $CD8^+$ T cells, which will then kill that cell to stop the infection. For this reason, $CD8^+$ T cells are also called cytotoxic or killer T cells.

MHC class II molecules present antigens only to **$CD4^+$ T cells**, as the binding is mediated by CD4.[11] MHC class II molecules are only expressed on the surface of immune cells, particularly B cells and dendritic cells.[10] For example, an antigen is taken up by dendritic cells at the site of inflammation and is transported to the closest SLT, such as a lymph node, where it is presented to circulating $CD4^+$ T cells. When a $CD4^+$ T cell is activated, it will further differentiate into the main subsets T_H1, T_H2 or T_H17, which tailor the cytokine response to the recognized pathogen (intracellular bacteria, helminth parasites, extracellular bacteria, fungi, etc.).[12, 13] Independent of the subset, $CD4^+$ T cells can either be follicular helper T cells (T_{FH}) or effector T cells (T_{eff}). Follicular helper T cells T_{FH} associate with B cells in lymph nodes to form germinal centers. There, B cells undergo class switching to produce antibodies with a higher affinity to the pathogen. As effector T cells T_{eff}, they coordinate the immune response through cytokine excretion. Additionally, in the contraction phase 1-2 weeks after infection, they can become memory T cells. Those can be reactivated, if the pathogen reoccurs, thereby shortening the reaction time of the immune system.[14] This is the basis of immunity to a pathogen.

T and B cell receptors

For B and T cell receptors to "anticipate" so far unknown structures, a huge arsenal of receptors is needed. This is achieved by variable regions in each receptor that form the antigen binding site.[15] For structural integrity and functional signal transduction, constant regions make up the rest of the receptor. Multiple copies of the DNA sequences encoding for the variable regions are present in the germline cells.[16] In the development of B or T cells, these copies get randomly combined into the gene used to express the T or B cell receptor in each cell. This process is called somatic or V(D)J recombination and generates a unique repertoire of receptors from up to 10^{15} theoretically possible variants. Practically, in mice, a variety of 2×10^6 T cells with different TCR specificities are found, sufficient to recognize most foreign antigens.[17] For T cells, this happens only after an initial proliferation of T cell progenitors in the thymus.

Among this diversity of receptor specificities, there are inevitably ones that recognize antigens of the body itself. In a healthy individual, these are eliminated. A concept of how this works was introduced by Sir Frank Macfarlane Burnet as clonal selection.[18] For predicting adaptive immunity, he was awarded the Nobel prize in 1960. Meanwhile, the concept has been refined, but is still valid in principle. T cells should only recognize foreign antigens presented to them on MHC molecules. [19] This is ensured by positive and negative clonal selection.

Positive clonal selection

Immature T cells in the thymus are **double positive for CD4 and CD8** and can, in principle, interact with both classes of MHC molecules. Both classes are expressed in the thymic cortex. Whether a cell interacts with MHC class I or class II molecules decides, however, which of the co-receptors will continue to be expressed.[19] This determines the later functionality of the respective cell as CD4$^+$ helper T cell or CD8$^+$ killer T cell and is called **positive selection**. 4 out of 5 immature T cells do not interact with either class of MHC molecules and are eliminated.[20]

Negative clonal selection

The second step in the thymus is **negative selection** of T cells that interact with autoantigens. To recognize those, self-peptides from other tissues are expressed in the thymus by the autoimmune regulator gene (AIRE).[21] If T cells react strongly to the resulting self-peptide:self MHC complexes on thymic cortical, medullary epithelial, or thymic dendritic cells, they are eliminated. In the end of the T cell maturation process, only 3-5% of initial T cell progenitors become functional T lymphocytes.[20]

Both, negative and positive selection are part of the central tolerance.[22] This protects self-tissues from the attack by mature T lymphocytes during their circulation between the blood and SLTs.

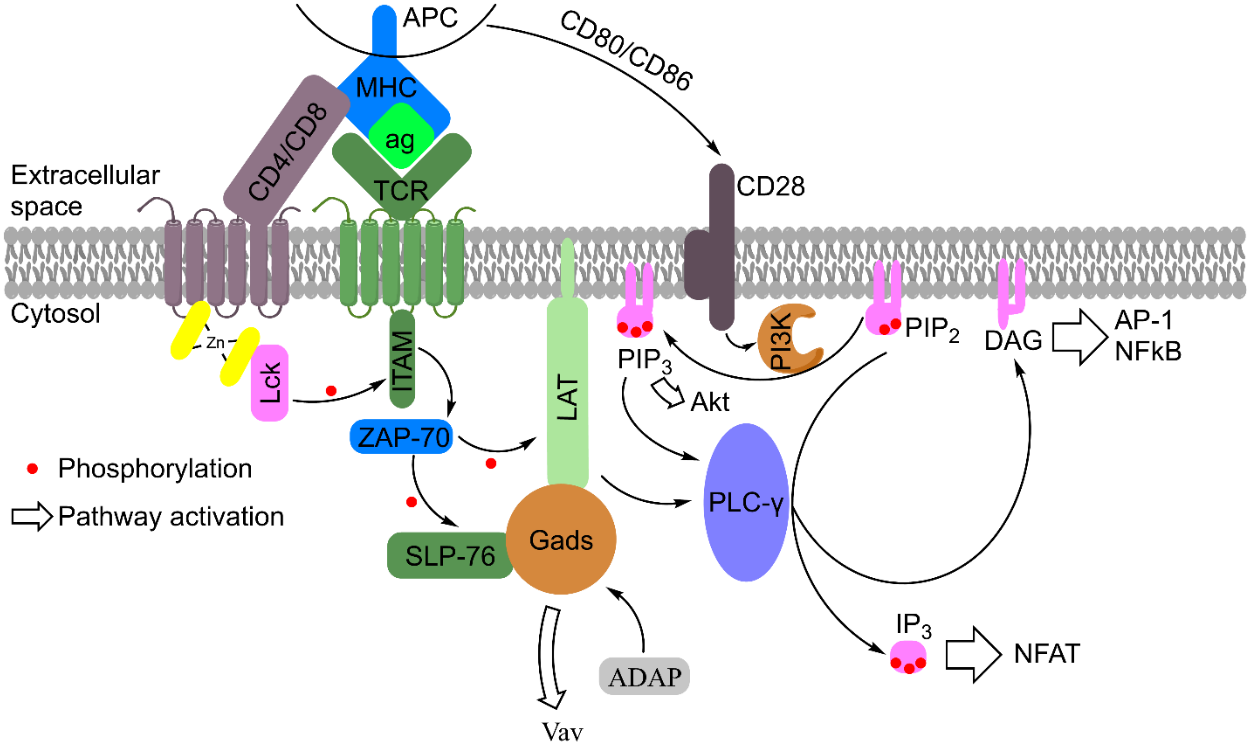

Figure 1. Graphic representation of interactions following TCR activation by the antigen (ag) presented by the antigen presenting cell (APC) on a MHC molecule. This ultimately leads to the activation of AP-1, NFκB, and NFAT.

2.1.2. Activation of T cells

Activated mature T cells can either neutralize recognized cells in case of CD8$^+$ killer T cells or initiate a full immune response in case of CD4$^+$ helper T cells. While they use different co-receptors, the signal cascade upon TCR activation is the same.

Signal transduction from the TCR

First, the TCR matches with its corresponding antigen:MHC complex (Figure 1).The binding of its co-receptor CD8 or CD4 to the respective MHC molecule on the APC activates Lck (lymphocyte specific protein tyrosine kinase). Lck then phosphorylates the cytosolic region on the TCR called the immunoreceptor tyrosine based activation motif (ITAM).[23, 24]. The phosphorylation of ARAM leads to the recruitment of the kinase ZAP-70, which phosphorylates LAT (linker for activation of T cells) and SLP-76 (SH2 domain containing leukocyte protein of 76kDa).[25] Together, both phosphorylated proteins form a complex with the adapter protein Gads.[26] This complex activates the phosphatidylinositol 3-kinase (PI 3-kinase) to catalyze the reaction of phosphatidylinositol 4,5-biphosphate (PIP_2) into phosphatidylinositol 3,4,5-triphosphate (PIP_3). On its own, the activation of the PI 3-kinase by the LAT:Gads:SLP-76 complex is only weak.[27] It is enhanced, however, by co-stimulatory activation of CD28 on the T cell by CD80 (B7.1) or CD86 (B7.2) presented on the APC.[28] PIP_3 is a second messenger with a hydrophobic tail anchored in the membrane, along which it can transduce a signal. In this context, it activates the Akt pathway, which leads to an increase in cellular metabolic activity necessary for proliferation.[29] Together with the LAT:Gads:SLP-76 complex, PIP_3 also activates PLC-γ (phospholipase C-γ) and Vav (a guainine nucleotide exchange factor).[30] ADAP is an adapter protein binding to the LAT:Gads:SLP-76 complex, leading to oligomerization of the complex.[31] Most likely, this is an additional mechanism to upregulate T cell activation. Together, these four proteins form the molecular basis of different aspects of T cell activation:

Akt activation leads to metabolic activation needed for extensive proliferation.

Vav activation leads to the rearrangement of the cytoskeleton.

PLC-γ activation leads to transcription factor activation.

ADAP recruitment modulates the response through oligomerization of the complex.

Additionally, other proteins and modulating mechanisms are involved as well in this pathway, many of which are actively investigated.[32, 26] This work, however, will focus on PLC-γ as key element in the downstream activation of IL-2 expression as a key cytokine stimulating T cell proliferation. PLC-γ catalyzes the reaction of PIP_2 into diacylglycerol (DAG), a membrane bound second messenger, and inositol 1,4,5-trisphosphate (IP_3), a soluble second messenger.[33] This is the first step in the pathways activating the transcription factors AP-1 (Activator protein-1), NFAT (Nuclear factor of activated T-cells), and NF-κB (nuclear factor κ-light-chain-enhancer of activated B cells). If all three are present, IL-2 expression is induced, which stimulates proliferation of activated T cells proliferation.

Activation of NF-κB

As shown in Figure 2, upstream of NF-κB, the D1 domain of PKC-θ (protein kinase C-θ) binds DAG and subsequently phosphorylates CARMA1 (caspase-recruitment domain membrane associated guanylate kinase).[34] CARMA1 is a scaffold protein, which forms the origin to oligomerize with BCL-10 and MALT1.[35] The resulting CBM complex recruits and activates TRAF-6 (tumor necrosis factor receptor-associated factor 6), which mediates ubiquitination of NEMO (NF-κB essential modulator).[36] Ubiquitination leads to the degradation of NEMO by the proteasome.[37, 38] As NEMO usually binds to and inactivates IKK (inhibitor of NF-κB kinase), IKK now can be activated by phosphorylation. This happens independently of the CBM complex by TAK1, which is ultimately also activated by PKC-θ. Phosphorylated IKK in turn phosphorylates the inhibitor of NF-κB (IκB) leading to its dissociation from NF-κB. NF-κB is then translocated into the nucleus where it activates the transcription of IL-2.

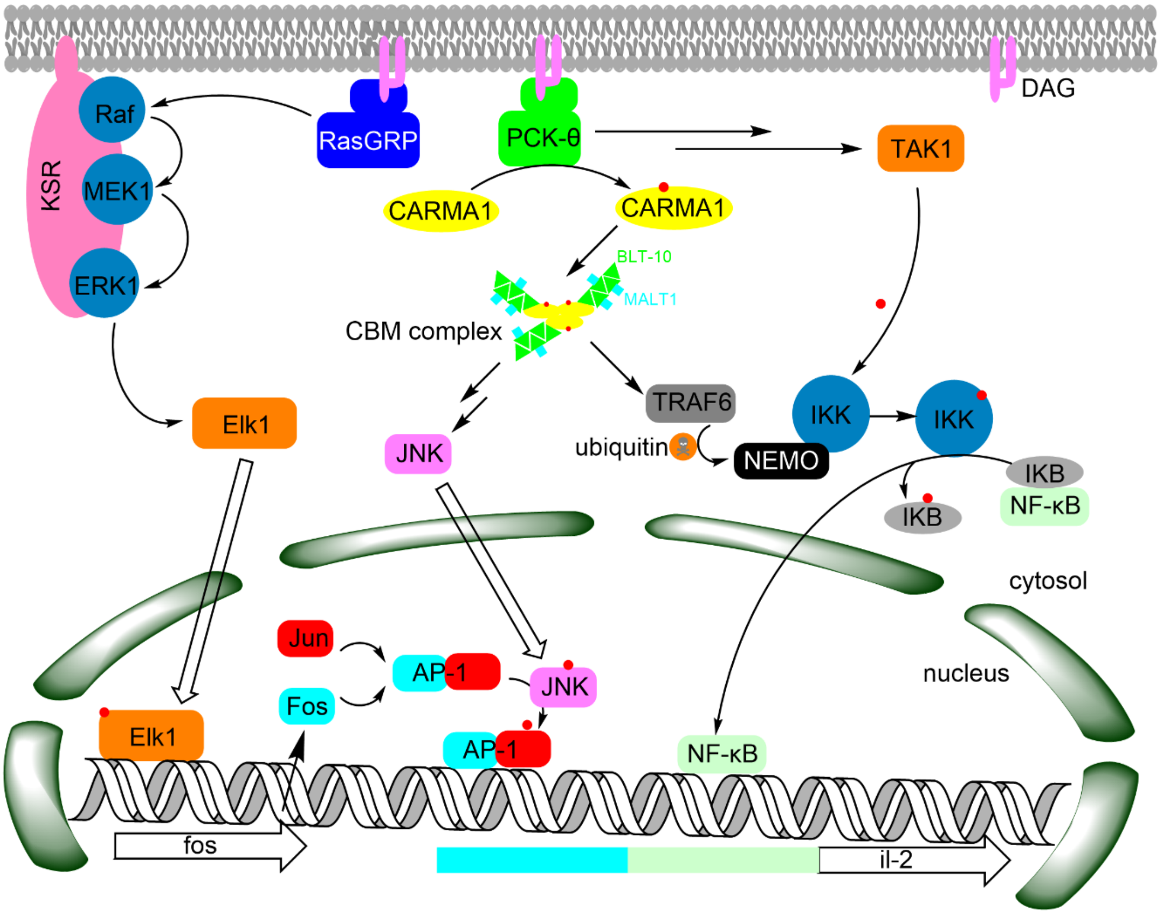

Figure 2. Induction of IL-2 transcription through AP-1 and NF-κB pathways by diacylglycerol (DAG).

Activation of AP-1

DAG in the plasma membrane binds the D1 domain of the soluble protein Ras-guanyl-releasing protein (RasGRP), thereby anchoring it in the plasma membrane (Figure 2).[39] This facilitates the exchange of guanosine diphosphate (GDP) for guanosine triphosphate (GTP) on the membrane bound kinase Ras. Ras then phosphorylates Raf, a mitogen activated protein kinase kinase kinase (MAPKKK).[40] Raf then phosphorylates MEK1 (MAPK/ERK kinase 1), a MAPKK, and MEK1 phosphorylates ERK (extracellular signal-regulated kinase), a MAPK. Similar cascades of MAP kinases are common for signal transduction and amplification in cellular pathways. All three MAP kinases are supported on the scaffold protein KSR (Kinase Suppressor of Ras) to enable a swift signal relay. Additionally, the scaffold protein is involved in the regulation of the cascade. In the end, ERK phosphorylates Elk-1 (E26 transformation-specific like protein 1), a transcription factor for the gene of Fos. When expressed, Fos forms the heterodimer AP-1 together with Jun. To activate AP-1 however, Jun needs to be phosphorylated. Through PCK-θ and CARMA1, which are also involved in NF-κB signaling, and a series of MAP kinases, the Jun kinase (JNK) is phosphorylated and translocated into the nucleus.[34] then, by phosphorylating Jun, JNK activates AP-1, which leads to the transcription of IL-2.

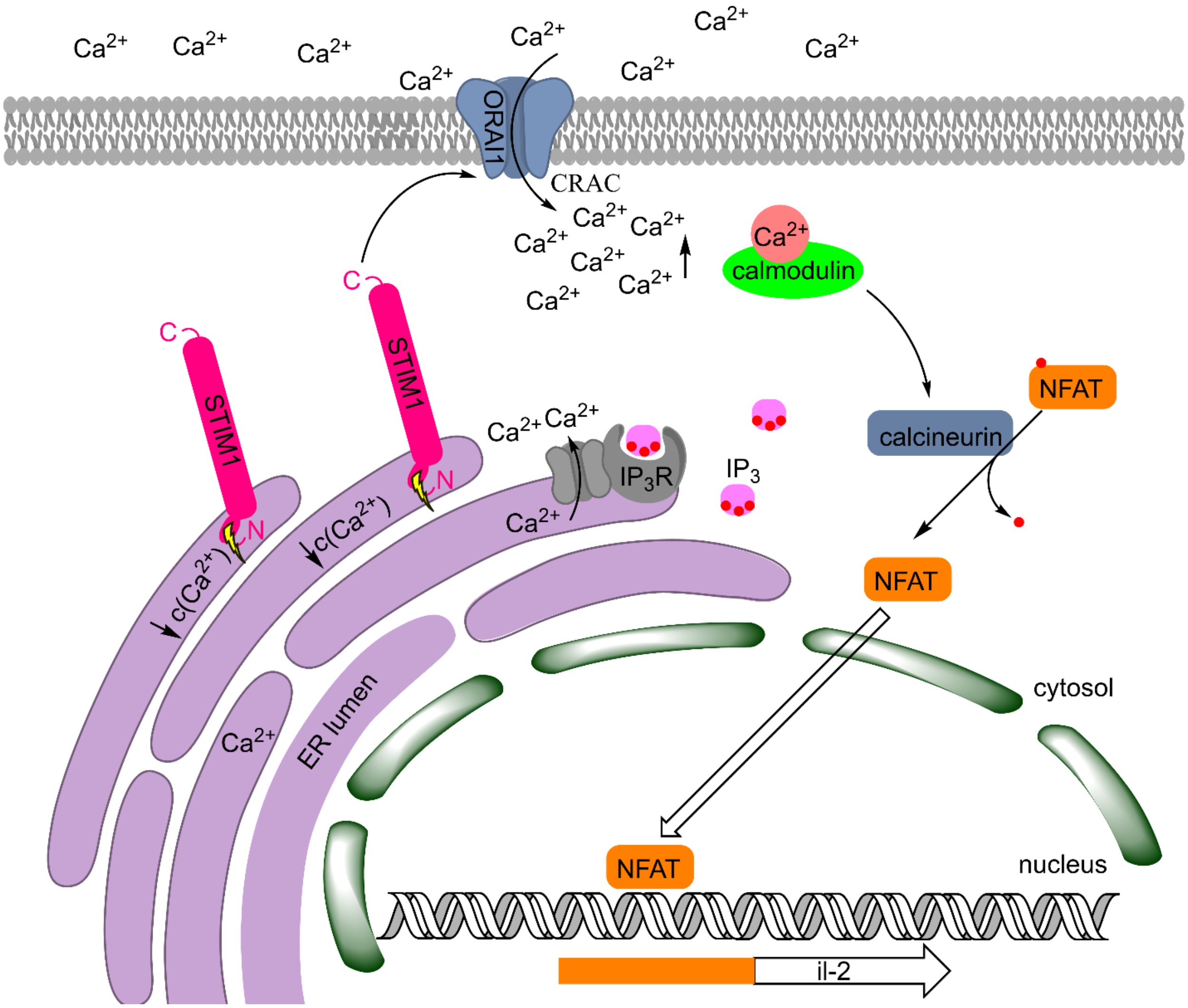

Figure 3. Induction of IL-2 transcription through the NFAT pathway by inositol 1,4,5-trisphosphate (IP_3).

Activation of NFAT

As shown in Figure 3, IP_3 activates the IP_3 receptor (IP_3R) located in the membrane of the endoplasmic reticulum (ER). This leads to the release of Ca^{2+} stored in the ER into the cytosol. This depletion of the endoplasmic Ca^{2+} storage prompts the opening of store operated Ca^{2+} channels in the plasma membrane.[41] These channels termed CRAC (calcium release-activated channels) consist of ORAI1 pore subunits and are activated by STIM1 transmembrane proteins located in the ER membrane. A decrease in Ca^{2+} concentration in the ER is sensed at the N-terminus of STIM1 molecules in the ER lumen. This leads to the oligomerization of STIM1 molecules at contact sites between the ER and the plasma membrane. There, the C-termini of STIM1 open the CRAC channels followed by an influx of Ca^{2+} into the cell. This prompts the cytoplasmic calcium sensing protein calmodulin to activate, among other proteins, calcineurin. The activated phosphatase calcineurin subsequently cleaves phosphates from NFAT located in the cytosol. Upon dephosphorylation, NFAT migrates into the nucleus to activate the expression of cytokines like IL-2 stimulating proliferation of T lymphocytes.

All three transcription factors, NF-κB, AP-1, and NFAT, are needed for the expression of IL-2. Thus, if one pathway is inhibited, it prevents the IL-2 mediated proliferation of activated T cells.

2.1.3. T cell regulation

By coordinating the immune response and neutralizing effected cells, T cells are a central element of the immune system. Thus, their regulation, and the regulation of this regulation, is essential to a functioning immune system, which will be outlined in the following.

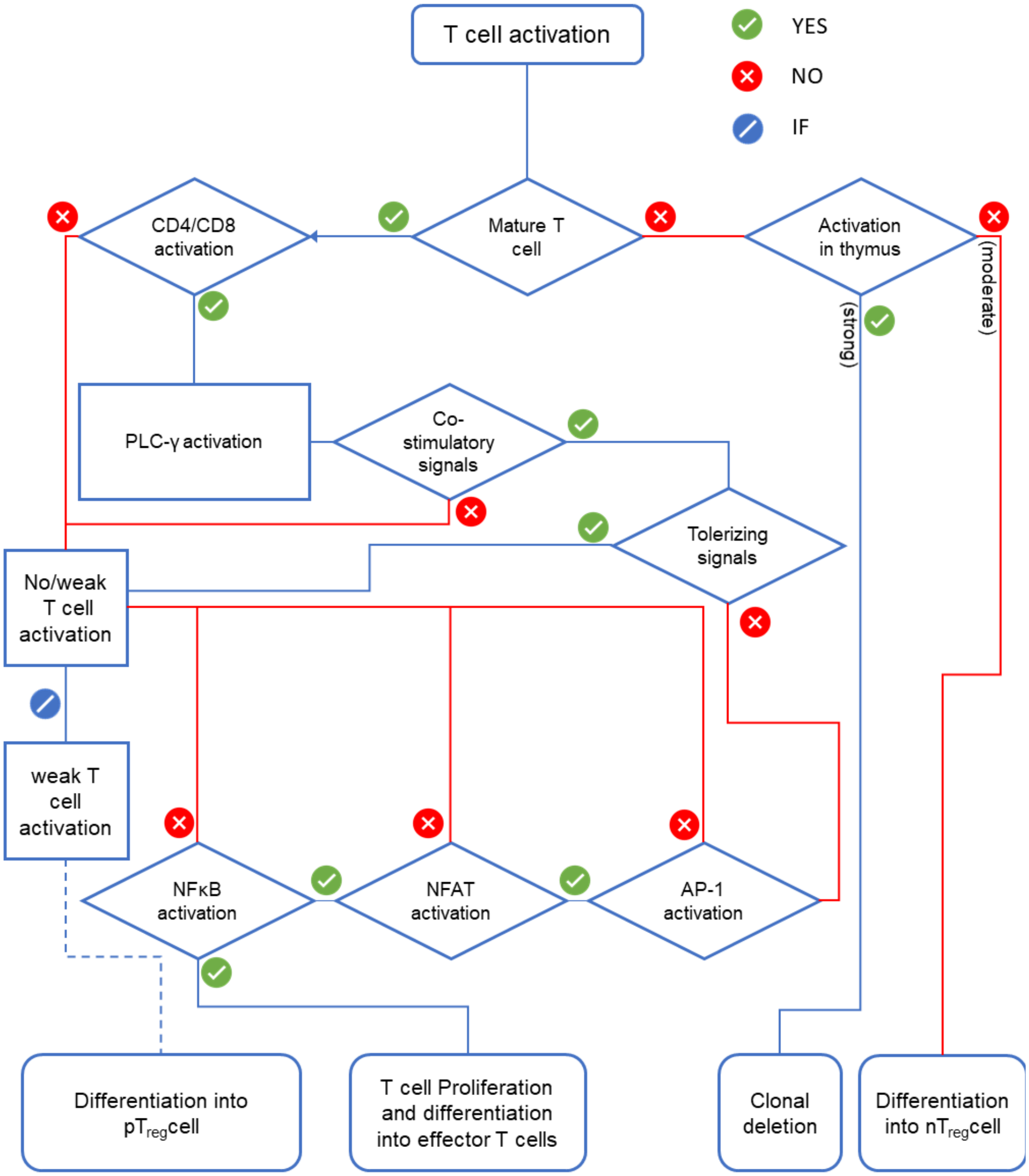

Figure 4. Schematic description of some factors determining the fate of a given T cell after activation. leading either towards T cell proliferation and subsequent differentiation into effector cells or towards the development of T_{reg} cells.

Regulation by APCs

In case of apoptotic cells, fragments are generated and taken up by macrophages.[42] As APCs, macrophages also present antigens on their surface Yet in this case, a recognition of the cell fragments could lead to autoimmunity. To prevent this, anti-inflammatory cytokines like transforming growth factor-β (TGF-β) and IL-10 are excreted by T_{reg} cells. Additionally, secretion of pro-inflammatory cytokines, like TNF-α, IL-1 or IL-12 is suppressed. If the function of macrophages to clear cell debris is impaired, it can lead to secondary necrosis of apoptotic cells. As it is accompanied by the release of TNFα, secondary necrosis can trigger an immune reaction. This malfunction is discussed as a possible origin of the autoimmune disease systemic lupus erythematosus (SLE), where autoantibodies against DNA and nucleus fragments are found.

Development of T_{reg} cells

While most T cells activated by self-peptide:self MHC complexes in the thymus undergo clonal selection, some $CD4^+$ T cells differentiate into $CD25^+$, $Foxp3^+$ **natural regulatory T cells (nT_{reg} cells)** with the purpose to suppress activation of other autoreactive T cells.[43] Similar to regular T cell activation, signals from the TCR, CD28, and IL-2 are necessary to induce nT_{reg} differentiation. The survival of autoreactive T cells as nT_{reg} cells in the thymus, however, seems to be dependent on the presence of TGF-β. In general, a strong activation (high affinity or long binding half-life $t_{1/2}$) of the TCR, a high ligand density, or a long duration of TCR signaling favor clonal selection over T_{reg} formation. Moderate activation, however, favors T_{reg} differentiation. Another factor is the age of the person. Most T_{reg} cells are produced in the thymus early in life and production declines over time. Later in life, regulatory T cells in the thymus are almost exclusively used as a reservoir to maintain the balance between regulatory and conventional T cells in circulation.[44] Together with positive and negative selection, this contributes to central tolerance.[22]

However, some autoreactive T cells evade central tolerance. As no pathogen is present during activation, the pro-inflammatory cytokine pattern from the innate immune system is missing. This can facilitate the differentiation into **peripheral regulatory T cells (pT_{reg} cells)**.[45] Thus, pT_{reg} cells can induce self-tolerance also to self-antigens not found in the thymus, thereby contributing to peripheral tolerance.[22] Analogous to the development of nT_{reg} cells from the thymus, the presence of TGF-β favors the differentiation into pT_{reg} cells. Recent research also points at the relevance of dendritic cells for this process.[46]

Different paths leading to either clonal selection, T cell activation or differentiation into T_{reg} cells are summarized in Figure 4.

Mechanisms of T_{reg} cell function

IL-2 is the main cytokine to promote proliferation in activated T cells.[47] While naïve T cells are not susceptible to IL-2, T_{reg} cells are. Thus, T_{reg} cells are constantly proliferating on some level to create a balance between conventional and regulatory T cells. Consequently, when a conventional T cell becomes activated and produces IL-2, the proliferation of T_{reg} cells increases as well. This increases the chance of a fitting T_{reg} cell to recognize an autoreactive T cell thereby preventing an autoreactive response. Four basic mechanisms, by which T_{reg} cells inhibit the immune response to autoantigen, are discussed: **Inhibitory cytokines**, **cytolysis**, **metabolic disruption**, and **modulation of dendritic cells**.[48]

IL-10 and TGF-β are the most prominent **inhibitory cytokines** produced by T_{reg} cells. While IL-10 seems to suppress local inflammation,[49] TGF-β increases the induction of pT_{reg} cells, a mechanism also exploited by tumors.[50]

The second mechanism, **cytolysis**, uses the perforin/granzyme pathway, which induces apoptosis in target cells.[51] This process is similar to the cytotoxic effects of $CD8^+$ T cells and Natural Killer (NK) cells. It is most likely used to kill APCs that present self-antigens, which can again be prevented by cells expressing inhibitors of granzyme B on their surface.[48] Also, other apoptosis inducing pathways like TRAIL-DR5 (tumor-necrosis-factor-related apoptosis-inducing ligand-death receptor 5) are investigated as mechanisms in regulatory T cells.

Metabolic disruption of effector T cells by regulatory T cells is another possible way of inhibition. One example is the capture of IL-2 by CD25. As IL-2 is needed for effector T cells to proliferate, the binding to CD25 on regulatory T cells can lead to a decrease of effector T cell proliferation.[48] This seems to be a mechanism specifically limiting activation of $CD8^+$ T cells.[52]

The fourth mechanism discussed is the **modulation of dendritic cells** as the most important APCs. There, T_{reg} cells have been shown to influence dendritic cells towards the production of immunosuppressive metabolites and the downregulation of co-stimulatory molecules. [53, 54]

The importance of each of these mechanisms *in vivo* is still unclear and so is their interplay.[48] As all of them rely on either cell-cell contact or local cytokine concentrations, a common prerequisite seems to be the spatial proximity to either effector T cells or dendritic cells.

2.1.4. Autoimmune diseases

Most autoimmune diseases can be explained with the failure of one or more regulatory mechanisms like in the case of SLE.[55] The variety of possible antigens from different organs, tissues, and cells in the human body generates a broad spectrum of clinical conditions considered as autoimmune diseases. Experimental evidence for autoimmunity can be obtained by transferring the reacting immune species into a healthy individual, where it will cause the same effects.[56] However, due to practical and ethical limitations of these experiments, the attribution is not always clear. In a review from 2012, Hayter and Cook counted 81 disorders with good evidence for autoimmunity.[57] Additionally, a range of autoimmune diseases with less clear evidence exists.[58] From data, mostly collected in the United States of America, the overall prevalence of autoimmune diseases is estimated at 4.5% with a higher prevalence in women (6.4%) than men (2.7%). Although the mechanisms leading to autoimmune diseases are not yet fully understood, the presence of autoreactive T cells are a common denominator of many autoimmune conditions. Examples are celiac disease[59], psoriasis[60], diabetes mellitus type I, rheumatoid arthritis[61] and multiple sclerosis[62]. Thus, the knowledge about signal transduction in T cells is used to find new treatment options for autoimmune diseases.

Origin

Much is known by now about cell types and compartments involved in the immune response. Some is known about the interactions between these actors. But least is known about the mechanisms leading the immune system to fail and cause an autoimmune disease. No solely responsible factor leading to autoimmune diseases was found. Thus, it can only be described as a complex interplay between environmental and genetic factors that increase or decrease the chance of an autoimmune reaction. With psoriasis alone, 1338 genes were found to be associated with the disease and, more recently, 101 gene loci that increase the risk for rheumatoid arthritis.[63, 64] However, some mutations can significantly increase the risk of autoimmunity. One example is the FOXP3 gene encoding a protein important to the function of T_{reg} cells.[65] Mutations in this gene often lead to Immune dysregulation, polyendocrinopathy, enteropathy, or immunodysregulation polyendocrinopathy enteropathy X-linked (IPEX) syndrome, a severe autoimmune disease effecting multiple organs and tissues.

Autoimmunity and transplantation

A special case in terms of immune diseases are transplantations of kidneys, lungs, blood, bone marrow or other organs.[66] There, instead of the immune system recognizing a self-antigen as foreign, a foreign organ or tissue introduced into the body is recognized. Two main concerns are associated with this. Firstly, the foreign organ elicits an immune response from the recipient, which, without immunosuppression, would lead to graft rejection. Secondly, especially in case of bone marrow transplants, the donor's immune system remaining in the transplant can attack the recipient. This is known as graft versus host disease (GvHD). Both, GvHD and graft rejection, need to be treated, similar to autoimmune diseases, with the use of immunosuppressant drugs.

Autoimmunity vs. Tumor Tolerance

Under normal circumstances, the immune system maintains a balance between immunity and tolerance.[65] While it defends the body against pathogens, it promotes tolerance to itself by preventing natural occurrences of autoreactive T cells or autoantibodies from becoming autoimmune diseases. Also, it avoids the tolerance of pathogens or abnormal cells that could otherwise develop into cancer. Thus, regulatory failures in the immune system can tip that scale in both directions. On one hand, the absence or lacking functionality of T_{reg} cells, for example by impairment of FOXP3, can lead to autoimmune disease. On the other hand, T_{reg} cells can promote tolerance against some tumors. [67] A therapeutic goal can thus be the depletion of the tumor of T_{reg} cells to break this tolerance. But, this could also lower the tolerance for self-antigens, which might then lead to the emergence of autoreactive T cells. To avoid these problems in practice, a strategy can be to only target specific subsets of T_{reg} cells and simultaneously support the immune reaction against the tumor itself. Thereby, the effect on the whole organism could be limited.

Therapy of autoimmune diseases

Generally, the treatment of autoimmune diseases focusses on the prevention of excessive immune responses to relieve symptoms and progression of the respective disease. A range of therapeutics has been developed over the last seven decades approaching different targets. For an overview about the drugs in question, the Anatomical Therapeutic Chemical (ATC) classification system of the World Health Organization Collaborating Centre for Drug Statistics Methodology (WHOCC) was used.[68] Information about classification, market introduction and mechanisms of action were obtained from the DrugBank 5.0 database (https://www.drugbank.ca).[69] This analysis focusses on immunosuppressant drugs (ATC classification L04) and only takes glucocorticoids, a class of corticosteroids (ATC classification S01BA), into account as a second option in the treatment of autoimmune diseases. Primarily anti-inflammatory drugs such as non-steroidal anti-inflammatory drugs (NSAIDs) were not considered. Thus, this analysis is not a manual to treat autoimmune diseases, but an overview of available immunosuppressant therapies.

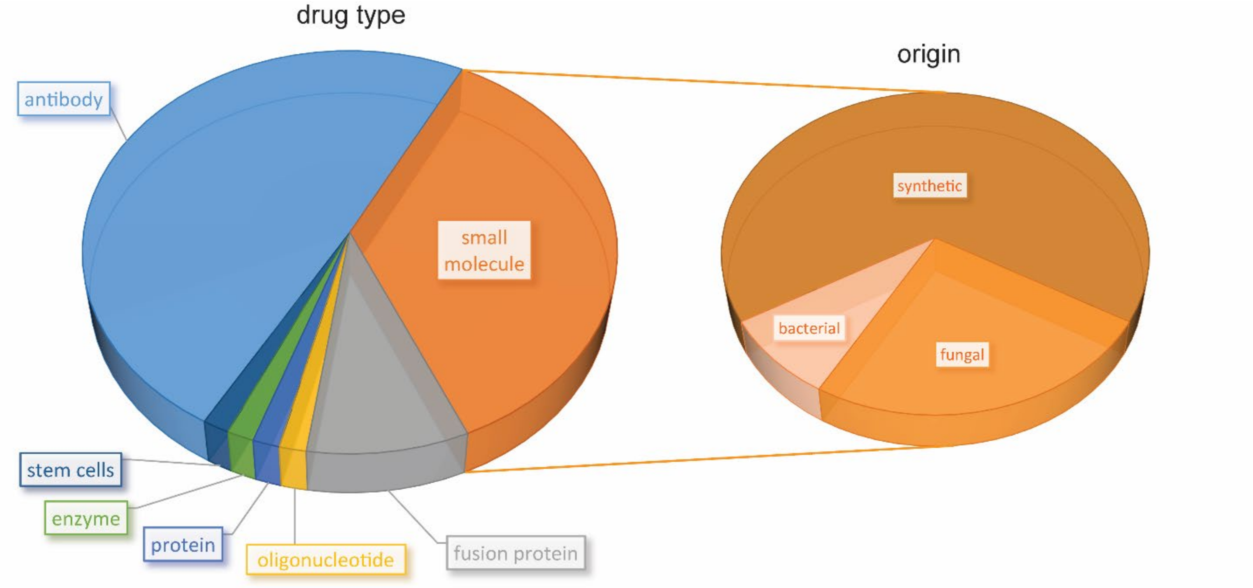

Figure 5. Distribution of drug types among immunosuppressant drugs contained in the ATC classification L04 (left) and distribution of structural origins among small molecule immunosuppressants (right).

Figure 5 shows the distribution of drug types among all immunosuppressant drugs classified in ATC L04. Almost half of the drugs in this category are, mostly monoclonal, antibodies with different target proteins in the immune system. The second largest group are small molecules acting through diverse mechanisms. The third largest group are fusion proteins targeting interleukins of co-stimulatory signals in the activation of T cells. Additionally, some more unusual treatments such as oligonucleotides, enzymes, or fat derived stem cells are used. Glucocorticoids are not classified as "immunosuppressants" in the ATC classification system and thus are not included in Figure 5. They are, however, important in the management of autoimmune diseases.

Glucocorticoids

Glucocorticoids are used for many indications, but are can be valuable in the management of inflammatory and autoimmune diseases. Several different glucocorticoids are available with different pharmacological profiles. There, dexamethasone, a drug now also considered in the treatment of acute COVID-19, is an example for a drug with a longer biological half-life, while cortisol is an example for a glucocorticoid with a shorter half-life.[70] Several mechanisms contribute to the action of glucocorticoids.[71] On a genomic basis, glucocorticoids bind to the glucocorticoid receptor. This leads to the suppression of inflammatory cytokines and the induction of anti-inflammatory cytokines. These effects, as they impact the expression of cytokines and require diffusion into the cell to reach the cytoplasmic glucocorticoid receptors, need some time to develop after administration. Short term effects are mediated primarily by membrane associated glucocorticoid receptors, for example on T cells. This needs higher doses, but leads to a broad impairment of signaling and thus, a rapid quenching of inflammation.

Because of these effects, glucocorticoids could be seen as the magic bullet against inflammatory diseases. However, they also effects glucose levels, adrenal hormones, and the musculoskeletal system. This leads to severe side effects, which primarily depend on the dose and the longitude of the treatment. In conclusion, although it is an important therapy, the necessity for high doses of glucocorticoids in the treatment of autoimmune diseases makes them less suited for long term disease management.

Antibody based therapies

The first immunosuppressant antibody therapeutics were approved in 1981 using equine anti-lymphocyte immunoglobulins. After inoculation of horses with human T lymphocytes, the equine immune system produces immunoglobulins against human T lymphocytes. Those are isolated and administered in humans to prevent lymphocytes from rejecting a transplant, for example hematopoietic stem cells.[72] Antibodies obtained in this way are polyclonal antibodies as they are produced by a group of different equine B cells reacting to T lymphocytes. Monoclonal antibodies are obtained from only one B cell clone with a defined receptor specificity, which is selected and fused to a myeloma cell in the lab to obtain hybridoma cells.[73] This can be used to target specific epitopes. Antibodies are macromolecules. This requires them to be administered either intravenously or subcutaneously to enable the uptake and avoid their degradation in the gastrointestinal tract. As antibodies itself are also foreign structures, they themselves can induce an immune reaction.[74] When antibodies against the drug are formed, this can result in a loss of activity and requires alternative treatments. Nowadays, to lower the risk of immunogenicity, humanized antibodies can be engineered, which contain constant regions from humans. A range of more or less humanized monoclonal antibodies is currently used as immunosuppressant drugs. One target for antibodies is C5, a component of the complement pathway in the innate immune system. Other antibodies are designed to inhibit the function of pro-inflammatory cytokines. For this, they target interleukins (e.g. IL-1, IL-6, or IL-23), their receptors (e.g. for IL-2 or IL-6), or TNF-α. Also, cell type specific clusters of differentiation, for example CD20 on B cells, can be used to limit the effect of the treatment on this cell type. Overall, the specificity of monoclonal antibodies is of great value in the treatment of autoimmune diseases, but their administration is limited by the necessity for injecting them and their possible immunogenicity.

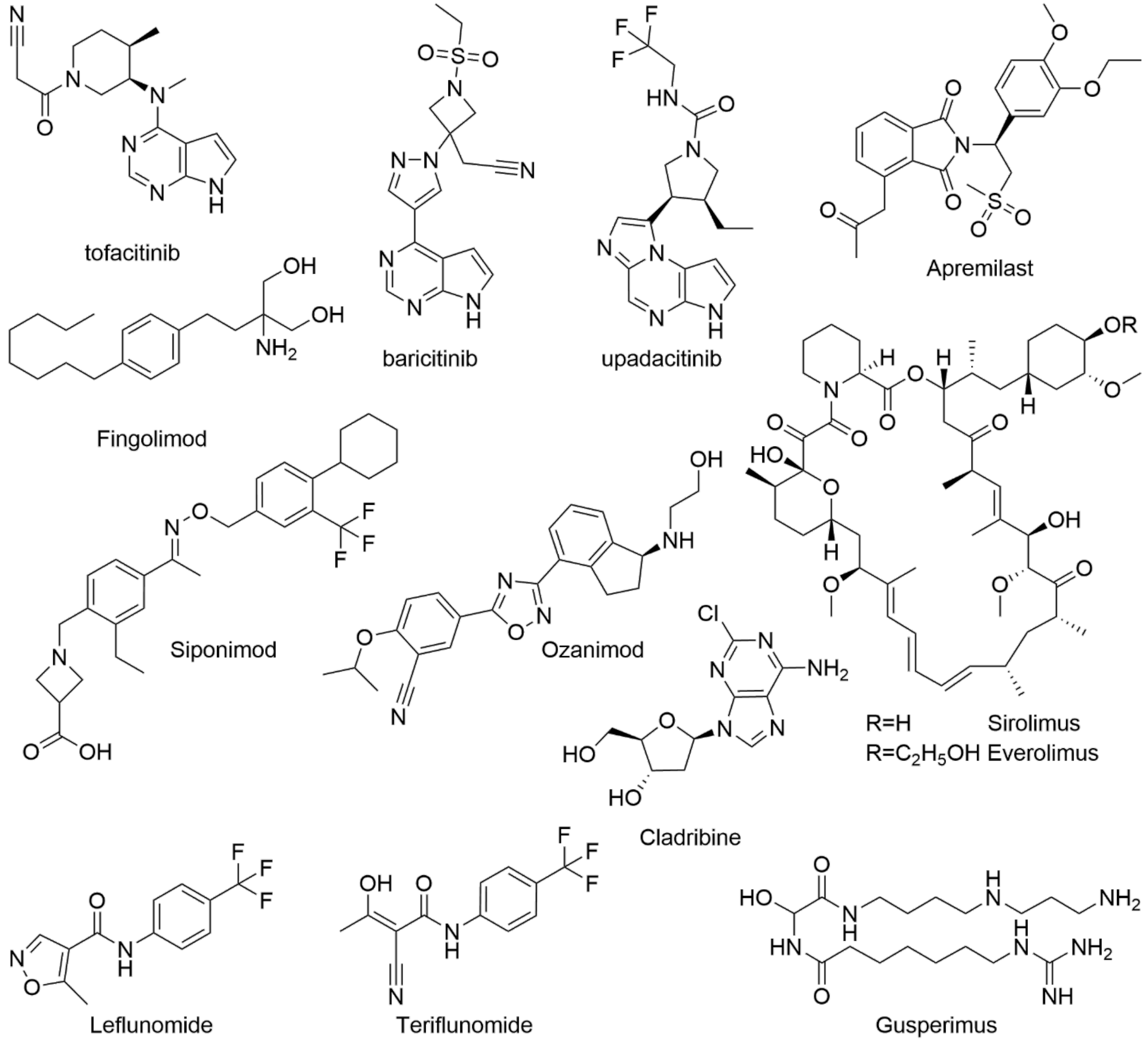

Figure 6. Small molecule drugs listed in the Anatomical Therapeutic Chemical (ATC) Classification System as selective immunosuppressants (L04AA).

Cell based therapies

A field of active investigation is the use of induced T_{reg} cells (iT_{reg} cells), which are primed *in vitro* for the antigen(s) in question. This yields either monoclonal iT_{reg} cells against one specific antigen or polyclonal iT_{reg} cells against different antigens present on target cells. Administered to the patient, they are intended to restore tolerance against the respective antigen and could therefore stop the autoimmune response. The first clinical trials on this new form of therapy have been conducted for GvHD and Type I diabetes. Since then, two treatments have been approved ("Kyriah" from Novartis and "Yescarta" from Kite, now Gilead) for different forms of leukemia in 2017.[75] Both treatments are based on the expression of a chimeric antigen receptor (CAR) in T cells previously collected from the patient. The CAR-T cells recognize CD19 expressed on leukemic cells and leads to their destruction. However, as this process is individual to each patient, it is very laborious and expensive. This warrants significant developments in the field to find a broader application.

Small molecule drugs

Several small molecule drugs are currently used for the treatment of autoimmune diseases like rheumatoid arthritis, psoriasis, and multiple sclerosis. In the ATC classification system, three groups of compounds contain small molecule drugs. Small molecule drugs considered selective immunosuppressants are shown in Figure 6, calcineurin inhibitors in Figure 7, and other immunosuppressants in Figure 8.

While compounds like cyclosporine prevent T cell proliferation by inhibiting calcineurin in the NFAT pathway, selective immunosuppressants have different mechanisms of action. Drugs like leflunomide or mycophenolic acid inhibit the synthesis of nucleotides needed for DNA polymerization and thereby inhibit the proliferation of fast-growing cells like activated T cells. Tofacitinib and its more recent analogues baricitinib and upacitinib are inhibitors of Janus kinases (JAK) thereby blocking the reaction to pro-inflammatory cytokines. Sirolimus (also known as rapamycin) and its derivative everolimus are inhibitors of the complement system through the mammalian target for rapamycin (mTOR), which in turn inhibits T cells activation and proliferation. Fingolimod is an example for a modulator of the sphingosine-1-phosphate receptor. Sphingosine-1-phosphate is a phospholipid and second messenger inducing the emigration of T cells from lymphoid tissues.[76] In this manner, fingolimod prevents autoreactive T lymphocytes from reaching their target tissues, a mechanism beneficial in the treatment of multiple sclerosis. Apremilast is an inhibitor of the phosphodiesterase 4 (PDE4), which prevents the formation of cyclic adenosine monophosphate (cAMP), a ubiquitous second messenger involved in the immune response.[77]

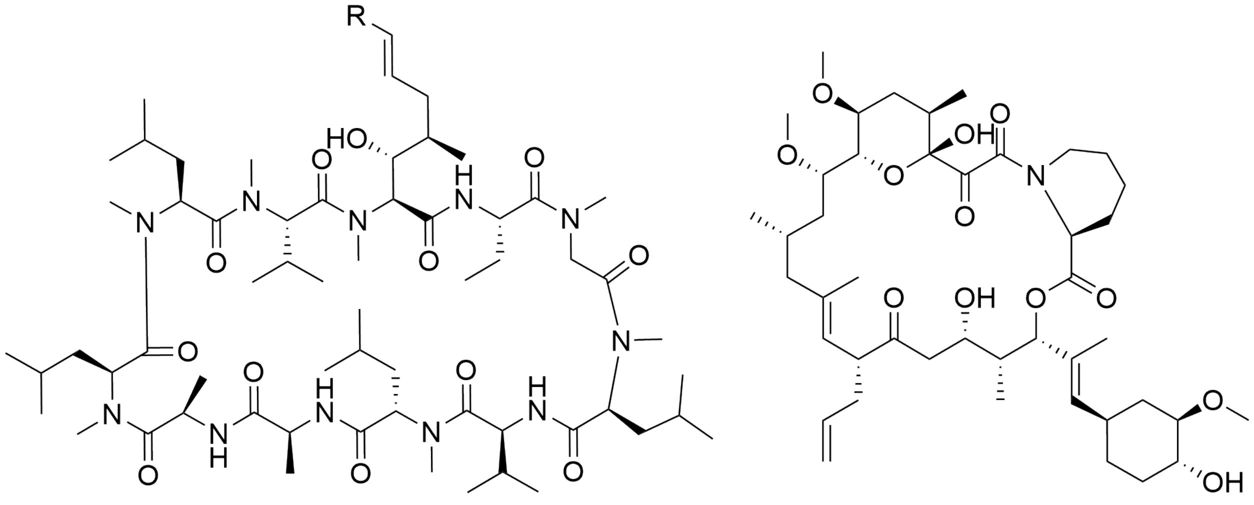

R=CH3 Ciclosporin

R=$CHCH_2$ Voclosporin

tacrolimus

Figure 7. Small molecule drugs listed in the Anatomical Therapeutic Chemical (ATC) Classification System as calcineurin inhibitors (L04AD).

While some of the “other immunosuppressants” like methotrexate or azathioprine also target nucleotide synthesis of fast proliferating cells, the mechanisms of immunomodulation by thalidomide or dimethyl fumarate are not clear.

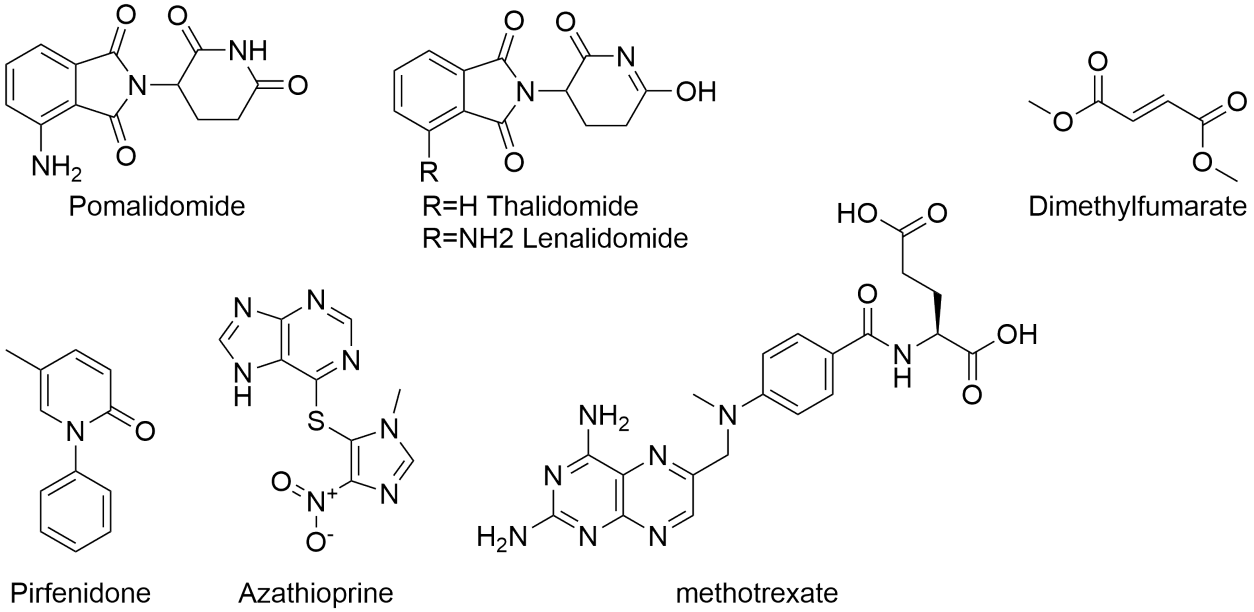

Figure 8. Small molecule drugs listed listed in the Anatomical Therapeutic Chemical (ATC) Classification System as other immunosuppressants (L04AX).

Natural products as new immunosuppressive drugs

A breakdown of structural origins of small molecule immunosuppressant drugs shows two thirds of the structures to be of synthetic origin, counting compounds like cladribine, which are inspired by primary metabolites like nucleotides. Although new methods for the discovery of new chemical entities have been introduced over the last decades, natural products are still the most important source of new chemical entities in the development of new drugs.[78] Plants contain a vast diversity of chemical entities over all plant families. Considering that all immunosuppressant drugs with a natural product background are of either fungal or bacterial origin, plant derived natural products are, so far, underexplored in this area. To identify possible new lead structures from plants, a library of plant extracts obtained by sequential extraction with solvents of low, intermediate, and high polarity can be used.[79] In an academic setting, this is a good tradeoff between the use of crude extracts, where compounds like tannins can interfere with the respective assay, and pure natural products, which require extensive isolation effort.[80] Additionally, as they have been used with some evidence over a long period of time, focused libraries of traditionally used plants, for example in Traditional Chinese Medicine (TCM), could increase the probability of finding active extracts.[81] Generally, the advances in modern technologies like HPLC-(HR)MS, preparative HPLC, centrifugal partition chromatography (CPC), or NMR have significantly reduced the time needed for dereplication, isolation, and identification of compounds.

Finding new immunosuppressant natural products

To, however, find new immunosuppressant lead compounds an appropriate assay is crucial. It should be compatible with the use of extracts, thus preferring a cell based assay over one using isolated proteins. Also, it should enable a medium or high throughput of extracts and, in the next step, micro fractions obtained from HPLC. And, it should model immune suppression *in vivo* as closely as possible. All these criteria are met by an assay monitoring the proliferation inhibition of primary T cells utilizing carboxyfluorescein diacetate succinimidyl ester (CFSE).[82] For this assay, T cells are isolated from human blood samples and incubated with the dye. After washing of the excess dye, T cells are activated with anti-human CD3 and anti-human CD28 antibodies, thus imitating the activation of the TCR in the presence of co-stimulatory signals. This is either performed in the presence of only medium, cyclosporine A as positive control, camptothecin as control for apoptosis induction, or a test substance. The negative control is not stimulated. After 72 h, the cells are analyzed by a fluorescence activated cell sorter (FACS). With each cell division, the fluorescence in the cells divided between two cells. This allows the identification of proliferating cells, non-proliferating cells and dead cells, which lost their fluorescence. In this manner, extracts inhibiting the proliferation of human T cells can be identified and their activity can be distinguished from cytotoxic or apoptosis inducing extracts. The assay is also applicable to the use for HPLC activity profiling. The chromatographic data (retention times, UV spectra, mass spectra) can be used to tentatively identify compounds in the extract. This is then used to dereplicate known substances and to prioritize the isolation of possibly active constituents of the extract.

References

1. Davidson, A. and B. Diamond. Autoimmune Diseases. **New England Journal of Medicine 2001**; 345: 340-350

2. Medzhitov, R. Recognition of microorganisms and activation of the immune response. **Nature 2007**; 449: 819-826

3. Takeda, K. and S. Akira. Toll-Like Receptors. **Curr. Protoc. Immunol. 2015**; 109:

4. Fernandez, E. J. and E. Lolis. Structure, Function, and Inhibition of Chemokines. **Annu. Rev. Pharmacol. Toxicol. 2002**; 42: 469-499

5. Murphy, K. and C. Weaver. Chapter 1: Basic Concepts in Immunology. In: K. Murphy and C. Weaver eds, Janeway's immunobiology Garland Science; **2016**

6. Edelman, G. M. Antibody Structure and Molecular Immunology. **Science 1973**; 180: 830-840

7. Picker, L. J. and E. C. Butcher. Physiological and Molecular Mechanisms of Lymphocyte Homing. **Annu. Rev. Immunol. 1992**; 10: 561-591

8. Garcia, K. C. and E. J. Adams. How the T Cell Receptor Sees Antigen—A Structural View. **Cell 2005**; 122: 333-336

9. Bouvier, M. Accessory proteins and the assembly of human class I MHC molecules: a molecular and structural perspective. **Mol. Immunol. 2003**; 39: 697-706

10. Steimle, V., C. Siegrist, A. Mottet, B. Lisowska-Grospierre and B. Mach. Regulation of MHC class II expression by interferon-gamma mediated by the transactivator gene CIITA. **Science 1994**; 265: 106-109

11. Mellman, I. and R. M. Steinman. Dendritic Cells. **Cell 2001**; 106: 255-258

12. Kang, J. and N. Malhotra. Transcription Factor Networks Directing the Development, Function, and Evolution of Innate Lymphoid Effectors. **Annu. Rev. Immunol. 2015**; 33: 505-538

13. Ruterbusch, M., K. B. Pruner, L. Shehata and M. Pepper. In Vivo CD4+ T Cell Differentiation and Function: Revisiting the Th1/Th2 Paradigm. **Annu. Rev. Immunol. 2020**; 38: 705-725

14. Omilusik, K. D. and A. W. Goldrath. The origins of memory T cells. **Nature 2017**; 552: 337-339

15. Schatz, D. G., M. A. Oettinger and M. S. Schlissel. V(D)J Recombination: Molecular Biology and Regulation. **Annu. Rev. Immunol. 1992**; 10: 359-383

16. Tonegawa, S., A. M. Maxam, R. Tizard, O. Bernard and W. Gilbert. Sequence of a mouse germ-line gene for a variable region of an immunoglobulin light chain. **PNAS 1978**; 75: 1485-1489

17. Casrouge, A., E. Beaudoing, S. Dalle, C. Pannetier, J. Kanellopoulos and P. Kourilsky. Size Estimate of the αβ TCR Repertoire of Naive Mouse Splenocytes. **J. Immunol. 2000**; 164: 5782-5787

18. Burnet, F. M. S. The clonal selection theory of acquired immunity. Nashville: Vanderbilt University Press; **1959**

19. Cosgrove, D., S. H. Chan, C. Waltzinger, C. Benoist and D. Mathis. The thymic compartment responsible for positive selection of CD4+ T cells. **Int. Immunol. 1992**; 4: 707-710

20. Merkenschlager, M., D. Graf, M. Lovatt, U. Bommhardt, R. Zamoyska and A. G. Fisher. How Many Thymocytes Audition for Selection? **J. Exp. Med. 1997**; 186: 1149-1158

21. Anderson, M. S. Projection of an Immunological Self Shadow Within the Thymus by the Aire Protein. **Science 2002**; 298: 1395-1401

22. Khan, U. and H. Ghazanfar. T Lymphocytes and Autoimmunity. In: Elsevier; **2018**: 125-168

23. Iwashima, M., B. Irving, N. Van Oers, A. Chan and A. Weiss. Sequential interactions of the TCR with two distinct cytoplasmic tyrosine kinases. **Science 1994**; 263: 1136-1139

24. Murphy, K. and C. Weaver. Chapter 7: Lymphocyte Receptor Signaling. In: K. Murphy and C. Weaver eds, Janeway's immunobiology Garland Science; **2016**

25. Wardenburg, J. B., C. Fu, J. K. Jackman, H. Flotow, S. E. Wilkinson, D. H. Williams, R. Johnson, G. Kong, A. C. Chan and P. R. Findell. Phosphorylation of SLP-76 by the ZAP-70 Protein-tyrosine Kinase Is Required for T-cell Receptor Function. **J. Biol. Chem. 1996**; 271: 19641-19644

26. Yablonski, D. Bridging the Gap: Modulatory Roles of the Grb2-Family Adaptor, Gads, in Cellular and Allergic Immune Responses. **Front. Immunol. 2019**; 10:
27. Acuto, O. and F. Michel. CD28-mediated co-stimulation: a quantitative support for TCR signalling. **Nat. Rev. Immunol. 2003**; 3: 939-951
28. Appleman, L. J., A. A. F. L. Van Puijenbroek, K. M. Shu, L. M. Nadler and V. A. Boussiotis. CD28 Costimulation Mediates Down-Regulation of p27kip1 and Cell Cycle Progression by Activation of the PI3K/PKB Signaling Pathway in Primary Human T Cells. **J. Immunol. 2002**; 168: 2729-2736
29. Osaki, M., M. Oshimura and H. Ito. PI3K-Akt pathway: Its functions and alterations in human cancer. **Apoptosis 2004**; 9: 667-676
30. Bustelo, X. R. Regulatory and Signaling Properties of the Vav Family. **Mol. Cell Biol. 2000**; 20: 1461-1477
31. Coussens, N. P., R. Hayashi, P. H. Brown, L. Balagopalan, A. Balbo, I. Akpan, J. C. D. Houtman, V. A. Barr, P. Schuck, E. Appella and L. E. Samelson. Multipoint Binding of the SLP-76 SH2 Domain to ADAP Is Critical for Oligomerization of SLP-76 Signaling Complexes in Stimulated T Cells. **Mol. Cell Biol. 2013**; 33: 4140-4151
32. Barreira, M., S. Rodríguez-Fdez and X. R. Bustelo. New insights into the Vav1 activation cycle in lymphocytes. **Cell. Signal. 2018**; 45: 132-144
33. Yang, Y. R., J. H. Choi, J.-S. Chang, H. M. Kwon, H.-J. Jang, S. H. Ryu and P.-G. Suh. Diverse cellular and physiological roles of phospholipase C-γ1. **Adv. Biol. Regul. 2012**; 52: 138-151
34. Blonska, M. and X. Lin. CARMA1-mediated NF-κB and JNK activation in lymphocytes. **Immunol. Rev. 2009**; 228: 199-211
35. David, L., Y. Li, J. Ma, E. Garner, X. Zhang and H. Wu. Assembly mechanism of the CARMA1–BCL10–MALT1–TRAF6 signalosome. **PNAS 2018**; 115: 1499-1504
36. Shambharkar, P. B., M. Blonska, B. P. Pappu, H. Li, Y. You, H. Sakurai, B. G. Darnay, H. Hara, J. Penninger and X. Lin. Phosphorylation and ubiquitination of the IκB kinase complex by two distinct signaling pathways. **The EMBO Journal 2007**; 26: 1794-1805
37. Goldstein, G., M. Scheid, U. Hammerling, D. H. Schlesinger, H. D. Niall and E. A. Boyse. Isolation of a polypeptide that has lymphocyte-differentiating properties and is probably represented universally in living cells. **PNAS 1975**; 72: 11-15
38. Wilkinson, K. D. The discovery of ubiquitin-dependent proteolysis. **PNAS 2005**; 102: 15280-15282
39. Ebinu, J. O., S. L. Stang, C. Teixeira, D. A. Bottorff, J. Hooton, P. M. Blumberg, M. Barry, R. C. Bleakley, H. L. Ostergaard and J. C. Stone. RasGRP links T-cell receptor signaling to Ras. **Blood 2000**; 95: 3199-3203
40. Shaw, A. S. and E. L. Filbert. Scaffold proteins and immune-cell signalling. **Nat. Rev. Immunol. 2009**; 9: 47-56
41. Hogan, P. G., R. S. Lewis and A. Rao. Molecular Basis of Calcium Signaling in Lymphocytes: STIM and ORAI. **Annu. Rev. Immunol. 2010**; 28: 491-533
42. Mahajan, A., M. Herrmann and L. E. Muñoz. Clearance Deficiency and Cell Death Pathways: A Model for the Pathogenesis of SLE. **Front. Immunol. 2016**; 7:
43. Savage, P. A., D. E. J. Klawon and C. H. Miller. Regulatory T Cell Development. **Annu. Rev. Immunol. 2020**; 38: 421-453
44. Vianna, P. H. O., F. B. Canto, J. S. Nogueira, C. F. C. G. Nunes, A. C. Bonomo and R. Fucs. Critical influence of the thymus on peripheral T cell homeostasis. **Immun. Inflamm. Dis. 2016**; 4: 474-486
45. Kretschmer, K., I. Apostolou, D. Hawiger, K. Khazaie, M. C. Nussenzweig and H. Von Boehmer. Inducing and expanding regulatory T cell populations by foreign antigen. **Nat. Immunol. 2005**; 6: 1219-1227
46. Iberg, C. A. and D. Hawiger. Natural and Induced Tolerogenic Dendritic Cells. **J. Immunol. 2020**; 204: 733-744

47. Sakaguchi, S., N. Mikami, J. B. Wing, A. Tanaka, K. Ichiyama and N. Ohkura. Regulatory T Cells and Human Disease. **Annu. Rev. Immunol. 2020**; 38: 541-566
48. Vignali, D. A. A., L. W. Collison and C. J. Workman. How regulatory T cells work. **Nat. Rev. Immunol. 2008**; 8: 523-532
49. Rubtsov, Y. P., J. P. Rasmussen, E. Y. Chi, J. Fontenot, L. Castelli, X. Ye, P. Treuting, L. Siewe, A. Roers, W. R. Henderson, W. Muller and A. Y. Rudensky. Regulatory T Cell-Derived Interleukin-10 Limits Inflammation at Environmental Interfaces. **Immunity 2008**; 28: 546-558
50. Clayton, A., J. P. Mitchell, J. Court, M. D. Mason and Z. Tabi. Human Tumor-Derived Exosomes Selectively Impair Lymphocyte Responses to Interleukin-2. **Cancer Res. 2007**; 67: 7458-7466
51. Grossman, W. J., J. W. Verbsky, B. L. Tollefsen, C. Kemper, J. P. Atkinson and T. J. Ley. Differential expression of granzymes A and B in human cytotoxic lymphocyte subsets and T regulatory cells. **Blood 2004**; 104: 2840-2848
52. Chinen, T., A. K. Kannan, A. G. Levine, X. Fan, U. Klein, Y. Zheng, G. Gasteiger, Y. Feng, J. D. Fontenot and A. Y. Rudensky. An essential role for the IL-2 receptor in T_{reg} cell function. **Nat. Immunol. 2016**; 17: 1322-1333
53. Cederbom, L., H. Hall and F. Ivars. CD4+CD25+ regulatory T cells down-regulate co-stimulatory molecules on antigen-presenting cells. **Eur. J. Immunol. 2000**; 30: 1538-1543
54. Fallarino, F., U. Grohmann, K. W. Hwang, C. Orabona, C. Vacca, R. Bianchi, M. L. Belladonna, M. C. Fioretti, M.-L. Alegre and P. Puccetti. Modulation of tryptophan catabolism by regulatory T cells. **Nat. Immunol. 2003**; 4: 1206-1212
55. Murphy, K. and C. Weaver. Chapter 15: Autoimmunity and Transplantation. In: K. Murphy and C. Weaver eds, Janeway's immunobiology Garland Science; **2016**
56. Wraith, D. C., D. E. Smilek, D. J. Mitchell, L. Steinman and H. O. McDevitt. Antigen recognition in autoimmune encephalomyelitis and the potential for peptide-mediated immunotherapy. **Cell 1989**; 59: 247-255
57. Hayter, S. M. and M. C. Cook. Updated assessment of the prevalence, spectrum and case definition of autoimmune disease. **Autoimmun. Rev. 2012**; 11: 754-765
58. American Autoimmune Related Diseases Association, I. "Autoimmune Disease List." Retrieved 08.10.19, 2019, from https://www.aarda.org/diseaselist/.
59. Di Sabatino, A. and G. R. Corrazza. Coeliac disease. **Lancet 2009**; 373: 1480-1493
60. Lowes, M. A., A. M. Bowcock and J. G. Krueger. Pathogenesis and therapy of psoriasis. **Nature 2007**; 445: 866-873
61. Skapenko, A., J. Leipe, P. E. Lipsky and H. Schulze-Koops. The role of the T cell in autoimmune inflammation. **Arthrit. Res. Ther. 2005**; 7 S4-S14
62. Pilli, D., A. Zou, F. Tea, R. C. Dale and F. Brilot. Expanding Role of T Cells in Human Autoimmune Diseases of the Central Nervous System. **Front. Immunol. 2017**; 8: 652
63. Zhou, X., J. G. Krueger, M.-C. J. Kao, E. Lee, F. Du, A. Menter, W. H. Wong and A. M. Bowcock. Novel mechanisms of T-cell and dendritic cell activation revealed by profiling of psoriasis on the 63,100-element oligonucleotide array. **Physiol. Genomics 2003**; 13: 69-78
64. Okada, Y., D. Wu, G. Trynka, T. Raj, C. Terao, K. Ikari, Y. Kochi, K. Ohmura, A. Suzuki, S. Yoshida, R. R. Graham, A. Manoharan, W. Ortmann, T. Bhangale, J. C. Denny, R. J. Carroll, A. E. Eyler, J. D. Greenberg, J. M. Kremer, D. A. Pappas, L. Jiang, J. Yin, L. Ye, D.-F. Su, J. Yang, G. Xie, E. Keystone, H.-J. Westra, T. Esko, A. Metspalu, X. Zhou, N. Gupta, D. Mirel, E. A. Stahl, D. Diogo, J. Cui, K. Liao, M. H. Guo, K. Myouzen, T. Kawaguchi, M. J. H. Coenen, P. L. C. M. Van Riel, M. A. F. J. Van De Laar, H.-J. Guchelaar, T. W. J. Huizinga, P. Dieudé, X. Mariette, S. Louis Bridges Jr, A. Zhernakova, R. E. M. Toes, P. P. Tak, C. Miceli-Richard, S.-Y. Bang, H.-S. Lee, J. Martin, M. A. Gonzalez-Gay, L. Rodriguez-Rodriguez, S. Rantapää-Dahlqvist, L. Ärlestig, H. K. Choi, Y. Kamatani, P. Galan, M. Lathrop, S. Eyre, J. Bowes, A. Barton, N. De Vries, L. W. Moreland, L. A. Criswell, E. W. Karlson, A. Taniguchi, R. Yamada, M. Kubo, J. S. Liu, S.-C. Bae, J. Worthington, L. Padyukov, L. Klareskog, P. K. Gregersen, S. Raychaudhuri, B. E. Stranger, P. L. De Jager, L. Franke, P. M.

Visscher, M. A. Brown, H. Yamanaka, T. Mimori, A. Takahashi, H. Xu, T. W. Behrens, K. A. Siminovitch, S. Momohara, F. Matsuda, K. Yamamoto and R. M. Plenge. Genetics of rheumatoid arthritis contributes to biology and drug discovery. **Nature 2014**; 506: 376-381

65. Bacchetta, R., F. Barzaghi and M.-G. Roncarolo. From IPEX syndrome to FOXP3 mutation: a lesson on immune dysregulation. **Annals of the New York Academy of Sciences 2018**; 1417: 5-22

66. Perkey, E. and I. Maillard. New Insights into Graft-Versus-Host Disease and Graft Rejection. **Annu. Rev. Pathol.-Mech. Dis. 2018**; 13: 219-245

67. Tanaka, A. and S. Sakaguchi. Regulatory T cells in cancer immunotherapy. **Cell Res. 2017**; 27: 109-118

68. WHO. Collaborating Centre for Drug Statistics Methodology, ATC classification index with DDDs. In. Oslo, Norway; **2020**

69. Wishart, D. S., Y. D. Feunang, A. C. Guo, E. J. Lo, A. Marcu, J. R. Grant, T. Sajed, D. Johnson, C. Li, Z. Sayeeda, N. Assempour, I. Iynkkaran, Y. Liu, A. Maciejewski, N. Gale, A. Wilson, L. Chin, R. Cummings, D. Le, A. Pon, C. Knox and M. Wilson. DrugBank 5.0: a major update to the DrugBank database for 2018. **Nucleic Acids Res. 2018**; 46: D1074-D1082

70. Moon, C. Dexamethasone to the rescue. **Nat. Rev. Immunol. 2020**:

71. Yasir, M., A. Goyal, P. Bansal and S. Sonthalia. Corticosteroid Adverse Effects. In, StatPearls. Treasure Island (FL): StatPearls Publishing LLC.; **2020**

72. Hagen, P., J. E. Wagner, T. E. Defor, M. Dolan, M. Arora, E. Warlick, D. Weisdorf and C. G. Brunstein. The effect of equine antithymocyte globulin on the outcomes of reduced intensity conditioning for AML. **Bone Marrow Transplant. 2014**; 49: 1498-1504

73. Milstein, C. The hybridoma revolution: an offshoot of basic research. **Bioessays 1999**; 21: 966-973

74. Davda, J., P. Declerck, S. Hu-Lieskovan, T. P. Hickling, I. A. Jacobs, J. Chou, S. Salek-Ardakani and E. Kraynov. Immunogenicity of immunomodulatory, antibody-based, oncology therapeutics. **J. Immunother. Cancer 2019**; 7:

75. Ferreira, L. M. R., Y. D. Muller, J. A. Bluestone and Q. Tang. Next-generation regulatory T cell therapy. **Nat. Rev. Drug Discov. 2019**; 18: 749-769

76. Matloubian, M., C. G. Lo, G. Cinamon, M. J. Lesneski, Y. Xu, V. Brinkmann, M. L. Allende, R. L. Proia and J. G. Cyster. Lymphocyte egress from thymus and peripheral lymphoid organs is dependent on S1P receptor 1. **Nature 2004**; 427: 355-360

77. Fertig, B. A. and G. S. Baillie. PDE4-Mediated cAMP Signalling. **J. Cardiovasc. Dev. Dis. 2018**; 5:

78. Newman, D. J. and G. M. Cragg. Natural Products as Sources of New Drugs over the Nearly Four Decades from 01/1981 to 09/2019. **J. Nat. Prod. 2020**; 83: 770-803

79. Potterat, O. and M. Hamburger. Combined use of extract libraries and HPLC-based activity profiling for lead discovery: potential, challenges, and practical considerations. **Planta Med. 2014**; 80: 1171-1181

80. Koehn, F. E. High impact technologies for natural products screening. In: F. Petersen and R. Amstutz eds, Natural Compounds as Drugs Volume I. Basel: Birkhäuser Basel; **2008**: 175-210

81. Hamburger, M. Unravelling the Potential of Natural Products – Biological Profiling of Extracts and New Molecules. **Chimia 2006**; 60: 14-18

82. Quah, B. J. and C. R. Parish. The use of carboxyfluorescein diacetate succinimidyl ester (CFSE) to monitor lymphocyte proliferation. **J. Vis. Exp. 2010**; 44: e2259

2.2. Absolute Configurations of Natural Products

2.2.1. The issue of chirality

Chirality describes the mirror-symmetry between non-superimposable objects like hands. Even though both hands seem identical (not considering scars or wedding rings), it is not possible to superimpose them by only rotating or translating them (Figure 9). The difference between both hands is probably one of the oldest known examples for a chiral object and the word “chiral” is derived from the ancient Greek word for hand, χείρ (*cheir*).

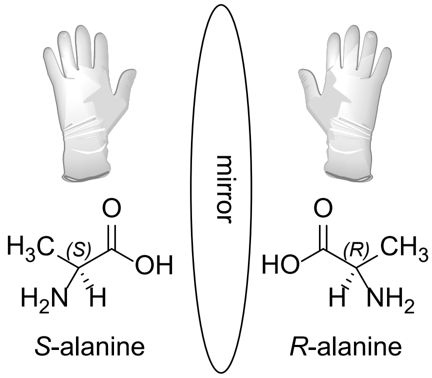

Figure 9. Representation of chirality in organic chemistry.

In chemistry, chirality is important as a property of organic molecules containing at least one carbon with four different substituents, for example the amino acid alanine. (*S*)- and (*R*)-alanine are mirror images. As they are non-superimposable using only mathematically proper operations (rotation, translation), they are **enantiomers** of each other. The description of one specific mirror image is its **absolute configuration (AC)**. If two molecules are only mirror images regarding some stereogenic centers, but not all, they are diastereomers.[83] While enantiomers are chemically equivalent, diastereomers are not. Thus, enantiomers appear the same in most analytical techniques like HPLC, UV, IR, and NMR, but diastereomers do not. Enantiomers are only distinguishable when interacting with other chiral elements, making them behave as diastereomers. Examples are chiral HPLC stationary phases, chiral shift reagents in NMR, or the interaction with polarized light. Different methods applying this principle can be used to assign the absolute configuration of a molecule by distinguishing enantiomers.

Another source of chirality in molecules are rotational barriers. In atropoisomerism, the rotation around a bond is hindered by large substituents resulting in two stable atropoisomers differing in conformation. This is the case for substituted biphenyls[84] but can also occur in natural products like abyssomyxin C and atrop-abyssomycin C[85]. On a larger scale, this is also the case for secondary structures of proteins or DNA, which are inherently chiral. But, although the methods described in the following are also applied to these cases, this work focuses on the absolute configurations of natural products.

Chirality in natural products

Many natural compounds contain at least one chiral center. For primary metabolites, the chirality of these centers was mostly stable in evolution. Glucose naturally occurs as D-glucose and natural amino acids are always present in the L-configuration, when referring to the Fischer nomenclature.[86] The chirality of secondary metabolites however is much less conserved as their structures were subject to more evolutionary variability.[87] This is illustrated by different biological effects of enantiomers, for example by insect pheromones.[88]

On one hand, this three dimensional diversity makes natural products a valuable source for new lead structures. On the other hand, it poses a challenge for drug development. The most infamous example is that of thalidomide, where only the *R*-enantiomer was found to be responsible for the desired sedative effect.[89] The drug itself was administered as a racemate and caused teratogenic side-effects, but also racemizes under physiological conditions, if only one enantiomer is given. Thus, it is almost impossible to find out, if only one or both enantiomers are responsible for the long term side effects. This case illustrates both the challenges and the necessity for the rigorous investigation of chiral properties in drug discovery. And, due to the extensive media coverage, it has initiated an awareness for chirality in drug design that is present until today.[90] The other reason for the importance of absolute configurations in drug discovery is more recent. As more and more screening procedures are done *in silico*, three dimensional input structures are needed to study the interactions with target proteins. Thus, each enantiomer or diastereomer needs to be screened separately. For a compound with *n* chiral carbons in its structure, 2^n structures need to be screened individually. This increases the needed computational effort exponentially with each additional undefined chiral carbon in a structure. And, if a hit is produced on a specific absolute configuration, it might not be the one existing in nature.[91] But, if the naturally occurring absolute configuration of a compound is known, only this configuration needs to be screened. And, if it is active, it can be made available for wet-lab experiments.

Optical rotation

The measurement of Optical Rotation (OR) is the oldest variant to distinguish enantiomers.[92] It measures the rotation of linearly polarized light when shone through a chiral sample, which can be a crystal, a solution, or a vapor. At any used wavelength, the angle observed for a rotation α_λ behaves analogous to the Beer-Lambert-Bouguer law.[93-95] It is proportional to the path length l, the concentration c and the specific optical rotation $[\alpha]_\lambda$ of the compound. As this effect is dependent on the wavelength it could at first only be observed at available single wavelengths.[96] These were the principal Fraunhofer lines of which the D line (Na line) at 589 nm is used to date in most OR measurements. This is illustrated by the conventional use of $[\alpha]_D^{25}$, which indicates the OR value to be measured at 589 nm and 25°C. Two corresponding enantiomers always give the same specific optical rotation, but exhibit opposite signs. This inherent property can be used to identify enantiomers and to determine their optical purities.

Determining the relative configuration

In compounds possessing more than one stereo center, the knowledge of configurations of stereo centers relative to each other is the **relative configuration (RC)**. Most commonly, relative configurations are determined by NMR. There, apart from using coupling constants (J_{HH} and J_{CH}), the Nuclear Overhauser Effect (NOE) is of great value.[97, 98] This is implemented in Nuclear Overhauser Effect SpectroscopY (NOESY) or Rotating frame nuclear Overhauser Effect SpectroscopY (ROESY) experiments, which identify protons closer than 5 Å from each other. NOESY gives positively phased peaks for smaller molecules and negatively phased peaks for macromolecules (Figure 10). The sign depends on the product of the spectrometer's angular frequency ω_0 and the molecular rotational correlation time τ_c. However, if $\omega_0\tau_c \approx 1$, no NOE effect is observed.[99] This is mostly the case for "intermediately" sized molecules between 1000 and 2000 Da.[98] In general, both experiments give similar information. But, to avoid signals close to zero, ROESY is often used for molecules larger than 500 Da. Another difference are the artefacts observed in the spectra. In NOESY, COSY correlations can in some cases be observed, while in ROESY, TOCSY crosspeaks can appear. This requires careful evaluation of the spectra.

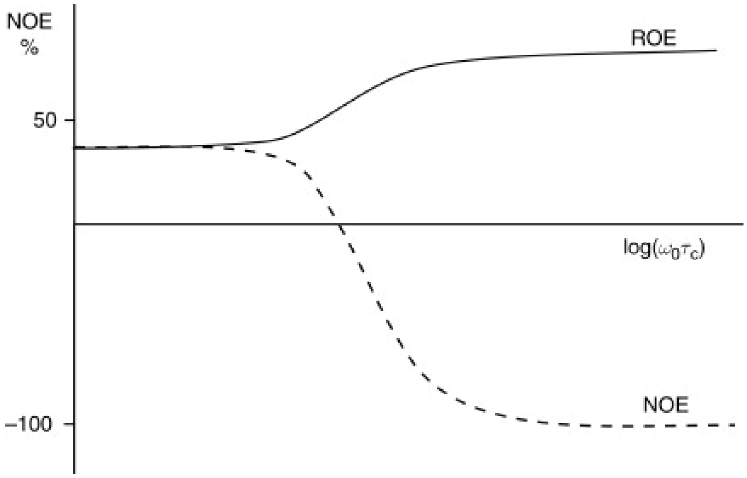

Figure 10. Strength and sign of observed NOE and ROE effects depending on $log(\omega_0\tau_c)$. Republished with permission of Elsevier, from Claridge, 2009[98]; permission conveyed through Copyright Clearance Center, Inc.

A crosspeak in either NOESY or ROESY indicates a close contact between two protons. This information can be combined into a three dimensional model of the molecule. This works best in rigid structures with known conformations (e.g. chair conformation of six-membered rings). As this is recorded over the whole measuring time, information from crosspeaks between conformationally flexible groups in a molecules is often ambiguous (see examples (B) and (D) in Figure 11).

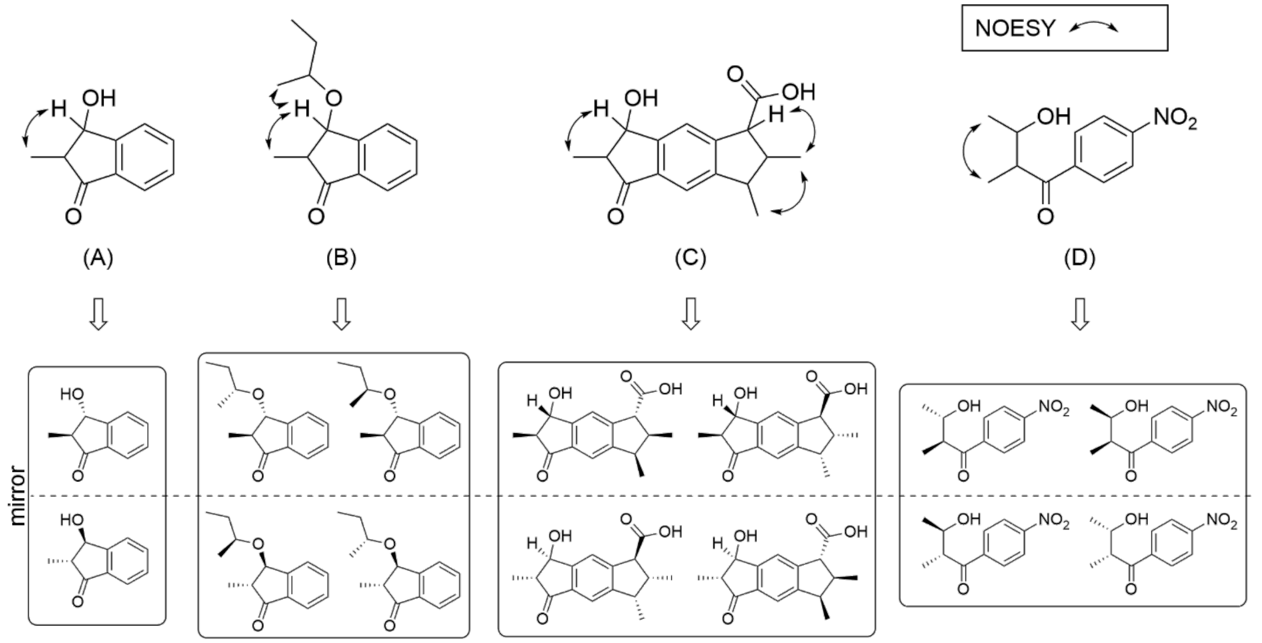

Figure 11. Imaginary examples of different molecules analyzed with NOESY. (A) Full relative configuration (B) Part of relative configuration (C) Relative configurations for independent parts of the molecule (D) No information on relative configuration. The planar structures with observed NOESY contacts are shown in the upper part. ACs compliant with the NOESY data are shown below with enantiomer pairs divided by the mirror plane (dashed line).

Thus, after critical assessment of the data, the result from NOESY or ROESY analysis can be (A) a full relative configuration, (B) a relative configuration with one or more undefined stereogenic centers, (C) independent relative configurations for different parts of the molecule, or (D) no information about the relative configuration (Figure 11). Which case is true for a specific molecule determines the further strategy to determine the absolute configuration.

2.2.2. Electronic Circular Dichroism (ECD)

A common way to determine the absolute configuration is electronic circular dichroism (ECD). As modern instruments only need minute amounts (<100 µg) of sample, it is ideal for natural product research. A good knowledge of the investigated structure, however, is necessary for valid results.

Introduction

Right and left handed circularly polarized light can be absorbed differently by chiral compounds depending on the wavelength. This circular dichroism (CD) can be measured, in principle, in the whole electromagnetic spectrum.[100] As a convention, the absorption of the right handed circularly polarized light (A_R) is subtracted from the absorption of the left handed circularly polarized light (A_R) for each wavelength:

$$CD = A_L - A_R \qquad (1)$$

The measured CD is usually obtained from the instrument as ellipticity θ in the unit millidegree [mdeg] and can be transformed into CD using the following equation:[101]

$$\theta\ (mdeg) = 33000\ CD \qquad (2)$$

To yield a value independent of concentration (c [mol/L]) or pathlength (l [cm]) in the cell used, the Beer-Lambert-Bouguer law is employed:[93-95]

$$\Delta\boldsymbol{\varepsilon} = \boldsymbol{\varepsilon_L} - \boldsymbol{\varepsilon_R} = \frac{\boldsymbol{CD}}{\boldsymbol{c * l}} \qquad (3)$$

The values of $\Delta\varepsilon$ [$M^{-1}cm^{-1}$] for two enantiomers at any given wavelength have opposite signs. As it is a differential spectroscopy (Equation 1), a CD effect can only be measured, if a corresponding absorption A is observed. The relation between CD and absorption A can be expressed by the dissymmetry factor g:

$$\boldsymbol{g} = \frac{\Delta\boldsymbol{\varepsilon}}{\boldsymbol{\varepsilon}} = \frac{\boldsymbol{CD}}{\boldsymbol{A}} \qquad (4)$$

Usually, g is between 10^{-3}-10^{-5} as the CD effect is significantly smaller than the corresponding absorption. Thus, compared to absorption spectra, stronger light sources and more sensitive detectors are needed to measure CD spectra.[101] Generally, circular dichroism can be measured in the far UV region (130-195 nm), the UV-Vis region (195-750 nm), the near infrared region (1,000-2,500 nm), and the infrared region (2,500-12,500 nm).[102, 103] Due to practical limitations, however, the most common applications of CD are ECD in the UV-Vis region followed by Vibrational Circular Dichroism (VCD) and Raman Optical Activity (ROA) in the infrared region (2,500-12,500 nm or 3500-750 cm^{-1}). Equations 1-4 are valid for all CD experiments. The measurement of Optical Rotations at different wavelengths, or Optical Rotation Dispersion (ORD) does not *per se* use CD, but is related to it through the Kramers-Kronig relation.[104]

Theory of ECD

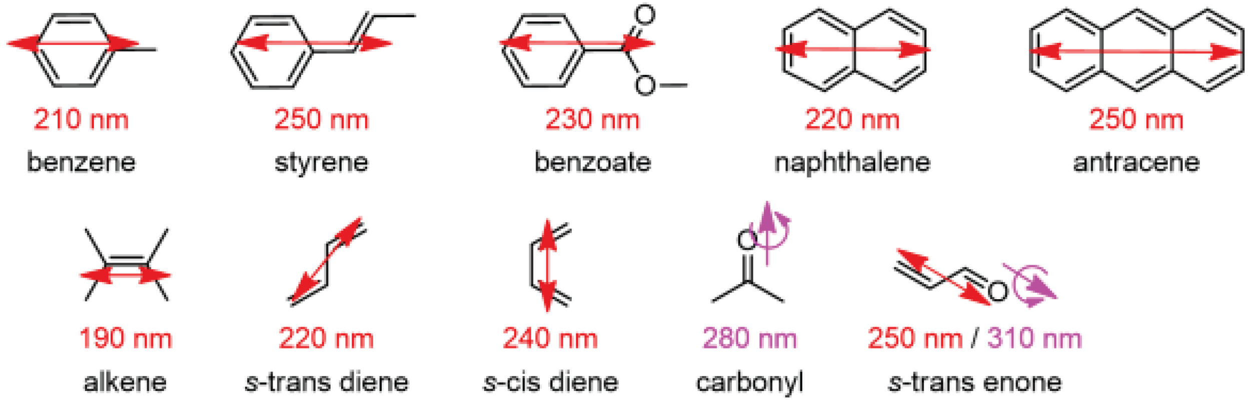

Figure 12. Examples of simple organic chromophores with their main transitions. Electronic transition dipoles are shown in red, magnetic ones in purple. Republished with permission of Royal Society of Chemistry, from Berova *et al.*, 2007[101]; permission conveyed through Copyright Clearance Center, Inc. Reproduced with permission from Berova *et al.*

As ECD is complementary to UV/Vis-spectroscopy, a suitable chromophore is needed. Some common chromophores with their respective typical absorption frequencies are shown in Figure 12. Each transfer of an electron from state “i” to state “j” can be divided into a linear charge displacement with an electronic dipole $\vec{\mu}_{ij}$ as well as the electron’s rotation causing a magnetic transition dipole $\vec{m}_{ij}$. Together, both determine the oscillator strength f_{ij}, which is proportional to the intensity of the respective UV absorption:

$$f_{ij} \approx \left|\vec{\mu}_{ij}\right|^2 + \left|\vec{m}_{ij}\right|^2 \tag{4}$$

In contrast, the CD effect is dependent on the rotational strength R_{ij} of an electronic transition, which is determined by the scalar product of the transition dipoles:

$$R_{ij} \approx \vec{\mu}_{ij} \cdot \vec{m}_{ij} \tag{5}$$

Therefore, if the dipole vectors $\vec{\mu}_{ij}$ and $\vec{m}_{ij}$ are not orthogonal, R_{ij} is $\neq 0$ and a Cotton effect (CE) can be observed.

Interpretation of ECD spectra

Simple examples of chromophores are helical 1,3-dienes, where the angle C=C-C=C is $\neq 0$ and can be either positive or negative (Figure 13).

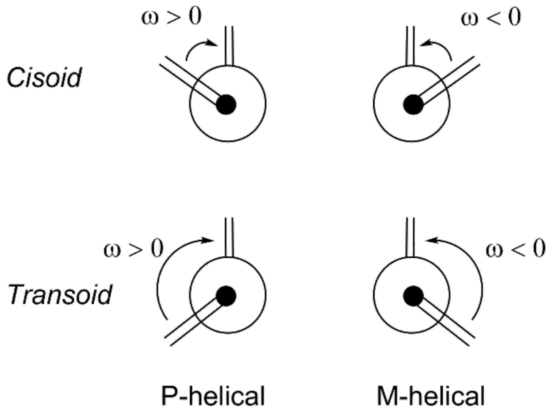

Figure 13. Nonplanar conformations of 1,3-dienes. The sign gives the respective sign of the angle ω.

1,3-dienes generals absorb light in the UV region around 220 nm for *cis*-1,3-dienes and around 240 nm for *trans*-1,3-dienes. For both configurations, the respective electron transitions from the π-Molecular Orbital (MO) of one double bond and to the π*-MO of the other double bond ($\pi \rightarrow \pi^*$). As it is mainly an electron transfer in space, the effect of the electronic dipole $\vec{\mu}_{ij}$ is significantly larger than of the magnetic dipole $\vec{m}_{ij}$. This is classified as an allowed transition. As the rotational strength R_{ij} and its sign depend on the angle ω, ECD is sensitive towards conformational changes This must be considered in the interpretation of ECD spectra.

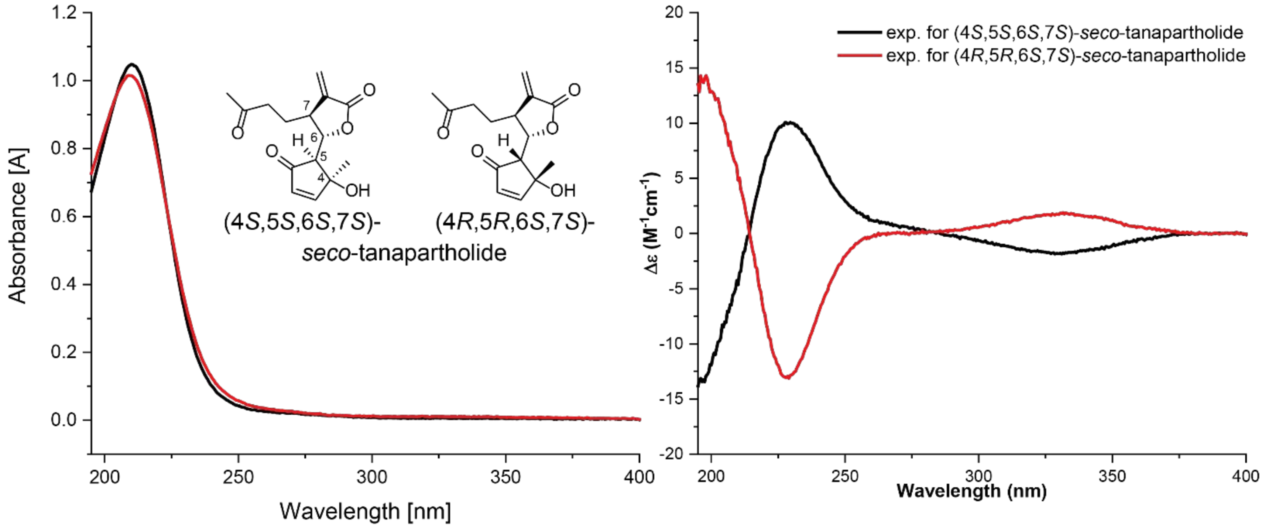

Figure 14. UV- (left) and ECD spectra (right) of two diastereomeric *seco*-tanapartholides isolated from *Artemisia argyi*.

In the case of 1,3-enones, additional to the $\pi \rightarrow \pi^*$ transition absorption band (K-band) a weaker one around 310 nm is observed (R-band). It arises due to the transition of an electron from a non-binding n-MO of the oxygen to an antibonding π*-MO ($n \rightarrow \pi^*$-transition). This is an example for a “forbidden” transition, as the contribution of the magnetic dipole $\vec{m}_{ij}$ is stronger than that of the electronic dipole $\vec{\mu}_{ij}$.[105] The different magnitudes of transitions can be observed in the case of two *seco*-tanapartholides from *Artemisia argyi* shown in Figure 14.[106] There, one *trans*-enone and one *cis*-enone are present. Generally, the ECD contribution of the *cis*-enone-chromophore is weaker than that of the *trans*-enone. This leads to opposite spectra for opposite configurations next to the *trans*-enone. The CE at 230 nm originating from the $\pi \rightarrow \pi^*$ transition is exemplary and corresponds to significant absorption in the UV-spectrum. The $n \rightarrow \pi^*$-transition, however, which causes the CE at 330 nm does only show very little UV absorption.

Starting from these effects observed in simple compounds, empirical rules for the interpretation of ECD spectra have been proposed. Examples are the Diene Helicity Rule[107] and the Quadrant Rule[108] for dienes, the Enone Helicity Rule[109] for enones, and sector rules[110] for aromatic chromophores. These rules, together with different semi-empirical calculations, have been used intensively to gain insights into ECD spectra before *ab initio* calculations were affordable, but can still give insights today.[111]

Ab initio calculations

Ab initio calculations use approximations of the Schrödinger equation to simulate data *in silico* without the input of experimental data.[112] For example, absorption phenomena can be deducted from this description of a physical system over time. As the Schrödinger equation itself can only be solved for a system consisting of one hydrogen atom, approximations are used. This was successfully implemented by Parr, Craig, and Ross in 1950 for benzene.[113] Nowadays, density functional theory (DFT), which is based on the calculation of molecular orbitals, is most commonly used. For ECD, as excited states are necessary for the calculation of electronic absorption, time-dependent DFT (TDDFT) is used. The specific method used for a calculation is described by the "Level of Theory" which is defined by the functional and the basis set. While the functional describes the correlation between electrons, the basis set describes the electron wave function. A common level of theory is the B3LYP functional (Becke, 3-parameter Lee-Young-Parr) used in combination with the basis set 6-31G(d,p). For more accuracy, optimized functionals like CAM-B3LYP and larger basis sets like 6-31G+(3df,2p) including more orbitals can be used. As this usually comes with significantly higher computational cost, a good balance between accuracy and computational cost needs to be found. These level of theories are accessible, for example, with Gaussian.[114]

Ab initio calculations of ECD spectra

Ab initio calculations allow for a convenient interpretation of ECD spectra. Instead of interpreting spectra of new molecules using empirical rules or by comparing them to spectra of compounds with known ACs, they can be compared to spectra generated individually for all stereoisomers. This extends the scope of ECD to include also unknown compounds. A comprehensive review on calculating ECD spectra was published in 2016 by Gennaro Pescitelli and Torsten Bruhn.[115] It outlines the calculation procedure and gives a guide to a good computational practice. As *ab initio* calculations can only predict the ECD spectrum of one conformation at a time, ideally, all stable conformers should be calculated. Usually, a conformational search in a force field, either through molecular dynamics or molecular modeling, is used to identify the conformers representing energy minima. Then, for each selected conformer, geometry and frequencies are optimized in a first *ab initio* calculation at the respective level of theory. With the resulting structure, the excited states are calculated using TDDFT, which simulates the absorption of light by the electrons. This calculation yields the electronic dipole $\vec{\mu}_{ij}$ and the magnetic transition dipole $\vec{m}_{ij}$ together as rotational strength dependent on the wavelength. On its own, a line spectrum is generated, which needs to be fitted with Gaussian or Laurentzian curves to be comparable to the experimental spectrum. Finally, the calculated ECD spectra of each conformer are combined based on the Boltzmann distribution between the respective conformers:

$$p \propto e^{\frac{\Delta E}{kT}}$$

Limitations of ECD

Although ECD is a very useful technique, its applicability is limited in molecules:

- That lack a chromophore
- For which the relative configuration is not known
- For which no stable conformers in solution can be identified

If a suitable chromophore is present and a ECD spectrum was recorded, the approach depends on the knowledge of the relative configuration. The different possibilities were outlined for cases (A)-(D) above (Figure 11). In case (A), where the full relative configuration was deduced from NMR, only one of the enantiomers needs to be calculated. If the relative configuration is correct and the *ab initio* calculation was done correctly, either the calculated spectrum or its mirror image can be overlaid with the experimental data. In case (B), one configuration from each enantiomer pair needs to be calculated. Ideally, one of them, or their mirror image, fits the experimental data and the respective AC can be assigned. If the undefined stereo center does not significantly impact the calculated ECD spectrum, only the rest of the molecule can be assigned. This gives a partial AC and the remaining stereo center needs to be assigned in another fashion. Case (C) also needs the calculation of one configuration from each pair of possible enantiomers. If only one of the calculated spectra or their mirror image fits, the AC can be assigned. Otherwise, it can only be used to possibly exclude ACs and other methods are needed to complete the assignment. Due to the flexibility in case (D), no information about the relative configuration is available and the conformational search is more challenging. Thus, even if one configuration from each pair of enantiomers is calculated, it is often not possible to assign the AC. In any case, before an AC is finally assigned by ECD, the result should be checked self-critically to avoid misassignments. Some questions to address for that matter are:

- Was the conformational search appropriate for the molecule?
- Was the level of theory appropriate for the molecule?
- Was the fit of the line-spectrum appropriate?
- Was there a bias in the spectra comparison?

If a compound lacks a chromophore, ECD is not suited to solve the AC. A shift into the infrared region of the electromagnetic spectrum, however, could do the trick.

2.2.3. Vibrational Circular Dichroism (VCD)

Vibrational interactions in the infrared range can be used to study absolute configurations of organic molecules. For this, over the last five decades, Raman optical activity (ROA) and vibrational circular dichroism (VCD) have been developed to measure vibrational optical activity (VOA).[116] As VCD is more commonly used, it is the main topic in this chapter.

History of VCD

The principal challenge in VCD is the signal strength, which is around four magnitudes smaller than that from ECD.[117] Thus, although the effect was predicted earlier, first VCD effects were only measured in the 1970s.[118, 119] The second challenge is the interpretation of VCD spectra, which relies almost exclusively on quantum mechanical calculations. These most often use the Born-Oppenheimer approximation for the Schrödinger equation to calculate electrons and nuclei separately. For VCD however, as the movement of the nucleus defines a vibration the electronic contribution to the magnetic transition cannot be calculated.[120] Thus, calculations using only the Born-Oppenheimer approximation were not suited as comprehensive descriptions of VCD phenomena.[117, 121] An approach to calculate VCD spectra *ab initio* became only available around ten years after the first measurements.[122] After further development in the 1990s towards routine DFT calculations, commercially available FT-VCD instruments, and the possibility to measure liquid samples, VCD became more broadly applicable to the study of ACs of organic compounds.[123, 120] As of today, its application in the field of natural product research field is still underexplored. Possible reasons could be the necessary sample quantity (>3 mg), the lack of knowledge about the method, and the lack of available instrumentation.

Theory of VCD

VCD measures the CD effect in the infrared region between 500 and 4000 cm^{-1}. Like in ECD, the sign of the CD effect is opposite for enantiomers and its amplitude proportional to the rotational strength. The rotational strength in turn originates from the electric and magnetic dipole transition moments.[124] As more bands can be used than in ECD, the method is very sensitive to conformational changes and can be used to determine configurations and conformations of a molecule. This potentially yields more information, but also makes the interpretation of VCD spectra a challenging task.

Empirical rules

Due to its late introduction, the only relatively recent advent of commercial VCD instruments, and the inherent complexity of VCD spectra, empirical rules comparable to the ones for ECD have not been established. An approach to understand VCD spectra in more detail is the visualization of the vibrational transition current density (VTCD).[125] This method, however, needs itself extensive computational effort, which, so far, is only feasible for smaller systems (Figure 15).[126] Thus, the interpretation of experimental VCD spectra relies almost entirely on the comparison to *ab initio* calculated spectra.

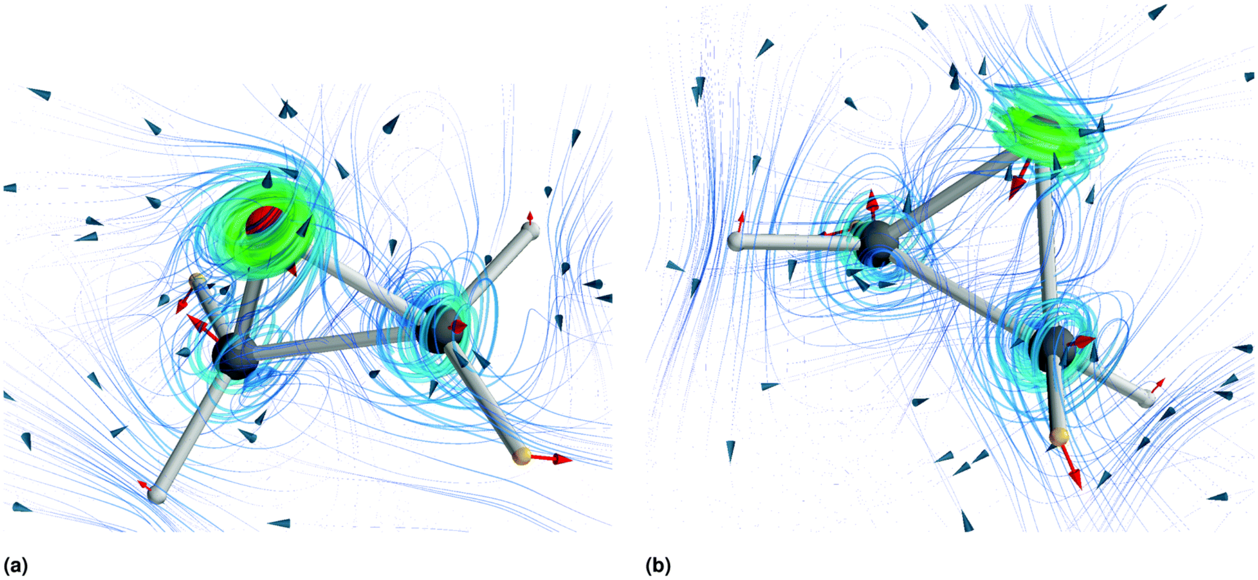

Figure 15. 3D representation of the VTCD vector field for the 4th normal modes of d2ox by means of a streamline object. The red arrows depict the charge-weighted nuclear displacement vector for the normal mode. Republished with permission of Royal Society of Chemistry, from Fusè *et al.*, 2019[126]; permission conveyed through Copyright Clearance Center, Inc.

Ab initio calculation of VCD spectra

Different methods like DFT and gauge-invariant atomic orbitals (GIAO) have been adapted for the *ab initio* calculation of VCD spectra. Between those, the B3LYP functional was found to be a suitable compromise between accuracy and computational cost.[127] In the *ab initio* calculation itself, the vibrations of the molecule as well as their dipole strengths and rotational strengths are calculated. As this does not need the calculation of excited states, it is computationally less demanding compared to ECD. Nevertheless, as VCD spectra are highly sensitive to configurational and conformational changes, a rigorous conformational search is needed as a basis for any reliable *ab initio* calculation.

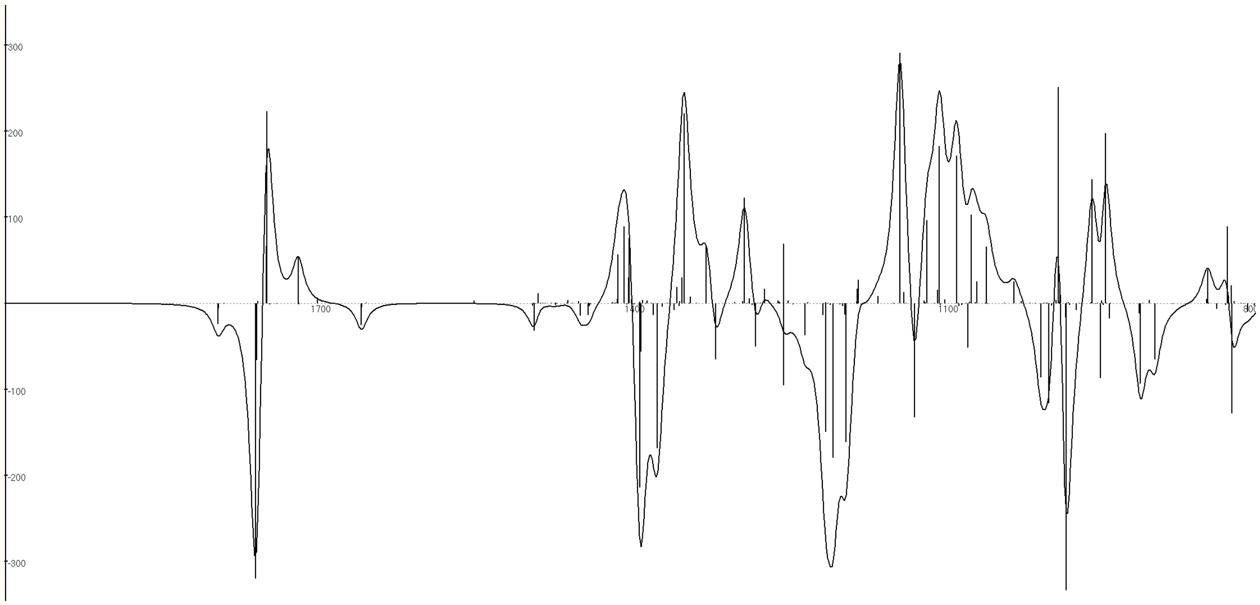

Figure 16. ***Ab initio*** **calculated transitional rotational strengths of (4*S*,5*S*,6*S*,7*S*)-*seco*-tanapartholide displayed as line spectrum with a Lorentzian fit using a bandwidth of 7 cm^{-1}. (from VCDSpecTech[128])**

When all relevant global minima are found, dipole and rotational strengths of bands in IR/VCD are calculated *ab initio* with their respective energies. The energies correspond to the wavenumbers, but are only consistent inside the calculation. Thus, the calculated spectra need to be scaled to the experimental ones prior to comparison. In the end, for comparison to measured data, band broadening is simulated with either a Lorentzian or a Gaussian fit as shown in Figure 16. The bandwidth should reflect the band broadening observed in the corresponding experimental spectrum.

Interpretation of VCD spectra

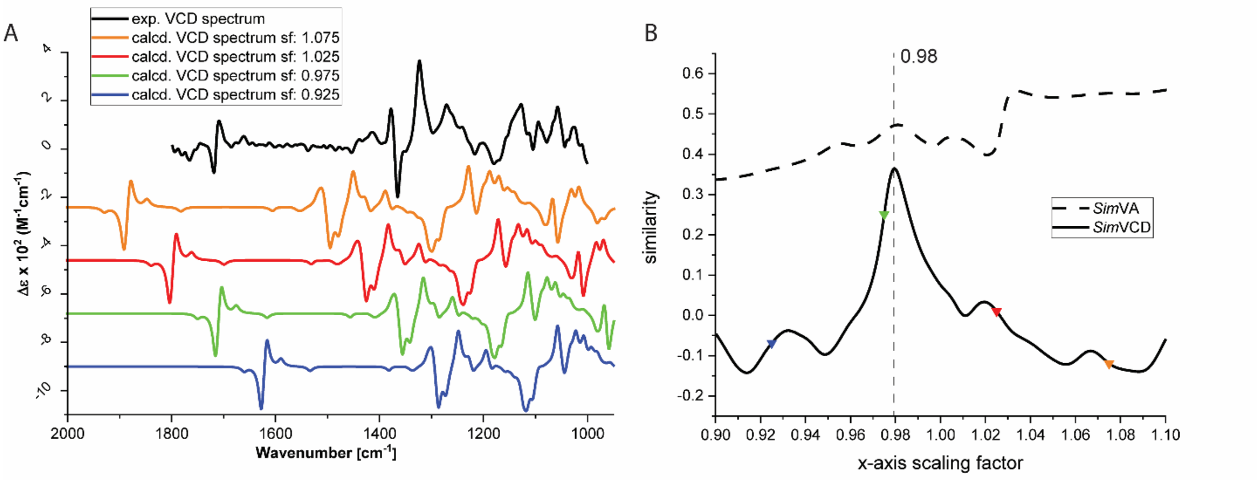

Figure 17. (A) Comparison of the experimental VCD spectrum of (4*S*,5*S*,6*S*,7*S*)-*seco*-tanapartholide with its calculated spectrum plotted at x-axis scaling factors (sf.) 0.925, 0.975, 1.025, and 1.075. (B) ***Sim*****VCD and** ***Sim*****VA indices plotted over the x-axis scaling factor comparing the experimental to the calculated VCD spectra shown in (A).**

VCD spectra contain significantly more bands than ECD spectra (Figure 17A). To interpret the multitude of bands, particularly in the crowded fingerprinting region between 1400 and 900 cm^{-1} needs special care. Thus, in order to avoid human bias in this comparison, algorithms comparing the similarity between spectra have been developed.[129, 128] One example is the calculation of similarity indices from the overlap between calculated and experimental spectra. This results in *Sim*VA for the comparison of IR spectra and *Sim*VCD for the comparison of VCD spectra (Figure 17B). *Sim*VA and *Sim*VCD can assume values from -1 to 1 where "1" corresponds to a perfect fit of the spectra and "-1" to a perfect fit to the opposite enantiomer. If *Sim*VCD ≈ 0, the spectra do not correspond at all. In Figure 17B, the ideal overlap between calculated and measured VCD spectrum is found at a scaling factor of 0.98. This should also be in agreement with a maximum in *Sim*VA. As the bands in the corresponding IR spectrum are usually broader compared to the VCD spectrum, maxima in *Sim*VA are less pronounced. This shows the influence of the bandwidth used to fit the spectrum on the values *Sim*VA and *Sim*VCD. To avoid false attributions, the fitted bandwidth should be similar to the measured bands. As this is individual for each measured spectrum, the values of *Sim*VA and *Sim*VCD for all diasteromers can only be used as relative values and no absolute threshold can be defined. For this, the similarity plots of *Sim*VA and *Sim*VCD against the x-axis scaling factor are compared between all possible diastereomers. While *Sim*VA assumes similar values between different calculated configurations, the configuration with the highest *Sim*VCD value is the most likely fit for the correct absolute configuration. This should be verified by a visual comparison of characteristic bands at the respective x-axis scaling factor. If both, computational and visual comparison, show significant differences and are consistent, the AC can be assigned with good confidence.

2.2.4. Strategies towards an Absolute Configuration

Unfortunately, non-destructive spectroscopic methods like OR, ECD, and VCD are not applicable in all cases. Thus, other methods have to be considered as well and are described in the following.

Total Synthesis

A historically important method to determine the absolute configuration is the **total synthesis** of a suspected structure or all possible diastereomers for comparison. Then, chiral properties like OR, ECD, or others can be compared to the isolated natural product, thereby identifying the absolute configuration. To synthesize natural products with defined absolute configurations, precursors of known chirality and stereoselective reactions are used. A famous example is the synthesis of the antimalarial drug artemisinin in 1982.[130] Total synthesis ideally gives the absolute configuration together with the possibility of synthesizing close derivatives of lead structures to explore structural features responsible for the activity. However, it is a very time consuming and in some cases near impossible task to synthesize natural products[131]. Therefore, not all compounds can or should be synthesized, as is outlined nicely by a comment from Philip Ball in 2015.[132]

Defined Degradation

One faster and often easier method is the defined degradation of the molecule. There, known reactions are employed to break down the molecule into simpler fragments. Those are then compared to already known molecules or can be synthesized in an easier fashion[133]. One example of this is the original identification of hazaleanins A and B isolated from *Fagara rhetza* in 1992.[134] In this work, some compounds from *T. asiatica* were hydrolyzed to identify the sugars and the configurations of the aglycons. This approach can take very different forms depending on the compound, but is usually limited by the quantities available for experiments. While hydrolyzed sugars can be identified from minute amounts via GCMS analysis, most other reactions require larger amounts to identify the products via NMR or other means.

X ray Crystallography

Another way to determine a molecules relative and, under the right conditions, absolute configuration is **X ray diffraction** on a suitable single crystal of the compound. For this, it is mounted on the tip of a needle in the diffractometer and monochromatic X rays are shot at it in a very concentrated parallel beam. The X-rays interact with the electrons in the ordered crystal lattice and get diffracted. The observed diffraction pattern on the detector are discrete dots of varying intensity, which correspond to the crystal lattice. This measurement is repeated at different angles of the crystal and taken together, the three dimensional crystal lattice can be defined. This can be compared to combining pictures of an object from all sides into a three-dimensional object, for example in a computer game.[135] However, X ray diffraction patterns are not direct images of the molecules. They arise from constructive interferences between X rays diffracted from the crystal planes. Thus, only interferences that follow Bragg's law[136] are observed:

$$n\lambda = 2d\ sin\theta$$

It depends on the wavelength λ, the distance between the planes d, the angle of the diffracted ray θ, and the order of the diffraction n. As wavelength and angle of the diffracted rays are known, the distance between the planes can be calculated. Through Fourier transformation, the information of all measurements is combined into a three-dimensional model of the electron cloud of the molecule. The atoms are then fit into the cloud leading to the three-dimensional model of the crystallized molecule or its enantiomer. This is hindered by the "phase problem", as only the intensity but not the phase of the diffracted light is measured.[137] Thus, the phase is initially guessed and subsequently optimized. While this usually works well for small molecules, protein structures require more effort.[138] In any case, however, whether this can be solved, and which resolution of the structure is reached depends on the quality of the acquired data. Apart from the type of X ray radiation used, the data quality also influences, if the absolute configuration can be identified. Therefore, if a crystal is available, X ray diffraction is a reliable method to determine at least the relative, and ideally the absolute configuration of a compound. Yet, crystallizing some compounds, especially with low sample quantities, can prove rather difficult. This limits the application of single crystal X ray diffraction significantly.

Mosher ester analysis

Mosher ester analysis is a **derivatization method** to determine the absolute configuration of secondary alcohols or amines.[139] In this method, a compound is esterified with both enantiomers of Mosher's acid separately (Figure 18) leading to two diastereomeric Mosher's esters[140].

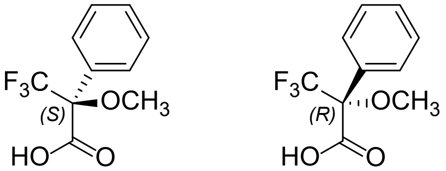

Figure 18. Mosher's acids.

Differences in ^{1}H NMR or ^{19}F NMR are then used to identify the absolute configuration at that stereogenic center. Here, the focus will be on ^{1}H NMR, as this is more commonly used. The chemical shifts (δ_R) of the protons surrounding the chiral alcohol (α) in the ester with the (*R*)-Mosher's acid are subtracted from the ones (δ_S) in the (*S*)-Mosher's ester. To interpret these results, the magnetic shielding from the benzene ring in the Mosher ester is used.[141, 142]

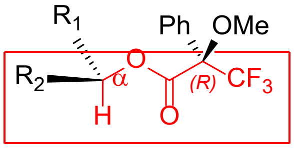

Figure 19. Visualization of the plane through a (*R*)-Mosher's ester (modified from Ohtani *et al.*[140])

For the main conformer present in the ester, a theoretical plane through the CF_3-group, the ester bond and the chiral carbon C_α is constructed (Figure 19). Protons belonging to R_1 in Figure 19 are on the same side of this plane as the benzene ring. Thus, their chemical shifts in the ester with the (*R*)-Mosher's acid are found more upfield in the ^{1}H-spectrum compared to the ester with the (*S*)-Mosher's acid. After subtraction (δ_R - δ_S), the sign for protons belonging to R_1 will be negative, while the sign for protons belonging to R_2 will be positive. This allows the determination of the absolute configuration. The limitation of this method is the dependence on the ideal configuration. In most cases, this conformation is the dominant one. However, if this conformation is sterically impaired, the method will lead to inconclusive results.[140] The derivatization reaction has been optimized over time since its first use, for example by using the acid chloride.[143] Another limitation is the amount needed for the derivatization reaction as it needs to be performed with both Mosher acids and the product needs to be enough for ^{1}H NMR analysis. This excludes Mosher ester analysis as a possibility in case of limited amounts available.

Other methods

Apart from chiroptical methods, total synthesis, defined degradation, Xray diffraction, and the Mosher ester analysis there are several other notable methods for relative or absolute configurational assignment. Most are related to the ones above and essentially share some of the characteristics but are less used because of availability or practicability. Nevertheless, in specific cases, they can provide answers to questions outside the scope of standard methods. Thus, they should be shortly mentioned in the following.

Complementary to total synthetic approaches, there are different kinds of **semi-synthetic approaches**. Some of them use natural products as starting materials for their chemical synthesis whereas others feed synthetically modified natural products to either isolated biosynthetic enzymes, cell extracts or whole cells to achieve products similar to the natural compound.[144] Related to Xray diffraction, **Xray powder diffraction** has been developed in the last three decades for crystallographic analyses without the need of a well grown crystal.[145, 146] However, as the angles are unknown and overlap in this method, it is used more commonly used to identify known substances by their fingerprint.[147] Analogously to Mosher's ester method, other derivatization methods for NMR have been developed to identify absolute configurations, also involving other functional groups.[148, 149] Other derivatization reactions aim at making compounds accessible to ECD or VCD. Another modern method to determine the absolute configuration of a molecule is the Coulomb explosion method. Opposed to all other methods, it is a more direct method, which visualizes the explosion shadow of a molecule. Unfortunately, this method is, so far, too limited in terms of molecule complexity to be of use for most natural products.[150]

Overall, a spectrum of methods is available to determine the AC of a compound. In the end the decision, which ones to use for a given molecule depends primarily on the availability of chromophores, sample, time, and resources. Nevertheless, given nowadays possibilities and necessities for characterizing natural products, it should be at least attempted for any given compound. And, even if this is not successful, the published data can be used to compare it to future efforts.

References:

83. Cotton, F. A. Chemical applications of group theory. New York: Wiley; **1990**

84. Moss, G. P. Basic terminology of stereochemistry (IUPAC Recommendations 1996). In, **Pure and Applied Chemistry**; **1996**: 2193

85. Nicolaou, K. C. and S. T. Harrison. Total Synthesis of Abyssomicin C and atrop-Abyssomicin C. **2006**; 45: 3256-3260

86. Fujii, N. and T. Saito. Homochirality and life. **2004**; 4: 267-278

87. Nina Theis and Manuel Lerdau. The Evolution of Function in Plant Secondary Metabolites. **Int. J. Plant Sci. 2003**; 164: S93-S102

88. Mori, K. Bioactive natural products and chirality. **2011**; 23: 449-462

89. Eriksson, T., S. Björkman, B. Roth and P. Höglund. Intravenous Formulations of the Enantiomers of Thalidomide: Pharmacokinetic and Initial Pharmacodynamic Characterization in Man. **2000**; 52: 807-817

90. Ito, T., H. Ando and H. Handa. Teratogenic effects of thalidomide: molecular mechanisms. **Cell. Mol. Life Sci. 2011**; 68: 1569-1579

91. Brooks, W. H., W. C. Guida and K. G. Daniel. The significance of chirality in drug design and development. **Curr. Top. Med. Chem. 2011**; 11: 760-770

92. Arago, F. J. D. Mémoire sur une modification remarquable qu'éprouvent les rayons lumineux dans leur passage à travers certains corps diaphanes et sur quelques autres nouveaux phénomènes d'optique. **Mémoires de la classe des sciences mathématiques et physiques de l'Institut de France. 1811**; 1: 93-134

93. Bouguer, P. Essai d'optique sur la gradation de la lumière. Paris, France: Claude Jombert; **1729**

94. Lambert, J. H. Photometria sive de mensura et gradibus luminis, colorum et umbrae [Photometry, or, On the measure and gradations of light intensity, colors, and shade]. Augsburg, Germany: Eberhardt Klett; **1760**

95. Beer, A. Bestimmung der Absorption des rothen Lichts in farbigen Flüssigkeiten. **Ann. Phys. (Berl.) 1852**; 86: 78-88

96. Arndtsen, A. Sur la polarisation circulaire de la lumiere dans divers liquides. **Ann. Chim. Phys. 1858**; 3: 403-421

97. Overhauser, A. W. Polarization of Nuclei in Metals. **Phys. Rev. 1953**; 92: 411-415

98. Claridge, T. D. W. Chapter 8 - Correlations through space: The nuclear Overhauser effect. In: T. D. W. Claridge ed, Tetrahedron Organic Chemistry Series: Elsevier; **2009**: 247-302

99. Bothner-By, A. A., R. L. Stephens, J. Lee, C. D. Warren and R. W. Jeanloz. Structure determination of a tetrasaccharide: transient nuclear Overhauser effects in the rotating frame. **J. Am. Chem. Soc. 1984**; 106: 811-813

100. Polavarapu, P. L. Chiroptical spectroscopy: fundamentals and applications. Boca Raton: CRC Press; **2016**

101. Berova, N., L. D. Bari and G. Pescitelli. Application of electronic circular dichroism in configurational and conformational analysis of organic compounds. **Chem. Soc. Rev. 2007**; 36: 914

102. Guo, C., R. D. Shah, R. K. Dukor, T. B. Freedman, X. Cao and L. A. Nafie. Fourier transform vibrational circular dichroism from 800 to 10,000cm^{-1}: Near-IR-VCD spectral standards for terpenes and related molecules. **Vib. Spectrosc 2006**; 42: 254-272

103. Burck, J., S. Roth, D. Windisch, P. Wadhwani, D. Moss and A. S. Ulrich. UV-CD12: synchrotron radiation circular dichroism beamline at ANKA. **J. Synchrotron Radiat. 2015**; 22: 844-852

104. Polavarapu, P. L. Kramers−Kronig Transformation for Optical Rotatory Dispersion Studies. **J. Phys. Chem. A 2005**; 109: 7013-7023

105. Kwit, M., P. Skowronek, J. Gawronski, J. Frelek, M. Woznica and A. Butkiewicz. Some Inherently Chiral Chromophores—Empirical Rules and Quantum Chemical Calculations. In: N. Berova, P. L.

Polavarapu, K. Nakanishi and R. W. Woody eds, Comprehensive Chiroptical Spectroscopy. Hoboken, New Jersey: John Wiley & Sons; **2012**: 37-72

106. Reinhardt, J. K., A. M. Klemd, O. Danton, M. De Mieri, M. Smiesko, R. Huber, T. Burgi, C. Grundemann and M. Hamburger. Sesquiterpene lactones from *Artemisia argyi*: Absolute configuration and immunosuppressant activity. **J. Nat. Prod. 2019**; 82: 1424-1433

107. Moscowitz, A., E. Charney, U. Weiss and H. Ziffer. Optical activity in skewed dienes. **J. Am. Chem. Soc. 1961**; 83: 4661-4663

108. Moriarty, R. M., H. E. Paaren, U. Weiss and W. B. Whalley. A quadrant rule for the prediction of chiroptical effects of optically active homoannular cisoid dienes. **J. Am. Chem. Soc. 1979**; 101: 6804-6810

109. Snatzke, G. Circulardichroismus-VIII Modifizierung der Octandenregel für α,β-ungesättigte Ketone: Theorie. **Tetrahedron 1965**; 21: 413-419

110. Smith, H. E. Chiroptical Properties of the Benzene Chromophore. A Method for the Determination of the Absolute Configurations of Benzene Compounds by Application of the Benzene Sector and Benzene Chirality Rules. **Chem. Rev. 1998**; 98: 1709-1740

111. Snatzke, G. Circular Dichroism and Absolute Conformation: Application of Qualitative MO Theory to Chiroptical Phenomena. **Angewandte Chemie, International Edition in English 1979**; 18: 363-377

112. Schrödinger, E. An Undulatory Theory of the Mechanics of Atoms and Molecules. **Phys. Rev. 1926**; 28: 1049-1070

113. Parr, R. G., D. P. Craig and I. G. Ross. Molecular Orbital Calculations of the Lower Excited Electronic Levels of Benzene, Configuration Interaction Included. **J. Chem. Phys. 1950**; 18: 1561-1563

114. Frisch, M. J., G. W. Trucks, H. B. Schlegel, G. E. Scuseria, M. A. Robb, J. R. Cheeseman, G. Scalmani, V. Barone, B. Mennucci, G. A. Petersson, H. Nakatsuji, M. Caricato, X. H. Li, H. P., A. F. Izmaylov, J. Z. Bloino, G., J. L. Sonnenberg, M. Hada, M. Ehara, K. Toyota, R. Fukuda, J. Hasegawa, M. Ishida, T. Nakajima, Y. Honda, O. Kitao, H. Nakai, T. Vreven, J. A. Montgomery, Jr., J. E. Peralta, F. Ogliaro, M. J. Bearpark, J. Heyd, E. N. Brothers, K. N. Kudin, V. N. Staroverov, R. Kobayashi, J. Normand, K. Raghavachari, A. P. Rendell, J. C. Burant, S. S. Iyengar, J. Tomasi, M. Cossi, N. Rega, N. J. Millam, M. Klene, J. E. Knox, J. B. Cross, V. Bakken, C. Adamo, J. Jaramillo, R. Gomperts, R. E. Stratmann, O. Yazyev, A. J. Austin, R. Cammi, C. Pomelli, J. W. Ochterski, R. L. Martin, K. Morokuma, V. G. Zakrzewski, G. A. Voth, P. Salvador, J. J. Dannenberg, S. Dapprich, A. D. Daniels, O. Farkas, J. B. Foresman, J. V. Ortiz, J. Cioslowski and D. J. Fox. Gaussian 09. In. Wallingfort, CT, USA: Gaussian, Inc.; **2009**

115. Pescitelli, G. and T. Bruhn. Good Computational Practice in the Assignment of Absolute Configurations by TDDFT Calculations of ECD Spectra. **Chirality 2016**; 28: 466-474

116. Nafie, L. A. Vibrational optical activity: From discovery and development to future challenges. **Chirality 2020**; 32: 667-692

117. Schellman, J. A. Vibrational optical activity. **J. Chem. Phys. 1973**; 58: 2882

118. Holzwarth, G., E. C. Hsu, H. S. Mosher, T. R. Faulkner and A. Moscowitz. Infrared circular dichroism of carbon-hydrogen and carbon-deuterium stretching modes. Observations. **J. Am. Chem. Soc. 1974**; 96: 251-252

119. Nafie, L. A., T. A. Keiderling and P. J. Stephens. Vibrational circular dichroism. **J. Am. Chem. Soc. 1976**; 98: 2715-2723

120. Joseph-Nathan, P. and B. Gordillo-Román. Vibrational Circular Dichroism Absolute Configuration Determination of Natural Products. In: A. D. Kinghorn, H. Falk and J. Kobayashi eds, Progress in the Chemistry of Organic Natural Products 100. Cham: Springer International Publishing; **2015**: 311-452

121. Nafie, L. A. and T. B. Freedman. Vibronic coupling theory of infrared vibrational transitions. **J. Chem. Phys. 1983**; 78: 7108-7116

122. Stephens, P. J. Theory of vibrational circular dichroism. **J. Phys. Chem. 1985**; 89: 748-752

123. Nafie, L. A., M. Diem and D. W. Vidrine. Fourier transform infrared vibrational circular dichroism. **J. Am. Chem. Soc. 1979**; 101: 496-498

124. Magyarfalvi, G., G. Tarczay and E. Vass. Vibrational circular dichroism. **Wiley Interdiscip. Rev.-Comput. Mol. Sci. 2011**; 1: 403-425

125. Nafie, L. A. Electron Transition Current Density in Molecules. 1. Non-Born−Oppenheimer Theory of Vibronic and Vibrational Transitions. **J. Phys. Chem. A 1997**; 101: 7826-7833

126. Fusè, M., F. Egidi and J. Bloino. Vibrational circular dichroism under the quantum magnifying glass: from the electronic flow to the spectroscopic observable. **Phys. Chem. Chem. Phys. 2019**; 21: 4224-4239

127. Stephens, P. J., F. J. Devlin, C. F. Chabalowski and M. J. Frisch. Ab Initio Calculation of Vibrational Absorption and Circular Dichroism Spectra Using Density Functional Force Fields. **J. Phys. Chem. 1994**; 98: 11623-11627

128. Covington, C. L. and P. L. Polavarapu. CDSpecTech: A single software suite for multiple chiroptical spectroscopic analyses. **Chirality 2017**; 29: 178-192

129. Polavarapu, P. L. and C. L. Covington. Comparison of experimental and calculated chiroptical spectra for chiral molecular structure determination. **Chirality 2014**; 26: 539-552

130. Schmid, G. and W. Hofheinz. Total synthesis of qinghaosu. **J. Am. Chem. Soc. 1983**; 105: 624-625

131. Veitch, G. E., E. Beckmann, B. J. Burke, A. Boyer, S. L. Maslen and S. V. Ley. Synthesis of Azadirachtin: A Long but Successful Journey. **2007**; 46: 7629-7632

132. Ball, P. Chemistry: Why synthesize? **2015**; 528: 327-329

133. Green, M. E., J. C. Rech and P. E. Floreancig. Stereochemical Assignment of the C1−C6 Fragment of Psymberin by Synthesis and Natural Product Degradation. **Org. Lett. 2005**; 7: 4117-4120

134. Shibuya, H., Y. Takeda, R.-s. Zhang, A. Tanitame, Y.-L. Tsai and I. Kitagawa. Indonesian Medicinal Plants. IV. On the Constituents of the Bark of *Fagara rhetza* (Rutaceae). (2). Lignan Glycosides and Two Apioglucosides. **Chem. Pharm. Bull. (Tokyo) 1992**; 40: 2639-2346

135. Poznanski, A. (**2014**). "Visual Revolution of the Vanishing of Ethan Carter." The Astronauts Retrieved 16.02.2020, 2020, from http://www.theastronauts.com/2014/03/visual-revolution-vanishing-ethan-carter/.

136. Bragg, W. H. and W. L. Bragg. The reflection of X-rays by crystals. **Proceedings of the Royal Society of London. Series A, Containing Papers of a Mathematical and Physical Character 1913**; 88: 428-438

137. Taylor, G. The phase problem. **Acta Crystallogr. Sect. D. Biol. Crystallogr. 2003**; 59: 1881-1890

138. Cowtan, K. Phase Problem in X-ray Crystallography, and Its Solution. In, eLS; **2003**

139. Dale, J. A. and H. S. Mosher. Nuclear magnetic resonance enantiomer regents. Configurational correlations via nuclear magnetic resonance chemical shifts of diastereomeric mandelate, O-methylmandelate, and .alpha.-methoxy-.alpha.-trifluoromethylphenylacetate (MTPA) esters. **J. Am. Chem. Soc. 1973**; 95: 512-519

140. Ohtani, I., T. Kusumi, Y. Kashman and H. Kakisawa. High-Field FT NMR Application of Mosher's Method. The Absolute Configurations of Marine Terpenoids. **J. Am. Chem. Soc. 1990**; 113: 4092-4096

141. Haigh, C. W. and R. B. Mallion. Ring current theories in nuclear magnetic resonance. **Prog. Nucl. Magn. Reson. Spectrosc. 1979**; 13: 303-344

142. Wannere, C. S. and P. v. R. Schleyer. How Do Ring Currents Affect 1H NMR Chemical Shifts? **Org. Lett. 2003**; 5: 605-608

143. Hoye, T. R., C. S. Jeffrey and F. Shao. Mosher ester analysis for the determination of absolute configuration of stereogenic (chiral) carbinol carbons. **Nat. Protoc. 2007**; 2: 2451-2458

144. Kirschning, A. and F. Hahn. Merging Chemical Synthesis and Biosynthesis: A New Chapter in the Total Synthesis of Natural Products and Natural Product Libraries. **2012**; 51: 4012-4022

145. Harris, K. D. M. and M. Tremayne. Crystal Structure Determination from Powder Diffraction Data. **Chem. Mater. 1996**; 8: 2554-2570

146. Pan, Z., E. Y. Cheung, K. D. M. Harris, E. C. Constable and C. E. Housecroft. A Case Study in Direct-Space Structure Determination from Powder X-ray Diffraction Data: Finding the Hydrate Structure of an Organic Molecule with Significant Conformational Flexibility. **Cryst. Growth Des. 2005**; 5: 2084-2090
147. Thangadurai, S., J. T. Abraham, A. K. Srivastava, M. Nataraja Moorthy, S. K. Shukla and Y. Anjaneyulu. X-Ray Powder Diffraction Patterns for Certain .BETA.-Lactam, Tetracycline and Macrolide Antibiotic Drugs. **Anal. Sci. 2005**; 21: 833-838
148. Trost, B. M., J. L. Belletire, S. Godleski, P. G. McDougal, J. M. Balkovec, J. J. Baldwin, M. E. Christy, G. S. Ponticello, S. L. Varga and J. P. Springer. On the use of the O-methylmandelate ester for establishment of absolute configuration of secondary alcohols. **J. Org. Chem 1986**; 51: 2370-2374
149. Latypov, S. K., J. M. Seco, E. Quinoa and R. Riguera. Conformational Structure and Dynamics of Arylmethoxyacetates: DNMR Spectroscopy and Aromatic Shielding Effect. **J. Org. Chem 1995**; 60: 504-515
150. Herwig, P., K. Zawatzky, M. Grieser, O. Heber, B. Jordon-Thaden, C. Krantz, O. Novotny, R. Repnow, V. Schurig, D. Schwalm, Z. Vager, A. Wolf, O. Trapp and H. Kreckel. Imaging the Absolute Configuration of a Chiral Epoxide in the Gas Phase. **Science 2013**; 342: 1084-1086

2.3. Artemisia argyi

2.3.1. Traditional uses

Artemisia argyi, commonly known as “wormwood” or “Chinese mugwort”, is found in China, Korea and neighboring countries.[151] It is commercially grown in China with a long history in Quichun County (Hubei Province), from which its name (*Qi ai)* in Traditional Chinese Medicine (TCM) is derived. The herb or the leaves are used in TCM for various indications including abnormal menstruation, hematemesis, pregnancy bleeding, chronic bronchitis, bronchial asthma.[152] The triturated leaves are called “moxa” and are used for “moxibustion”. For moxibustion therapy, the drug is burnt in the form of cones or “cigars”. This is done on, or close to, the skin to warm acupoints treating a wide range of illnesses.[153, 154] Also, essential oils from the plant are used for different therapeutic applications, especially in the treatment of respiratory diseases.[153, 155]

2.3.2. Bioactivity

Bioactivities of *A. argyi* have been studied extensively in the past. Numerous studies have been published in Chinese journals describing effects of *A. argyi* extracts, preparations and applications. Examples are an *in vivo* study of preparations from *A. argyi* against chronic renal failure[156] and studies on the effects of moxibustion on rheumatoid arthritis or immune modulation in rats.[157, 158] Adjacent research on *A. argyi* addresses topics like constituents found in endophytic fungi from its roots[159] or the study of different bioactive water-soluble polysaccharides isolated from A. argyi.[160-162] Thus, to limit the scope of this work to a reasonable size, only studies in English dealing with extracts of or compounds isolated from *A. argyi* have been included.

The least common reports of activities from *A. argyi* are an **insecticidal activity** of the EtOH extract[163] and **antimicrobial activity** of its essential oils.[164] More commonly, **antineoplastic effects** were observed for *A. argyi* in several instances. This was found to be mediated through NF-κB inhibition and cytotoxicity in human gastric adenocarcinoma cells by an extract with 70% EtOH. From this, several active guaianolide sesquiterpene lactones were isolated.[165] In another study, inhibition of CCRF-CEM leukemia cells was reported. The active constituents scopoletin und isoscopoletin also inhibit a multi-drug resistant sub line of leukemia cells. This indicates a significantly different mechanism compared to established cytostatic drugs like doxorubicin or vincristine.[166] For Human Papillomavirus (HPV) 16, an inhibition of the oncoproteins E6 and E7 by an *A. argyi* MeOH extract is reported, which is attributed to jaceosidin as the active constituent.[167]

Anti-inflammatory activity in different settings is the most frequently mentioned activity of *A. argyi* extracts. Two studies used extracts with 70% EtOH, which were orally administered to mice or rats *in vivo*. Both found reduced inhibition markers, one in sensitized skin on mice, and the other in the gastric mucosa of rats.[168, 169] Another study found reduced inflammation after oral application of a MeOH extract in ovalbumin-induced asthmatic mice.[170] The essential oil from *A. argyi* was described to suppress an inflammatory response *in vitro* in LPS-induced RAW264.7 macrophages.[171]

The anti-inflammatory effect of the essential oil was found to be mediated by the inhibition of JAK/STAT1/3.[171] For extracts from *A. argyi*, activity was previously attributed to polyphenols as it was traced to enriched fractions.[172] However, only the flavone jaceosidin was described to inhibit nitric oxide (NO) production.[173] All other compounds isolated from *A. argyi* related to anti-inflammatory or immunosuppressant activities were sesquiterpene lactones or their dimers.[174] As mechanisms for these compounds, NF-κB inhibition and inhibition of NO production were described.[175-178, 165] With this large potential in mind, the goal of this work was to identify and characterize potential immunosuppressant lead compounds from an *A. argyi* extract.

2.3.3. Constituents of *Artemisia argyi*

The transcriptome of *A. argyi* has been sequenced and a wide range of genes involved in the synthesis of secondary metabolites was identified. From this study, the presence of several alkaloid classes, different flavonoids, phenolic compounds and a wide range of terpenoids could be expected.[179] To compare this to the published compounds from *A. argyi*, the following list of publications was compiled (Table 1).

Table 1. List of publications reporting compounds isolated from *A. argyi*. Compound classes are described only considering the scaffold. Most sesquiterpenes (guaianolides, eudesmanolides, germacranolides) are present as sesquiterpene lactones.

Reference	Described activity	Described compound "classes"	# of isolated Compounds	Extraction method
Adams, 2006[166]	Inhibition of CCRF-CEM leukaemia cells	Coumarins	2	Dried leaves, EtOAc extract
Chemesova, 1990[180]	-	Flavones	3	Dried aerial parts, 70% EtOH extract
Kim, 2019[181]	Protection against contrast-induced cytotoxicity by iodixanol in LLC-PK1 cells	Coumarins Phenylpropanes Phenolic acids Indole alkaloid	14	Dried leaves, MeOH extract
Lao, 1984[182]	-	Triterpenes Phenolic acids Fatty acid ethyl esters	12 (1 new)	Dried plants, MeOH extract
Lee, 2002[183]	Farnesyl transferase inhibition	Guaianolide dimers	7 (5 new)	Dried leaves, MeOH extract
Lee, 2018[184]	Protection against contrast-induced cytotoxicity by iodixanol in LLC-PK1 cells	Flavonoids	19	Dried leaves, MeOH extract
LV, 2013[185]	Antioxidants	Caffeic acid esters	3 (1 new)	Dried leaves, 80% EtOH extract
Lv, 2018[186]	Anticoagulation	Flavone Flavone glycoside	2 new	Dried leaves, 95%

Reference	Described activity	Described compound "classes"	# of isolated Compounds	Extraction method
				EtOH extract
Nakasugi, 2000[187]	Antimutagenicity	Flavones	11	Dried leaves, MeOH extract
Reinhardt, 2019[106]	T cell proliferation inhibition NF-κB inhibition NFAT inhibition	(seco-)Guaianolides Eudesmanolides Guaianolide dimers Flavones	18 (5 new)	Dried aerial parts, EtOAc extract
Seo, 2003[188]	Farnesyl transferase inhibition	Flavones	6	Dried aerial parts, MeOH extract
Song, 2014[189]	-	Norneolignan Coumarines Phenolic compounds	6 (1 new)	Dried leaves, 80% EtOH extract
SUN, 2020[165]	Human gastric adenocarcinoma inhibition NF-κB inhibition	Guaianolides Moniterpene δ-lactone	12 (6 new)	Dried leaves, 70% EtOH extract
Wang, 2013[175]	nitric oxide (NO) inhibitory activity in BV-2 microglial cells	unusual guaianolide fused with eudesmane Guaianolide/monoterpene heterodimer	2 new	Dried leaves, 95% EtOH extract
Wang, 2014[176]	nitric oxide (NO) inhibitory activity in BV-2 microglial cells Cytotoxicity	Guaianolides Eudesmanolides	19 (10 new)	Dried leaves, 95% EtOH extract
Xue, 2017[190]	Cytotoxicity	*Diseco*-guaianolide heterodimers	4 new	Dried leaves, CH_2Cl_2 extract
Xue, 2019[177]	NO inhibitory activity in RAW 264.7 cells	Guaianolides Eudesmanolides Germacranolides	6 (2 new)	Dried leaves, CH_2Cl_2 extract

Reference	Described activity	Described compound "classes"	# of isolated Compounds	Extraction method
Xue, 2019[178]	NO inhibitory activity in RAW 264.7 cells	*Seco*-guaianolides *Seco*-guaianolide (hetero)dimers Guaianolide	10 (4 new)	Dried leaves, CH_2Cl_2 extract
Yoshikawa, 1996[191]	Vasorelaxant effect	Unusual Sesquiterpenes Guaianolides Triterpenes Octadecadienoic acids *trans*-o-Coumaric acid Coumarin (scopoletin) Flavonoids	16 (5 new)	Moxa/Dried leaves, MeOH extract
Yusupov, 1985[192]	-	Guaianolides Germacranolides	5	Flower heads/Dried leaves, $CHCl_3$ extract
Yusupov, 1991[193]	-	Guaianolide	1 new	Flower heads/Dried leaves, $CHCl_3$ extract
Zhang, 2019[194]	COX inhibition	Sesquiterpene lactone dimer Terpene trimer Guaianolides Germacranolides Eudesmanolides	12 (4 new)	Dried leaves, 95% EtOH extract
Zhang, 2019[195]	Cytotoxicity	Guaianolides Eudesmanolides (7-8 lactonized)	6 (3 new)	Dried leaves, EtOAc extract
Zhang, 2020[196]	α-glycosidase inhibition	Triterpenes	4 (2 new)	Dried leaves, 95% EtOH extract
Zhang, 2020[174]	Anti-inflammatory NF-κB inhibition	Eudesmanolides	1 new	Dried leaves, 95% EtOH extract

From this, the most common compound classes found in *A. argyi* are flavonoids and sesquiterpenes. Most isolated sesquiterpenes are either guaiane- or eudesmane-type sesquiterpene lactones. As monoterpenes define much of its olfactory impression, they are almost exclusively found in the essential oil of *A. argyi*.[197] The only exception to this is the presence of some monoterpenes fused with one or two guaiane-type sesquiterpene lactones resulting in the unusual structures of isoartemisolide[175] and artemargyinolide A[194] (Figure 20).

Other unusual structures originate from aldol condensations of guaiane-type sesquiterpene lactones with *diseco*-guaianolides (artemisianes A-D).[190] In addition, sesquiterpene lactone dimers connected by an ester bond are found. These exist as combination of guaianolides with eudesmanolides (artemillinin A),[175] guaianolides with *seco*-guaianolides (artemisiane A)[178], and *diseco*- with *seco*-guaianolides (artemisiane C).[178] Examples of different terpene (hetero-)dimers isolated from *A. argyi* are shown in Figure 20. A close to comprehensive review of natural disesquiterpenoids was done recently by Ying-Hong Ma and coworkers.[198]

When comparing this list to the transcriptome,[179] the overall dominance of terpenoid structures in *A. argyi* is no surprise. Triterpenes, coumarins, phenylpropanoids, and flavonoids are expected to be found. However, compared to the transcriptome alkaloids are underrepresented among the isolated compounds. Only one simple indole alkaloid (1-H-indole-3-carboxylic acid) is described so far even though genes for the synthesis of isoquinoline, tropane, piperidine and pyridine alkaloids are present in the transcriptome of *A. argyi*. In any case, the broad diversity of terpenes forms a vast reservoir of potential lead compounds.

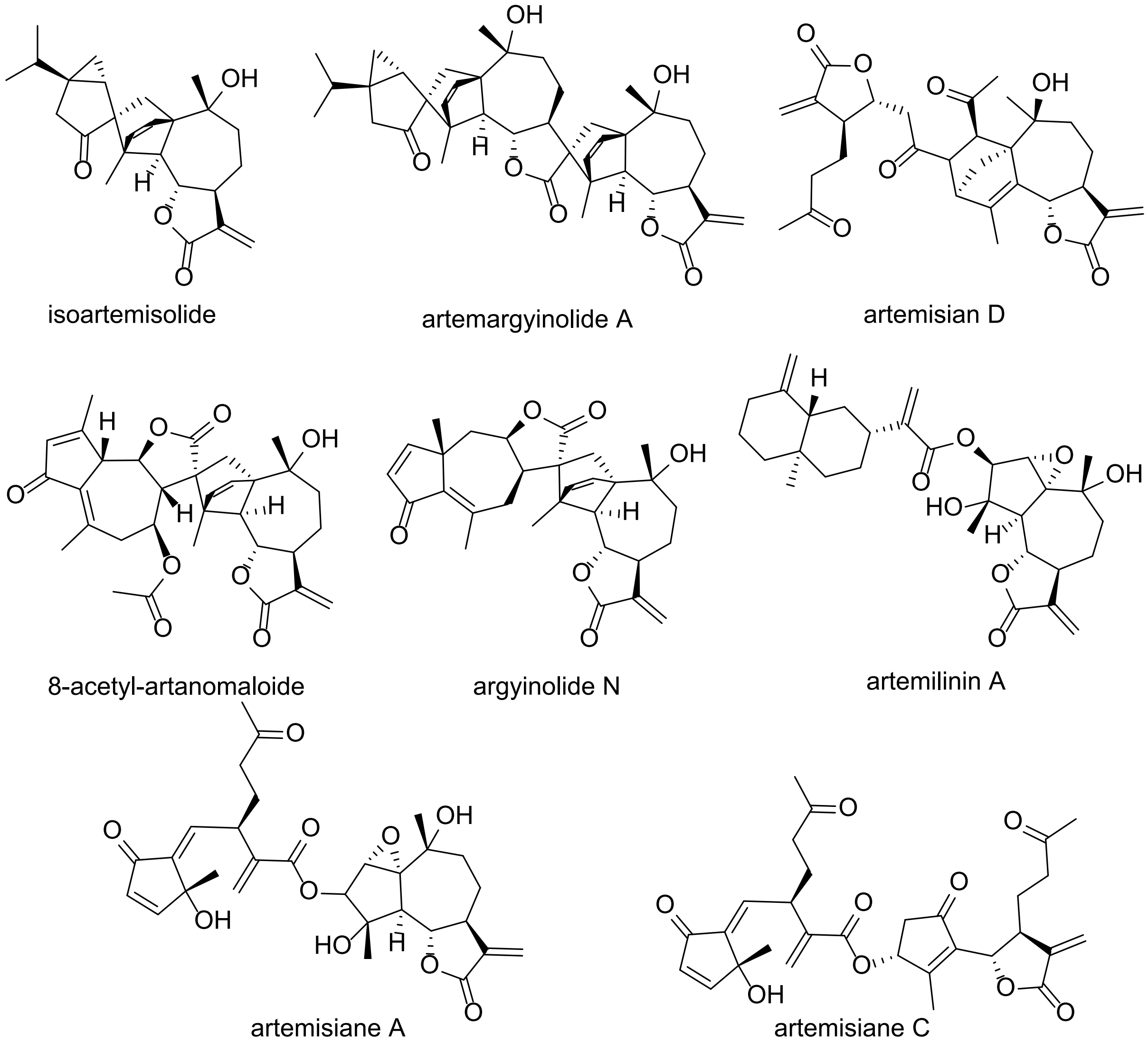
isoartemisolide
artemargyinolide A
artemisian D
8-acetyl-artanomaloide
argyinolide N
artemilinin A
artemisiane A
artemisiane C

Figure 20. Examples of fused sesquiterpene lactones isolated from *A. argyi*.

2.3.4. Absolute configurations of sesquiterpene lactones

Sesquiterpene lactones are so far the most frequently isolated compounds from *A. argyi*. The complexity and diversity of their structures features them as a worthwhile group of compounds to work on.[199] Most sesquiterpene lactones contain multiple stereogenic centers, in case of artemargyinolide A, up to 15.[194] This warrants suitable strategies for resolving the configuration of these molecules.

Relative Configuration

Most sesquiterpene lactones from *A. argyi* belong to groups (A) or (B) (Figure 11) as the ring structure of guaiane- or eudesmane-type sequiterpene lactones provides a relatively rigid scaffold to identify the relative positions of most protons using NMR.

Absolute configuration

For the identification of absolute configurations of sesquiterpene lactones from *A. argyi* ECD is commonly used.[176, 178, 195] This leads to the proposal of empirical rules for many cases of smaller compounds earlier.[200] Nowadays, the experimental ECD spectra are usually compared to *ab initio* calculated spectra of possible stereoisomers, for example calculated with the B3LYP functional in combination with either 6-31G or 6-311G as basis set.[175, 176, 190, 106, 177, 178, 195, 165] This procedure works in the case of group (A) and in the case of group (B), if the non-defined stereogenic centers do not affect the chromophore. Thus, for group (B), all possible diastereomers need to be calculated. This way, the influence of the stereogenic centers in question can be determined.

Most chromophores present in sesquiterpene lactones are trans-enones. Thus, only two transitions, a medium $\pi \rightarrow \pi^*$ transition around 250 nm as well as a weak $n \rightarrow \pi^*$-transition around 330 nm, are available for interpretation. With CD in the UV region (190 – 600 nm), this usually permits the distinction of enantiomers but not the differentiation between a multitude of possible stereoisomers. If enough material (ca. 3 mg) is available, VCD can be used on sesquiterpene lactones with good chances of success.

In conclusion, circular dichroism is very useful for the assignment of absolute configurations to sesquiterpene lactones. The rigidity of most ring systems allows a reliable calculation of *ab initio* spectra for comparison to experimental data. This is true for ECD as well as for VCD. However, both methods need to be applied with caution to avoid misassignments. But, especially in combination, even difficult cases can be solved.

References

106. Reinhardt, J. K., A. M. Klemd, O. Danton, M. De Mieri, M. Smiesko, R. Huber, T. Burgi, C. Grundemann and M. Hamburger. Sesquiterpene lactones from *Artemisia argyi*: Absolute configuration and immunosuppressant activity. **J. Nat. Prod. 2019**; 82: 1424-1433

151. (**2020**). Retrieved 13.03.2020, 2020, from http://www.agroatlas.ru/en/content/weeds/Artemisia_argyi/.

152. Liu, D., Y. Chen, X. Wan, N. Shi, L. Huang and D. Wan. *Artemisiae argyi* Folium and its geo-authentic crude drug *qi ai*. **J. Tradit. Chin. Med. 2017**; 4: 20-23

153. Tang, W. and G. Eisenbrand. Handbook of Chinese medicinal plants. Weinheim: Wiley-VCH **2011**

154. Adams, J. D., C. Garcia and G. Garg. Mugwort (*Artemisia vulgaris , Artemisia douglasiana , Artemisia argyi*) in the Treatment of Menopause, Premenstrual Syndrome, Dysmenorrhea and Attention Deficit Hyperactivity Disorder. **Chin. Med. 2012**; 3: 116-123

155. Abad, M. J., L. M. Bedoya, L. Apaza and P. Bermejo. The Artemisia L. Genus: A Review of Bioactive Essential Oils. **Molecules 2012**; 17: 2542-2566

156. Chen, F., T. Zou and F. Qin. Effect of Kangshen granule on kidney function and micro-inflammation state in patients with non-dialysis chronic renal failure. **Shiyong Linchuang Yiyao Zazhi 2015**; 19: 103-105

157. Wei, K., D. Zhang, C. Dou, X. Ma, L. Yang, H.-g. Wu, J. Hong, Y. Zhu, C. Zhang, J. Liu, L. Wu and Y. Huang. Study on the regulating effect of moxibustion on NF-κB p65, TNF-α, and IL-1β in colons of CD rats. **Shijie Zhongyiyao 2013**; 8: 862-866, 870

158. Zheng, B.-z., L. Hu, X.-g. Song, L. He, Z.-j. Wu, R.-l. Cai, C. Zhang, F. Zhou and J. Yao. Effects of moxibustion on expressions of hypothalamic POMC and PDYN mRNA in rats with rheumatoid arthritis. **Zhongguo Zhenjiu 2013**; 33: 433-437

159. Shi, X.-S., H.-L. Li, X.-M. Li, D.-J. Wang, X. Li, L.-H. Meng, X.-W. Zhou and B.-G. Wang. Highly oxygenated polyketides produced by *Trichoderma koningiopsis* QA-3, an endophytic fungus obtained from the fresh roots of the medicinal plant *Artemisia argyi*. **Bioorg. Chem. 2020**; 94: 103448

160. Bao, X., H. Yuan, C. Wang, J. Liu and M. Lan. Antitumor and immunomodulatory activities of a polysaccharide from Artemisia argyi. **Carbohydr. Polym. 2013**; 98: 1236-1243

161. Zhang, P., B. Shi, T. Li, Y. Xu, X. Jin, X. Guo and S. Yan. Immunomodulatory effect of *Artemisia argyi* polysaccharide on peripheral blood leucocyte of broiler chickens. **Journal of Animal Physiology and Animal Nutrition 2018**; 102: 939-946

162. Tseng, C.-P., Y.-L. Huang, Y.-W. Chang, H.-R. Liao, Y.-L. Chen and P.-W. Hsieh. Polysaccharide-containing fraction from *Artemisia argyi* inhibits tumor cell-induced platelet aggregation by blocking interaction of podoplanin with C-type lectin-like receptor 2. **J. Food Drug Anal. 2020**; 28: 115-123

163. Ahmed, M., Q. Peiwen, Z. Gu, Y. Liu, A. Sikandar, D. Hussain, A. Javeed, J. Shafi, M. F. Iqbal, R. An, H. Guo, Y. Du, W. Wang, Y. Zhang and M. Ji. Insecticidal activity and biochemical composition of *Citrullus colocynthis*, *Cannabis indica* and *Artemisia argyi* extracts against cabbage aphid (*Brevicoryne brassicae* L.). **Sci. Rep. 2020**; 10:

164. Xiang, F., J. Bai, X. Tan, T. Chen, W. Yang and F. He. Antimicrobial activities and mechanism of the essential oil from *Artemisia argyi* Levl. et Van. var. argyi cv. Qiai. **Ind. Crops. Prod. 2018**; 125: 582-587

165. Sun, Y.-W., Y. Ju, C.-H. Liu, K.-C. Du and D.-L. Meng. Polyhydroxyl guaianolide terpenoids as potential NF-κB inhibitors induced cytotoxicity in human gastric adenocarcinoma cell line. **Bioorg. Chem. 2020**; 95: 103551

166. Adams, M., T. Efferth and R. Bauer. Activity-Guided Isolation of Scopoletin and Isoscopoletin, the Inhibitory Active Principles towards CCRF-CEM Leukaemia Cells and Multi-Drug Resistant CEM/ADR5000 Cells, from *Artemisia argyi*. **Planta Med 2006**; 72: 862-864

167. Lee, H.-G., K.-A. Yu, W.-K. Oh, T.-W. Baeg, H.-C. Oh, J.-S. Ahn, W.-C. Jang, J.-W. Kim, J.-S. Lim, Y.-K. Choe and D.-Y. Yoon. Inhibitory effect of jaceosidin isolated from *Artemisia argyi* on the function of E6 and E7 oncoproteins of HPV 16. **J. Ethnopharmacol. 2005**; 98: 339-343

168. Han, H. M., S. J. Kim, J. S. Kim, B. H. Kim, H. W. Lee, Y. T. Lee and K. H. Kang. Ameliorative effects of *Artemisia argyi* Folium extract on 2,4-dinitrochlorobenzene-induced atopic dermatitis-like lesions in BALB/c mice. **Mol. Med. Report. 2016**; 14: 3206-3214

169. Li, S., S. Zhou, W. Yang and D. Meng. Gastro-protective effect of edible plant *Artemisia argyi* in ethanol-induced rats via normalizing inflammatory responses and oxidative stress. **J. Ethnopharmacol. 2018**; 214: 207-217

170. Shin, N.-R., H.-W. Ryu, J.-W. Ko, S.-H. Park, H.-J. Yuk, H.-J. Kim, J.-C. Kim, S.-H. Jeong and I.-S. Shin. *Artemisia argyi* attenuates airway inflammation in ovalbumin-induced asthmatic animals. **J. Ethnopharmacol. 2017**; 209: 108-115

171. Chen, L.-L., H.-J. Zhang, J. Chao and J.-F. Liu. Essential oil of *Artemisia argyi* suppresses inflammatory responses by inhibiting JAK/STATs activation. **J. Ethnopharmacol. 2017**; 204: 107-117

172. Kim, S., S. Lee, V. Venkatarame Gowda Saralamma, S. Ha, P. Vetrivel, K. Desta, J. Choi, W. Lee, S. Shin and G. S. Kim. Polyphenol mixture of a native Korean variety of *Artemisia argyi* H. (Seomae mugwort) and its anti-inflammatory effects. **Int. J. Mol. Med. 2019**; 44: 1741-1752

173. Nam, Y., M. Choi, H. Hwang, M.-G. Lee, B.-M. Kwon, W.-H. Lee and K. Suk. Natural Flavone Jaceosidin is a Neuroinflammation Inhibitor. **Phytother. Res. 2013**; 27: 404-411

174. Zhang, L.-B., H.-H. Zhu, L.-M. Guo and J.-L. Lv. Artemargyinolide E, a new sesquiterpene lactone from *Artemisia argyi* inhibits inflammatory responses via down-regulating NF-κB signaling pathway. **Phytochem. Lett. 2020**; 36: 17-23

175. Wang, S., J. Li, J. Sun, K.-W. Zeng, J.-R. Cui, Y. Jiang and P.-F. Tu. NO inhibitory guaianolide-derived terpenoids from *Artemisia argyi*. **Fitoterapia 2013**; 85: 169-175

176. Wang, S., J. Sun, K. Zeng, X. Chen, W. Zhou, C. Zhang, H. Jin, Y. Jiang and P. Tu. Sesquiterpenes from *Artemisia argyi*: Absolute Configurations and Biological Activities. **European Journal of Organic Chemistry 2014**; 2014: 973-983

177. Xue, G.-M., J.-F. Xue, C.-G. Zhao, Z.-Z. Zhao, Y.-J. Sun, K. Du, H.-W. Li and W.-S. Feng. Sesquiterpenoids from *Artemisia argyi* and their NO production inhibitory activity in RAW264.7 cells. **Nat. Prod. Res. 2019**: 1-8

178. Xue, G.-M., D.-R. Zhu, T.-Y. Zhu, X.-B. Wang, J.-G. Luo and L.-Y. Kong. Lactone ring-opening seco-guaianolide involved heterodimers linked via an ester bond from *Artemisia argyi* with NO inhibitory activity. **Fitoterapia 2019**; 132: 94-100

179. Liu, M., J. Zhu, S. Wu, C. Wang, X. Guo, J. Wu and M. Zhou. De novo assembly and analysis of the *Artemisia argyi* transcriptome and identification of genes involved in terpenoid biosynthesis. **Sci. Rep. 2018**; 8:

180. Chemesova, I. I. and É. V. Boiko. Flavonoids of *Artemisia argyi*. **Chem. Nat. Compd. 1990**; 26: 713-713

181. Kim, K. O., D. Lee, N. T. Hiep, J. H. Song, H.-J. Lee, D. Lee and K. S. Kang. Protective Effect of Phenolic Compounds Isolated from Mugwort (*Artemisia argyi*) against Contrast-Induced Apoptosis in Kidney Epithelium Cell Line LLC-PK1. **Molecules 2019**; 24:

182. Lao, A., Y. Fujimoto and T. Tatsuno. Studies on the constituents of *Artemisia argyi* LEVL et VANT. **Chem. Pharm. Bull. (Tokyo) 1984**; 32: 723-727

183. Lee, S.-H., H.-K. Kim, J.-M. Seo, H.-M. Kang, J. H. Kim, K.-H. Son, H. Lee, B.-M. Kwon, J. Shin and Y. Seo. Arteminolides B, C, and D, New Inhibitors of Farnesyl Protein Transferase from *Artemisia argyi*. **J. Org. Chem 2002**; 67: 7670-7675

184. Lee, D., C.-E. Kim, S.-Y. Park, K. Kim, N. Hiep, D. Lee, H.-J. Jang, J. Lee and K. Kang. Protective Effect of *Artemisia argyi* and Its Flavonoid Constituents against Contrast-Induced Cytotoxicity by Iodixanol in LLC-PK1 Cells. **Int. J. Mol. Sci. 2018**; 19: 1387

185. Lv, J.-L., J.-A. Duan, B. Shen and Y.-Y. Yin. Caffeic Acid Esters from *Artemisia argyi* and their Antioxidant Activities. **Chem. Nat. Compd. 2013**; 49: 8-11
186. Lv, J.-L., Z.-Z. Li and L.-B. Zhang. Two new flavonoids from *Artemisia argyi* with their anticoagulation activities. **Nat. Prod. Res. 2017**; 32: 632-639
187. Nakasugi, T., M. Nakashima and K. Komai. Antimutagens in Gaiyou (*Artemisia argyi* Levl. et Vant.). **Journal of Agricultural and Food Chemistry 2000**; 48: 3256-3266
188. Seo, J.-M., H.-M. Kang, K.-H. Son, J. H. Kim, C. W. Lee, H. M. Kim, S.-I. Chang and B.-M. Kwon. Antitumor Activity of Flavones Isolated from *Artemisia argyi*. **Planta Med. 2003**; 69: 218-222
189. Song, C., Y.-Q. Li, Y.-M. Yan, M. Hu and Q.-Z. Zhang. A new Norneolignan from the Leaves of the Traditional Chinese Medicine *Artemisia argyi*. **Chem. Nat. Compd. 2014**; 50: 414-416
190. Xue, G.-M., C. Han, C. Chen, L.-N. Li, X.-B. Wang, M.-H. Yang, Y.-C. Gu, J.-G. Luo and L.-Y. Kong. Artemisians A–D, Diseco-guaianolide Involved Heterodimeric [4 + 2] Adducts from *Artemisia argyi*. **Org. Lett. 2017**; 19: 5410-5413
191. Yoshikawa, M., H. Shimada, H. Matsuda, J. Yamahara and N. Murakami. Bioactive Constituents of Chinese Natural Medicines. I. New Sesquiterpene Ketones with Vasorelaxant Effect from Chinese Moxa, the Processed Leaves of *Artemisia argyi* LEVL. et VANT.: Moxartenone and Moxartenolid. **Chem. Pharm. Bull. (Tokyo) 1996**; 44: 1656-1662
192. Yusupov, M. I., S. Z. Kasymov, G. P. Sidyakin and E. V. Boiko. Lactones of *Artemisia argyi*. **Chem. Nat. Compd. 1985**; 21: 379-380
193. Yusupov, M. I., S. K. Zakirov, I. D. Sham'Yanov, V. M. Malikov and A. Abdusamatov. 11,13-Dihydroarteglasin A - A new guaianolide from *Artemisia argyi*. **Chem. Nat. Compd. 1991**; 26: 473-474
194. Zhang, L.-B. and J.-L. Lv. Sesquiterpenoids from *Artemisia argyi* and their COXs inhibitory activities. **Fitoterapia 2019**; 139: 104372
195. Zhang, L., Y.-M. Yan, S.-X. Wang, Z. Ren and Y.-X. Cheng. Three new sesquiterpenoids with cytotoxic activity from Artemisia argyi. **Nat. Prod. Res. 2019**:
196. Zhang, L.-B., J.-J. Chang, L.-M. Guo and J.-L. Lv. Triterpenoids with α-glucosidase inhibitory activity from *Artemisia argyi*. **J. Asian Nat. Prod. Res. 2020**; 22: 241-248
197. Huang, H.-C., H.-F. Wang, K.-H. Yih, L.-Z. Chang and T.-M. Chang. Dual Bioactivities of Essential Oil Extracted from the Leaves of *Artemisia argyi* as an Antimelanogenic versus Antioxidant Agent and Chemical Composition Analysis by GC/MS. **Int. J. Mol. Sci. 2012**; 13: 14679-14697
198. Ma, Y.-H., X.-X. Dou and X.-H. Tian. Natural disesquiterpenoids: an overview of their chemical structures, pharmacological activities, and biosynthetic pathways. **Phytochem. Rev. 2020**:
199. Abad Martínez, M. J., L. M. B. Del Olmo, L. A. Ticona and P. B. Benito. The *Artemisia* L. Genus: A Review of Bioactive Sesquiterpene Lactones. In: Atta-ur-Rahman ed, Stud. Nat. Prod. Chem.: Elsevier; **2012**: 43-65
200. Stöcklin, W., T. G. Waddel and T. A. Geissmann. Circular dichroism and optical rotatory dispersion of sesquiterpene lactones. **Tetrahedron 1970**; 26: 2397-2410

2.4. Toddalia asiatica

2.4.1. Traditional uses

Toddalia asiatica is a plant distributed in most parts of Asia and Africa.[201] It is widely used in both African and Asian traditional medicine practice. Judging from a survey in Uganda, Tanzania and Kenya, all parts of the plant are used with the root bark being the most common. Most often, it is used against stomach problems, followed by malaria and coughs as indications.[202] Surveys in Kenya and Zimbabwe corroborate the use of *T. asiatica* as traditional treatment for malaria.[203, 204] These and more indications have been described for the use in Indian Traditional Medicine.[205] In TCM, the roots of *T. asiatica* are known under the name "Fei Long Zhang Xue", but are not commonly used.[206]

2.4.2. Bioactivity

Although the treatment of stomach problems is common in practice, most available studies focus on **antiplasmodial or antimalarial activity**. Several screenings among traditionally used plants for antiplasmodial activity found *T. asiatica* extracts to be active *in vitro*.[207, 208] This was also confirmed in *in vivo* xenograft models.[209] Apart from that, **antidiabetic and antihyperlipidemic effects** of the leaf extract were observed *in vivo*.[210, 211] Also, analgesic and immunosuppressive effects were observed *in vivo*.[212, 213] Related to immunosuppression, effects on collagen-induced arthritis *in vivo* are described. [214] *In vitro*, spasmolytic activity is described in one study.[215] In the process of understanding these bioactivities, a range of compounds was isolated.

2.4.3. Constituents of Toddalia asiatica

Several studies into compounds from *T. asiatica* were performed. The results from an extensive literature survey are summarized in Table 2.

Table 2. List of publications reporting compounds isolated from *T. asiatica*. Compound classes are described only considering the scaffold.

Reference	Described activity	Described compound "classes"	# of isolated compounds	Extraction method
Sharma, 1980[216]	-	Coumarin Dimeric coumarins	2 (1 new)	Roots, 95% EtOH
Sharma, 1981[217]	-	Coumarins	5 (2 new)	Roots, 95% EtOH
Sharma, 1982[218]	-	benzophenanthridines triterpenes	7 (1 new)	Roots, 95% EtOH
Ishii, 1983[219]	-	coumarin	1	-
Ishii, 1991[220]	-	Coumarin-quinolone-dimer	1 new	Root bark
Ishii, 1992[221]	-	coumarins	5	Root bark
Chen, 1993[222]	-	benzoquinolines	1 new	Root bark, MeOH

Reference	Described activity	Described compound "classes"	# of isolated compounds	Extraction method
Ishii, 1993[223]	-	Coumarin dimer	1	
Gakunju, 1995[224]	Antimalarial activity	Benzophenanthrene (nitidine)	1	Root bark, CH_2Cl_2
Tsai, 1997[225]	-	Dimeric coumarin Cyclohexyl amides benzophenanthrenes	7 (3 new)	Roots, MeOH
Tsai, 1998[226]	Anti-platelet aggregation	Coumarins Alkaloids	30 (2 new)	Roots, MeOH
Oketch-Rabah, 2000[227]	Antiplasmodial	Coumarin	1	Roots, EtOAc
Iwasaki, 2006[228]	Tumor selective cytotoxicity	dihydronitidine	1	Stem, 50% EtOH
Iwasaki, 2010[229]	Tumor selective cytotoxicity	benzophenanthrenes	2	Stem, 50% EtOH
Karundai Raj, 2012[230]	antimicrobial	coumarins	2	Leaves, EtOAc[a]
Hu, 2014[231]	Cytotoxic, antimicrobial, antifungal	Diverse alkaloids	18 (8 new)	Roots, 80% EtOH
Lin, 2014[232]	Phosphodiesterase-4 inhibitors	Coumarins Coumarin dimers	21 (7 new)	Roots, 95% EtOH
Phatchana, 2014[233]	cytotoxicity	Coumarins Phenolics Coumarin dimer	16	Stem bark, EtOAc[b]
Watanabe, 2014[234]	Enhancement of Differentiation and lipolysis in adipocytes	coumarins	3	Stems, MeOH
Hu, 2015[235]	-	Amides	4 (3 new)	Root, 80% EtOH
Watanabe, 2015[236]	Inhibition of Osteoclastogenesis, enhancement of Osteoblastogenesis	coumarins	1	Stems, MeOH
Hirunwong, 2016[237]	Cytotoxicity antimalarial	Coumarins terpenealkaloid	18 (2 new)	Root, hexane[b]

Reference	Described activity	Described compound "classes"	# of isolated compounds	Extraction method
Li, 2017[238]	-	Coumarins phenolics	42 (9 new)	Stems, 95% EtOH
Kumagai, 2018[239]	Anti-inflammatory	Coumarins	2	Stems, MeOH
Sukieum, 2018[240]	cytotoxicity	Benzophenanthrenes coumarins	17	Root, EtOAC and MeOH

Concluding from this, coumarins are most often isolated from *T. asiatica* followed by benzophenthrene alkaloids. Typical are coumarins with a 5,7-methoxy substitution pattern as well as nitidine and related alkaloids.[229, 232] Nitidine was also concluded to be responsible, at least in part, for the antimalarial activity of *T. asiatica*.[241] Other alkaloids like 8-methoxynorchelerythrine and toddayanis were also found to have antimalarial effects.[237] Significantly lower activity has been observed for a coumarin from *T. asiatica*.[227] For the possible use of compounds from *T. asiatica*, the absolute configurations of the compounds are needed. While most isolated compounds from *T. asiatica* do not possess stereogenic centers, coumarins and glycosylated coumarins need to be studied in more detail.

2.4.4. Absolute configurations of glycosylated coumarins

The representative coumarin from *T. asiatica*, toddalolactone, has only one stereogenic center, which can be assigned using OR, ECD or NMR with Eu(hfc)$_3$.[221] For glycosylated coumarins, six stereogenic centers need to be addressed. Thus, further steps are required to determine the absolute configurations of glycosylated coumarins.

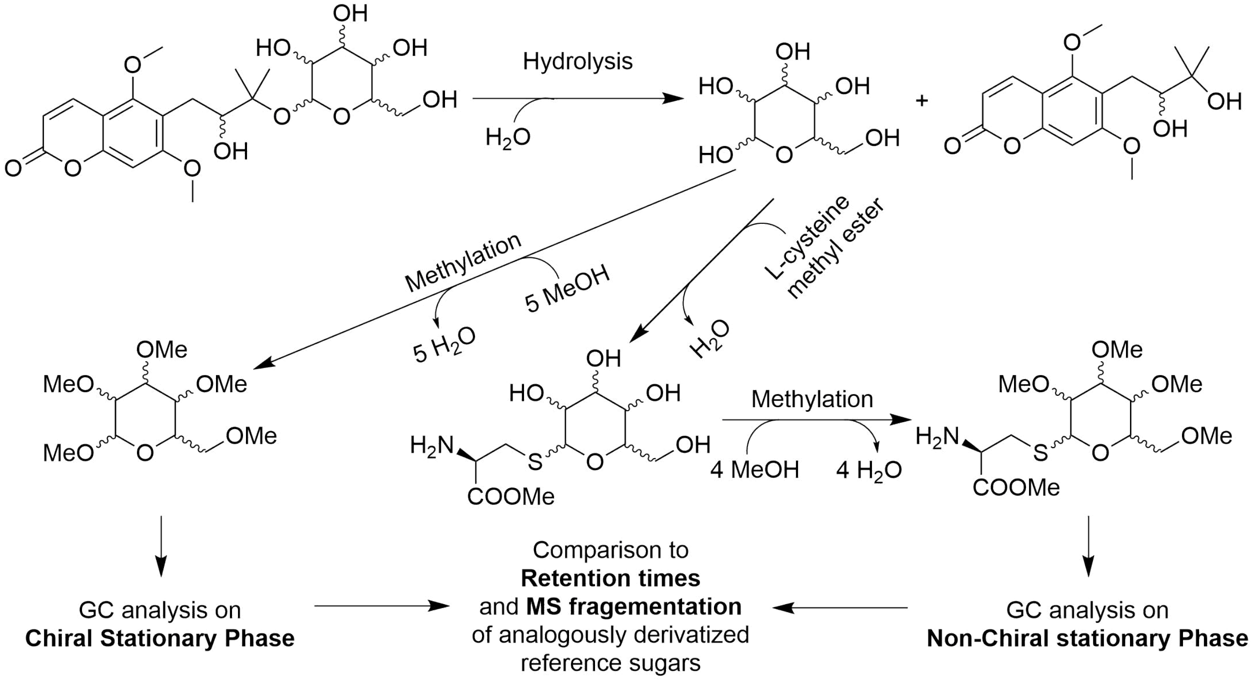

Figure 21. Scheme showing exemplary derivatization steps for GCMS analysis of a coumarin glycoside.

First, the identity of the sugar is determined. Using ^{13}C NMR and NOE data, the relative configuration of the sugar moiety can be determined in good confidence. Secondly, for an assignment of the sugar, GCMS can be used.[242] For this, a small amount of the compound is hydrolyzed and the sugars are obtained from the aqueous phase. Exemplary derivatization steps necessary for GCMS analysis of sugars are outlined in Figure 21. It is important to note that references of all possible sugars should be run with the same method as the sample. This way, false positive results from similar retention times can be avoided. The organic phase of the hydrolyzed sample can be used to identify the absolute configuration of the aglycone. It is however necessary to double check the resulting structure with NMR, as changes can occur through the hydrolysis conditions. If this is not the case, the absolute configuration can be determined through enantioselective HPLC, ECD, OR, or by using NMR with a shift reagent like $Eu(hfc)_3$.

Another option, as soon as the identity of the sugar is known, is *ab initio* calculation of NMR data for the full molecule as by then only diastereoisomers need to be distinguished. For this, all possible stereoisomers are calculated *ab initio* and the ^{13}C and ^{1}H NMR data is compared to the experimental data using the DP4 probability algorithm.[243] More recently, the precision of this method was improved and extended to the use of unscaled data resulting in the DP4+ probability algorithm.[244]

In conclusion, several suitable methods are well established to identify the absolute configurations of glycosylated coumarins. In the end, the choice depends mostly on the amount of compound available. Especially the spectroscopic analysis of the hydrolyzed aglycone is only feasible, if enough material can be spared.

References

201. (**2020**). "*Toddalia asiatica*, US National Plant Germplasm System." Retrieved 24.04.2020, 2020, from https://npgsweb.ars-grin.gov/gringlobal/taxonomydetail.aspx?36738.
202. Orwa, J. A., I. J. O. Jondiko, R. J. A. Minja and M. Bekunda. The use of Toddalia asiatica (L) Lam. (Rutaceae) in traditional medicine practice in East Africa. **J. Ethnopharmacol. 2008**; 115: 257-262
203. Katuura, E., P. Waako, J. Ogwal-Okeng and R. Bukenya-Ziraba. Traditional treatment of malaria in Mbarara District, western Uganda. **Afr. J. Ecol. 2007**; 45: 48-51
204. Ngarivhume, T., C. I. E. A. Van'T Klooster, J. T. V. M. De Jong and J. H. Van Der Westhuizen. Medicinal plants used by traditional healers for the treatment of malaria in the Chipinge district in Zimbabwe. **J. Ethnopharmacol. 2015**; 159: 224-237
205. Rajkumar, M., R. H. Chandra, K. Asres and C. Veeresham. *Toddalia asiatica* (Linn.) Lam.-A Comprehensive Review. **Pharmacogn Rev. 2008**; 2: 386-397
206. Zhou, J., G. Xie and X. Yan. Isolated Compounds (T-Z) References TCM Plants and Congeners: Springer Berlin Heidelberg; **2011**
207. Katuura, E., P. Waako, J. R. S. Tabuti, R. Bukenya-Ziraba and J. Ogwal-Okeng. Antiplasmodial activity of extracts of selected medicinal plants used by local communities in western Uganda for treatment of malaria. **Afr. J. Ecol. 2007**; 45: 94-98
208. Muregi, F. W., A. Ishih, T. Miyase, T. Suzuki, H. Kino, T. Amano, G. M. Mkoji and M. Terada. Antimalarial activity of methanolic extracts from plants used in Kenyan ethnomedicine and their interactions with chloroquine (CQ) against a CQ-tolerant rodent parasite, in mice. **J. Ethnopharmacol. 2007**; 111: 190-195
209. Orwa, J. A., L. Ngeny, N. M. Mwikwabe, J. Ondicho and I. J. O. Jondiko. Antimalarial and safety evaluation of extracts from *Toddalia asiatica* (L) Lam. (Rutaceae). **J. Ethnopharmacol. 2013**; 145: 587-590
210. Stephen Irudayaraj, S., C. Sunil, V. Duraipandiyan and S. Ignacimuthu. Antidiabetic and antioxidant activities of *Toddalia asiatica* (L.) Lam. leaves in Streptozotocin induced diabetic rats. **J. Ethnopharmacol. 2012**; 143: 515-523
211. Irudayaraj, S. S., C. Sunil, V. Duraipandiyan and S. Ignacimuthu. In vitro antioxidant and antihyperlipidemic activities of *Toddalia asiatica* (L) Lam. Leaves in Triton WR-1339 and high fat diet induced hyperlipidemic rats. **Food and Chemical Toxicology 2013**; 60: 135-140
212. Kariuki, H. N., T. I. Kanui, A. Yenesew, N. Patel and P. M. Mbugua. Antinocieptive and anti-inflammatory effects of *Toddalia asiatica* (L) Lam. (Rutaceae) root extract in Swiss albino mice. **Pan. Afr. Med. J. 2013**; 14: 133-133
213. Kimang'A, A., J. Gikunju, D. Kariuki and M. Ogutu. Safety and analgesic properties of ethanolic extracts of *Toddalia asiatica* (L) Lam. (rutaceae) used for central and peripheral pain management among the east african ethnic communities. **Ethiop. J. Health Sci. 2016**; 26: 55
214. Yang, K., L. Tong, C. Chen, P. Zhang, H. Pi, H. Ruan and J. Wu. Therapeutic effects of extracts from Radix *Toddaliae* Asiaticae on collagen-induced arthritis in Balb/c mice. **J. Ethnopharmacol. 2013**; 146: 355-362
215. Lakshmi, V., S. Kapoor, K. Pandey and G. K. Patnaik. Spasmolytic activity of *Toddalia asiatica* var. Floribunda. **Phytother. Res. 2002**; 16: 281-282
216. Sharma, P. N., A. Shoeb, R. S. Kapil and S. P. Popli. Toddasin, a new dimeric coumarin from *Toddalia asiatica*. **Phytochemistry 1980**; 19: 1258-1260
217. Sharma, P. N., A. Shoeb, R. S. Kapil and S. P. Popli. Toddanol and toddanone, two coumarins from *Toddalia asiatica*. **Phytochemistry 1981**; 20: 335-336
218. Sharma, P. N., A. Shoeb, R. S. Kapil and S. P. Popli. 8-hydroxydihydrochelerythrine and arnottianamide from roots of *Toddalia asiatica*. **Phytochemistry 1982**; 21: 252-253

219. Ishii, H., J. Kobayashi and T. Ishikawa. Toddalenone: A new coumarin from *Toddalia asiatica* (T. aculeata). Structural establishment based on the chemical conversion of limettin into toddalenone. **Chem. Pharm. Bull. (Tokyo) 1983**; 31: 3330-3333
220. Ishii, H., J.-I. Kobayashi and T. Ishikawa. Toddacoumalone, a novel mixed dimer of coumarin and quinolone from *Toddalia asiatica* (L.) Lam. (*T. aculeata* pers.). **Tetrahedron Letters 1991**; 32: 6907-6910
221. Ishii, H., J.-I. Kobayashi, E. Sakurada and T. Ishikawa. The absolute stereochemistries of (+)-toddalolactone and its related chiral coumarins from *Toddalia asiatica* (l.) lam. (*T. aculeata* pers.) and their optical purities. **J. Chem. Soc., Perkin Trans. 1 1992**; 1: 1681-1684
222. Chen, I.-S., I.-L. Tsai, S.-J. Wu, W.-S. Sheen, T. Ishikawa and H. Ishii. Toddaquinoline from formosan *Toddalia asiatica*. **Phytochemistry 1993**; 34: 1449-1451
223. Ishii, H., J.-I. Kobayashi, K.-I. Yamaguchi and T. Ishikawa. Toddalosin, a New Biscoumarin, from *Toddalia asiatica* (L.) LAM. (*T. aculeata* PERS.). **Chem. Pharm. Bull. (Tokyo) 1993**; 41: 1655-1656
224. Gakunju, D. M., E. K. Mberu, S. F. Dossaji, A. I. Gray, R. D. Waigh, P. G. Waterman and W. M. Watkins. Potent antimalarial activity of the alkaloid nitidine, isolated from a Kenyan herbal remedy. **Antimicrob. Agents Chemother. 1995**; 39: 2606-2609
225. Ian-Lih, T., F. Song-Chwan, T. Ishikawa, C. Chin-Teng and C. Ih-Sheng. N-cyclohexyl amides and a dimeric coumarin from formosan *Toddalia asiatica*. **Phytochemistry 1997**; 44: 1383-1386
226. Tsai, I.-L., M.-F. Wun, C.-M. Teng, T. Ishikawa and I.-S. Chen. Anti-platelet aggregation constituents from formosan *Toddalia asiatica*. **Phytochemistry 1998**; 48: 1377-1382
227. Oketch-Rabah, H. A., J. W. Mwangi, J. Lisgarten and E. K. Mberu. A new antiplasmodial coumarin from *Toddalia asiatica* roots. **Fitoterapia 2000**; 71: 636-640
228. Iwasaki, H., H. Oku, R. Takara, H. Miyahira, K. Hanashiro, Y. Yoshida, Y. Kamada, T. Toyokawa, K. Takara and M. Inafuku. The tumor specific cytotoxicity of dihydronitidine from *Toddalia asiatica* Lam. **Cancer Chemother. Pharmacol. 2006**; 58: 451-459
229. Iwasaki, H., T. Okabe, K. Takara, T. Toda, M. Shimatani and H. Oku. Tumor-selective cytotoxicity of benzo[c]phenanthridine derivatives from *Toddalia asiatica* Lam. **Cancer Chemother. Pharmacol. 2010**; 65: 719-726
230. Karunai Raj, M., C. Balachandran, V. Duraipandiyan, P. Agastian and S. Ignacimuthu. Antimicrobial activity of Ulopterol isolated from *Toddalia asiatica* (L.) Lam.: A traditional medicinal plant. **J. Ethnopharmacol. 2012**; 140: 161-165
231. Hu, J., X. Shi, J. Chen, X. Mao, L. Zhu, L. Yu and J. Shi. Alkaloids from *Toddalia asiatica* and their cytotoxic, antimicrobial and antifungal activities. **Food Chemistry 2014**; 148: 437-444
232. Lin, T. T., Y. Y. Huang, G. H. Tang, Z. B. Cheng, X. Liu, H. B. Luo and S. Yin. Prenylated coumarins: natural phosphodiesterase-4 inhibitors from *Toddalia asiatica*. **J. Nat. Prod. 2014**; 77: 955-962
233. Phatchana, R. and C. Yenjai. Cytotoxic coumarins from *Toddalia asiatica*. **Planta Med. 2014**; 80: 719-722
234. Watanabe, A., T. Kato, Y. Ito, I. Yoshida, T. Harada, T. Mishima, K. Fujita, M. Watai, K. Nakagawa and T. Miyazawa. Aculeatin, a coumarin derived from *Toddalia asiatica* (L.) Lam., enhances differentiation and lipolysis of 3T3-L1 adipocytes. **Biochemical and Biophysical Research Communications 2014**; 453: 787-792
235. Hu, J., X. Shi, X. Mao, J. Chen and H. Li. Amides from the Roots of *Toddalia asiatica*. **Chem. Nat. Compd. 2015**; 51: 726-729
236. Watanabe, A., M. Kumagai, T. Mishima, J. Ito, Y. Otoki, T. Harada, T. Kato, M. Yoshida, M. Suzuki, I. Yoshida, K. Fujita, M. Watai, K. Nakagawa and T. Miyazawa. Toddaculin, Isolated from of *Toddalia asiatica* (L.) Lam., Inhibited Osteoclastogenesis in RAW 264 Cells and Enhanced Osteoblastogenesis in MC3T3-E1 Cells. **PLoS One 2015**; 10: e0127158
237. Hirunwong, C., S. Sukieum, R. Phatchana and C. Yenjai. Cytotoxic and antimalarial constituents from the roots of *Toddalia asiatica*. **Phytochem. Lett. 2016**; 17: 242-246

238. Li, W., J.-S. Zhang, J.-L. Huang, M.-H. Jiang, Y.-K. Xu, A. Ahmed, S. Yin and G.-H. Tang. New prenylated coumarins from the stems of *Toddalia asiatica*. **RSC Advances 2017**; 7: 31061-31068

239. Kumagai, M., A. Watanabe, I. Yoshida, T. Mishima, M. Nakamura, K. Nishikawa and Y. Morimoto. Evaluation of Aculeatin and Toddaculin Isolated from *Toddalia asiatica* as Anti-inflammatory Agents in LPS-Stimulated RAW264 Macrophages. **Biological and Pharmaceutical Bulletin 2018**; 41: 132-137

240. Sukieum, S., W. Sang-Aroon and C. Yenjai. Coumarins and alkaloids from the roots of *Toddalia asiatica*. **Nat. Prod. Res. 2018**; 32: 944-952

241. Gakunju, D. M., E. K. Mberu, S. F. Dossaji, A. I. Gray, R. D. Waigh, P. G. Waterman and W. M. Watkins. Potent antimalarial activity of the alkaloid nitidine, isolated from a Kenyan herbal remedy. **Antimicrobial Agents and Chemotherapy 1995**; 39: 2606-2609

242. Severi, J. A., O. Fertig, I. Plitzko, W. Vilegas, M. Hamburger and O. Potterat. Oleanane saponins and glycerogalactolipids from the leaves of *Guapira graciliflora*. **Helv. Chim. Acta 2010**; 93: 1058-1066

243. Smith, S. G. and J. M. Goodman. Assigning Stereochemistry to Single Diastereoisomers by GIAO NMR Calculation: The DP4 Probability. **J. Am. Chem. Soc. 2010**; 132: 12946-12959

244. Grimblat, N., M. M. Zanardi and A. M. Sarotti. Beyond DP4: an Improved Probability for the Stereochemical Assignment of Isomeric Compounds using Quantum Chemical Calculations of NMR Shifts. **J. Org. Chem 2015**; 80: 12526-12534

3. Results and Discussion

3.1. Sesquiterpene Lactones from *Artemisia argyi*: Absolute Configuration and Innunosuppressant Activity

Jakob K. Reinhardt†, Amy M. Klemd†, Ombeline Danton, Maria De Mieri, Martin Smieško, Roman Huber, Thomas Bürgi, Carsten Gründemann, Matthias Hamburger

J Nat Prod. 2019, 82, 1424-1433. doi: 10.1021/acs.jnatprod.8b00791

A library of extracts from plants used in Chinese Traditional Medicine was screened for inhibition of T lymphocyte proliferation. An ethyl acetate extract from aerial parts of *Artemisia argyi* showed promising activity and was submitted to HPLC-based activity profiling to track the active compounds. From the most active time window, three guaianolides (**1**, **2** and **5**) and two seco-tanapartholides (**3** and **4**) were identified and, in a less active time window five new sesquiterpene lactones (**8-11**, **17**), along with six known sesquiterpene lactones and two known flavonoids. The absolute configurations of compounds **1**, **2**, **5-10**, **13-15**, **17**, and **18** were established by comparison of experimental with calculated electronic circular dichroism (ECD) spectra. For seco-tanapartholides B (**3**) and A (**4**), ECD yielded ambiguous results, and their absolute configurations were determined by comparing experimental and calculated vibrational circular dichroism (VCD) spectra. Compounds **1-5** showed significant, non-cytotoxic inhibition of T lymphocyte proliferation, with IC_{50} values between 1.0 and 3.7 μM.

Extraction of plant material, isolation, recording and interpretation of analytical data for structure elucidation (HPLC-PDA-ELCD-ESI-MS, 1D and 2D NMR [with support from Maria De Mieri and Ombeline Danton], optical rotation, ECD), interpretation of data from VCD measurements (measurements and some advice from Thomas Bürgi), quantum chemical calculations of ECD and VCD spectra (some advice from Martin Smieško), writing of the manuscript draft, and preparation of figures were my contributions to this publication.

T-lymphocyte proliferation inhibition experiments as well as preparation of the results and discussion part "Immunosuppressant activity" as well as the experimental parts "Ethics Statement", "Preparation and Cultivation of Human Peripheral Lymphocytes" "T Cell Proliferation Assay" and "Determination of Apoptosis and Necrosis of T Cells" in the manuscript draft done by other first coauthor Amy Zimmermann-Klemd.

†*contributed equally to this work*

Jakob K. Reinhardt

Downloaded via UNIV OF BASEL on December 2, 2020 at 12:22:27 (UTC).
See https://pubs.acs.org/sharingguidelines for options on how to legitimately share published articles.

JOURNAL OF NATURAL PRODUCTS

Article

Cite This: J. Nat. Prod. 2019, 82, 1424−1433

pubs.acs.org/jnp

Sesquiterpene Lactones from *Artemisia argyi*: Absolute Configuration and Immunosuppressant Activity

Jakob K. Reinhardt,[†,#] Amy M. Klemd,[‡,#] Ombeline Danton,[†] Maria De Mieri,[†] Martin Smieško,[§] Roman Huber,[‡] Thomas Bürgi,[⊥] Carsten Gründemann,[‡] and Matthias Hamburger*,[†]

[†]Pharmaceutical Biology, Pharmacenter, University of Basel, Klingelbergstrasse 50, 4056 Basel, Switzerland

[‡]Center for Complementary Medicine, Institute for Infection Prevention and Hospital Epidemiology, Faculty of Medicine, University of Freiburg, Breisacher Straße 115 B, 79106 Freiburg, Germany

[§]Department of Molecular Modeling, University of Basel, Klingelbergstrasse 50, 4056 Basel, Switzerland

[⊥]Department of Physical Chemistry, University of Geneva, 30 Quai Ernest Ansermet, 1211 Geneva, Switzerland

Supporting Information

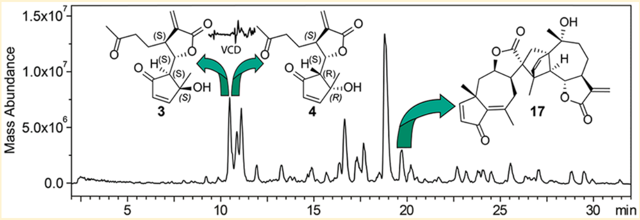

ABSTRACT: A library of extracts from plants used in Chinese Traditional Medicine was screened for inhibition of T lymphocyte proliferation. An ethyl acetate extract from aerial parts of *Artemisia argyi* showed promising activity and was submitted to HPLC-based activity profiling to track the active compounds. From the most active time window, three guaianolides (**1**, **2**, and **5**) and two *seco*-tanapartholides (**3** and **4**) were identified and, in a less active time window, five new sesquiterpene lactones (**8**−**11**, **17**), along with six known sesquiterpene lactones and two known flavonoids. The absolute configurations of compounds **1**, **2**, **5**−**10**, **13**−**15**, **17**, and **18** were established by comparison of experimental with calculated electronic circular dichroism (ECD) spectra. For *seco*-tanapartholides B (**3**) and A (**4**), ECD yielded ambiguous results, and their absolute configurations were determined by comparing experimental and calculated vibrational circular dichroism (VCD) spectra. Compounds **1**−**5** showed significant, noncytotoxic inhibition of T lymphocyte proliferation, with IC_{50} values between 1.0 and 3.7 μM.

Immune malfunction is characterized by the body's inability to adequately differentiate between non-self and self-antigen structures. In immune deficiencies, the immune system fails to identify and eliminate pathogens, while in autoimmune diseases it fails to recognize endogenous cells from one's self.[1] Autoimmune diseases such as type I diabetes, rheumatoid arthritis, or multiple sclerosis are characterized by an increased T cell proliferation.[2] Presently, no causal therapies are available, and autoimmune diseases are typically treated symptomatically with immunosuppressive drugs.[3] As these substances often show severe side effects, the search for compounds with new modes of action and fewer adverse effects is warranted. Natural products have a successful track record for providing immunosuppressive compounds with unique modes of action, such as cyclosporine A, tacrolimus, rapamycin, mycophenolic acid, and myriocin.[4] Compared to actinomycetes and fungi, higher plants have been much less investigated as a source for immunosuppressive lead compounds. In an effort to explore the potential of plant secondary metabolites, a focused library of extracts from plants used in Traditional Chinese Medicine (TCM) was screened for their ability to inhibit T cell proliferation in vitro.

RESULTS AND DISCUSSION

Compound Isolation and Structure Elucidation. A library of 435 extracts was screened at a single concentration of 20 μg/mL for the ability to inhibit T lymphocyte proliferation.[5] A total of 40 extracts inhibited proliferation by ≥70% without exhibiting cytotoxicity at this concentration. This was verified by annexin V and propidium iodide (PI) double staining. These extracts were then tested at four concentrations ranging from 3 to 100 μg/mL. The ethyl acetate extract from aerial parts of *Artemisia argyi* Levl. et Vant. (Asteraceae) exhibited significant activity (IC_{50} 16.2 μg/mL) and was submitted to HPLC-based activity profiling.[6,7] Microfractions were collected and tested at four different dilutions, and a theoretical IC_{50} value was calculated and normalized to 100% (residual proliferation) as a measure of activity.

Pronounced inhibition of T cell proliferation was found in the time window of 10−12 min, and moderate activity in the window of 16−20 min (Figure 1). Preparative isolation of compounds **1**−**18** for structure elucidation and biological testing was achieved by a combination of open column chromatography on silica gel and semipreparative and preparative HPLC on C_{18} and cyano columns.

The UV spectra of compounds **1**−**11**, **13**−**15**, and **18** showed absorption maxima between 200 and 220 nm, while compounds

Received: September 17, 2018
Published: June 5, 2019

ACS Publications © 2019 American Chemical Society and American Society of Pharmacognosy

DOI: 10.1021/acs.jnatprod.8b00791
J. Nat. Prod. 2019, 82, 1424−1433

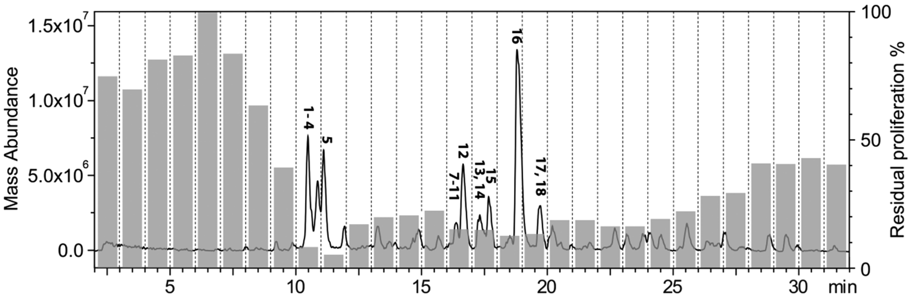

Figure 1. HPLC-ESIMS (base peak chromatogram) and activity profile (gray bars) of a EtOAc extract of *A. argyi*. Residual proliferation levels of T lymphocytes are expressed in % on inoculation with 1 min HPLC microfractions. Bold numbers in the chromatogram refer to compounds **1**−**18**.

Chart 1

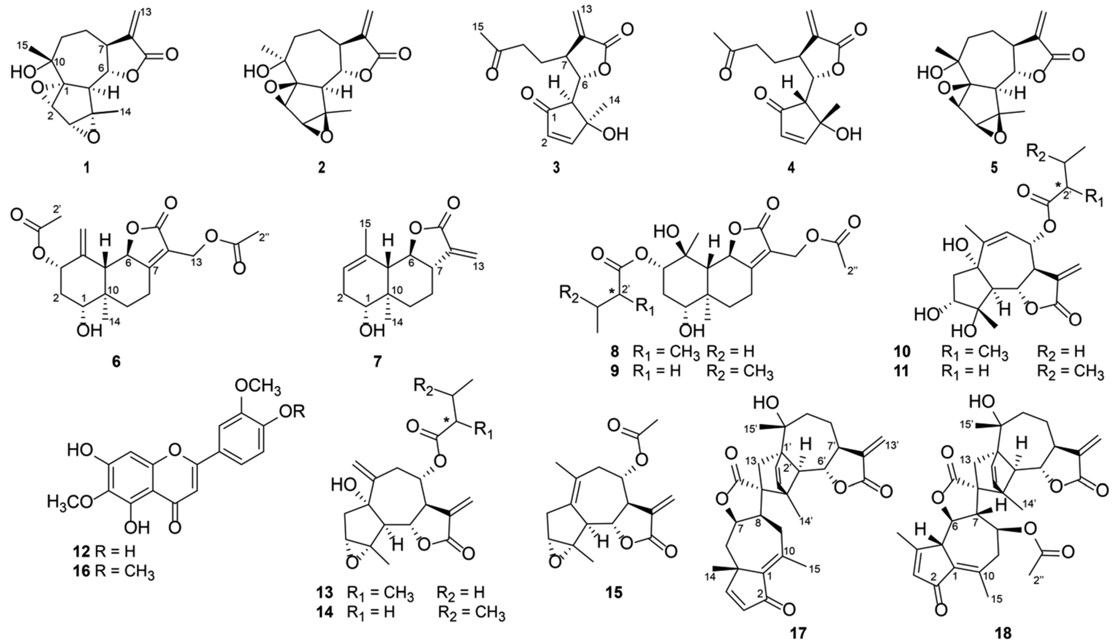

12 and **16** exhibited two UV maxima between 270 and 275 nm and 340−345 nm indicative of flavones.[8]

Compounds **6** and **7** were identified as the known eudesmanolide sesquiterpene lactones eudesmaafraglaucolide (**6**)[9] and santamarin (**7**).[10] The absolute configuration of **6** has not been established up to now and was determined by electronic circular dichroism (ECD) in comparison to the calculated spectrum as (1*R*,3*S*,5*S*,6*R*,10*R*) (Figure S42, Supporting Information).

3*α*,4*α*-Epoxyrupicoline D (**13**) and E (**14**) were isolated as a mixture and identified by comparison of their NMR spectra with published data (Table S5, ORTEP diagram in Figure S68, Supporting Information).[11] Compound **14** crystallized from the mixture, but the X-ray diffraction data were not of sufficient quality (Flack parameter (0.10(19)) to determine the absolute configuration. An ECD spectrum was recorded for the mixture and compared with the corresponding calculated spectra (Figure S67, Supporting Information). Thus, the absolute configuration of the scaffold in **13** and **14** was established as (1*S*,3*R*,4*S*,5*R*,6*S*,7*R*,8*S*). Given the lack of a suitable chromophore in the vicinity of C-2′, the absolute configuration of this stereocenter in **13** could not be determined by ECD.

Arteglasin A (**15**) was isolated as white crystals and identified by X-ray diffraction analysis (Table S7, ORTEP diagram in Figure S70, Supporting Information). NMR data were in good agreement with literature values.[12] The absolute configuration of **15** was determined as (3*R*,4*S*,5*S*,6*S*,7*R*,8*S*) (Flack parameter = 0.06 (15)) and confirmed by comparison of experimental and calculated ECD spectra (Figure S69, Supporting Information).

The flavones jaceosidin (**12**) and eupatilin (**16**) had been previously reported from *Artemisia argyi*.[13]

The NMR data of **1**, **2**, and **5** indicated that they are stereoisomers possessing a planar structure corresponding to that of canin (**1**).[14] Two of them were identified as canin (**1**) and artecanin (**5**) (Figure 2).[15]

The ECD spectrum of **1** exhibited a strong positive Cotton effect (CE) at 200 nm and a broad negative CE at 250 nm (Figure 3). The calculated spectrum for (1*R*)-canin was in good agreement with the experimental data obtained. An independent confirmation of the absolute configuration was obtained from the vibrational circular dichroism (VCD) spectrum that was compared to the calculated spectra of **1**, **2**, and **5** (at the B3LYP/6-31+G(d,p) level of theory) (Figure 4). For an unbiased comparison of VCD spectra, similarity indices *Sim*VA (for vibrational absorption) and *Sim*VCD were calculated with VCD SpecTech.[16] Similarity indices calculated for scaling factors between 0.939 and 1.009 are shown in Figure 4. The maximal value of *Sim*VCD was determined for (1*R*)-canin (**1**) at a wavenumber scale factor of 0.9865, which was used to plot the calculated spectra. A visual inspection of the main bands at 1772

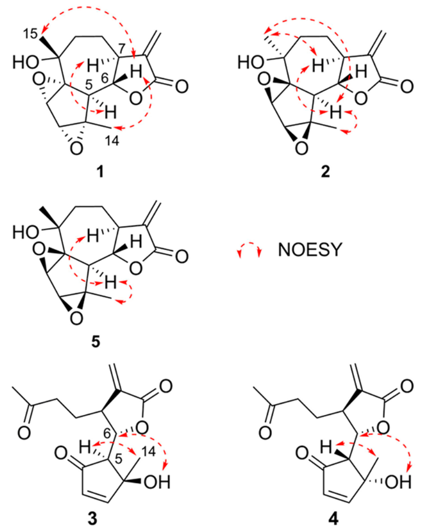

Figure 2. Selected NOESY correlations for compounds **1**−**5**.

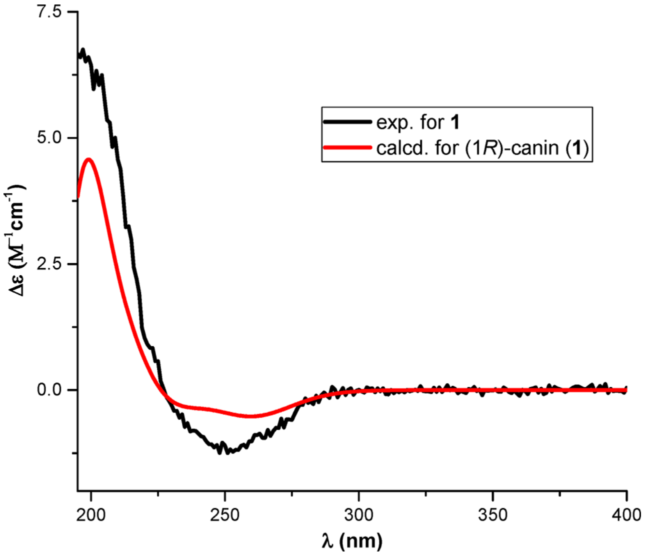

Figure 3. Comparison of experimental and calculated ECD spectra for compound **1** in MeOH.

(−), 1260 (+), 1205 (−), and 1150 (−) cm^{-1} in the VCD confirmed the assignment of the absolute configuration as (1*R*)-canin (**1**).

The absolute configuration of **5** was determined as (1*S*,2*R*,3*S*,4*R*,5*S*,6*S*,7*S*,10*R*), corresponding to (1*S*)-artecanin, by comparison of the experimental and calculated ECD spectra (Figure S38, Supporting Information). Additionally, the VCD spectrum of **5** was measured in DMSO-d_6 and compared to the computed spectra of compounds **1**, **2**, and **5** (Figure S40, Supporting Information). Although the relative configuration of **5** was clearly established from the NOESY correlations, the experimental VCD spectrum showed the best fit with the calculated spectrum of **1** when an automated comparison was used. Visual comparison of the experimental and the calculated spectra of **1** and **5** showed that they were all very similar with respect to the major CEs (e.g., 1277 (+), 1257 (+), 1215 (−), 1154 (−), and 1133 (+) cm^{-1}). However, a positive CE at 1385 cm^{-1} was seen in the experimental and calculated spectra of **5**, whereas a negative CE was present at this wavenumber in the calculated spectrum of **1**.

In contrast to **1** and **5**, compound **2** exhibited NOESY correlations between Me-15 (δ_H 1.41), H-5 (δ_H 2.26), and H-7 (δ_H 2.57), placing them in an α-orientation opposite H-6 (δ_H 4.12). A NOESY correlation between H-5 and Me-14 indicated a β-orientation of the two epoxy groups as in **5**. Therefore, compound **2** was the 10-epimer of artecanin. A compound with this structure was previously published as 10-*epi*-canin.[17] The structural assignment was at that time solely based on ^1H NMR data, but some of the published chemical shifts differed significantly from those measured for **2** (e.g., H-5 and H-7 reported: δ_H 2.62 and 3.40; measured for **2**: δ_H 2.26 and 2.57 ppm, Table S1, Supporting Information). Thus, the structural assignment for the previously published 10-*epi*-canin is likely incorrect. The absolute configuration of **2** was determined as (1*S*,2*R*,3*S*,4*R*,5*S*,6*S*,7*S*,10*S*) by comparison of experimental and calculated ECD spectra (Figure S17, Supporting Information).

Compounds **3** and **4** were obtained as stereoisomers with the planar structure of *seco*-tanaparatholides.[17,18] The ^1H and ^{13}C NMR chemical shifts of **3** and **4** differed slightly, but the compounds exhibited the same correlations in their COSY, HMBC, and NOESY spectra (Table S2 and Figures S18−S29, Supporting Information). For both compounds, a NOESY correlation between H-5 (**3** δ_H 2.23, **4** δ_H 2.50) and Me-14 (**3** δ_H 1.41, **4** δ_H 1.45) was used to establish their orientations as *cis*-α or *cis*-β. The scalar coupling between H-6 and H-7 (**3** $J_{6,7}$ 3.1, **4** $J_{6,7}$ 5.8) indicated a *trans* orientation of H-6 (**3** δ_H 4.45, **4** δ_H 4.52) and H-7 (**3** δ_H 3.27, **4** δ_H 3.50). The dihedral angles between these two protons in the two most populated conformers in chloroform were determined as −115° and 132° for compound **3** and as 132° and 120° for compound **4**. Both the relative configurations of (4*S**,5*S**,6*S**,7*S**)-*seco*-tanapartholide B (**3**) and (4*R**,5*R**,6*S**,7*S**)-*seco*-tanapartholide A (**4**) were in accord with the NMR data, and only the *J* values between geminal H-5 and H-6 differed (**3** $J_{5,6}$ 7.3, **4** $J_{5,6}$ 2.1). On the basis of this difference, Kawazoe et al. previously postulated **3** as (4*S**,5*S**,6*S**,7*S**) and **4** as (4*R**,5*R**,6*S**,7*S**).[19] However, the two most populated conformers of compound **3** showed dihedral angles of 172° and 77° between H-5 and H-6, while angles of 72° and 173° were obtained for compound **4**. Thus, an assignment based on geminal *J* values was ambiguous.

Compounds **3** and **4** had enantiomer-like ECD spectra (Figure 5) but, given that the compounds had been separated on nonchiral stationary phases, could not be enantiomers. Calculated ECD spectra of **3** and **4** (absolute configuration as drawn) reproduced these CEs, although the experimental spectrum of **3** could also be explained by the computed enantiomeric spectrum of **4** and vice versa. Thus, the absolute configuration of **3** was either (4*S*,5*S*,6*S*,7*S*) or (4*S*,5*S*,6*R*,7*R*), and that of **4** was (4*R*,5*R*,6*S*,7*S*) or (4*R*,5*R*,6*R*,7*R*).

The experimental VCD spectrum of **3** in chloroform (Figure 6) was compared to calculated spectra of the (4*S*,5*S*,6*S*,7*S*) (**3**) and the (4*R*,5*R*,6*S*,7*S*) (**4**) stereoisomer. A good fit between the experimental and calculated spectra of **3** was obtained with a scaling factor of 0.9815 and confirmed by a visual comparison of major CEs at 1271 (+), 1323 (+), 1365 (−), 1380 (+), 1711 (+), and 1718 (+) cm^{-1} in the measured and calculated IR and VCD spectra. Hence, the absolute configuration of **3** was established as (4*S*,5*S*,6*S*,7*S*). In the same manner (Figure S31, Supporting Information) the absolute configuration of **4** was determined as (4*R*,5*R*,6*S*,7*S*).

Argyinolides K (**8**) and L (**9**) were obtained as an inseparable mixture. In the HRESIMS, the sodium adduct ion (*m*/*z* =

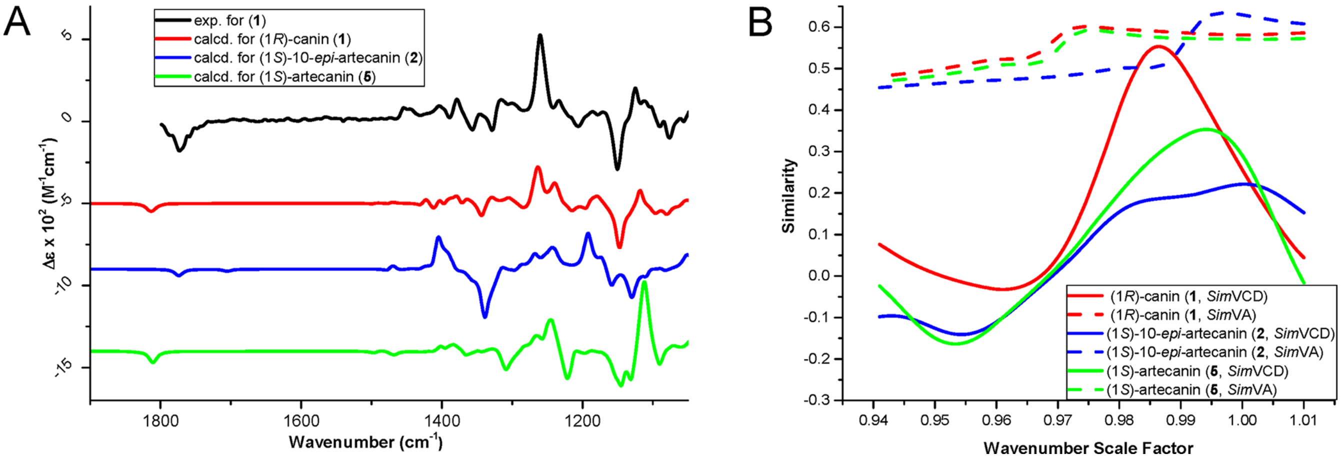

Figure 4. Comparison of experimental and computed VCD spectra in chloroform for compound **1**. The region of 1900−1050 cm^{-1} is shown (A). Similarities (*Sim*VA and *Sim*VCD) of the experimental VA and VCD spectra of **1** to the calculated spectra of possible stereoisomers were plotted as functions of wavenumber scale factor (B). The wavenumber scale factor corresponding to the maximal *Sim*VCD value in B (0.9865) was used to scale the computed spectra in A.

447.2018 $[\text{M} + \text{Na}]^+$, calcd for $C_{22}H_{32}O_8Na$ 447.1989) indicated a molecular formula of $C_{22}H_{32}O_8$ for both compounds. Analysis of ^{1}H NMR and ^{13}C NMR data (Table 1) pointed to a eudesmanolide scaffold similar to that in **6**, but with the methylene group replaced by an sp^3-hybridized carbon (C-4, δ_C = 72.8) connected to a methyl group (Me-15 δ_H = 1.29, δ_C = 17.7) and a hydroxy group. Additional methyl signals were assigned to a 2-methylbutyryl moiety in **8** (Me-4′, δ_H 0.87, dd, J = 7.5, 7.5; Me-5′, δ_H 1.07, d, J = 7.0), a 3-methylbutyryl moiety in **9** (Me-4′/5′ δ_H 0.92, d, J = 6.7), and an acetyl group (Me-2″, δ_H 2.01, δ_C 20.6) in both compounds. Me-2″ showed HMBC correlations to C-13 (δ_H 4.72, δ_C 54.6). HMBC correlations between H-3 (δ_H = 4.60) and both butyryl carbonyl carbons (**8** δ_C = 175.0; **9** δ_C = 171.6) led to the identification of two regioisomers. The ratio between **8** and **9** was estimated as 2:1, based on the integrals of the Me-4′ (**8** δ_H = 0.87; **9** δ_H = 0.92) and Me-5′ (**8** δ_H = 1.07; **9** δ_H = 0.92) resonances in the ^{1}H NMR spectrum. This ratio was confirmed by the integration of the Me-15 resonances (**8** δ_H = 1.29; **9** δ_H = 1.28). The relative configurations of **8** and **9** were determined from the NOESY

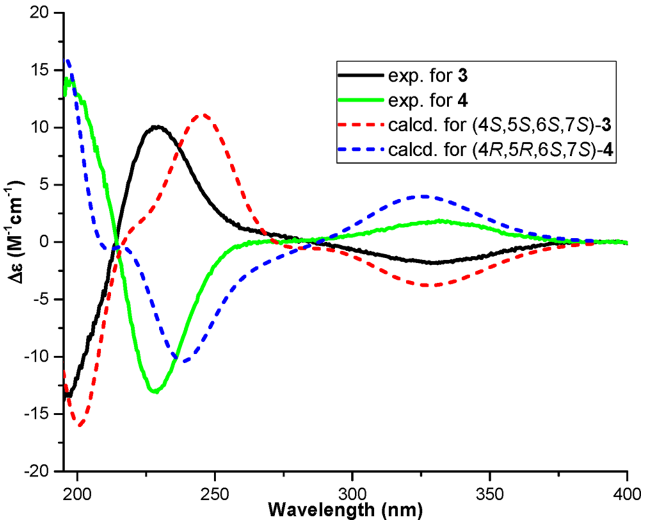

Figure 5. Comparison of experimental and calculated ECD spectra of **3** and **4** in MeOH.

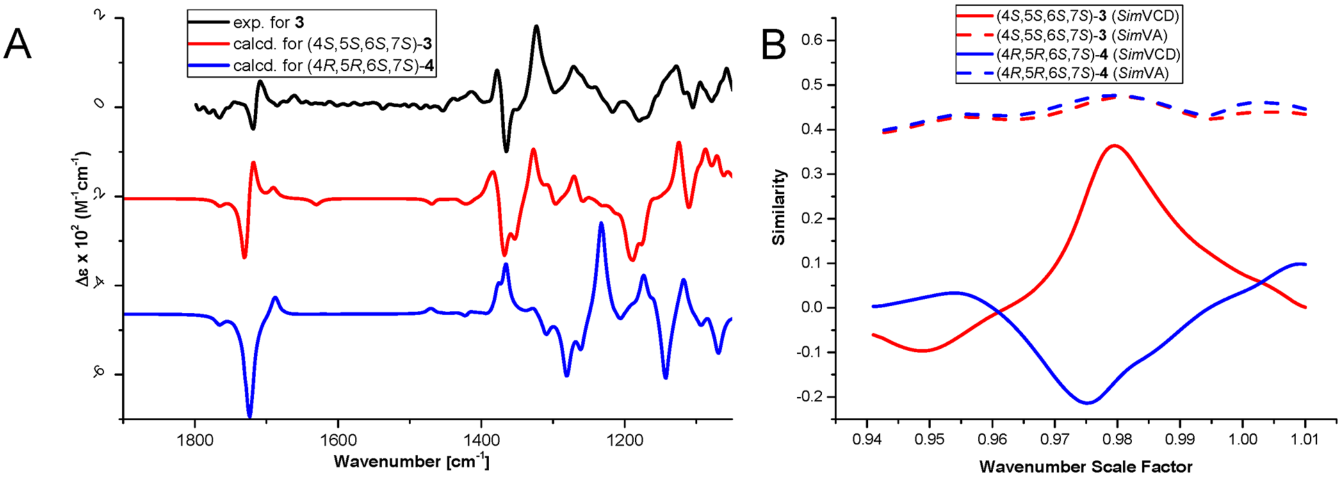

Figure 6. Comparison of experimental and computed VCD spectra in $CDCl_3$ for compound **3**. The region of 1900−1050 cm^{-1} is shown (A). Similarities (*Sim*VA and *Sim*VCD) of the experimental VA and VCD spectra of **3** to the calculated spectra of possible stereoisomers were plotted as functions of wavenumber scale factor (B). The wavenumber scale factor corresponding to the maximal *Sim*VCD value in B (0.9810) was used to scale the computed spectra in A.

DOI: 10.1021/acs.jnatprod.8b00791
J. Nat. Prod. 2019, 82, 1424−1433

spectrum. Only the configuration at C-2′ in **8** could not be determined (Figure 7).

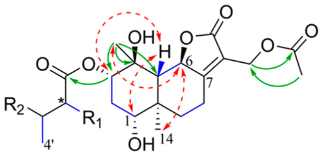

8 $R_1 = CH_3$ $R_2 = H$
9 $R_1 = H$ $R_2 = CH_3$

Figure 7. Selected COSY (blue bonds), HMBC (green arrows), and NOESY correlations (red arrows) for compounds **8** and **9**.

The ECD spectrum of the mixture (Figure S51, Supporting Information) showed maxima at 200 and 252 nm together with a minimum at 228 nm. Spectra were calculated for **9** and for both possible stereoisomers of **8**. The three spectra showed a positive CE at 200 nm and negative CEs between 215 and 235 nm. Only the maximum at 252 nm in the experimental spectrum was not reproduced in the calculations. Therefore, the absolute configurations of the rings in compounds **8** and **9** were established as (1*R*,4*S*,5*S*,6*R*,10*R*). Due to the limited amount available, it was not possible to measure the VCD spectrum of the mixture as an attempt to establish the absolute configuration of C-2′ in **8**.

Argyinolide M (**10**) gave a molecular formula of $C_{20}H_{28}O_7$ (HRESIMS data *m*/*z* 403.1750 [M + Na]$^+$, calcd for $C_{20}H_{28}O_7Na$, 403.1727), which suggested seven degrees of unsaturation. NMR data (Table 2, Figures S52−57, Supporting Information) indicated a guaianolide scaffold similar to that in a previously published compound.[20] In compound **10**, a 2-methylbutyryl group was attached at C-8, as indicated by the HMBC correlations between H-8 (δ_H 5.24) and C-1′ (δ_C 175.2). The relative configuration of **10** was established through NOESY correlations (Figure 8), and the absolute configuration of the scaffold of **10** was determined via comparison of experimental and computed ECD spectra (Figure S58, Supporting Information) as (1*S*,3*R*,4*S*,5*R*,6*S*,7*R*,8*S*). As in the case of **8**, the absolute configuration at C-2′ could not be established.

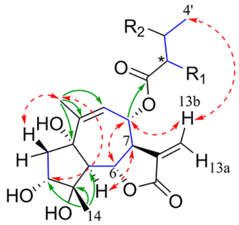

10 $R_1 = CH_3$ $R_2 = H$
11 $R_1 = H$ $R_2 = CH_3$

Figure 8. Selected COSY (blue bonds), HMBC (green arrows), and NOESY correlations (red arrows) for compounds **10** and **11**.

Argyinolide N (**11**) was determined as being a regioisomer of **10** containing a 3-methylbutyryl unit instead of a 2-methylbutyryl group at C-8. Apart from the resonances attributed to the side chain, correlations in COSY, HMBC, and NOESY spectra were similar to those of **10**. The UV and ECD spectra were measured (Figures S65 and S66, Supporting Information). A strong positive CE at 195 nm in the calculated ECD spectrum was in agreement with the experimental data. However, the strong negative CE at 220 nm and a weak positive CE at 250 nm were not present in the experimental spectrum, and an unambiguous assignment of the absolute configuration was thus not possible for compound **11**.

Compound **18** was identified as 8-acetylarteminolide.[21] Its relative, but not its absolute configuration, has been reported previously. The absolute configuration was established as (5*S*,6*R*,7*R*,8*S*,12*S*,1′*R*,4′*R*,5′*S*,6′*S*,7′*S*,10′*R*) by comparison of measured and calculated ECD and VCD spectra (Figures S77, S78, and S79, Supporting Information).

Argyinolide O (**17**) gave a molecular formula of $C_{30}H_{34}O_6$ (HRESIMS *m*/*z* 513.2261 [M + Na]$^+$, calcd for $C_{30}H_{34}O_6Na$, 513.2248), corresponding to 14 degrees of unsaturation. Inspection of the NMR data (Table 3, Figures S71−76, Supporting Information) indicated that the molecule **17** consists of two distinct portions, each containing a γ-lactone ring. Thus, the structure of **17** resembled that of **18**, with one sesquiterpene portion being identical in these compounds.[21] In the other portion of **17**, a contiguous spin system between C-6 and C-9 was determined from the COSY spectrum (Figure 9). Substituents at the bridgehead C-5 were characterized by HMBC correlations from Me-14 (δ_H 1.27) to C-4 (δ_C 155.3), C-5 (δ_C 38.4), and C-6 (δ_C 39.5). The orientation of the cyclopentenone ring was established by diagnostic HMBC correlations from the olefinic protons H-3 and H-4 to C-1, C-2, and C-5. A γ-lactone moiety was attached to the seven-membered ring at C-8 (δ_C 43.7) and C-7 (δ_C 75.4). The linkage of the two sesquiterpene portions A and B was established by HMBC correlations. Me-14′ (δ_C 16.1) and the diastereotopic protons at C-13 (δ_H 1.62, 2.50) of portion B, and H-8 (δ_H 2.32) of portion A, exhibited HMBC cross-peaks with C-12 (δ_C 61.3), and H_2-13 also with C-1′. The relative configuration of **17** was established via a series of diagnostic ROESY correlations (Figure 9). Correlations between H-5′ (δ_H 2.96), H-7′ (δ_H 3.39), and H_α-13 (δ_H 2.50, correlations not drawn in Figure 9) and between H-6′ (δ_H 4.00), H-2′ (δ_H 6.17), H_β-13 (δ_H 5.35), and H_β-9 (δ_H 6.17) indicated their respective cofacial orientation and thus helped determine the linkage of the lactone ring at C-6′ (δ_C 79.6) and C-7′ (δ_C 43.0) as *trans*. The β-orientation of Me-15′ (δ_H 1.38) was indicated by a ROESY cross-peak with H-2′. The configuration of C-12 was established through correlations between Me-14′ (δ_H 1.54) and H-7 (δ_H 4.77) and between H-3′ (δ_H 5.90) and H-8 (δ_H 2.32). The UV and ECD spectra of **17** were measured and compared to calculated data (Figures S74 and S75, Supporting Information). A strong negative CE in the ECD spectrum at 210 nm was present in the calculated spectrum, but not the broad negative CE occurring in the experimental spectrum between 230 and 290 nm. Considering the relative magnitudes of the absorption maxima in the UV

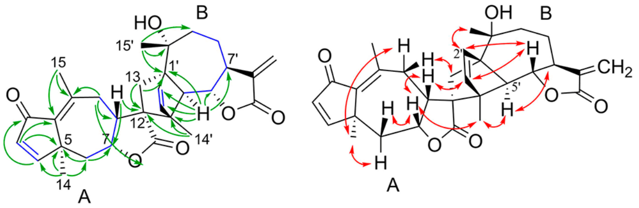

Figure 9. Selected COSY (blue bonds), HMBC (green arrows), and ROESY for compound **17**. For better visibility, ROESY correlations (red arrows) are shown in a spatial representation (right). A and B refer to the two sesquiterpene lactone portions.

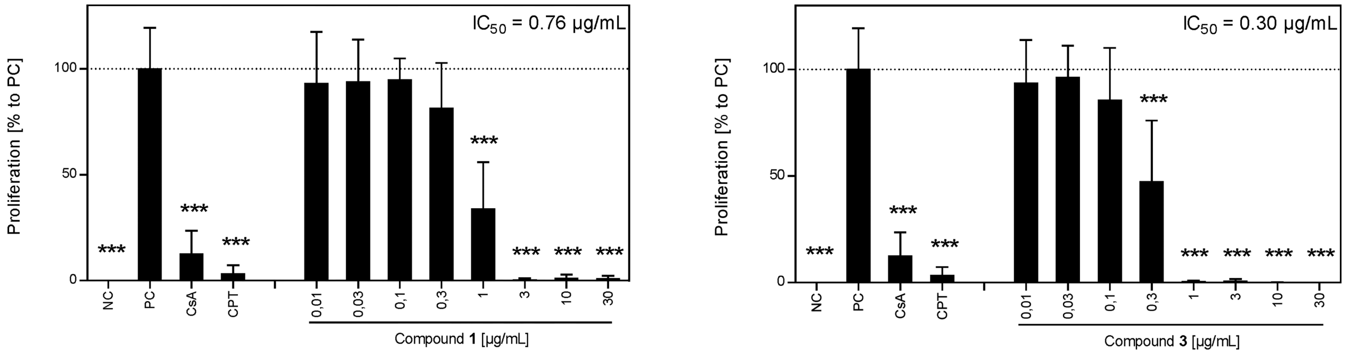

Figure 10. Inhibitory effects of compounds **1** and **3** on the proliferation of T lymphocytes. Data of three independent experiments were summarized and depicted as means ± standard deviation in relation to the untreated, stimulated control (PC; = 100% ± SD). Nonstimulated cells were used as the negative control (NC), cyclosporin A (CsA) was used as a known inhibitor of T cell proliferation, and camptothecin (CPT) was used as a known inducer of apoptosis. $^*p < 0.05$, $^{**}p < 0.01$, $^{***}p < 0.001$.

spectrum, the negative CE at 210 nm was considered as being more relevant, and the absolute configuration assigned tentatively as (5*S*,7*R*,8*R*,12*S*,1′*R*,4′*R*,5′*S*,6′*S*,7′*S*,10′*R*). This is also in accord with the absolute configuration of compound **18**.

The absolute configurations of canin (**1**) and its stereoisomers **2** and **5** had not been previously determined, and the representation of their structures since their first description in 1969 followed a previous convention.[15] We determined the absolute configurations of canin (**1**) and artecanin (**5**) using ECD and VCD in combination with ab initio calculations. In addition, the absolute configurations of other sesquiterpene lactones were determined if a reliable assignment of such information was lacking. However, this was not established for the 2-methylbutyryl side chain in compounds **8**, **10**, and **14**, due to the lack of a suitable chromophore in proximity, and the limited amounts of pure compounds precluded the measurement of VCD spectra. In the case of *seco*-tanapartholides B (**3**) and A (**4**), the rotatable bond between the two chromophores impeded an assignment of the absolute configuration via ECD. However, analysis of the VCD spectra proved to be successful. For compounds **1**, **5**, and **18**, a comparison of experimental and computed VCD spectra confirmed the absolute configuration determined by ECD, and for arteglasin A (**15**) the X-ray crystallographic data supported the assigned absolute configuration. Automated comparison of VCD spectra using *Sim*VCD and *Sim*VA proved to be helpful in the case of **1**, **3**, **4**, and **18**. However, a visual examination of spectra is warranted to avoid false attributions, as would have been the case with compound **5**.

Immunosuppressant Activity. Compounds were tested for their ability to inhibit proliferation of stimulated T lymphocytes at a concentration range of 0.01−30 µg/mL. FACS analyses of the forward and side scatters in the proliferation experiments were used to simultaneously assess immunosuppressive activity and cytotoxicity. The results for compounds **1** and **3** are shown in Figure 10, and IC$_{50}$ values for all compounds tested were determined (Table 4, Figure S2, Supporting Information).

Compounds **3**, **4**, and **15** and the mixture of **13** and **14** significantly inhibited T lymphocyte proliferation, having IC$_{50}$ values of <2 µM. For **3** and **4**, beginning cytotoxicity was seen at a concentration that was 10-fold higher than the IC$_{50}$ value in the T-cell proliferation assay. For compound **15**, signs of cytotoxicity were observed at a concentration that was 3-fold higher than the IC$_{50}$ value. Compounds **1**, **5**, and **18** were less active (IC$_{50}$ ≤ 4 µM), and compounds **6**−**9**, **12**−**14**, and **16** had no significant activity in the T-cell proliferation assay. When comparing the activity profile (Figure 1) with the IC$_{50}$ values of pure compounds, it appeared that sesquiterpenes **1** and **3**−**5** contribute to a large extent to the activity of the extract.

Table 1. ^{1}H and ^{13}C NMR Spectroscopic Data (500 MHz, $CDCl_3$) for Compounds **8** and **9**

	8		**9**		
position	δ_C, type	δ_H (J in Hz)	δ_C, type	δ_H (J in Hz)	HMBC[b]
1	73.3, CH	3.29, dd (11.9, 3.7)	73.3, CH	3.29, dd (11.9, 3.7)	9, 10, 14
2α	33.3, CH_2	1.59[a]		1.59[a]	1, 3, 4, 10
2β		1.76, m	33.3, CH_2	1.76, m	1, 4, 10
3	76.6, CH	4.60, dd (12.5, 4.6)	76.6, CH	4.60, dd (12.5, 4.6)	1′, 4, 15
4	72.8, C		72.8, C		
5	56.0, CH	1.41, d (11.3)	56.0, CH	1.41, d (11.3)	4, 6, 9, 10, 14, 15
6	79.2, CH	5.32, d (11.3)	79.2, CH	5.32, d (11.3)	4, 5, 7, 11, 12
7	171.8, C		171.8, C		
8a	22.3, CH_2	2.92, dd (13.3, 2.3)	22.3, CH_2	2.92, dd (13.3, 2.3)	
8b		2.39[a]		2.39[a]	9, 11
9a	39.6, CH_2	2.06, dd (13.3, 5.0)[a]	39.6, CH_2	2.06, dd (13.3, 5.0)[a]	
9b		1.12, m		1.12, m	
10	40.6, C		40.6, C		
11	117.8, C		117.8, C		
12	171.0, C		171.0, C		
13	54.6, CH_2	4.72, s	54.6, CH_2	4.72, s	1”, 7, 11, 12
14	13.0, CH_3	0.98, s	13.0, CH_3	0.98, s	1, 5, 9, 10
15	17.8, CH_3	1.29, s	17.8, CH_3	1.28, s	3, 4, 5
1′	175.0, C		171.6, C		
2′	40.5, CH	2.37[a]	43.1, CH_2	2.17, dd (7.0, 4.9)	1′, 3′, 4′, 5′
3′a	26.4, CH_2	1.58[a]	25.6, CH	2.00[a]	1′,[c] 4′, 5′
3′b		1.46, ddq (13.9, 7.5, 6.9)			1′,[c] 4′,[c] 5′[c]
4′	11.2, CH_3	0.87, dd (7.5, 7.5)	22.2, CH_3	0.92, d (6.7)	2′, 3′
5′	16.4, CH_3	1.07, d (7.0)	22.2, CH_3	0.92, d (6.7)	1′,[c] 2′, 3′
1″	170.1, C		170.1, C		
2″	20.6, CH_3	2.01, s[a]	20.6, CH_3	2.01, s[a]	1′, 13

[a] Overlapped signals. [b] HMBC spectrum for compounds **8** and **9** as observed in the mixture. [c] Observed solely for compound **8**. [d] Observed solely for compound **9**.

DOI: 10.1021/acs.jnatprod.8b00791
J. Nat. Prod. 2019, 82, 1424−1433

Table 2. ^{1}H and ^{13}C NMR Spectroscopic Data (500 MHz, DMSO-d_6) for **10** and **11**

	10			**11**[b]	
position	δ_C, type	δ_H (J in Hz)	HMBC	δ_C, type	δ_H (J in Hz)
1	78.4, C			78.4, C	
2α	46.8, CH_2	1.61, dd (14.2, 4.3)[a]	1, 3, 4, 10	46.8, CH_2	1.61, dd (14.2, 3.8)
2β		2.62, dd (14.2, 6.0)	1, 3, 4, 5, 10		2.61, dd (14.2, 6.0)
3	77.6, CH	3.55, dd (6.0, 4.7)	1, 4, 5	77.5, CH	3.55, dd (6.0, 4.0)
4	79.2, C			79.2, C	
5	60.6, CH	2.28, d (9.8)	1, 4, 6, 7, 10, 14,	60.7, CH	2.28, d (9.8)[a]
6	75.4, CH	4.38, dd (9.8, 9.8)	4, 5, 7, 8	75.4, CH	4.38, dd (9.6, 9.6)
7	41.2, CH	4.15, dddd (9.8, 9.8, 3.4, 3.2)	5, 6, 11, 12	41.1, CH	4.14, dddd (9._, 9.5, 3.1, 2.4)
8	72.5, CH	5.24, dd (9.8, 4.9)	1′, 9, 10, 11	72.5, CH	5.24, dd (9.8, 4.3)
9	121.4, CH	5.33, brd (4.9)	1, 7, 10, 15	121.6, CH	5.34, d (4.3)
10	143.9, C			143.7, C	
11	138.7, C			138.5, C	
12	169.4, C			169.4, C	
13a	120.9, CH_2	6.06, d (3.4)	7, 8, 11, 12	121.0, CH_2	6.05, d (3.1)
13b		5.54, d (3.0)	7, 8, 12		5.57, d (2.4)
14	23.1, CH_3	1.24, s	3, 4, 5	23.1, CH_3	1.24, s
15	24.9, CH_3	1.81, s	1, 9, 10	24.9, CH_3	1.81, s
1′	175.2, C			171.9, C	
2′	40.3, CH	2.41, ddq (13.7, 13.7, 7.0)	1′, 3′, 4′, 5′	42.4, CH_2	2.26, d (7.0)
3′a	26.0, CH_2	1.65, m[a]	1′, 2′, 4′, 5′	25.1, CH	2.02, m
3′b		1.44, ddq (13.7, 13.7, 7)	1′, 2′, 4′, 5′		
4′	11.5, CH_3	0.88, dd (7.2, 7.2)	2′, 3′	22.1, CH_3	0.93, d (6.4)[a]
5′	16.4, CH_3	1.10, d (7.0)	1′, 2′, 3′	22.1, CH_3	0.93, d (6.4)[a]

[a] Overlapping signals. [b] HMBC data for the core structure were identical to those of **10**.

Table 3. ^{1}H and ^{13}C NMR Spectroscopic Data (500 MHz, $CDCl_3$) for **17**

position	δ_C, type	δ_H (J in Hz)	HMBC
1	130.7, C		
2	185.5, C		
3	126.1, CH	6.21, d (9.8)	1, 5
4	155.3, CH	6.78, d (9.8)	2, 6, 10, 14
5	38.4, C		
6α	39.5, CH_2	2.45, dd (15.3, 2.1)	4, 5, 7, 8, 14
6β		1.57, dd (15.3, 4.9)	4, 5, 14
7	75.4, CH	4.77, ddd (4.9, 4.9, 2.1)	6, 9
8	43.7, CH	2.32[a]	9, 11, 12
9α	28.3, CH_2	2.04, m	1, 8, 10, 12
9β		2.67, dd (13.7, 6.7)	1, 7, 8, 10
10	155.4, C		
11	180.1, C		
12	61.3, C		
13α	37.6, CH_2	2.50, d (11.9)	1′, 2′, 8, 10, 11, 12
13β		1.62, d (11.9)	2′, 5′, 8, 11, 12
14	24.9, CH_3	1.27, s	4, 5, 6
15	10.8, CH_3	1.90, s[a]	1, 10
1′	63.2, C		
2′	139.0, CH	6.17, d (5.8)	1′, 3′, 4′, 5′
3′	137.1, CH	5.90, d (5.8)	1′, 2′, 4′, 5′, 14′
4′	61.4, C		
5′	65.2, CH	2.96, d (10.0)	1′, 2′, 3′, 4′, 6′, 7′, 13
6′	79.6, CH	4.00, dd (9.8, 9.8)	5′, 8′
7′	43.0, CH	3.39, m	
8′α	23.6, CH_2	2.28[a]	6′, 7′, 9′
8′β		1.45, m	10′
9′a	34.8, CH_2	1.89, m;[a] 1.83[a]	1′, 7′, 10′
9′b		1.83, m[a]	1′, 8′, 10′
10′	72.4, C		
11′	170.3, C		
12′	140.5, C		
13′a	118.7, CH_2	6.07, d (3.7)	7′, 11′, 12′
13′b		5.35, d (3.4)	7′, 11′
14′	16.1, CH_3	1.54, s	3′, 4′, 5′, 12
15′	29.9, CH_3	1.38, s	1′, 9′, 10

[a] Overlapping signals.

■ EXPERIMENTAL SECTION

General Experimental Procedures. Optical rotations were measured at a concentration of 1 mg/mL in chloroform utilizing a PerkinElmer 341 polarimeter with a 10 cm microcell. UV and ECD spectra were recorded in methanol (66−400 μg/mL) on a Chirascan CD spectrometer using 1 mm path precision cells (110 QS, Hellma Analytics). IR and VCD spectra were recorded on a Bruker PMA 50 accessory coupled to a Tensor 27 Fourier transform infrared spectrometer. A photoelastic modulator (Hinds PEM 90) set at l/4 retardation was used to modulate the handedness of the circular-polarized light. Demodulation was performed by a lock-in amplifier (SR830 DSP). An optical low-pass filter (<1800 cm^{-1}) in front of the photoelastic modulator was used to enhance the signal/noise ratio. Solutions of 3−8 mg in 130−400 μL of deuterated solvent ($CDCl_3$ or DMSO-d_6) were prepared and measured in a transmission cell equipped with CaF_2 windows and a 200 μm spacer. The VCD spectrum of the pure solvent served as the reference and was subtracted from the VCD spectrum of the compound in order to eliminate artifacts. For both the sample and the reference, ca. 24 000 scans at 4 cm^{-1} resolution were averaged. NMR data were recorded on a Bruker Avance III NMR spectrometer operating at 500.13 MHz for ^{1}H and 125.77 MHz for ^{13}C nuclei. ^{1}H NMR data and COSY, HSQC, HMBC, and NOESY spectra were measured at 18 °C in a 1 mm TXI probe with a z-gradient. ^{13}C NMR/DEPTQ spectra were recorded at 23 °C in 3 mm tubes with a 5 mm BBI probe. Spectra were analyzed by Bruker TopSpin 3.0 and ACDLabs Spectrus Processor. Either a Bruker Kappa Apex 2 diffractometer or a Stoe StadiVari diffractometer equipped with a Pilatus 300 K detector was used to collect X-ray diffraction data. The structure was solved with Superflip[22] and refined using Crystals.[23] HPLC-PDA-ELSD-ESIMS data were recorded in the positive mode on a Shimadzu LC-MS/MS 8030 triple quadrupole MS connected via a T-splitter (1:10) to a Shimadzu HPLC system consisting of degasser, binary high-pressure mixing pump, autosampler, column oven, and diode array detector, and via a T-splitter to an Alltech 3300 ELSD detector. Data acquisition and processing was performed with LabSolution software. Semipreparative HPLC separations were carried out with an Agilent HP 1100 Series system consisting of a quaternary pump, autosampler, column oven, and a diode array detector (G1315B). Chemstation software was used for data acquisition and processing. Waters SunFire C_{18} (3.5 μm, 3.0 × 150 mm i.d., equipped with a guard column 10 × 3.0 mm i.d.), SunFire Prep C_{18} (5 μm, 10 × 150 mm i.d., equipped with a guard column 10 × 10 mm i.d.), and SunFire Prep C_{18} OBD (5 μm, 30 × 150 mm i.d., equipped with a guard column 10 × 20 mm i.d.) columns were used for analytical, semipreparative, and preparative separations, respectively. HPLC-grade methanol, acetonitrile (Scharlau Chemie), and water from a Milli-Q water purification system (Merck Millipore) were used for

DOI: 10.1021/acs.jnatprod.8b00791
J. Nat. Prod. 2019, 82, 1424−1433

Table 4. In Vitro Inhibitory Concentrations of *Artemisia argyi* Extract and Selected Constituents Leading to Inhibition of T-Cell Proliferation by 50% (IC_{50}) in [μg/mL] (Middle Column) and [μM] (Right Column)

compound[a]	IC_{50} [μg/mL] ± SD	IC_{50} [μM] ± SD
1	0.8 ± 0.3	2.7 ± 0.9
3	0.3 ± 0.1	1.0 ± 0.4
4	0.3 ± 0.1	1.2 ± 0.3
5	1.0 ± 0.3	3.7 ± 1.1
6	5.0 ± 2.2	13.8 ± 5.9
7	4.9 ± 1.3	19.6 ± 5.3
8 + **9** (ratio 2:1)	7.1 ± 3.9	16.8 ± 9.2
12	1.9 ± 0.6	5.8 ± 1.7
13 + **14** (ratio 1:1)	0.7 ± 0.2	1.8 ± 0.4
15	0.6 ± 0.2	1.9 ± 0.7
16	4.0 ± 0.5	11.7 ± 1.4
18	1.7 ± 0.7	3.2 ± 1.3
CsA	0.3 ± 0.2	0.2 ± 0.2
extract	16.1 ± 3.6	

[a] Compounds **2**, **10**, **11**, and **17** were not tested due to the limited amounts available.

HPLC separations. The mobile phase used for analytical HPLC contained 0.1% formic acid. An analytical Nucleodur 100-5 CN column (5.0 μm, 4.0 × 125 mm i.d.) and a semipreparative Nucleodur 100-5 CN column (5.0 μm, 10.0 × 150 mm i.d.) (both Macherey-Nagel) were used for normal-phase HPLC separations. NMR spectra were recorded in $CDCl_3$ (Sigma-Aldrich) or DMSO-d_6 (Armar Chemicals). Technical-grade solvents purified by distillation were used for extraction and open column chromatography. Silica gel (63–200 μm and 15–40 μm, Merck) was used for open column chromatography. HRESIMS data were measured on a LQT XL Orbitrap mass spectrometer (Thermo Scientific) via direct injection.

Plant Material. *Artemisia argyi* whole plants, batch number 150788859, were purchased from Peter Weinfurth, Bochum, Germany, in March 2016. A voucher specimen (number 00 979) has been deposited at the Division of Pharmaceutical Biology, University of Basel, Switzerland.

Microfractionation. Microfractionation of *A. argyi* EtOAc extract was carried out by analytical RP-HPLC on an LC-MS 8030 system (Shimadzu) connected with an FC 204 fraction collector (Gilson). A solution of 10 mg/mL extract in DMSO was prepared. In total, three injections were performed: 2 × 30 μL using only DAD for detection for collection (0.6 mg of extract in total) and 1 × 10 μL with UV-ELSD-ESIMS detection without collection. Water with 0.1% formic acid (A) and acetonitrile with 0.1% formic acid (B) were used as mobile phase. The gradient was 5% to 100% B in 30 min followed by 5 min at 100% B. Fractions of 1 min each were collected from minute 2 to minute 32, resulting in 30 microfractions in total. Microfractions of two successive injections of the extract were collected into the corresponding wells of a 96-deep-well plate. The plate was dried in a Genevac EZ-2 evaporator.

Extraction and Isolation. A 400 g aliquot of plant material was ground using a M20 universal mill (IKA). The powdered material was mixed with 400 g of sea sand and percolated with EtOAc (ca. 12 L) to afford 42 g of crude extract. A portion (20 g) of the extract was fractionated by column chromatography (CC) on silica gel (80 × 5 cm, 63–200 μm) using a gradient of *n*-hexane–EtOAc–MeOH (95:5:0 to 0:100:0 to 0:50:50) as mobile phase. Fractions A–R were combined based on TLC patterns (silica gel, *n*-hexane–EtOAc, 70:30, 50:50, and 35:65, respectively; detection with 1% ethanolic vanillin and 10% sulfuric acid, followed by heating). Fraction M (80 mg) was submitted to preparative RP-HPLC [H_2O (A), MeCN (B); 15 → 100% B (0–30 min), 100% B (30–35 min), flow rate 25 mL/min; sample concentration 100 mg/mL in DMSO; injection volume 700 μL], yielding jaceosidin (**12**, 8.7 mg, t_R 15.1 min), santamarin (**7**, 3.9 mg, t_R 16.0 min), and eupatilin (**16**, 21.8 mg, t_R 17.4 min). Fraction P (769 mg) was submitted to preparative RP-HPLC [H_2O (A), MeCN (B); 25 → 60% B (0–30 min), 60 → 100% B (30–32 min), 100% B (32–37 min), flow rate 20 mL/min; sample concentration 100 mg/mL in DMSO; injection volume 1000 μL], yielding fractions P_1–P_{26}. Fraction P_5 afforded crystals of artecanin (**5**, 18.5 mg). P_{14} consisted of eudesmaafraglaucolide (**6**, 15.9 mg, t_R 15.6 min), and P_{17} was found to be a mixture of **8** and **9** (2.0 mg, t_R 18.8 min). P_{26} consisted of 8-acetylarteminolide (**18**, 7 mg, t_R 28.0 min). P_3 was purified by semipreparative HPLC on a Nucleodur 100-5 CN column [*n*-heptane (A), isopropanol (B); 5% B (0–3 min), 5 → 15% B (3–6 min), 15% (6–16 min), flow rate 3 mL/min; sample concentration 20 mg/mL in 2:1 isopropanol–*n*-heptane; injection volume 75 μL] to afford canin (**1**, 2.9 mg, t_R 16.2 min), *seco*-tanapartholides B (**3**, 8.1 mg, t_R 16.9 min) and A (**4**, 4.8 mg, t_R 17.9 min), and 10-*epi*-artecanin (**2**, 0.8 mg, t_R 18.8 min). Fraction K (452 mg) was separated by preparative RP-HPLC [H_2O (A), MeCN (B); 45% (0–2 min), 45 → 70% B (2–30 min), 60 → 100% B (30–31 min), 100% B (31–40 min), flow rate 20 mL/min; sample concentration 75 mg/mL in DMSO; injection volume 100–900 μL]. K_{11} consisted of a mixture of 3α,4α-epoxyrupicolines E and D (**13** and **14**, 2.3 mg, t_R 21.3 min). Crystals formed in the vial were identified by X-ray crystallography as 3α,4α-epoxyrupicolin E (**14**). K_5 consisted of arteglasin A (**15**, 3.0 mg, t_R 14.7 min). From a second portion of extract (20 g) a targeted isolation of compounds **8** and **9** was performed. For this, the extract was fractionated on an MPLC glass column (Büchi) packed with silica gel (40 × 7 cm, 15–40 μm) utilizing an Interchim Puriflash 4100 system [*n*-hexane (A), EtOAc (B); 20% B (0–15 min) 20 → 30% B (15–20 min), 30% B (15–50 min), 30 → 80% (50–80 min), 80% (80–130 min), 80 → 95% (130–160 min), 95% (160–215 min), flow rate 30 mL/min; sample introduction via dry load, with 20 g of extract adsorbed on 40 g silica gel 15–40 μm]. Separation was monitored by HPLC-ESIMS, and fractions containing the target molecules were combined, dried, and submitted to preparative RP-HPLC [H_2O (A), MeCN (B); 25% B (0–3 min), 25 → 30% B (3–10 min), 30% B (10–40 min); flow rate 20 mL/min; sample concentration 130 mg/mL in DMSO; injection volume 900 μL]. This separation yielded compounds **10** (1.9 mg, t_R 27.3 min) and **11** (1.7 mg, t_R 29.8 min) and a peak (5.4 mg, t_R 36.1 min), which was further purified by semipreparative HPLC (Nucleodur 100-5 CN) [H_2O (A), MeCN (B); 17 → 20% B (0–27 min), 20 → 100% B (27–29 min), 100% B (29–40 min); flow rate 4 mL/min; sample concentration 20 mg/mL in DMSO; injection volume 100 μL] to afford a mixture of **8** and **9** (1.4 mg, t_R 20.3 min).

*Canin (**1**):* white solid; $[\alpha]_D^{25}$ +7 (*c* 0.1 g/100 mL, CH_2Cl_2); UV λ_{max} (MeOH) (log ε) 209 (4.0) nm; ECD (MeOH, *c* 0.96 mM, 0.1 cm); Δε +4.0 (202 nm) −0.9 (252 nm); ^1H and ^{13}C NMR, see Table S1, Supporting Information; HRESIMS *m*/*z* 301.1054 $[M + Na]^+$ (calcd for $C_{15}H_{18}O_5Na$, 301.1052).

*10-epi-Canin (**2**):* UV λ_{max} (MeOH) (log ε) 207 (3.9) nm; ECD (MeOH, *c* 0.54 mM, 0.1 cm); Δε +4.9 (195 nm) −0.8 (257 nm); ^1H and ^{13}C NMR, see Table S1, Supporting Information; HRESIMS *m*/*z* 301.1057 $[M + Na]^+$ (calcd for $C_{15}H_{18}O_5Na$, 301.1052).

*(−)-seco-Tanapartholide B (**3**):* colorless gum; $[\alpha]_D^{25}$ −62 (*c* 0.1 g/100 mL, CHCl3); UV λ_{max} (MeOH) (log ε) 213 (4.2) nm; ECD (MeOH, *c* 0.60 mM, 0.1 cm); Δε +10.0 (228 nm) −1.8 (330 nm); ^1H and ^{13}C NMR see Table S2, Supporting Information; HRESIMS *m*/*z* 301.1055 $[M + Na]^+$ (calcd for $C_{15}H_{18}O_5Na$, 301.1052).

*(+)-seco-Tanapartholide A (**4**):* colorless gum; $[\alpha]_D^{25}$ +79 (*c* 0.1 g/100 mL, $CHCl_3$); UV λ_{max} (MeOH) (log ε) 209 (4.2) nm; ECD (MeOH, *c* 0.60 mM, 0.1 cm); Δε −13.1 (228 nm) +1.8 (330 nm); ^1H and ^{13}C NMR, see Table S2, Supporting Information; HRESIMS *m*/*z* 301.1057 $[M + Na]^+$ (calcd for $C_{15}H_{18}O_5Na$, 301.1052).

*Artecanin (**5**):* UV λ_{max} (MeOH) (log ε) 211 (4.2), 208 (3.7) nm; ECD (MeOH, *c* 1.44 mM, 0.1 cm); Δε +2.7 (202 nm), −0,5 (251 nm); ^1H and ^{13}C NMR, see Table S1, Supporting Information; HRESIMS *m*/*z* 301.1054 $[M + Na]^+$ (calcd for $C_{15}H_{18}O_5Na$, 301.1052).

*Eudesmaafraglaucolide (**6**):* white solid; UV λ_{max} (MeOH) (log ε) 215 (4.0), 288 (2.7) nm; ECD (MeOH, *c* 1.1 mM, 0.1 cm); Δε +3.2 (217 nm), −0.8 (243 nm); ^1H and ^{13}C NMR, see Table S3, Supporting Information; HRESIMS *m*/*z* 387.1431 $[M + Na]^+$ (calcd for $C_{19}H_{24}O_7Na$, 387.1414).

Santamarin (7): white solid; UV λ_{max} (MeOH) (log ε) 211 (4.2), 273 (3.8), 334 (3.9) nm; ECD (MeOH, *c* 0.26 mM, 0.1 cm); $\Delta\varepsilon$ +2.4 (202 nm); ^{1}H and ^{13}C NMR, see Table S3, Supporting Information; HRESIMS *m*/*z* 271.1317 [M + Na]$^+$ (calcd for $C_{15}H_{20}O_3Na$, 271.1305).

Argyinolides K (8) and L (9): white solid; UV λ_{max} (MeOH) (log ε) 210 (3.7) nm; ECD (MeOH, *c* 0.85 mM, 0.1 cm); $\Delta\varepsilon$ −2.4 (225 nm); ^{1}H and ^{13}C NMR see Table 1; HRESIMS *m*/*z* 447.2018 [M + Na]$^+$ (calcd for $C_{24}H_{31}O_8Na$, 447.1989).

Argyinolide M (10): yellow solid; UV λ_{max} (MeOH) (log ε) 200 (4.0) nm; ECD (MeOH, *c* 0.79 mM, 0.1 cm); $\Delta\varepsilon$ +8.5 (195 nm) −0.4 (255 nm); ^{1}H and ^{13}C NMR see Table 2; HRESIMS *m*/*z* 403.1750 [M + Na]$^+$ (calcd for $C_{20}H_{28}O_7Na$, 403.1727).

(+)-Argyinolide N (11): yellow solid; $[\alpha]_D^{25}$ +20 (*c* 0.15 g/100 mL, $CHCl_3$); UV λ_{max} (MeOH) (log ε) 200 (4.1) nm; ECD (MeOH, *c* 0.79 mM, 0.1 cm); $\Delta\varepsilon$ +9.0 (195 nm) −0.5 (256 nm); ^{1}H and ^{13}C NMR see Table 2; HRESIMS *m*/*z* 403.1748 [M + Na]$^+$ (calcd for $C_{20}H_{28}O_7Na$, 403.1727).

Jaceosidin (12): yellow solid; ^{1}H and ^{13}C NMR, see Table S4, Supporting Information; HRESIMS *m*/*z* 353.0649 [M + Na]$^+$ (calcd for $C_{17}H_{14}O_7Na$, 353.0656).

3α,4α-Epoxyrupicolines D and E (13 and 14): UV λ_{max} (MeOH) (log ε) 285 (2.8) nm; ratio 1:1; identification by ^{1}H and ^{13}C NMR, see Table S5, Supporting Information; HRESIMS *m*/*z* 385.1634 [M + Na]$^+$ (calcd for $C_{20}H_{26}O_6Na$, 385.1622).

(+)-Arteglasin A (15): $[\alpha]_D^{25}$ +86 (*c* 0.07 g/100 mL, $CHCl_3$); UV λ_{max} (MeOH) (log ε) 195 (4.2) nm; ECD (MeOH, *c* 0,65 mM, 0.1 cm); $\Delta\varepsilon$ +7.4 (209 nm) −1.0 (231 nm); ^{1}H and ^{13}C NMR, see Table S5, Supporting Information; HRESIMS *m*/*z* 327.1220 [M + Na]$^+$ (calcd for $C_{17}H_{20}O_5Na$, 327.1203).

Eupatilin (16): yellow solid; identification by ^{1}H and ^{13}C NMR see Table S4, Supporting Information; HRESIMS *m*/*z* 367.0808 [M + Na]$^+$ (calcd for $C_{18}H_{16}O_7Na$, 367.0788).

(−)-Argyinolide N (17): white solid; $[\alpha]_D^{25}$ −120 (*c* 0.08 g/100 mL, $CHCl_3$); UV λ_{max} (MeOH) (log ε) 205 (4.2) nm; ECD (MeOH, *c* 0.31 mM, 0.1 cm); $\Delta\varepsilon$ +12.3 (195 nm), +27.5 (207 nm); ^{1}H and ^{13}C NMR see Table 3; HRESIMS *m*/*z* 513.2261 [M + Na]$^+$ (calcd for $C_{30}H_{34}O_6Na$, 513.2248).

(+)-8-Acetylarteminolide (18): white solid; $[\alpha]_D^{25}$ +27 (*c* 0,1 g/100 mL, $CHCl_3$); UV λ_{max} (MeOH) (log ε) 253 (3.8) nm; ECD (MeOH, *c* 0.73 mM, 0.1 cm); $\Delta\varepsilon$ −8.4 (210 nm), +0.7 (240 nm), −1.2 (269 nm); ^{1}H and ^{13}C NMR, see Table S6, Supporting Information; HRESIMS *m*/*z* 571.2313 [M + Na]$^+$ (calcd for $C_{32}H_{36}O_8Na$, 571.2308).

X-ray Analysis of 3α,4α-Epoxyrupicolin E (14). A crystal of **14** with the dimensions 0.11 × 0.13 × 0.21 mm, obtained as a colorless block from $CHCl_3$, was mounted on a Bruker Kappa Apex 2 diffractometer and was kept at 123 K during data collection (CCDC 1862952). The orthorhombic space group $P2_12_12_1$ was observed using Cu Kα radiation ($\hat{L}$ = 1.541 78 Å, a = 9.1487(7) Å, b = 10.3308(7) Å, c = 20.0261(14) Å, $\alpha = \beta = \gamma$ = 90°, V = 1892.7(2) Å^3), giving 3419 independent reflections. The structure was solved with Superflip[22] and refined using Crystals.[23] Non-hydrogen atoms were refined anisotropically, and hydrogen atoms were fixed at the calculated positions. The final indices were R = 0.0473, R_w = 0.0496 and goodness of fit = 1.0832.

X-ray Analysis of Arteglasin A (15). A crystal of **15** with the dimensions 0.05 × 0.09 × 0.14 mm, obtained as a colorless block from $CHCl_3$, was mounted on a Stoe StadiVari diffractometer equipped with a Pilatus 300 K detector and was kept at 123 K during data collection (CCDC 1862953). The orthorhombic space group $P2_12_12_1$ was observed using Ga Kα radiation ($\hat{L}$ = 1.341 43 Å, a = 19.8206(4) Å, b = 9.5646(2) Å, c = 8.4390(2) Å, $\alpha = \beta = \gamma$ = 90°, V = 1599.83(6) Å^3), giving 3101 independent reflections. Non-hydrogen atoms were refined anisotropically, and hydrogen atoms were fixed at the calculated positions. The final indices were R = 0.0265, R_w = 0.0294 and goodness of fit = 1.1151.

Computational Methods. Conformational analysis was performed with Schrödinger MacroModel 9.8 (Schrödinger, LLC, New York, USA) employing the OPLS2005 (optimized potential for liquid simulations) force field in H_2O or chloroform for ECD or VCD calculations, respectively. Selected conformers within a 8 kcal/mol energy window from the global minimum were submitted to geometrical optimization and energy calculation applying density functional theory (DFT) with the Beck's nonlocal three-parameter exchange and correlation functional and the Lee−Yang−Parr correlation functional level (B3LYP), using the B3LYP/6-31G** basis set, the SCRF method, and the CPMC model for solvation (MeOH for ECD calculations) with the Gaussian 09 program package.[24] Vibrational analysis was done at the same level to confirm minima. Excitation energy (denoted by wavelength in nm), rotator strength (R_{str}), dipole velocity (R_{vel}), and dipole length (R_{len}) were calculated in MeOH by TD-DFT/B3LYP/6-31G(d,p). ECD curves were obtained on the basis of rotator strengths with a half-band of 0.3 eV using SpecDis v1.64.[25] Vibrational frequencies (given as wavenumbers in cm^{-1}), rotator strength (R_{str}), IR intensity (IR_{inten}), and dipole strength (R_{str}) were calculated in chloroform or dimethyl sulfoxide with B3LYP/6-31+G(d,p). While the conformational search for compounds measured in chloroform was also performed in chloroform, it was carried out in water for samples measured in methanol or DMSO-d_6. VCD curves were obtained on the basis of rotator strengths with a bandwidth of 10 cm^{-1} using VCDspecTech v22.0.[26,27] ECD and VCD spectra were calculated from the spectra of individual conformers according to their contribution calculated by Boltzmann weighting. Comparison was done visually and by calculation of similarity indices (*Sim*VA, *Sim*VCD) which were generated by VCDspecTech v22.0.[16] The SimVCD values were plotted against the scaling factors of the x axis, and graphs compared between the different stereoisomers.

Ethics Statement. Patients gave their written consent to donate blood for scientific research. All experiments conducted on human material were approved by the Ethics Committee of the University of Freiburg (55/14).

Preparation and Cultivation of Human Peripheral Lymphocytes. Peripheral blood mononuclear cells (PBMCs) were isolated from the blood of healthy adult donors obtained from the Blood Transfusion Centre (University Medical Center, Freiburg, Germany). Venous blood was centrifuged on a LymphoPrep gradient (density: 1.077 g/cm^3, 20 min, 500*g*, 20 °C; Progen). After centrifugation, cells were washed twice with phosphate-buffered saline (PBS) and subsequently cultured in RPMI 1640 medium supplemented with 10% heat-inactivated fetal calf serum (GE Healthcare Life Sciences), 2 mM L-glutamine, 100 U/mL penicillin, and 100 U/mL streptomycin (all from Life Technologies). The cells were cultured at 37 °C in a humidified incubator with a 5% CO_2/95% air atmosphere.

T Cell Proliferation Assay. Lymphocytes were isolated, washed twice in cold PBS, and resuspended in PBS at a concentration of 5 × 10^6 cells/mL. Cells were stained for 10 min at 37 °C with carboxyfluorescein diacetate succinimidyl ester (CFSE; 5 μM: Sigma-Aldrich, St. Louis, MO, USA). The staining was stopped by washing twice with complete medium. Stained lymphocytes (2 × 10^6 cells/mL) were stimulated with anti-human CD3 (clone HIT3a) and anti-human CD28 (clone 28.2) mAbs (each 100 ng/mL; eBioscience) in the presence of either medium, cyclosporin A (CsA; 4.16 μM; Novartis Pharma), camptothecin (CPT; 300 μM; Tocris), or plant extracts/single compounds (concentration range 0.01−100 μg/mL) and incubated for 72 h. The negative control remained unstimulated. Flow cytometric analysis of the cell division was performed using a FACSCalibur instrument (BD Biosciences).

Determination of Apoptosis and Necrosis of T Cells. Lymphocytes were isolated, washed twice in cold PBS, and resuspended in medium at a concentration of 2 × 10^6 cells/mL. Cells were stimulated with anti-human CD3 (clone HIT3a) and anti-human CD28 (clone 28.2) mAbs (each 100 ng/mL; eBioscience) in the presence of either medium, camptothecin (CPT; 300 μM; Tocris), 0.5% Triton-X 100, or plant extracts/single compounds (concentration range 0.01−100 μg/mL) and cultivated for 48 h. The negative control remained unstimulated. Cultured cells were washed with PBS and stained with annexin V-FITC using the apoptosis-detection kit (eBioscience) according to the manufacturer's instructions. Propidium iodide (eBioscience) was added, and cells were stained for 15 min at room temperature in the dark. Apoptosis and necrosis rates were determined by flow cytometric analysis using a FACSCalibur instrument (BD Biosciences).

Testing of Microfractions. The dried microfractions in 96-deep-well plates were dissolved in 25 μL of DMSO by sonication and mixing with a pipet. Of these stock solutions, dilutions of 1:1, 1:3, 1:10, and 1:30 were prepared and tested in duplicates for T lymphocyte proliferation inhibition as described above. Assuming an equal distribution of 200 ng substance in each of the microfractions, theoretical IC_{50} values were calculated to be used as a relative measure of activity. They were normalized to 100% with the highest value representing 100%.

■ ASSOCIATED CONTENT

Supporting Information

The Supporting Information is available free of charge on the ACS Publications website at DOI: 10.1021/acs.jnatprod.8b00791.

T lymphocyte proliferation inhibition data for compounds **1**, **3−5**, **15**, and **18**; ^{1}H and ^{13}C NMR data for compounds **1−7**, **12−16**, and **18**; experimental and computed ECD spectra of compounds **2**, **5−11**, **13−15**, **17**, and **18**; experimental and computed VCD spectra of compounds **4** and **18**; 1D and 2D NMR spectra of compounds **1−5**, **8−11**, and **17**; table of crystallographic data and ORTEP diagrams for compounds **14** and **15** (PDF)

Crystallographic data for **14** (CIF)

Crystallographic data for **15** (CIF)

■ AUTHOR INFORMATION

Corresponding Author

*Tel: +41 61 267 14 25. Fax: +41 61 267 14 74. E-mail: matthias.hamburger@unibas.ch.

ORCID

Maria De Mieri: 0000-0001-5567-2072
Martin Smieško: 0000-0003-2758-2680
Thomas Bürgi: 0000-0003-0906-082X
Matthias Hamburger: 0000-0001-9331-273X

Author Contributions

[#]J. K. Reinhardt and A. M. Klemd contributed equally to this work.

Notes

The authors declare no competing financial interest.

■ ACKNOWLEDGMENTS

ECD spectra were measured at the Biophysics Facility, Biozentrum, University of Basel. X-ray diffraction was measured by Dr. Markus Neuburger at the Laboratory for Chemical Crystallography, University of Basel.

■ REFERENCES

(1) Lleo, A.; Invernizzi, P.; Gao, B.; Podda, M.; Gershwin, M. E. *Autoimmun. Rev.* **2010**, *9*, A259−A266.

(2) Chaplin, D. D. *J. Allergy Clin. Immunol.* **2010**, *125*, S3−23.

(3) Her, M.; Kavanaugh, A. *J. Allergy Clin. Immunol.* **2016**, *137*, 19−27.

(4) Taylor, A. L.; Watson, C. J.; Bradley, J. A. *Crit. Rev. Oncol./Hematol.* **2005**, *56*, 23−46.

(5) Quah, B. J.; Parish, C. R. *J. Visualized Exp.* **2010**, *44*, No. e2259.

(6) Potterat, O.; Hamburger, M. *Nat. Prod. Rep.* **2013**, *30*, 546−64.

(7) Potterat, O.; Hamburger, M. *Planta Med.* **2014**, *80*, 1171−81.

(8) Harborne, J. B.; Mabry, T. J.; Mabry, H. *The Flavonoids*; Academic Press: New York, 1975.

(9) Jakupovic, J.; Klemeyer, H.; Bohlmann, F.; Graven, E. H. *Phytochemistry* **1988**, *27*, 1129−1133.

(10) Romo de Vivar, A.; Jimenez, H. *Tetrahedron* **1965**, *21*, 1741−1745.

(11) Jin, H. Z.; Lee, J. H.; Lee, D.; Hong, Y. S.; Kim, Y. H.; Lee, J. J. *Phytochemistry* **2004**, *65*, 2247−2253.

(12) Lee, K. H.; Matsueda, S.; Geissman, T. A. *Phytochemistry* **1971**, *10*, 405−410.

(13) Nakasugi, T.; Nakashima, M.; Komai, K. *J. Agric. Food Chem.* **2000**, *48*, 3256−3266.

(14) Lee, K. H.; Simpson, R. F.; Geissman, T. A. *Phytochemistry* **1969**, *8*, 1515−1521.

(15) Hewlett, M. J.; Begley, t. l. M. J.; Groenewegen, W. A.; Heptinstall, S.; Knight, D. W.; May, J.; Salan, U.; Toplis, D. *J. Chem. Soc., Perkin Trans. 1* **1996**, *1*, 1979−1986.

(16) Polavarapu, P. L.; Covington, C. L. *Chirality* **2014**, *26*, 539−52.

(17) Bohlmann, F.; Zdero, C. *Phytochemistry* **1982**, *21*, 2543−2549.

(18) Tan, R. X.; Jakupovic, J.; Bohlmann, F.; Jia, Z. J.; Huneck, S. *Phytochemistry* **1991**, *30*, 583−587.

(19) Kawazoe, K.; Tsibouchi, Y.; Abdullah, N.; Takaishi, Y.; Shibata, H.; Higuti, T.; Hori, H.; Ogawa, M. *J. Nat. Prod.* **2003**, *66*, 538−539.

(20) Ahmed, A. A.; El-Moghazy, S. A.; El-Shanawany, M. A.; Abdel-Hani, H. F.; Karchedy, J.; Sturtz, G.; Dalley, K.; Paré, P. W. *J. Nat. Prod.* **2004**, *67*, 1705−1710.

(21) Lee, S.-H.; Kang, H.-M.; Song, H.-C.; Lee, H.; Lee, U. C.; Son, K.-H.; Kim, S.-H.; Kwona, B.-M. *Tetrahedron* **2000**, *56*, 4711−4715.

(22) Palatinus, L.; Chapuis, G. *J. Appl. Crystallogr.* **2007**, *40*, 786−790.

(23) Betteridge, P. W.; Carruthers, J. R.; Cooper, R. I.; Prout, K.; Watkin, D. J. *J. Appl. Crystallogr.* **2003**, *36*, 1487−1487.

(24) Frisch, M. J.; Trucks, G. W.; Schlegel, H. B.; Scuseria, G. E.; Robb, M. A.; Cheeseman, J. R.; Scalmani, G.; Barone, V.; Mennucci, B.; Petersson, G. A.; Nakatsuji, H.; Caricato, M.; Li, X. H. H. P.; Izmaylov, A. F.; Bloino, J. Z. G.; Sonnenberg, J. L.; Hada, M.; Ehara, M.; Toyota, K.; Fukuda, R.; Hasegawa, J.; Ishida, M.; Nakajima, T.; Honda, Y.; Kitao, O.; Nakai, H.; Vreven, T.; Montgomery, J. A., Jr.; Peralta, J. E.; Ogliaro, F.; Bearpark, M. J.; Heyd, J.; Brothers, E. N.; Kudin, K. N.; Staroverov, V. N.; Kobayashi, R.; Normand, J.; Raghavachari, K.; Rendell, A. P.; Burant, J. C.; Iyengar, S. S.; Tomasi, J.; Cossi, M.; Rega, N.; Millam, N. J.; Klene, M.; Knox, J. E.; Cross, J. B.; Bakken, V.; Adamo, C.; Jaramillo, J.; Gomperts, R.; Stratmann, R. E.; Yazyev, O.; Austin, A. J.; Cammi, R.; Pomelli, C.; Ochterski, J. W.; Martin, R. L.; Morokuma, K.; Zakrzewski, V. G.; Voth, G. A.; Salvador, P.; Dannenberg, J. J.; Dapprich, S.; Daniels, A. D.; Farkas, O.; Foresman, J. B.; Ortiz, J. V.; Cioslowski, J.; Fox, D. J. *Gaussian 09*; Gaussian, Inc.: Wallingford, CT, USA, 2009.

(25) Bruhn, T.; Schaumlöffel, A.; Hemberger, Y. *SpecDis* v1.64; University of Würzburg: Germany, 2015.

(26) Covington, C. L.; Polavarapu, P. L. *VCDspecTech* v22.0; https://sites.google.com/site/cdspechtech1/, 2017.

(27) Covington, C. L.; Polavarapu, P. L. *Chirality* **2017**, *29*, 178−192.

Supporting Information

Sesquiterpene Lactones from *Artemisia argyi*: Absolute Configuration and Immunosuppressant Activity

Jakob K. Reinhardt,[†,#] *Amy M. Klemd,*[‡,#] *Ombeline Danton,*[†] *Maria De Mieri,*[†] *Martin Smieško,*[§]
Roman Huber,[‡] *Thomas Bürgi,*[⊥] *Carsten Gründemann,*[‡] *Matthias Hamburger*[†,]*

[†]Pharmaceutical Biology, Pharmacenter, University of Basel, Klingelbergstrasse 50, 4056 Basel,
Switzerland

[‡]Center for Complementary Medicine, Institute for Infection Prevention and Hospital
Epidemiology, Faculty of Medicine, University of Freiburg, Breisacher Straße 115 B, 79106
Freiburg, Germany

[§]Department of Molecular Modeling, University of Basel, Klingelbergstrasse 50, 4056 Basel,
Switzerland

[⊥]Department of Physical Chemistry, University of Geneva, 30 Quai Ernest Ansermet, 1211
Geneva, Switzerland

[#]equally contributed to this work

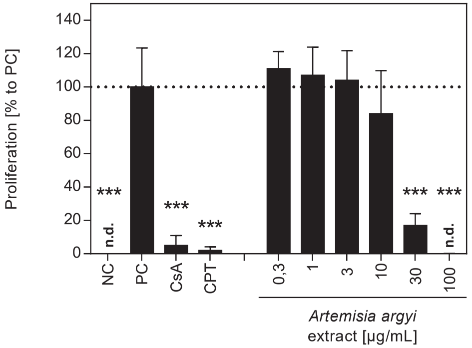

Figure S1. Inhibitory effects of *A. argyi* EtOAc extract on the proliferation of T lymphocytes. Data of three independent experiments were summarized and depicted as means ± standard deviation in relation to the untreated, stimulated control (PC; = 100% ± SD). *P < 0.05, **P < 0.01, ***P < 0.001.

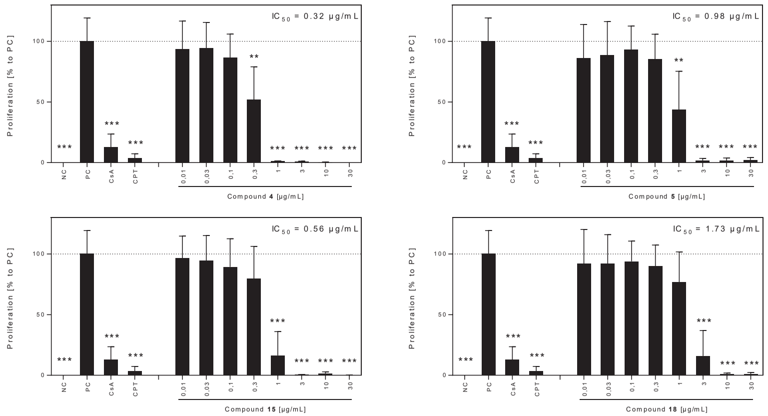

Figure S2. Inhibitory effects of compounds **4**, **5**, **15**, and **18** on the proliferation of T lymphocytes. Data of three independent experiments were summarized and depicted as means ± standard deviation in relation to the untreated, stimulated control (PC; = 100% ± SD). *P < 0.05, **P < 0.01, ***P < 0.001.

Table S2. ^{1}H and ^{13}C NMR Spectroscopic Data (500 MHz, $CDCl_3$) for compounds **3** and **4**.

	3		**4**	
position	δ_C, type	δ_H (*J* in Hz)	δ_C, type	δ_H (*J* in Hz)
1	204.8, C		204.9, C	
2	132.9, CH	5.94, d (5.8)	133.4, CH	6.01, d (5.8)
3	165.9, CH	7.33, d (5.8)	167.2, CH	7.44, d (5.8)
4	77.9, C		77.3, C	
5	58.1, CH	2.23, d (7.3)	56.6, CH	2.50, m[a]
6	80.6, CH	4.45, dd (7.3, 3.1)	79.7, CH	4.52, dd (5.8, 2.1)
7	40.7, CH	3.27, m	39.7, CH	3.50, m
8	28.2, CH_2	1.70, m	26.1, CH_2	1.84, m
9	39.4, CH_2	2.39, m	39.4, CH_2	2.49, m[a]
10	207.8, C		207.3, C	
11	137.8, C		137.8, C	
12	169.6, C		169.2, C	
13	124.1, CH_2	6.06, d (2.1)	122.7, CH_2	6.15, d (2.7)
		5.51, d (1.8)		5.54, d (2.4)
14	30.0, CH_3	1.41, s	30.0, CH_3	1.45, s
15	28.7, CH_3	1.99, s	27.2, CH_3	2.08, s

[a]Overlapping signals

Table S1. ^{1}H and ^{13}C NMR Spectroscopic Data (500 MHz, $CDCl_3$) for compounds **1**, **2**, and **5**.

	1		**2**[c]		**5**[b]	
position	δ_C, type	δ_H (*J* in Hz)	δ_C, type	δ_H (*J* in Hz)	δ_C, type	δ_H (*J* in Hz)
1	79.8, C		78.2, C		77.8, C	
2	58.7, CH	3.47, d (0.9)	55.4, CH	3.54, d (0.9)	56.0, CH	3.63, br. s
3	58.3, CH	3.28, d (0.9)	57.6, CH	3.35, d (0.9)	57.0, CH	3.40, br. S
4	73.7, C		71.8, C		70.2, C	
5	50.3, CH	2.55, d (11.9)	44.7, CH	2.26, d (10.7)	42.5, CH	2.81, d (11.0)
6	78.3, CH	4.22, dd (11.9, 9.5)	81.1, CH	4.12, dd(10.7, 10.7)	82.4, CH	3.91, dd (11.0, 10.4)
7	45.2a, CH	3.39, m	51.3, CH	2.57, m	44.0, CH	3.25, m
8	23.7, CH_2	2.35, m	20.2, CH_2	1.98, m	22.2, CH_2	2.10, m
		1.52, m[a]		1.62, m[a]		1.45, m[a]
9	34.3, CH_2	2.01, ddd (15.0, 6.1, 4.3)	42.2, CH_2	2.17, ddd (15.6, 6.4, 2.8)	37.0, CH_2	1.68, m
		1.83, ddd (15.0, 10.7, 6.1)		1.80, ddd (15.0, 11.4, 3.2)		
10	72.4, C		69.4, C		70.4, C	
11	139.6, C		138.8, C		139.6, C	
12	169.4, C		169.2, C		169.8, C	
13	120.2, CH_2	6.21, d (3.4)	118.3, CH_2	6.16, d (3.1)	118.8, CH_2	6.02, d (3.7)
		5.50, d (3.1)		5.44, d (3.1)		5.57, d (3.4)
14	19.4, CH_3	1.57, s[a]	19.6, CH_3	1.57, s[a]	19.6, CH_3	1.41, s[a]
15	27.2, CH_3	1.16, s	27.6, CH_3	1.41, s	26.9, CH_3	0.94, s

[a]Overlapping signals, [b]Measured in DMSO, [c]^{13}C extracted from ^{1}H–^{13}C 2D inverse-detected experiments. [d]Apparent multiplet

Table S3. ^{1}H and ^{13}C NMR Spectroscopic Data (500 MHz, CDCl$_3$) for compounds **6** and **7**.

	6		**7**	
position	δ_C, type	δ_H (J in Hz)	δ_C, type	δ_H (J in Hz)
1	74.9, CH	3.41, dd (11.8, 4.4)[a]	75.2, CH	3.67, dd (10.1, 6.7)[a]
1'	170.7, C			
1''	169.7, C			
2	36.8, CH$_2$	1.54, q (11.9)	32.8, CH$_2$	2.39, m[a]
		2.08, m		1.98, m
2'	20.8, CH	1.96, s		
2''	20.9, CH$_3$	2.03, s[a]		
3	70.3, CH	5.004, m[a]	121.3, CH	5.35, brs
4	140.5, C		133.5, C	
5	52.5, CH	1.67, d (10.8)	51.1, CH	2.34, d (11.6)[a]
6	77.8, CH	4.95, d (10.8)	81.5, CH	3.94, m[a]
7	172.3, C		51.0, C	2.49, m
8	22.5, CH$_2$	2.37, td (14.0, 5.5)	21.2, CH$_2$	1.64, qd (12.5, 3.0)
		2.94, brdd (14.6, 2.8)		2.08, m[a]
9	36.3, CH$_2$	2.06, brdd (13.3, 5.0)[a]	34.2, CH$_2$	2.07, m[a]
		2.21, ddd (12.8, 5.8, 1.8)		1.31, td (13.2, 4.1)
10	41.3, C		40.9, C	
11	119.4, C		170.8, C	
12	168.3, C		138.9, C	
13	54.8, CH$_2$	4.68, d (2.4)	116.9, CH$_2$	5.40, d (3.8)
				6.07, d (3.1)
14	10.4, CH$_3$	0.83, td (13.5, 4.4)	11.0, CH$_3$	0.88, s
15	107.9, CH$_3$	5.003, s[a]	23.3, CH$_3$	1.84, s
		5.12, s		

[a]Overlapping signals

Table S4. ^{1}H and ^{13}C NMR Spectroscopic Data (500 MHz, CDCl$_3$) for compounds **12** and **16**.

	12		**16**	
position	δC, type	δH (J in Hz)	δC, type	δH (J in Hz)
2	162.7, C		163.4, C	
3	101.8, CH	6.76, s	103.4, CH	6.79, s
4	181.2, C		182.3, C	
4a	103.0, C		104.2, C	
5	151.8, C		152.8, C	
6	130.5, C		131.4, C	
7	156.8, C		157.3, C	
8	93.4, CH	6.57, s	94.4, CH	6.56, s
8a	151.6, C		152.5, C	
1'	120.6, C		122.9, C	
2'	109.2, CH	7.48, m[a]	109.4, CH	7.44, d (2.0)
3'	147.1, C		149.0, CH	
4'	149.8, C		152.2, C	
5'	114.8, CH	6.93, d (8.8)	111.7, C	7.02, d (8.5)
6'	119.4, CH	7.49, m[a]	120.1, CH	7.55, dd (8.5, 2.0)
OCH3-6	59.0, CH$_3$	3.77, s	60.0, CH$_3$	3.77, s
OCH3-3'	55.0, CH$_3$	3.89, s	55.9, CH$_3$	3.85, s
OCH3-4'			55.8, CH$_3$	3.82, s
OH-5		12.97, brs		12.97, brs

[a]Overlapping signals

Table S5. ^{1}H and ^{13}C NMR Spectroscopic Data (500 MHz, CDCl$_3$) for compounds **13** - **15**.

position	**13**[b]		**14**[b]		**15**[c]	
	δC, type	δH (*J* in Hz)	δC, type	δH (*J* in Hz)	δC, type	δH (*J* in Hz)
1	81.8, C		81.8, C		136.3, C	
2a	40.9, CH$_2$	2.21, brd (15.3)[a]	40.9, CH$_2$	2.21, brd (15.3)[a]	33.0, CH$_2$	2.63, d (17.7)
2b		1.89, bd (15.3)		1.89, brd (15.3)		2.41[a]
3	64.3, CH	3.54, brs	64.3, CH	3.54, brs	63.1, CH	3.32, s
4	67.4, C		67.4, C		66.5, C	
5	61.0, CH	2.33, dd (11.3, 3.1)	61.0, CH	2.33, dd (11.3, 3.1)	51.2, CH	3.01, d (10.7)
6	75.2, CH	3.92, ddd (11.1, 9.1, 6.4)	75.2, CH	3.92, ddd (11.1, 9.1, 6.4)	77.7, CH	3.64, dd (10.2, 10.2)
7	46.8, CH	3.23, m	46.8, CH	3.23, m	56.1, CH	3.06, dddd(10.2, 10.2, 2.9, 2.9)
8	73.1, CH	4.95, m	73.1, CH	4.95, m	70.1, CH	4.71, ddd (10.7, 10.7, 1.8)
9a	35.4, CH$_2$	2.55, ddd (15.2, 7.3, 2.9)	35.4, CH$_2$	2.55, ddd (15.2, 7.3, 2.9)	41.2, CH$_2$	2.42[a]
9b		2.26, m[a]		2.26, m[a]		2.15, dd (13.6, 2.0)
10	140.7, C		140.7, C		127.9, C	
11	168.7, C		168.7, C		168.3, C	
12	136.6, C		136.6, C		136.8, C	
13a	122.7, CH$_2$	6.18, d (3.4)	122.7, CH$_2$	6.18, d (3.4)	120.1, CH$_2$	6.07, d (3.0)
13b		5.60, dd (4.7, 3.2)[d]		5.60, dd (4.7, 3.2)[d]		5.48, d (3.0)
14	18.6, CH$_3$	1.63, s	18.6, CH$_3$	1.63, s	18.6, CH$_3$	1.59, s
15	118.0, CH$_3$	5.53, brd (3.4) 4.98, brs	118.0, CH$_3$	5.53, brd (3.4) 4.98, brs	21.9, CH$_3$	1.66, s
1'	175.9, C		172.4, C		169.4, C	
2'	41.5, CH	2.42, ddq (13.9, 13.9, 7.0)	43.5, CH$_2$	2.25, m[a]	20.7, CH$_3$	2.04, s
3'a	26.4, CH$_2$	1.73, m	25.6, CH	2.14, tqq (6.7, 6.7, 6.7)		
3'b		1.49, m				
4'	11.8, CH$_3$	0.94, dd (7.5, 7.5)	22.43, CH$_3$	0.98, d (6.7)[a]		
5'	16.8, CH$_3$	1.19, d (7.0)	22.46, CH$_3$	0.99, d (6.7)[a]		

[a]Overlapping signals, [b]Measured in DMSO, [c]^{13}C extracted from ^{1}H−^{13}C 2D inverse-detected experiments. [d]Apparent multiplet

Table S6. ^{1}H and ^{13}C NMR Spectroscopic Data (500 MHz, CDCl$_3$) for compound **18**.

position	**18**		
	δC, type	δH (*J* in Hz)	HMBC
1	134.1, C		
2	194.8, C		
3	136.2, CH	6.15, s	1, 2, 4, 5, 14,
4	170.1, C		
5	51.9, CH	3.26, d (10.0)	1, 4, 6, 7
6	80.1, CH	3.99, dd (10.4, 10.4)	1, 7
7	59.2, CH	2.72, dd (10.8, 10.8)	4', 5, 6, 8, 9, 12
8	68.3, CH	4.75, ddd (10.6, 10.6, 1.7)	1'', 7
9a	44.5, CH$_2$	2.48, dd (12.7, 10.8)	1, 7, 8, 15
9b		2.28, m[a]	1, 7, 8, 15
10	143.8, C		
11	178.6, C		
12	61.3, C		
13a	40.2, CH$_2$	2.63, d (11.6)	1', 2', 4', 10', 11
13b		1.86, d (11.9)	1', 2', 5', 7, 11
14	20.2, CH$_3$	2.28, s[a]	3, 4, 5
15	20.5, CH$_3$	2.36, s	1, 9, 10
1'	63.0, C		
2'	137.5, CH	5.85, d (5.8)	1', 3'
3'	136.4, CH	5.81, d (5.5)	1', 2', 5', 12, 14'
4'	57.9, C		
5'	66.9, CH	3.04, d (9.8)	1', 2', 6', 7'
6'	79.2, CH	3.96, dd (9.6, 9.6)	5', 8', 12
7'	43.1, CH	3.30, m	6'
8'a	23.5, CH$_2$	2.22, m	9'
8'b		1.38, m	7'
9'a	34.6, CH$_2$	1.82, m	1', 7', 8', 10', 15'
9'b		1.75, m	8'
10'	72.5, C		
11'	170.4, C		
12'	140.6, C		
13'	118.8, CH$_2$	6.01, d (3.4) 5.29, d (3.0)	7', 11', 12' 7', 11', 12'
14'	17.0, CH$_3$	1.44, s	3', 4', 5', 12
15'	29.8, CH$_3$	1.27, s	1', 8', 9', 10'
1''	168.9, C		
2''	21.6, CH$_3$	1.96, s	1'', 8

[a]overlapping signals

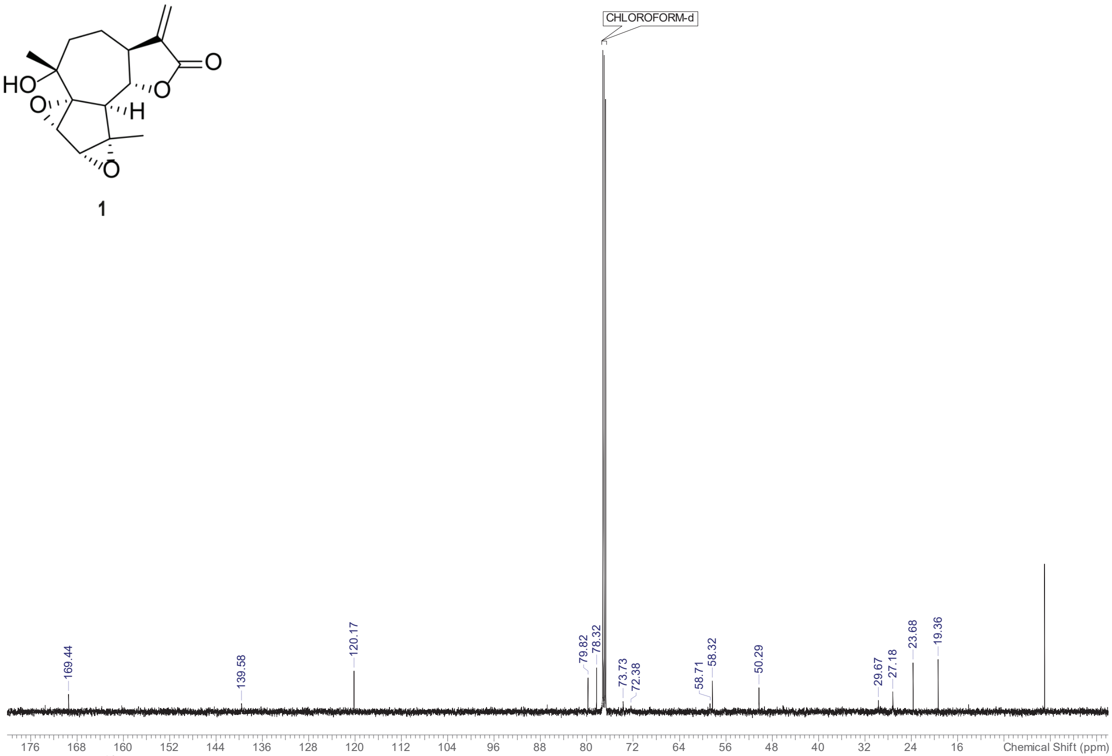

Figure S4. ^{13}C spectrum of compound **1** (125 MHz, $CDCl_3$).

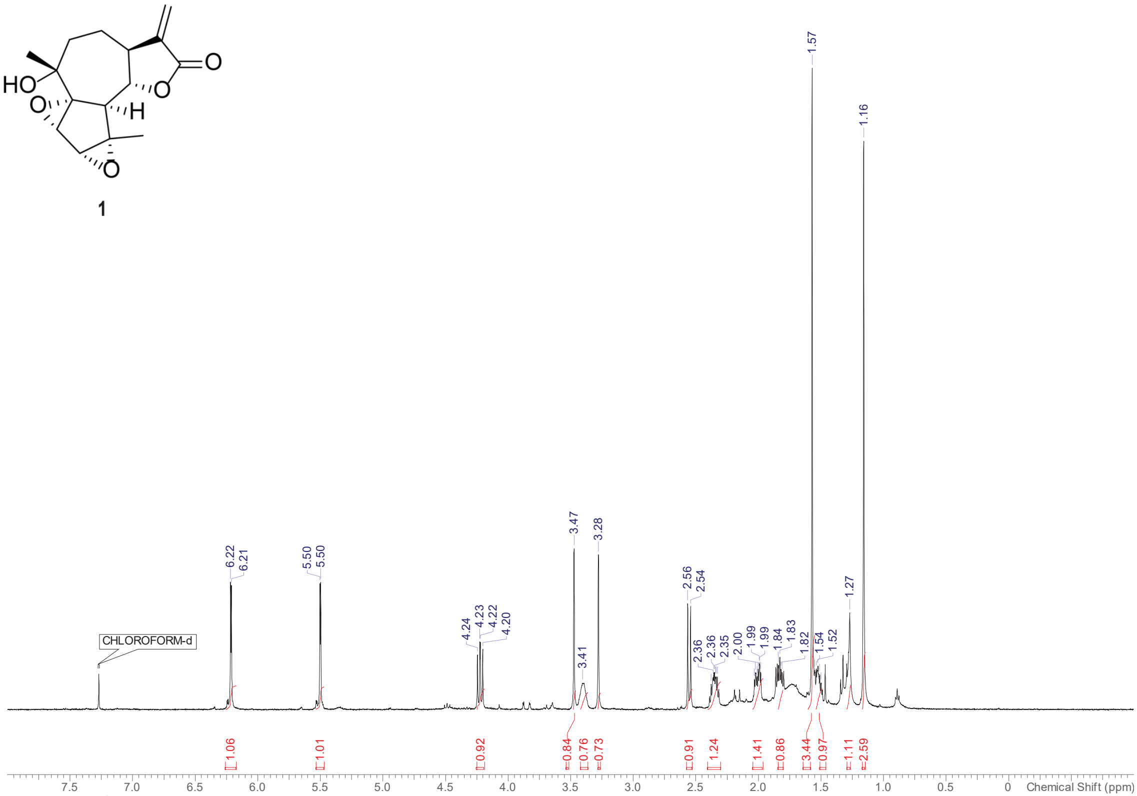

Figure S3. ^{1}H NMR spectrum of compound **1** (500 MHz, $CDCl_3$).

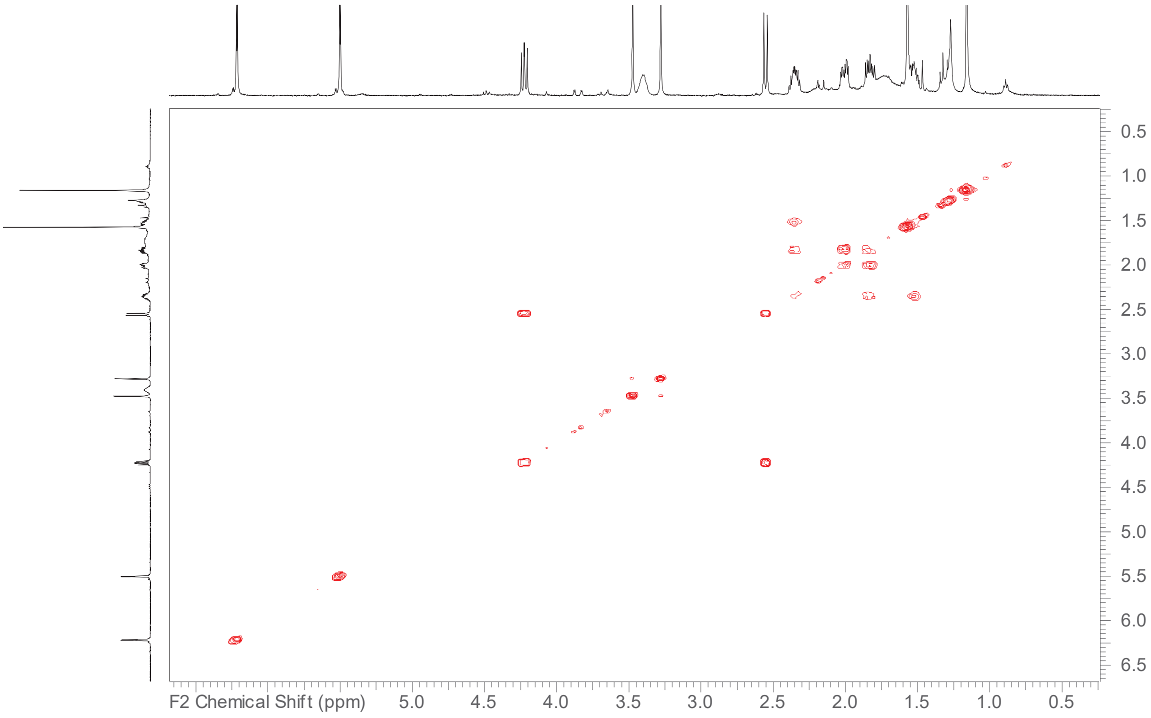

Figure S6. ^{1}H-^{1}H COSY spectrum of compound **1** (500 MHz, $CDCl_3$).

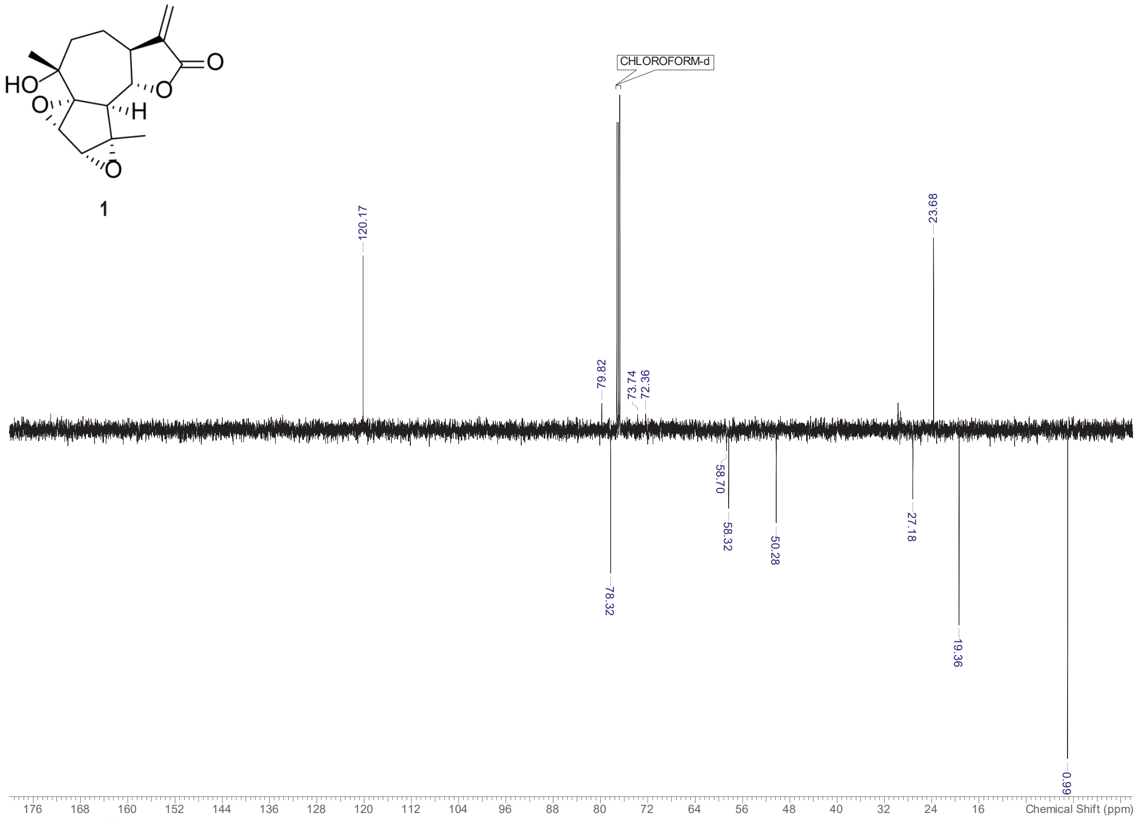

Figure S5. ^{13}C-DEPTq spectrum of compound **1** (125 MHz, $CDCl_3$).

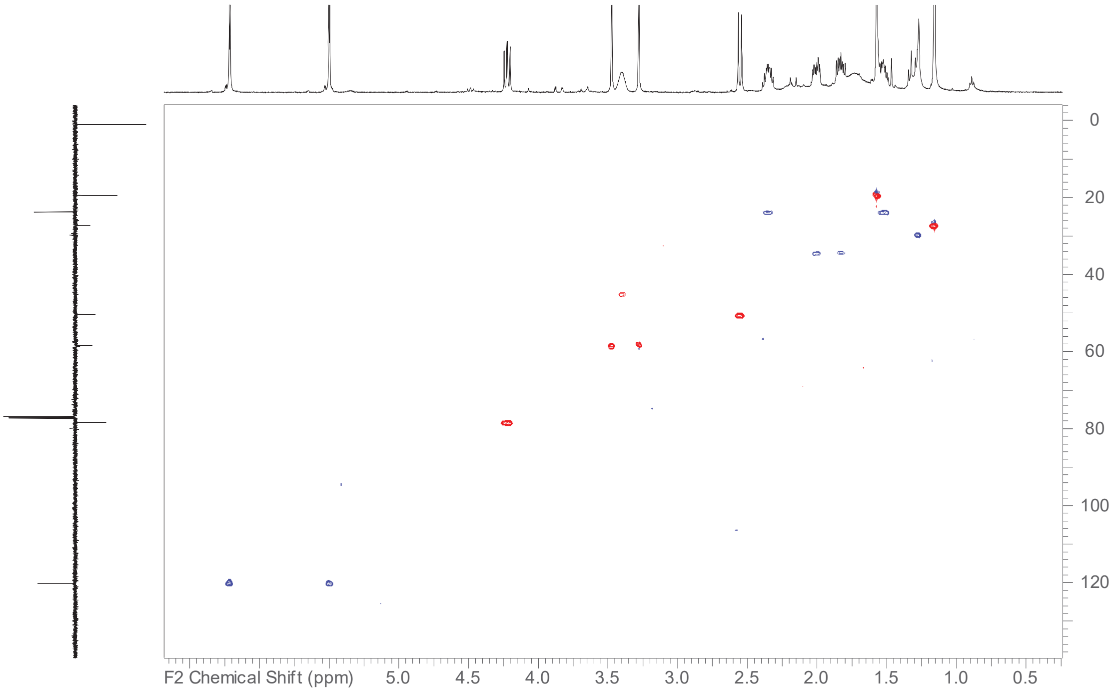

Figure S8. HSQC-DEPT spectrum of compound **1** (500 MHz, $CDCl_3$).

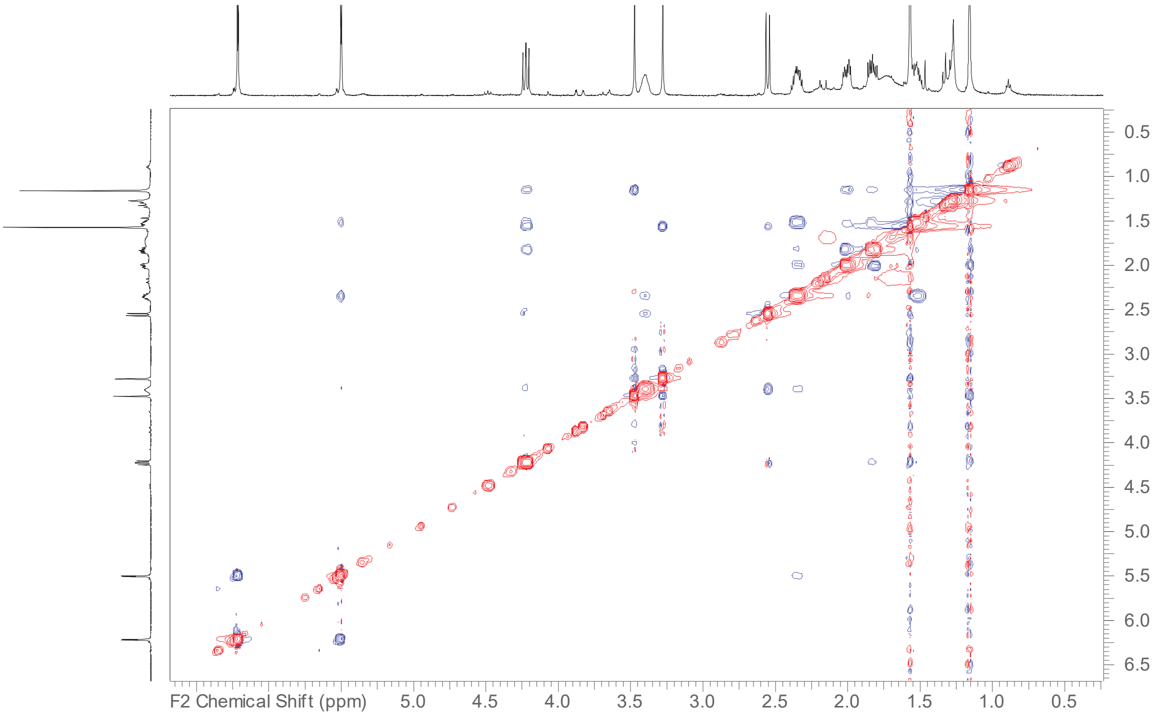

Figure S7. . ^{1}H-^{1}H NOESY spectrum of compound **1** (500 MHz, $CDCl_3$).

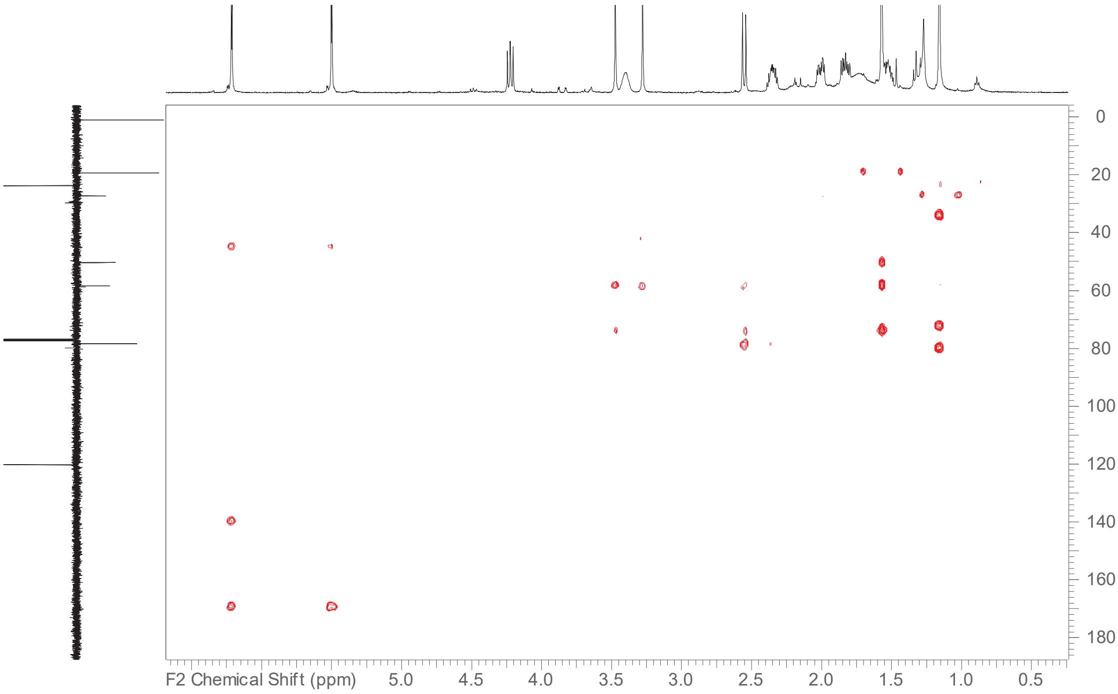

Figure S9. HMBC spectrum of compound **1** (500 MHz, CDCl$_3$).

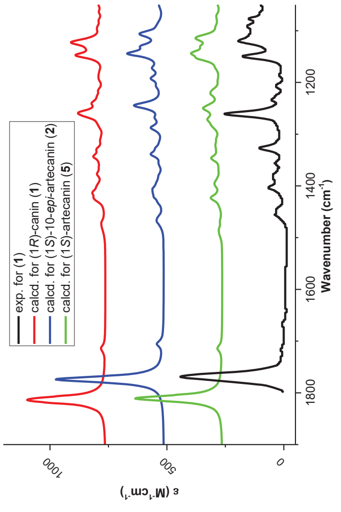

Figure S10. Comparison of experimental and computed IR spectra in chloroform for compound **1** in the region 1900-1050 cm^{-1}. Computed spectra (compounds **1**, **2** and **5**) were scaled according to the overall maximal *Sim*VCD value (0.9865).

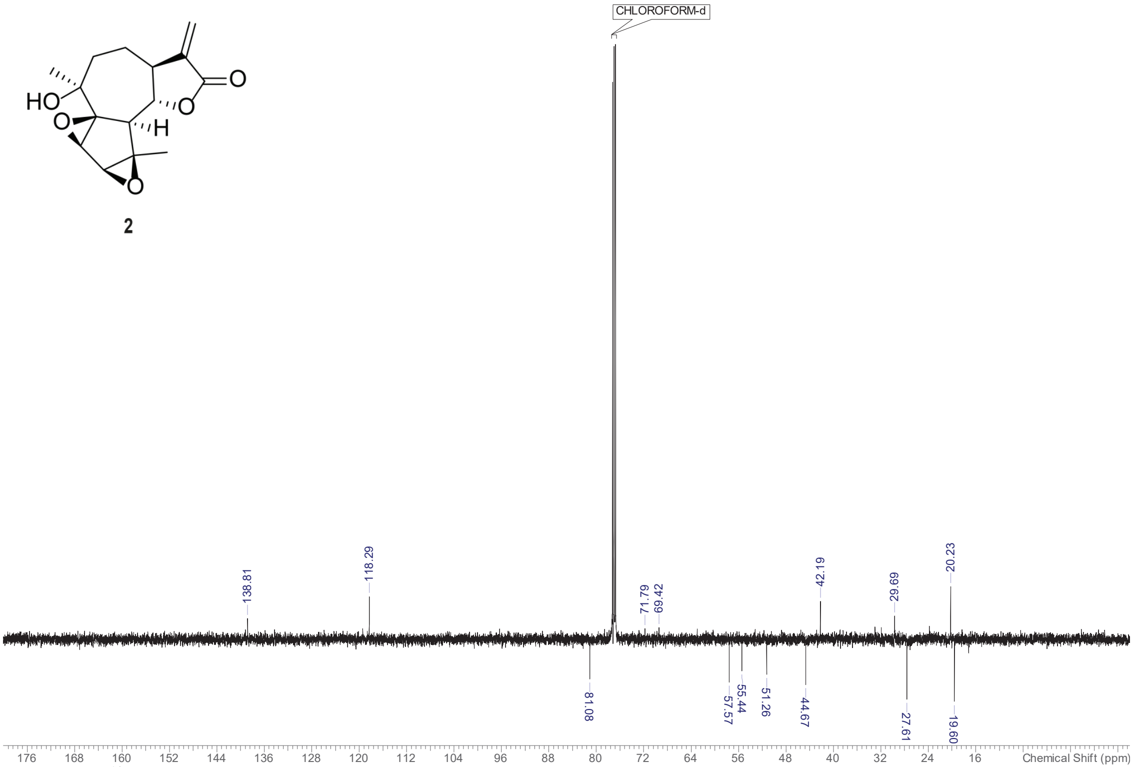

2

Figure S12. ^{13}C-DEPTq spectrum of compound **2** (125 MHz, CDCl$_3$).

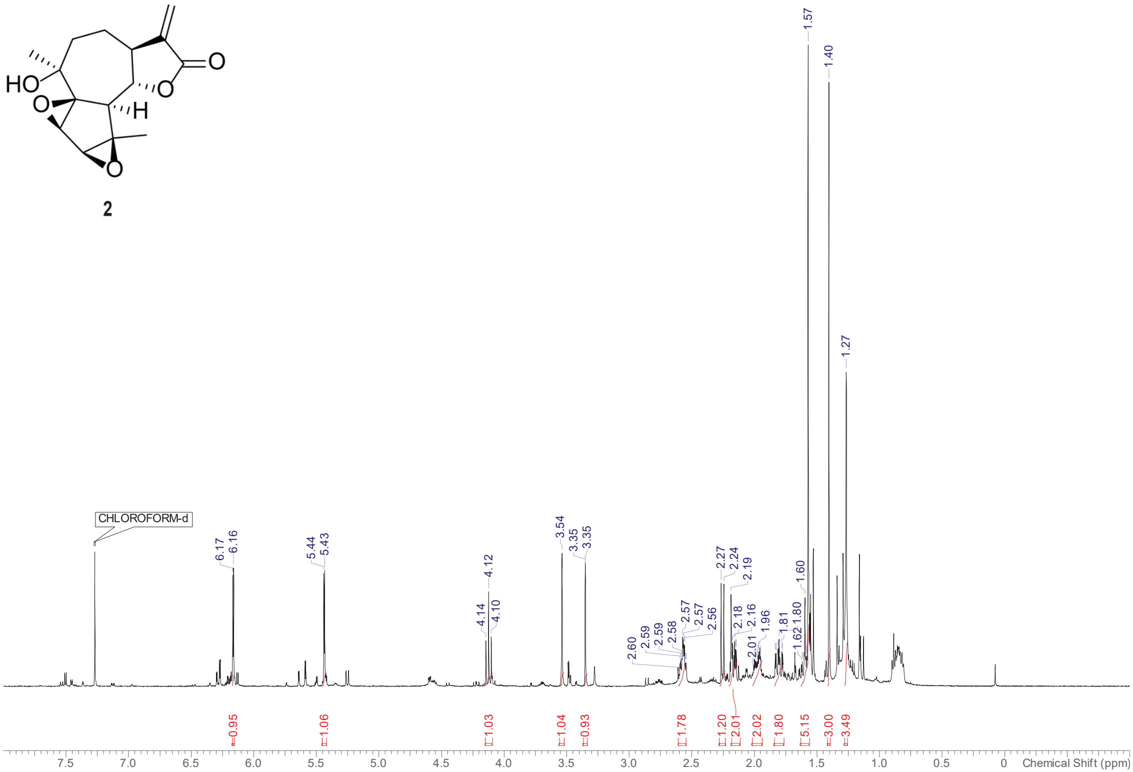

2

Figure S11. ^{1}H NMR spectrum of compound **2** (500 MHz, CDCl$_3$).

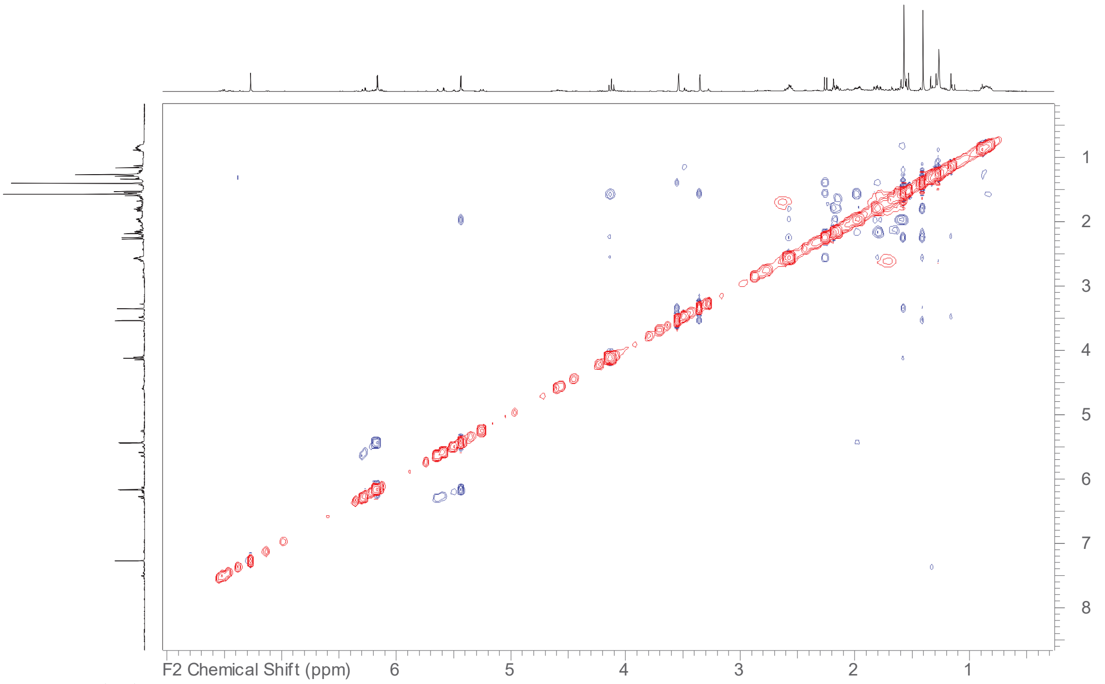

Figure S14. ^{1}H-^{1}H NOESY spectrum of compound **2** (500 MHz, CDCl$_3$).

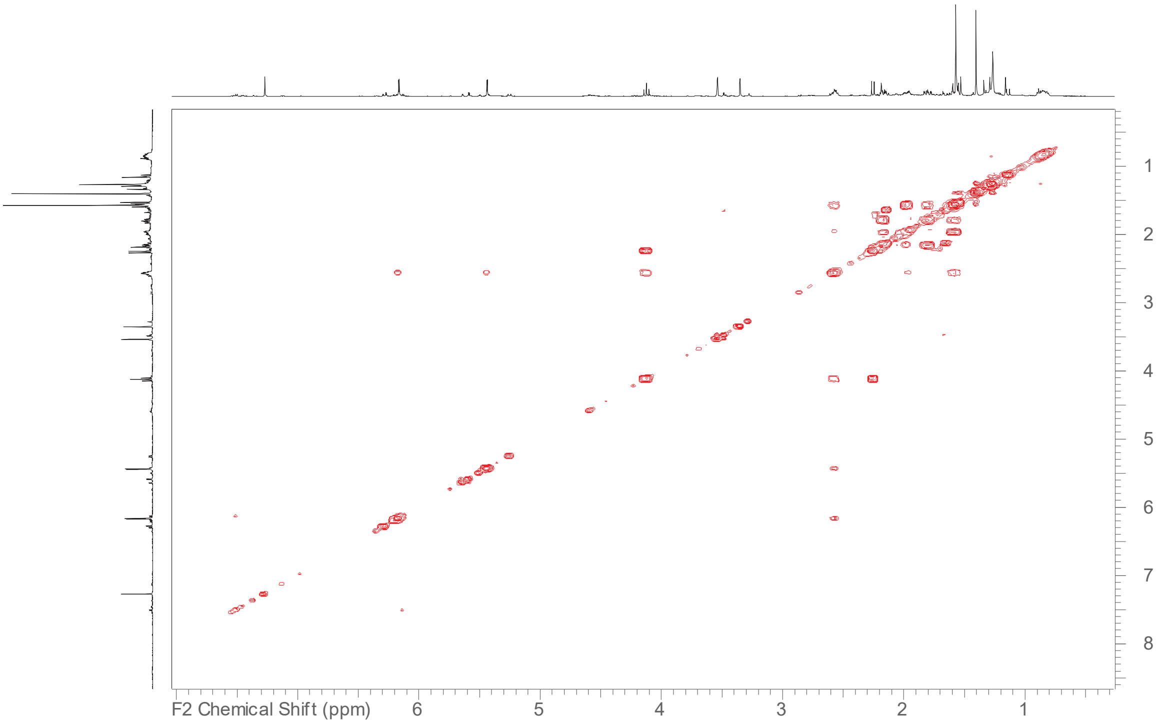

Figure S13. ^{1}H-^{1}H COSY spectrum of compound **2** (500 MHz, CDCl$_3$).

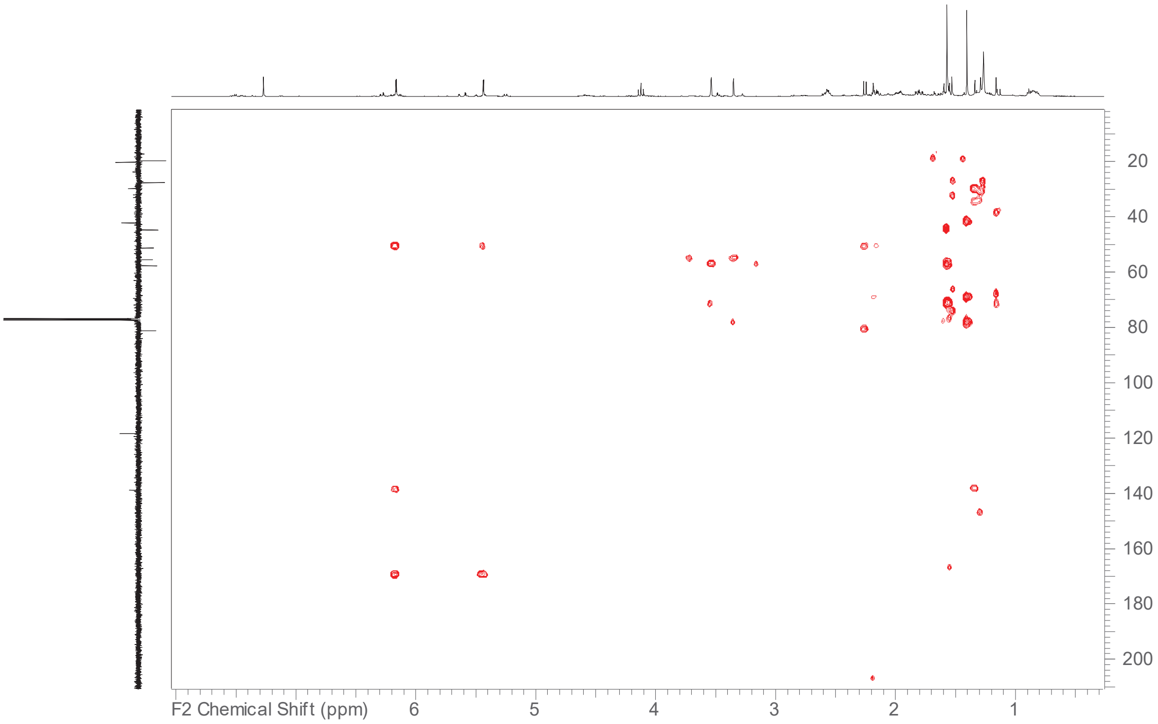

Figure S16. HMBC spectrum of compound **2** (500 MHz, CDCl$_3$).

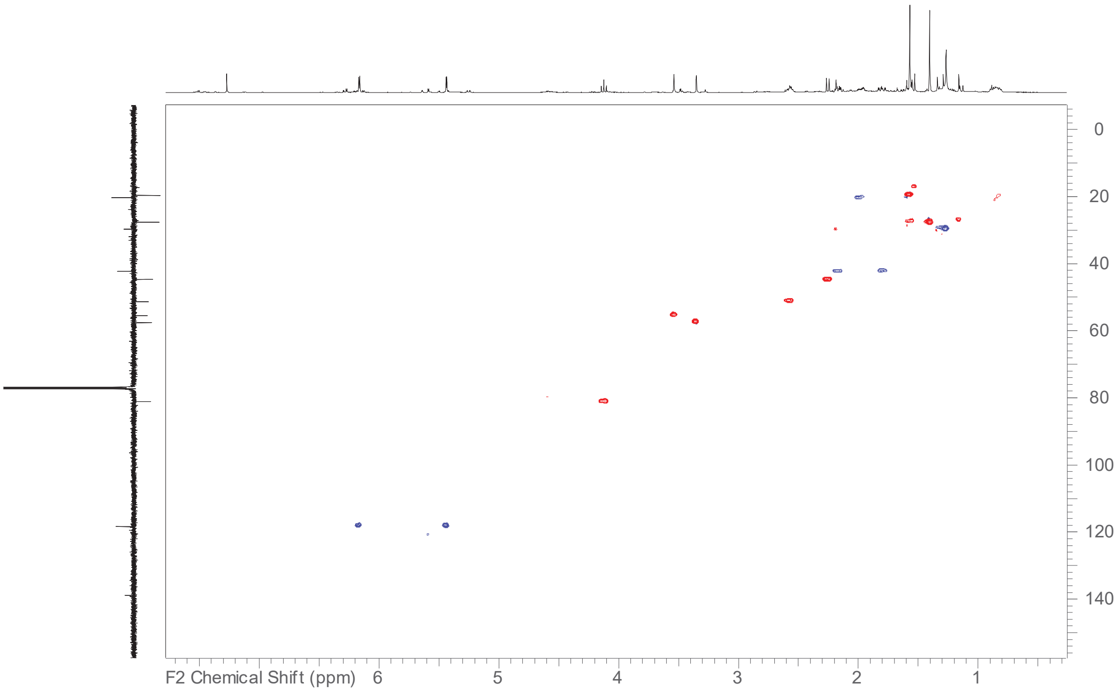

Figure S15. HSQC-DEPT spectrum of compound **2** (500 MHz, CDCl$_3$).

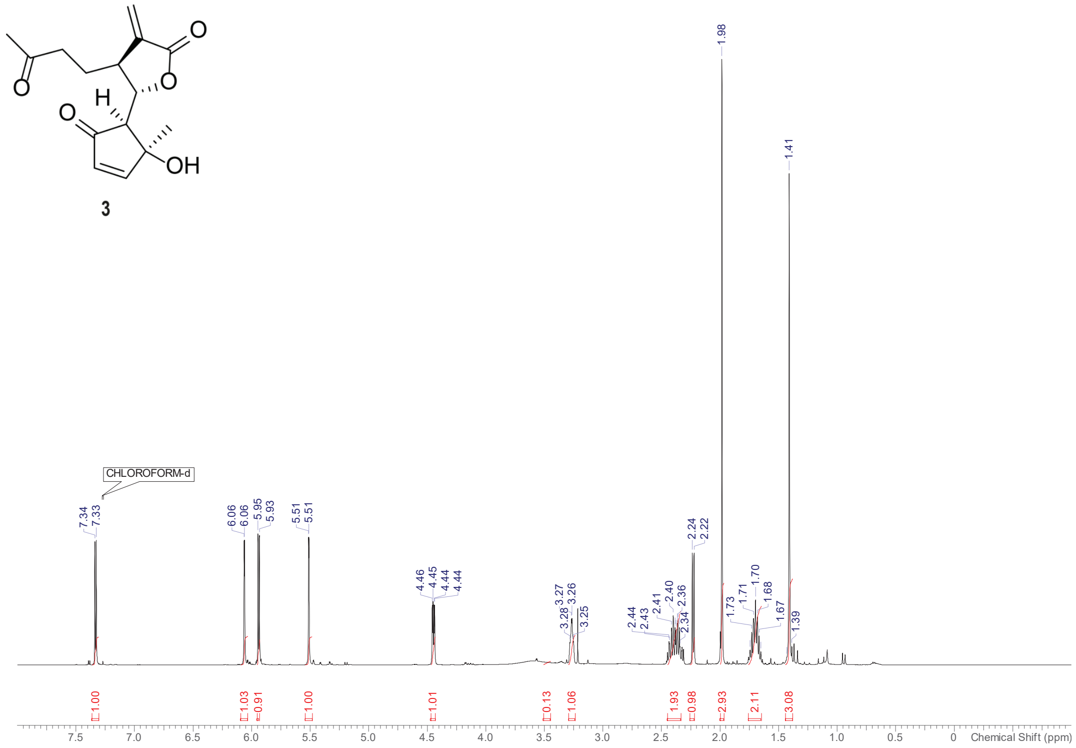

Figure S18. ^{1}H NMR spectrum of compound **3** (500 MHz, $CDCl_3$).

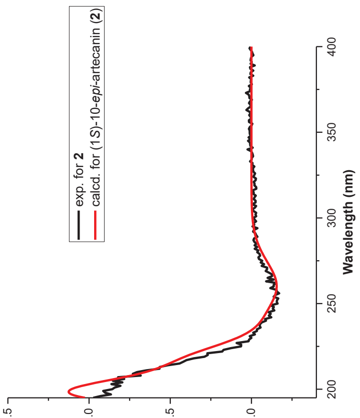

Figure S17. Comparison of experimental and computed ECD spectra for compound **2** in MeOH.

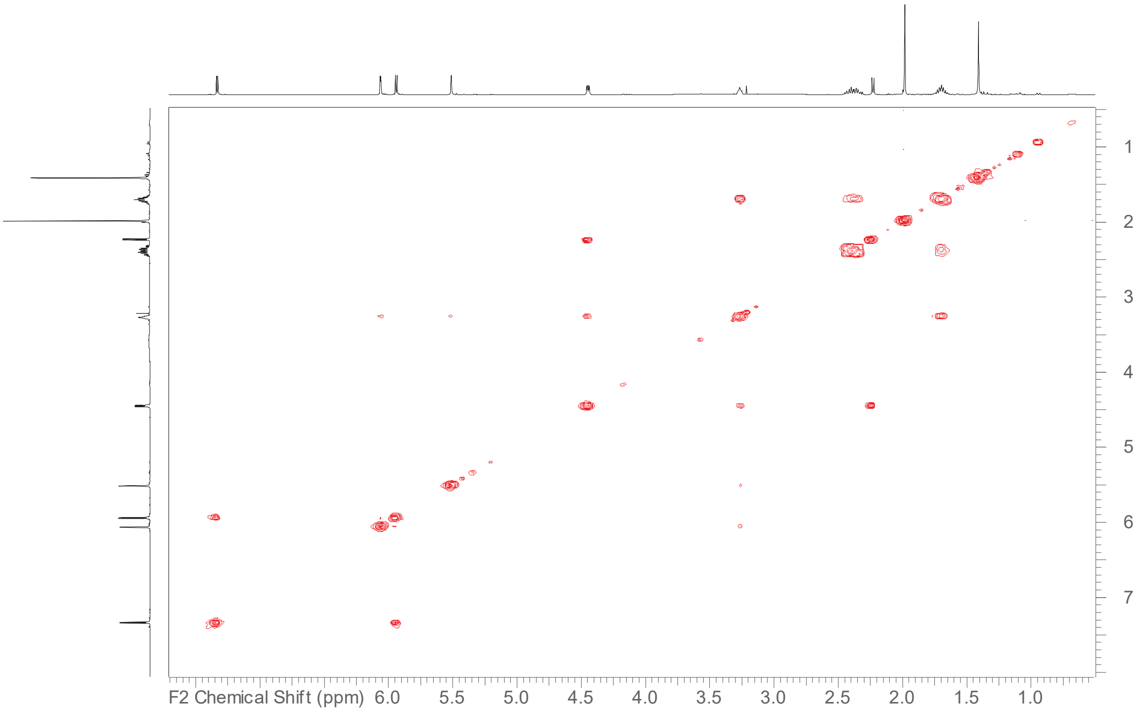

Figure S20. 1H 1H COSY spectrum of compound **3** (500 MHz, CDCl3).

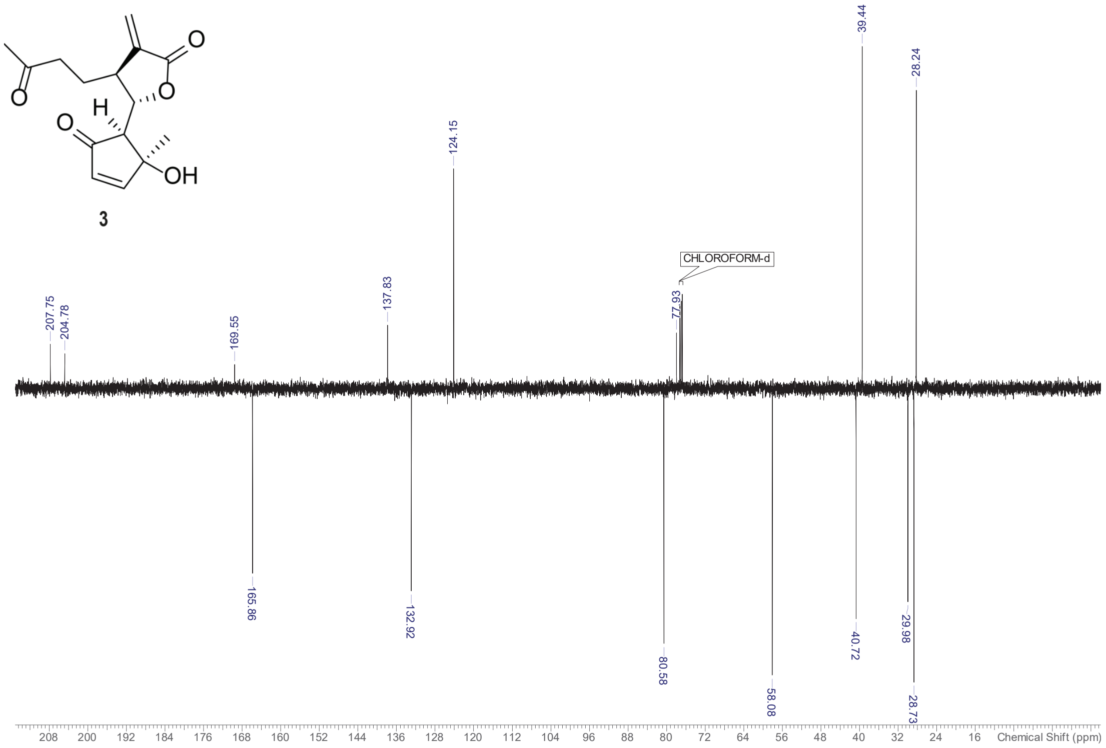

Figure S19. ^{13}C-DEPTq spectrum of compound **3** (125 MHz, $CDCl_3$).

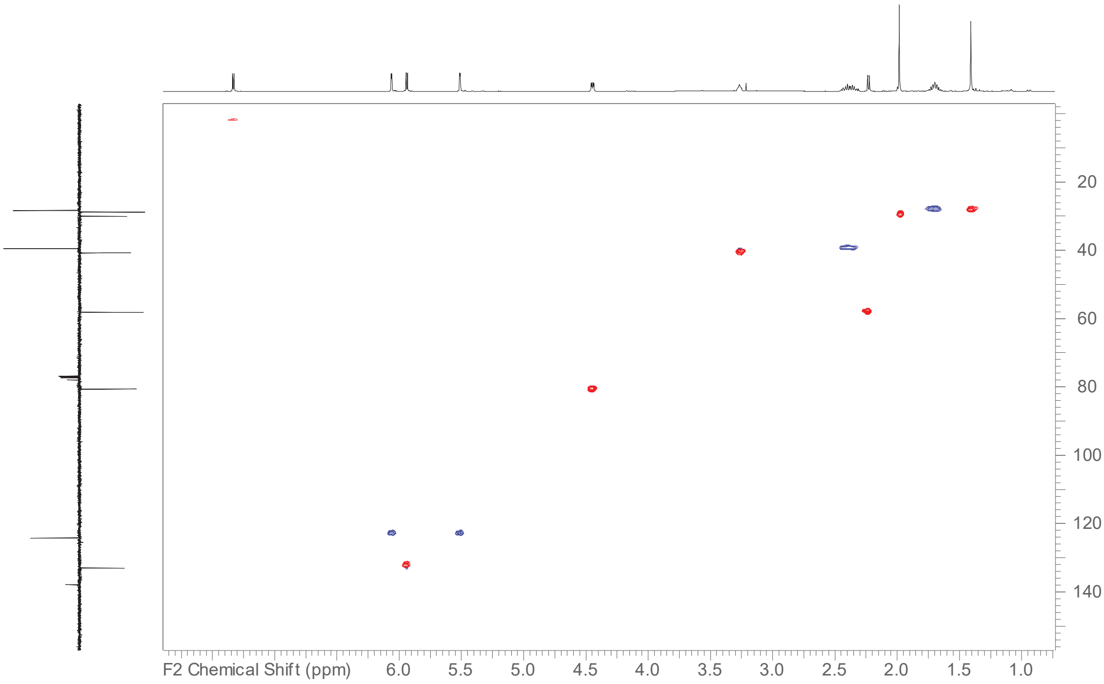

Figure S22. HSQC-DEPT spectrum of compound **3** (500 MHz, CDCl3).

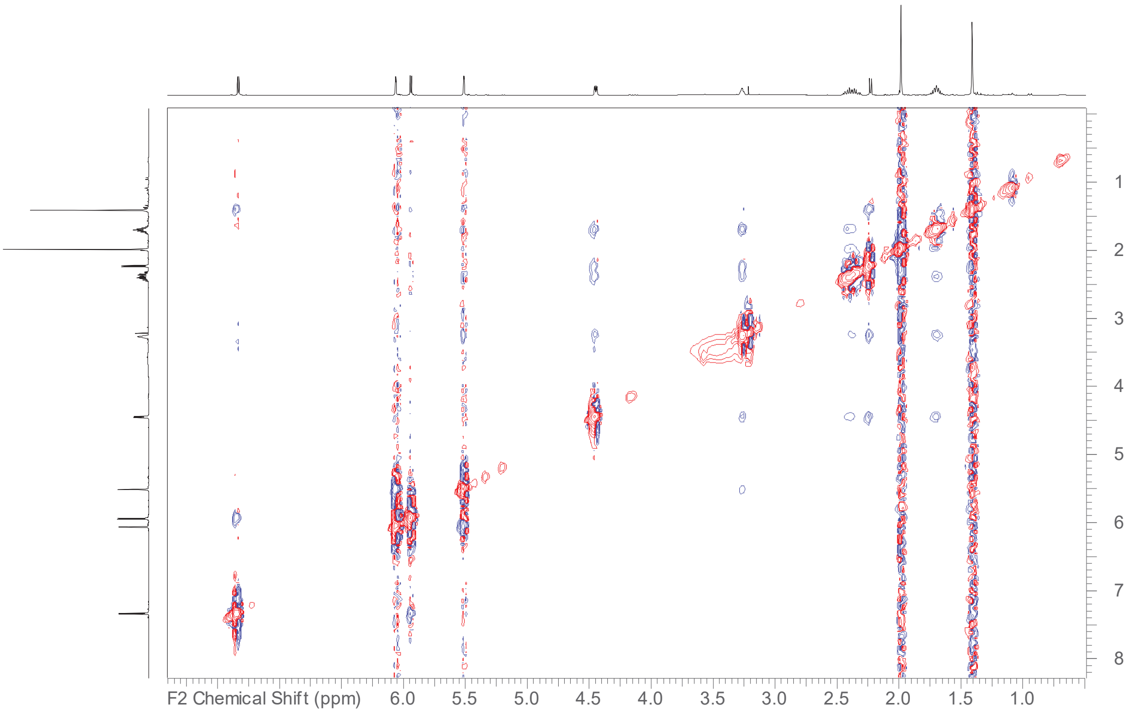

Figure S21. 1H 1H NOESY spectrum of compound **3** (500 MHz, CDCl3)

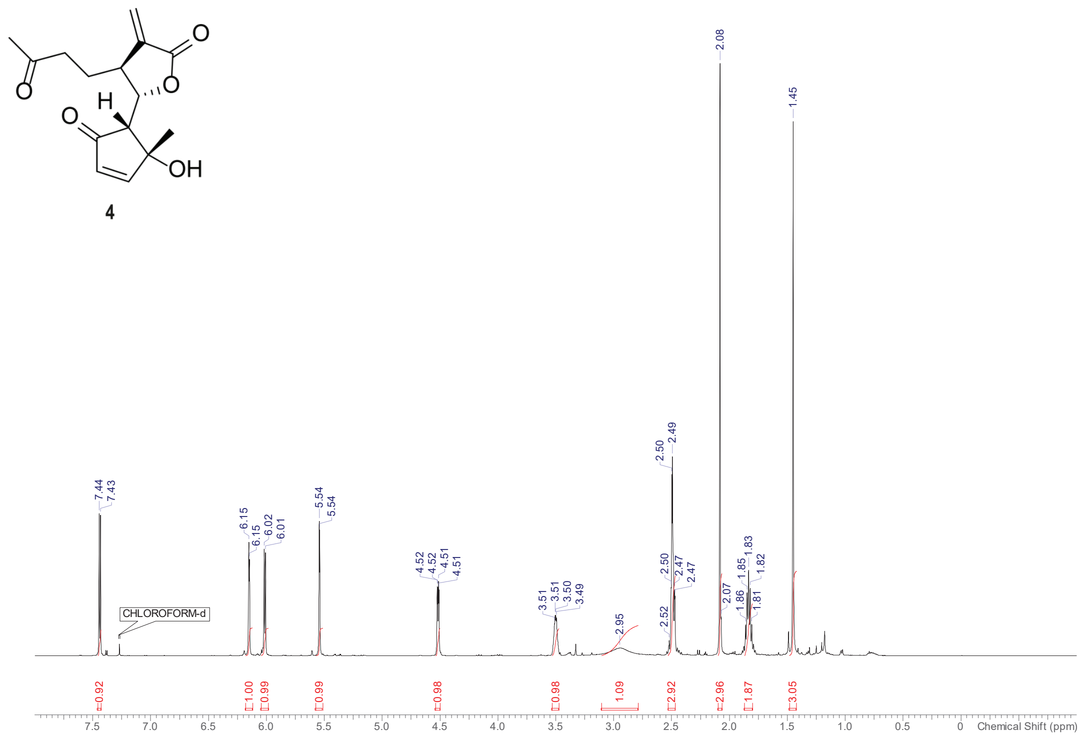

Figure S24. ^{1}H NMR spectrum of compound **4** (500 MHz, CDCl$_3$).

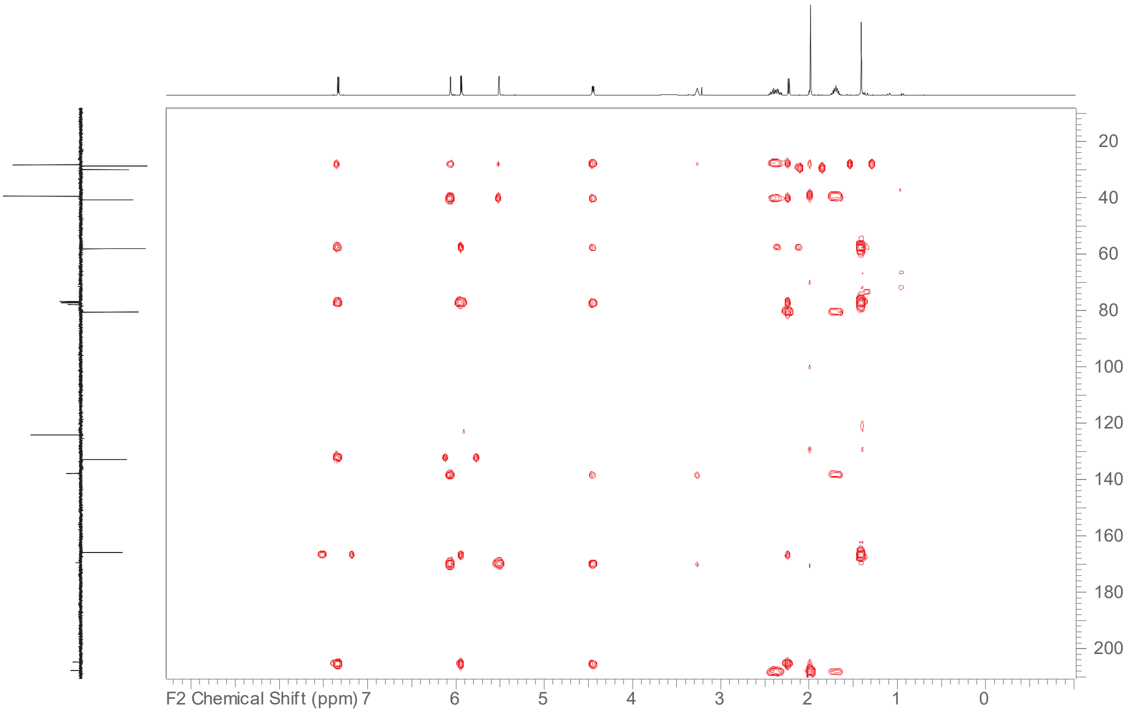

Figure S23. HMBC spectrum of compound **3** (500 MHz, CDCl3).

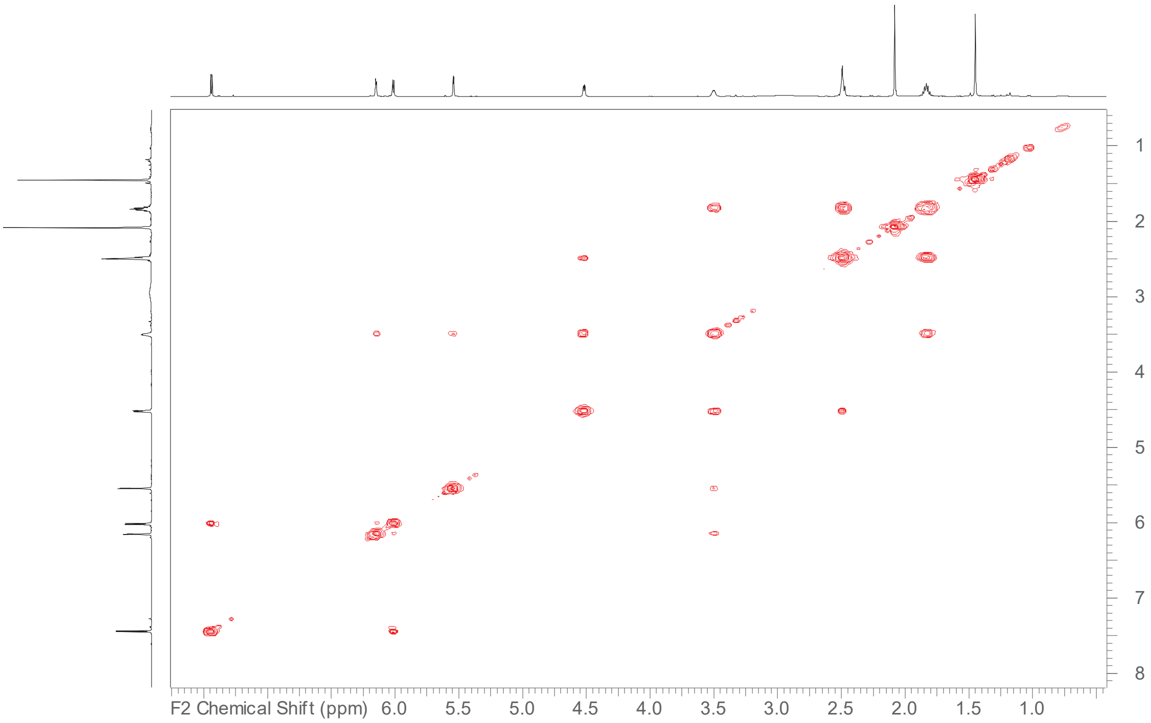

Figure S26. ^{1}H-^{1}H COSY spectrum of compound **4** (500 MHz, CDCl$_3$).

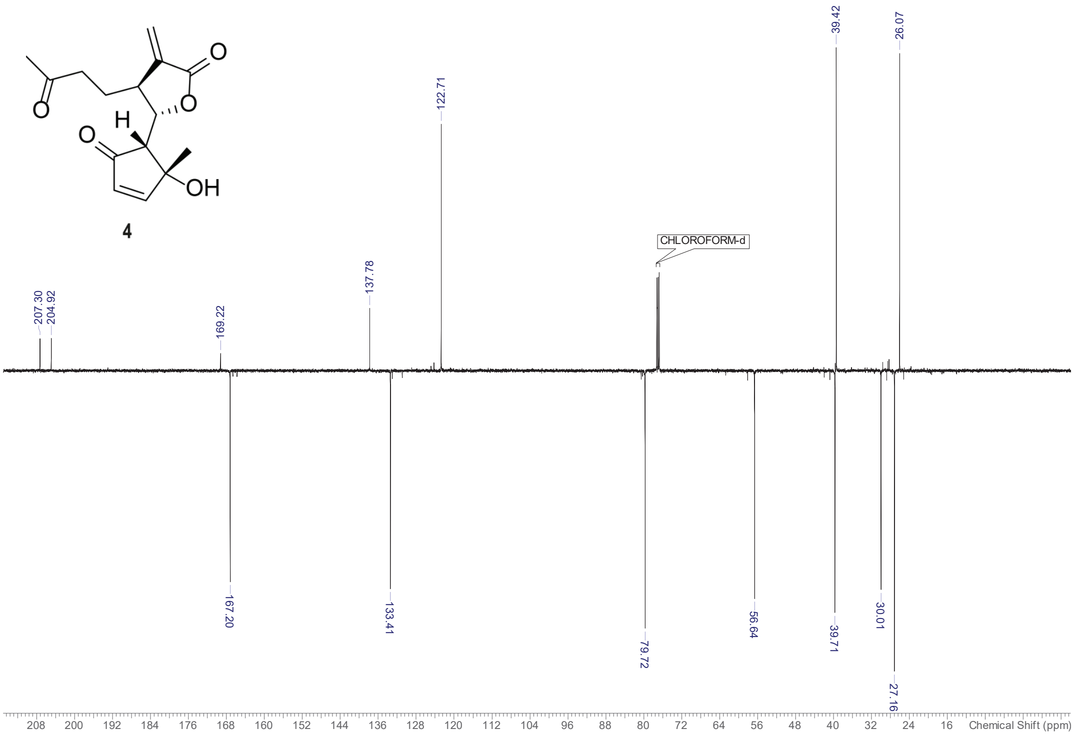

Figure S25. ^{13}C-DEPTq spectrum of compound **4** (125 MHz, CDCl$_3$).

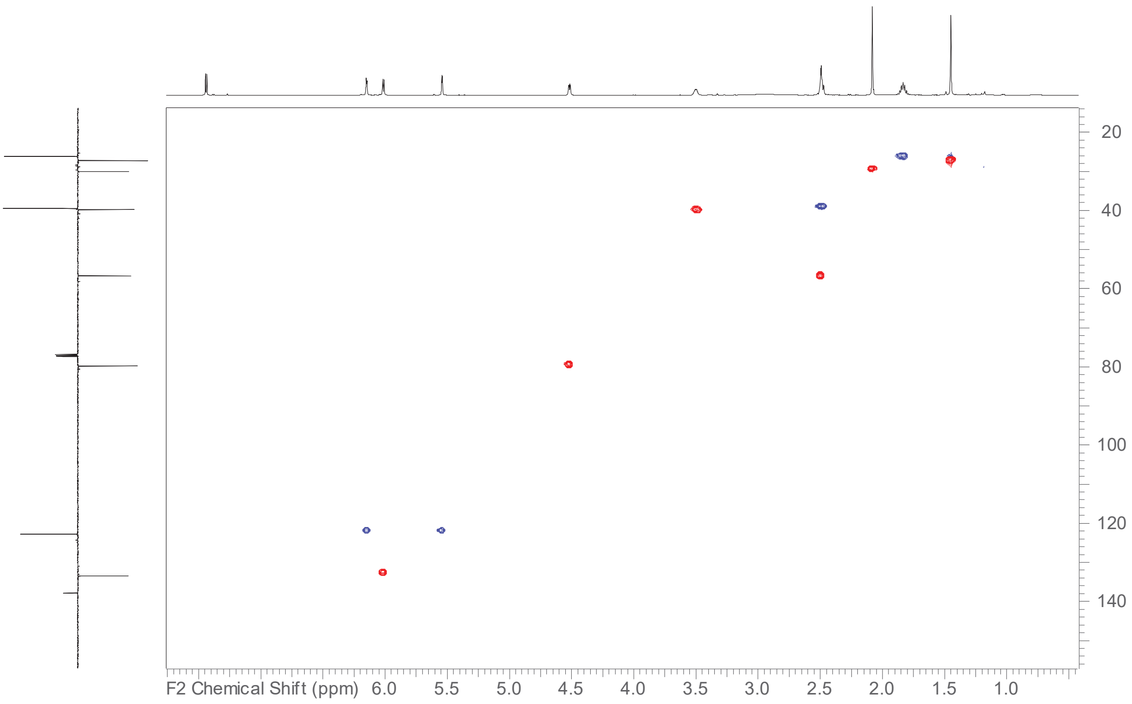

Figure S28. HSQC-DEPT spectrum of compound **4** (500 MHz, $CDCl_3$).

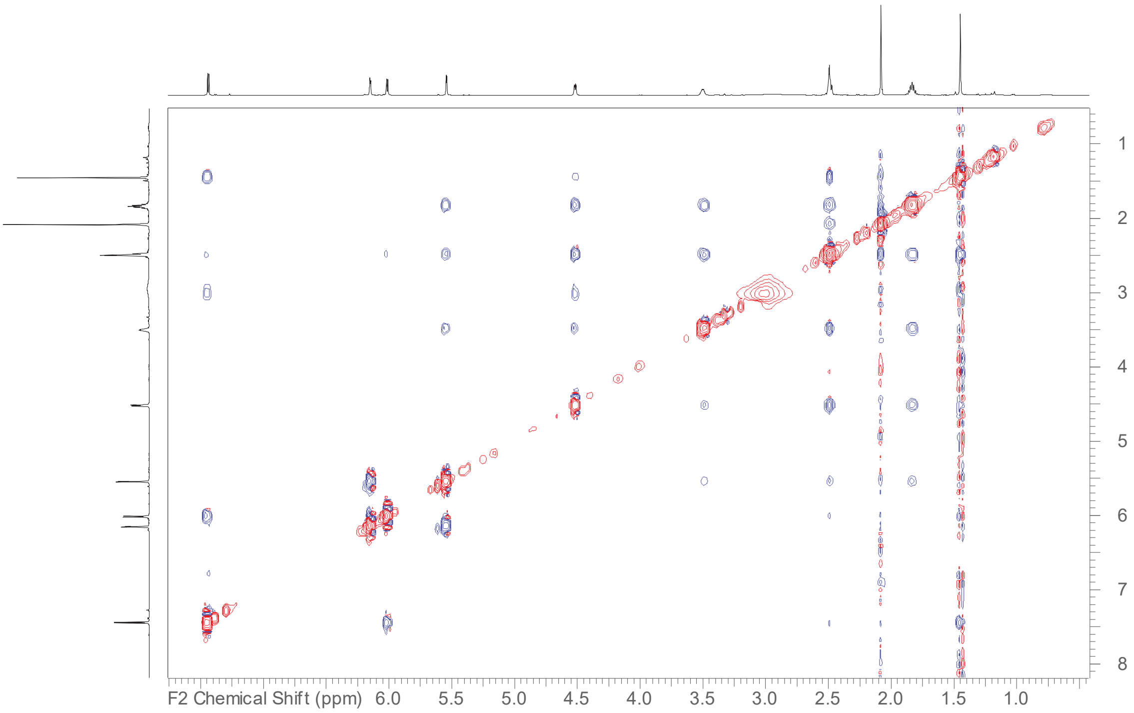

Figure S27. ^1H-^1H NOESY spectrum of compound **4** (500 MHz, $CDCl_3$).

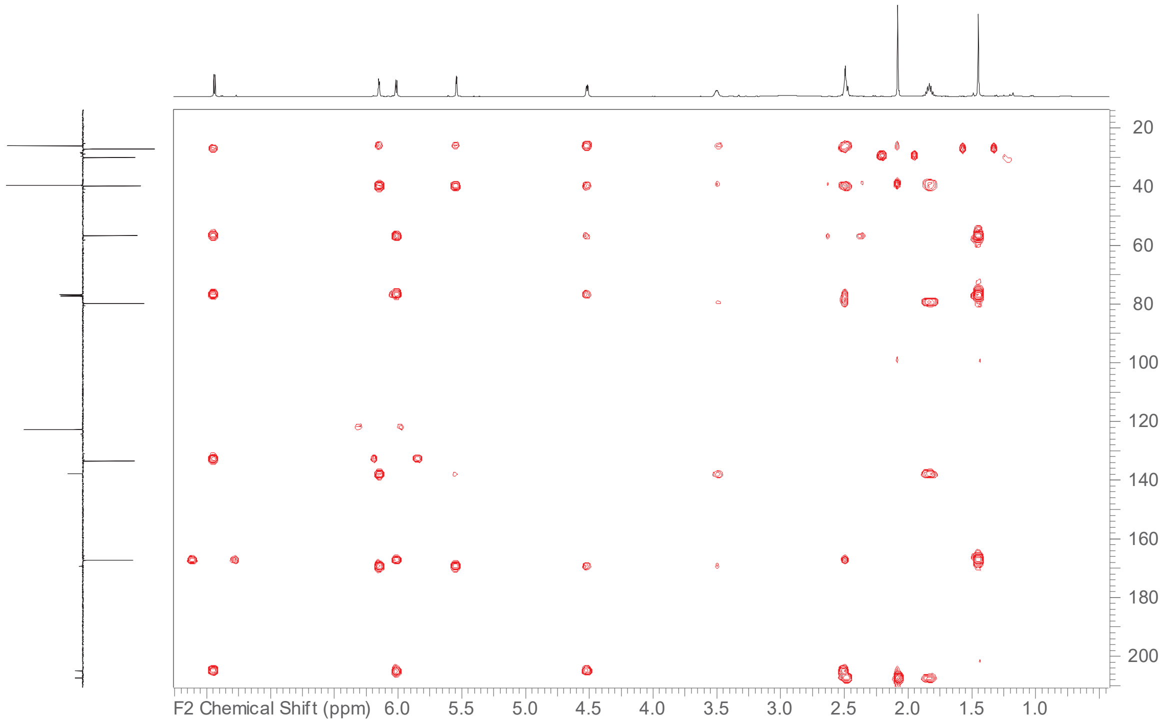

Figure S29. HMBC spectrum of compound **4** (500 MHz, $CDCl_3$).

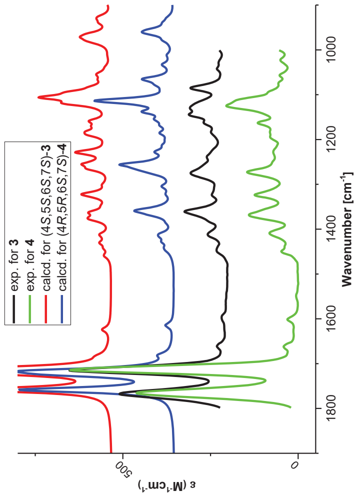

Figure S30. Comparison of experimental and computed IR spectra in chloroform for compounds **3**and **4** in the region 1900-1050 cm^{-1}. Computed spectra (compounds **3** and **4**) were scaled according to the overall maximal *Sim*VCD value (0.9795).

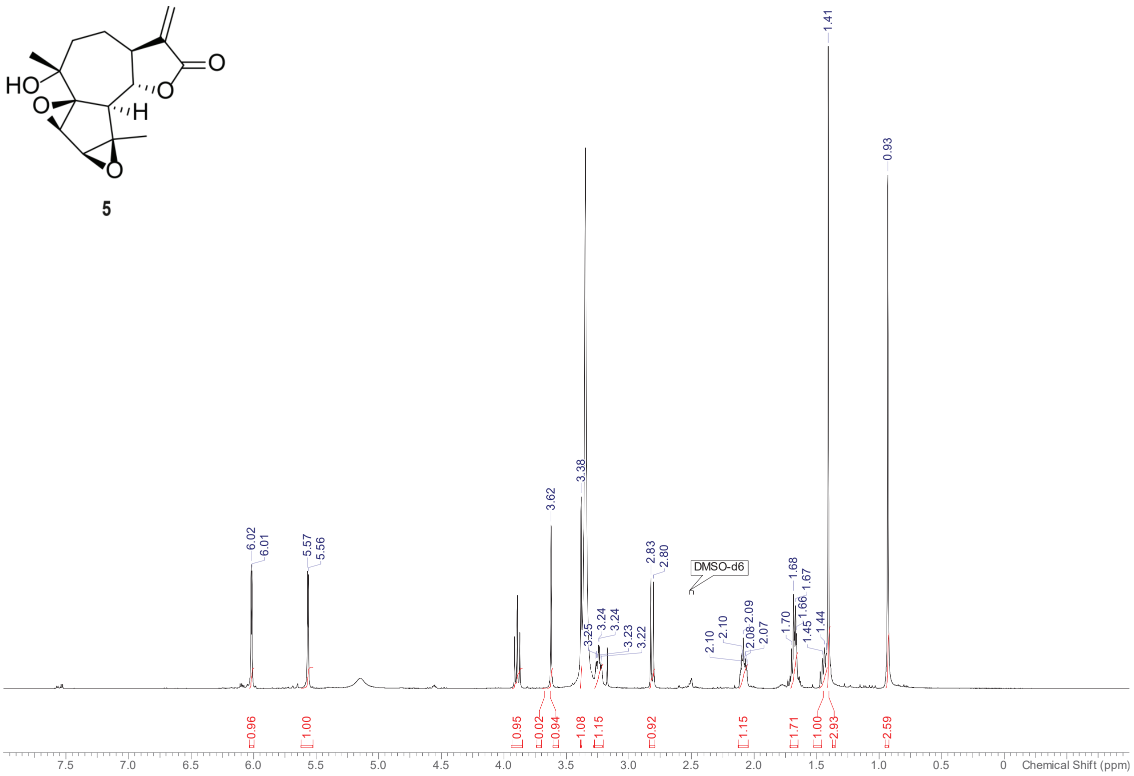

Figure S32. ^{1}H NMR spectrum of compound **5** (500 MHz, DMSO).

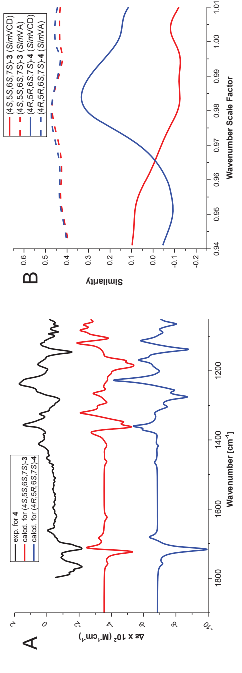

Figure S31. Comparison of experimental and computed VCD spectra in chloroform for compound **4.** The region of 1900-1050 cm^{-1} is shown (A). Similarities (*Sim*VA and *Sim*VCD) of the experimental VA and VCD spectra of **4** to the calculated spectra of possible stereoisomers were plotted as functions of wavenumber scale factor (B). The wavenumber scale factor corresponding to the maximal *Sim*VCD value in B (0.9795) was used to scale the computed spectra in A.

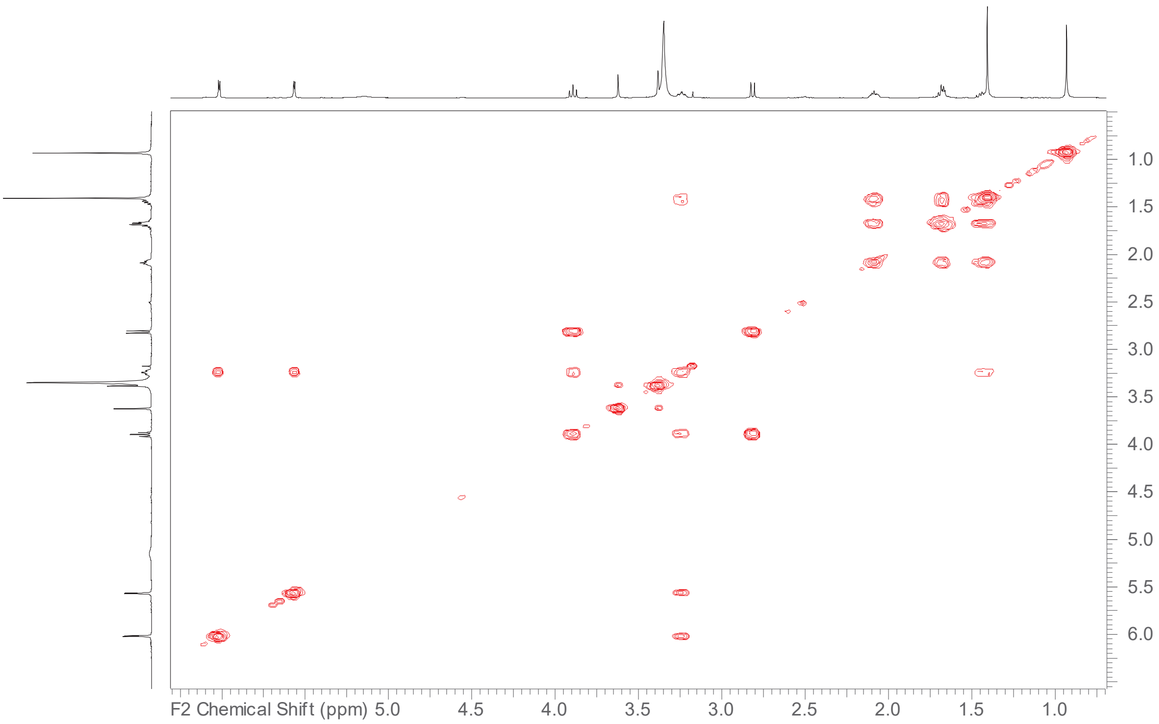

Figure S34. ^{1}H-^{1}H COSY spectrum of compound **5** (500 MHz, DMSO).

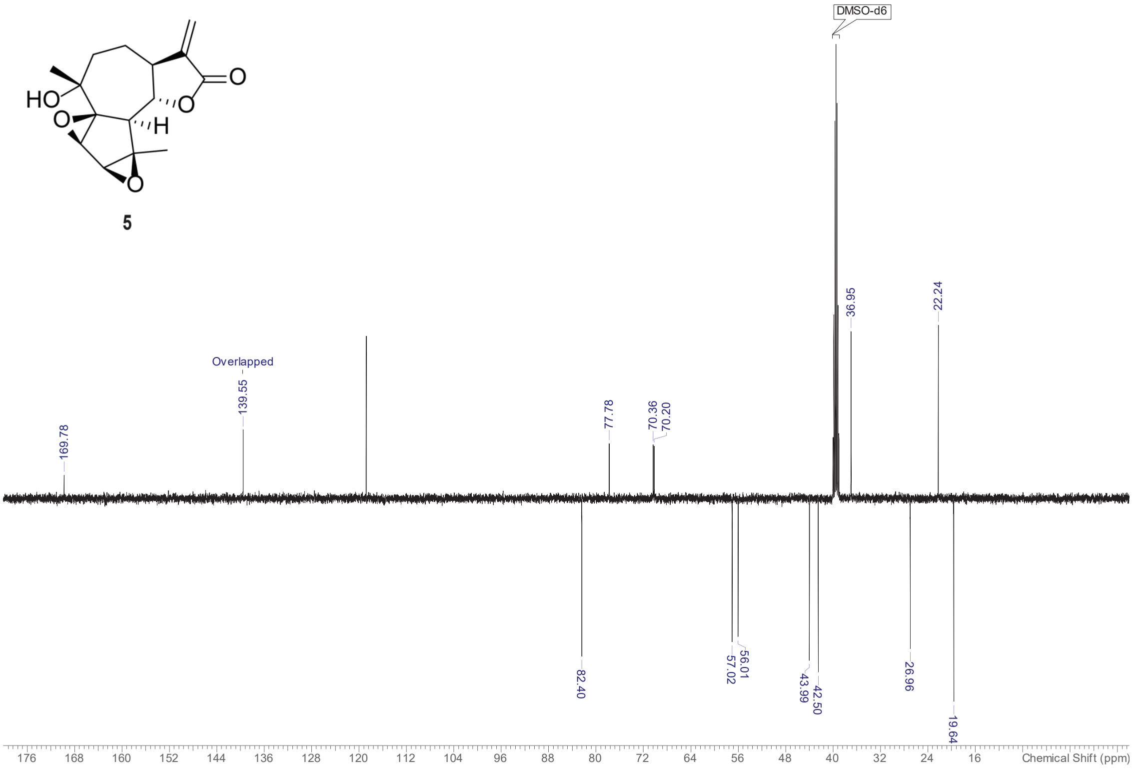

Figure S33. ^{13}C-DEPTq spectrum of compound **5** (125 MHz, DMSO).

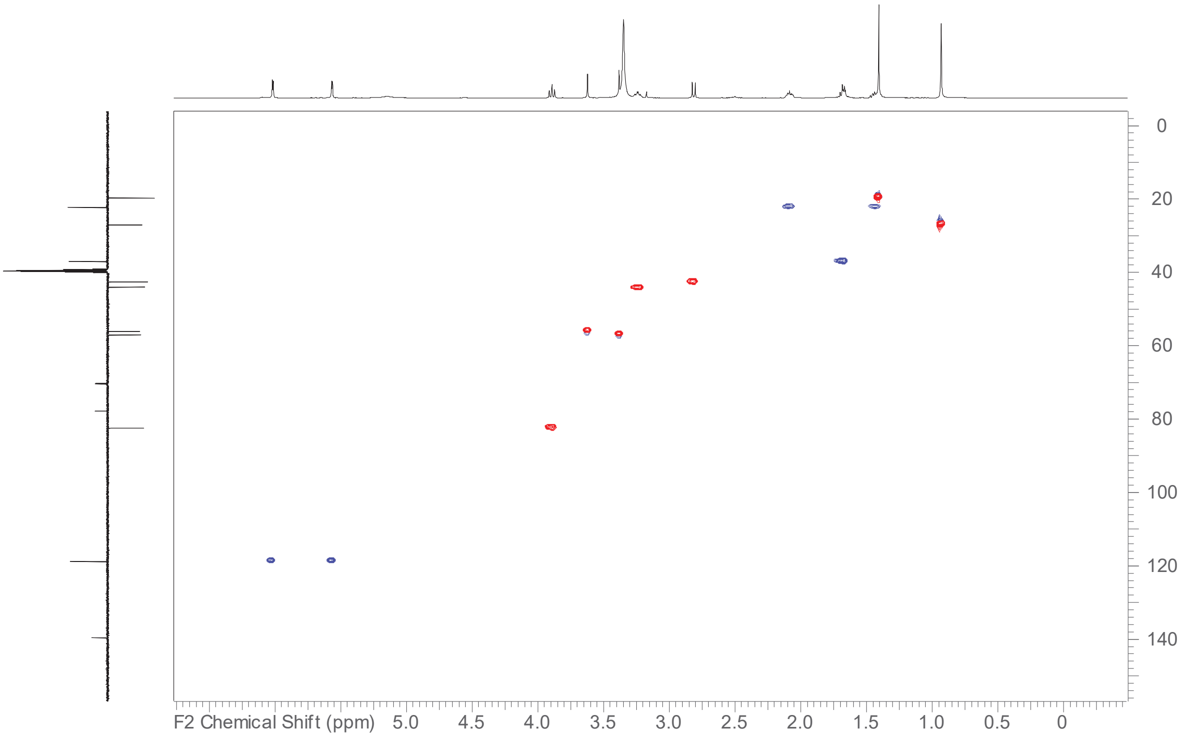

Figure S36. HSQC-DEPT spectrum of compound **5** (500 MHz, DMSO).

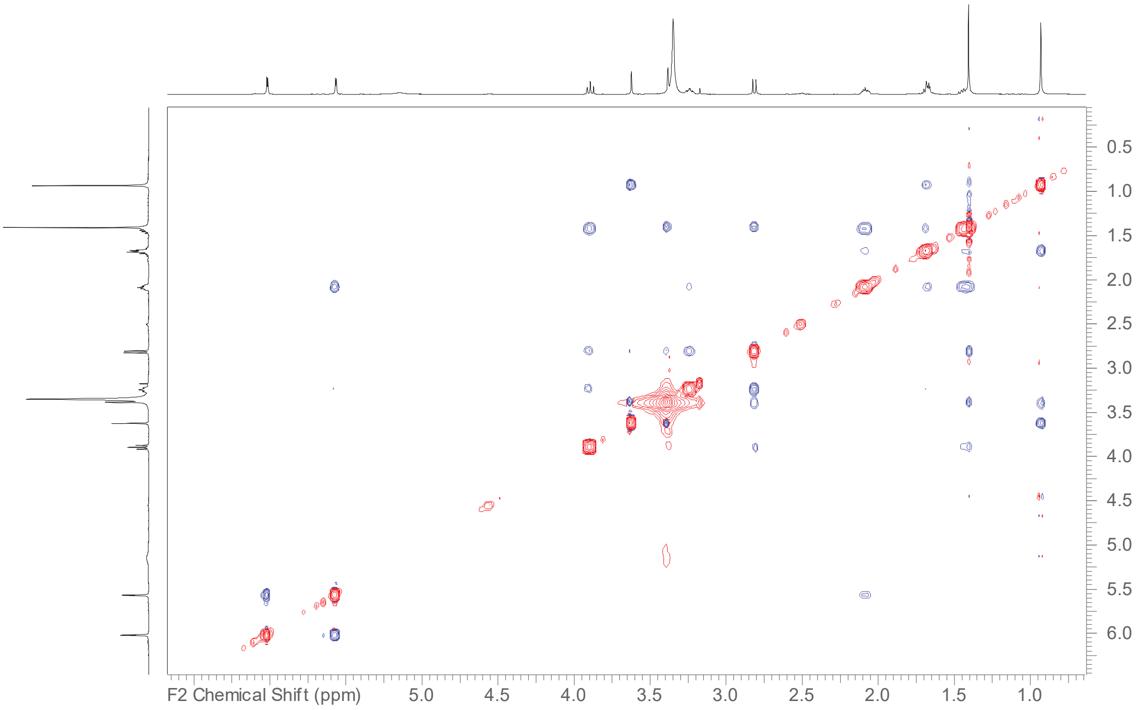

Figure S35. ^{1}H-^{1}H NOESY spectrum of compound **5** (500 MHz, DMSO).

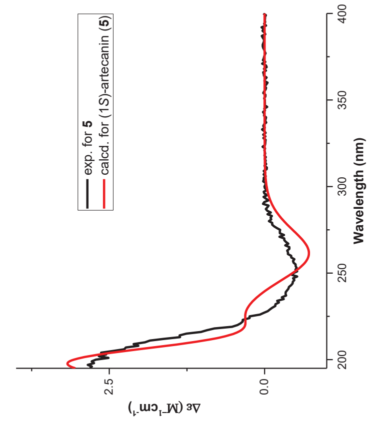

Figure S38. Comparison of experimental and computed ECD spectra for compound **5** in MeOH.

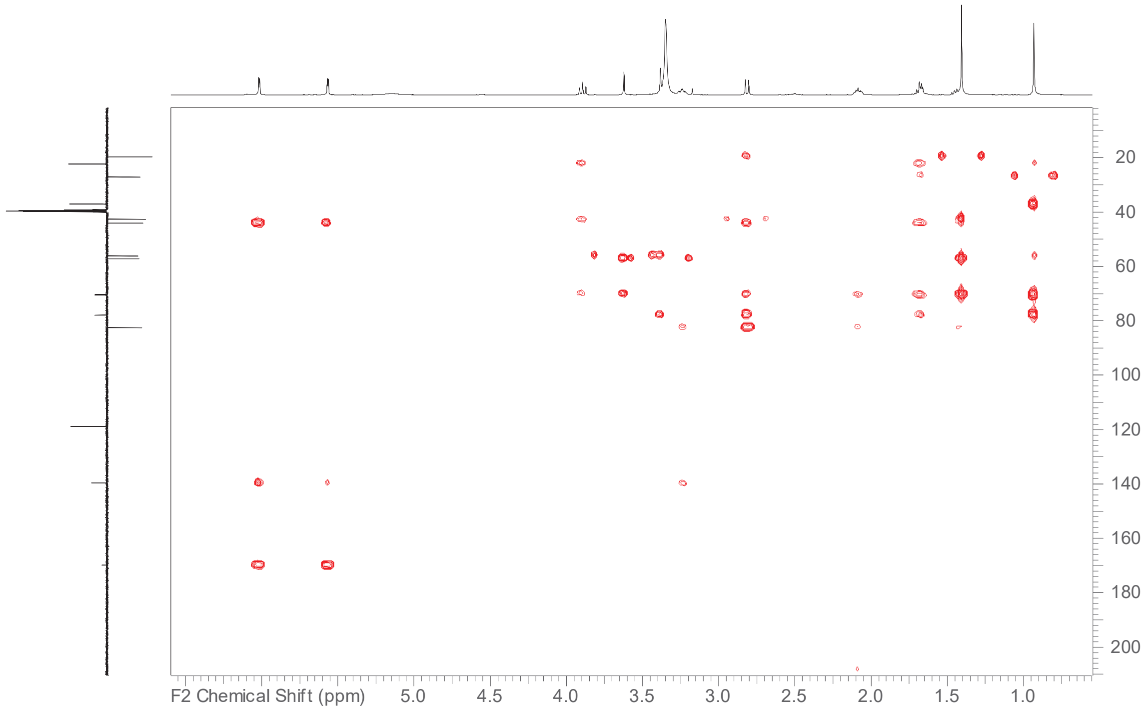

Figure S37. HMBC spectrum of compound **5** (500 MHz, DMSO).

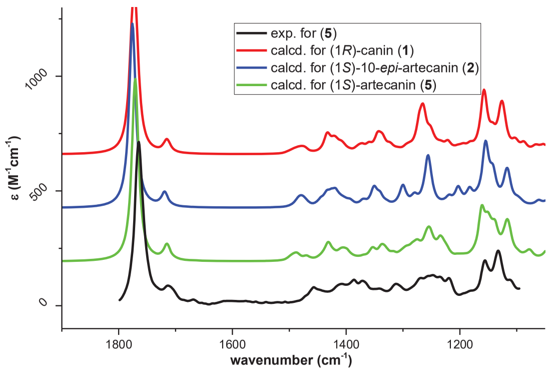

Figure S39. Comparison of experimental and computed IR spectra in DMSO-d_6 for compound **5** in the region 1900-1050 cm^{-1}. Computed spectra (compounds **1**, **2** and **5**) were scaled according to the overall maximal *Sim*VCD value (0.9955).

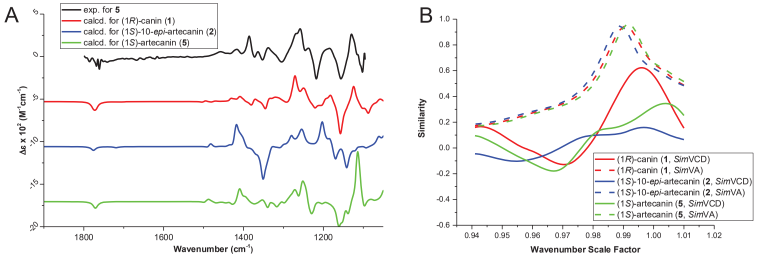

Figure S40. Comparison of experimental and computed VCD spectra in DMSO-d_6 for compound **5.** The region of 1900-1050 cm^{-1} is shown (A). Similarities (*Sim*VA and *Sim*VCD) of the experimental VA and VCD spectra of **5** to the calculated spectra of possible stereoisomers were plotted as functions of wavenumber scale factor (B). The wavenumber scale factor corresponding to the maximal *Sim*VCD value in B (0.9955) was used to scale the computed spectra in A.

.

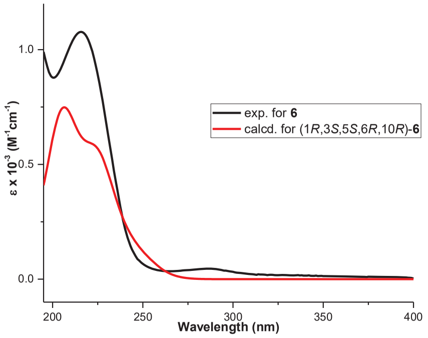

Figure S41. Comparison of experimental and computed UV spectra for compound **6** in MeOH.

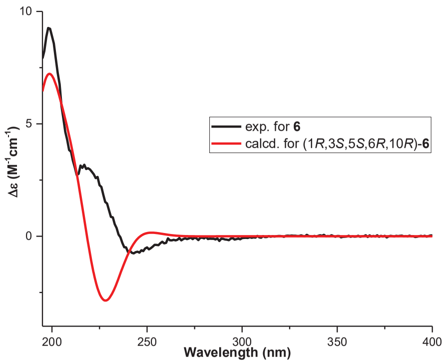

Figure S42. Comparison of experimental and computed ECD spectra for compound **6** in MeOH.

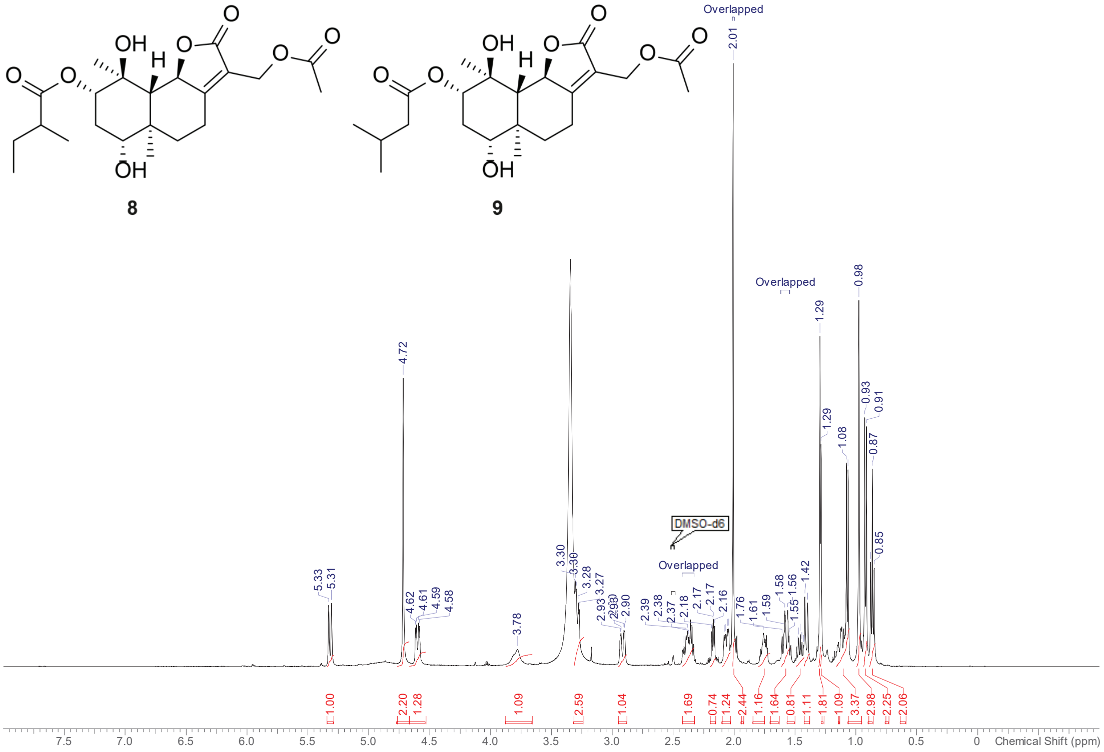

Figure S44. ^{1}H NMR spectrum of compounds **8** and **9** (500 MHz, DMSO).

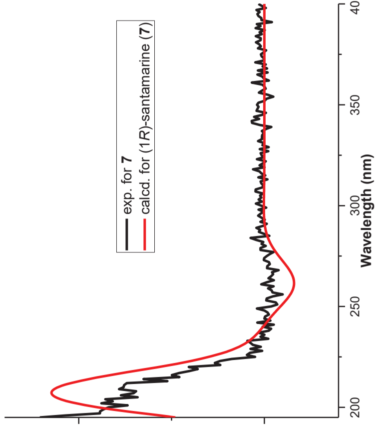

Figure S43. Comparison of experimental and computed ECD spectra for compound **7** in MeOH.

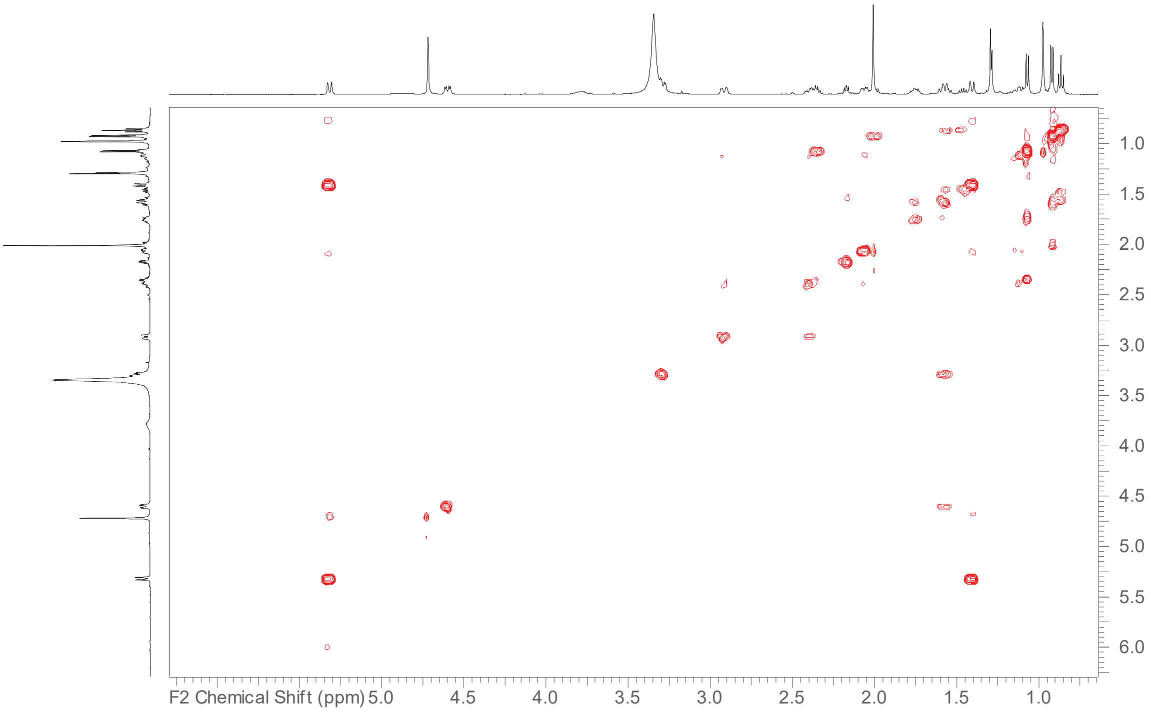

Figure S46. ^1H-^1H COSY spectrum of compounds **8** and **9** (500 MHz, $CDCl_3$).

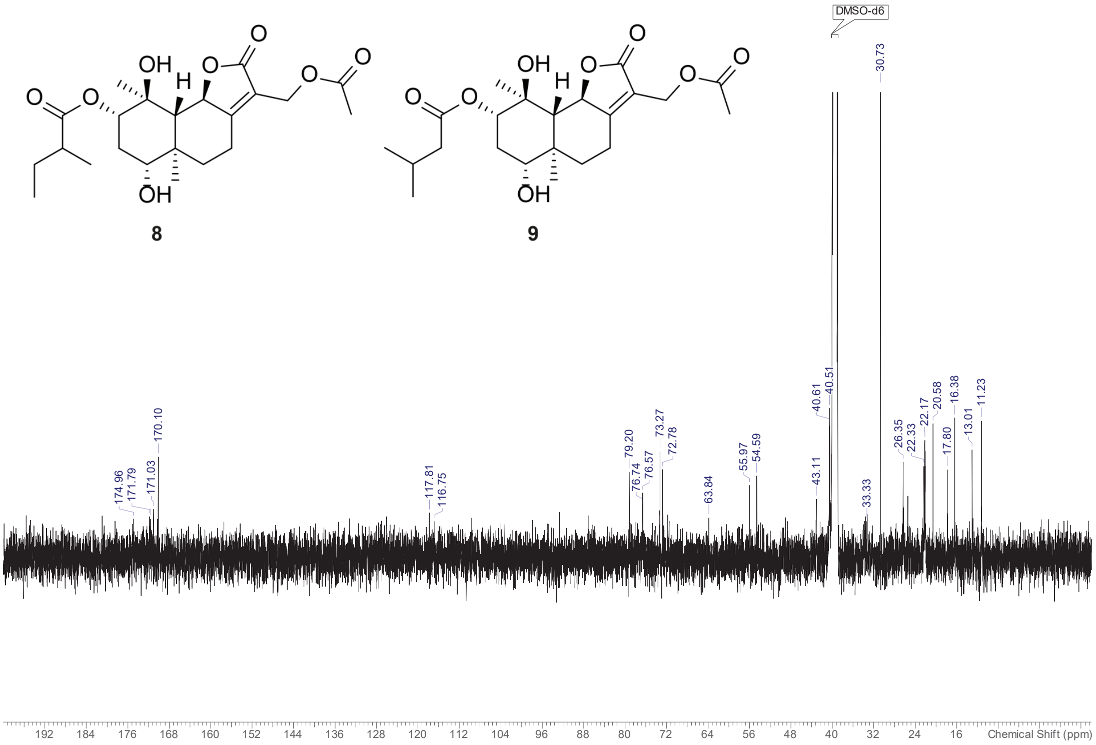

Figure S45. ^{13}C NMR spectrum of compounds **8** and **9** (125 MHz, $CDCl_3$).

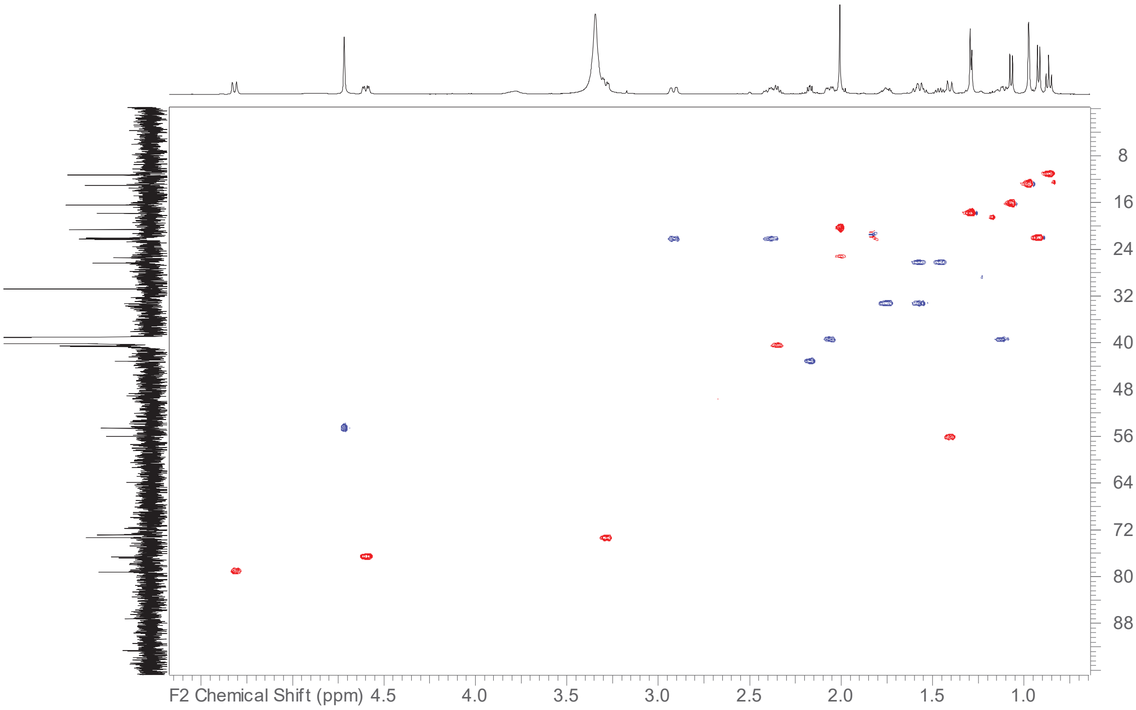

Figure S48. HSQC-DEPT spectrum of compounds **8** and **9** (500 MHz, CDCl$_3$).

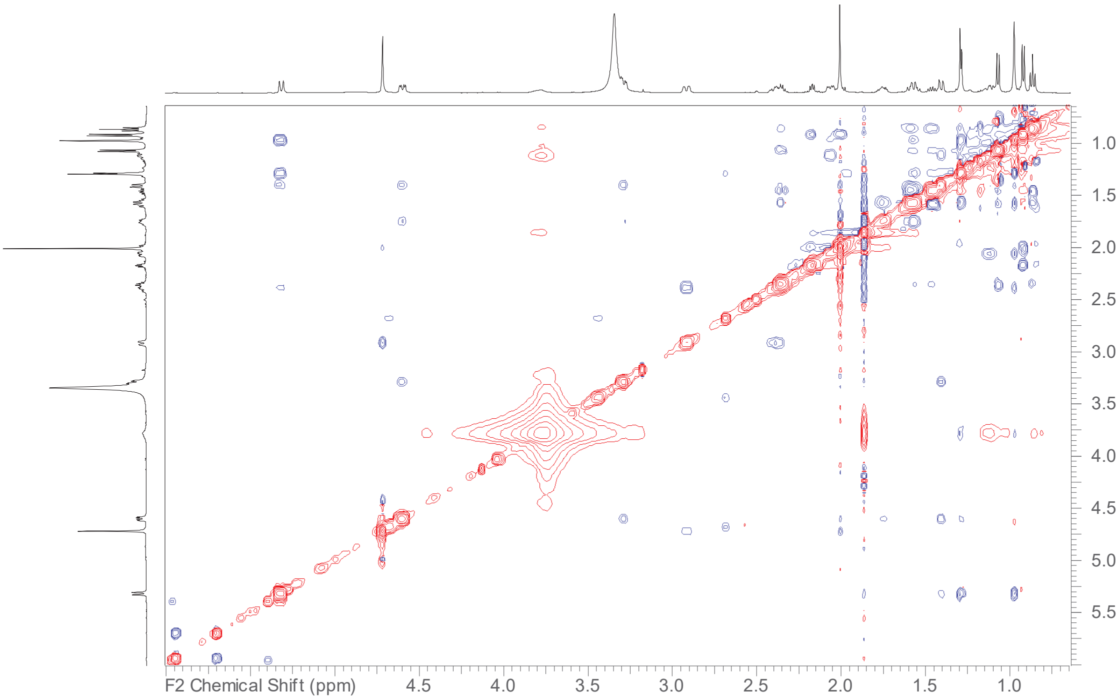

Figure S47. . ^{1}H-^{1}H NOESY spectrum of compounds **8** and **9** (500 MHz, CDCl$_3$).

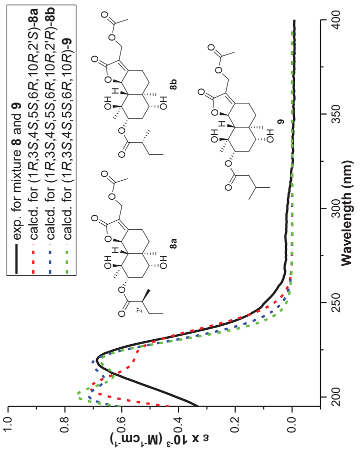

Figure S50. Comparison of experimental and computed UV spectra for compound **11** in MeOH.

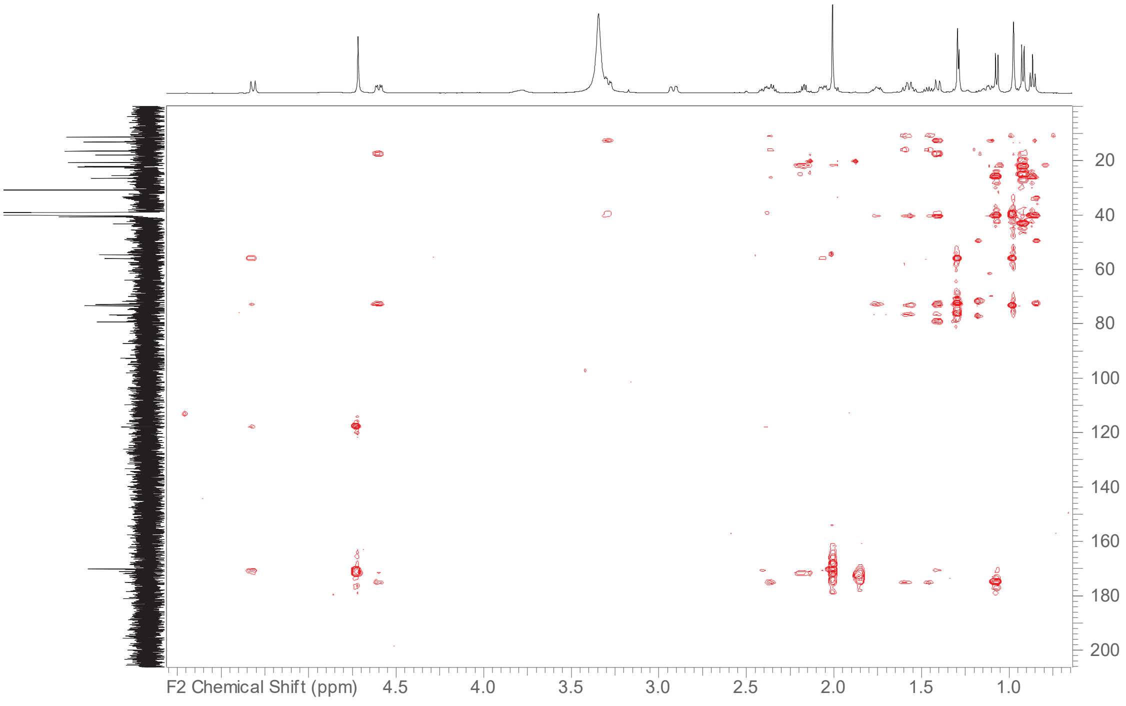

Figure S49. HMBC spectrum of compounds **8** and **9** (500 MHz, $CDCl_3$).

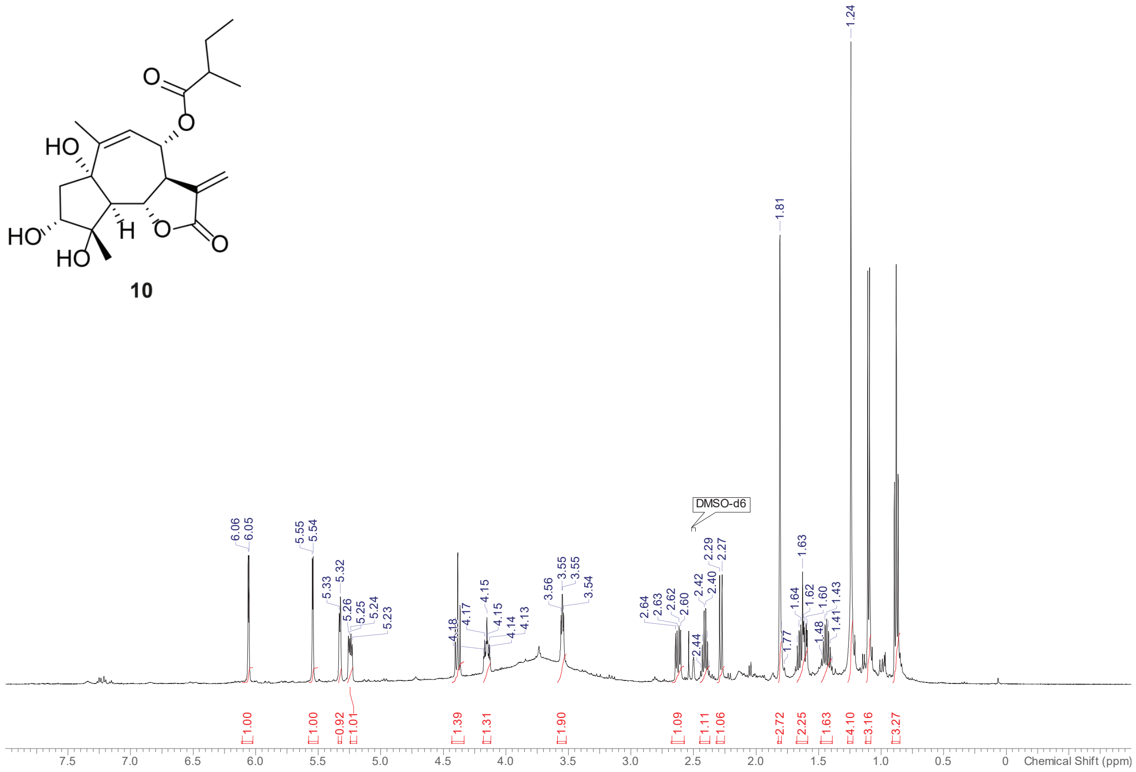

Figure S52. ^{1}H NMR spectrum of compound **10** (500 MHz, DMSO).

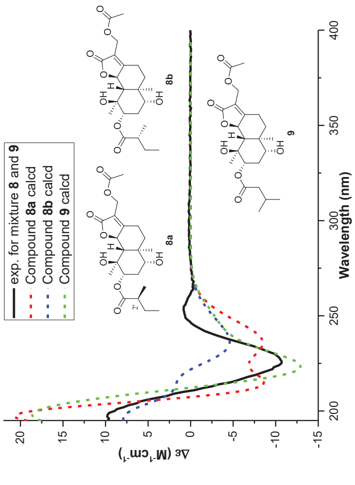

Figure S51. Comparison of the experimental ECD spectrum for the mixture of compounds **8** and **9** in MeOH to the computed spectra of **8a**, **8b**, and **9**.

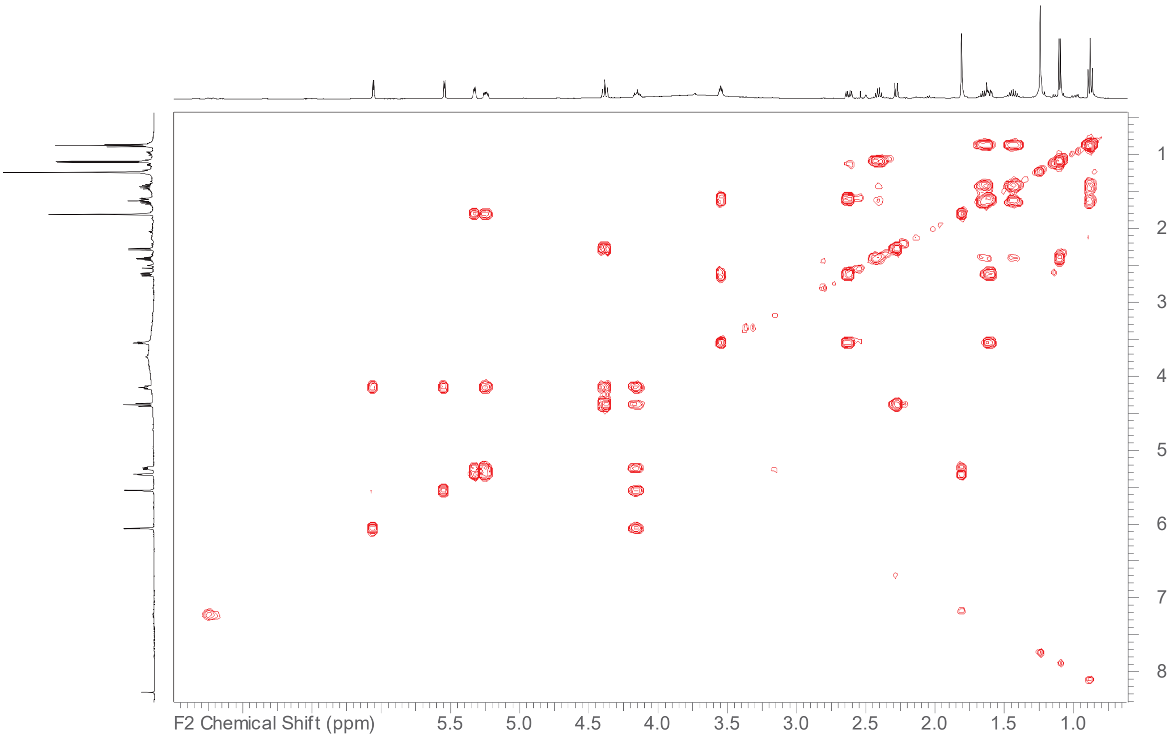

Figure S54. ^{1}H-^{1}H COSY spectrum of compound **10** (500 MHz, DMSO).

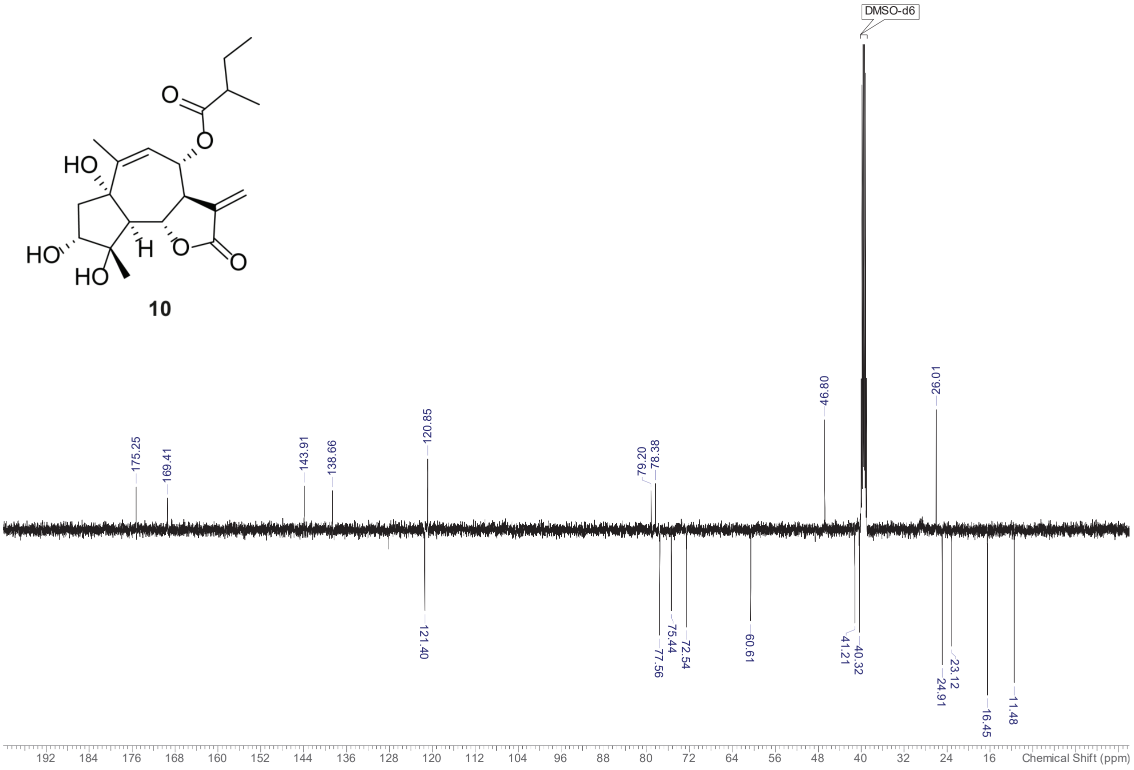

Figure S53. ^{13}C-DEPTq spectrum of compound **10** (125 MHz, DMSO).

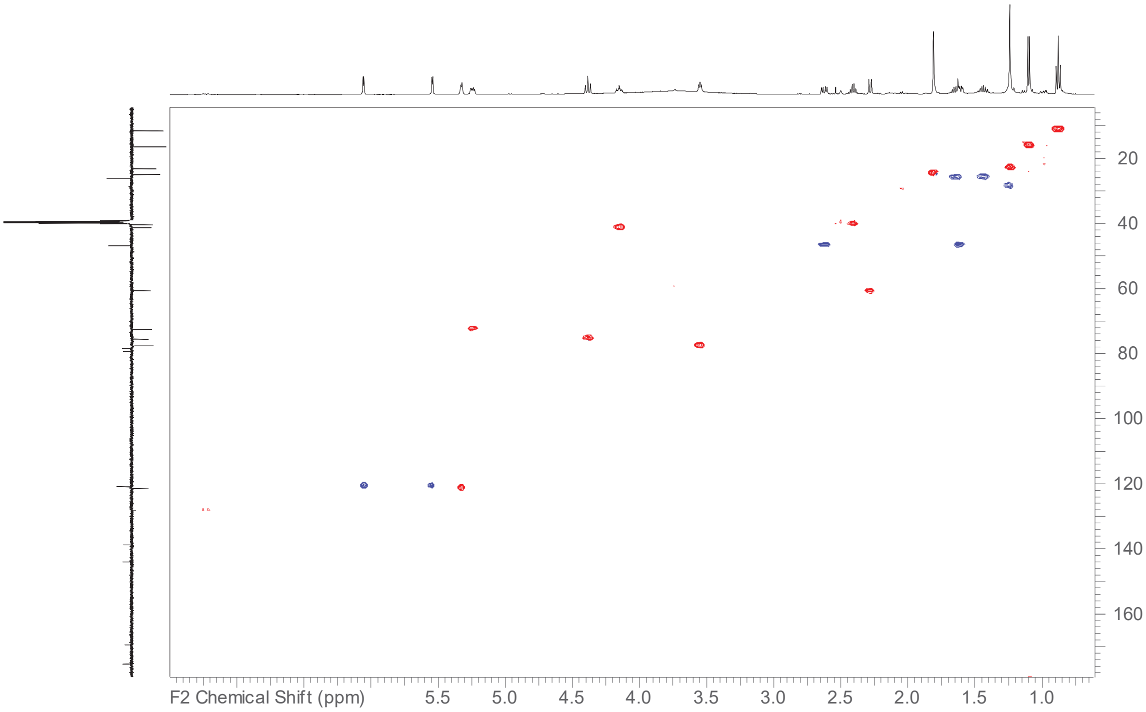

Figure S56 HSQC-DEPT spectrum of compound **10** (500 MHz, DMSO).

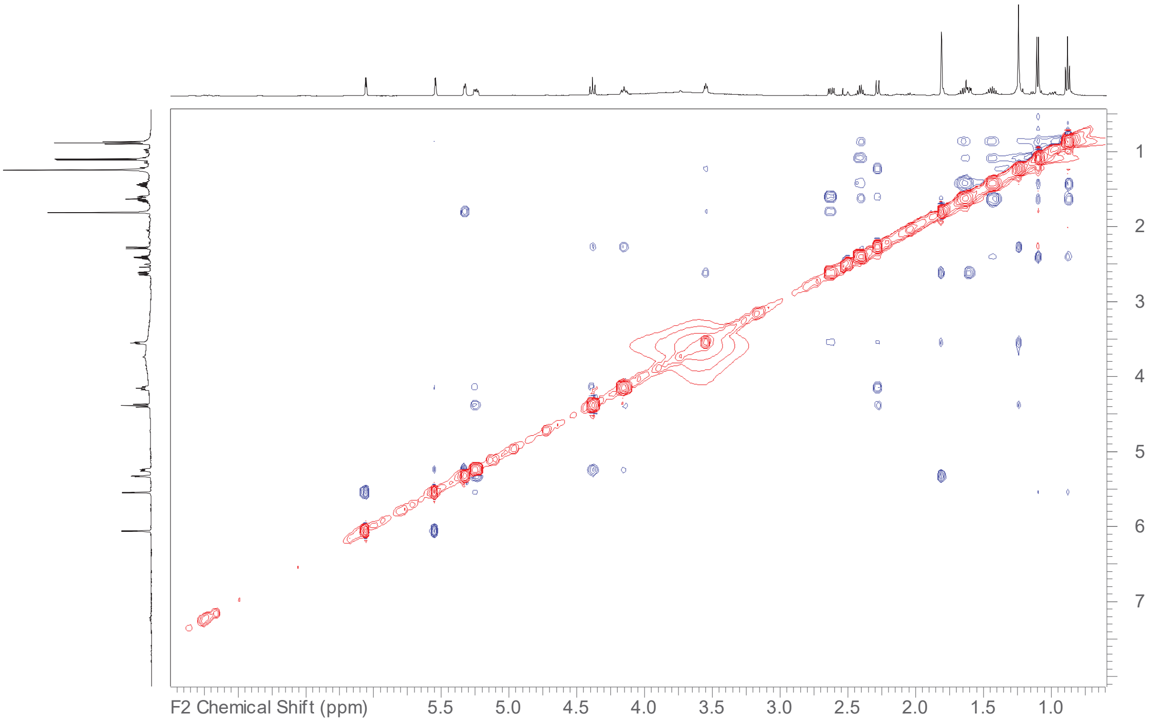

Figure S55. ^{1}H-^{1}H NOESY spectrum of compound **10** (500 MHz, DMSO).

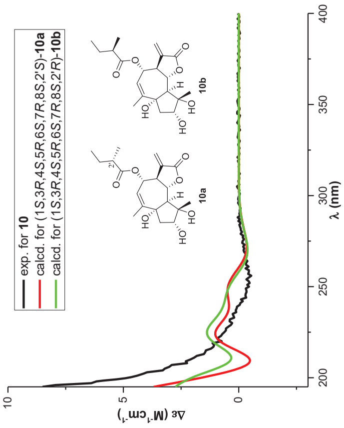

Figure S58. Comparison of the experimental ECD spectrum for compound **10** in MeOH to the computed spectra of **10a** and **10b**.

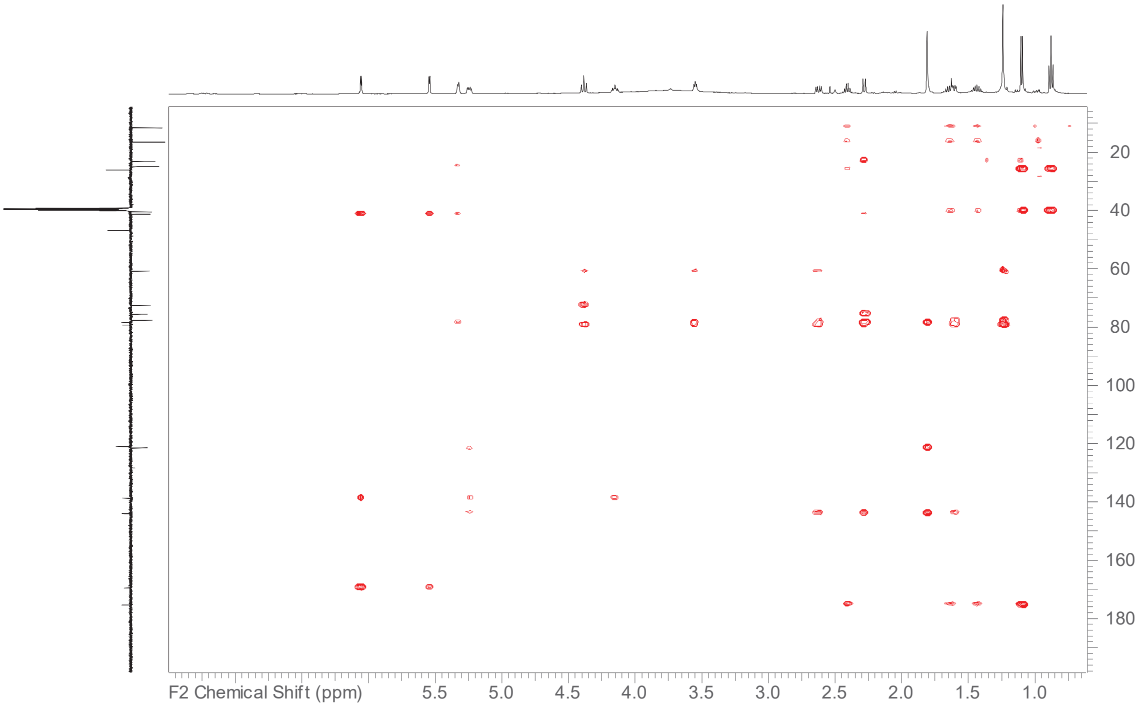

Figure S57. HMBC spectrum of compound **10** (500 MHz, DMSO).

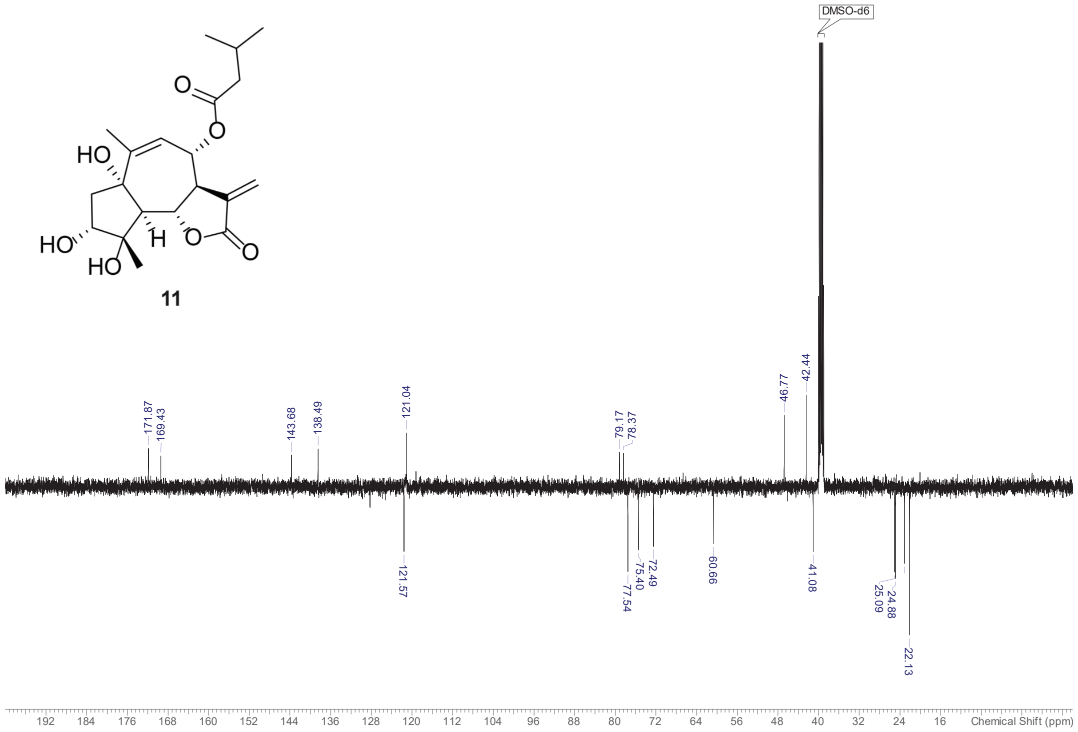

Figure S60. ^{13}C-DEPTq spectrum of compound **11** (125 MHz, DMSO).

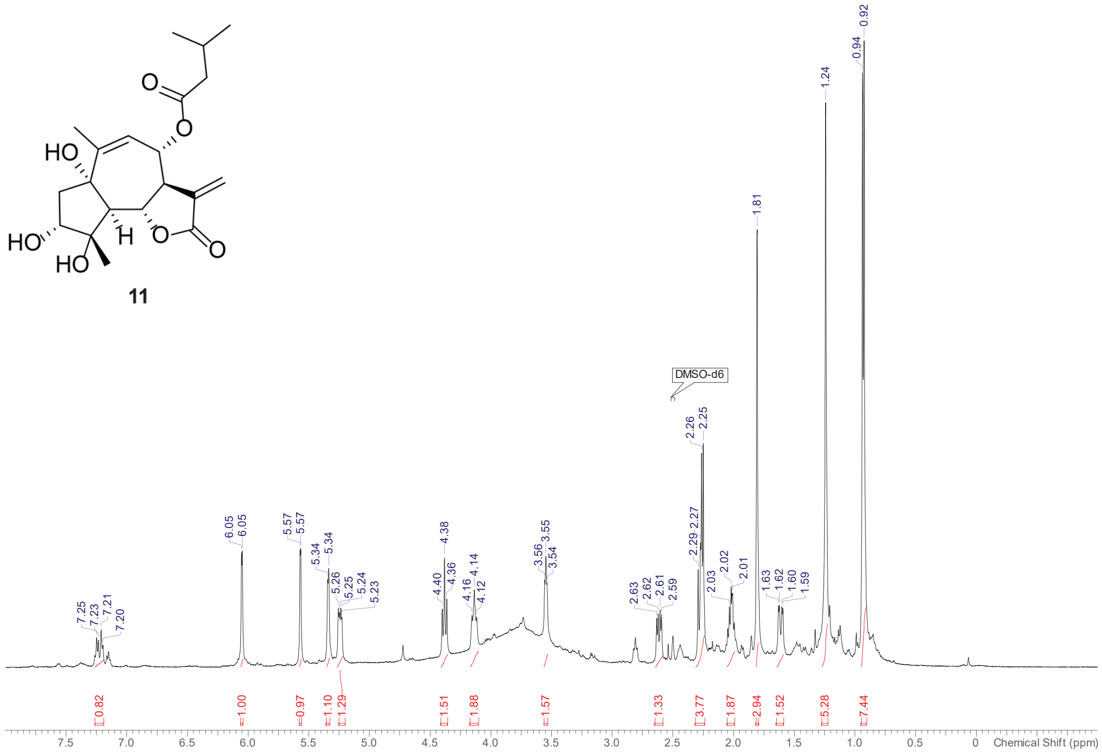

Figure S59. ^{1}H NMR spectrum of compound **11** (500 MHz, DMSO).

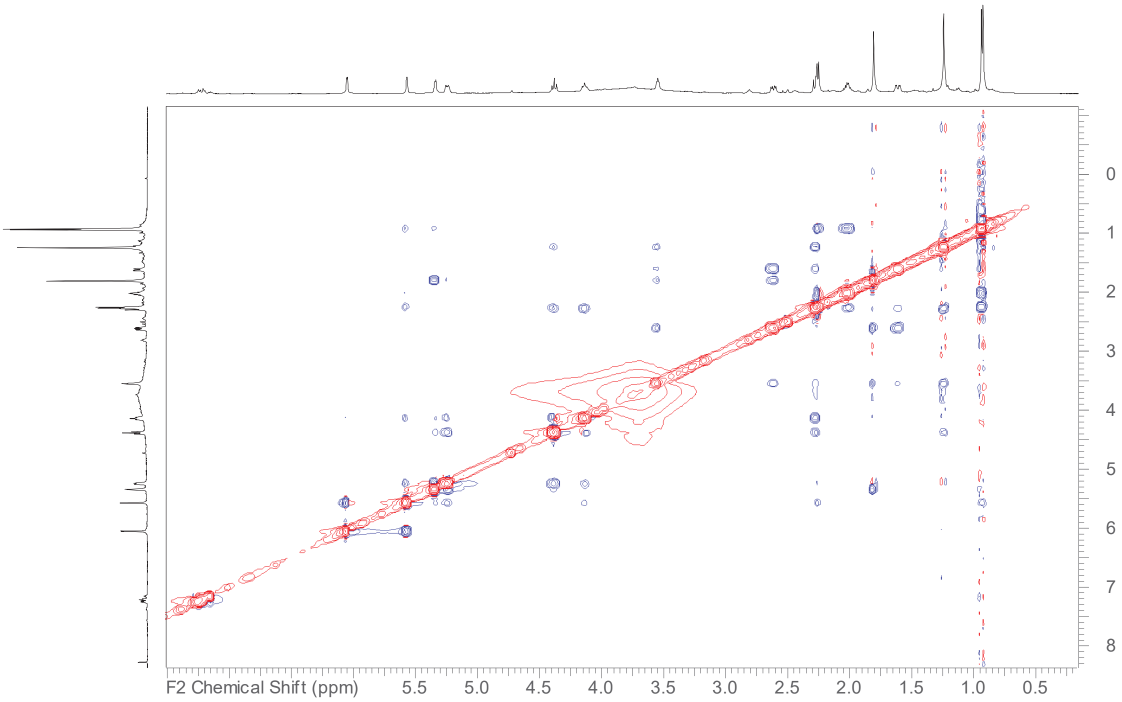

Figure S62. ^{1}H-^{1}H NOESY spectrum of compound **11** (500 MHz, DMSO).

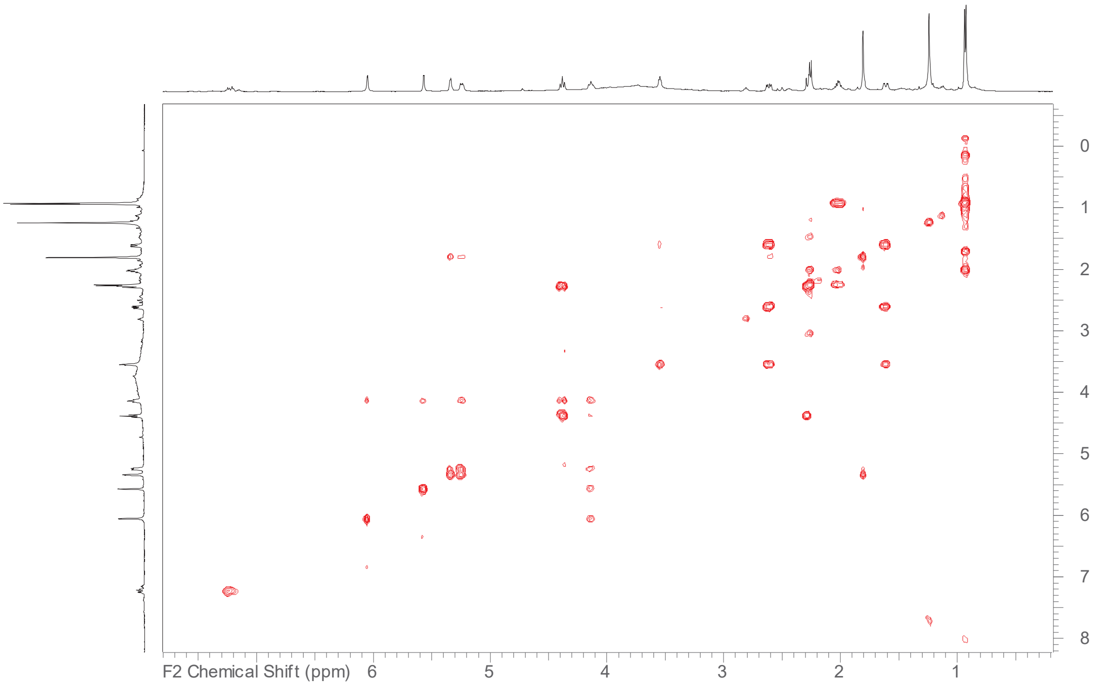

Figure S61. ^{1}H-^{1}H COSY spectrum of compound **11** (500 MHz, DMSO).

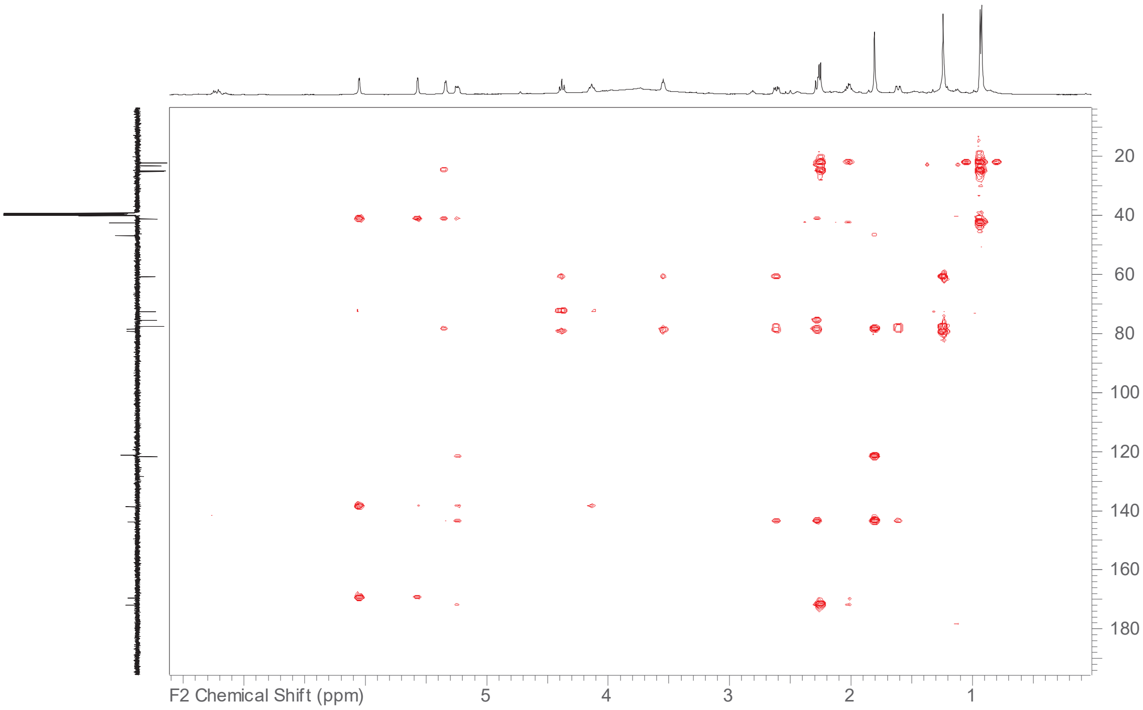

Figure S64. HMBC spectrum of compound **11** (500 MHz, DMSO).

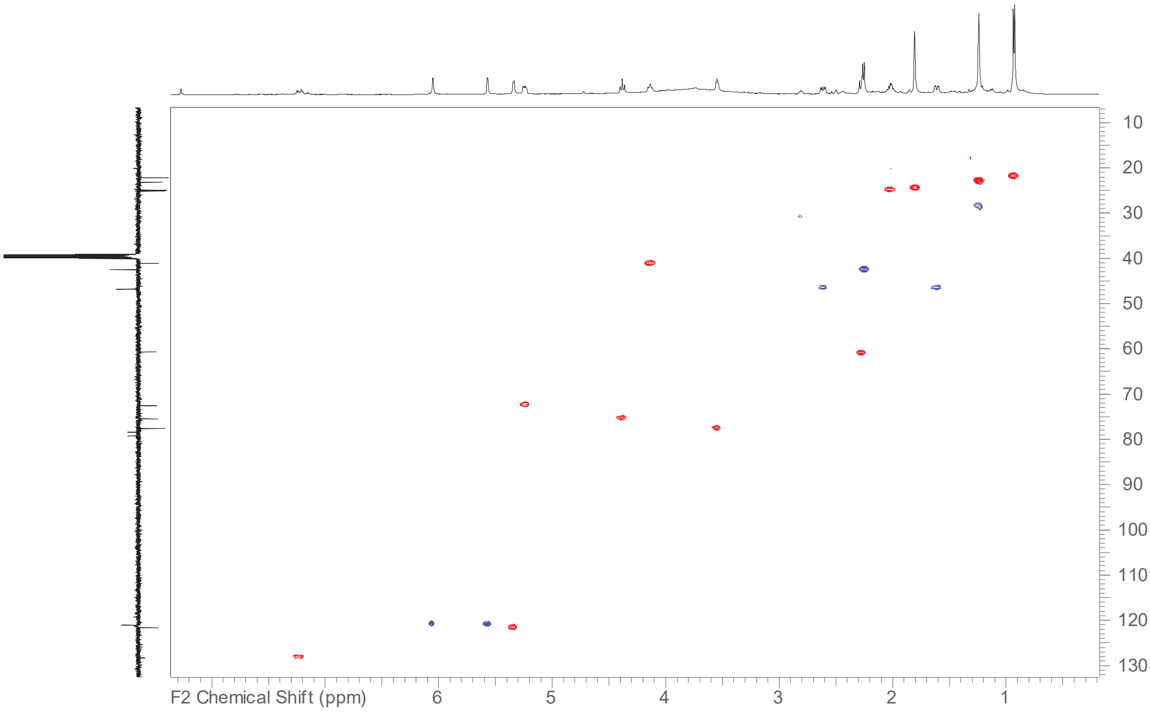

Figure S63. HSQC-DEPT spectrum of compound **11** (500 MHz, DMSO).

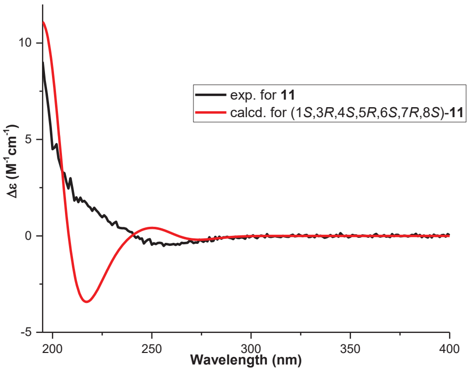

Figure S66. Comparison of experimental and computed ECD spectra for compound **11** in MeOH.

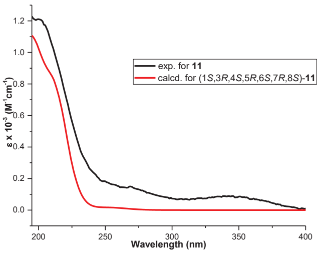

Figure S65. Comparison of experimental and computed UV spectra for compound **11** in MeOH.

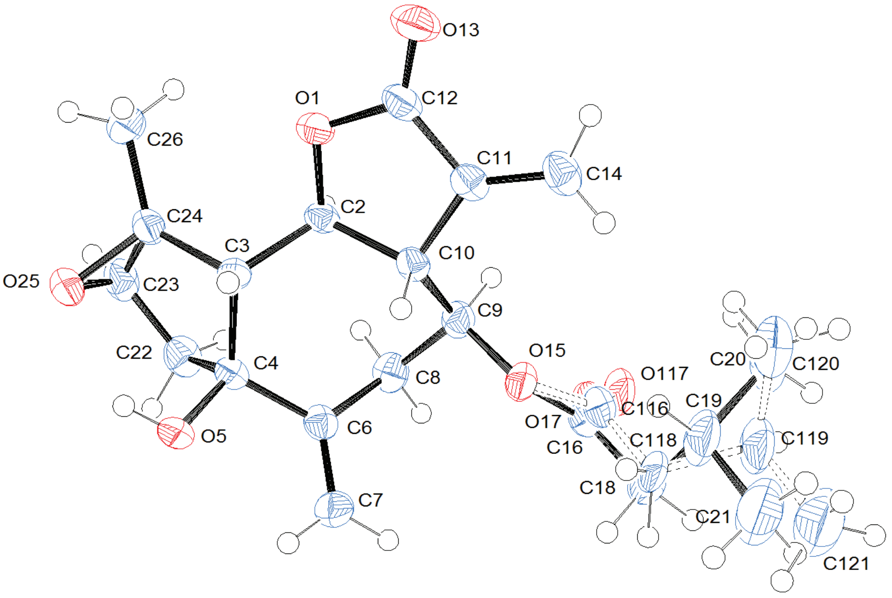

Figure S68. ORTEP diagram of compound **14** from the X-ray diffraction experiment.

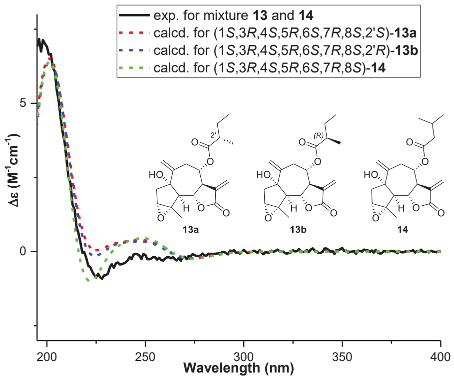

Figure S67. Comparison of experimental ECD spectrum of the mixture of compounds **13** and **14** in MeOH (270 μg/mL) to the computed spectra of **13a**, **13b**, and **14**. Combined curves were mixed in the ratio of 1:1 as determined between compounds **13** and **14** via ^{1}H NMR.

Table S7. Crystal data for **14** and **15**.

	14	**15**
formula	$C_{20}H_{26}O_6$	$C_{17}H_{20}O_5$
formula weight	362.42	304.34
Z, calculated density	4, 1.272 Mg * m^{-3}	4, 1.263 Mg * m^{-3}
F (000)	775.997	647.996
description and size of crystal	colorless block, 0.11 * 0.13 * 0.21 mm^3	colorless block, 0.05 * 0.09 * 0.14 mm^3
absorption coefficient	0.769	0.487
min/max transmission	0.90 / 0.92	0.98 / 0.98
temperature	123 K	123 K
radiation (wavelength)	CuK_α (Î = 1.54178 Å)	GaK_α (Î = 1.34143 Å)
Crystal system, space group	orthorhombic, $P2_12_12_1$	orthorhombic, $P2_12_12$
a	9.1487(7) Å	19.8206(4) Å
b	10.3308(7) Å	9.5646(2) Å
c	20.0261(14) Å	8.4390(2) Å
Î±	90°	90°
Î²	90°	90°
Î³	90°	90°
V	1892.7(2) $Å^3$	1599.83(6) $Å^3$
min/max Î¸	4.816 Å / 68.964 Å	3.881 Å / 57.257 Å
number of collected reflections	25073	33193
number of independent reflections	3419 (merging r = 0.032)	3101 (merging r = 0.024)
number of observed reflections	3485 I>2.0\σ(I)	3274 I>2.0\σ(I)
number of refined parameters	295	200
R	0.0473	0.0265
R_w	0.0496	0.0294
goodness of fit	1.0832	1.1151
Flack parameter	0.10 (19)	0.06(15)

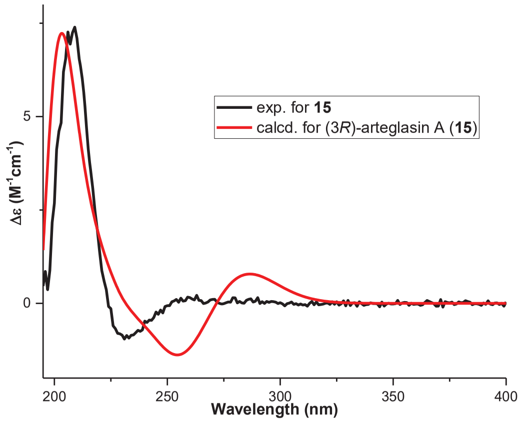

Figure S69. Comparison of experimental and computed ECD spectra for compound **15** in MeOH.

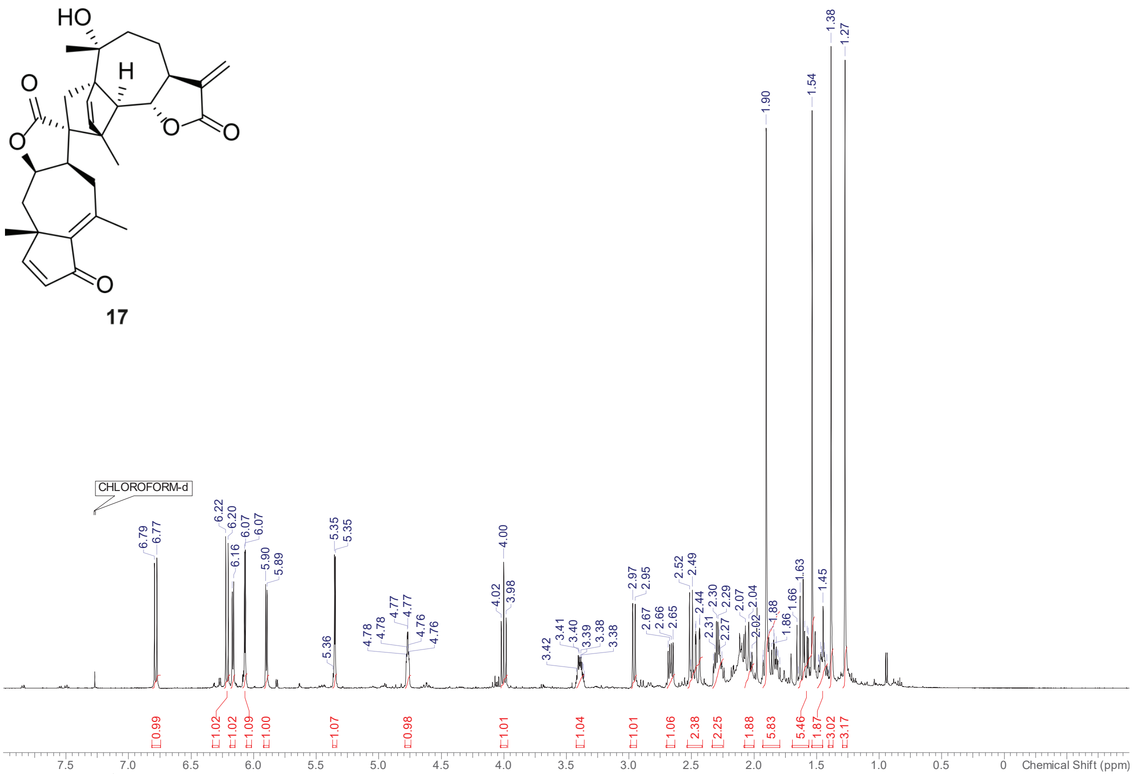

Figure S71. ^{1}H NMR spectrum of compound **17** (500 MHz, $CDCl_3$).

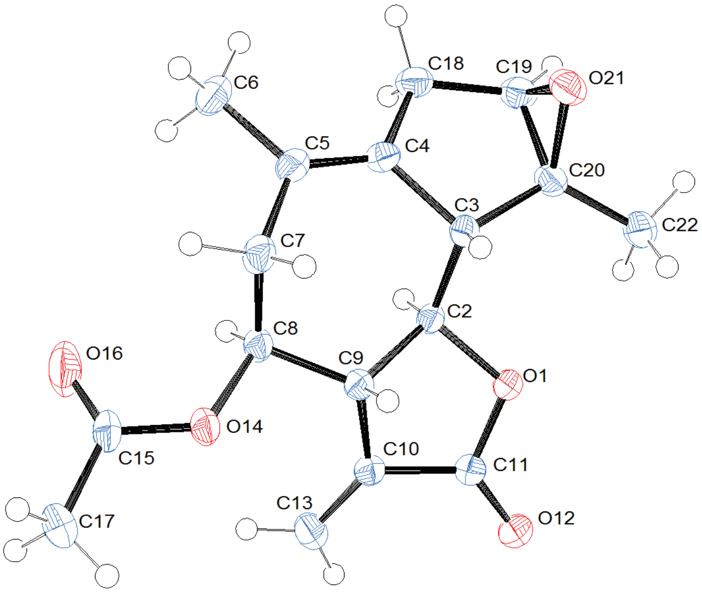

Figure S70. ORTEP diagram of compound **15** from the X-ray diffraction experiment.

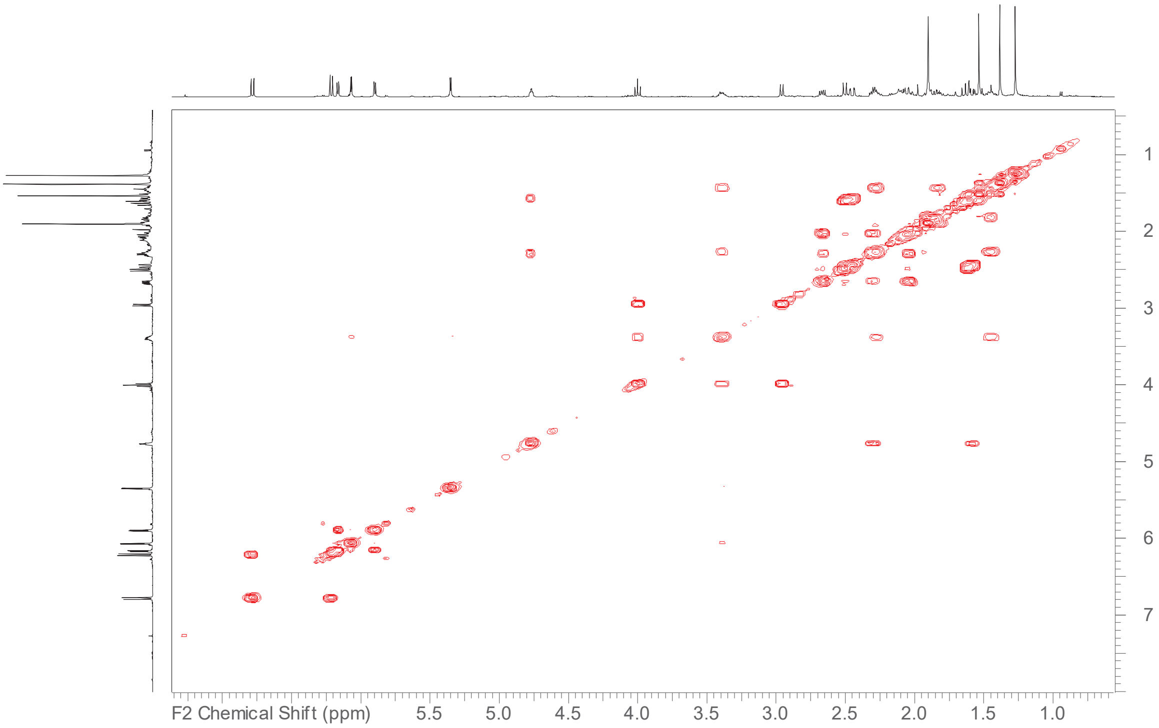

Figure S73. ^{1}H-^{1}H COSY spectrum of compound **17** (500 MHz, CDCl$_3$).

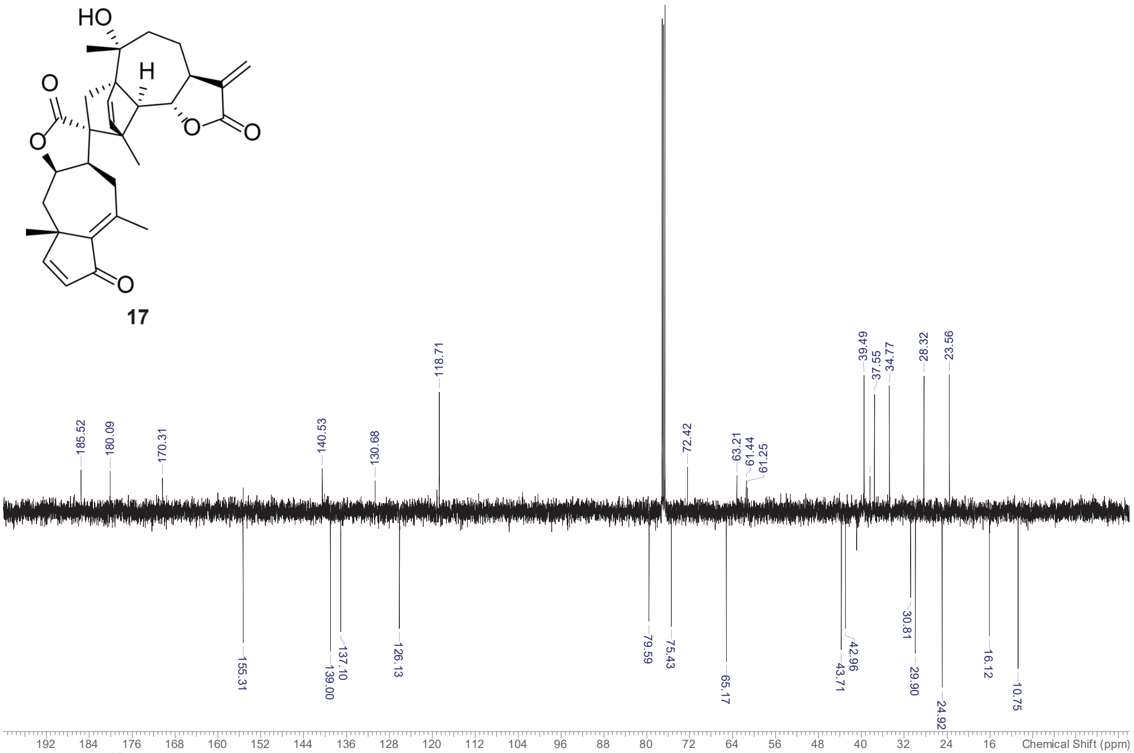

Figure S72. ^{13}C-DEPTq spectrum of compound **17** (125 MHz, CDCl$_3$)

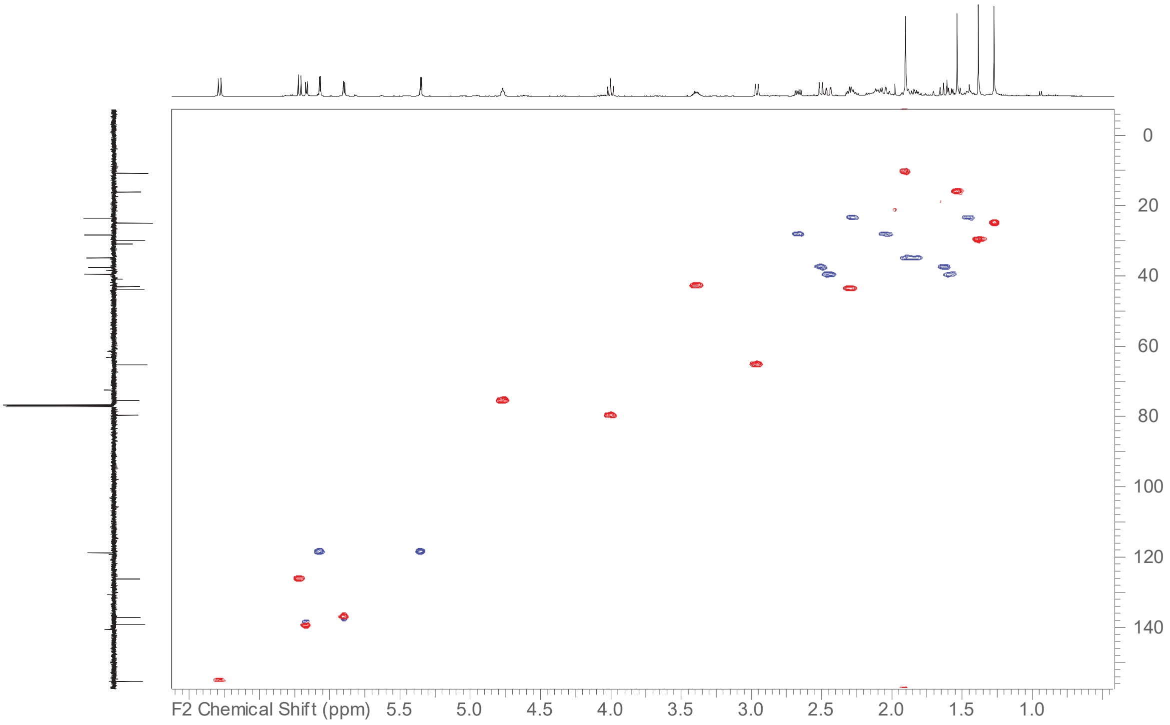

Figure S75. HSQC-DEPT spectrum of compound **17** (500 MHz, $CDCl_3$).

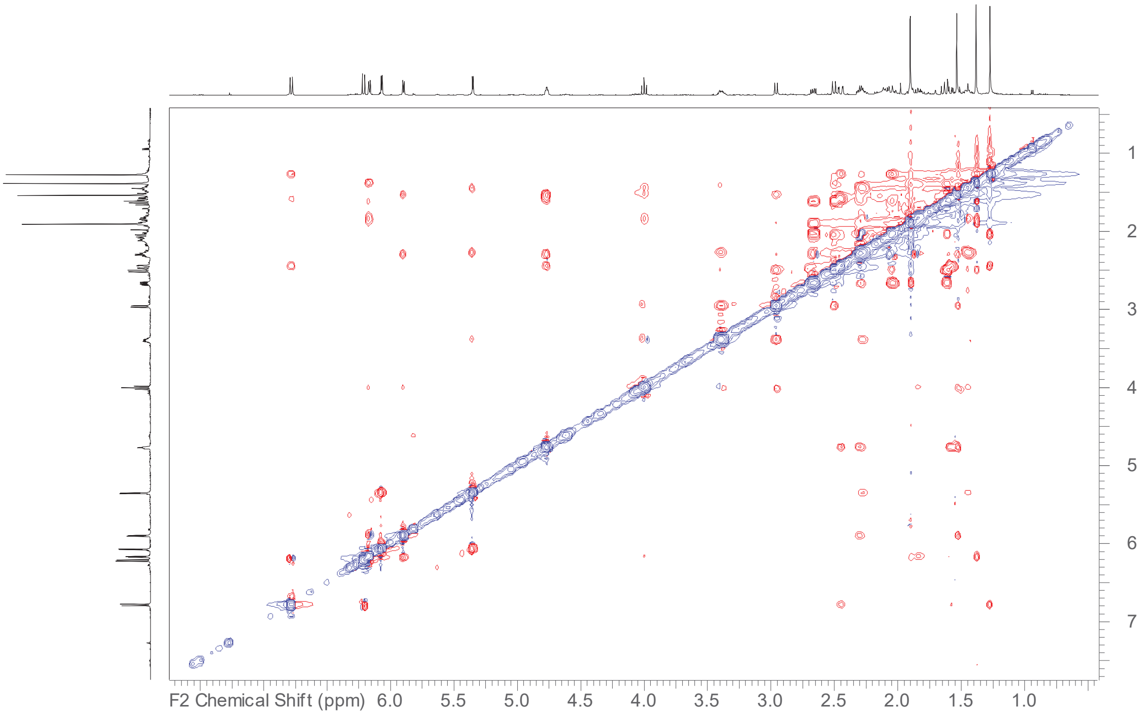

Figure S74. ^1H-^1H NOESY spectrum of compound **17** (500 MHz, $CDCl_3$).

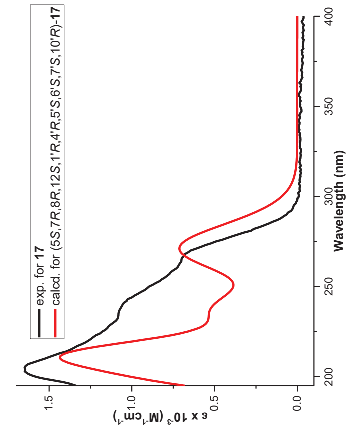

Figure S77. Comparison of experimental and computed UV spectra for compound **17** in MeOH.

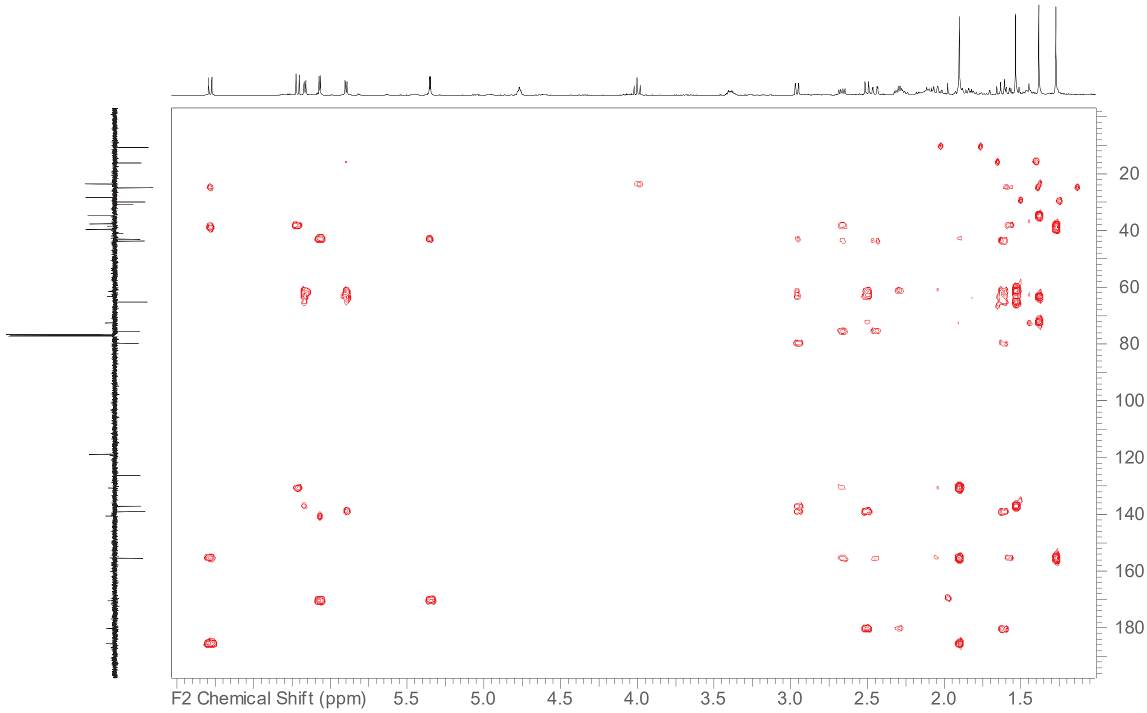

Figure S76. HMBC spectrum of compound **17** (500 MHz, CDCl$_3$).

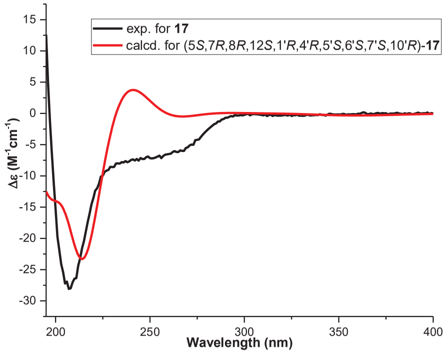

Figure S78. Comparison of experimental and computed ECD spectra for compound **17** in MeOH.

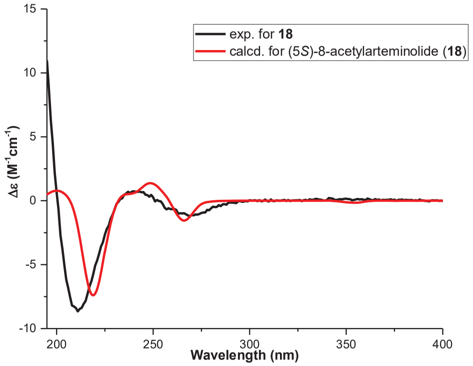

Figure S79. Comparison of experimental and computed ECD spectra for compound **18** in MeOH.

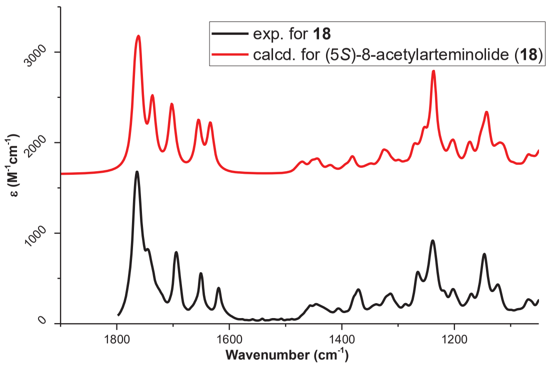

Figure S80. Comparison of experimental and computed IR spectra in chloroform for compound **18** in the region 1900 1050 cm^{-1}. Computed spectrum of **18** was scaled according to the maximal SimVCD value (0.9845).

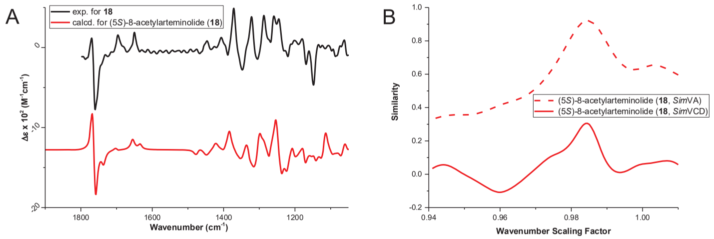

Figure S81. Comparison of experimental and computed VCD spectra in chloroform for compound **18.** The region of 1900-1050 cm^{-1} is shown (A). Similarities (*Sim*VA and *Sim*VCD) of the experimental VA and VCD spectra of **18** to the calculated spectra of possible stereoisomers were plotted as functions of wavenumber scale factor (B). The wavenumber scale factor corresponding to the maximal *Sim*VCD value in B (0.9845) was used to scale the computed spectra in A.

3.2. Immunosuppressive Activity of *Artemisia argyi* Extract and Isolated Compounds

Amy M. Zimmermann-Klemd[†], Jakob K. Reinhardt[†], Anna Morath, Wolfgang W. Schamel, Peter Steinberger, Judith Leitner, Roman Huber, Matthias Hamburger, Carsten Gründemann

Front. Pharmacol. 2020, 11, 402. doi: 10.3389/fphar.2020.00402

The need for novel drugs for the treatment of autoimmune diseases is high, since available pharmaceuticals often have substantial side effects and limited efficacy. Natural products are a good starting point in the development of immunosuppressive leads. Since enhanced T cell proliferation is a common feature of autoimmune diseases, we investigated the T cell proliferation inhibitory potential of an extract library of plants used in traditional Chinese medicine. Using a newly established cell-based screening platform, an ethyl acetate extract of *Artemisia argyi* H.Lév. & Vaniot (Asteraceae, *A. argyi*) was found to suppress the proliferation of human primary T lymphocytes in vitro in an IL-2-dependent manner. Flow cytometry- and ELISA-based techniques further demonstrated that the *A. argyi* extract reduced the activation and function of T cells. Transcription factor analysis and flow cytometric calcium influx investigations indicated that the immunomodulatory effect was based on specific modification of T cell signaling in a non-cytotoxic manner which is mediated via the NFAT pathway and a non-sequestrant inhibition of the calcium influx. A series of guaianolide and seco-guaianolide sesquiterpene lactones, as well as a flavonoid, were identified in a previous study as the bioactive compounds in the *A. argyi* extract. The effects of these bioactive compounds were compared to those of the crude extract. The tested sesquiterpene lactones act via the transcription factor NFAT and NF-kB, thereby exhibiting their immunosuppressive potential, but have an overall effect on T cell biology on a more-downstream level than the crude *A. argyi* extract.

Preparation of the tested extract, selection of compounds, preparation of chemical structures, writing of manuscript draft regarding results and discussion on "Effects of isolated compounds", and the discussion of other tested Asteraceae were my contributions to this publication. Other than that, I contributed to the design, implementation of the research, and in finalizing the manuscript.

[†] *contributed equally to this work*

Jakob K. Reinhardt

frontiers in Pharmacology

ORIGINAL RESEARCH
published: 08 April 2020
doi: 10.3389/fphar.2020.00402

Immunosuppressive Activity of *Artemisia argyi* Extract and Isolated Compounds

Amy M. Zimmermann-Klemd[1†], Jakob K. Reinhardt[2†], Anna Morath[3,4,5], Wolfgang W. Schamel[3,4,6], Peter Steinberger[7], Judith Leitner[7], Roman Huber[1], Matthias Hamburger[2] and Carsten Gründemann[8]*

[1] Center for Complementary Medicine, Institute for Infection Prevention and Hospital Epidemiology, Faculty of Medicine, University of Freiburg, Freiburg, Germany, [2] Pharmaceutical Biology, Pharmacenter, University of Basel, Basel, Switzerland, [3] Signalling Research Centres BIOSS and CIBSS, University of Freiburg, Freiburg, Germany, [4] Faculty of Biology, University of Freiburg, Freiburg, Germany, [5] Spemann Graduate School of Biology and Medicine, University of Freiburg, Freiburg, Germany, [6] Center for Chronic Immunodeficiency, Medical Center Freiburg and Faculty of Medicine, University of Freiburg, Freiburg, Germany, [7] Center for Pathophysiology, Infectiology, and Immunology, Institute of Immunology, Medical University of Vienna, Vienna, Austria, [8] Translational Complementary Medicine, Department of Pharmaceutical Sciences, University of Basel, Basel, Switzerland

OPEN ACCESS

Edited by:
Judit Hohmann,
University of Szeged, Hungary

Reviewed by:
Edgar Serfling,
Julius Maximilian University of Würzburg, Germany
Orazio Taglialatela-Scafati,
University of Naples Federico II, Italy

***Correspondence:**
Carsten Gründemann
carsten.gruendemann@unibas.ch

†These authors have contributed equally to this work

Specialty section:
This article was submitted to Ethnopharmacology, a section of the journal Frontiers in Pharmacology

Received: 17 December 2019
Accepted: 17 March 2020
Published: 08 April 2020

Citation:
Zimmermann-Klemd AM, Reinhardt JK, Morath A, Schamel WW, Steinberger P, Leitner J, Huber R, Hamburger M and Gründemann C (2020) Immunosuppressive Activity of Artemisia argyi Extract and Isolated Compounds. Front. Pharmacol. 11:402. doi: 10.3389/fphar.2020.00402

The need for novel drugs for the treatment of autoimmune diseases is high, since available pharmaceuticals often have substantial side effects and limited efficacy. Natural products are a good starting point in the development of immunosuppressive leads. Since enhanced T cell proliferation is a common feature of autoimmune diseases, we investigated the T cell proliferation inhibitory potential of an extract library of plants used in traditional Chinese medicine. Using a newly established cell-based screening platform, an ethyl acetate extract of *Artemisia argyi* H.Lév. & Vaniot (Asteraceae, *A. argyi*) was found to suppress the proliferation of human primary T lymphocytes *in vitro* in an IL-2-dependent manner. Flow cytometry- and ELISA-based techniques further demonstrated that the *A. argyi* extract reduced the activation and function of T cells. Transcription factor analysis and flow cytometric calcium influx investigations indicated that the immunomodulatory effect was based on specific modification of T cell signaling in a non-cytotoxic manner which is mediated *via* the NFAT pathway and a non-sequestrant inhibition of the calcium influx. A series of guaianolide and *seco*-guaianolide sesquiterpene lactones, as well as a flavonoid, were identified in a previous study as the bioactive compounds in the *A. argyi* extract. The effects of these bioactive compounds were compared to those of the crude extract. The tested sesquiterpene lactones act *via* the transcription factor NFAT and NF-κB, thereby exhibiting their immunosuppressive potential, but have an overall effect on T cell biology on a more-downstream level than the crude *A. argyi* extract.

Keywords: Artemisia, immunosuppression, interleukin-2, T cell signalling, sesquiterpene lactones

INTRODUCTION

T cells play a major role in the immune system. A complex mechanism of antigen recognition and signal transduction ensures a highly specific and highly efficient clearance of pathogens.

Upon T cell activation, several adaptor molecules and signaling proteins are phosphorylated to initiate three main axis of signal transduction in T cells. In this process, phosphatidylinositol-4,5-bisphosphate (PIP_2) is hydrolyzed to generate inositol-1,4,5-trisphosphate (IP_3) and diacylglycerol (DAG). While DAG is membrane associated, IP_3 binds to the IP_3 receptor in the membrane of the endoplasmic reticulum (ER) leading to calcium ER store depletion. Upon calcium ER store depletion, release-activated channels (CRAC channels) mediate a strong store-operated calcium entry (SOCE) (Hogan et al., 2010). The rising calcium concentration in the cytosol causes dephosphorylation and thereby unmasking of the nuclear location sequence of the nuclear factor of activated T cells (NFAT) *via* second messenger and phosphatase activation (Srikanth et al., 2017). On a further axis the mitogen-activated protein kinase (MAPK) pathway is triggered, resulting the formation of activator protein 1 (AP-1) and its nuclear transport (Myers et al., 2019). The third axis induces phosphorylation of nuclear factor of the kappa-light-polypeptide-gene enhancer in B cells inhibitor (IκB), leading to its degradation. Subsequently, the nuclear factor kappa-light-chain enhancer of activated B cells (NF-κB) is released for nuclear transport (Sun, 2012). The transcription factors NFAT, NF-κB, and AP-1 all bind to the *interleukin-2* (*il-2)* gene to allow transcription and secretion of interleukin-2 (IL-2) (Myers et al., 2019). IL-2 autocrinally stimulates T cell proliferation, and thus, is crucial for a proper immune response. Consequently, IL-2 can be linked to immune overreactions.

Overreaction of the immune system can be linked to autoimmune diseases such as rheumatoid arthritis or multiple sclerosis (Chaplin, 2010; Wang et al., 2015). The treatment of autoimmune diseases usually involves different classes of immunosuppressive drugs (Her and Kavanaugh, 2016). Glucocorticoids inhibit the function of immune cells as the activated glucocorticoid receptor directly interferes with the transcription factors NF-κB and AP-1 (van der Laan and Meijer, 2008; Frenkel et al., 2015; Wang et al., 2017). Glucocorticoids are quite effective, but this potency is accompanied by a range of side effects (Ramamoorthy and Cidlowski, 2016). Drugs such as cyclophosphamide or mycophenolate interfere with the cell cycle and, thereby, inhibit lymphocyte proliferation (Allison, 2000; Wang et al., 2015). Despite their clinical efficacy, these drugs also show severe side effects (Allison, 2000; Wang et al., 2015). Biopharmaceuticals, also called biologics, are widely used due to minor toxicity and high levels of specificity. They intervene strongly in the immune system and, therefore, lead to an increased susceptibility to infections and paradoxical inflammation (Her and Kavanaugh, 2016; Moroncini et al., 2017; Wagner, 2019). Small-molecule drugs (e.g., cyclosporine A, tacrolimus, or tofacitinib) interfering in T cell signaling lead to a suppression of T cell proliferation by addressing different molecular targets (Allison, 2000; Tedesco and Haragsim, 2012; Wiseman, 2016), and they all show adverse effects, such as nephrotoxicity and an increased susceptibility to infections (Allison, 2000).

Hence, compounds with novel modes of action and fewer side effects are needed. Natural products remain a promising source for the discovery and development of new drugs. A recent analysis emphasized their relevance by demonstrating that one third of new chemical entities (NCEs) approved by the Food and Drug Administration (FDA) between 1981 and 2014 were based on natural products (Newman and Cragg, 2016). Plant secondary metabolites possess high structural diversity which has likely evolved for serving different biological functions (Atanasov et al., 2015).

Aiming the discovery of new plant derived drugs, we recently tested a library of 435 extracts from plants used in traditional Chinese medicine (TCM), whereby immunosuppressive activity and inhibition of T lymphocyte proliferation *in vitro,* without apparent cytotoxicity, was targeted. One of the best hits in this library was an ethyl acetate extract of *Artemisia argyi* H. Lév. & Vaniot (Asteraceae). *A. argyi* (also called "Chinese mugwort") grows in China, Japan, and Korea and is traditionally used for the treatment of abdominal pain, dysmenorrhea, uterine hemorrhage, and inflammation (Yun et al., 2016). In previous studies, fatty acids, essential amino acids, sesquiterpene lactones, coumarins, sterols, terpenes, and polyphenols were the main compound classes isolated from *A. argyi* (Bao et al., 2013; Kim et al., 2015). *A. argyi* was recently shown to have anti-inflammatory properties (Yun et al., 2016). The anti-inflammatory effects were supported by *in vivo* experiments that showed reduced cytokine levels and immune infiltration in mouse models for contact dermatitis (Yun et al., 2016) and allergic asthma (Shin et al., 2017). The anti-inflammatory properties of *A. argyi* were linked to some compounds in the extracts, such as the flavonoids jaceosidin, eupatilin, and luteolin, and to a sesquiterpene dimer. These compounds were recently shown to decrease the production of inflammatory mediators and cytokines (Zeng et al., 2014; Li et al., 2018).

We previously showed that the *A. argyi* extract inhibited the proliferation of stimulated human T lymphocytes *in vitro*, and a series of related guaianolides and *seco*-guaianolides was found to be responsible for most of the inhibitory effects of the extract (Reinhardt et al., 2019). In the present study, we aimed to further

---

Abbreviations: AP-1, activator protein 1; APC, allophycocyanin; CD, cluster of differentiation; CFSE, carboxyfluorescein succinimidyl ester; CPT, camptothecin; CsA, cyclosporine A; CRAC channel, calcium release activated channel; DAG, diacylglycerine; DMSO, dimethyl sulfoxide; EDTA, ethylenediaminetetraacetic acid; ELISA, enzyme-linked immunosorbent assay; ER, endoplasmic reticulum; FACS, fluorescence-activated cell sorting; FCS, fetal bovine serum; FDA, Food and Drug Administration; FITC, Fluorescein isothiocyanate; GFP, green fluorescent protein; HPLC, High-performance liquid chromatography; IFN-, interferon-; IκB, nuclear factor of kappa light polypeptide gene enhancer in B-cells inhibitor; IL-, interleukin; IC_{50}, half maximal inhibitory concentration; IP3, inositol 1,4,5-trisphosphate; mAb, monoclonal antibody; MAPK, mitogen-activated protein kinase; NCEs, new chemical entities; NFAT, Nuclear factor of activated T-cells; NF-κB, nuclear factor kappa-light-chain-enhancer of activated B cells; p, p-value; Par, parthenolide; PIP_2, phosphatidylinositol 4,5-bisphosphate; PBMC, peripheral blood mononuclear cell; PBS, phosphate buffered saline; PE, phycoerythrin; PI, propidium iodide; PMA, phorbol-12-myristat-13-acetate; RPMI, Roswell Park Memorial Institute medium; SD, standard deviation; SOCE, store-operated calcium entry; TNF-α, tumor necrosis factor alpha; TCM, traditional Chinese medicine; TCR, T cell receptor.

substantiate the rationale for the use of *A. argyi* as an anti-inflammatory herbal drug. We here address the effects of *A. argyi* extract and selected compounds on the activation and function of T cells *in vitro*, as well as the effects of these compounds on relevant signaling pathways.

MATERIALS AND METHODS

Ethics Approval Statement

Written informed consent was obtained from patients prior to blood donation for research purposes. All experiments conducted on human material were approved by the Ethics Committee of the University of Freiburg (55/14; 11.02.2014). All performed methods are compliant with the regulations of the Ethics Committee of the University of Freiburg.

Preparation and Cultivation of Human Peripheral Lymphocytes

Preparation and cultivation of human peripheral lymphocytes were performed as indicated (Zimmermann-Klemd et al., 2019). Briefly, peripheral blood mononuclear cells (PBMCs) were isolated from the blood of healthy adult donors, which was obtained from a blood transfusion center (University Medical Center, Freiburg, Germany). Venous blood was centrifuged on a LymphoPrep™ gradient (1.077 g/cm^3, 20 min, 500 × g, 20°C; Progen, Heidelberg, Germany). After centrifugation cells were washed twice with phosphate buffered saline (PBS) and subsequently cultured in Roswell Park Memorial Institute medium (RPMI) 1640 medium supplemented with 10% heat-inactivated fetal calf serum, 2 mM L-glutamine, 100 U/ml penicillin, and 100 U/ml streptomycin (all from Life Technologies, Paisley, UK). Cells were cultured at 37°C in a humidified incubator with a 5% CO_2/95% air atmosphere.

Activation and Treatment of Lymphocytes

Lymphocytes were activated with anti-CD3 (clone OKT3) and anti-CD28 (clone 28.2) mAbs (each 100 ng/ml; both from eBioscience, Frankfurt, Germany) in the presence of medium; cyclosporine A (CsA; 4.16 µM; Sandimmun 50 mg/ml, Novartis Pharma, Basel, Switzerland); camptothecin (CPT; 300 µM: Tocris, Bristol, UK); 0.5% Triton-X 100; plant extract; or isolated compounds from *A. argyi*, as described previously (Zimmermann-Klemd et al., 2019). After cultivation, the cells were used in biological tests.

Determination of Apoptosis and Necrosis of T Cells

Determination of apoptosis and necrosis of T cells was performed as described previously (Zimmermann-Klemd et al., 2019). Cells were treated for 48 h. Cultured cells were washed with PBS and stained with Annexin V-FITC using the apoptosis detection kit (eBioscience, Frankfurt, Germany) according to instructions of the manufacturer. Propidium iodide (PI; eBioscience, Frankfurt, Germany) was added, and cells were stained for 15 min at room temperature in the dark. The proportion of apoptotic/necrotic lymphocytes was determined by flow cytometric analysis (FACSCalibur instrument; BD Biosciences, Franklin Lakes, NJ).

Determination of T Cell Proliferation

The proliferation of T lymphocytes was determined using carboxyfluorescein diacetate succinimidyl ester (CFSE) staining, as described previously (Parish et al., 2009; Gründemann et al., 2012). Lymphocytes were isolated, washed twice in cold PBS, and resuspended in PBS at a concentration of 5 × 10^6 cells/ml. Cells were stained for 10 min at 37°C with CFSE (5 µM; Sigma-Aldrich, St. Louis, MO). The staining reaction was stopped by washing twice with a complete medium. Stained cells were treated for 72 h. The progress of cell division was determined by flow cytometric analysis (FACSCalibur instrument; BD Biosciences, Franklin Lakes, NJ).

Analysis of Activation Marker of T Cells

The activation state of T lymphocytes was determined *via* cell-surface analysis of CD25 and CD69, as previously reported (Gründemann et al., 2014). Briefly, cells were treated for 24 h. Then, cells were washed with PBS and stained with PE-labeled, anti-CD25 mAbs; FITC-labeled, anti-CD69; and, for the differentiation of CD4$^+$ and CD4$^-$ T cells, with APC-labeled, anti-CD4 mAbs (all from eBioscience, Frankfurt, Germany) for 20 min at 4°C. Afterward, cells were washed twice with PBS, resuspended, and transferred into FACS vials. The expression of CD25 and CD69 was measured for CD4$^+$ and CD4$^-$ T cells, respectively, by flow cytometric analysis (FACSCalibur instrument; BD Biosciences, Franklin Lakes, NJ).

Determination of Cytokine Secretion

After 20 h of treatment, cells were restimulated with PMA (50 ng/ml; Sigma-Aldrich, Taufkirchen, Deutschland) and ionomycin (500 ng/ml; Sigma-Aldrich, Taufkirchen, Deutschland) for 4 h. Supernatants were stored at –20°C. The amount of cytokines was quantified using ELISA technique according to manufacturer's instructions (Affymetrix, Frankfurt, Germany).

Determination of Cytokine-Producing Cells

Cells were treated for 20 h, as described in section 2.3, and restimulated with PMA (50 ng/ml; Sigma-Aldrich, Taufkirchen, Deutschland) and ionomycin (500 ng/ml; Sigma-Aldrich, Taufkirchen, Germany) for an additional 4 h at 37°C. During this time, they were additionally treated with GolgiPlug (0.5 µl; BD Biosciences, Heidelberg, Germany). After incubation, cells of each sample were divided into three approaches: one for the determination of IL-2, one for the determination of TNFα, one for the determination of IFN-γ. The cells were fixed with 100 µl of 4% PFA (Morphisto, Frankfurt, Germany) for 10 min at room temperature and washed with PBS. Afterward, permeabilization was performed using 100 µl of 1× BD Perm/Wash Puffer (BD Biosciences, Heidelberg, Germany) per sample for 15 min at 4°C. Finally, cells were stained with 1 µl anti-IL-2 or anti-IFN-γ (both Affymetrix, Frankfurt, Germany) for 30 min at 4°C. After two washing steps samples were analyzed by flow cytometric analysis (FACS LSR Fortessa Instrument; BD Biosciences, Franklin Lakes, NJ).

Analysis of T Cell Degranulation

A CD107a surface staining was performed, as described previously (Gründemann et al., 2013), to determine the T cell degranulation capacity. Cells were treated for 20 h and then restimulated for 4 h with PMA (50 ng/ml; Sigma-Aldrich, Taufkirchen, Deutschland) and ionomycin (500 ng/ml; Sigma-Aldrich, Taufkirchen, Deutschland). To each well containing 200 µl of cell suspension, 2.5 µl (~0.25 µg) of PE-conjugated, anti-CD107a mAbs (eBioscience, Frankfurt, Germany) was added. After incubation at 37°C for 1 h, 2 µl of 1/10 diluted GolgiStop (Becton Dickinson, Franklin Lakes, NJ) was added per well, and the cells were incubated for another 3 h. Samples were analyzed by flow cytometric analysis (FACSCalibur instrument; BD Biosciences, Franklin Lakes, NJ).

Reporter Cell Experiments for the Determination of NFAT-, NF-κB-, and AP-1 Activity

A 96 well F-bottom cell culture plate was coated with anti-human CD3 mAb (clone OKT3, 1 µg/ml, 50 µl/well) or PBS (unstim. control) at 4°C over-night. Reporter cells (Jutz et al., 2016) were harvested, washed twice with PBS, and seeded in a 5% FCS RPMI cell culture medium (0.15×10^6 cells in 200 µl/well). Cells were treated with inhibitors (1 nM SP100030 for AP-1, 5 µg/ml cyclosporine A for NFAT, and 20 µM parthenolide for NF-κB), plant extract or isolated compounds from *A. argyi* or remained untreated (unstim. control, stim. control). Cells were incubated at 37°C for 8 h (AP-1) or 24 h (NFAT and NF-κB). Cells were washed twice with PBS and the expression of eGFP was determined by flow cytometric analysis (FACSCalibur instrument; BD Biosciences, Franklin Lakes, NJ).

Determination of Intracellular Calcium

Jurkat cells (0.5×10^6) were stained in 200 µl RPMI medium, containing 1% FCS, 2.6 µM Fluo3 AM (Life Technologies, Carlsbad, California), 5.5 µM FuraRed AM (Invitrogen, Carlsbad, California), and 0.1% (w/v) Pluronic F-127 (Invitrogen, Carlsbad, California) in the presence of test substances (30 µg/ml *A. argyi* extract or 10 µg/ml compound/compound mix; merely for the determination of the calcium ER store depletion) for 45 min at 37°C. For differentiation of calcium ER store depletion and SOCE, the staining solution was further supplemented with 0.6 mM ethylenediaminetetraacetic acid (EDTA). Cell suspensions were gently mixed every 10 min. After staining cells were resuspended in 100 µl of 1% FCS RPMI medium containing the test substance (30 µg/ml *A. argyi* extract or 10 µg/ml compound/compound mix; merely for the determination of the calcium ER store depletion). For the measurement of calcium influx, 50 µl of cell suspension were prewarmed (37°C, 5 min) in 700 µl of 1% FCS RPMI medium supplemented with 0.6 mM EDTA (for differentiation of ER store depletion and SOCE) and the test substance (30 µg/ml *A. argyi* extract or 10 µg/ml compound/compound mix; merely for the determination of the calcium ER store depletion). Baseline calcium levels were determined by flow cytometric measurement (FACS CyAn ADP; Beckman Coulter, Brea, California) for 1 min. Afterward, calcium influx was induced *via* stimulation with anti-CD3 mAbs (clone OKT3, 1 µg/ml). After 2 min, the test substance (30 µg/ml *A. argyi* extract or 10 µg/ml compound/compound mix) was added, followed, 30 s later, by the addition of calcium dichloride (1 mM). Calcium influx was measured for 5 min.

Analysis of Data

For statistical analysis, data were processed with Microsoft Excel and SPSS software (Version 22.0, IBM, Armonk, USA). Statistical significance was determined with the SPSS software by a one-way ANOVA followed by Dunnett's *post hoc* pairwise comparisons. Values are presented as mean ± standard deviation (SD) for the indicated number of independent experiments. The asterisks represent significant differences from controls (*$p < .05$).

Tested Compounds

The compounds used in this work were isolated from *A. argyi* ethyl acetate extract in a previous study (Reinhardt et al., 2019).

RESULTS

Anti-Proliferative Effects of the *A. argyi* Extract on T Lymphocytes

Previously, we evaluated the effect of 435 plant extracts from a focused extract library of TCM plants on the proliferative capacity of primary expanded human T lymphocytes *in vitro*. The ethyl acetate extract of *A. argyi* inhibited the proliferation of human T lymphocytes in a concentration-dependent manner, with a half maximal inhibitory concentration (IC_{50}) of 16.2 µg/ml (Reinhardt et al., 2019) (**Figure 1A**). The focused library also comprised extracts from other plants of the Asteraceae family (**Supplement 2**), but none of these exhibited notable activity in the assay.

To verify that the observed immunosuppressive activity was not due to cytotoxicity of the extract, flow cytometry analysis was performed to analyze the apoptosis and necrosis events of the cells. Using Annexin V/PI double staining, we found that the *A. argyi* extract had no toxic effects in the concentration range that was used for the mechanistic studies (**Figures 1B, C**).

Effects of the *A. argyi* Extract on T Lymphocyte Function

Next, the effect of the *A. argyi* extract on the effector function of human T cells was examined. Stimulation of T lymphocytes *via* the T cell receptor (TCR) leads to the expression of the activation markers CD25 and CD69. We found that after TCR stimulation the treatment of T cells with the *A. argyi* extract significantly and concentration-dependently lowered CD25 and CD69 expressions (**Figures 2A, B**). This was the case in both the $CD4^+$ and $CD4^-$ T cells. In addition, we observed a significantly reduced CD25 expression of $CD4^-$ T cells after treatments with low concentrations (3 and 10 µg/ml) of the *A. argyi* extract (**Figure 2A**).

Upon activation, T cells secrete IL-2, which is important for proliferation, and interferon-γ (IFN-γ), which defines T cell function. The *A. argyi* extract significantly suppressed IL-2 as well as the IFN-γ secretion capacity of activated T lymphocytes (**Figures 2C, D**).

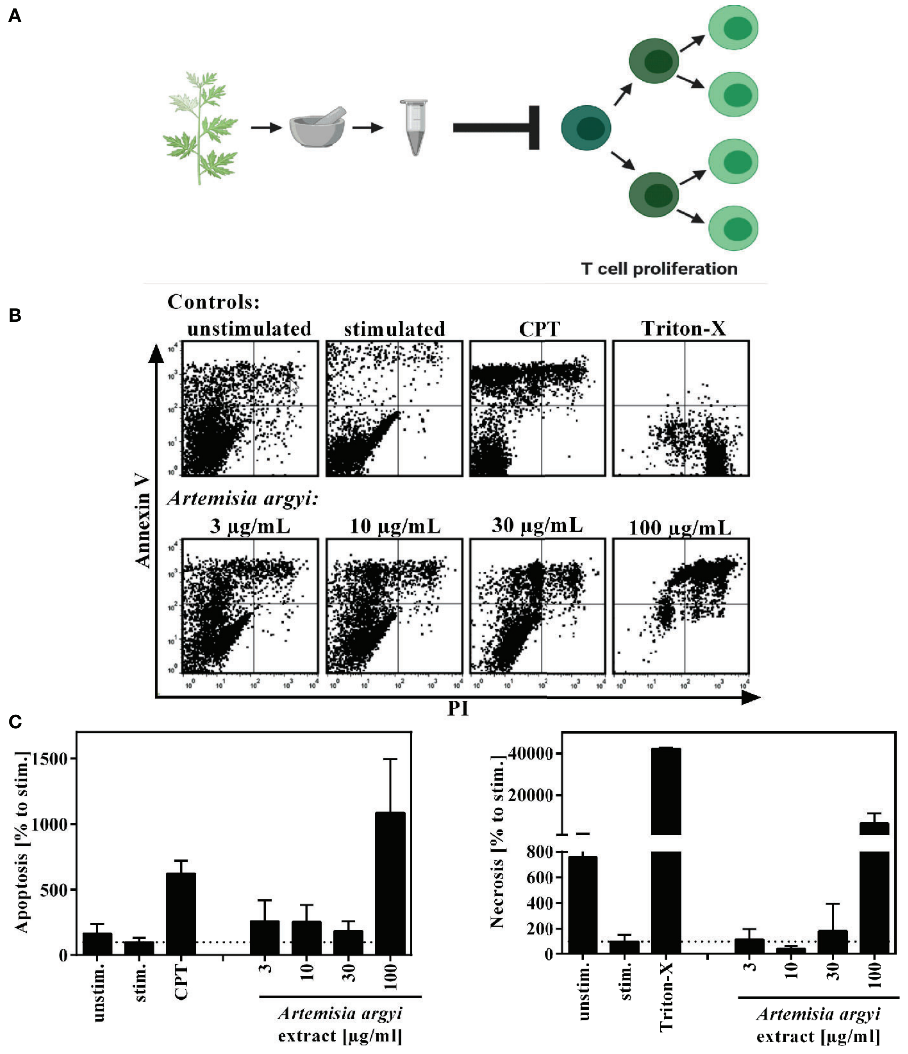

FIGURE 1 | Overview of recently published results **(A)** and effect of the *A. argyi* extract on the viability of T lymphocytes **(B, C)**. Expanded human lymphocytes (2 × 10^5) were left unstimulated (unstim.) or were stimulated (stim.) with anti-CD3 and anti-CD28 mAbs (100 ng each) and incubated for 48 h with medium (unstim., stim.), camptothecin (CPT; 300 µM), Triton-X 100 (0.5%) or the *A. argyi* extract. Annexin V-FITC and PI double stainings were performed after incubation. The proportions of viable, necrotic, and apoptotic cells were determined by flow cytometry. Data are depicted as dot plots **(B)**, and the proportion of apoptotic/necrotic lymphocytes in relation to the stimulated control was determined from two independent experiments. Data are depicted as mean ± SD **(C)**.

Influence of the *A. argyi* Extract on the Transcription Factors AP-1, NFAT, and NF-κB

To understand how the activation and proliferation of human T cells is inhibited by the *A. argyi* extract, we analyzed the effect of the *A. argyi* extract on the transcription factors AP-1, NFAT, and NF-κB. All three transcription factors regulate the transcription of the *il-2* gene, which is a key regulator in these processes. Jurkat T cell reporter lines (Ratzinger et al., 2014; Jutz et al., 2016), in which eGFP is fused to the response elements of these transcription factors, were used for this purpose. After stimulation with anti-CD3 mAbs, activity of the transcription factors was quantified *via* flow cytometry. The treatment with the *A. argyi* extract did not change the anti-CD3-induced AP-1 activity in comparison to untreated activated AP-1 reporter cells (**Figure 3A**). In contrast, NFAT and NF-κB activity was reduced in a concentration-dependent manner by the *A. argyi* extract (**Figures 3B, C**). In summary, the reporter cell experiments pointed to a specific suppression of NFAT and NF-κB activities, but not to suppression of AP-1.

Effects of the *A. argyi* Extract on TCR-Induced Calcium Signaling

The previous experiments demonstrated that the *A. argyi* extract lowered activity of NFAT, which was induced by TCR triggering. Influx of calcium ions into the cytosol is upstream regulated of NFAT activation (Robert et al., 2011). Hence, we performed

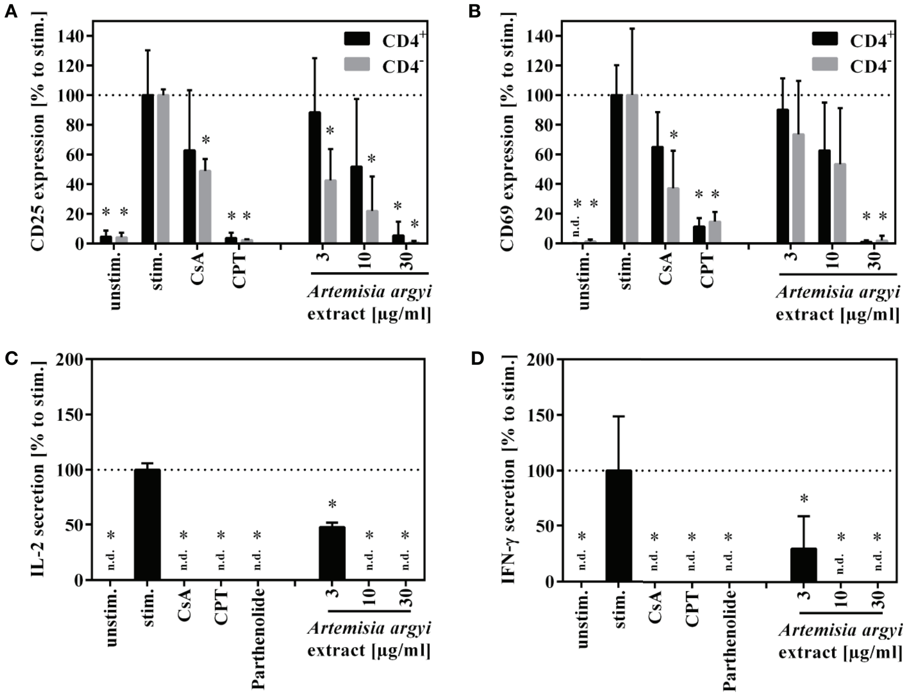

FIGURE 2 | Effects of *A. argyi* extract on the function of T lymphocytes. For **(A, B)**, lymphocytes (2×10^5) were left unstimulated (unstim.) or were activated with anti-CD3 and anti-CD28 mAbs (100 ng each and incubated for 24 h with medium (unstim., stim.), cyclosporine A (CsA; 4.16 µM), camptothecin (CPT; 300 µM), or the *A. argyi* extract. Cells were stained with anti-CD69-FITC and anti-CD4-APC **(A)** or anti-CD25-PE and anti-CD4-APC **(B)**. Expression of surface markers (CD69, CD25, CD4) was analyzed by flow cytometry, and the amounts of activated $CD4^+$ and $CD4^-$ T lymphocytes were determined. For **(C, D)** expanded lymphocytes (2×10^5) were incubated for 20 h with medium (unstim., stim.), cyclosporine A (CsA; 4.16 µM), camptothecin (CPT; 300 µM), parthenolide (20 µM) or the *A. argyi* extract. Subsequently, the cells were stimulated with PMA/Ionomycin for 4 h at 37°C. IL-2 **(C)** and IFN-γ **(D)** were quantified in the supernatants by ELISA. The results of three different experiments are summarized and are depicted as mean ± SD in relation to the untreated, stimulated control. *$p < 0.05$. n.d.= below detection limit.

calcium flux experiments to determine whether the calcium influx to the cytosol was impaired. Inhibition of calcium influx would prevent the translocation of NFAT to the nucleus and, consequently suppress NFAT activity.

Jurkat cells were stained with the calcium indicators Fluo3 and FuraRed and treated with the *A. argyi* extract. Subsequently, calcium influx was induced by TCR stimulation using an anti-CD3 mAbs. The experiments demonstrated that the treatment of the cells with the *A. argyi* extract led to a complete suppression of the calcium influx (**Figures 4A, B**).

Next, we sought to characterize the inhibition of the calcium influx. Jurkat cells were treated with the *A. argyi* extract or the calcium ion chelator EDTA to determine whether the inhibition was mediated *via* chelation of calcium. As expected, a strong calcium influx was measured for untreated cells (control) after TCR stimulation (**Figure 4C**). This influx was prevented in EDTA-treated cells but restored by the addition of calcium dichloride to the medium (**Figure 4C**). In contrast, in cells treated with the *A. argyi* extract, the calcium influx capability could not be restored with the addition of increasing concentrations of calcium dichloride (**Figure 4C**). This suggested that the *A. argyi* extract did not inhibit the calcium influx through calcium chelating properties.

Upon TCR activation by antigen binding, the opening of a calcium channel in the membrane of the ER initiates calcium release from ER stores (ER store depletion). The depletion of these intracellular calcium stores causes the formation of calcium release-activated channels (CRAC) channels, which in turn leads to a strong influx of calcium from the extracellular space to the cytosol (store-operated calcium entry, SOCE) and allows replenishment of the calcium stores in the ER (Robert et al., 2011). To discriminate between these two options, we stained Jurkat cells with Fluo3 and FuraRed in a medium supplemented with EDTA. During the staining process, the cells were treated with the *A. argyi* extract in a calcium-free setting to ensure a calcium-free, extracellular compartment. Cells were stimulated *via* TCR to induce the calcium influx. Given that the SOCE was prevented, calcium store depletion could be measured. In comparison to the untreated cells (control), treatment with the extract lowered calcium ER store depletion (**Figure 4D**). To determine whether the SOCE was also inhibited by the *A. argyi* extract, or just prevented due to the lacking depletion of ER calcium store, we stained Jurkat cells with Fluo3 and FuraRed in a medium supplemented with EDTA, and induced the calcium ER store depletion by TCR stimulation. Next, the extract and calcium dichloride were added and the SOCE was measured.

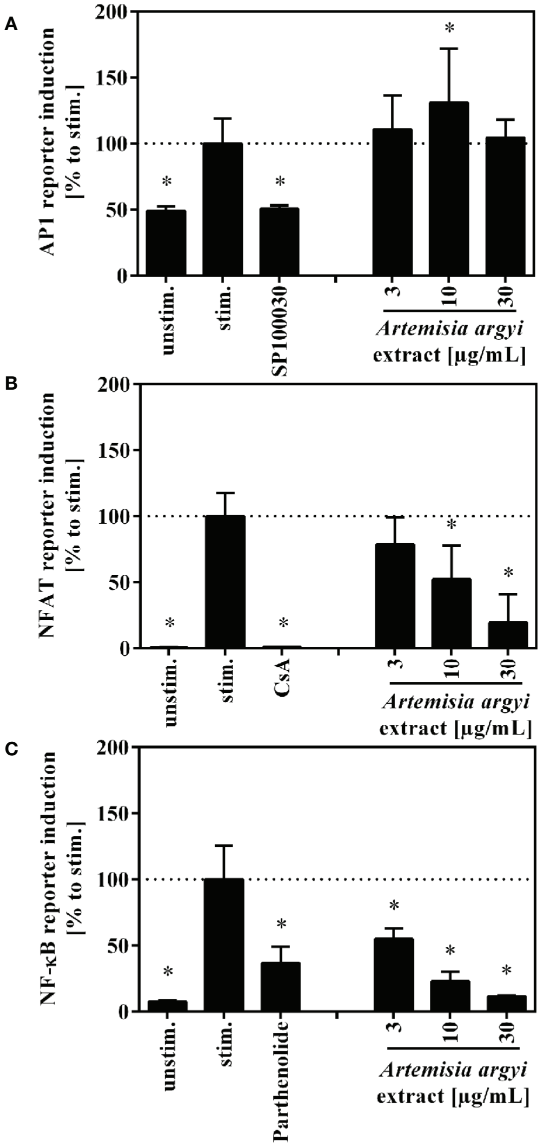

FIGURE 3 | Effect of the *A. argyi* extract on the activity of transcription factors AP-1 **(A)**, NFAT **(B)** and NFκB **(C)** in Jurkat T cells. Jurkat reporter cells (0.15 × 10^6) were seeded on a cell culture plate, coated with anti-CD3 mAbs, and incubated with medium, inhibitors (AP-1: 1 nM SP100030, NFAT: 4.16 µM CsA, NF-κB: 20 µM parthenolide) or the *A. argyi* extract in different concentrations for 8 (AP-1) or 24 h (NFAT and NF-κB). The GFP expression was measured by flow cytometry after incubation. The results of three independent experiments are summarized and depicted as mean ± SD. $^*p < 0.05$.

The medium of control cells was supplemented with calcium dichloride directly after depletion of the intracellular calcium stores. The results showed that the *A. argyi* extract also lowered the SOCE from the extracellular space (**Figure 4D**).

In summary, the strong reduction of calcium influx upon TCR stimulation after treatment with the *A. argyi* extract resulted from suppression of the ER calcium store depletion and a reduction of the SOCE.

Effects of Isolated *A. argyi* Compounds on the Activation and Function of T Lymphocytes

We previously isolated a series of sesquiterpene lactones and flavones from the active extract (**Figure 7A**), some of which showed significant inhibitory effects on T lymphocyte proliferation (Reinhardt et al., 2019) (**Figure 1A**). Several of the most-active compounds were tested: two stereoisomeric guaianolides, artecanin and canin (**1** and **5**), artanomaloide (**2**), arteglasin A (**3**) differing from **1** and **2** in the decoration of the 7-membered ring, the moderately active flavone jaceosidin (**4**), and two stereoisomeric *seco*-guaianolides, *seco*-tanapartholides B and A (**6** and **7**) (**Figure 5**).

To better understand their contribution to the activity of the extract, their influence on activation, cytokine production, and degranulation capacity of human T lymphocytes was investigated.

The compounds **1**, **2**, **3**, **5,** and the compound mix significantly reduced the expression of CD25 in $CD4^-$ and $CD4^+$ T cells at 10 and/or 3 µg/ml. Compound **6** suppressed the CD25 expression in $CD4^+$ T cells at all tested concentration levels, while compound **7** suppressed it at 10 and 3 µg/ml. Compounds **6** and **7** had no significant effect on $CD4^-$ T cells. The isolated flavone **4** showed no effect on CD25 expression (**Figure 6A**).

All isolated compounds, with the exception of compound **4**, significantly and strongly suppressed IL-2-producing cells at 10 µg/ml. While the effect was only miniscule for the flavone (**4**), compounds **1**, **3**, **5**-**7**, and the mix also showed significant inhibition at 3 µg/ml. A similar pattern was observed for the suppression of tumor necrosis factor α-(TNFα) and IFN-γ-producing cells. The strongest suppression of IL-2- and IFN-γ-producing cells was observed from compound **6** (**Figure 6B**).

Upon release of perforin and granzymes, T lymphocytes express the lysosomal-associated membrane protein 1 (LAMP-1, CD107a) on their surface. Analysis of the LAMP-1 surface expression, showed concentration-dependent effects for the mixture of all compounds and the *A. argyi* extract (**Figure 6C**).

Effects of Isolated *A. argyi* Compounds on the Transcription Factors NFAT and NF-κB

Jurkat-based NFAT and NF-κB reporter experiments were performed to shed light on the interaction of compounds by manipulation the T lymphocyte signaling. For the sesquiterpene lactones, but not for the flavone (**4**), a concentration-dependent, suppressive effect on the NFAT pathway was found, with IC_{50} values < 10 µM (< 3 µg/ml) (**Figures 7C, D**). Likewise, NF-κB activity was significantly decreased by all compounds except compound **4** (**Figures 7B, D**). We here focused on the effects of the *A. argyi* extract and isolated compounds on the NFAT signaling pathway.

Thus we tested whether the isolated compounds were able to inhibit TCR-induced calcium signaling. To this end, we looked at both the ER calcium store depletion (**Supplement 1**, left panel) and the SOCE (**Supplement 1**, right panel), using the methodology, described above. Single compounds and a mixture of all isolated compounds were tested with the assumption that the mixture would, at least in part, mimic the activity of the whole extract.

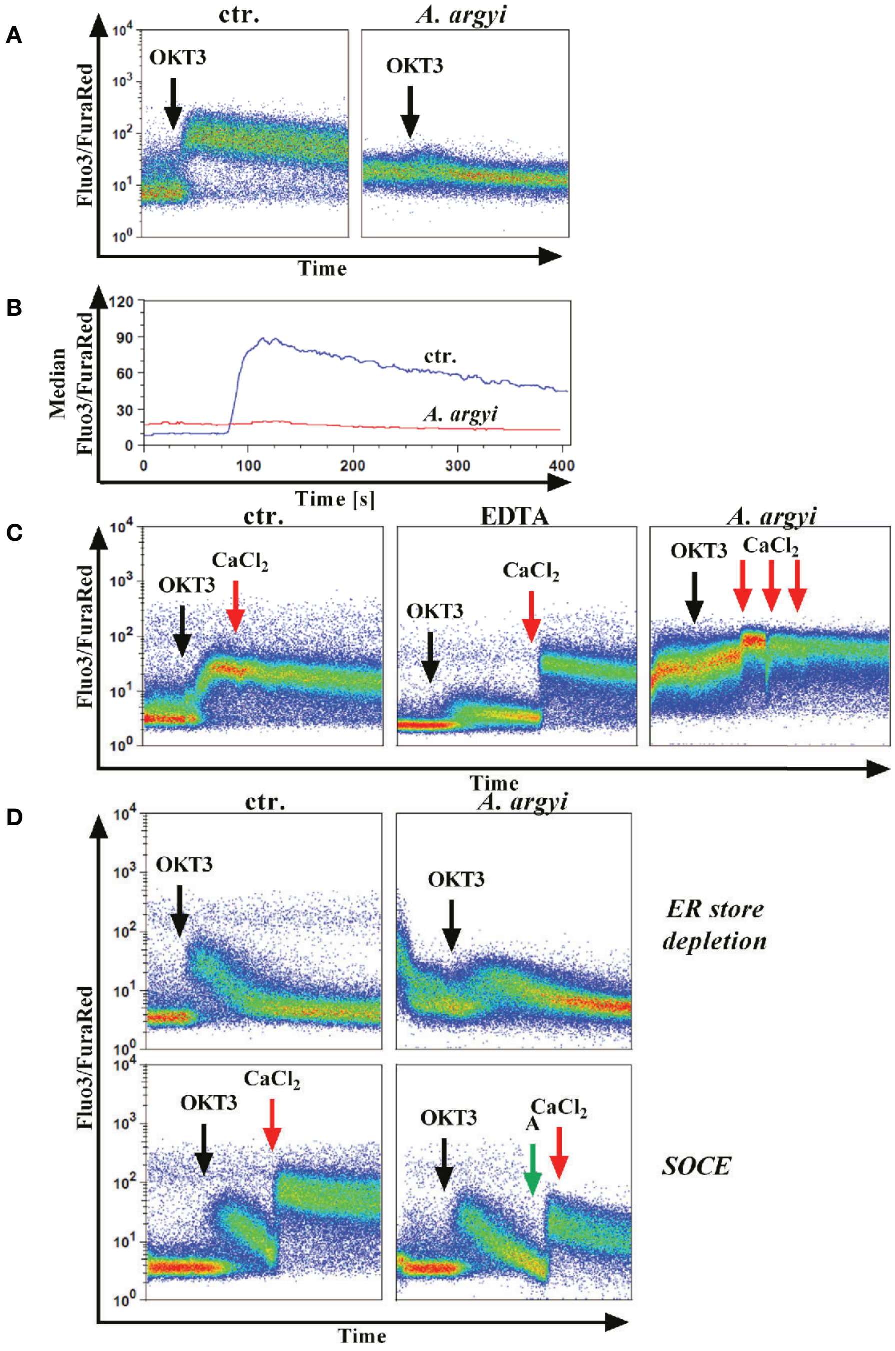

FIGURE 4 | Effect of the *A. argyi* extract on the calcium influx in Jurkat T cells. Jurkat cells (0.5 × 10^6) were stained with Fluo3 and FuraRed for 45 min at 37°C in the presence of medium, 0.6 mM EDTA or 30 µg/ml *A. argyi* extract. The results show the anti-CD3-induced (black arrows) calcium influx as the Fluo3/FuraRed ratio **(A)** and the median of this ratio **(B)** for untreated cells (ctr.) and cells treated with 30 µg/ml *A. argyi* extract. Calcium influx was induced by anti-CD3 stimulation (black arrows) of the TCR **(C)**, and, after 1 min 1 mM calcium dichloride was added (red arrows). The calcium influx (ratio Fluo3/FuraRed) of untreated cells (ctr.), cells treated with 0.6 mM EDTA, and cells treated with 30 µg/ml *A. argyi* extract are shown. The ER store depletion in presence of the *A. argyi* extract was analyzed **(D)**. Jurkat cells (0.5 × 10^6) were stained with Fluo3 and FuraRed in a calcium-free medium for 45 min at 37°C. To determine the ER calcium store depletion, 30 µg/ml *A. argyi* extract was present in the medium during staining and measurement, and the ER store depletion was triggered by TCR stimulation (black arrows). The control cells remained untreated. For determination of the SOCE, cells were stained, and the ER calcium store depletion was induced by TCR stimulation (black arrows). After 2 min 30 µg/ml *A. argyi* extract (green arrows) were added and, after another 30 s, 1 mM calcium dichloride (red arrows) was added. For the control (ctr.), 1 mM calcium dichloride was added directly after depletion of the ER calcium store. The results show the calcium influx (the ratio Fluo3/FuraRed) of the untreated cells (ctr.) and the cells treated with 30 µg/ml *A. argyi* extract.

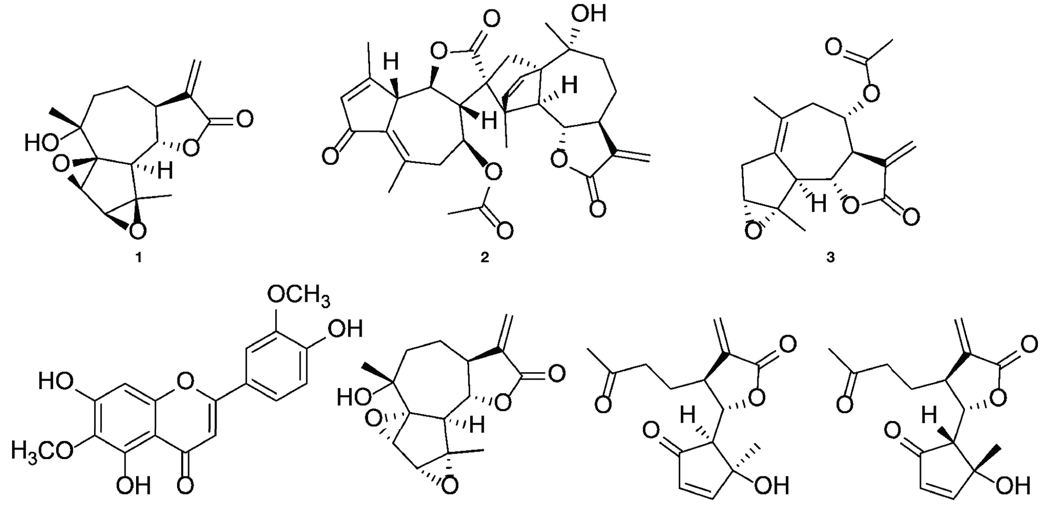

FIGURE 5 | Chemical structures of (1*S*)-artecanin **(1)**, 8-acetyl-artanomaloide **(2)**, arteglasin A **(3)**, jaceosidin **(4)**, (1*R*)-canin **(5)**, (4*S*, 5*S*, 6*S*, 7*S*)- and (4*R*, 5*R*, 6*S*, 7*S*) -*seco*-tanapartholide **(6** and **7)**.

The *A. argyi* extract was used as a control. A slight inhibition of calcium influx from the ER combined with a significant time delay was observed for compound **5**. A similar delay was observed for the compound mix and, to a lesser extent, for compounds **1**, **6**, and **7**. Compounds **2** and **3** increased the intensity of the calcium influx. However, neither the single compounds nor the compound mix inhibited the calcium influx as effectively as did the *A. argyi* extract (**Supplement 1**).

DISCUSSION

We recently found that an ethyl acetate extract of *A. argyi* suppressed the *in vitro* proliferation of human primary T lymphocytes in a concentration-dependent, non-cytotoxic manner (**Figure 1**) and we also isolated a series of compounds that were responsible for this activity (Reinhardt et al., 2019).

Stimulation of TCR promotes the surface expression of the transmembrane C-type lectin CD69 and the alpha-chain of the IL-2 receptor (CD25) on T cells (Malek, 2008). The *A. argyi* extract lowered the expression of both activation markers (**Figures 2A, B**) and of IL-2 production (**Figure 2C**) in stimulated T lymphocytes. As IL-2 is pivotal for lymphocyte proliferation, inhibition of IL-2 production could explain the observed inhibition of T cell proliferation. Further, the IFN-γ secretion was reduced after treatment with the *A. argyi* extract (**Figure 2D**). Our findings provide evidence for IL-2-mediated, anti-inflammatory properties of the extract, likely *via* IL-2-mediated T lymphocyte proliferation inhibition, and thereby corroborate the traditional use of *A. argyi* as an anti-inflammatory herbal drug (Yun et al., 2016).

The IL-2-dependent suppression of T lymphocyte proliferation by the *A. argyi* extract is linked to suppression of the transcription factors NFAT and NF-κB (**Figures 3B, C**), while AP-1 activity was not affected (**Figure 3A**). ER calcium store depletion and the SOCE were inhibited *via* a non-sequestrant mechanism (**Figures 4A–D**). Our observation that it is impossible to restore the calcium influx by generating an overage of calcium dichloride in the outer cell compartment points to an irreversible blockage of the calcium channels. Otherwise, binding and dissociation homeostasis would trigger a stronger calcium influx without binding of the active constituent(s) of the *A. argyi* extract to the calcium channels. The effect of the extract was comparable to that of the calcium chelator EDTA. Inhibition of the ER calcium store depletion and SOCE explain the observed reduced NFAT activity.

To correlate the effects found for the *A. argyi* extract to the compounds from the extract, selected T cell proliferation-inhibiting compounds were investigated analogously. Jaceosidin (**4**) showed no effect on either NFAT or NF-κB reporter cells, which is in accord with its weak inhibition of all three pro-inflammatory cytokines tested. A comparable inhibition of TNFα expression by jaceosidin (**4**) has been reported (Li et al., 2018). Thus, it is unlikely for jaceosidin to contribute significantly to the observed activity of the extract. All tested sesquiterpene lactones were shown to inhibit NFAT and NF-κB binding to the DNA. The inhibition of DNA binding of NF-κB can presumably be compared to the effects published for other sesquiterpene lactones, such as helenalin (a guaianolide) and parthenolide (a germacranolide) (García-Piñeres et al., 2001; García-Piñeres et al., 2004). Parthenolide inhibits the IκB kinase complex β (IKKβ) by alkylating a cysteine residue in its activation loop (Kwok et al., 2001). Less is known about the effect of sesquiterpene lactones on the NFAT pathway, which was the focus of this work. Only helenalin was previously shown to suppress abundance and nuclear translocation of NFATc2 (Berges et al., 2009). The stereoisomeric guaianolides artecanin (**1**) and canin (**5**), as well as the guaianolide dimer **2** and arteglasin A (**3**) showed very similar effects to the *A. argyi* extract in general. However, in the ER

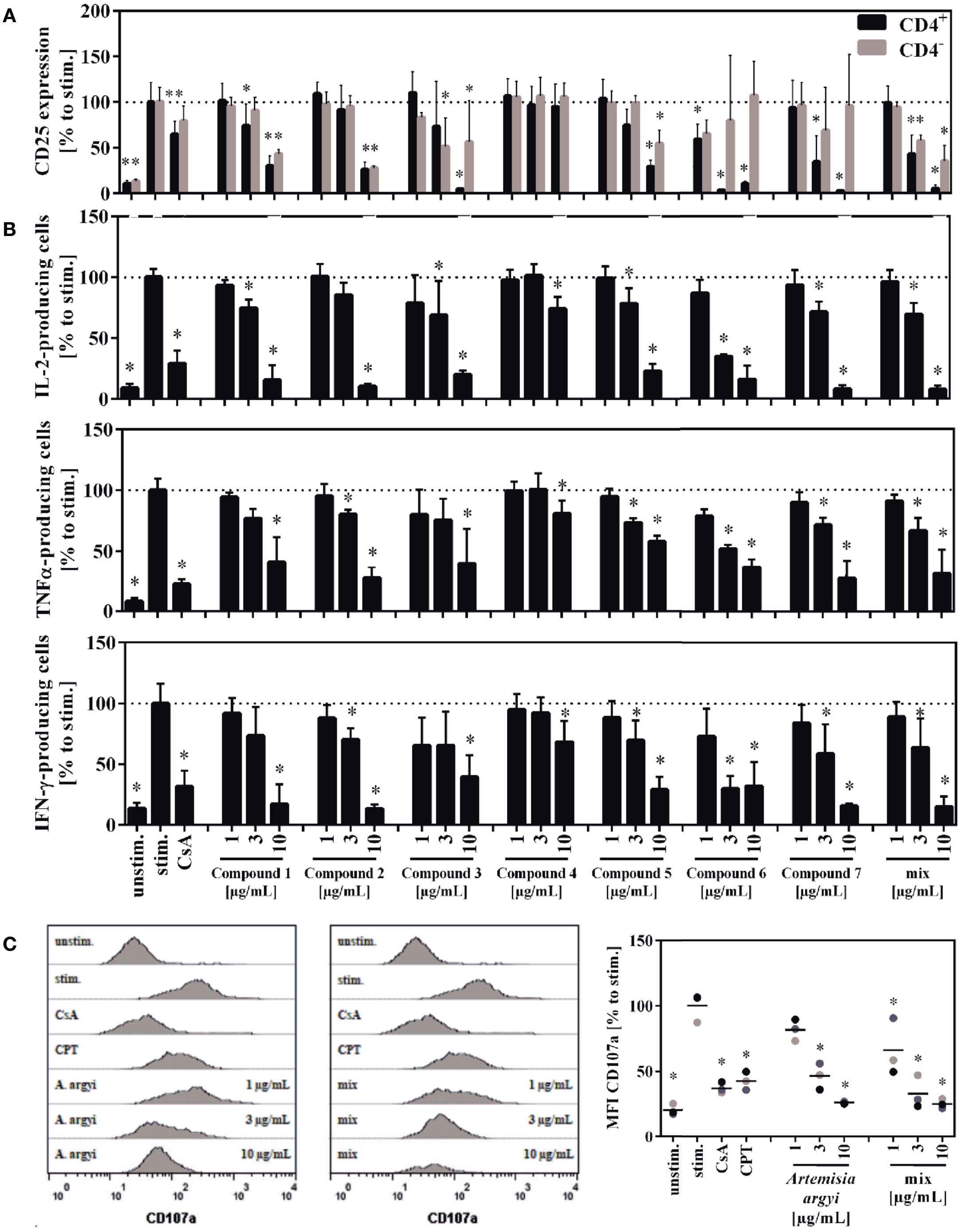

FIGURE 6 | Effect of the isolated compounds and the compound mix on activation **(A)** IL-2-, TNFα-, and IFN-γ-producing T cells **(B)** and the degranulation capacity of T cells **(C)**. For **(A),** lymphocytes (2 × 10^6) were stimulated with anti-CD3 and anti-CD28 mAbs (100 ng each) and incubated for 48 h with medium (unstim., stim.), cyclosporine A (CsA; 4.16 µM), the compounds, the compounds mixture, or the *A. argyi* extract **(B)**. Cells were re-stimulated with PMA (500 µg/ml) and ionomycin (500 ng/ml) and treated with GolgiPlug for 4 h. The cells were fixed, permeabilized, and stained with anti-IL-2, anti-TNFα or anti-IFN-γ mAbs. The amount of IL-2-, TNFα-, and IFN-γ-secreting cells was determined *via* flow cytometry. Results from four independent experiments were summarized and are depicted as mean ± SD in relation to the untreated, stimulated control. *$p < 0.05$. For **(C)** lymphocytes (2 × 10^5) were stimulated with anti-CD3 and anti-CD28 mAbs (100 ng each). Afterward, cells were incubated for 20 h with medium (unstim., stim.), cyclosporine A (CsA; 4.16 µM), camptothecin (CPT; 300 µM), the compound mixture, or the *A. argyi* extract. Cells (except the unstim. control) were restimulated with PMA (500 µg/ml) and ionomycin (500 ng/ml) for 4 h and stained with anti-CD107a-PE. The amount of degranulating T lymphocytes, as indicated by a CD107a surface expression, was determined *via* flow cytometry. Data are depicted as histogram plots, and data of three independent experiments are summarized as mean ± SD. *$p < 0.05$.

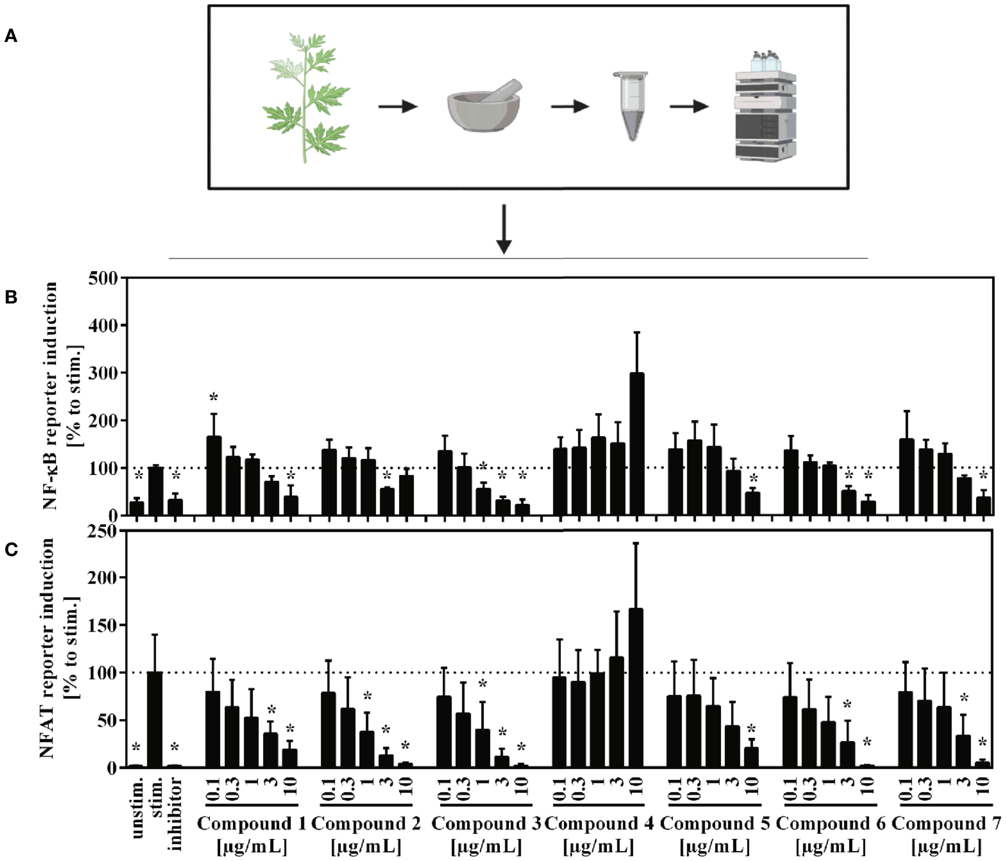

D

Compound	NF-kB IC$_{50}$ [μg/mL]	NF-kB IC$_{50}$ [μM]	NFAT IC$_{50}$ [μg/mL]	NFAT IC$_{50}$ [μM]
1	1.7	6.1	1.3	4.7
2	1.7	3.1	0.9	1.6
3	0.6	2.0	1.1	3.6
4	no inhib.	no inhib.	no inhib.	no inhib.
5	2.6	9.3	2.6	9.3
6	1.8	6.5	1.9	6.8
7	2.2	7.9	2.4	8.6

FIGURE 7 | Overview of the published fractionation process **(A)** and effect of the A. argyi compounds on NF-κB **(B)** and NFAT **(C)** activity and corresponding IC$_{50}$ values **(D)** in Jurkart T cells. Jurkat reporter cells (0.15 × 10^6) were seeded on a culture plate, coated with anti-CD3 mAbs, and incubated with medium, inhibitors (NFAT: 4.16 μM CsA, NF-κB: 20 μM parthenolide) or *A. argyi* compounds in different concentrations for 24 h. The GFP expression was measured by flow cytometry. The results of three independent experiments are summarized and depicted as mean ± SD. *$p < 0.05$ **(B, C)**. The calculated IC$_{50}$ values are presented in μg/ml and in μM, as stated **(D)**.

store depletion and for the SOCE, the activity of the single compounds was not comparable to that of the extract. Only canin (**5**), but not its stereoisomer artecanin (**1**), showed some inhibition of ER store depletion, which did not affect the SOCE. Thus, canin (**5**) might be part of the explanation for the inhibition of the ER store depletion by the *A. argyi* extract. The specific CD25 inhibition by the two *seco*-guaianolides **6** and **7** in CD4$^+$ cells but not inCD4$^-$ cells is unusual and deserves further investigation. However, this inhibition is not reflected in the activity of the *A. argyi* extract. Although most of the observed activity from the *A. argyi* extract can be attributed to the presence of the tested guaianolides and *seco*-guaianolides, none of the isolated compounds showed sufficient inhibition of the ER calcium store depletion or the SOCE (**Supplement 1**). This was also true for a mixture of the compounds, suggesting that other, as yet unidentified compounds in the extract are responsible for this activity.

The initial screening (Reinhardt et al., 2019) included extracts from additional herbal drugs of the family Asteraceae, but none of these inhibited T cell proliferation at the concentrations tested. The lack of activity can be possibly explained, by an absence of sesquiterpene lactones from the extracts (*Carthamus tinctorius*, *Artemisia scoparia,* and *Artemisia apiacaea*). So far, sesquiterpene lactones have only been reported from *Artemisia capillaris* (Feng et al., 2017) and *Centipeda minima* (Eisenbrand and Tang, 2011), and their concentrations in the plants were very low, in the range of 0.001% in *A. capillaris* (Wu et al., 2012; Feng et al., 2017). Furthermore, the strength of T cell proliferation inhibition may also depend on the specific sesquiterpene scaffold, as significant differences were observed between eudesmanes, guaianolides, and *seco*-guaianolides (Reinhardt et al., 2019). All reported sesquiterpene lactones from *C. minima* are structurally related to helenalin, which is a known NF-κB inhibitor (Lyss et al., 1997; Eisenbrand and Tang, 2011).

We ascertained different modes of action for the capacity of the *A. argyi* extract to inhibit the proliferation of T cells. We demonstrated that the *A. argyi* extract, as well as different guaianolides isolated from it, inhibited the activity of NFAT and NF-κB. Moreover, the crude extract suppressed the TCR-induced calcium influx, but neither the isolated single compounds nor a mixture of these sesquiterpene lactones showed similar effects. This suggests that the *A. argyi* extract likely contains compounds affecting signaling on a more upstream target than the compounds isolated thus far. Our findings corroborate the notion of a multitarget effect of herbal extracts possibly resulting in pharmacological synergism (Fürst and Zündorf, 2015; Colalto, 2018). The study also demonstrates that the established cell-based screening platform approach is a powerful tool for identifying and characterizing potential immunosuppressive leads from natural product sources.

DATA AVAILABILITY STATEMENT

The datasets generated for this study are available on request to the corresponding author.

ETHICS STATEMENT

The studies involving human participants were reviewed and approved by Ethics Committee of the University of Freiburg, Engelberger Straße 21, 79106 Freiburg. The patients/participants provided their written informed consent to participate in this study.

AUTHOR CONTRIBUTIONS

AZ-K performed the experiments, analyzed the data, prepared the figures, and wrote the draft manuscript. JR prepared **Figure 5** and wrote the draft manuscript regarding results and discussion on "Effects of isolated compounds" and the discussion of other tested Asteraceae. JR, AM, WS, PS, JL, RH, MH, and CG contributed to the design, implementation of the research, and in finalizing the manuscript.

FUNDING

Gefördert durch die Deutsche Forschungsgemeinschaft (DFG) im Rahmen der Exzellenzstrategie des Bundes und der Länder – EXC – 2189 – Projektnummer 390939984. (Funded by the Deutsche Forschungsgemeinschaft (DFG, German Research Foundation) under Germany's Excellence strategy – EXC – 2189 – Project ID: 390939984.) Furthermore, this work was financially supported by the Software AG Foundation, DAMUS-DONATA e.V. and PRIAM-based foundation.

ACKNOWLEDGMENTS

We appreciate the excellent technical assistance of Kerstin Fehrenbach, Orlando Fertig and Moritz Winker, Seema Devi and Carmen Steinborn.

SUPPLEMENTARY MATERIAL

The Supplementary Material for this article can be found online at: https://www.frontiersin.org/articles/10.3389/fphar.2020.00402/full#supplementary-material

REFERENCES

Allison, A. C. (2000). Immunosuppressive drugs: the first 50 years and a glance forward. *Immunopharmacology* 47, 63–83. doi: 10.1016/S0162-3109(00)00186-7

Atanasov, A. G., Waltenberger, B., Pferschy-Wenzig, E.-M., Linder, T., Wawrosch, C., Uhrin, P., et al. (2015). Discovery and resupply of pharmacologically active plant-derived natural products: A review. *Biotechnol. Adv.* 33, 1582–1614. doi: 10.1016/j.biotechadv.2015.08.001

Bao, X., Yuan, H., Wang, C., Liu, J., and Lan, M. (2013). Antitumor and immunomodulatory activities of a polysaccharide from Artemisia argyi. *Carbohydr. Polym.* 98, 1236–1243. doi: 10.1016/j.carbpol.2013.07.018

Berges, C., Fuchs, D., Opelz, G., Daniel, V., and Naujokat, C. (2009). Helenalin suppresses essential immune functions of activated CD4+ T cells by multiple mechanisms. *Mol. Immunol.* 46, 2892–2901. doi: 10.1016/j.molimm.2009.07.004

Chaplin, D. D. (2010). Overview of the Immune Response. *J. Allergy Clin. Immunol.* 125, S3–23. doi: 10.1016/j.jaci.2009.12.980

Colalto, C. (2018). What phytotherapy needs: Evidence-based guidelines for better clinical practice. *Phytother. Res.* 32, 413–425. doi: 10.1002/ptr.5977

Eisenbrand, G., and Tang, W. (2011). *Handbook of Chinese Medicinal Plants: Chemistry, Pharmacology, Toxicology* Vol. I+II. Eds. W. Tang and G. Eisenbrand (Weinheim: Wiley-VCH), 1150. doi: 10.1002/mnfr.201190015

Fürst, R., and Zündorf, I. (2015). Evidence-Based Phytotherapy in Europe: Where Do We Stand? *Planta Med.* 81, 962–967. doi: 10.1055/s-0035-1545948

Feng, J., Jin, Y.-J., Jia, J.-J., Cao, J.-F., Wang, Y.-T., and Li, X.-F. (2017). Sesquiterpene Lactones from Artemisia capillaris*. *Chem. Nat. Compd.* 53, 978–979. doi: 10.1007/s10600-017-2176-z

Frenkel, B., White, W., and Tuckermann, J. (2015). Glucocorticoid-Induced Osteoporosis. *Adv. Exp. Med. Biol.* 872, 179–215. doi: 10.1007/978-1-4939-2895-8_8

García-Piñeres, A. J., Castro, V., Mora, G., Schmidt, T. J., Strunck, E., Pahl, H. L., et al. (2001). Cysteine 38 in p65/NF-kappaB plays a crucial role in DNA binding inhibition by sesquiterpene lactones. *J. Biol. Chem.* 276, 39713–39720. doi: 10.1074/jbc.M101985200

García-Piñeres, A. J., Lindenmeyer, M. T., and Merfort, I. (2004). Role of cysteine residues of p65/NF-kappaB on the inhibition by the sesquiterpene lactone parthenolide and N-ethyl maleimide, and on its transactivating potential. *Life Sci.* 75, 841–856. doi: 10.1016/j.lfs.2004.01.024

Gründemann, C., Koehbach, J., Huber, R., and Gruber, C. W. (2012). Do plant cyclotides have potential as immunosuppressant peptides? *J. Nat. Prod.* 75, 167–174. doi: 10.1021/np200722w

Gründemann, C., Thell, K., Lengen, K., Garcia-Käufer, M., Huang, Y.-H., Huber, R., et al. (2013). Cyclotides Suppress Human T-Lymphocyte Proliferation by an Interleukin 2-Dependent Mechanism. *PloS One* 8, e68016. doi: 10.1371/journal.pone.0068016

Gründemann, C., Lengen, K., Sauer, B., Garcia-Käufer, M., Zehl, M., and Huber, R. (2014). Equisetum arvense (common horsetail) modulates the function of inflammatory immunocompetent cells. *BMC Complement. Altern. Med.* 14, 283. doi: 10.1186/1472-6882-14-283

Her, M., and Kavanaugh, A. (2016). Alterations in immune function with biologic therapies for autoimmune disease. *J. Allergy Clin. Immunol.* 137, 19–27. doi: 10.1016/j.jaci.2015.10.023

Hogan, P. G., Lewis, R. S., and Rao, A. (2010). Molecular basis of calcium signaling in lymphocytes: STIM and ORAI. Annu. *Rev. Immunol.* 28, 491–533. doi: 10.1146/annurev.immunol.021908.132550

Jutz, S., Leitner, J., Schmetterer, K., Doel-Perez, I., Majdic, O., Grabmeier-Pfistershammer, K., et al. (2016). Assessment of costimulation and coinhibition in a triple parameter T cell reporter line: Simultaneous measurement of NF-κB, NFAT and AP-1. *J. Immunol. Methods* 430, 10–20. doi: 10.1016/j.jim.2016.01.007

Kim, J. K., Shin, E.-C., Lim, H.-J., Choi, S. J., Kim, C. R., Suh, S. H., et al. (2015). Characterization of Nutritional Composition, Antioxidative Capacity, and Sensory Attributes of Seomae Mugwort, a Native Korean Variety of Artemisia argyi H. Lév. & Vaniot. *J. Anal. Methods Chem.* 2015. doi: 10.1155/2015/916346

Kwok, B. H., Koh, B., Ndubuisi, M. I., Elofsson, M., and Crews, C. M. (2001). The anti-inflammatory natural product parthenolide from the medicinal herb Feverfew directly binds to and inhibits IkappaB kinase. *Chem. Biol.* 8, 759–766. doi: 10.1016/S1074-5521(01)00049-7

Li, S., Zhou, S., Yang, W., and Meng, D. (2018). Gastro-protective effect of edible plant Artemisia argyi in ethanol-induced rats via normalizing inflammatory responses and oxidative stress. *J. Ethnopharmacol.* 214, 207–217. doi: 10.1016/j.jep.2017.12.023

Lyss, G., Schmidt, T. J., Merfort, I., and Pahl, H. L. (1997). Helenalin, an anti-inflammatory sesquiterpene lactone from Arnica, selectively inhibits transcription factor NF-kappaB. *Biol. Chem.* 378, 951–961. doi: 10.1515/bchm.1997.378.9.951

Malek, T. R. (2008). The Biology of Interleukin-2. *Annu. Rev. Immunol.* 26, 453–479. doi: 10.1146/annurev.immunol.26.021607.090357

Moroncini, G., Calogera, G., Benfaremo, D., and Gabrielli, A. (2017). Biologics in Inflammatory Immune-mediated Systemic Diseases. *Curr. Pharm. Biotechnol.* 18, 1008–1016. doi: 10.2174/1389201019666171226152448

Myers, D. R., Wheeler, B., and Roose, J. P. (2019). mTOR and other effector kinase signals that impact T cell function and activity. *Immunol. Rev.* 291, 134–153. doi: 10.1111/imr.12796

Newman, D. J., and Cragg, G. M. (2016). Natural Products as Sources of New Drugs from 1981 to 2014. *J. Nat. Prod.* 79, 629–661. doi: 10.1021/acs.jnatprod.5b01055

Parish, C. R., Glidden, M. H., Quah, B. J. C., and Warren, H. S. (2009). "Use of the Intracellular Fluorescent Dye CFSE to Monitor Lymphocyte Migration and Proliferation," in *Current Protocols in Immunology*. Eds. J. E. Coligan, B. E. Bierer, D. H. Margulies, E. M. Shevach and W. Strober (Hoboken, NJ, USA: John Wiley & Sons, Inc.). doi: 10.1002/0471142735.im0409s84

Ramamoorthy, S., and Cidlowski, J. A. (2016). Corticosteroids-Mechanisms of Action in Health and Disease. *Rheumatol. Dis. Clin. North Am.* 42, 15–31. doi: 10.1016/j.rdc.2015.08.002

Ratzinger, F., Haslacher, H., Poeppl, W., Hoermann, G., Kovarik, J. J., Jutz, S., et al. (2014). Azithromycin suppresses CD4(+) T-cell activation by direct modulation of mTOR activity. *Sci. Rep.* 4, 7438. doi: 10.1038/srep07438

Reinhardt, J. K., Klemd, A. M., Danton, O., De Mieri, M., Smieško, M., Huber, R., et al. (2019). Sesquiterpene Lactones from Artemisia argyi: Absolute Configuration and Immunosuppressant Activity. *J. Nat. Prod.* 82, 1424–1433. doi: 10.1021/acs.jnatprod.8b00791

Robert, V., Triffaux, E., Savignac, M., and Pelletier, L. (2011). Calcium signalling in T-lymphocytes. *Biochimie* 93, 2087–2094. doi: 10.1016/j.biochi.2011.06.016

Shin, N.-R., Ryu, H.-W., Ko, J.-W., Park, S.-H., Yuk, H.-J., Kim, H.-J., et al. (2017). Artemisia argyi attenuates airway inflammation in ovalbumin-induced asthmatic animals. *J. Ethnopharmacol.* 209, 108–115. doi: 10.1016/j.jep.2017.07.033

Srikanth, S., Woo, J. S., Sun, Z., and Gwack, Y. (2017). Immunological Disorders: Regulation of Ca2+ Signaling in T Lymphocytes. *Adv. Exp. Med. Biol.* 993, 397–424. doi: 10.1007/978-3-319-57732-6_21

Sun, Z. (2012). Intervention of PKC-θ as an immunosuppressive regimen. *Front. Immunol.* 3, 225. doi: 10.3389/fimmu.2012.00225

Tedesco, D., and Haragsim, L. (2012). Cyclosporine: A review. *J. Transplant.* doi: 10.1155/2012/230386

van der Laan, S., and Meijer, O. C. (2008). Pharmacology of glucocorticoids: Beyond receptors. *Eur. J. Pharmacol.* 585, 483–491. doi: 10.1016/j.ejphar.2008.01.060

Wagner, U. (2019). Biologika in der Rheumatologie. *Internist* 60, 1036–1042. doi: 10.1007/s00108-019-00676-0

Wang, L., Wang, F.-S., and Gershwin, M. E. (2015). Human autoimmune diseases: a comprehensive update. *J. Intern. Med.* 278, 369–395. doi: 10.1111/joim.12395

Wang, Q., Jiang, H., Li, Y., Chen, W., Li, H., Peng, K., et al. (2017). Targeting NF-kB signaling with polymeric hybrid micelles that co-deliver siRNA and dexamethasone for arthritis therapy. *Biomaterials* 122, 10–22. doi: 10.1016/j.biomaterials.2017.01.008

Wiseman, A. C. (2016). Immunosuppressive Medications. *Clin. J. Am. Soc Nephrol.* 11, 332–343. doi: 10.2215/CJN.08570814

Wu, P., Su, M.-X., Wang, Y., Wang, G.-C., Ye, W.-C., Chung, H.-Y., et al. (2012). Supercritical fluid extraction assisted isolation of sesquiterpene lactones with antiproliferative effects from Centipeda minima. *Phytochemistry* 76, 133–140. doi: 10.1016/j.phytochem.2012.01.003

Yun, C., Jung, Y., Chun, W., Yang, B., Ryu, J., Lim, C., et al. (2016). Anti-Inflammatory Effects of Artemisia Leaf Extract in Mice with Contact Dermatitis In Vitro and In Vivo. *Mediators Inflammation* 2016. doi: 10.1155/2016/8027537

Zeng, K.-W., Wang, S., Dong, X., Jiang, Y., and Tu, P.-F. (2014). Sesquiterpene dimer (DSF-52) from Artemisia argyi inhibits microglia-mediated neuroinflammation via suppression of NF-κB, JNK/p38 MAPKs and Jak2/Stat3 signaling pathways. *Phytomedicine* 21, 298–306. doi: 10.1016/j.phymed.2013.08.016

Zimmermann-Klemd, A. M., Konradi, V., Steinborn, C., Ücker, A., Falanga, C. M., Woelfle, U., et al. (2019). Influence of traditionally used Nepalese plants on wound healing and immunological properties using primary human cells in vitro. *J. Ethnopharmacol.* 235, 415–423. doi: 10.1016/j.jep.2019.02.034

Conflict of Interest: The authors declare that the research was conducted in the absence of any commercial or financial relationships that could be construed as a potential conflict of interest.

Copyright © 2020 Zimmermann-Klemd, Reinhardt, Morath, Schamel, Steinberger, Leitner, Huber, Hamburger and Gründemann. This is an open-access article distributed under the terms of the Creative Commons Attribution License (CC BY). The use, distribution or reproduction in other forums is permitted, provided the original author(s) and the copyright owner(s) are credited and that the original publication in this journal is cited, in accordance with accepted academic practice. No use, distribution or reproduction is permitted which does not comply with these terms.

Supporting Information

Immunosuppressive activity of *Artemisia argyi* extract and isolated compounds

Amy M. Zimmermann-Klemd[1‡], Jakob K. Reinhardt[2‡], Anna Morath[3,4,5], Wolfgang W. Schamel[3,4,6], Peter Steinberger[7], Judith Leitner[7], Roman Huber[1], Matthias Hamburger[2], Carsten Gründemann[8*]

[1]Center for Complementary Medicine, Institute for Infection Prevention and Hospital Epidemiology, Faculty of Medicine, University of Freiburg, Freiburg, Germany

[2]Pharmaceutical Biology, Pharmacenter, University of Basel, Basel, Switzerland

[3]Signalling Research Centres BIOSS and CIBSS, University of Freiburg, Freiburg, Germany

[4]Faculty of Biology, University of Freiburg, Freiburg, Germany

[5]Spemann Graduate School of Biology and Medicine, University of Freiburg, Freiburg, Germany

[6]Center for Chronic Immunodeficiency, Medical Center Freiburg and Faculty of Medicine, University of Freiburg, Freiburg, Germany

[7]Center for Pathophysiology, Infectiology, and Immunology, Institute of Immunology, Medical University of Vienna, Vienna, Austria

[8]Translational Complementary Medicine, Department of Pharmaceutical Sciences, University of Basel, Basel, Switzerland

[‡] contributed equally to this work

*** Correspondence:**

Prof. Dr. Carsten Gründemann, PhD

carsten.gruendemann@unibas.ch

Keywords: Artemisia, immunosuppression, Interleukin-2, T cell signaling, sesquiterpene lactones

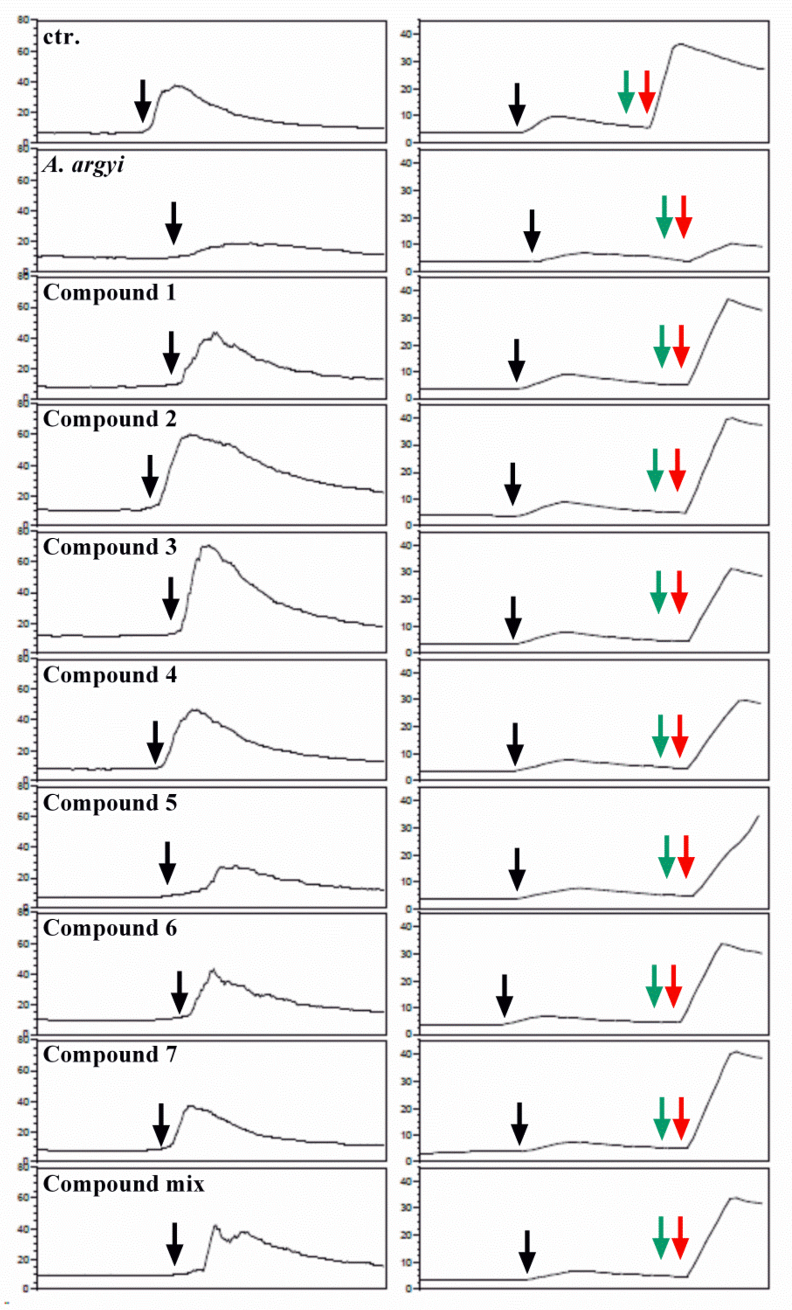

Supplement 1: Effect of isolated compounds and compound mix on the calcium flux in Jurkat T cells, in comparison to *A. argyi* extract. Jurkat cells (0.5 x 10^6) were stained with Fluo3 and FuraRed in calcium-free medium for 45 min at 37°C. During the staining process and measurement 30 µg/mL *A. argyi* extract or 10 µg/mL of the compounds, or 10 µg/mL of compound mix were present in the medium (only left panel). The calcium flux was induced by addition of the anti-CD3 mAbs (black arrows). For the investigation of SOCE, extract, compounds or compound mix were added (green arrows) after ER store depletion and calcium dichloride was supplemented (red arrows) subsequently. The results show the kinetics of calcium flux (median Fluo3/FuraRed) of untreated cells and cells treated with 30 µg/mL *A. argyi* or 10 µg/mL of each compound.

Supplement 2: Table of all tested Asteraceae.

Family	**Species**	**Organ**	**Extracts**
Asteraceae	*Centipeda minima*	Herb	EtOAc ASE
Asteraceae	*Centipeda minima*	Herb	DCM ASE
Asteraceae	*Centipeda minima*	Herb	MeOH ASE
Asteraceae	*Carthamus tinctorius*	Flowers/Buds	EtOAc ASE
Asteraceae	*Carthamus tinctorius*	Flowers/Buds	DCM ASE
Asteraceae	*Carthamus tinctorius*	Flowers/Buds	MeOH ASE
Asteraceae	*Artemisia apiacea*	Herb	EtOAc
Asteraceae	*Artemisia apiacea*	Herb	DCM ASE
Asteraceae	*Artemisia apiacea*	Herb	MeOH ASE
Asteraceae	*Artemisia argyi*	Herb	EtOAc
Asteraceae	*Artemisia argyi*	Herb	DCM ASE
Asteraceae	*Artemisia argyi*	Herb	MeOH ASE
Asteraceae	*Artemisia capillaris*	Herb	EtOAc
Asteraceae	*Artemisia capillaris*	Herb	DCM ASE
Asteraceae	*Artemisia capillaris*	Herb	MeOH ASE
Asteraceae	*Artemisia scoparia*	Herb	EtOAc
Asteraceae	*Artemisia scoparia*	Herb	DCM ASE
Asteraceae	*Artemisia scoparia*	Herb	MeOH ASE

3.3. Compounds from *Toddalia asiatica*: Immunosuppressant activity and absolute configurations

Jakob K. Reinhardt, Amy M. Zimmermann-Klemd, Ombeline Danton, Martin Smieško, Carsten Gründemann, Matthias Hamburger

J Nat Prod. 2019, 82, 1424-1433. doi: 10.1021/acs.jnatprod.8b00791

In a screening of an extract library from plants used in Traditional Chinese Medicine (TCM) the MeOH extract of *Toddalia asiatica* inhibited proliferation of human primary T cells with an IC_{50} of 25.8 µg/mL. Activity in the extract was tracked by HPLC activity profiling, and a total of 15 compounds was characterized. Two compounds, toddalic acid (**6**) and toddanolic acid (**7**), were new natural products, and two recently published compounds, 2’*R*-toddalolactone-3’-O-β-D-glucopyranoside (**10**) and 2’*S*-toddalolactone-2’-O-β-D-glucopyranoside (**11**), were described in detail for the first time. The absolute configurations of compounds **8**, **9**, **10**, **12**, **13** and **15** were determined by comparison of experimental and calculated ECD spectra. For glycosides **9** and **10**, ECD data and enantioselective HPLC of the aglycons after enzymatic hydrolysis confirmed the results. Nitidine chloride (**4**) inhibited proliferation of primary human T cells with an IC_{50} of 0.37 µM.

Extraction of plant material, isolation, recording and interpretation of analytical data for structure elucidation (HPLC-PDA-ELCD-ESI-MS, 1D and 2D NMR [with support from Ombeline Danton], optical rotation, ECD), interpretation of data from VCD measurements (measurements and some advice from Thomas Bürgi), quantum chemical calculations of ECD and VCD spectra (some advice from Martin Smieško), writing of the manuscript draft, and preparation of figures (with the exception of Figure 3) were my contributions to this publication. [T-lymphocyte proliferation inhibition experiments as well as their description in the experimental part were done by Amy Zimmermann-Klemd.]

Jakob K. Reinhardt

JOURNAL OF NATURAL PRODUCTS

pubs.acs.org/jnp Article

Compounds from *Toddalia asiatica*: Immunosuppressant Activity and Absolute Configurations

Jakob K. Reinhardt, Amy M. Zimmermann-Klemd, Ombeline Danton, Martin Smieško, Carsten Gründemann, and Matthias Hamburger*

Cite This: *J. Nat. Prod.* 2020, 83, 3012−3020 Read Online

ACCESS | Metrics & More | Article Recommendations | Supporting Information

Downloaded via UNIV OF BASEL on December 2, 2020 at 12:18:48 (UTC). See https://pubs.acs.org/sharingguidelines for options on how to legitimately share published articles.

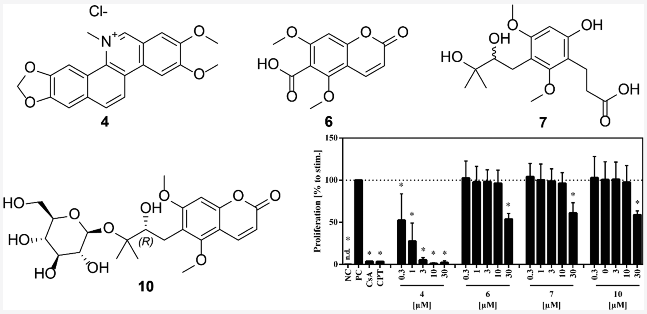

ABSTRACT: In a screening of an extract library from plants used in Traditional Chinese Medicine the MeOH extract of *Toddalia asiatica* inhibited proliferation of human primary T cells with an IC_{50} of 25.8 μg/mL. Activity in the extract was tracked by HPLC activity profiling, and a total of 15 compounds were characterized. Three compounds, toddalic acid (**6**) and both enantiomers (**7a** and **7b**) of toddanolic acid (**7**), were new natural products, and two recently published compounds, (2′*R*)-toddalolactone 3′-*O*-*β*-D-glucopyranoside (**10**) and (2′*S*)-toddalolactone 2′-*O*-*β*-D-glucopyranoside (**11**), were described in detail for the first time. The absolute configurations of compounds **8**, **9**, **10**, **12**, **13**, and **15** were determined by comparison of experimental and calculated ECD spectra. For glucosides **9** and **10**, ECD data and chiral-phase HPLC of the aglycones after enzymatic hydrolysis confirmed the results. Nitidine chloride (**4**) inhibited proliferation of primary human T cells with an IC_{50} of 0.4 μM.

Under normal conditions the immune system is able to differentiate between self and nonself.[1] However, autoimmune diseases can develop if this function is impaired. In rheumatoid arthritis, for example, autoreactive T cells attack the synovial lining of the joints, resulting in tissue destruction and inflammation.[2] Autoimmune diseases are typically treated with immunosuppressive drugs, but therapy may be accompanied by severe side effects.[3] Thus, there is a need for better-tolerated treatment options. To find new natural product leads with immunosuppressive activity, a library of extracts from plants used in Traditional Chinese Medicine (TCM) was screened for their ability to inhibit T cell proliferation in vitro. The MeOH extract from roots of *Toddalia asiatica* Lam. (Rutaceae) was a promising hit, as it showed an IC_{50} value of 25.8 μg/mL without concomitant cytotoxicity (Figure S1, Supporting Information). *T. asiatica* grows in most parts of Asia and Africa.[4] Its roots are only occasionally used in TCM (Fei Long Zhang Xue),[5] but more commonly as an antimalarial drug in different African countries.[6,7] The phytochemistry of *T. asiatica* has been widely studied, and numerous coumarins, alkaloids, and phenolic compounds have been isolated from the roots of the plant.[8−10] Most notably, a structurally diverse set of coumarins have been identified, including glucosides and prenylated derivatives.

RESULTS AND DISCUSSION

The active compounds in the extract were tracked by HPLC-based activity profiling.[11] The overlay of an analytical HPLC chromatogram and the activity of 1 min microfractions collected is shown in Figure S2 (Supporting Information). Inhibition of T cell proliferation was found in the microfractions eluted at 14, 15, and 26 min. Compounds **3**−**10** in the time windows of activity were subsequently isolated by a combination of liquid−liquid partitioning, centrifugal countercurrent chromatography, preparative flash chromatography, and HPLC on RP stationary phases. In addition, compounds **1**, **2**, and **11**−**15** were isolated from adjacent regions in the HPLC chromatogram (Figure S2, Supporting Information). The active fraction at 26 min contained a minor peak with the same mass as nitidine (**4**). However, this peak was not found after further fractionation of the extract.

Compound **1** was identified as syringic acid by analysis of HRESIMS and NMR data (Table S1, Supporting Information) and comparison with literature data.[12]

Compound **2** had a molecular formula of $C_{21}H_{23}NO_5$ (HRESIMS data *m*/*z* 370.1646 $[M + H]^+$, calcd for $C_{21}H_{24}NO_5^+$, 370.1649). With the aid of 1D and 2D NMR data recorded at 23 and 60 °C (Table S2) and comparison

Received: May 22, 2020
Published: October 1, 2020

ACS Publications
© 2020 American Chemical Society and American Society of Pharmacognosy

https://dx.doi.org/10.1021/acs.jnatprod.0c00564

Chart 1

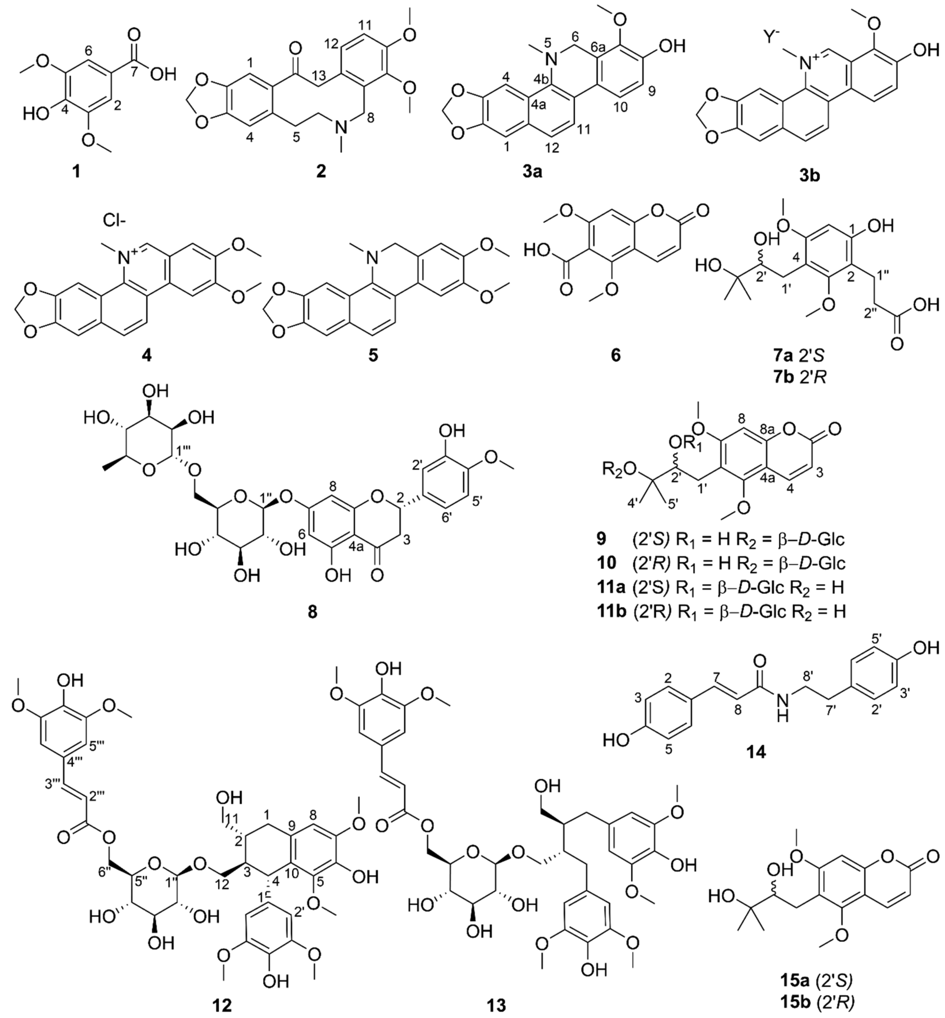

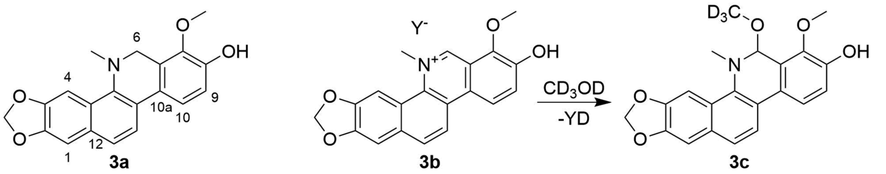

Figure 1. Isolated mixture of compounds **3a** and **3b** and proposed reaction of compound **3b** to yield **3c**.

with literature data, compound **2** was identified as allocryptopine.[13]

Fagaridine (**3b**, identical to isofagaridine[14]) was obtained as the major compound in a 4:1 mixture with dihydrofagaridine (**3a**).[15] Both were identified by comparison of their NMR data (Table S3, Supporting Information) with the literature.[14,15] To prepare fagaridine (**3b**) as the respective chloride for biological testing, the mixture was passed through an ion-exchange resin. In the resulting compound a change was observed for the chemical shifts of C-6 (δ_C 86.3) and H-6 (δ_H 5.53). The presence of a methoxy group at C-6 was supported by an HMBC correlation of H-6 to a carbon at δ_C 51.8. However, no correlating protons were seen in the HSQC-DEPT spectrum. This suggested the formation of the pseudobase of fagaridine in the presence of methanol-d_4 used for the NMR measurements (Figure 1). Indeed, similar reactions have been described before.[16,17]

Compound **4** was identified as nitidine by analysis of its 1D and 2D NMR spectra in DMSO-d_6 with trifluoracetic acid (Table S4, Supporting Information). Nitidine chloride was successively prepared using an ion-exchange resin.[18] The ^{1}H NMR shifts in DMSO-d_6 (Table S4, Supporting Information) and MS data (HRESIMS data m/z 348.1223 $[M]^+$, calcd for $C_{21}H_{18}NO_4^+$, 348.1230) were in good agreement with published data.[19]

Compound **5** was identified as dihydronitidine (Table S4, Supporting Information).[20,21]

For compound **6**, a molecular formula of $C_{12}H_{10}O_6$ (HRESIMS data m/z 251.0542 $[M + H]^+$, calcd for $C_{12}H_{11}O_6^+$, 251.0550) was determined, which, in combination with 1D and 2D NMR data (Table 1), suggested a coumarin. However, no signals for the proposed carboxylic acid moiety at C-6 appeared in the HMBC and ^{13}C NMR spectra. The compound was methylated with trimethylsilyl diazomethane

Table 1. ^{1}H and ^{13}C NMR Spectroscopic Data (500 MHz, Methanol-d_4) for Compounds 6 and 6a

	6		6a	
position	δ_C, type	δ_H (J in Hz)	δ_C, type[a]	δ_H (J in Hz)
2	163.2, C		162.2, C	
3	113.2, CH	6.24, d (9.8)	113.5, CH	6.28, d (9.8)
4	140.9, CH	8.03, d (9.8)	140.0, CH	8.02, d (9.8)
4a	108.2, C		108, C	
5	155.2, C		156.3, C	
6	118.7[a], C		115.1, C	
7	161.7, C		161.6, C	
8	96.1, CH	6.74, s	96.3, CH	6.79, s
8a	157.4, C		158.1, C	
11	[c]		167.1, C	
12	63.4, CH_3	3.99, s	63.7, CH_3	3.92, s
13	57.1, CH_3	3.90, s	57.1, CH_3	3.90, s[b]
14			52.9, CH_3	3.89, s[b]

[a] ^{13}C extracted from ^{1}H−^{13}C 2D inverse-detected experiments. [b] Overlapping signals. [c] Signal not found.

(TMS-DAM) to obtain methyl ester **6a** (Figure S17, Supporting Information) with a molecular formula of $C_{13}H_{12}O_6$ (HRESIMS data m/z 265.0706 $[M + H]^+$, calcd for $C_{13}H_{13}O_6^+$, 265.0707), and the structure was corroborated by NMR data as the methyl ester of **6**. Thus, toddalic acid (**6**) was confirmed as a new coumarin and only similar to buntasin, another naturally occurring coumarin carboxylic acid found in some *Citrus* species.[22]

Table 2. ^{1}H and ^{13}C NMR Spectroscopic Data (500 MHz, Methanol-d_4) for Compound 7

position	δ_C, type	δ_H (J in Hz)	HMBC
1	156.7, C		
2	114.1, C		
3	159.9, C		
4	113.5, C		
5	158.9, C		
6	96.7, CH	6.30, s	1, 2, 4, 5
7	62.2, CH_3	3.75, s[a]	3
8	56.1, CH_3	3.76, s[a]	5
1′	27.2, CH_2	2.66, dd (13.7, 10.1)	3, 4, 5, 2′, 3′
1′		2.86[a]	3, 4, 5, 2′, 3′
2′	79.9, CH	3.56, dd (9.8, 2.8)	1′, 3′, 4
3′	74.2, C		
4′	25.4, CH_3	1.23, s[a]	2′, 3′, 5′
5′	25.8, CH_3	1.22, s[a]	2′, 3′, 4′
1″	20.9, CH_2	2.87[a]	2, 2″, 3″
2″	35.3, CH_2	2.54, t (8.2, 8.2)	1″, 3″
3″	178.1, C		

[a] Overlapping signals.

The molecular formula of compound **7** was determined as $C_{16}H_{22}O_7$ (HRESIMS data m/z 327.1437 $[M - H]^-$, calcd for $C_{16}H_{23}O_7^-$, 327.1449). NMR data (Table 2) indicated an aromatic ring bearing one hydroxy group, two methoxy groups (CH_3-7 and CH_3-8; δ_H 3.75 and 3.76), a 2-methylbutan-2,3-diol side chain, and a propionic acid residue (C-3″; δ_C 178.1). The location of substituents on the aromatic ring were determined with the aid of ^{13}C NMR and HMBC data, leading to the 2D structure of **7**. To determine the absolute configuration at C-2′, an ECD spectrum was recorded and compared to *ab initio* calculated spectra of the enantiomers (Figure S3(B), Supporting Information). The measured ECD spectrum had a low signal-to-noise ratio and showed no significant features of an expected $\pi \rightarrow \pi^*$ transition at 220 nm hinting at a scalemic mixture. The enantiomers were subsequently separated by chiral-phase HPLC. ECD spectra (Figure S3(B), Supporting Information) and the specific rotations of the single enantiomers were recorded. The specific rotations and ECD values for compound **7b** were smaller than could be expected. This was most likely due to an impurity not observed in the NMR. Comparison to the *ab initio* calculated ECD spectra identified **7a** as (−)-(2′*S*)-toddanolic acid and **7b** as (+)-(2′*R*)-toddanolic acid.

The 2D structure of compound **8** (Table S5, Supporting Information) corresponded to that of hesperidin.[23,24]

Compounds **9** and **10** were identified by 1D and 2D NMR data analysis as toddalolactones bearing a sugar moiety at C-3′. Hydrolysis and subsequent GCMS analysis of the sugar afforded D-glucose in both cases. Therefore, **9** and **10** were epimers at C-2′, and this was corroborated by a difference in ^{13}C chemical shifts of CH_3-4′ (δ_C 21.9 in **9** and δ_C 23.0 in **10**) and CH_3-5′ (δ_C 24.0 in **9** and δ_C 23.4 in **10**). Compound **9** showed a specific rotation of $[\alpha]_D^{25}$ −45 and $[\alpha]_D^{25}$ −2.5 for **10**. The (2′*S*)-epimer (**9**) was reported earlier by Lin et al. with a specific rotation of $[\alpha]_D^{25}$ −44.[25] In a recent publication, however, the (2′*R*)-epimer **10** was reported as the "enantiomer" of the (2′*S*)-epimer, with ^{13}C NMR data virtually identical to those of Lin's (2′*S*)-epimer, but with exactly opposite specific rotations.[26] This was highly unexpected in light of our data, and the absolute configuration of C-2′ in both compounds was therefore examined in detail.

The absolute configuration at C-2′ was determined by ECD. The experimental spectra of **9** and **10** showed Cotton effects (CEs) at 225, 253, and 330 nm with opposite signs. In the calculated spectra (Figure 2) the sign for the CE at 330 nm was negative for both epimers. Therefore, the CEs at 225 and 253 nm were used for the assignment. The two negative CEs measured for **9** were in good agreement with the calculated CEs for (2′*S*)-toddalolactone 3′-*O*-*β*-D-glucopyranoside. The spectrum measured for **10** showed positive CEs at 225 and 253 nm. The observed CE at 225 nm matched with a positive CE

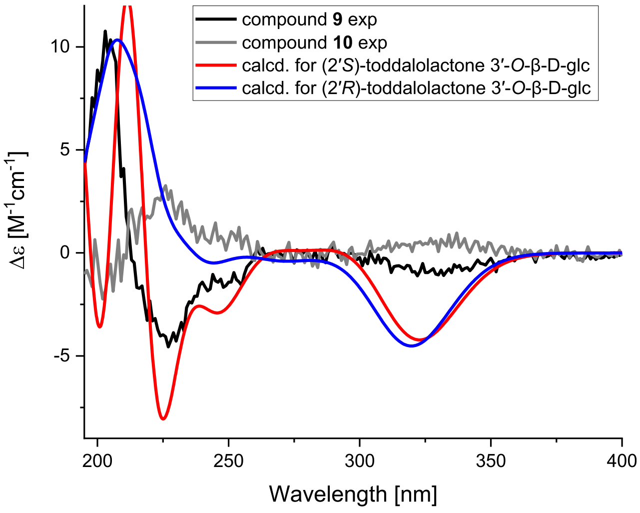

Figure 2. Comparison of experimental and calculated ECD spectra of compounds **9** and **10** in MeOH (calcd spectrum shifted +5 nm).

Table 3. ^1H and ^{13}C NMR Spectroscopic Data (500 MHz, Methanol-d_4) for Compounds 9, 10, and 11

	9		**10**		**11**	
pos.	δ_C, type	δ_H (J in Hz)	δ_C, type	δ_H (J in Hz)	δ_C, type	δ_H (J in Hz)
2	163.5, C		163.5, C		163.7, C	
3	112.7, CH	6.22, d (9.8)	112.7, CH	6.20, d (9.6)	112.6, CH	6.21, d (9.5)
4	141.3, CH	8.00, d (9.8)	141.4, CH	7.97, d (9.6)	141.6, CH	7.98, d (9.5)
4a	108.5, C		108.5, C		108.5, C	
5	157.7, C		157.8, C		157.9, C	
6	120.3, C		120.4, C		120.0, C	
7	163.7, C		163.9, C		164.1, C	
8	96.4, CH	6.72, s	96.4, CH	6.69, s	96.3, CH	6.71, s
8a	156.2, C		156.3, C		156.4, C	
9	64.0, CH_3	3.90, s[a]	64.0, CH_3	3.88, s[a]	64.2, CH_{33}	3.90, s[a]
10	56.9, CH_3	3.91, s[a]	56.9, CH_3	3.88, s[a]	56.9, CH	3.90, s[a]
1′	27.2, CH_2	2.90, dd (13.6, 10.1)	27.2, CH_2	2.89, dd (13.7, 9.8)	27.0, CH_2	2.98, dd (13.7, 10.0)
1′		2.79, dd (13.6, 2.0)		2.76, dd (13.7, 2.4)		2.72, d (13.7)
2′	77.6, CH	3.81[a]	77.2, CH	3.79[a]	88.1, CH	3.87[a]
3′	82.0, C		81.6, C		75.1, C	
4′	21.9, CH_3	1.36, s[a]	23.0, CH_3	1.34, s[a]	24.3, CH_3	1.30, s
5′	24.0, CH_3	1.35, s[a]	23.4, CH_3	1.35, s[a]	26.6, CH_3	1.25, s
1″	98.7, CH	4.57, d (7.6)[a]	98.3, CH	4.55, d (7.6)[a]	106.1, CH	4.20, d (7.0)
2″	75.3, CH	3.22, dd (8.4, 7.6)	75.5, CH	3.19, dd (9.5, 7.6)	76, CH	3.06[a]
3″	78.1, CH	3.4, dd (8.4, 8.4)	78.3, CH	3.38, dd (9.5, 7.9)	78.1, CH	3.23[a]
4″	71.7, CH	3.32[a]	71.8, CH	3.31[a]	71.7, CH	3.06[a]
5″	77.8, CH	3.29[a]	77.9, CH	3.28[a]	77.3, CH	2.90, m
6″	62.8, CH_2	3.65, dd (11.7, 5.0)	62.9, CH_2	3.66, dd (11.7, 4.7)	62.9, CH_2	3.22[a]
6″		3.82, m[a]		3.82[a]		3.26[a]

[a] Overlapping signals.

in the calculated spectrum of (2′*R*)-toddalolactone 3′-*O*-*β*-D-glucopyranoside, but no interpretable CE was seen in the calculated spectrum at 253 nm. To corroborate the assignments, compounds **9** and **10** were subjected to acid hydrolysis with HCl.[25] This led to an almost quantitative formation of ketone **9a** and, via a rearrangement, to aldehyde **9b** (Figures S18 and S81−S84, Supporting Information) and a small amount of the aglycones. Using chiral-phase chromatography on a Daicel Chiralpak IG column, the aglycone of **9** was identified as (2′*S*)-toddalolactone, and that of **10** as (2′*R*)-toddalolactone (Figure S128, Supporting Information). Enzymatic hydrolysis of **9** and **10** with cellulase was used to obtain the aglycones in sufficient amounts for ECD and specific rotation (SR) analysis (Figures S123−S126, Supporting Information). ECD identified the aglycone of **9** as the (2′*S*) enantiomer, and the one from **10** as the (2′*R*)-enantiomer (Figure S8, Supporting Information). Collectively, compound **9** was identified as (2′*S*)-toddalolactone 3′-*O*-*β*-D-glucopyranoside and compound **10** as (2′*R*)-toddalolactone 3′-*O*-*β*-D-glucopyranoside. Coumarin **10** has been recently reported, but the assignment of its absolute configuration was solely based on OR data and a questionable correlation with previously known glucoside **9**.[26]

Compound **11** had a molecular formula of $C_{22}H_{30}O_{11}$ (HRESIMS data *m*/*z* 493.1672 $[M + Na]^+$, calcd for $C_{22}H_{30}O_{11}Na^+$, 493.1680), and 1D and 2D NMR data (Table 3) identified it as toddalolactone 2′-*O*-*β*-D-glucopyranoside.[26] As the absolute configuration of **11** was hitherto only based on SR data, an ECD spectrum was recorded and compared to calculated spectra of both possible epimers (Figure S9, Supporting Information). However, the calculated spectra were highly similar; thus the analysis was inconclusive. Acidic hydrolysis of **11** afforded the aglycone together with the respective ketone and aldehyde (Figure S18, Supporting Information). The aglycone was identified via chiral-phase HPLC as (2′*S*)-toddalolactone (Figure S128, Supporting Information), and compound **11** was conclusively identified as (2′*S*)-toddalolactone 2′-*O*-*β*-D-glucopyranoside.

A molecular formula of $C_{39}H_{48}O_{17}$ was determined for compound **12** (HRESIMS data *m*/*z* 811.2758 $[M + Na]^+$, calcd for $C_{39}H_{48}O_{17}Na^+$, 811.2784). Using 1D and 2D NMR data, compound **12** was identified as hazaleanin B (Table S7, Supporting Information), which was previously reported from *Fagara rhetza* (Rutaceae)[27] and Zhuyeqing Liquor.[28] ECD analysis corroborated the published absolute configuration as (2*R*,3*R*,4*S*)-hazaleanin B (Figure S11, Supporting Information).

Compound **13** had a molecular formula of $C_{39}H_{50}O_{17}$ (HRESIMS data *m*/*z* 813.2916 $[M + Na]^+$, calcd for $C_{39}H_{50}O_{17}Na^+$, 813.2940). By 1D and 2D NMR analysis **13** was identified as hazaleanin A.[27] ECD data analysis was used to independently confirm the absolute configuration. Owing to the high conformational flexibility of **13**, the conformational analysis was performed not in bulk but in explicit MeOH by means of molecular dynamics simulations. A comparison of the experimental and calculated spectra (spectra in Figure S13, selected conformers in Figures S19−S22, Supporting Information) resulted in the assignment of **13** as (2*S*,3*S*)-hazaleanin in accordance with the findings of Shibuya et al.[27] This is the first report of the presence of hazaleanins A and B in *T. asiatica*.

Compound **14** was identified by 1D and 2D NMR data as *p*-coumaroyltyramine (Table S8, Supporting Information).[29]

Compound **15** had a molecular formula of $C_{16}H_{20}O_6$ (HRESIMS data *m*/*z* 309.1329 $[M + Na]^+$, calcd for $C_{16}H_{20}O_6Na^+$, 309.1333), and 1D and 2D NMR data (Table S9, Supporting Information) identified the compound as

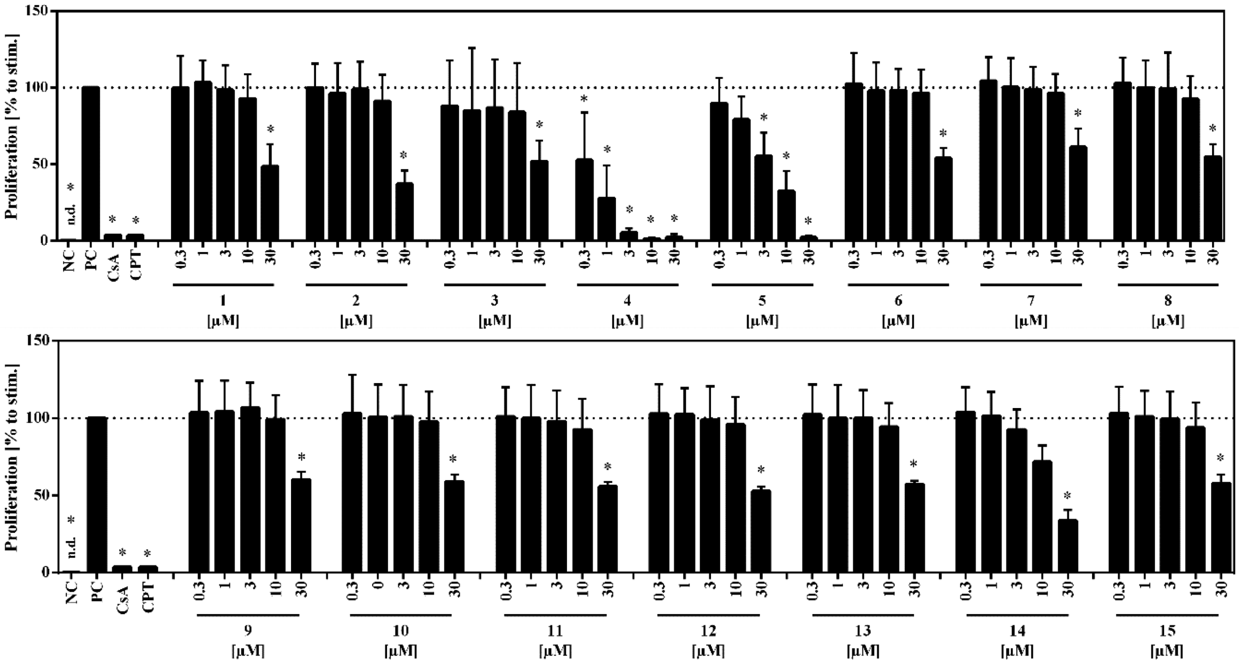

Figure 3. Inhibitory effects of compounds **1**−**15** on the proliferation of human T lymphocytes. Human PBMCs (2×10^5) were stained with CFSE and stimulated with anti-CD3 and anti-CD28 monoclonal antibodies (mAbs, 100 ng/mL each). Unstimulated cells served as a negative control (NC). Afterward, cells were incubated for 72 h in the presence of medium (PC), cyclosporin A (CsA; 4.16 μM), camptothecin (CPT; 300 μM), or compounds **1**−**15** at concentrations between 0.3 and 30 μM. Cell division was analyzed by flow cytometry. The percentage of proliferating cells was normalized to the stimulated control and depicted as mean ± standard deviation. $n = 3$. $^*p < 0.05$.

toddalolactone.[25,30] The negative sign of the specific rotation suggested (2′*S*)-toddalolactone (**15a**).[25] This was supported by the ECD spectrum, which was compared to the calculated spectra of both enantiomers **15a** and **15b** (Figure S15, Supporting Information). The SR of **15** ($[\alpha]_D^{25}$ −10) compared to (2′*S*)-toddalolactone (**15a**) obtained by enzymatic hydrolysis of **9** ($[\alpha]_D^{25}$ −51) indicated the enantiomeric excess of **15a** as 20%. This analysis was corroborated by a ^{1}H NMR experiment in the presence of the shift reagent Eu(hfc)$_3$[31] (29% enantiomeric excess of **15a**) and chiral-phase HPLC on a Daicel Chiralpak IG column (25% enantiomeric excess of **15a**).

In conclusion, a total of 15 compounds were isolated from the MeOH extract of *T. asiatica*, of which toddalic acid (**6**) and toddanolic acid (**7**) were new natural products. Although compound **10**, the 2′-epimer of **9**, was reported recently, we provide here the first full structural assignment and spectroscopic data. The co-occurrence of **9** and **10** indicates that both enantiomers of toddalolactone are naturally present in the plant.[32] The carboxylic moiety at C-6 in coumarin **6** is unusual from a biosynthetic perspective, and only one similar naturally occurring coumarin has been reported so far.[22] Toddanolic acid (**7**) is structurally related to toddalolactone (**15**). An artifactual formation of **7** can be ruled out given that an opening of the lactone ring and reduction of the double bond would require conditions (e.g., basic pH, metal catalyst, and NaBH$_4$) far from the ones used during the isolation.[33,34]

Compounds **1**−**15** were tested for their ability to suppress the proliferation of stimulated human primary T lymphocytes in vitro. Compounds **1**−**3** and **6**−**15** showed slight inhibition of T cell proliferation at the highest test concentration of 30 μM. Compounds **4** and **5** concentration-dependently inhibited T cell proliferation with IC$_{50}$'s of 0.4 μM (R^2 = 0.7) and 6.7 μM (R^2 = 0.9), respectively (Figure 3). Cytotoxic effects were detected only at 10 and 30 μM concentrations for compound **4** and at 30 μM concentration for **5**. Nitidine chloride (**4**) has been previously found to modulate reactive microgliosis after traumatic brain injury at 0.1 μM, and inhibition of the ERK and NF-κB signaling pathways in microglia cells was reported.[35] Inhibition of T cell proliferation by nitidine chloride (**4**) observed in our study could thus be caused by inhibition of these pathways. Nitidine chloride reportedly also induces apoptosis in HCT116 human colorectal cancer cells via inhibition of ERK.[36] In conclusion, nitidine chloride (**4**) is a potential lead, with inhibition of T cell proliferation at submicromolar concentrations and an apparent cytotoxicity only at a 25-fold higher concentration. This possibility was also corroborated by a patent (CN102008474B) filed for the use of nitidine in the treatment of autoimmune diseases and resisting transplant rejection.[37] The related dihydronitidine (**5**) has been reported to selectively induce apoptosis in various tumor cell lines when tested at low micromolar concentrations.[38]

■ EXPERIMENTAL SECTION

General Experimental Procedures. Optical rotations were measured at concentrations between 0.4 and 1 mg/mL in MeOH on a PerkinElmer 341 polarimeter with a 10 cm microcell. UV and ECD spectra were recorded in MeOH (50−150 μg/mL) on a Chirascan CD spectrometer using 1 mm path precision cells (110 QS, Hellma Analytics). NMR data were recorded on a Bruker Avance III NMR spectrometer operating at 500.13 MHz for ^{1}H and 125.77 MHz for ^{13}C nuclei. ^{1}H NMR, COSY, HSQC, HMBC, and NOESY spectra were measured at 23 °C in a 1 mm TXI probe with a z-gradient. ^{13}C NMR/DEPTQ spectra were recorded at 23 °C in 3 mm tubes using a 5 mm BBI probe. For compound **2**, ^{1}H, COSY, HSQC, and HMBC spectra were also recorded at 60 °C. All spectra were analyzed using Bruker TopSpin 3.5 and ACDLabs NMR Workbook software suites. NMR spectra were recorded in CDCl$_3$ (Sigma-Aldrich), methanol-d_4, DMSO-d_6, or TFA (all Armar Chemicals). HPLC-PDA-ELSD-ESIMS data were recorded in the positive and negative mode on a Shimadzu LC-MS/MS 8030 triple quadrupole ESIMS system connected via a T-splitter (1:10) to a Shimadzu HPLC system consisting of a degasser, binary high-pressure mixing pump, autosampler, column oven, and diode array detector, and via a T-split to an Alltech 3300 ELSD detector. Data were acquired and processed with the LabSolution software suite. Semipreparative HPLC separations were carried out with an Agilent HP 1100 Series system consisting of a quaternary pump, autosampler, column oven, and a diode array detector (G1315B). Preparative HPLC separations were carried out using Agilent 1290 Infinity II preparative binary pumps and an Agilent 1100 DAD detector in line with an Agilent 6120 Quadropole LC/MS detector. The column effluent was collected via an active split (100:1) between HPLC columns and detectors. Chemstation software was used for data acquisition and processing. Waters SunFire C_{18} (3.5 μm, 3.0 × 150 mm i.d., equipped with a guard column 10 × 3.0 mm i.d.), SunFire Prep C_{18} (5 μm, 10 × 150 mm i.d., equipped with a guard column 10 × 10 mm i.d.), and SunFire Prep C_{18} OBD (5 μm, 30 × 150 mm i.d., equipped with a guard column 10 × 20 mm i.d.) columns were used for reverse-phase analytical, semipreparative, and preparative separations, respectively. Chiral-phase HPLC separations were performed at a flow rate of 1 mL/min on either a Daicel Chiralpak IG column (5 μm, 250 × 4.6 mm) eluted with 20% CH_3CN in H_2O for 10 min or a Daicel Chiralpak IF column (5 μm, 250 × 4.6 mm) eluted with 20% CH_3CN in H_2O, both containing 0.1% formic acid (FA), for 10 min. HPLC-grade MeOH, CH_3CN (Scharlau Chemie), and water from a Milli-Q water purification system (Merck Millipore) were used for HPLC separations. The mobile phase used for analytical HPLC contained 0.1% FA. Technical-grade solvents purified by distillation were used for extraction, open column chromatography, and CPC separations. Silica gel (15−40 μm, Merck) and C_{18} modified silica (RP-18 LiChroprep 25−40 μm) were used for open column chromatography. HRESIMS data were measured on an LQT XL Orbitrap mass spectrometer (Thermo Scientific) coupled to a Shimadzu LC-MS system equipped with a Waters SunFire C_{18} column (3.5 μm, 3.0 × 150 mm i.d., equipped with a guard column 10 × 3.0 mm i.d.). Trimethylsilyldiazomethane was purchased from Tokio Chemical Industry, and Lewatit MonoPlus SP 112 (Na^+ form), Eu(hfc)$_3$, and cellulase enzyme blend were from Sigma-Aldrich, Germany.

Plant Material. *T. asiatica* roots were purchased from Bozhou Swanf Commerce and Trade Co., Ltd. (Bozhou, China) in January 2018. A voucher specimen (number 0 1026) has been deposited at the Division of Pharmaceutical Biology, University of Basel, Switzerland.

Microfractionation. Microfractionation of *T. asiatica* MeOH extract was carried out by analytical RP-HPLC on an LC-MS 8030 system (Shimadzu) connected with an FC 204 fraction collector (Gilson). A solution of 10 mg/mL extract in DMSO was prepared, and three injections were performed: 2 × 30 μL for microfraction, using only the PDA (0.6 mg of extract in total), and 1 × 10 μL with PDA-ELSD-ESIMS detectors without microfractionation. Water containing 0.1% FA (solvent A) and CH_3CN with 0.1% FA (B) were used as a mobile phase. A linear gradient from 5 to 60% B in 30 min was followed by 5 min at 100% B. Microfractions of 1 min each were collected from the beginning of minute 2 to the end of minute 34. Corresponding microfractions of two successive injections were collected into the same wells of a 96-deep-well plate. The plates were dried in a Genevac EZ-2 evaporator.

Extraction and Isolation. *T. asiatica* roots were ground with a Retsch ZM1 centrifugal mill. A 740 g amount of the powdered roots was extracted with 4 × 2.2 L of DCM over 24 h. The remaining plant material was extracted with 3 × 2.2 L of MeOH over 24 h. The combined MeOH extracts were dried in vacuo and freeze-dried to afford 38.7 g of dry residue. A 35.7 g amount of MeOH extract was subjected to liquid−liquid partitioning using a two-phase system containing 928 mL of $CHCl_3$, 500 mL of MeOH, and 570 mL of H_2O. After removal of the organic phase, the aqueous phase was successively extracted with a mixture of 800 mL of $CHCl_3$ and 200 mL of MeOH, a mixture of 500 mL of $CHCl_3$ and 500 mL of MeOH, and a mixture of 1500 mL of $CHCl_3$ and 500 mL of MeOH. The organic layers were combined and dried *in vacuo*, yielding 17.3 g of an enriched fraction. A precipitate at the interface of the aqueous and the organic layers was collected separately, filtered, and washed with cold $CHCl_3$ and MeOH to give 548 mg of **8**. Aliquots of the enriched fraction (1.9 to 3.0 g per run) were subjected to centrifugal partition chromatography (CPC) using $CHCl_3$/MeOH/H_2O (25:30:20) at a flow rate of 5 mL/min in descending mode. Six fractions (A−F) were collected, and a switch to ascending mode gave four additional fractions (G−K). Fraction E (559 mg) was separated on a C_{18} column (25−40 μm, 5 × 47 cm) connected to an Interchim Puriflash 4100 system [water + 0.1% FA (A), CH_3CN + 0.1% FA (B); 27% B (0−5 min) 27 → 44% B (5−202 min), 44 → 100% (202−220 min), 100% (220−245 min); flow rate 22 mL/min; sample dissolved in 1.3 mL of MeOH], and fractions E_1−E_{16} were obtained. E_6 (6 mg) was purified by semipreparative RP HPLC [CH_3CN + 0.1% FA (A), H_2O + 0.1% FA (B); 18% B (0−20 min) 18 → 20% B (20−22 min), 20 → 100% (22−26 min), 100% (26−31 min); flow rate 4 mL/min; concentration 50 mg/mL in MeOH, injection volume 10−40 μL] to yield dihydronitidine (**5**, 0.6 mg). The rest of fraction E (600 mg) was chromatographed on a silica gel column (15−40 μm; 3.5 × 35 cm) connected to an Interchim Puriflash 4100 system [$CHCl_3$ (A), MeOH (B); 100% A (0−5 min) 0 → 2% B (5−10 min), 2 → 5% (10−20 min), 5 → 30% (20−110 min), 30 → 50% (110−175 min), 50 → 55% (175−190 min), 55 → 57% (190−191 min), 57 → 100% (191−205 min), 100% (205−260 min); flow rate 20 mL/min; solid state introduction, with the sample adsorbed on 3 g of silica gel (63−200 μm, Merck)], and 24 fractions (EA−EX) were obtained. Fraction EL (36 mg) was separated by preparative RP HPLC [CH_3CN + 0.1% FA (A), H_2O + 0.1% FA (B); 15% B (0−24 min) 15 → 25% B (24−35 min), 25 → 35% B (35−40 min), 35 → 60% B (40−45 min), 60 → 100% B (45−47 min), flow rate 25 mL/min; concentration 90 mg/mL in MeOH, injection volume 390 μL] to afford a mixture of **3a** and **3b** (3.5 mg). Fraction EN (9.3 mg) was recrystallized from MeOH/H_2O (1:2) to obtain syringic acid (**1**, 4.5 mg). Fraction EP (22 mg) was separated by preparative RP HPLC [CH_3CN + 0.1% FA (A), H_2O + 0.1% FA (B); 15% B (0−3 min) 30 → 35% B (3−16 min), 35 → 100% (16−20 min); flow rate 20 mL/min; concentration 55 mg/mL in MeOH/H_2O (1:3); injection volume 400 μL], and fractions EP_1−EP_4 were collected. EP_3 (5.8 mg) was purified by semipreparative RP HPLC [CH_3CN + 0.1% FA (A), H_2O + 0.1% FA (B); 24% B (0−20 min) 24 → 100% B (20−22 min), 100% B (22−27 min), flow rate 4 mL/min; concentration 2.5 mg/mL MeOH/H_2O (1:1), 3 injections with injection volumes 40−70 μL] to afford **12** (3.6 mg) and **13** (1.5 mg). Fraction EQ (60 mg) was separated by preparative RP HPLC [CH_3CN + 0.1% FA (A), H_2O + 0.1% FA (B); 23% B (0−30 min) 23 → 100% B (30−31 min), 100% B (31−36 min); flow rate 20 mL/min; concentration 83 mg/mL in MeOH/H_2O (1:3); 2 injections of 300−400 μL] to afford **9** (20 mg), **10** (11 mg), and **11** (5.1 mg). Fraction ET (55 mg) was dissolved in 700 μL MeOH/H_2O (3:1), and the supernatant was subjected to preparative HPLC [CH_3CN + 0.1% FA (A), H_2O + 0.1% FA (B); 13% B (0−2 min), 13 → 25% B (2−32 min), 25 → 29% (32−42 min), 29 → 60% (42−50 min), 60% (50−52 min), 60 → 100% B (52−55 min), flow rate 20 mL/min; concentration 75 mg/mL in MeOH/H_2O (3:1); injection volume 700 μL] to yield **2** (1.6 mg). Fraction EV (22 mg) was separated by preparative RP HPLC [CH_3CN + 0.1% FA (A), H_2O + 0.1% FA (B); 21% B (0−3 min) 21 → 29% B (3−24 min), 29 → 100% (24−30 min), flow rate 20 mL/min; concentration 55 mg/mL in MeOH/H_2O (1:1); injection volume 400 μL] to afford fractions EV_1−EV_5. Fraction EV_1 (5.8 mg) was purified by semipreparative RP HPLC [CH_3CN + 0.1% FA (A), H_2O + 0.1% FA (B); 11% B (0−30 min) 11 → 100% B (30−32 min), 100% B (32−38 min), flow rate 4 mL/min; concentration 33 mg/mL in MeOH/H_2O (1:2), 2 injections of 60 μL], to afford **6** (1.0 mg) and **7** (1.5 mg). As compound **7** was obtained as a scalemic mixture of both enantiomers, the enantiomers **7a** and **7b** were separated via chiral-phase HPLC on a Daicel Chiralpak IF column [CH_3CN + 0.1% FA (A), H_2O + 0.1% FA (B); 20% B (0−10 min), flow rate 1 mL/min; concentration of 5 mg/mL; 8 injections with 10 μL]. Compound **7b**

eluted at 7.3 min, and compound **7a** at 8.4 min. Fraction EW (58 mg) was dissolved in 580 μL MeOH and 10 μL of FA and subjected to preparative RP HPLC [CH_3CN (A), H_2O (B); 16% B (0−48 min), 16 → 100% B (48−53 min); flow rate 25 mL/min; concentration of 90 mg/mL; injection volume 550 μL], to afford **4** (10.1 mg). The hydrochloride of **4** was prepared via filtration over Lewatit MonoPlus SP 112 resin.

Syringic acid (1): white solid; ^1H and ^{13}C NMR, see Table S1, Supporting Information; HRESIMS m/z 181.0489 $[M + H - H_2O]^+$ (calcd for $C_9H_9O_4^+$, 181.0495).

Allocryptopine (2): colorless solid; ^1H and ^{13}C NMR, see Table S2, Supporting Information; HRESIMS m/z 370.1646 $[M + H]^+$ (calcd for $C_{21}H_{24}NO_5^+$, 370.1649).

Fagaridine and dihydrofagaridine (3b and 3a): red solid; ^1H and ^{13}C NMR, see Table S3, Supporting Information; HRESIMS m/z 334.1059 $[M]^+$ (calcd for $C_{20}H_{16}NO_4^+$, 334.1074).

Compound 3b: ^1H and ^{13}C NMR, see Table S3, Supporting Information.

Nitidine chloride (4): yellow solid; ^1H and ^{13}C NMR, see Table S4, Supporting Information; HRESIMS m/z 338.1223 $[M]^+$ (calcd for $C_{21}H_{18}NO_4^+$, 338.1230).

Dihydronitidine (5): light yellow solid; ^1H and ^{13}C NMR, see Table S4, Supporting Information; HRESIMS m/z 348.1220 $[M - H]^+$ (calcd for $C_{21}H_{18}NO_4^+$, 348.1230) and m/z 334.1064 $[M - CH_3]+$ (calcd for $C_{20}H_{16}NO_4^+$, 334.1074).

Toddalic acid (6): colorless solid; UV λ_{max} (MeOH) (log ε) 206 (4.4) nm, 323 (3.9) nm; ^1H and ^{13}C NMR, see Table 1; HRESIMS m/z 251.0542 $[M + H]+$ (calcd for $C_{12}H_{11}O_6^+$, 251.0550).

Compound 6a: colorless solid; ^1H and ^{13}C NMR, see Table 1; HRESIMS m/z 265.0706 $[M + H]^+$ (calcd for $C_{13}H_{13}O_6^+$, 265.0707).

Toddanolic acid (7): colorless solid; $[\alpha]_D^{25}$ −12 (c 0.07 g/100 mL, MeOH); UV λ_{max} (MeOH) (log ε) 204 (4.1), 281 (3.0) nm; ECD (MeOH, c 0.97 mM, 0.1 cm); $\Delta\varepsilon$ +1.49 (204 nm), −0.8 (230 nm); ^1H and ^{13}C NMR, see Table 2, Supporting Information; HRESIMS m/z 327.1437 $[M - H]^-$ (calcd for $C_{16}H_{23}O_7^-$, 327.1449).

(−)-(2′S)-Toddanolic acid (7a): colorless solid; $[\alpha]_D^{25}$ −20 (c 0.03 g/100 mL, MeOH); UV λ_{max} (MeOH) (log ε) 204 (4.5), 281 (3.3) nm; ECD (MeOH, c 0.48 mM, 0.1 cm); $\Delta\varepsilon$ −3.4 (205 nm), −1.2 (231 nm), −0.5 (273 nm).

(+)-(2′R)-Toddanolic acid (7b): colorless solid; $[\alpha]_D^{25}$ 32 (c 0.02 g/100 mL, MeOH); UV λ_{max} (MeOH) (log ε) 204 (4.5), 282 (3.4) nm; ECD (MeOH, c 0.32 mM, 0.1 cm); $\Delta\varepsilon$ +8.0 (205 nm), +2.6 (232 nm), +1.1 (275 nm).

(2′S)-Hesperidin (8): pale yellow solid; UV λ_{max} (MeOH) (log ε) 200 (4.8), 224 (4.5), 283 (4.3), 331 (3.6) nm; ECD (MeOH, c 0.32 mM, 0.1 cm); $\Delta\varepsilon$ +20.2(200 nm) +11.0 (223 nm), −10.4 (289 nm), +2.5 (334 nm); ^1H and ^{13}C NMR, see Table S5, Supporting Information; HRESIMS m/z 633.1778 $[M + Na]^+$ (calcd for $C_{28}H_{34}NaO_{15}^+$, 633.1790) (m/z 633.1778 $[M + Na]^+$, calcd for $C_{28}H_{34}NaO_{15}^+$, 633.1790).

(2′S)-Toddalolactone 3′-O-β-D-glycopyranoside (9): yellow solid; $[\alpha]_D^{25}$ −45 (c 0.14 g/100 mL, MeOH); UV λ_{max} (MeOH) (log ε) 205 (4.6), 226 (4.1), 330 (4.1) nm; ECD (MeOH, c 0.32 mM, 0.1 cm); $\Delta\varepsilon$ +10.8 (203 nm), −4.6 (227 nm), −1.7 (248 nm), −1.1 (332 nm); ^1H and ^{13}C NMR, see Table 3; HRESIMS m/z 493.1669 $[M + Na]^+$ (calcd for $C_{22}H_{30}O_{11}Na^+$, 493.1680).

Compounds 9a and 9b. ^1H and ^{13}C NMR, see Table S6, Supporting Information.

(2′R)-Toddalolactone 3′-O-β-D-glycopyranoside (10): yellow solid; $[\alpha]_D^{25}$ −2.5 (c 0.12 g/100 mL, MeOH); UV λ_{max} (MeOH) (log ε) 205 (4.6), 225 (4.2), 328 (4.0) nm; ECD (MeOH, c 0.21 mM, 0.1 cm); $\Delta\varepsilon$ −2.2 (202 nm), +2.6 (226 nm), +1.0 (251 nm), +0.9 (334 nm); ^1H and ^{13}C NMR, see Table 3; HRESIMS m/z 493.1670 $[M + Na]^+$ (calcd for $C_{22}H_{30}O_{11}Na^+$, 493.1680).

(2′S)-Toddalolactone 2′-O-β-D-glycopyranoside (11): yellow solid; $[\alpha]_D^{25}$ −46 (c 0.08 g/100 mL, MeOH); UV λ_{max} (MeOH) (log ε) 204 (4.5), 224 (4.1), 329 (3.9) nm; ECD (MeOH, c 0.32 mM, 0.1 cm); $\Delta\varepsilon$ +12.9 (204 nm), −5.2 (227 nm), −1.9 (248 nm), −1.5 (332 nm); ^1H and ^{13}C NMR, see Table 3; HRESIMS m/z 493.1672 $[M + Na]^+$ (calcd for $C_{22}H_{30}O_{11}Na$, 493.1680).

Hazaleanin B (12): yellow solid; $[\alpha]_D^{25}$ +14 (c 0.09 g/100 mL, MeOH); UV λ_{max} (MeOH) (log ε) 205 (5.0), 328 (4.3) nm; ECD (MeOH, c 0.13 mM, 0.1 cm); $\Delta\varepsilon$ +43.7 (203 nm), −18.5 (218 nm), +14.5 (244 nm), +4.3 (272 nm), −1.9 (287 nm); ^1H and ^{13}C NMR, see Table S7, Supporting Information; HRESIMS m/z 811.2758 $[M + Na]^+$ (calcd for $C_{39}H_{48}O_{17}Na$, 811.2784).

Hazaleanin A (13): white solid; $[\alpha]_D^{25}$ −9 (c 0.05 g/100 mL, MeOH); UV λ_{max} (MeOH) (log ε) 205 (4.9), 329 (4.2) nm; ECD (MeOH, c 0.13 mM, 0.1 cm); $\Delta\varepsilon$ +20.5 (208 nm), −7.3 (217 nm), +1.4 (239 nm); ^1H and ^{13}C NMR, see Table S7, Supporting Information; HRESIMS m/z 813.2916 $[M + Na]^+$ (calcd for $C_{39}H_{50}O_{17}Na$, 813.2940).

N-p-Coumaroyltyramine (14): yellowish solid; ^1H and ^{13}C NMR, see Table S8, Supporting Information; HRESIMS m/z 284.1274 $[M + H]^+$ (calcd for $C_{17}H_{18}NO_3$, 284.1281).

Toddalolactone (15): white solid; $[\alpha]_D^{25}$ −10 (c 0.07 g/100 mL, MeOH); UV λ_{max} (MeOH) (log ε) 205 (4.5), 225 (4.1), 330 (4.0) nm; ECD (MeOH, c 0.21 mM, 0.1 cm); $\Delta\varepsilon$ +3.1 (203 nm), −1.0 (229 nm); ^1H and ^{13}C NMR, see Table S9, Supporting Information; HRESIMS m/z 309.1329 $[M + Na]^+$ (calcd for $C_{16}H_{20}O_6Na$, 309.1333).

(2′S)-Toddalolactone (15a): colorless solid; $[\alpha]_D^{25}$ −51 (c 0.04 g/100 mL, MeOH); UV λ_{max} (MeOH) (log ε) 196 (4.8), 205 (4.7), 226 (4.4), 330 (4.1) nm; ECD (MeOH, c 0.21 mM, 0.1 cm); $\Delta\varepsilon$ +8.8 (203 nm), −6.3 (229 nm), −1.8 (256 nm), −1.7 (327 nm).

(2′R)-Toddalolactone (15b): colorless solid; $[\alpha]_D^{25}$ 50 (c 0.06 g/100 mL, MeOH); UV λ_{max} (MeOH) (log ε) 197 (4.7), 205 (4.6), 225 (4.3), 330 (4.0) nm; ECD (MeOH, c 0.21 mM, 0.1 cm); $\Delta\varepsilon$ +5.8 (225 nm), +2.7 (253 nm), +1.0 (329 nm).

Ion Exchange. The resin (Lewatit MonoPlus SP 112 (Na^+ form), 500 mg) was placed in a 3 mL glass vial with a magnetic stirrer. The resin was washed twice with 10 mL of HPLC grade MeOH while slowly stirring. Compound **2** or **4**, respectively, was dissolved in MeOH at a concentration of 1.7 mg/mL, added to the washed resin, and stirred until the color of the supernatant had faded. The supernatant was discarded, and the resin was washed twice with 10 mL of MeOH. Then, 1 mL of a 10% NaCl solution in H_2O/MeOH (1:1) was added while stirring, followed by 5 mL of MeOH. The supernatant was collected, and the step was repeated once again. The combined supernatants were dried under a flow of N_2, suspended in 1.5 mL of HPLC grade water, and centrifuged at 13 200 rpm for 8 min. The supernatant was discarded, and the precipitate was washed twice more with 1 mL of H_2O, yielding the respective chloride.

Preparation of 6a. Compound **6** (0.1 mg, 0.4 μmol) was dissolved in 75 μL of DCM and 25 μL of MeOH in a vial under an argon atmosphere, and 5 μL of trimethylsilyl diazomethane (0.6 M in *n*-hexane, 3 μmol) was added. The mixture was vortexed and allowed to stand at room temperature for 1 h. The reaction was stopped by the addition of 3.4 μL of 1.7 M acetic acid in H_2O. The reaction mixture was dried in a flow of N_2 to yield **6a**.

Enantiomeric Excess Determination of Toddalolactone (15). $Eu(hfc)_3$ (0.7 mg) was dissolved under argon in $CDCl_3$ at a concentration of 1.5 equiv of **15** per 120 μL, and the solution was transferred under argon to the mixture of **15a** and **15b**. The resulting solution was transferred into a 3 mm NMR tube under argon, and ^1H NMR spectra were recorded.

Acid Hydrolysis of 9, 10, and 11. Analogous to acid hydrolysis for GCMS sugar analysis,[24] approximately 1 mg of **9**, **10**, or **11**, respectively, was dissolved in 1 mL of 2 N aqueous HCl in a 4 mL sealable vial. The vial was placed in an oven at 105 °C for 105 min. After cooling, the mixture was extracted with EtOAc (3 × 1 mL). The organic layers were combined and dried under N_2. The aglycones **15a** and **15b**, respectively, were identified as minor compounds via chiral-phase HPLC on a Daicel Chiralpak IG column eluting with 20% CH_3CN. (2′R)-Toddalolactone (**15b**) eluted at 4.74 min, and (2′S)-toddalolactone (**15a**) at 4.93 min, respectively (Figure S128, Supporting Information). The major compounds recovered after hydrolysis of **9**, **10**, and **11**, respectively, were the ketone **9a** and the aldehyde **9b** (Figure S18, Supporting Information).

Enzymatic Hydrolysis of 9, 10, and 11. Approximately 1 mg of **9**, **10**, or **11** was dissolved in 100 μL of cellulase blend (Sigma-Aldrich, Cellulase, enzyme blend, SAE0020) diluted 1:1 with purified water. The mixture was stirred at 37 °C for 22.5 h. Afterward, the reaction mixture was diluted with 900 μL of H_2O and extracted with EtOAc (3 × 1 mL). The organic layers were combined and dried under N_2. Compounds **9** and **10** afforded their respective aglycone, while **11** was recovered unreacted.

Computational Methods. Conformational analysis was performed with Schrödinger MacroModel 11.0 (Schrödinger, LLC, New York) employing the OPLS2005 (optimized potential for liquid simulations) force field in H_2O for geometrical optimization in two steps. In the first step, a global minimum was searched using 20 000 or 30 000 steps, depending on the size of the molecule. In the second step, the global minimum was used for a conformational search (4000 steps) choosing the five conformers to be subjected to geometrical optimization and energy calculation applying DFT with Becke's nonlocal three-parameter exchange and correlation functional and the Lee−Yang−Parr correlation functional level (B3LYP), using the B3LYP/6-31G** basis set, the SCRF method, and the CPMC model for solvation (MeOH for ECD calculations) with the Gaussian 09 program package.[39] Excitation energy (denoted by wavelength in nm), rotator strength (R_{str}), dipole velocity (R_{vel}), and dipole length (R_{len}) were calculated in MeOH by TD-DFT/B3LYP/6-31G(d,p). ECD curves were obtained on the basis of rotator strengths with a half-band of 0.25 eV using SpecDis v1.71.[40]

Conformational Search for 13. The conformational flexibility and relative structural complexity of **13** required a more sophisticated conformational analysis. The 3D structures of all four stereoisomers were built in the Maestro modeling environment.[41] First, a conformational search was performed to obtain a reasonable starting conformation by sampling a total of 30 000 conformers using a mixed torsional/low-mode sampling method, extended torsional sampling, OPLS 2005 force field, and the implicit water solvent model in MacroModel.[42] The water solvent model was selected from the list of available implicit models (water, $CHCl_3$, octanol), because it offers properties closest to MeOH. Next, a periodic boundary system was created by placing the global minimum structure identified in the conformational search into a cubic system (edge length 50 Å) of preorganized MeOH molecules. The whole periodic boundary system was fully optimized using the default relaxation protocol implemented in Desmond,[43−45] composed of seven stages allowing the solvent molecules to optimally arrange with respect to the solute. The last frame of the equilibration stage was used as input for the production simulation in the total duration of 0.48 ms (NPT ensemble and standard conditions $T = 300$ K, $p = 101.325$ kPa) with frames being sampled every 480 ps (in total 1000 frames were saved per simulation). All MD simulations were done using Desmond software. The MD trajectories were postprocessed using the default clustering analysis of Desmond. Representative solute structures of the 10 most significant clusters were used as input for Gaussian 09 calculations as described earlier.

Ethics Statement. Patients gave their written consent to donate blood for scientific research. All experiments conducted on human material were approved by the Ethics Committee of the University of Freiburg (55/14; 11.02.2014), and all methods used were compliant with the regulations of the Ethics Committee.

Preparation and Cultivation of Human Peripheral Lymphocytes. Peripheral blood mononuclear cells (PBMCs) were isolated from the blood of healthy adult donors obtained from the Blood Transfusion Centre (University Medical Center, Freiburg, Germany). Venous blood was centrifuged on a LymphoPrep gradient (density: 1.077 g/cm^3, 20 min, 500g, 20 °C; Progen). After centrifugation, cells were washed twice with PBS and subsequently cultured in RPMI 1640 medium supplemented with 10% heat-inactivated fetal calf serum (GE Healthcare Life Sciences), 2 mM L-glutamine, 100 U/mL penicillin, and 100 U/mL streptomycin (all from Life Technologies). The cells were cultured at 37 °C in a humidified incubator with a 5% CO_2/95% air atmosphere.

T Cell Proliferation Assay. Lymphocytes were isolated, washed twice in cold PBS, and resuspended in PBS at a concentration of 5 × 10^6 cells/mL. Cells were stained for 10 min at 37 °C with carboxyfluorescein diacetate succinimidyl ester (CFSE; 5 μM: Sigma-Aldrich, St. Louis, MO, USA). The staining was stopped by washing twice with complete medium. Stained lymphocytes (2 × 10^6 cells/mL) were stimulated with anti-human CD3 (clone OKT3) and anti-human CD28 (clone 28.2) mAbs (each 100 ng/mL; eBioscience) in the presence of either medium, CsA (4.16 μM; Novartis Pharma), CPT (300 μM; Tocris), or plant extracts/single compounds (concentration range 0.3−30 μM) and incubated for 72 h. The negative control remained unstimulated. Flow cytometric analysis of the cell division was performed using a FACSCalibur instrument (BD Biosciences).

Determination of Apoptosis and Necrosis of T Cells. Lymphocytes were isolated, washed twice in cold PBS, and resuspended in medium at a concentration of 2 × 10^6 cells/mL. Cells were stimulated with anti-human CD3 (clone OKT3) and anti-human CD28 (clone 28.2) mAbs (each 100 ng/mL; eBioscience) in the presence of either medium, CPT (300 μM; Tocris), 0.5% Triton-X 100, or plant extracts and cultivated for 48 h. The negative control remained unstimulated. Cultured cells were washed with PBS and stained with annexin V-FITC using the apoptosis detection kit (eBioscience) according to the manufacturer's instructions. Propidium iodide (eBioscience) was added and cells were stained for 15 min at room temperature in the dark. Apoptosis and necrosis rates were determined by flow cytometric analysis using a FACSCalibur instrument (BD Biosciences).

Testing of Microfractions. The dried microfractions in 96-deep-well plates were dissolved in 25 μL of DMSO by sonication and mixing with a pipet. Of these stock solutions, dilutions of 1/1, 1/3, 1/10, and 1/30 were prepared and tested in duplicates for T lymphocyte proliferation inhibition as described above. Assuming an equal distribution of 200 ng substance in each of the microfractions, theoretical IC_{50} values were calculated as a relative measure of activity. They were normalized to 100%, with the highest value representing 100%.

Analysis of Data. For statistical analysis, data were processed with Microsoft Excel and SPSS software (IBM, version 22.0, Armonk, USA). Statistical significance was determined with the SPSS software. Statistical significance was determined with the SPSS software by a one-way ANOVA, followed by Dunnett's post hoc pairwise comparisons. Values are presented as mean ± SD for the indicated number of independent experiments. The asterisks represent significant differences from controls ($*p < 0.05$).

■ ASSOCIATED CONTENT

Supporting Information

The Supporting Information is available free of charge at https://pubs.acs.org/doi/10.1021/acs.jnatprod.0c00564.

> T lymphocyte proliferation data for *T. asiatica* MeOH extract, ^{1}H and ^{13}C NMR data for compounds **1−5**, **6a**, **8**, and **12−15**; experimental and computed ECD spectra of **7**, **8**, **11**, and **15** as well as UV spectra for compounds **7−13** and **15**; 1D and 2D NMR spectra and chiral-phase HPLC data (PDF)

■ AUTHOR INFORMATION

Corresponding Author

Matthias Hamburger − *Pharmaceutical Biology, Pharmacenter, University of Basel, 4056 Basel, Switzerland;* orcid.org/0000-0001-9331-273X; Phone: +41 61 207 14 25; Email: matthias.hamburger@unibas.ch; Fax: +41 61 207 14 74

Authors

Jakob K. Reinhardt − *Pharmaceutical Biology, Pharmacenter, University of Basel, 4056 Basel, Switzerland*

Amy M. Zimmermann-Klemd − *Center for Complementary Medicine, Institute for Infection Prevention and Hospital Epidemiology, Faculty of Medicine, University of Freiburg, 79106 Freiburg, Germany*

Ombeline Danton − *Pharmaceutical Biology, Pharmacenter, University of Basel, 4056 Basel, Switzerland*

Martin Smieško − *Pharmacenter, University of Basel, 4056 Basel, Switzerland;* orcid.org/0000-0003-2758-2680

Carsten Gründemann − *Pharmacenter, University of Basel, 4056 Basel, Switzerland*

Complete contact information is available at:
https://pubs.acs.org/10.1021/acs.jnatprod.0c00564

Notes

The authors declare no competing financial interest.

■ ACKNOWLEDGMENTS

C.G. is supported by PRIAM-BS (Verein Stiftungsprofessur für Integrative and Anthroposophische Medizin an der Universität Basel). ECD spectra were measured at the Biophysics Facility, Biozentrum, University of Basel. We are grateful to Andrea Treyer for measuring the HRESIMS data and to Orlando Fertig for technical support. Assunta Green, Daicel Technologies Europe, is gratefully acknowledged for providing the chiral-phase HPLC columns.

■ REFERENCES

(1) Davidson, A.; Diamond, B. *N. Engl. J. Med.* **2001**, *345* (5), 340−350.

(2) Skapenko, A.; Leipe, J.; Lipsky, P. E.; Schulze-Koops, H. *Arthrit. Res. Ther.* **2005**, *7*, S4−S14.

(3) Her, M.; Kavanaugh, A. *J. Allergy Clin. Immunol.* **2016**, *137* (1), 19−27.

(4) *Toddalia asiatica*; US National Plant Germplasm System. https://npgsweb.ars-grin.gov/gringlobal/taxonomydetail.aspx?36738 (24.04.2020).

(5) Zhou, J.; Xie, G.; Yan, X. *Isolated Compounds (T-Z) References TCM Plants and Congeners*; Springer: Berlin, Heidelberg, 2011; Vol. 5, p 455.

(6) Orwa, J. A.; Jondiko, I. J. O.; Minja, R. J. A.; Bekunda, M. *J. Ethnopharmacol.* **2008**, *115*, 257−262.

(7) Rajkumar, M.; Chandra, R. H.; Asres, K.; Veeresham, C. *Pharmacogn. Rev.* **2008**, *2* (4), 386−397.

(8) Li, W.; Zhang, J.-S.; Huang, J.-L.; Jiang, M.-H.; Xu, Y.-K.; Ahmed, A.; Yin, S.; Tang, G.-H. *RSC Adv.* **2017**, *7*, 31061−31068.

(9) Hu, J.; Shi, X.; Chen, J.; Mao, X.; Zhu, L.; Yu, L.; Shi, J. *Food Chem.* **2014**, *148*, 437−444.

(10) Hirunwong, C.; Sukieum, S.; Phatchana, R.; Yenjai, C. *Phytochem. Lett.* **2016**, *17*, 242−246.

(11) Potterat, O.; Hamburger, M. *Nat. Prod. Rep.* **2013**, *30*, 546−64.

(12) Tian, X.; Guo, S.; He, K.; Roller, M.; Yang, M.; Liu, Q.; Zhang, L.; Ho, C.-T.; Bai, N. *Nat. Prod. Res.* **2018**, *32* (3), 354−357.

(13) Takahashi, H.; Iguchi, M.; Onda, M. *Chem. Pharm. Bull.* **1985**, 33 (11), 4775−4782.

(14) Nakanishi, T.; Suzuki, M. *J. Nat. Prod.* **1998**, *61*, 1263−1267.

(15) Ishii, H.; Ishikawa, T.; Ichikawa, Y.; Sakamoto, M.; Ishikawa, M.; Takahashi, T. *Chem. Pharm. Bull.* **1984**, 32 (8), 2984−2994.

(16) Bunting, J. W. Heterocyclic Pseudobases. In *Advances in Heterocyclic Chemistry*; Katritzky, A. R.; Boulton, A. J., Eds.; Academic Press, 1980; Vol. 25, pp 1−82.

(17) Ramani, P.; Fontana, G. *Tetrahedron Lett.* **2008**, *49*, 5262−5264.

(18) Schramm, A.; Hamburger, M. *Fitoterapia* **2014**, *94*, 127−33.

(19) Lv, P.; Huang, K.; Xie, L.; Xu, X. *Org. Biomol. Chem.* **2011**, *9*, 3133−5.

(20) De, S.; Mishra, S.; Kakde, B. N.; Dey, D.; Bisai, A. *J. Org. Chem.* **2013**, *78*, 7823−7844.

(21) Arthur, H. R.; Ng, Y. L. *J. Chem. Soc.* **1959**, 4010−4012.

(22) Huang, S.-C.; Chen, M.-T.; Wu, T.-S. *Phytochemistry* **1989**, *28* (12), 3574−3576.

(23) Okamura, N.; Haraguchi, H.; Hashimoto, K.; Yagi, A. *Phytochemistry* **1994**, *37* (5), 1463−1466.

(24) Severi, J. A.; Fertig, O.; Plitzko, I.; Vilegas, W.; Hamburger, M.; Potterat, O. *Helv. Chim. Acta* **2010**, *93*, 1058−1066.

(25) Lin, T. T.; Huang, Y. Y.; Tang, G. H.; Cheng, Z. B.; Liu, X.; Luo, H. B.; Yin, S. *J. Nat. Prod.* **2014**, *77*, 955−62.

(26) Li, Y.; Sun, S.-W.; Zhang, X.-Y.; Liu, Y.; Liu, X.-H.; Zhang, S.; Wang, W.; Wang, J.; Wang, W. *Plants* **2020**, *9* (4), 428.

(27) Shibuya, H.; Takeda, Y.; Zhang, R.-s.; Tanitame, A.; Tsai, Y.-L.; Kitagawa, I. *Chem. Pharm. Bull.* **1992**, *40* (10), 2639−2346.

(28) Gao, H.-y.; Wang, H.-y.; Li, G.-y.; Du, X.-w.; Zhang, X.-t.; Han, Y.; Huang, J.; Li, X.-x.; Wang, J.-h. *Phytochem. Lett.* **2014**, *7*, 150−155.

(29) Chang, Y.-C.; Chen, C.-Y.; Chang, F.-R.; Wu, Y.-C. *J. Chin. Chem. Soc.* **2001**, *48*, 811−815.

(30) Sharma, P. N.; Shoeb, A.; Kapil, R. S.; Popli, S. P. *Phytochemistry* **1981**, *20*, 335−336.

(31) Ishii, H.; Kobayashi, J.-I.; Sakurada, E.; Ishikawa, T. *J. Chem. Soc., Perkin Trans. 1* **1992**, *1* (13), 1681−1684.

(32) Ishii, H.; Kobayashi, J.; Ishikawa, M.; Haginiwa, J.; Ishikawa, T. *Yakugaku Zasshi* **1991**, *111* (7), 365−375.

(33) El-Khatib, R. M.; Nassr, L. A.-M. E. *Spectrochim. Acta, Part A* **2007**, *67*, 643−648.

(34) Rao, G. K.; Gowda, N. B.; Ramakrishna, R. A. *Synth. Commun.* **2012**, *42*, 893−904.

(35) Yuan, Y.; Zhu, F.; Pu, Y.; Wang, D.; Huang, A.; Hu, X.; Qin, S.; Sun, X.; Su, Z.; He, C. *Brain, Behav., Immun.* **2015**, *48*, 287−300.

(36) Zhai, H.; Hu, S.; Liu, T.; Wang, F.; Wang, X.; Wu, G.; Zhang, Y.; Sui, M.; Liu, H.; Jiang, L. *Mol. Med. Rep.* **2016**, *13*, 2536−2542.

(37) Li, J.; Su, J.; Shan, L.; Zhang, S.; Zhang, W.; Dai, X.; Cao, X.; Yu, Y. Patent CN102008474B, 2010.

(38) Iwasaki, H.; Oku, H.; Takara, R.; Miyahira, H.; Hanashiro, K.; Yoshida, Y.; Kamada, Y.; Toyokawa, T.; Takara, K.; Inafuku, M. *Cancer Chemother. Pharmacol.* **2006**, *58*, 451−459.

(39) Frisch, M. J.; Trucks, G. W.; Schlegel, H. B.; Scuseria, G. E.; Robb, M. A.; Cheeseman, J. R.; Scalmani, G.; Barone, V.; Mennucci, B.; Petersson, G. A.; Nakatsuji, H.; Caricato, M.; Li, X. H. H. P.; Izmaylov, A. F.; Bloino, J. Z. G.; Sonnenberg, J. L.; Hada, M.; Ehara, M.; Toyota, K.; Fukuda, R.; Hasegawa, J.; Ishida, M.; Nakajima, T.; Honda, Y.; Kitao, O.; Nakai, H.; Vreven, T.; Montgomery, J. A., Jr.; Peralta, J. E.; Ogliaro, F.; Bearpark, M. J.; Heyd, J.; Brothers, E. N.; Kudin, K. N.; Staroverov, V. N.; Kobayashi, R.; Normand, J.; Raghavachari, K.; Rendell, A. P.; Burant, J. C.; Iyengar, S. S.; Tomasi, J.; Cossi, M.; Rega, N.; Millam, N. J.; Klene, M.; Knox, J. E.; Cross, J. B.; Bakken, V.; Adamo, C.; Jaramillo, J.; Gomperts, R.; Stratmann, R. E.; Yazyev, O.; Austin, A. J.; Cammi, R.; Pomelli, C.; Ochterski, J. W.; Martin, R. L.; Morokuma, K.; Zakrzewski, V. G.; Voth, G. A.; Salvador, P.; Dannenberg, J. J.; Dapprich, S.; Daniels, A. D.; Farkas, O.; Foresman, J. B.; Ortiz, J. V.; Cioslowski, J.; Fox, D. J. *Gaussian 09*; Gaussian, Inc.: Wallingford, CT, USA, 2009.

(40) Bruhn, T.; Schaumlöffel, A.; Hemberger, Y. *Spec Dis*, 1.64; University of Würzburg: Germany, 2015.

(41) *Maestro*, 11.0; Schrödinger, LLC: New York, NY, 2016.

(42) *Macro Model*, 11.0; Schrödinger, LLC: New York, NY, 2016.

(43) *Desmond Molecular Dynamics System*, 5.7; D. E. Shaw Research: New York, NY, 2019.

(44) *Desmond Interoperability Tools*, 11.0; Schrödinger, LLC: New York, NY, 2019.

(45) Bowers, K. J.; Chow, E.; Xu, H.; Dror, R. O.; Eastwood, M. P.; Gregersen, B. A.; Klepeis, J. L.; Kolossvary, I.; Moraes, M. A.; Sacerdoti, F. D.; Salmon, J. K.; Shan, Y.; Shaw, D. E. *Proceedings of the 2006 ACM/IEEE Conference on Supercomputing*; Association for Computing Machinery: Tampa, FL, 2006; pp 84-es.

Supporting Information

Compounds from *Toddalia asiatica*: Immunosuppressant Activity and Absolute Configurations

Jakob K. Reinhardt,[†] Amy M. Zimmermann-Klemd,[‡] Ombeline Danton,[†] Martin Smieško,[†]
Carsten Gründemann,[†] and Matthias Hamburger[†],*

[†]Pharmaceutical Biology, Computational Pharmacy, and Translational Complementary Medicine, Pharmacenter, University of Basel, Klingelbergstrasse 50, 4056 Basel, Switzerland

[‡]Center for Complementary Medicine, Institute for Infection Prevention and Hospital Epidemiology, Faculty of Medicine, University of Freiburg, Breisacher Straße 115 B, 79106 Freiburg, Germany

Table of Content

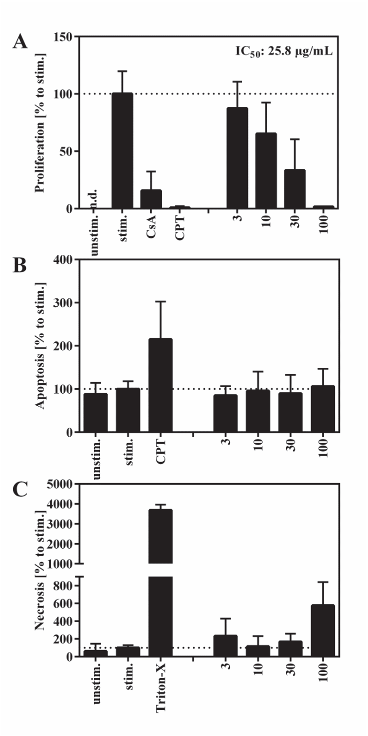

Figure S1. Inhibitory effects of *T. asiatica* MeOH extract on the proliferation (A) and viability (B, C) of T lymphocytes.

Human PBMCs (2 x 10^5) were stained with CFSE and stimulated with anti-CD3 and anti-CD28 monoclonal antibodies (mAbs, 100 ng/mL each). Unstimulated cells (unstim.) served as a control. Afterwards, cells were incubated for 72 h (A) or 48 h (B) in the presence of medium (unstim., stim.), cyclosporin A (CsA; 4.16 µM), camptothecin (CPT; 300 µM), Triton-X 100 (0.5%) or *T. asiatica* MeOH extract at increasing concentrations. (A) Cell division was analyzed by flow cytometry. The percentage of proliferating cells was normalized to the stimulated control and depicted as mean ± standard deviation. n=2. (B, C) Annexin V-FITC and PI double staining was performed. The proportions of viable, necrotic, and apoptotic cells were analyzed via flow cytometry. The amount of apoptotic (B) and necrotic (C) lymphocytes compared to the stimulated control was determined and depicted as mean ± standard deviation. n = 2.

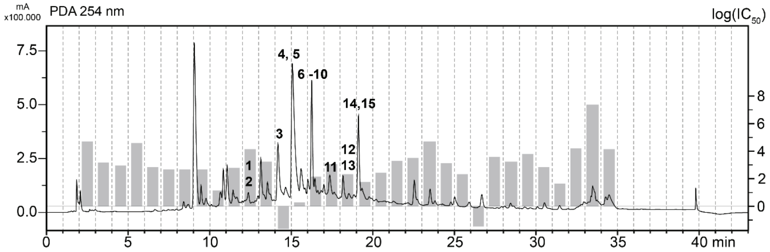

Figure S2. HPLC Chromatogram at 254 nm and activity profile (grey bars) of a MeOH extract of *T. asiatica* roots. Inhibition of T cell proliferation is presented as log(IC_{50}) calculated from dilutions of each microfraction assuming an average of 200 µg extract per microfraction. Bold numbers in the chromatogram refer to compounds **1-15**.

Table S1. ^1H and ^{13}C NMR Spectroscopic Data (500 MHz, methanol-d_4) for Compound **1**

	1[a]	
position	δ_C, type[a]	δ_H (*J* in Hz)
1	120.6, C	
2, 6	107.3, CH	7.32, s
3, 5	147.5, C	
4	140.5, C	
7	168.5, C	
8, 9	55.5, CH_3	3.87, s
OH		4.73, br s

[a] ^{13}C extracted from ^1H–^{13}C 2D inverse-detected experiments.

Table S3. ^{1}H and ^{13}C NMR Spectroscopic Data (500 MHz, DMSO-d_6/TFA ratio 10:1) for Compounds **3a**, **3b**, and **3c** (in methanol-d_4). Spectra of **3a** and **3b** were recorded in a mixture (molar ratio 4:1).

	3a		**3b**		**3c**	
position	δ_C, type[a]	δ_H (J in Hz)	δ_C, type[a]	δ_H (J in Hz)	δ_C, type[a]	δ_H (J in Hz)
1	104.9, CH	7.27[b]	104.5, CH	8.15, s	105.3, CH	7.13, s
2	149.2, C		149.0, C		149.4, C	
3	148.0, C		149.0, C		148.6, C	
4	98.6, CH	7.56, s	106.1, CH	7.53, s	101.0, CH	7.65, s
4a	123.5, C		120.4, C		128.0, C	
4b	134.4, C		131.7, C		138.9, C	
6	49.7, CH$_2$	4.46, s	150.1, CH	9.88, s	87.6, CH	5.53, s
6a	122.0, C		120.0, C		126.2, C	
7	145.3, C		143.7, C		146.7, C	
8	151.1, C		149.4, C		150.8, C	
9	117.3, CH	6.99, d (8.5)	130.8, CH	7.92, d (8.9)	118.4, CH	7.02, d (8.5)
10	120.2, CH	7.50, d (8.5)	119.3, CH	8.49[b]	120.1, CH	7.56, d (8.5)
10a	122.3, C		128.0, C		125.1, C	
10b	124.7, C		125.8, C		124.5, C	
11	120.4, CH	7.74, d (8.5)	118.7, CH	8.5[b]	124.5, CH	7.48, d (8.5)
12	127.3, CH	7.67, d (8.5)	131.2, CH	8.09[b]	120.6, CH	7.77, d (8.5)
12a	130.9, C		132.4, C		132.3, C	
13	102.0, CH$_2$	6.12, s	102.9, CH$_2$	6.26, s	102.3, CH$_2$	6.04, s
14	41.6, CH$_3$	2.75, s	52.4, CH$_3$	4.93, s	40.7, CH$_3$	2.74, s
15	60.7, CH$_3$	3.81, s	61.9, CH$_3$	4.15, s	61.9, CH$_3$	3.94, s
16					53.1, CD$_3$	[c]

[a] ^{13}C extracted from ^{1}H–^{13}C 2D inverse-detected experiments. [b] Overlapping signals. [c] Signal not found.

Table S2. ^{1}H and ^{13}C NMR Spectroscopic Data (500 MHz, DMSO-d_6) for Compound **2** at 23°C and 60°C.

	2 (at 23°C)		**2** (at 60°C)	
position	δ_C, type[a]	δ_H (J in Hz)	δ_C, type[a]	δ_H (J in Hz)
1	106.8, CH	7.01, s	107.1, CH	6.92, s[b]
2	145.3, C		144.8, C	
3	147.0, C		146.6, C	
4	109.2, CH	6.79, s	109.5, CH	6.76, s
4a	132.6, C		135.1, C	
5	28.2, CH$_2$	2.93[b]	30.0, CH$_2$	2.84, m
6	55.6, CH$_2$	2.87[b]	56.5, CH$_2$	2.49[b]
8	51.5, CH$_2$	3.93, br s	49.9, CH$_2$	3.67[b]
8a	[c]		129.0, C	
9	145.8, C		146.3, C	
10	150.4, C		150.4, C	
11	111.2, CH	6.92[b]	110.5, CH	6.86, d (8.5)
12	126.3, CH	6.94[b]	126.9, CH	6.91, d (8.5)[b]
12a	[c]		128.1, C	
13	[c]	[c]	45.1, CH$_2$	3.71[b]
14	[c, d]		[c]	
14a	129.6, C		131.7, C	
15	100.8, CH$_2$	5.99, s	100.4, CH$_2$	5.98, s
16	41.0, CH$_3$	2.15, s	40.3, CH$_3$	1.84, s
17	59.8, CH$_3$	3.70, s	59.6, CH$_3$	3.67, s[b]
18	55.3, CH$_3$	3.79, s	55.0, CH$_3$	3.78, s

[a] ^{13}C extracted from ^{1}H–^{13}C 2D inverse-detected experiments. [b] Overlapping signals. [c] Signal not found. [d] δ_C of C-14 not visible due to limited amount, expected at 194 ppm (Takahashi, 1985)

Table S4. ^{1}H and ^{13}C NMR Spectroscopic Data (500 MHz, DMSO-d_6) for Compounds **4** and **5**. Compound **4** in its crude form was measured in DMSO-d_6 + TFA ratio 2:1.

	4	Crude **4** in DMSO-d_6 and TFA		**5**	
position	δ_H (J in Hz)	δ_C, type^a	δ_H (J in Hz)	δ_C, type^a	δ_H (J in Hz)
1	7.77, s	106, CH	7.53, s	103.9, CH	7.28, s
2		148.9, C		146.9, C	
3		149.2, C		147.6, C	
4	8.37, s	104.7, CH	8.15, s	99.5, CH	7.51, s
4a		120, C		125.5, C	
4b		132.7, C		142, C	
6	9.91, s	151.3, CH	9.70, s	53.7, CH$_2$	4.08, s
6a		119.7, C		124.2, C	
7	7.94, s	109, CH	7.74, s	110.7, CH	6.96, s
8		152, C		148.6, C	
9		158.7, C		148.2, C	
10	8.31, s	103.4, CH	8.1, m	106.9, CH	7.42, s
10a		132.2, C		123.9, C	
10b		124.2, C		123.9, C	
11	8.90, d (9.2)	119.2, CH	8.60, d (8.9)	120, CH	7.83, d (8.9)
12	8.29, d (9.2)	130.3, CH	8.06, d (8.9)	123.4, CH	7.55, d (8.9)
12a		132.7, C		130.2, C	
13	6.34, s	103, CH$_2$	6.28, s	100.9, CH$_2$	6.11, s
14	4.91, s	51.8, CH$_3$	4.83, s	40.5, CH$_3$	2.50^b
15	4.24, s	56.5, CH$_3$	4.01, s	55.5, CH$_3$	3.81, s
16	4.05, s	57.4, CH$_3$	4.17, s	55.7, CH$_3$	3.87, s

^{a} ^{13}C extracted from ^{1}H–^{13}C 2D inverse-detected experiments. ^{b} Overlapping signals.

Table S5. ^{1}H and ^{13}C NMR Spectroscopic Data (500 MHz, DMSO-d_6) for Compound **8**

	8	
position	δ_C, type^a	δ_H (J in Hz)
2	77.9, CH	5.5, dd (11.9, 3.0)
3	41.7, CH$_2$	3.23, m
		2.80^b
4	196.5, C	
4a	103.1, C	
5	162.7, C	
6	96.2, CH	6.15^b
7	164.8, C	
8	95.3, CH	6.13^b
8a	162.2, C	
9	55.4, CH$_3$	3.78, s
1'	130.7, C	
2'	113.9, CH	6.95^b
3'	146.2, C	
4'	147.7, C	
5'	112.0, CH	6.93^b
6'	117.5, CH	6.90, m
1''	99.3, CH	4.97, d (7.3)
2''	72.7, CH	3.26^b
3''	76.0, CH	3.3, m
4''	69.4, CH	3.17^b
5''	75.3, CH	3.54, m
6''	65.8, CH$_2$	3.46^b
1'''	100.3, CH	4.55, m
2'''	70.0, CH	3.66, m
3'''	70.5, CH	3.46^b
4'''	71.8, CH	3.18^b
5'''	67.9, CH	3.43^b
6'''	17.4, CH$_3$	1.10, d (6.1)
OH		11.98, br s
OH		5.02, br d (3.7)
OH		4.48, br d (3.4)
OH		5.06, br d (4.9)
OH		8.96, br s
OH		4.32, br s
OH		5.29, br d (4.3)

^{a} ^{13}C extracted from ^{1}H–^{13}C 2D inverse-detected experiments. ^{b} Overlapping signals.

Table S6. ^{1}H and ^{13}C NMR Spectroscopic Data (500 MHz, CDCl3) for Compounds **9a** and **9b**. Spectra of **9a** and **9b** were recorded as mixture.

	9a		**9b**	
position	δ_C, type[a]	δ_H (J in Hz)	δ_C, type[a]	δ_H (J in Hz)
2	161.2, C		160.8, C	
3	112.6, CH	6.22, d (9.8)[b]	112.5, CH	6.22, d (9.5)[b]
4	138.6, CH	7.84, d (9.8)[b]	138.6, CH	7.82[b]
4a	107, C		107.1, C	
5	156.1, C		156.2, C	
6	114.6, C		116.2, C	
7	161.4, C		161.3, C	
8	95.4, CH	6.61, s	95.5, CH	6.59, s
8a	155.5, C		155.5, C	
9	63.1, CH_3	3.78, s	62.7, CH_3	3.79, s[b]
10	56, CH_3	3.82, s[b]	55.5, CH_3	3.81, s[b]
1'	35.5, CH_2	3.80[b]	30.9, CH2	2.84, s
2'	211.3, C		47, C	
3'	40.6, CH	2.77, spt (6x7.0)	204.7, CH	9.49, s
4'	18.3, CH_3	1.18, d (7.0)	21.5, CH_3	1.03, s
5'	18.3, CH_3	1.18, d (7.0)	21.5, CH_3	1.03, s

[a] ^{13}C extracted from ^{1}H–^{13}C 2D inverse-detected experiments. [b] Overlapping signals.

Table S7. ^{1}H and ^{13}C NMR Spectroscopic Data (500 MHz, methanol-d_4) for Compounds **12** and **13**.

	12		**13**	
position	δ_C, type	#	δ_C, type	δ_H (J in Hz)
1	34.0, CH_2	2.60, dd (14.9, 11.3)	36.3, CH_2	2.55[a]
		2.67, dd (14.9, 4.6)		
2	41.0, CH	1.68, m	44.0, CH	1.90, m
3	46.7, CH	2.16, m	41.3, CH	2.08, m
4	43.2, CH	4.33[a]	36.7, CH_2	2.53[a]
				2.67, dd (13.7, 6.7)
5	147.7, C		149.0, C[b]	
6	139.0, C		134.5, C[a]	
7	148.7, C		149.0, C[b]	
8	107.8, CH	6.5, s	107.4, CH[c]	6.32, s[c]
9	130.3, C		133.4, C	
10	126.4, C		107.4, CH[c]	6.32, s[c]
11	66.2, CH_2	3.56[a]	62.8, CH2	3.52[a]
		3.65, dd (10.8, 4.1)		3.64, dd (11.0, 5.5)
12	72.1, CH_2	3.52[a]	71.2, CH2	3.50[a]
		3.88, dd (9.8, 5.5)		4.01, dd (9.5, 5.8)
13	60.3, CH_3	3.37, s	56.7, CH3[d]	3.70, m[d]
14	56.6, CH_3	3.79, s	56.7, CH3[d]	3.70, m[d]
1'	139.5, C		133.1, C	
2', 6'	107.1, CH	6.43, s	107.2, CH	6.29, s
3', 5'	149.1, C		149.1, C	
4'	134.6, C		134.5, C[a]	
7', 8'	57.0, CH_3	3.74, s	56.8, CH_3	3.72, s
1''	105, CH	4.30[a]	104.8, CH	4.27, d (7.6)
2''	75.2, CH	3.31, dd (7.9, 7.6)	75.4, CH	3.26, t (7.9)
3''	78.2, CH	3.44,[a]	78.3, CH	3.40[a]
4''	71.9, CH	3.42[a]	72.2, CH	3.36[a]
5''	75.5, CH	3.53[a]	75.5, CH	3.53[a]
6''	64.9, CH_2	4.35[a]	64.8, CH_2	4.38, dd (11.9, 6.1)
		4.49, d (11.0)		4.50, d (11.3)
1'''	169.2, C		169.1, C	
2'''	115.8, CH	6.38, d (15.9)	115.8, CH	6.36, d (15.9)
3'''	147.5, CH	7.60, d (15.9)	147.5, CH	7.57, d (15.9)
4'''	126.7, C		126.8, C	
5''', 9'''	107.0, CH	6.84, s	107.0, CH	6.81, s
6''', 8'''	149.6, C		149.6, C	
10''', 11'''	57.0, CH_3		57.0, CH_3	3.82, s

[a] Overlapping signals, [b, c, d] pairs of chemically equivalent nuclei

Table S8. ^{1}H and ^{13}C NMR Spectroscopic Data (500 MHz, DMSO-d_6) for Compound **14**

	14	
position	δC, type	δH (*J* in Hz)
1	125.4, C	
2, 6	128.7, CH	7.37, d (8.5)
3, 5	115.5, CH	6.8, d (8.5)
4	158.7, C	
7	138.3, CH	7.32, d (15.6)
8	118.4, CH	6.41, d (15.6)
9	165.1, C	
1'	129.0, C	
2', 6'	129.0, CH	7.01, d (8.3)
3', 5'	114.8, CH	6.7, d (8.3)
4'	155.3, C	
7'	34.1, CH$_2$	2.66, t (7.3)
8'	40.1, CH$_2$	3.34, td (2x7.3, 5.5)
NH		7.95, t (5.5)

Table S9. ^{1}H and ^{13}C NMR Spectroscopic Data (500 MHz, CDCl$_3$) for Compound **15**, a mixture of both enantiomers (**15a** and **15b**).

	15	
position	δC, type	δH (*J* in Hz)
2	161.0, C	
3	112.8, CH	6.19, d (9.8)
4	138.7, CH	7.81, d (9.8)
4a	107.2, C	
5	155.9, C	
6	117.8, C	
7	161.4, C	
8	95.7, CH	6.61, s
8a	155.0, C	
11	63.2, CH$_3$	3.86, s
12	56.2, CH$_3$	3.87, s
1'	26.1, CH$_2$	2.75, dd (13.8, 10.1) 2.89, dd (13.8, 1.8)
2'	78.1, CH	3.60, dd (10.1, 1.8)
3'	72.9, C	
4'	23.6, CH$_3$	1.27, s[a]
5'	26.1, CH$_3$	1.28, s[a]

[a] Overlapping signals

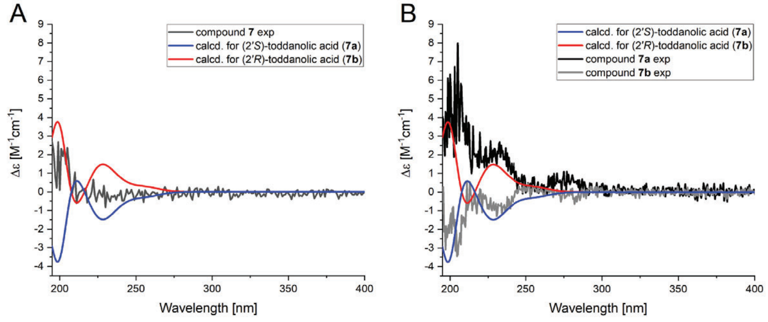

Figure S3. Experimental ECD Spectra of Compound **7** (A), and Compounds **7a** and **7b** (B) compared to the computed ECD spectra of **7a** and **7b** in MeOH (calcd. spectrum shifted by +5 nm).

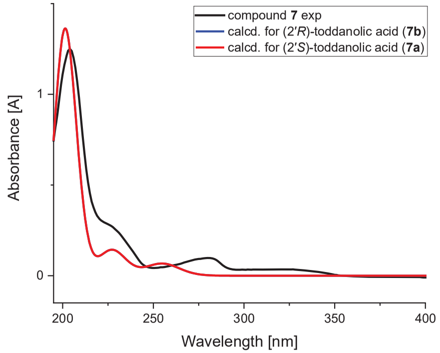

Figure S4. Experimental UV Spectrum of Compound **7** compared to the computed UV spectra of compounds **7a** and **7b** in MeOH (calcd. spectrum shifted by +5 nm).

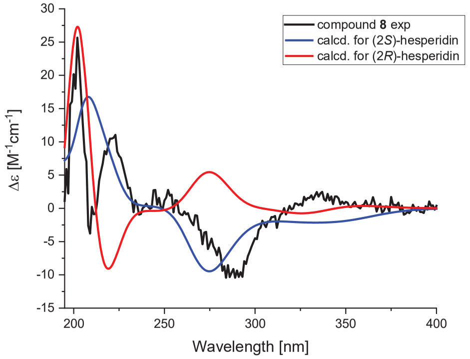

Figure S5. Experimental ECD Spectrum of Compound **8** compared to the computed ECD spectra of its diastereomers in MeOH.

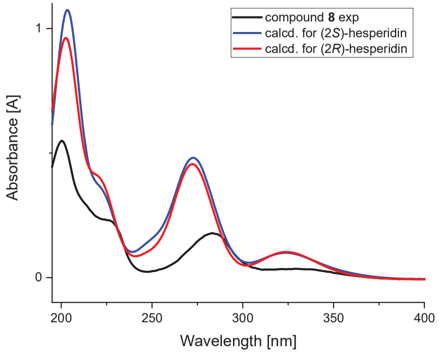

Figure S6. Experimental UV Spectrum of Compound **8** compared to the computed ECD spectra of its diastereomers in MeOH.

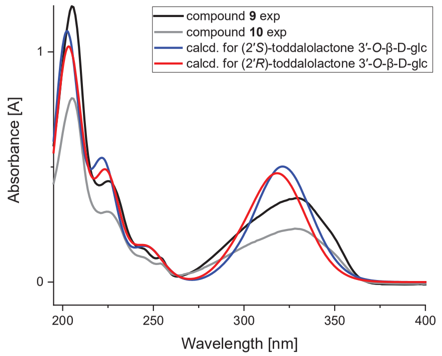

Figure S7. Experimental UV spectra of compounds **9** and **10** compared to the computed ECD spectra of possible diastereomers in MeOH (calcd. spectrum shifted by +5 nm).

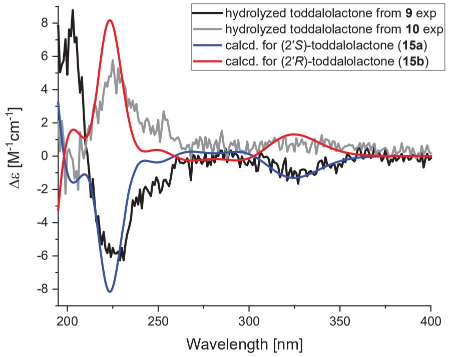

Figure S8. Experimental ECD spectra of aglycones from compounds **9** and **10**, and calculated spectra of (2’*S*)- and (2’*R*)-toddalolactone (calcd. spectrum shifted by +5 nm).

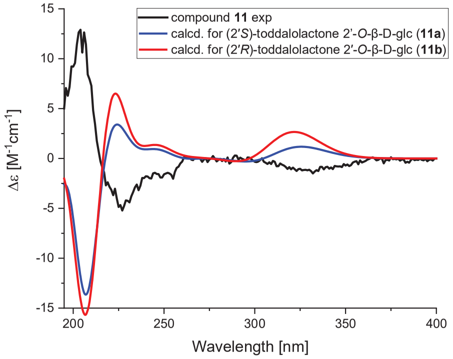

Figure S9. Experimental ECD Spectrum of Compound **11** compared to the computed ECD spectra of compounds **11a** and **11b** in MeOH (calcd. spectrum shifted by +5 nm).

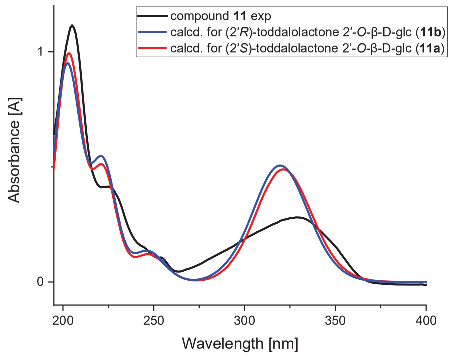

Figure S10. Experimental UV Spectrum of Compound **11** compared to the computed UV spectra of compounds **11a** and **11b** in MeOH (calcd. spectra shifted by +5 nm).

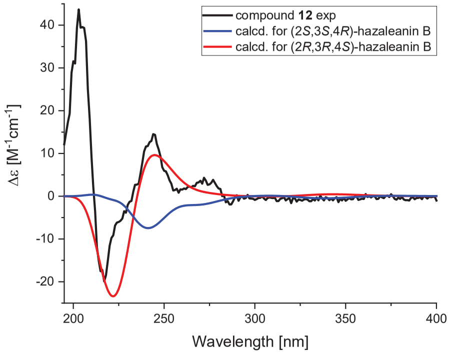

Figure S11. Experimental ECD Spectrum of Compound **12** and calculated spectra of both possible stereoisomers.

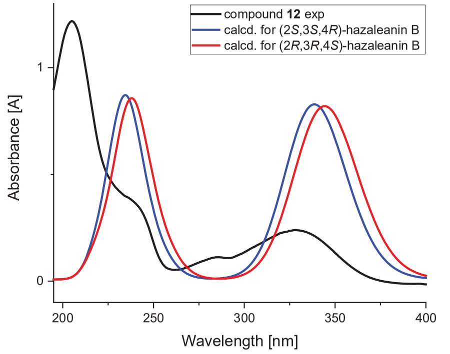

Figure S12. Experimental UV Spectrum of Compound **12** compared to computed UV spectra possible diastereomers in MeOH.

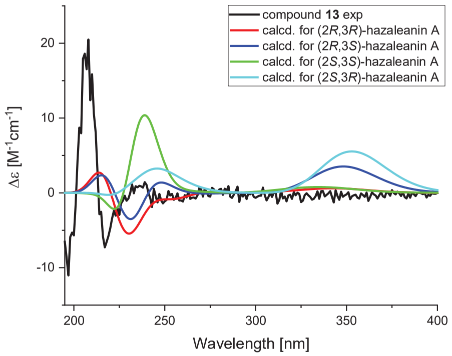

Figure S13. Experimental ECD Spectrum of Compound **13**, and calculated spectra of all four possible stereoisomers.

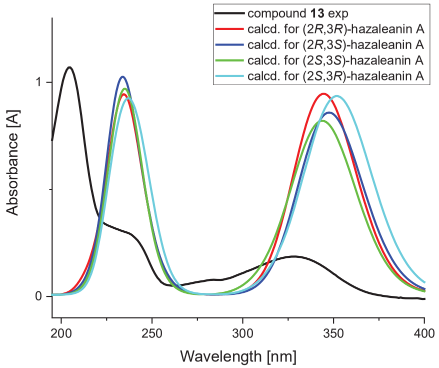

Figure S14. Experimental UV Spectrum of Compound **13** compared to computed UV spectra possible diastereomers in MeOH.

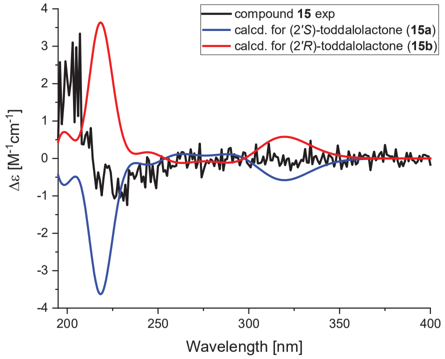

Figure S15. Experimental ECD Spectrum of Compound **15** compared to the computed ECD spectra of compounds **15a** and **15b** in MeOH.

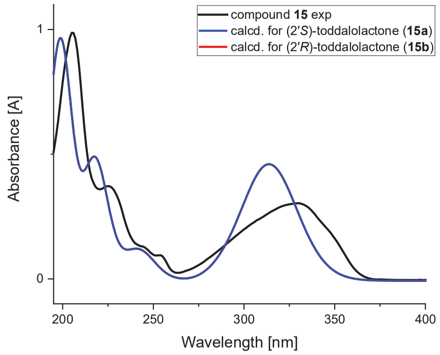

Figure S16. Experimental UV Spectrum of Compound **15** compared to the computed UV spectra of compounds **15a** and **15b** in MeOH.

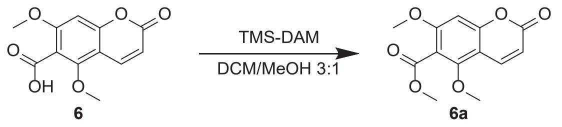

Figure S17. Methylation of compound **6**.

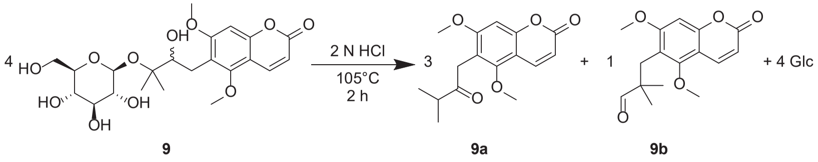

Figure S18. Major compounds obtained from acid hydrolysis of compound **9**. Analogously for compounds **10** and **11**.

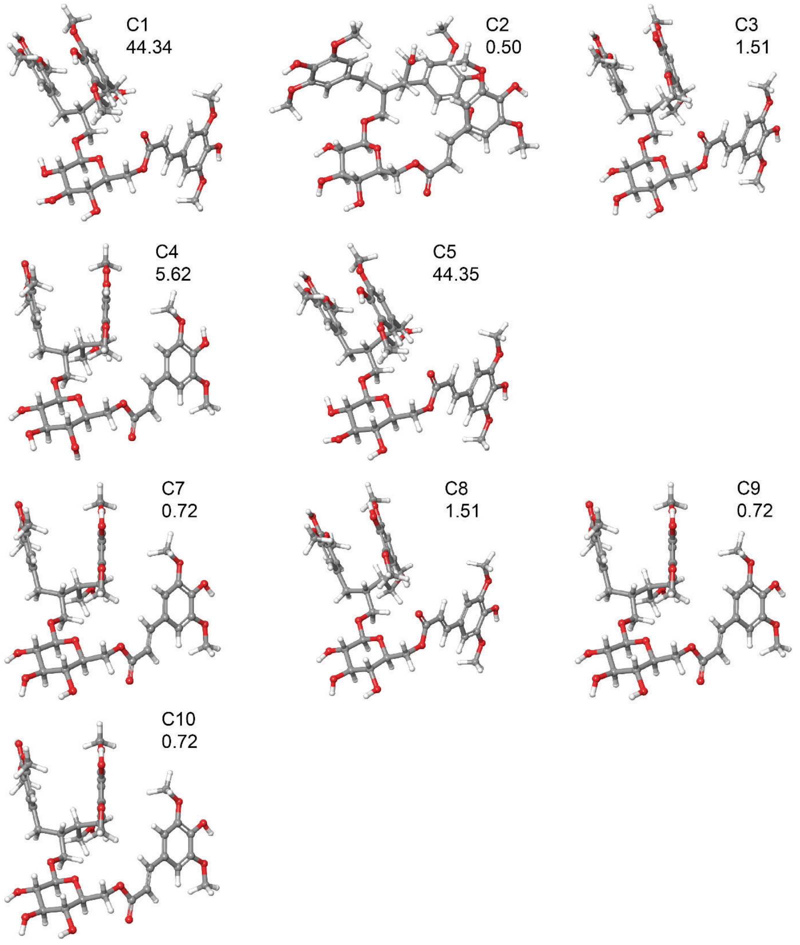

Figure S19. Conformers C1-C10 of (2*R*,3*R*)-hazaleanin A (**13**) calculated in explicit MeOH, which were used for *ab initio* calculation of conformer ECD spectra. The Boltzmann factor used to weigh the impact of each is displayed next to the conformer. The calculation of C6 was not successful.

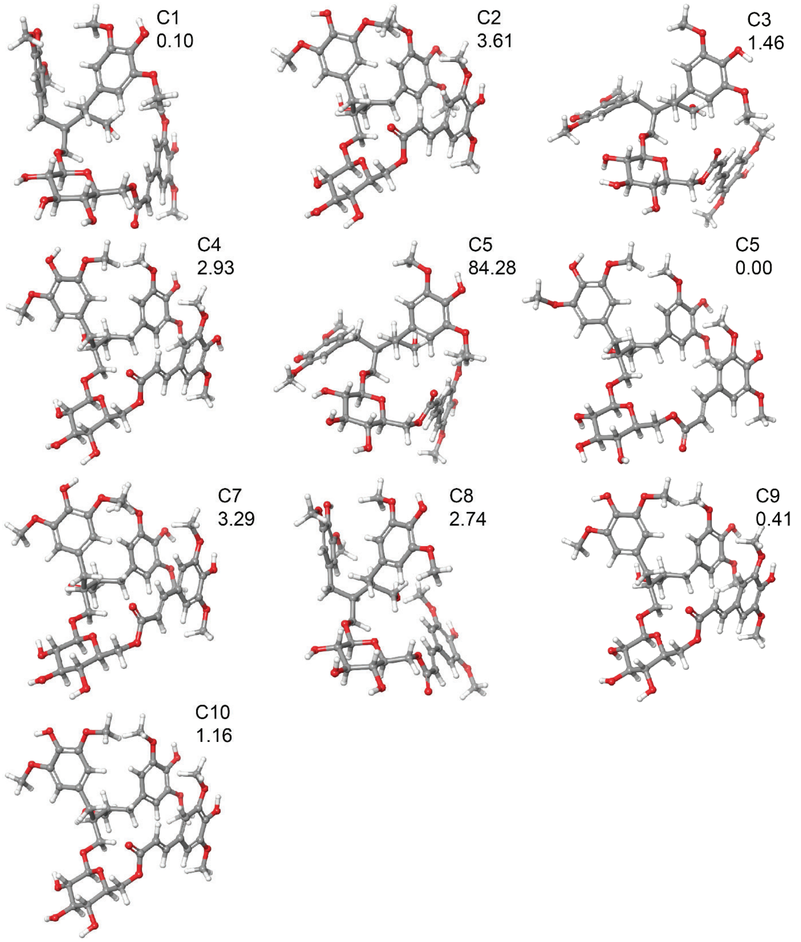

Figure S20. Conformers C1 - C10 of (2*R*,3*S*)-hazaleanin A (**13**) calculated in explicit MeOH, which were used for *ab initio* calculation of conformer ECD spectra. The Boltzmann factor used to weigh the impact of each is displayed next to the conformer.

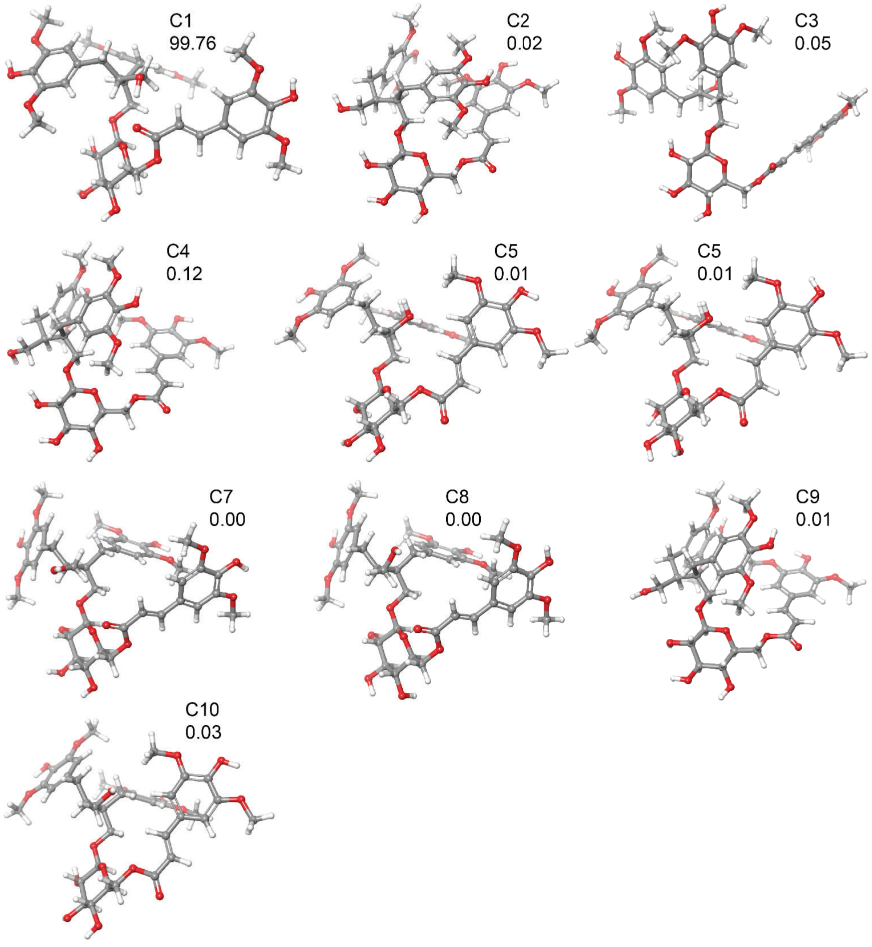

Figure S21. Conformers C1-C10 of (2*S*,3*R*)-hazaleanin A (**13**) calculated in explicit MeOH, which were used for *ab initio* calculation of conformer ECD spectra. The Boltzmann factor used to weigh the impact of each is displayed next to the conformer.

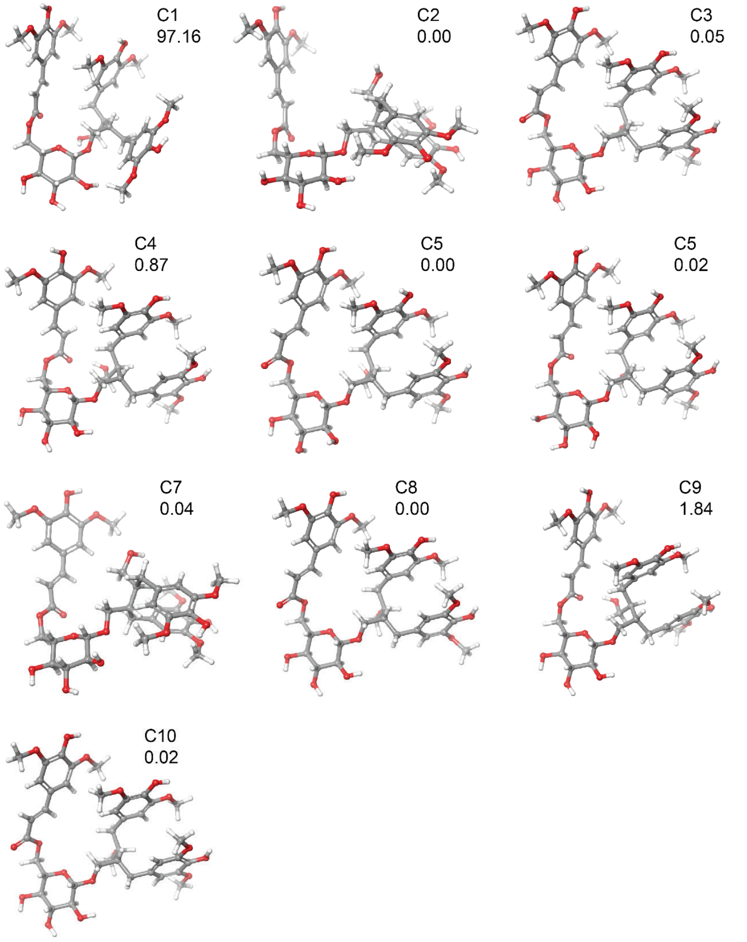

Figure S22. Conformers C1 - C10 of (2*S*,3*S*)-hazaleanin A (**13**) calculated in explicit MeOH, which were used for *ab initio* calculation of conformer ECD spectra. The Boltzmann factor used to weigh the impact of each is displayed next to the conformer.

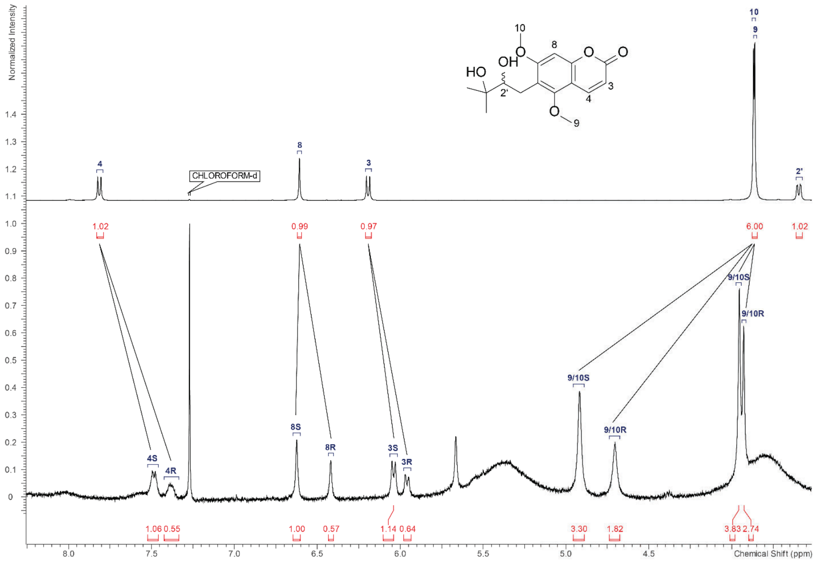

Figure S23. ^{1}H NMR spectra of compound **15** in $CHCl_3$ without shift reagent (upper spectrum) and with 1.5 eq $Eu(hfc)_3$ as shift reagent (lower spectrum). Signals originating from (2'*S*)-toddalolactone are labeled as "S" and from (2'*R*)-toddalolactone are "R". The assignment of CH_3-9 and CH_3-10 in the lower spectrum may be reversed.

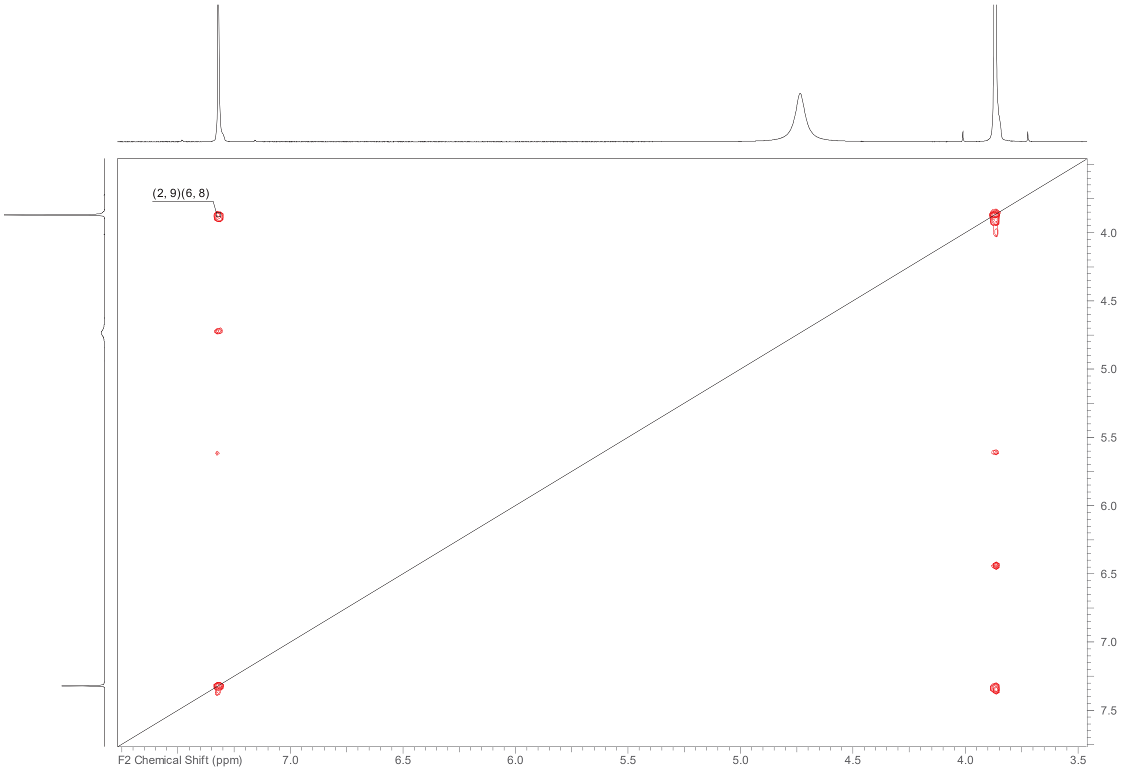

Figure S25. ^{1}H-^{1}H COSY Spectrum of Compound **1** (500 MHz, DMSO-d_6).

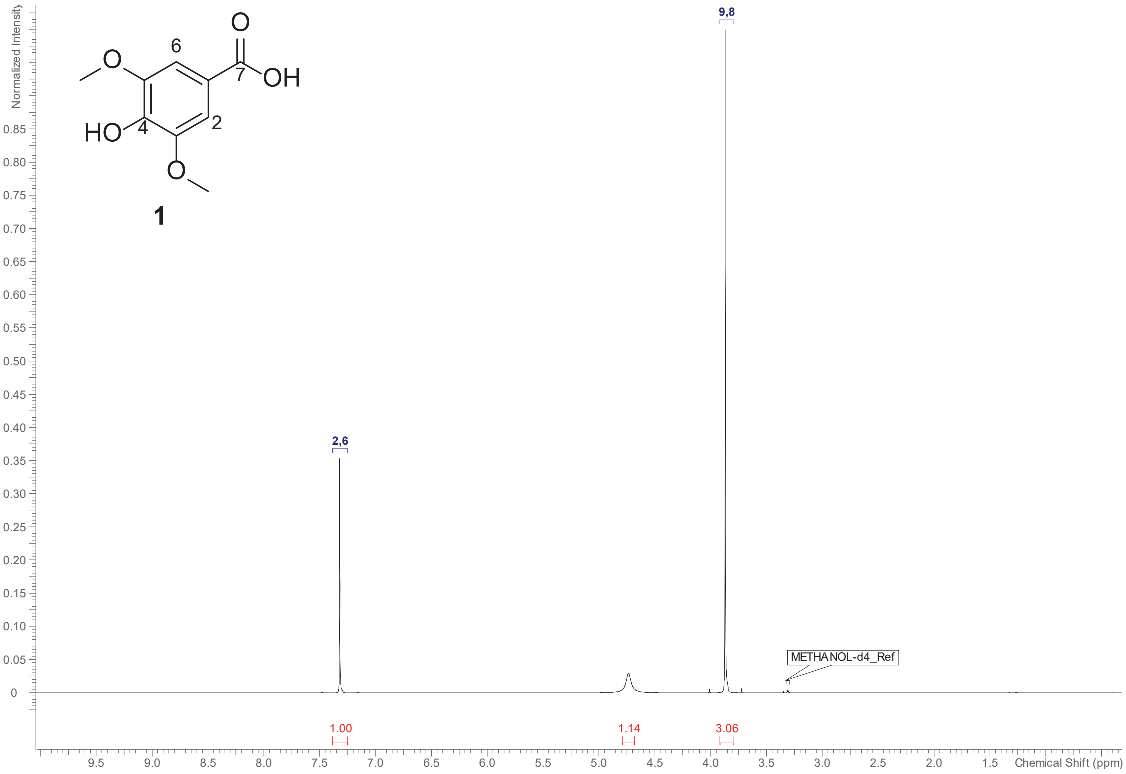

Figure S24. ^{1}H NMR Spectrum of Compound **1** (500 MHz, DMSO-d_6).

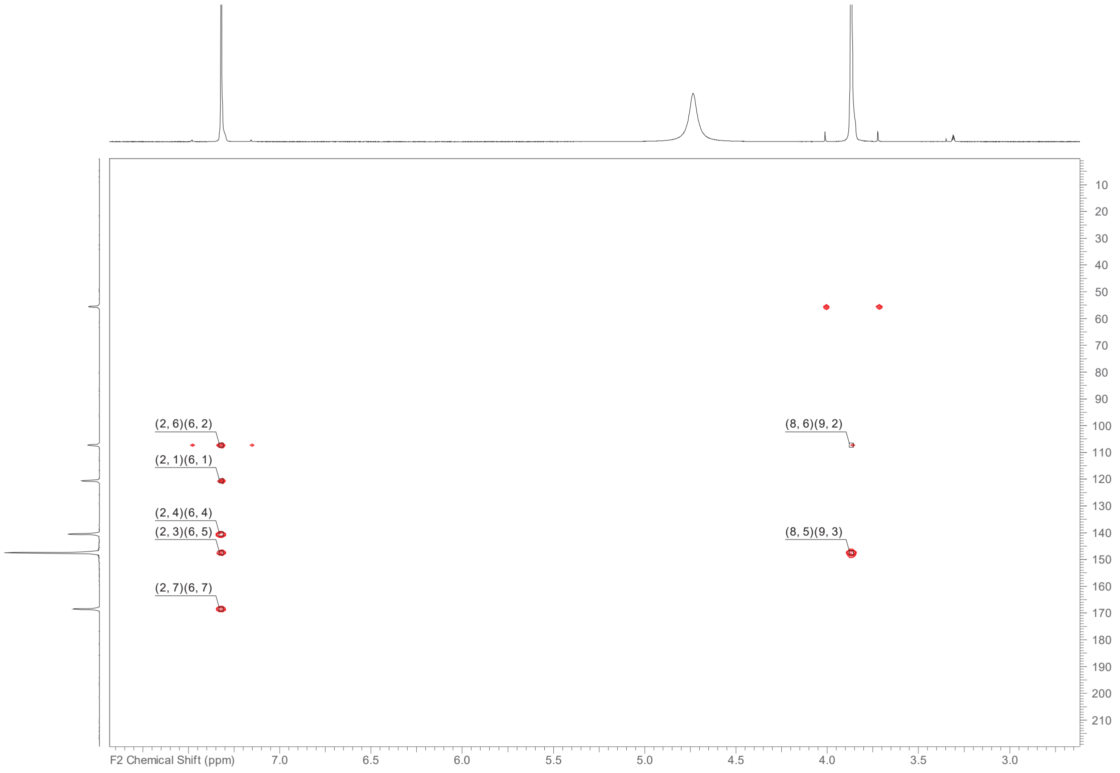

Figure S27. HMBC Spectrum of Compound **1** (500 MHz, DMSO-*d*$_6$, 23°C).

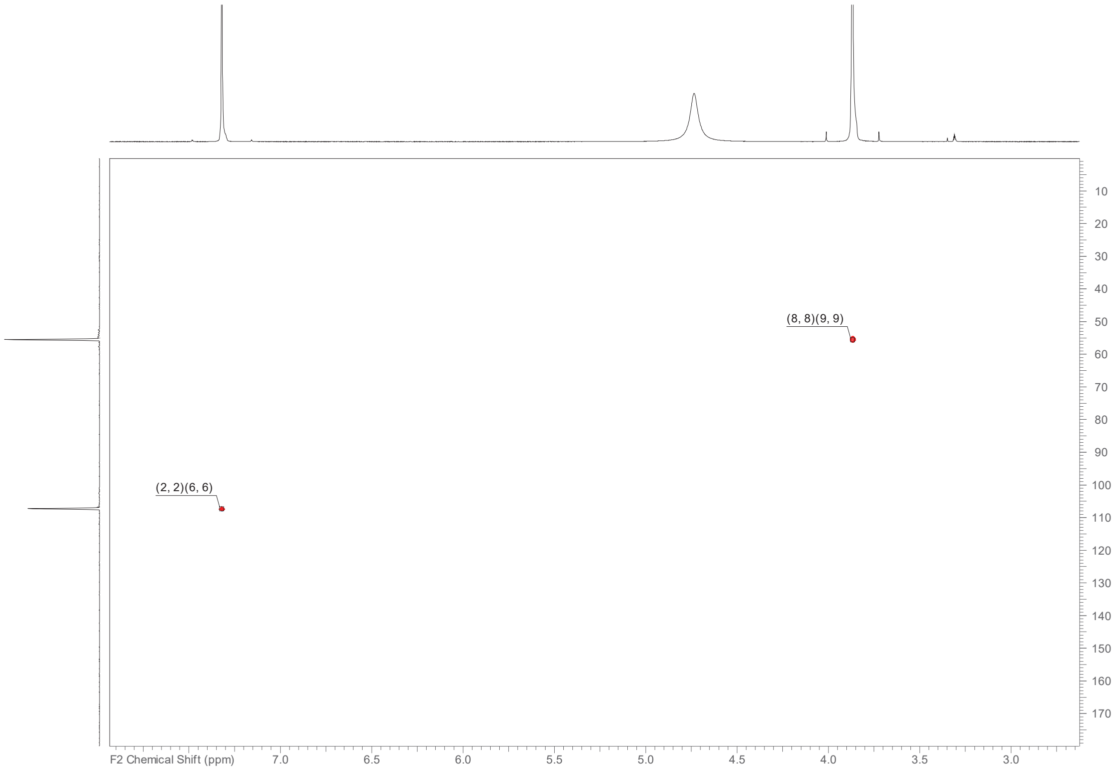

Figure S26. HSQC-DEPT Spectrum of Compound **1** (500 MHz, DMSO-*d*$_6$).

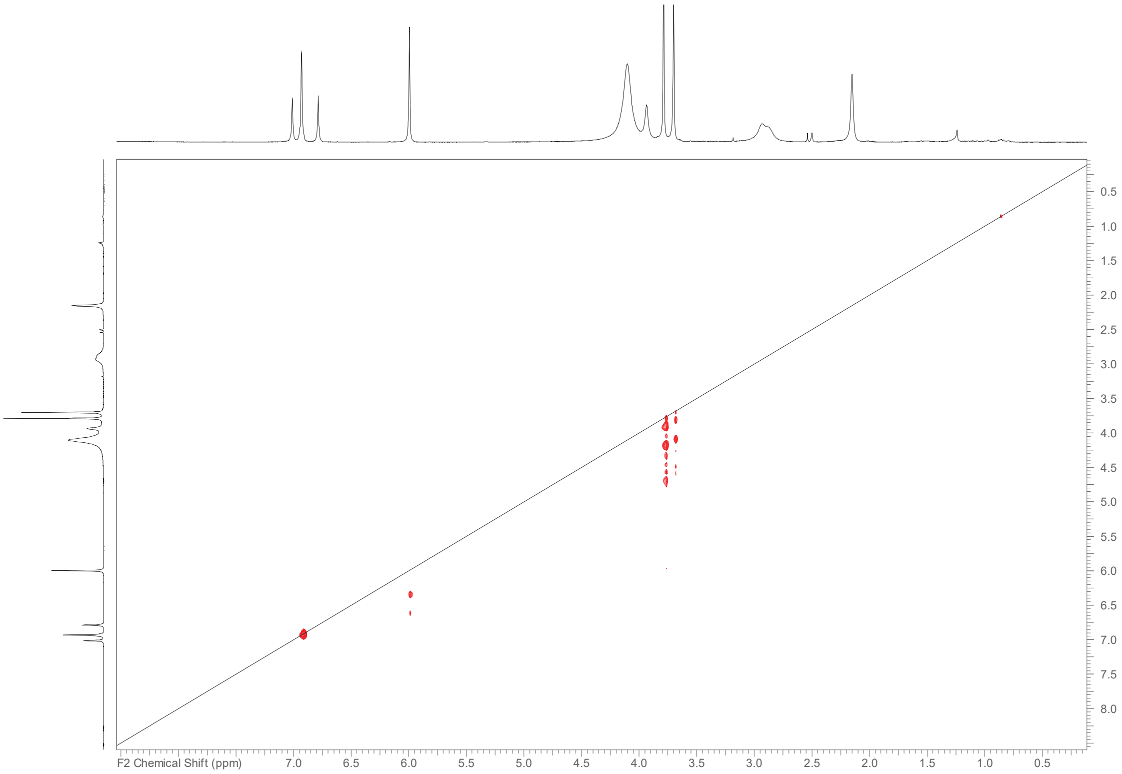

Figure S29. ^{1}H-^{1}H COSY Spectrum of Compound **2** (500 MHz, DMSO-d_6, 23°C).

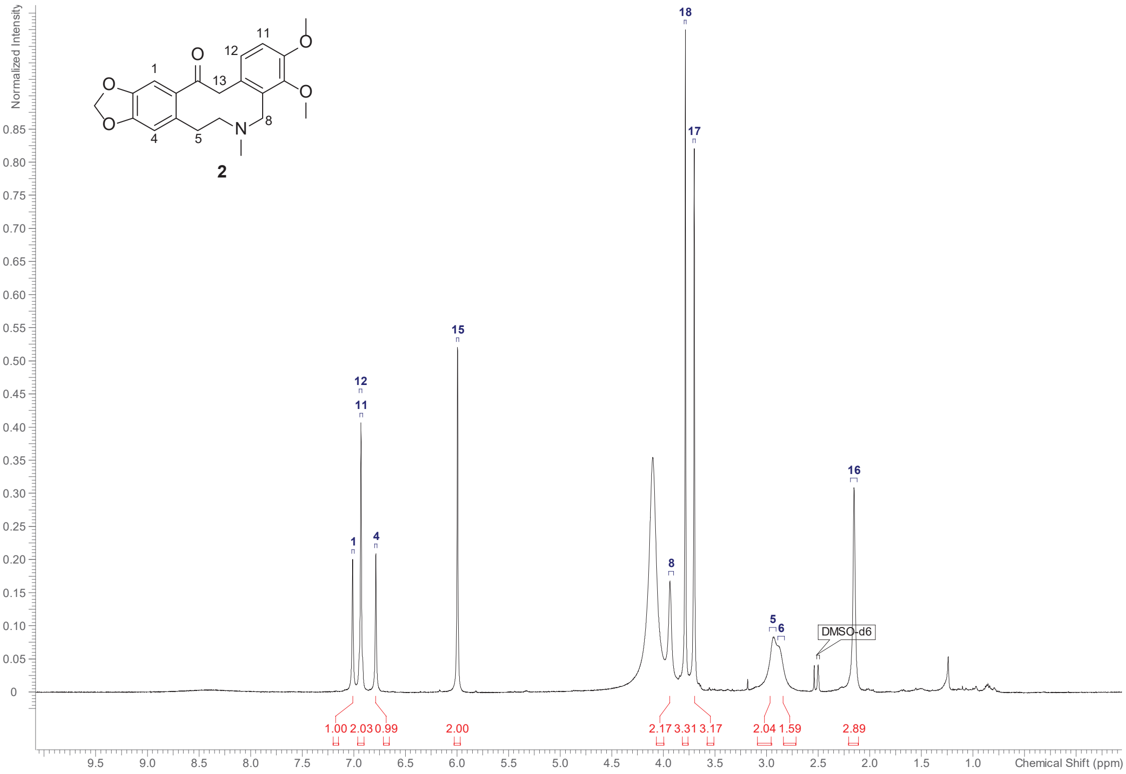

Figure S28. ^{1}H NMR Spectrum of Compound **2** (500 MHz, DMSO-d_6, 23°C).

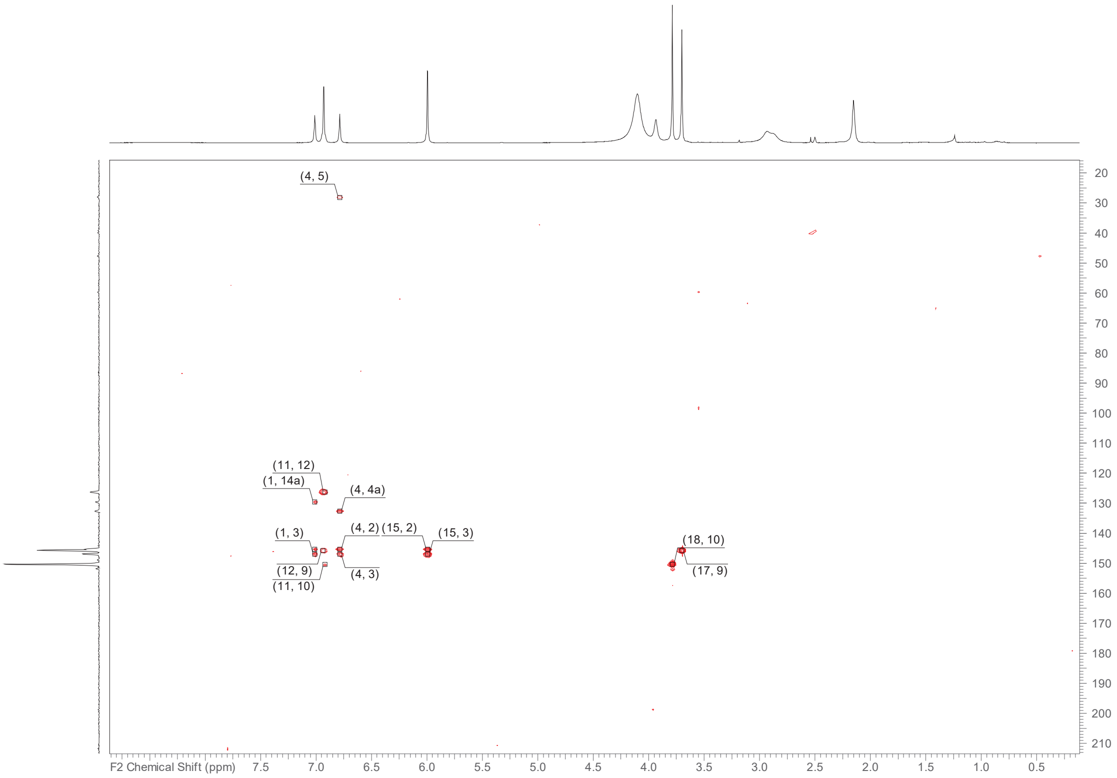

Figure S31. HMBC Spectrum of Compound **2** (500 MHz, DMSO-d_6, 23°C).

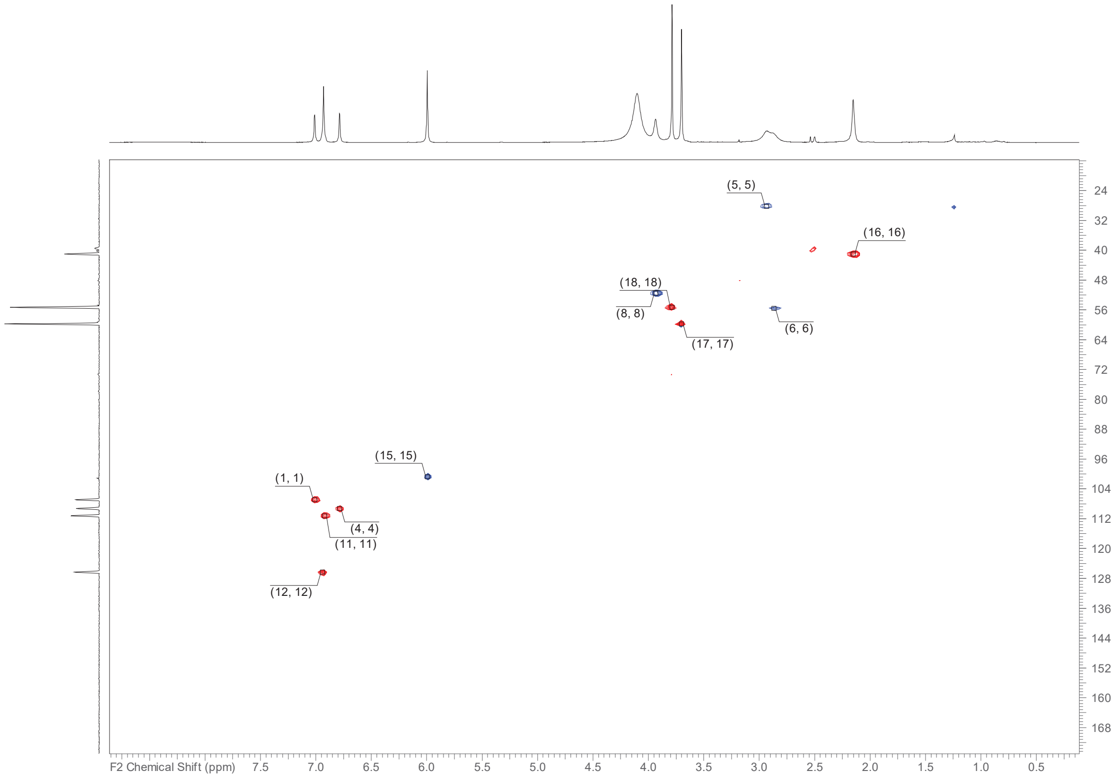

Figure S30. HSQC-DEPT Spectrum of Compound **2** (500 MHz, DMSO-d_6, 23°C).

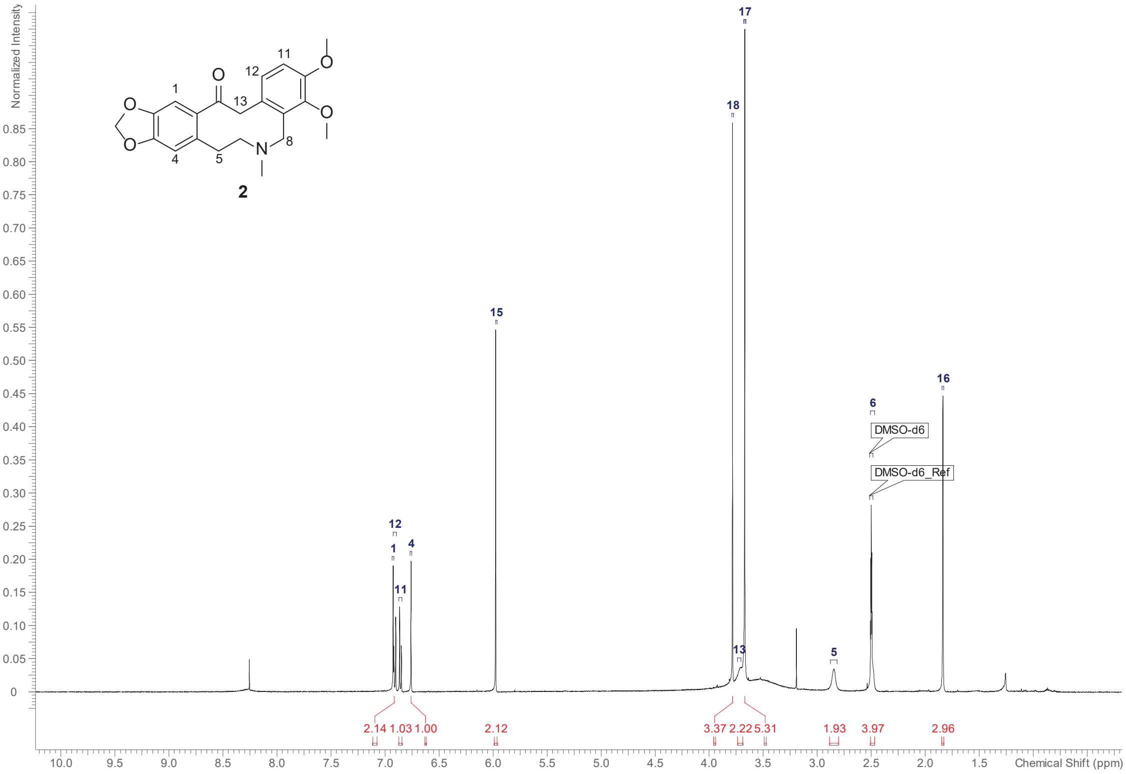

Figure S33. ^{1}H NMR Spectrum of Compound **2** (500 MHz, DMSO-d_6, 60°C).

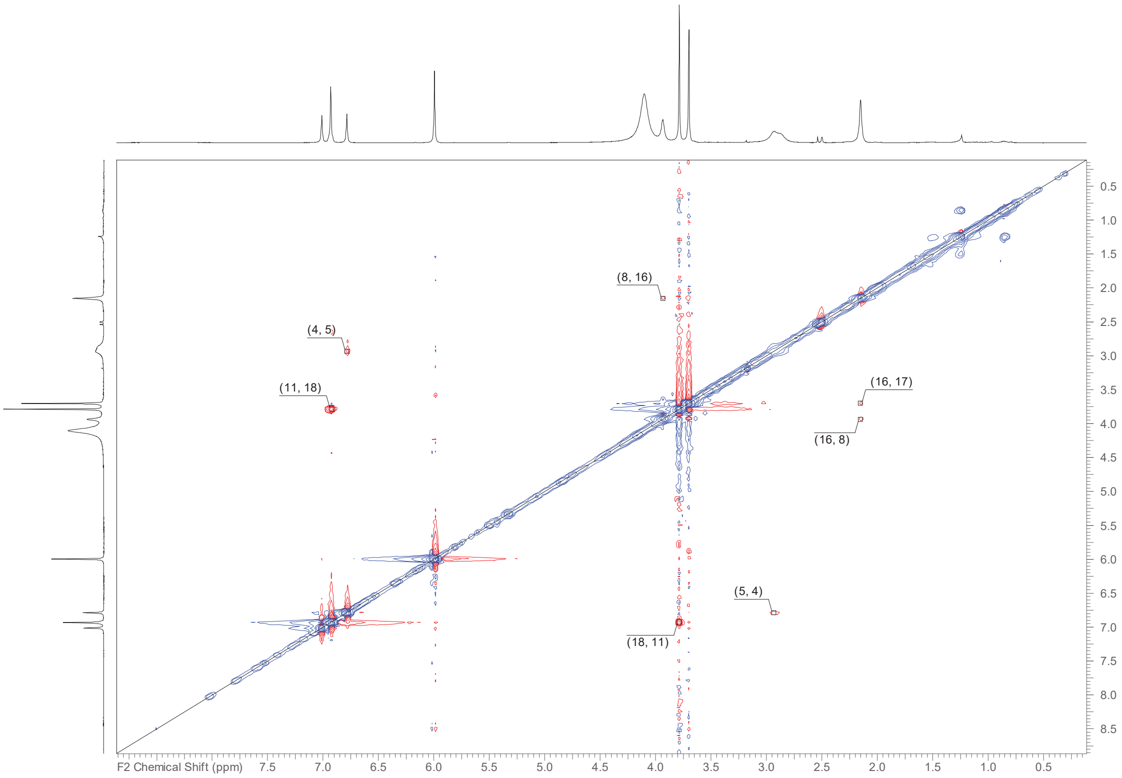

Figure S32. ^{1}H-^{1}H NOESY Spectrum of Compound **2** (500 MHz, DMSO-d_6, 23°C).

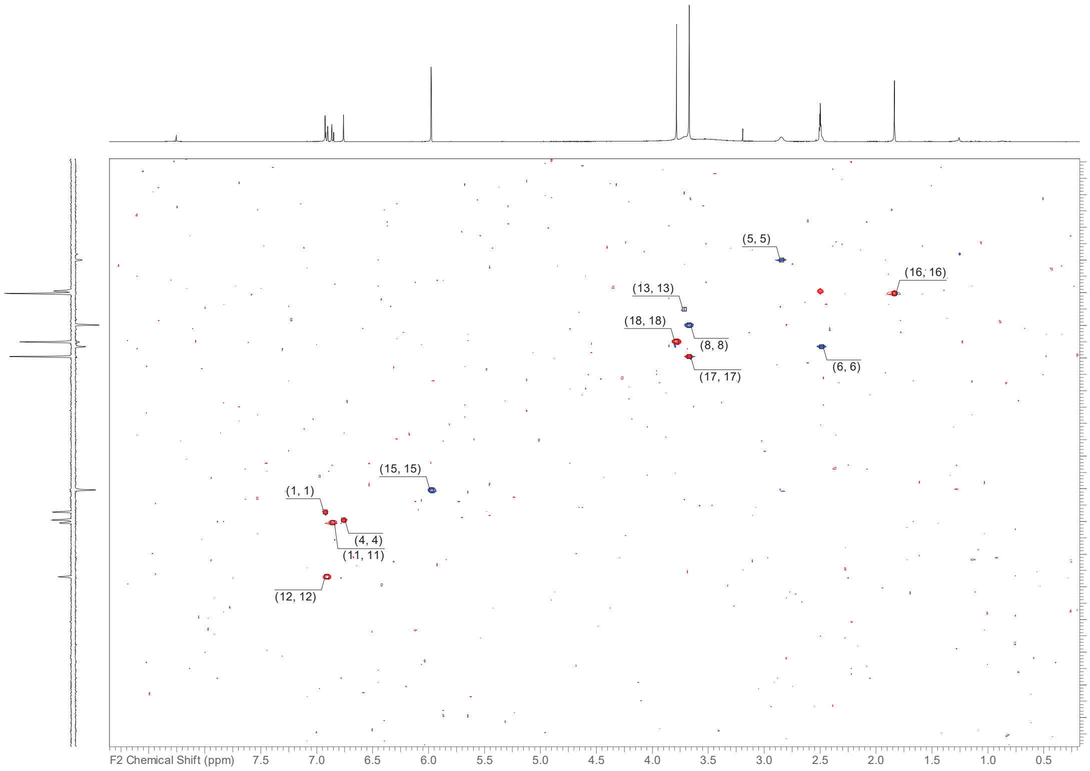

Figure S35. HSQC-DEPT Spectrum of Compound **2** (500 MHz, DMSO-*d*$_6$, 60°C).

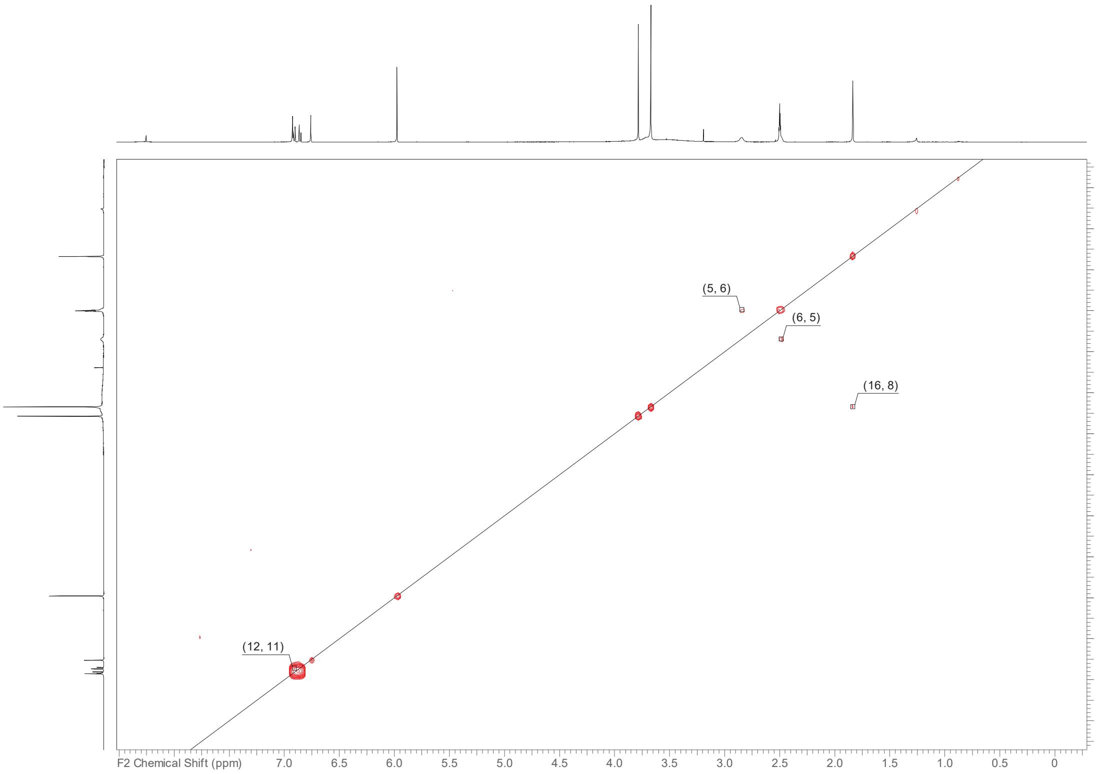

Figure S34. . ^{1}H-^{1}H COSY Spectrum of Compound **2** (500 MHz, DMSO-*d*$_6$, 60°C).

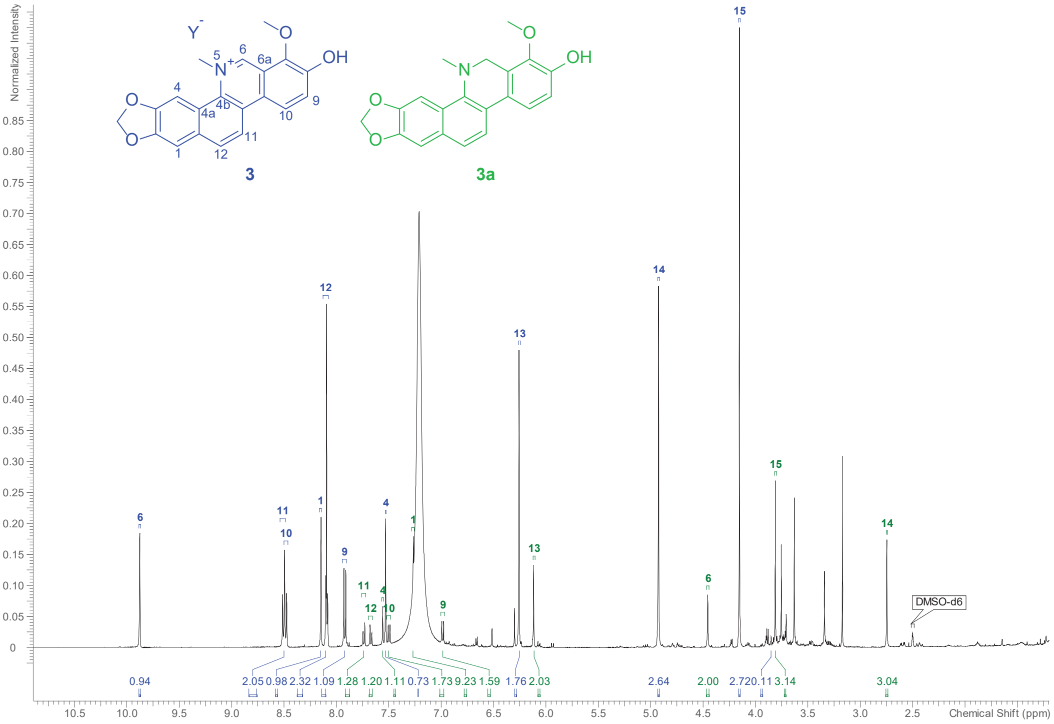

Figure S37. ^{1}H NMR Spectrum of Compound **3a** (blue) with **3b** (green, molar ratio 4:1, 500 MHz, DMSO-d_6 + TFA 10:1). Integrals are independently calculated for each compound.

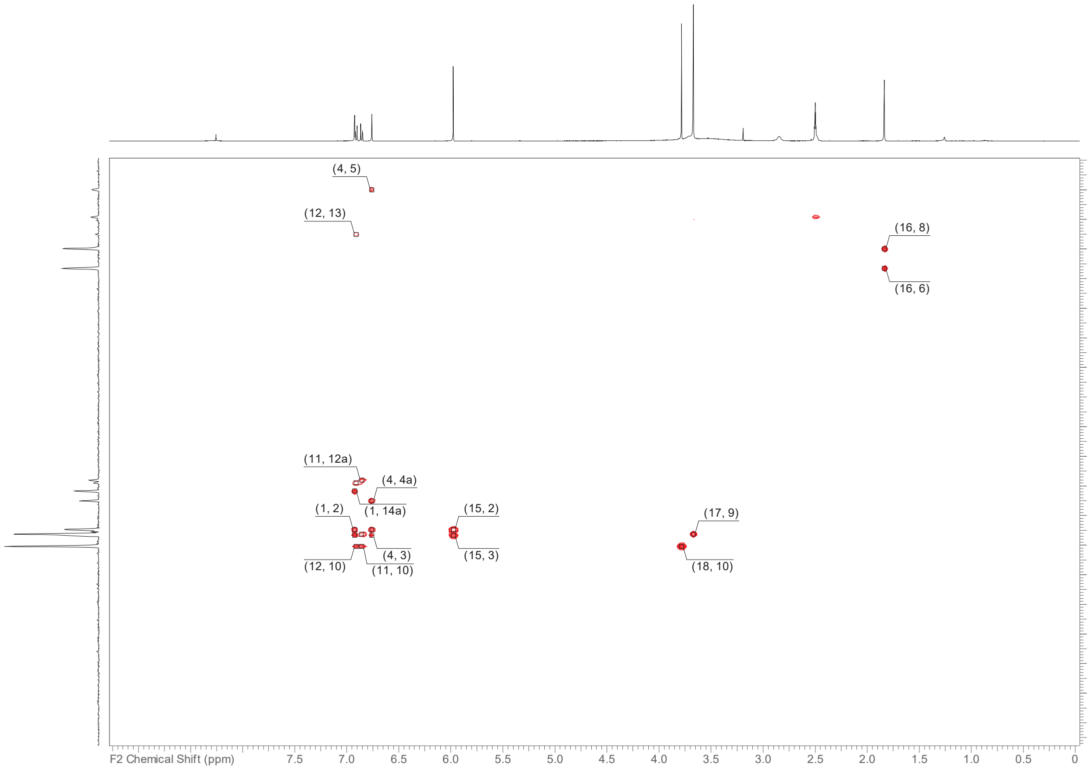

Figure S36. HMBC Spectrum of Compound **2** (500 MHz, DMSO-d_6, 60°C).

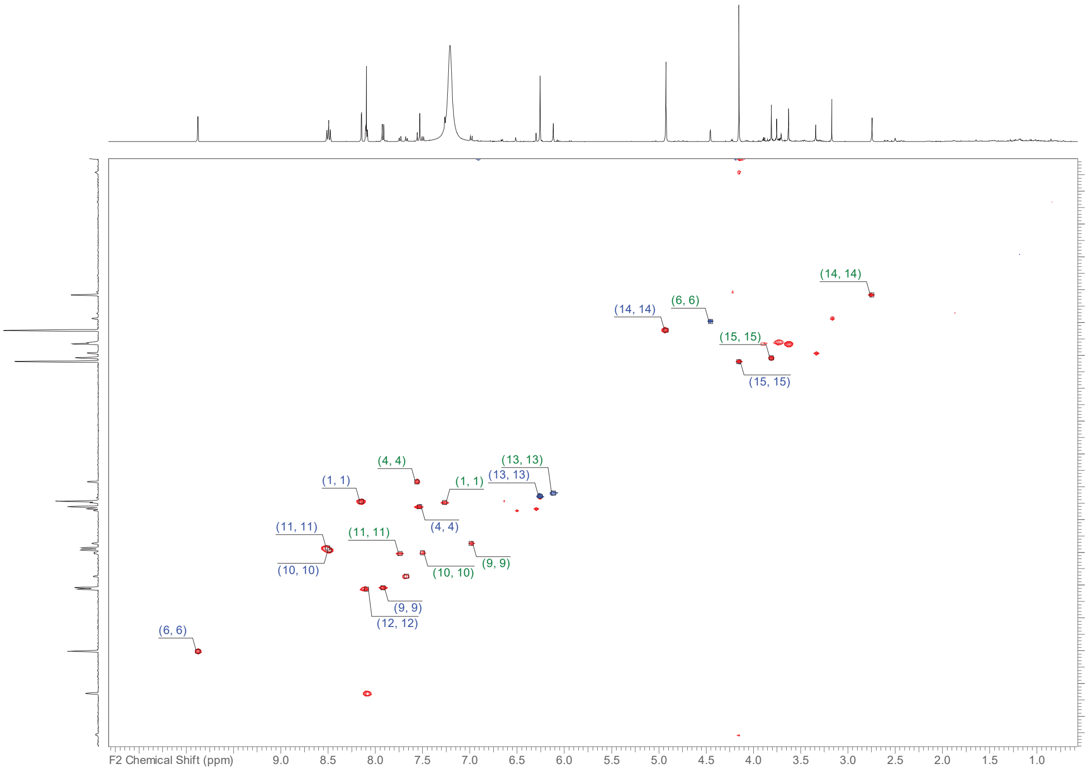

Figure S39. HSQC-DEPT Spectrum of Compound **3a** (blue) with **3b** (green, molar ratio 4:1, 500 MHz, DMSO-d_6 + TFA 10:1).

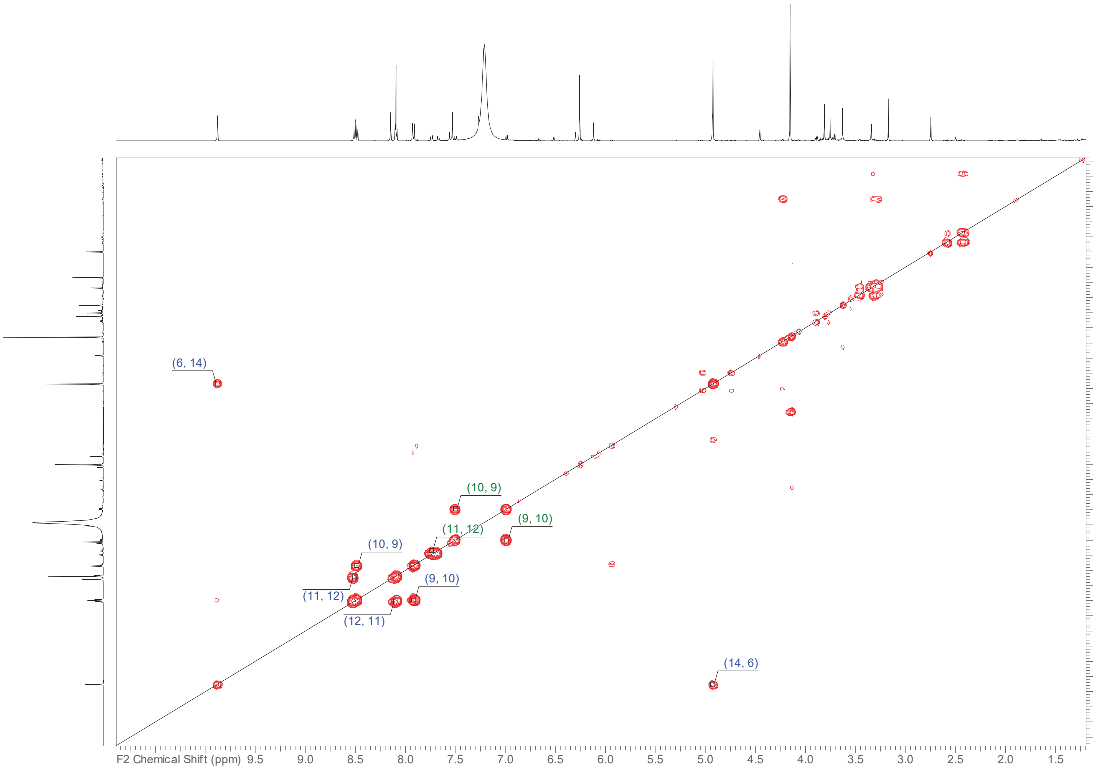

Figure S38. ^{1}H-^{1}H COSY Spectrum of Compound **3a** (blue) with **3b** (green, molar ratio 4:1, 500 MHz, DMSO-d_6 + TFA 10:1).

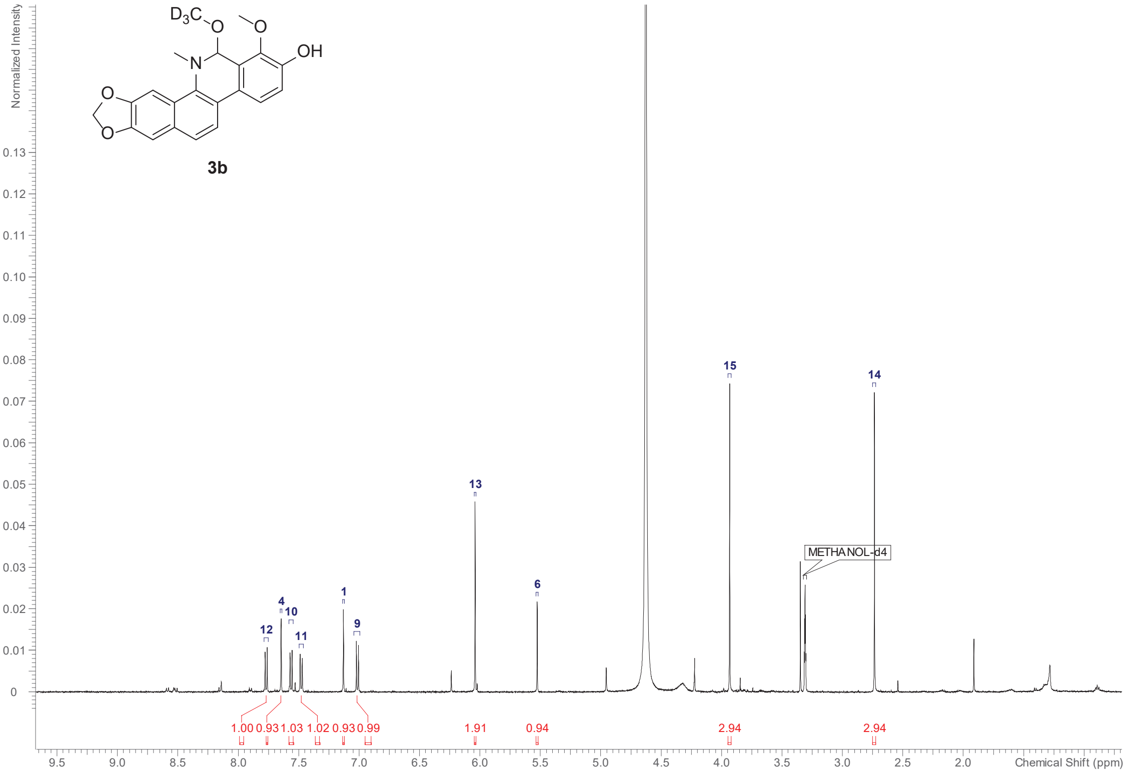

Figure S41. ^{1}H NMR Spectrum of Compound **3c** (500 MHz, methanol-*d*$_4$).

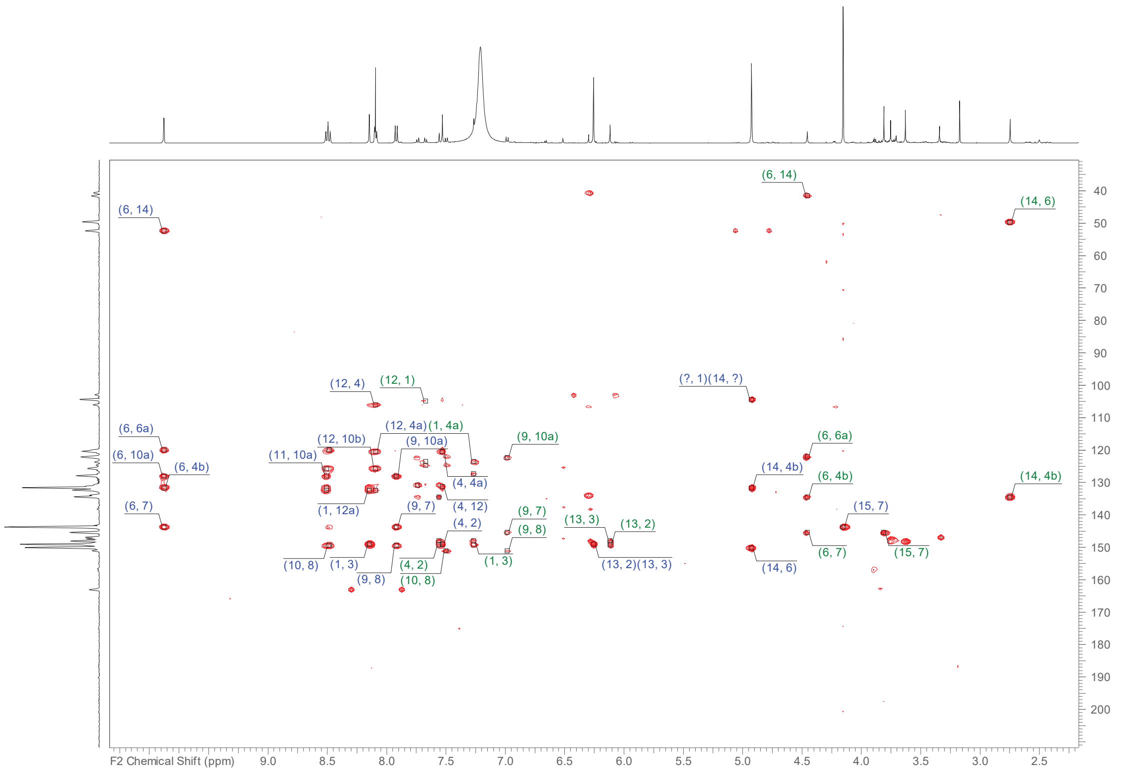

Figure S40. HMBC Spectrum of Compound **3a** (blue) with **3b** (green, molar ratio 4:1, 500 MHz, DMSO-*d*$_6$ + TFA 10:1).

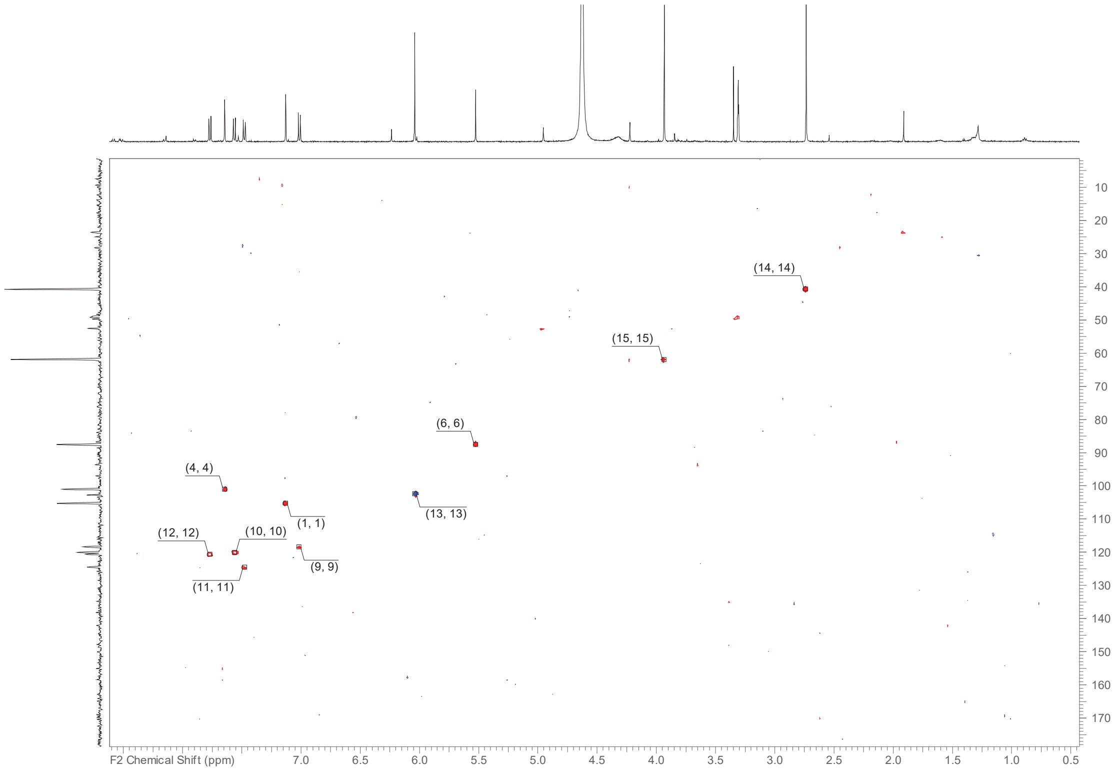

Figure S43. HSQC-DEPT Spectrum of Compound **3c** (500 MHz, methanol-*d*$_4$).

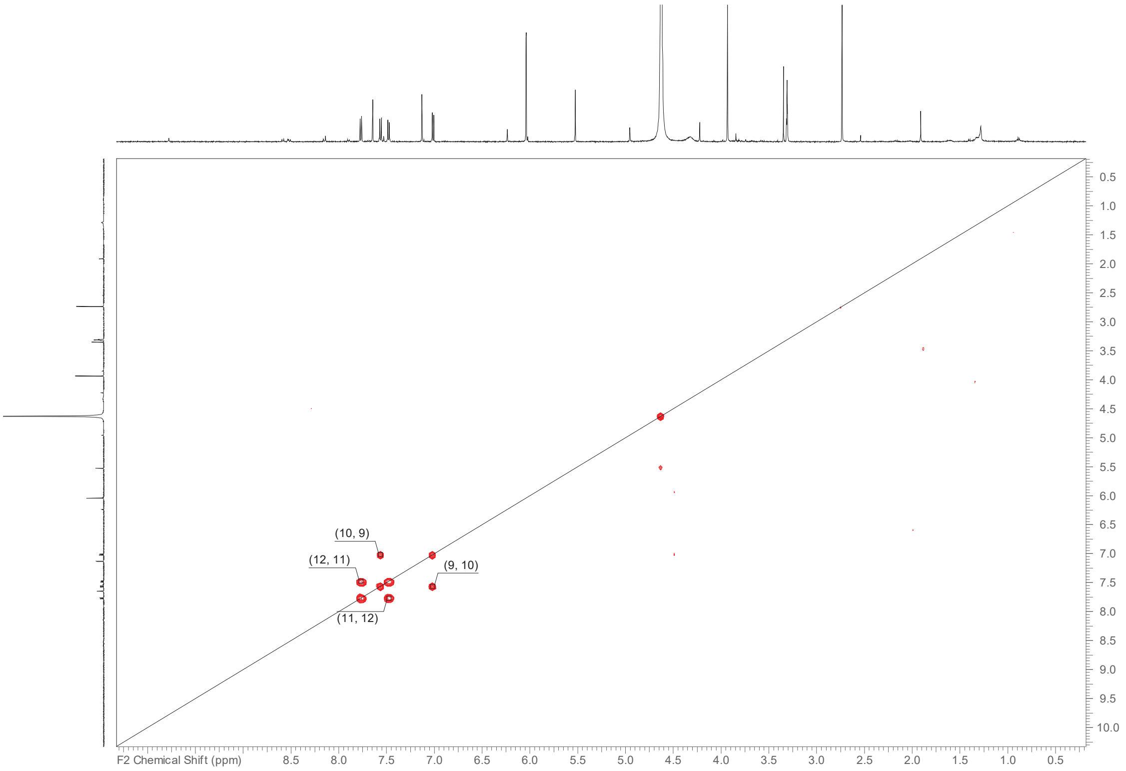

Figure S42. ^{1}H-^{1}H COSY Spectrum of Compound **3c** (500 MHz, methanol-*d*$_4$).

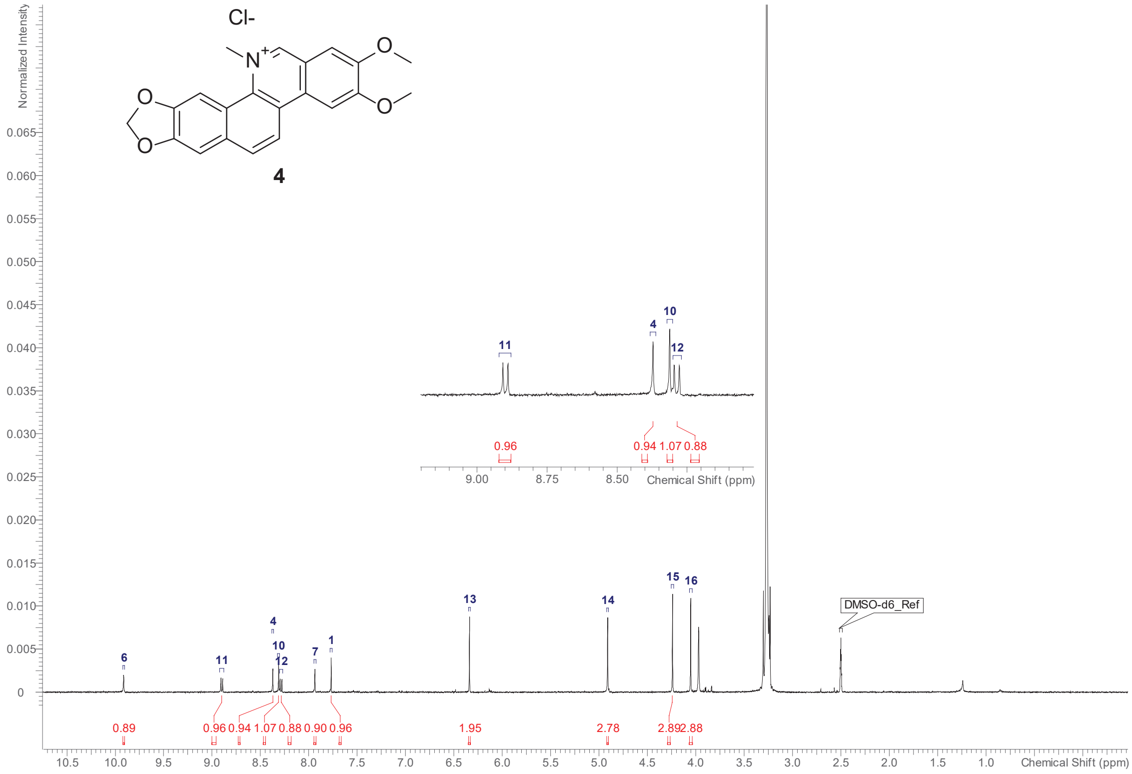

Figure S45. ^{1}H NMR Spectrum of Compound **4** (500 MHz, DMSO-d_6).

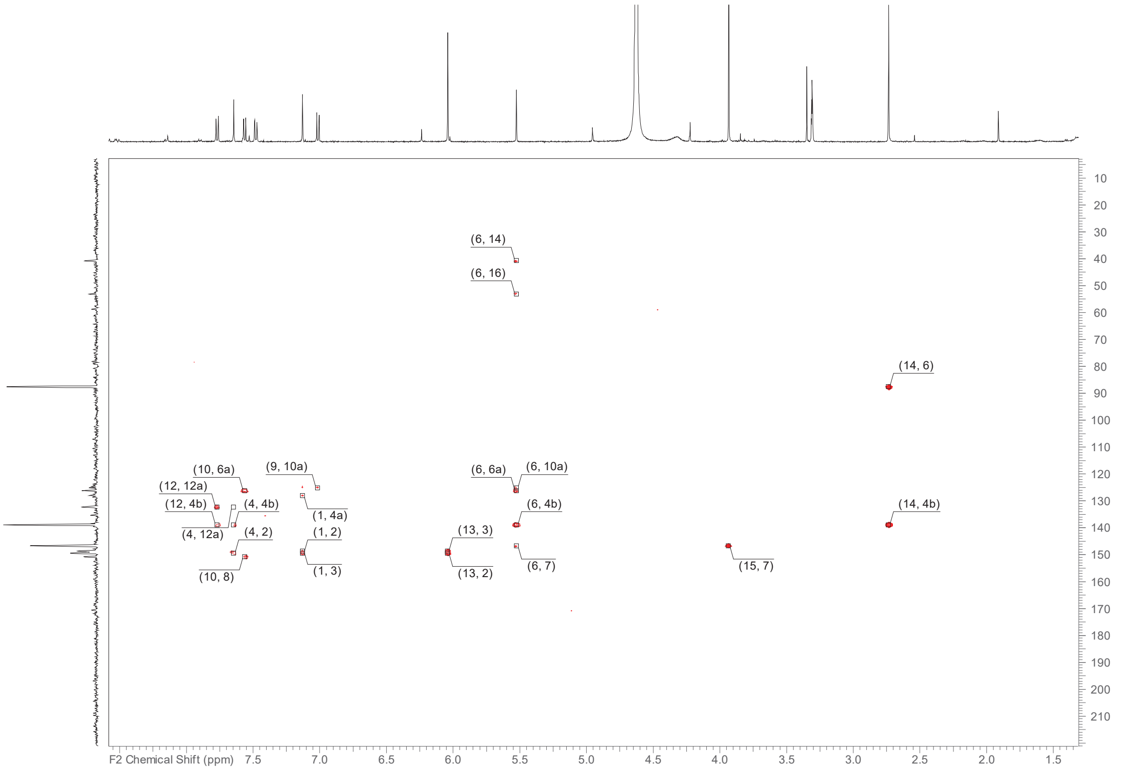

Figure S44. HMBC Spectrum of Compound **3c** (500 MHz, methanol-d_4).

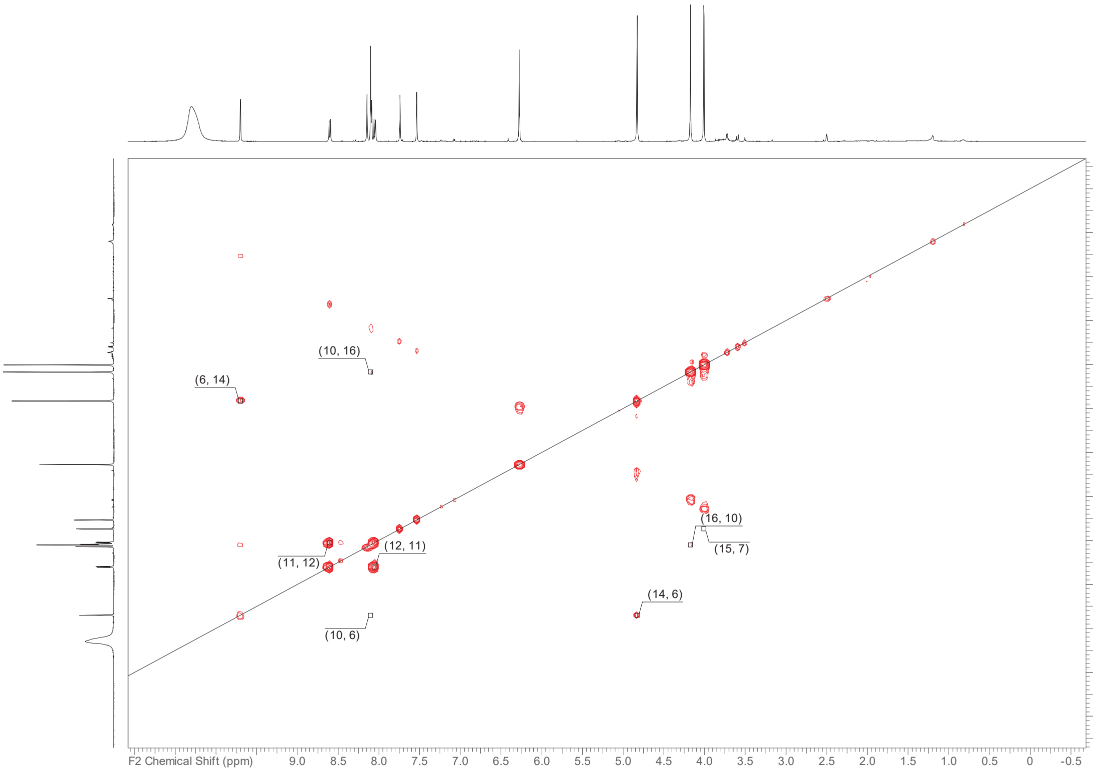

Figure S47. ^{1}H-^{1}H COSY Spectrum of Compound **4** (500 MHz, DMSO-d_6 + TFA ratio 2:1).

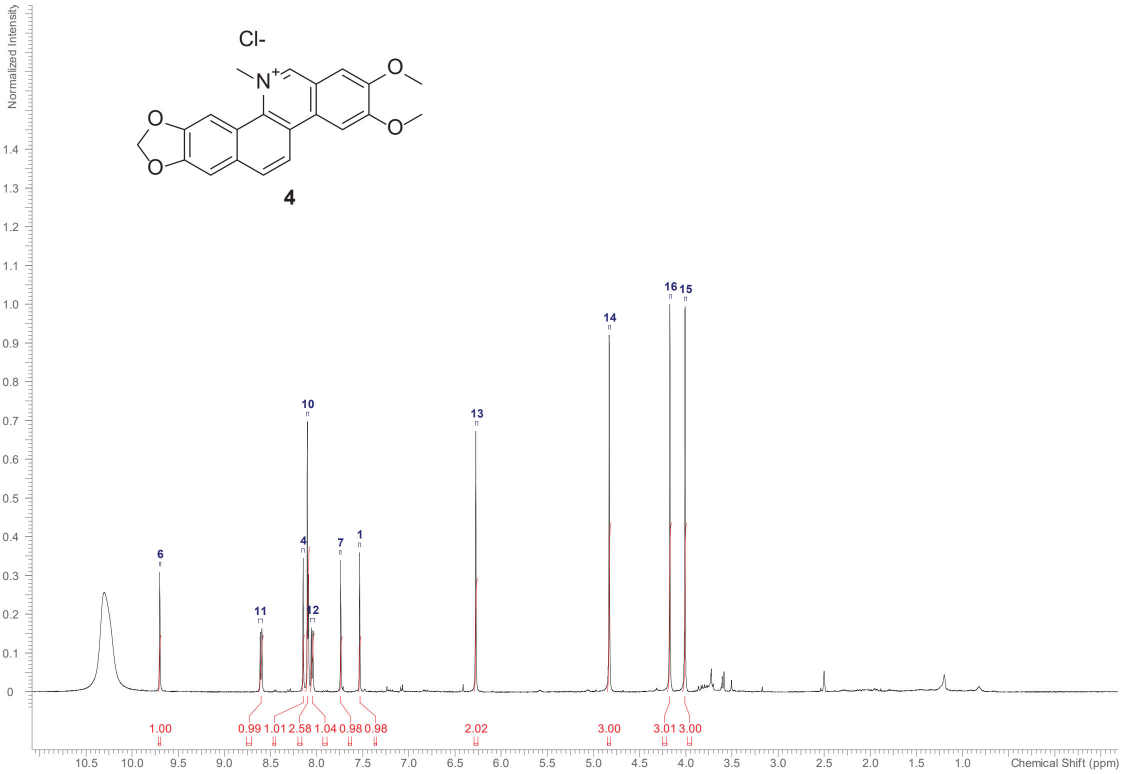

Figure S46. ^{1}H NMR Spectrum of Compound **4** (500 MHz, DMSO-d_6 + TFA ratio 2:1).

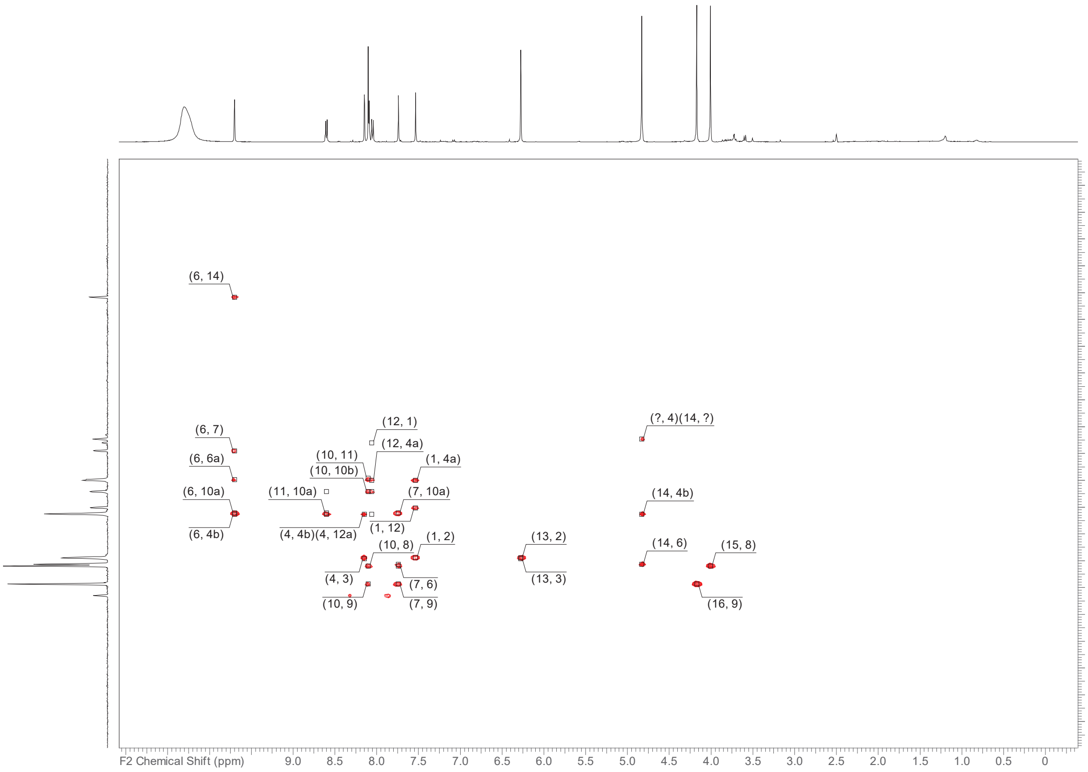

Figure S49. HMBC Spectrum of Compound **4** (500 MHz, DMSO-d_6 + TFA ratio 2:1).

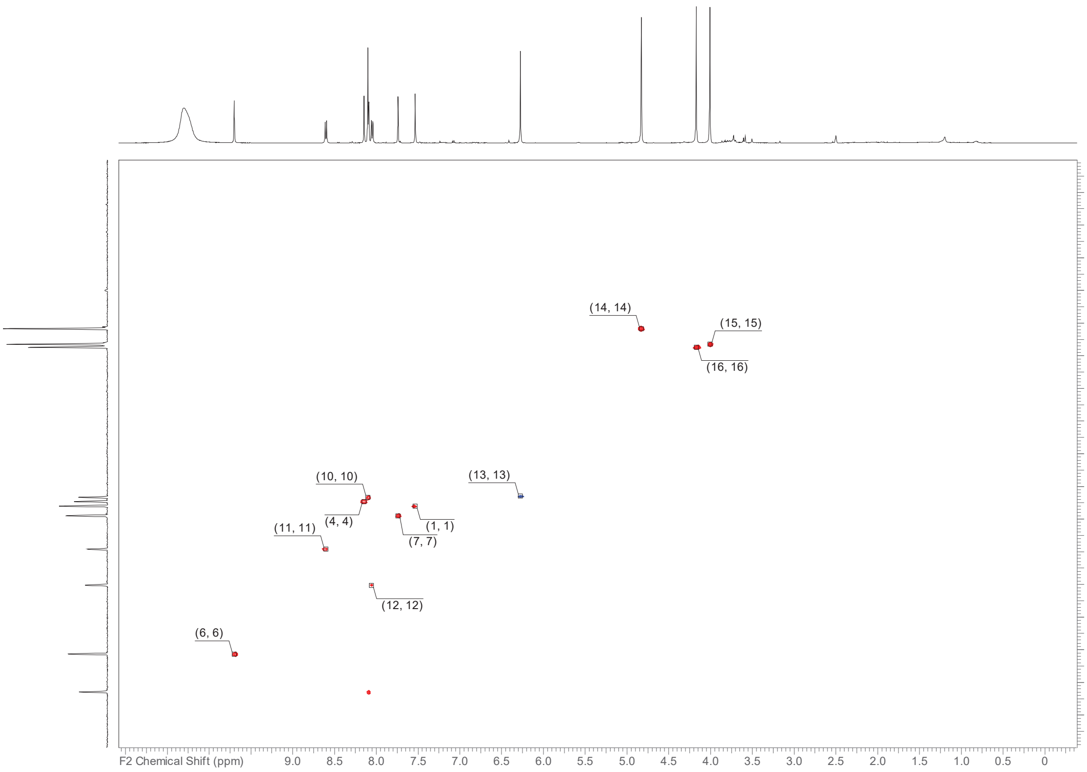

Figure S48. HSQC-DEPT Spectrum of Compound **4** (500 MHz, DMSO-d_6 + TFA ratio 2:1).

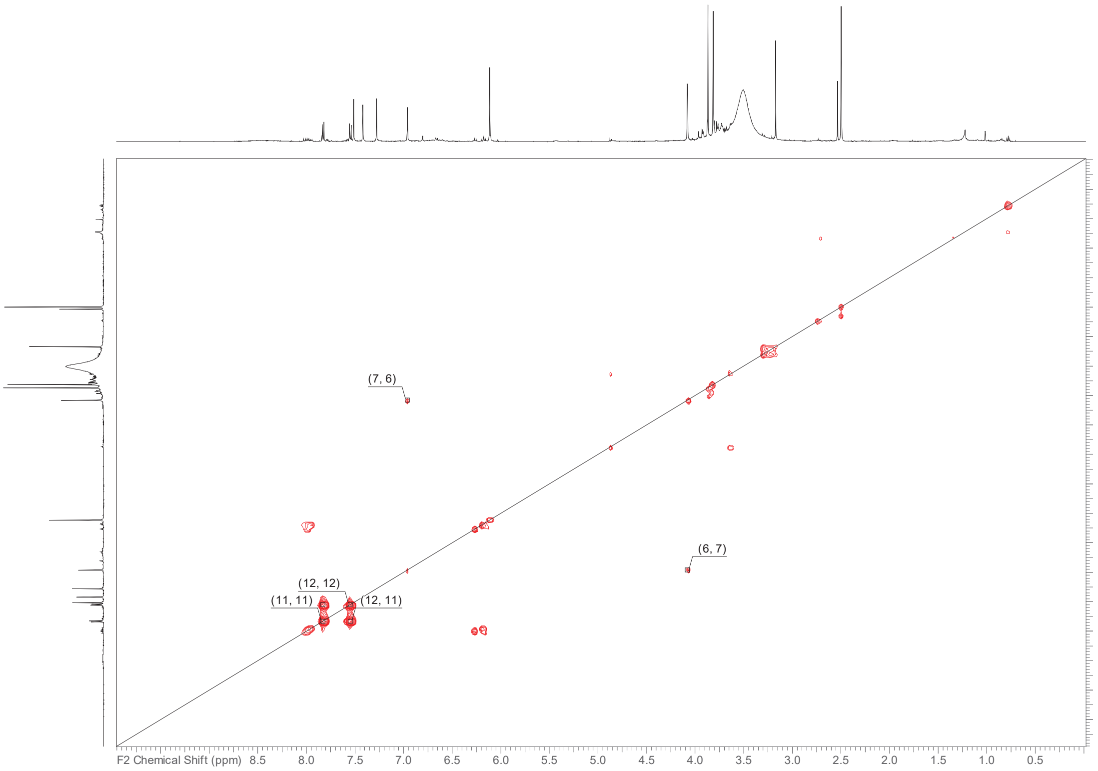

Figure S51. ^{1}H-^{1}H COSY Spectrum of Compound **5** (500 MHz, DMSO-d_6).

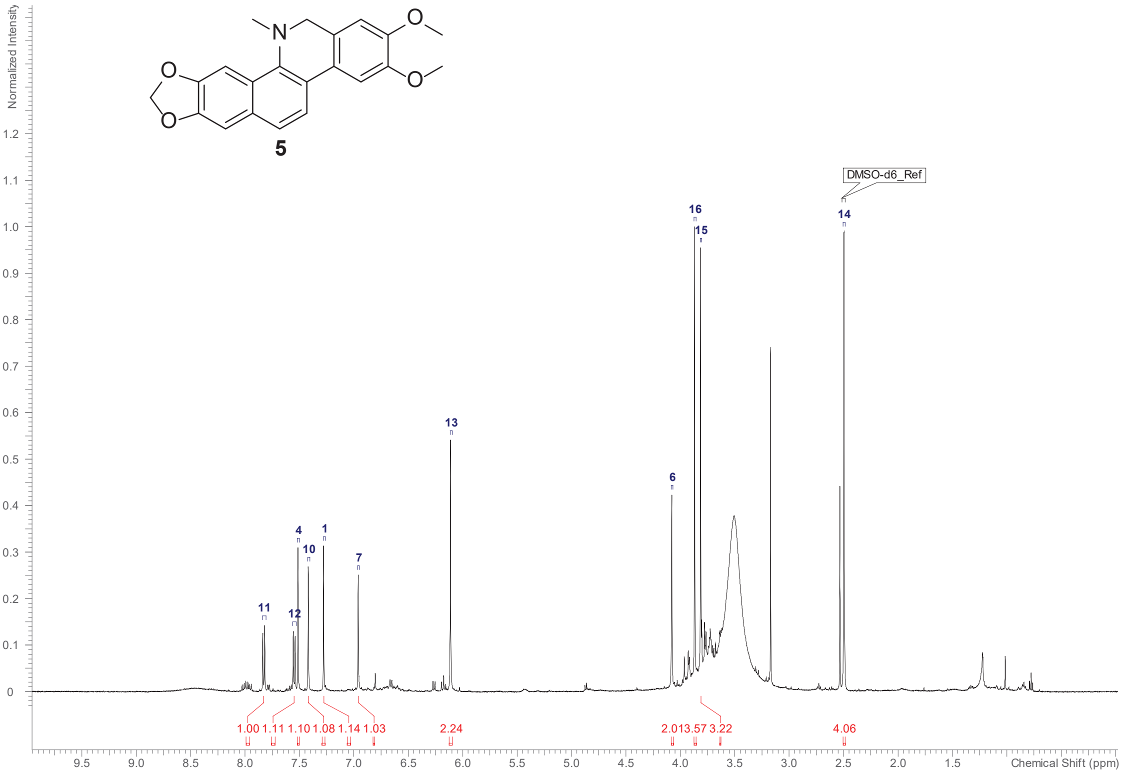

Figure S50. ^{1}H NMR Spectrum of Compound **5** (500 MHz, DMSO-d_6).

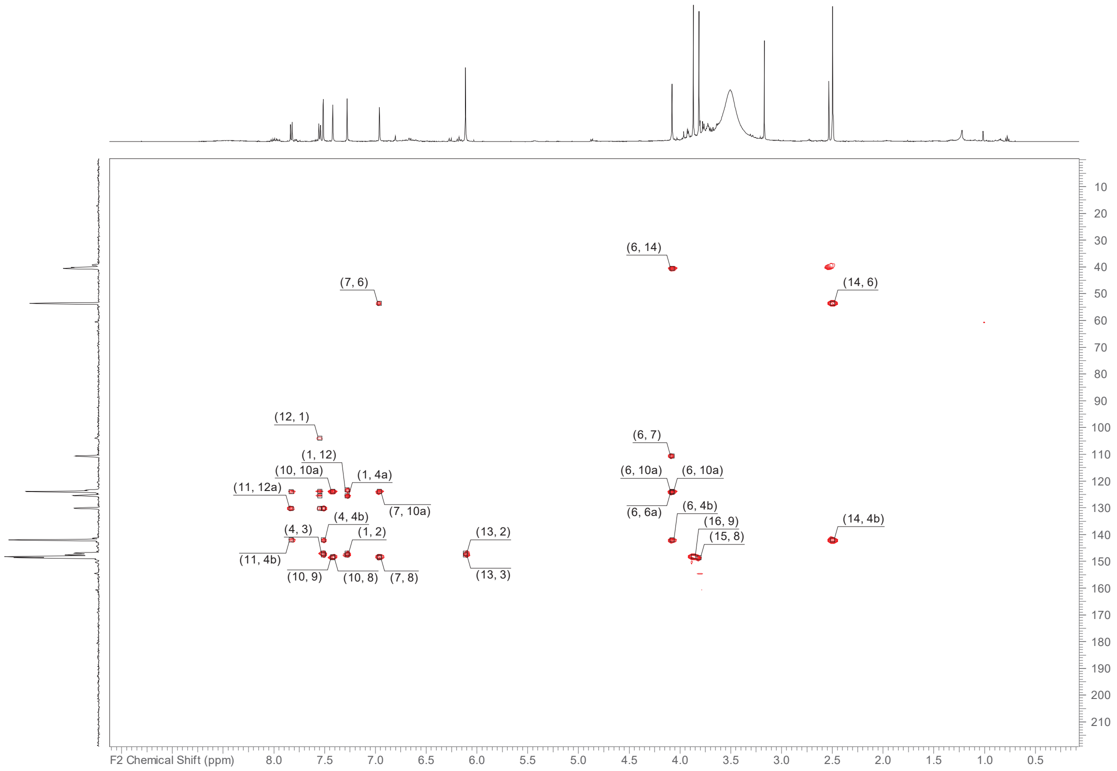

Figure S53. HMBC Spectrum of Compound **5** (500 MHz, DMSO-d_6).

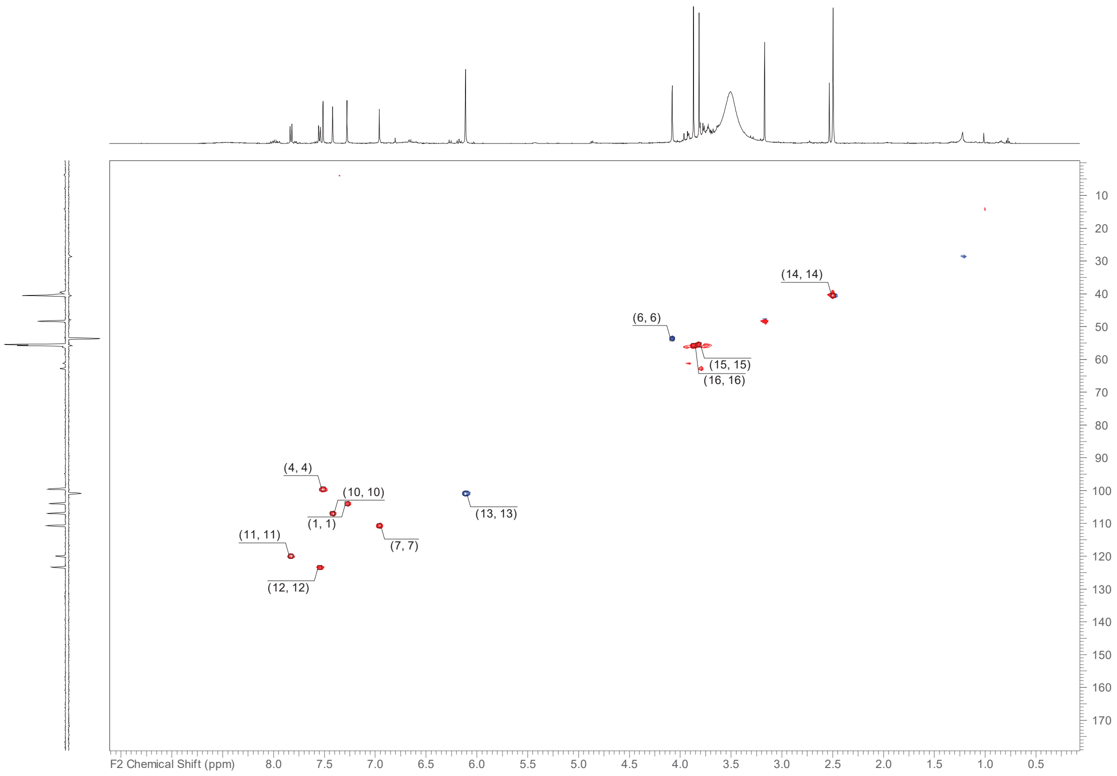

Figure S52. HSQC-DEPT Spectrum of Compound **5** (500 MHz, DMSO-d_6).

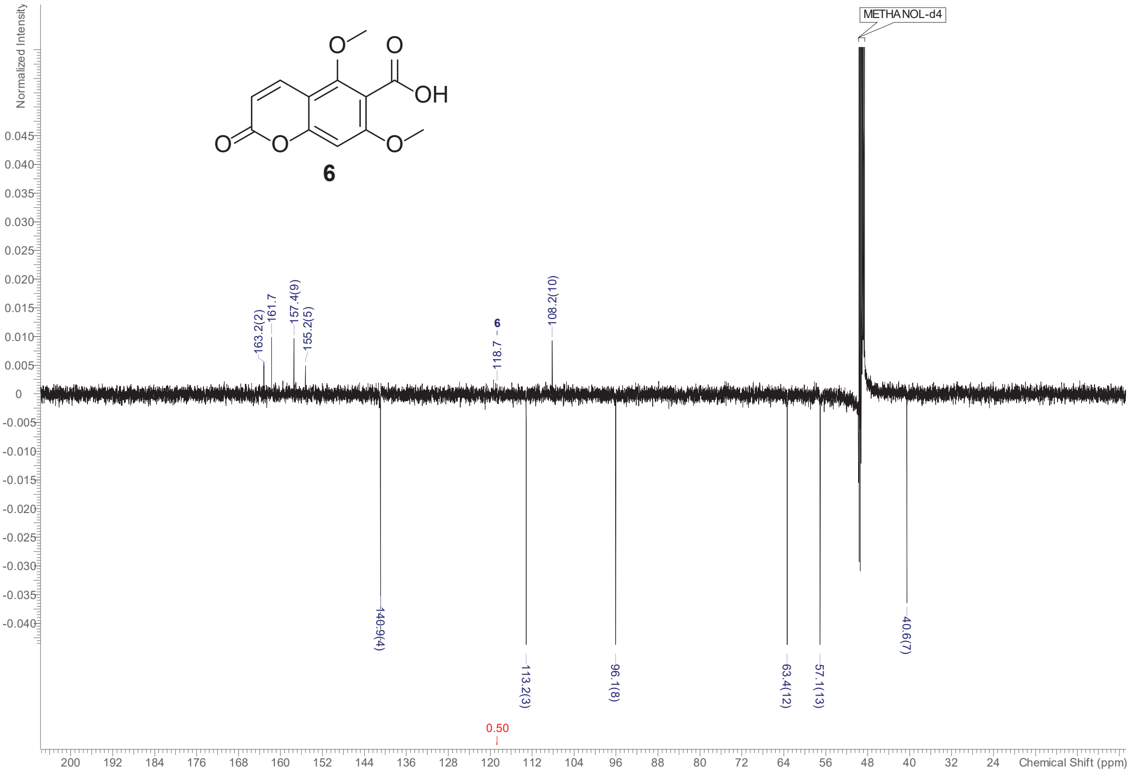

Figure S55. ^{13}C NMR Spectrum of Compound **6** (125 MHz, methanol-d_4).

Figure S54. ^{1}H NMR Spectrum of Compound **6** (500 MHz, methanol-d_4).

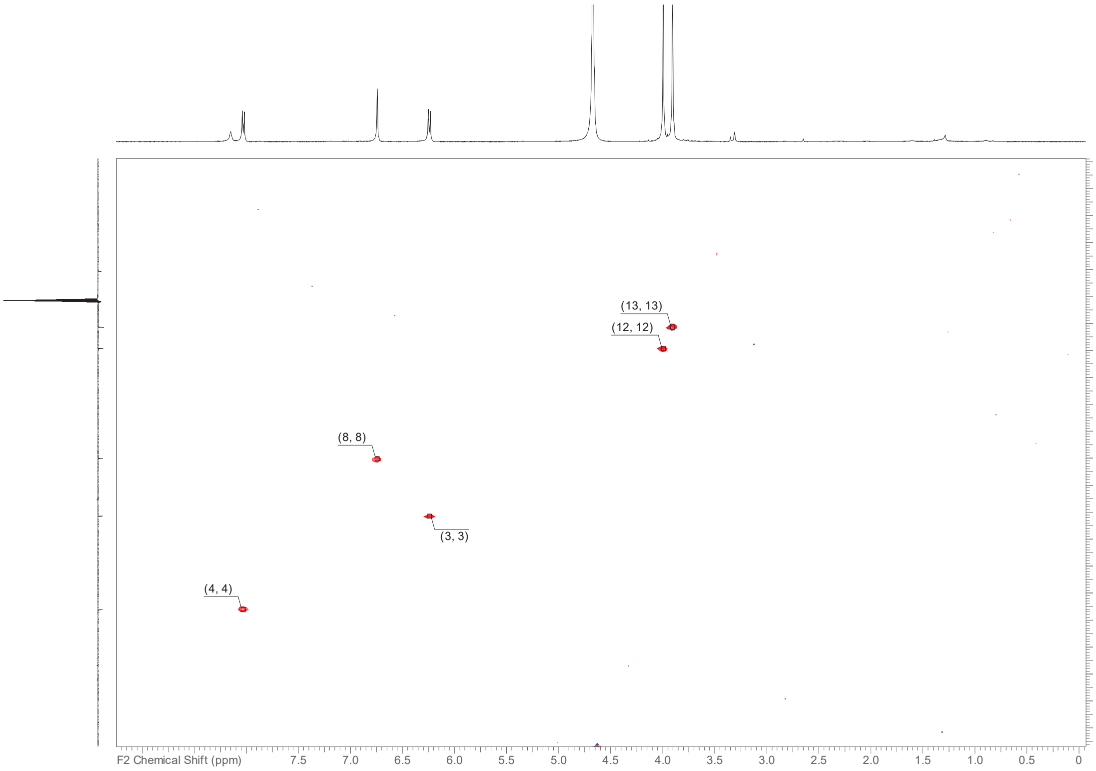

Figure S57. HSQC-DEPT Spectrum of Compound **6** (500 MHz, methanol-d_4).

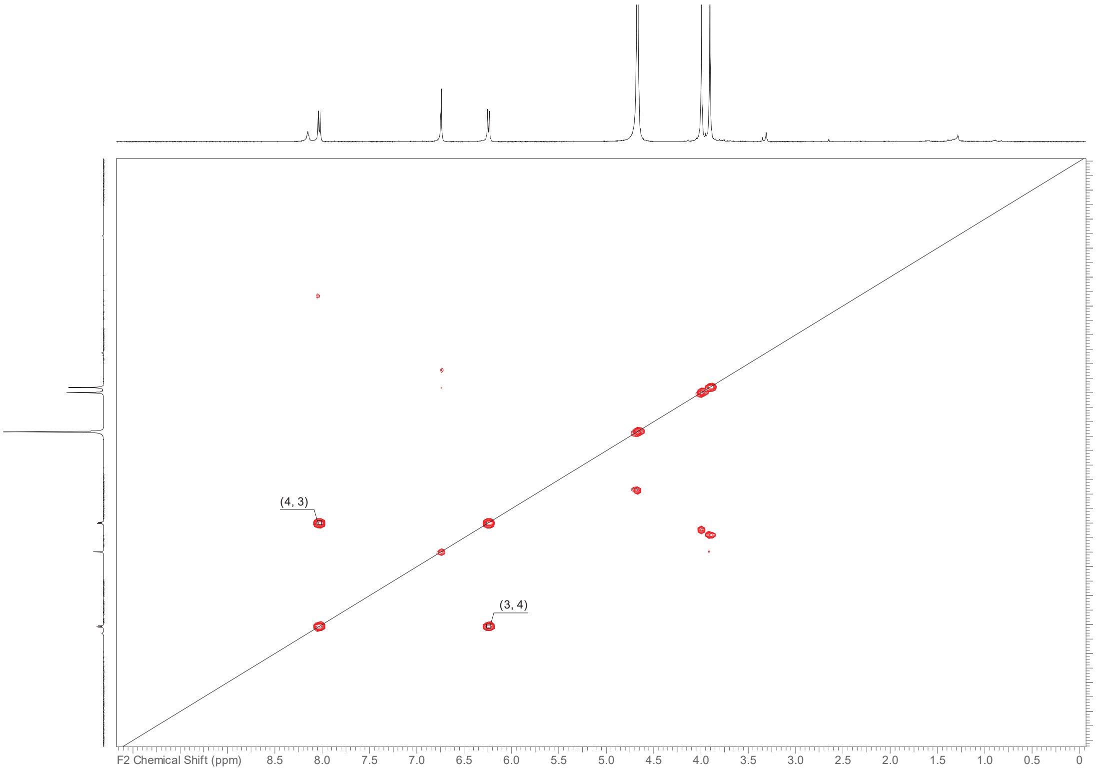

Figure S56. ^{1}H-^{1}H COSY Spectrum of Compound **6** (500 MHz, methanol-d_4).

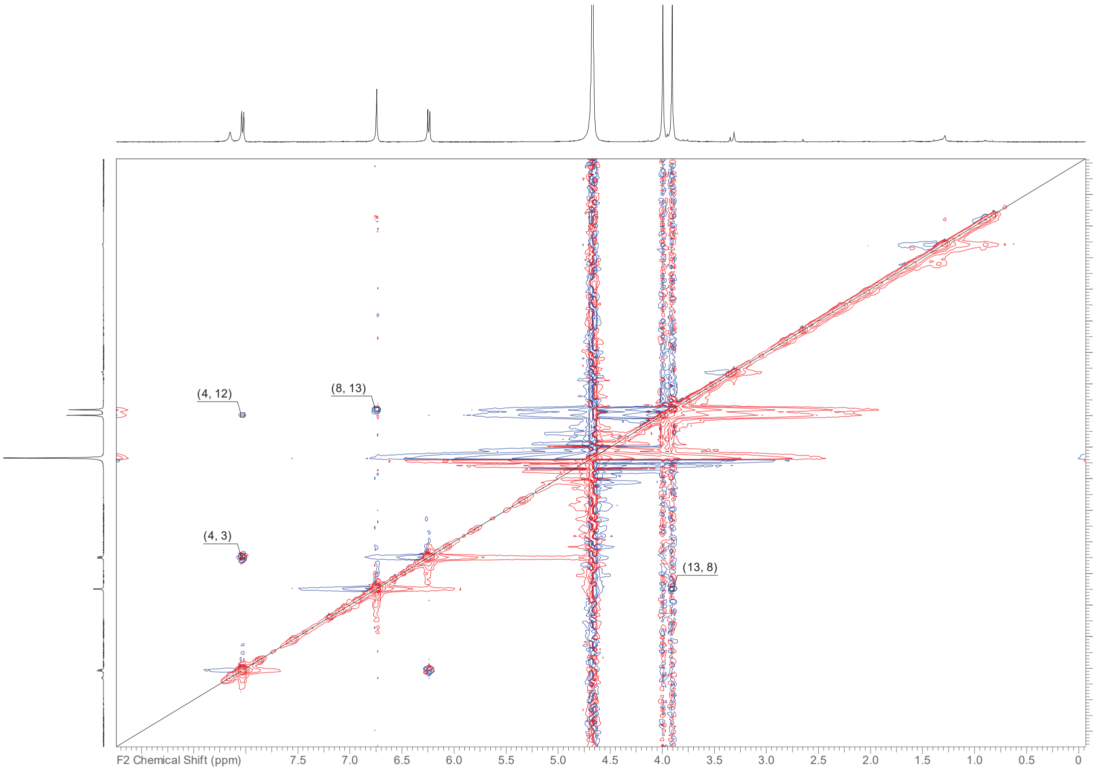

Figure S59. ^{1}H-^{1}H ROESY Spectrum of Compound **6** (500 MHz, methanol-d_4).

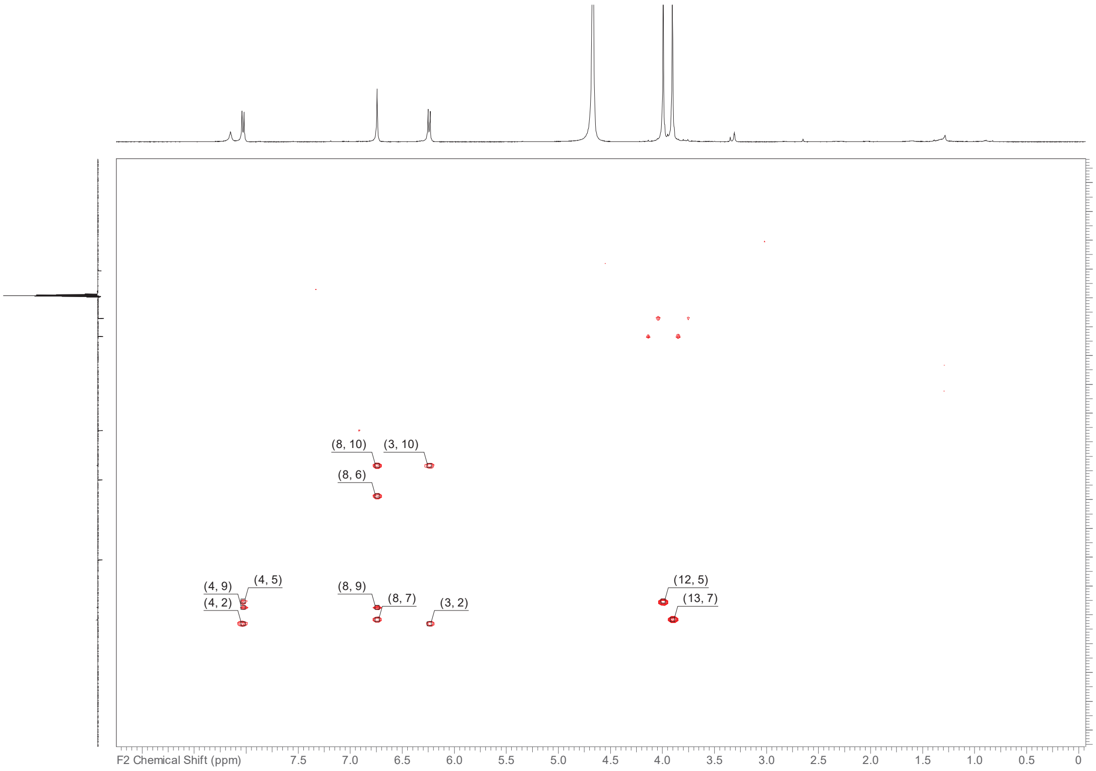

Figure S58. HMBC Spectrum of Compound **6** (500 MHz, methanol-d_4).

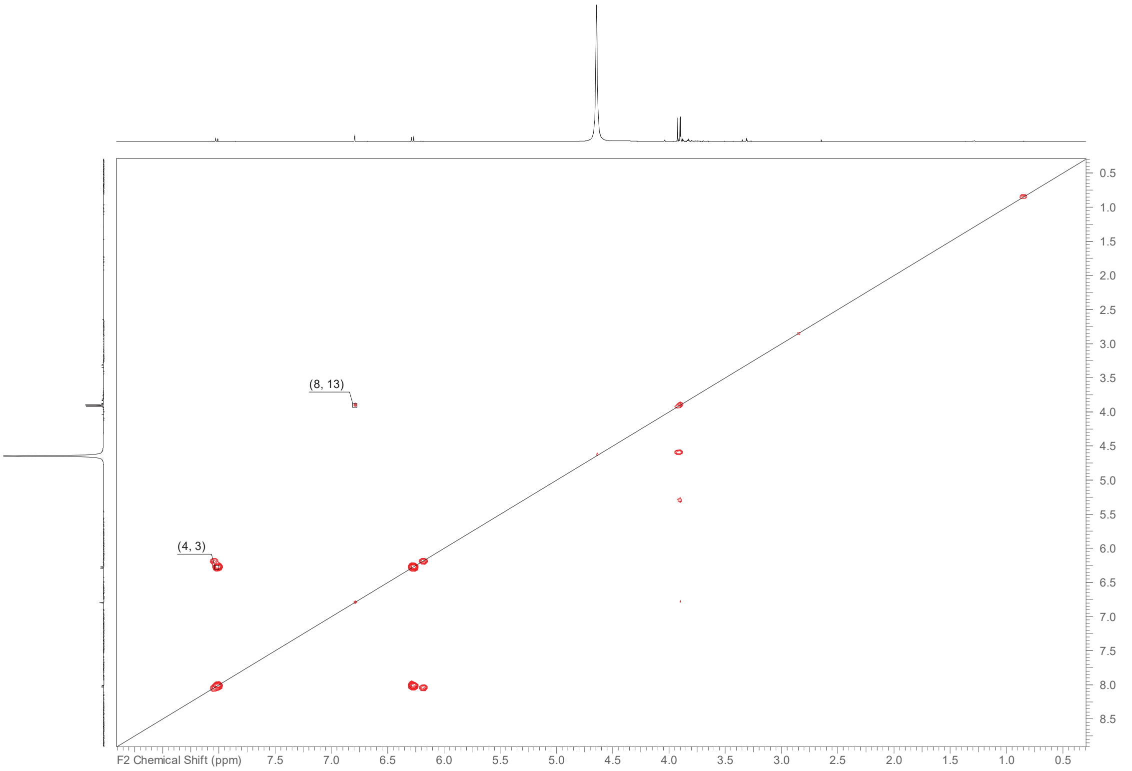

Figure S61. ^{1}H-^{1}H COSY Spectrum of Compound **6a** (500 MHz, methanol-*d$_4$*).

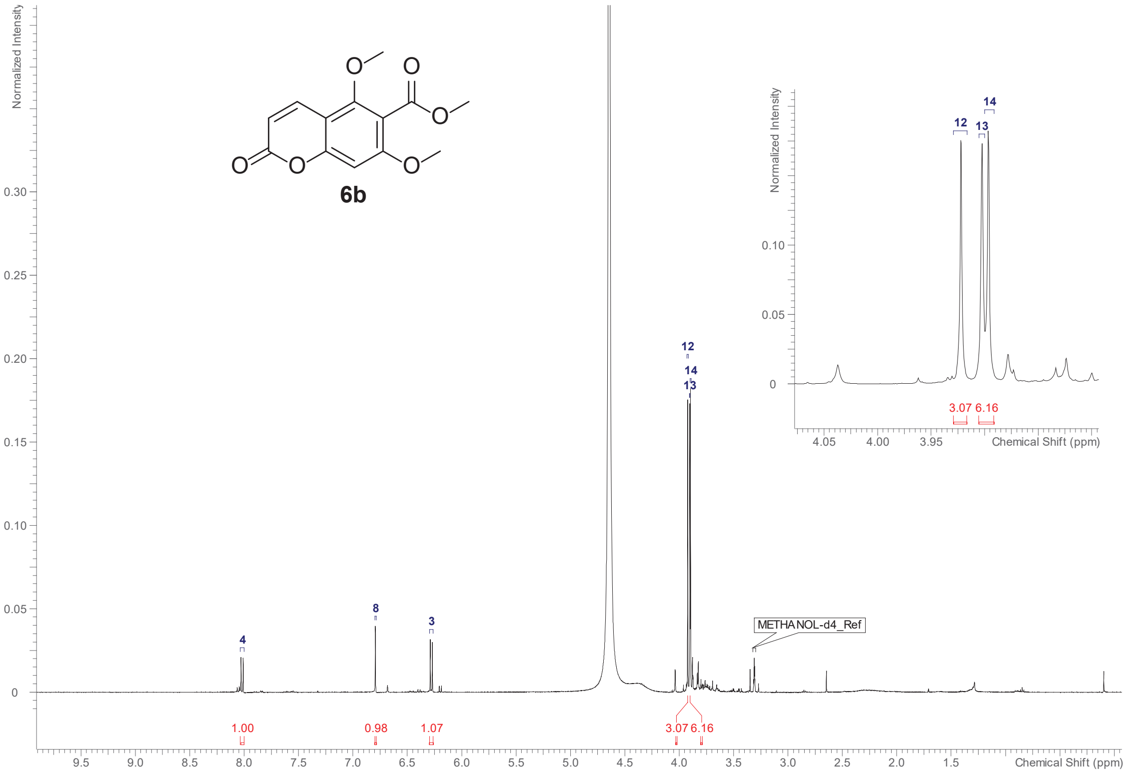

Figure S60. ^{1}H NMR Spectrum of Compound **6a** (500 MHz, methanol-*d$_4$*).

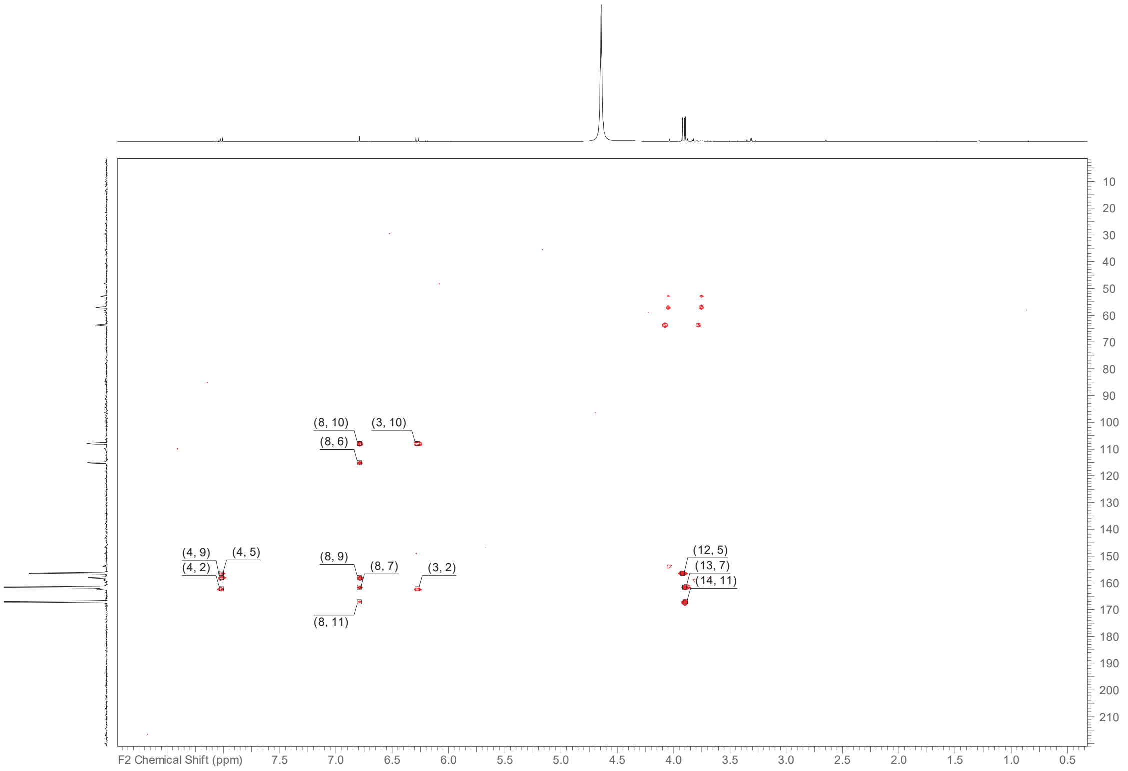

Figure S63. HMBC Spectrum of Compound **6a** (500 MHz, methanol-*d*$_4$).

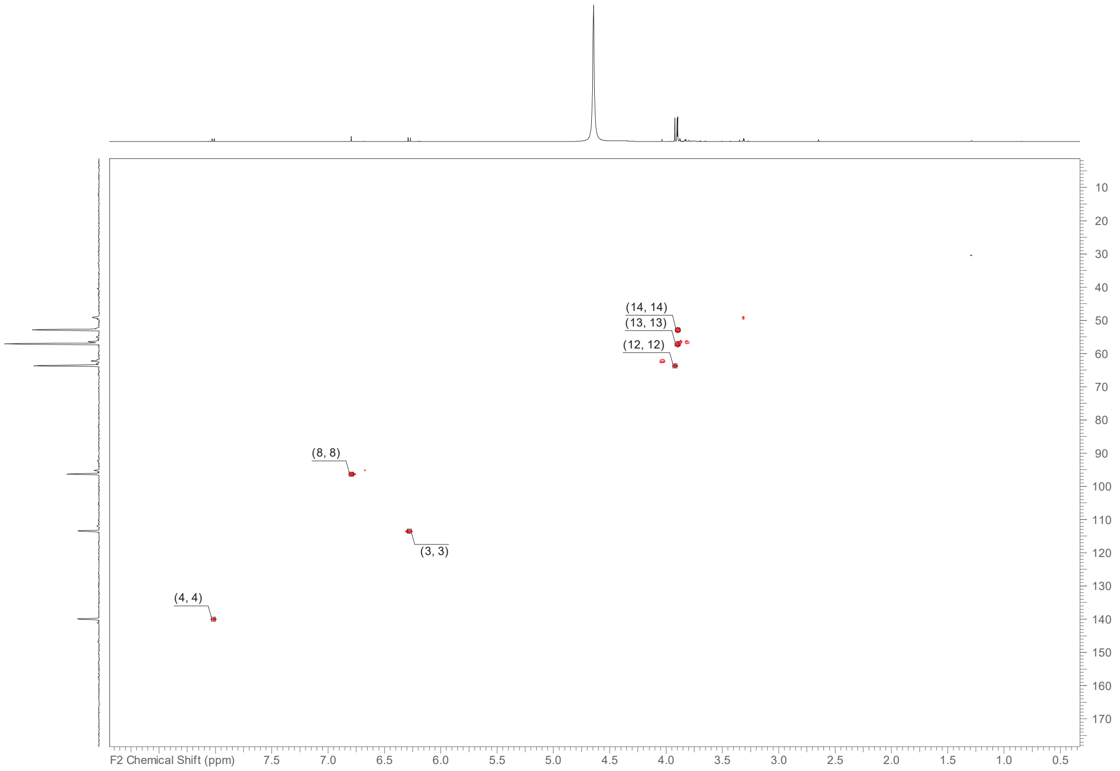

Figure S62. HSQC-DEPT Spectrum of Compound **6a** (500 MHz, methanol-*d*$_4$).

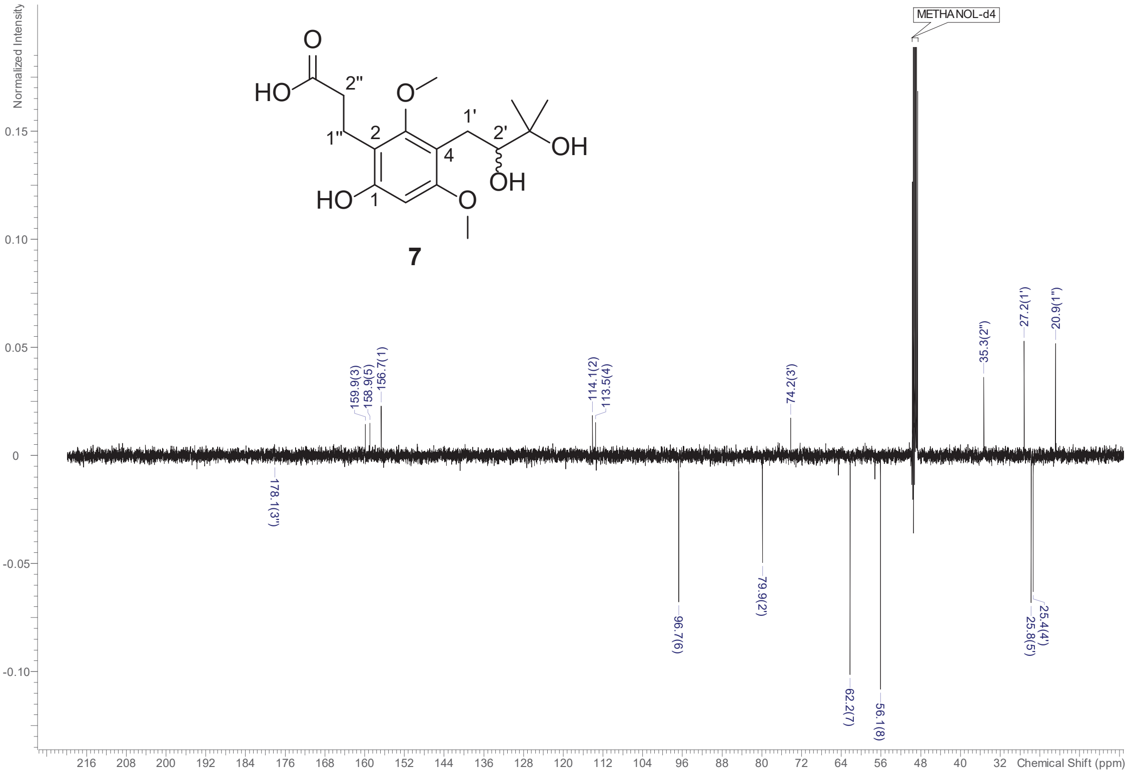

Figure S65. ^{13}C NMR Spectrum of Compound **7** with an impurity (ca. 10%) of **6** (125 MHz, methanol-d_4).

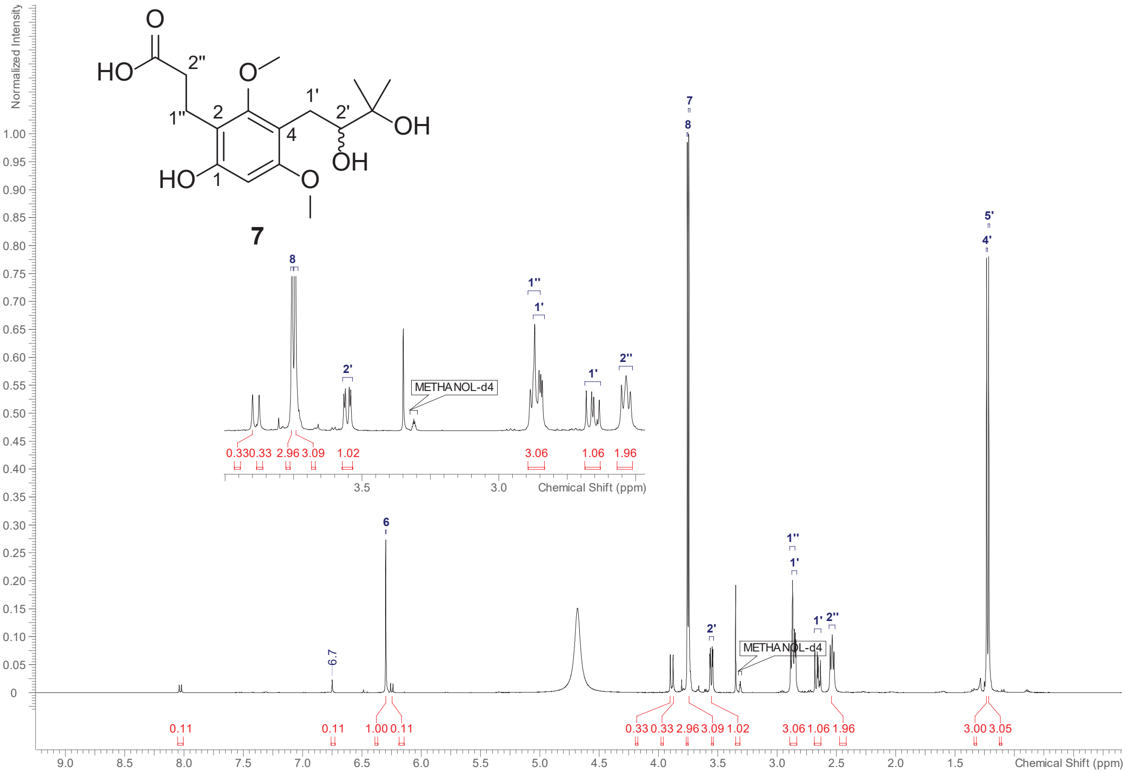

Figure S64. ^{1}H NMR Spectrum of Compound **7** with an impurity (ca. 10%) of **6** (500 MHz, methanol-d_4).

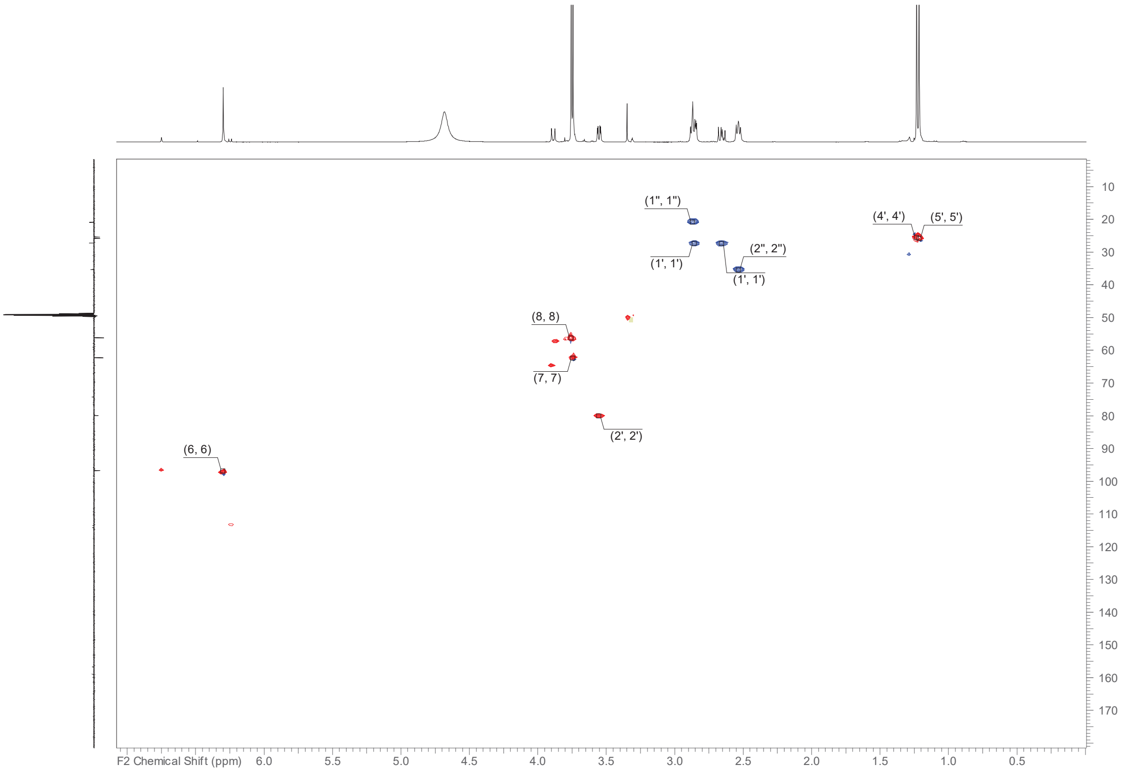

Figure S67. HSQC-DEPT Spectrum of Compound **7** with an impurity (ca. 10%) of **6** (500 MHz, methanol-d_4).

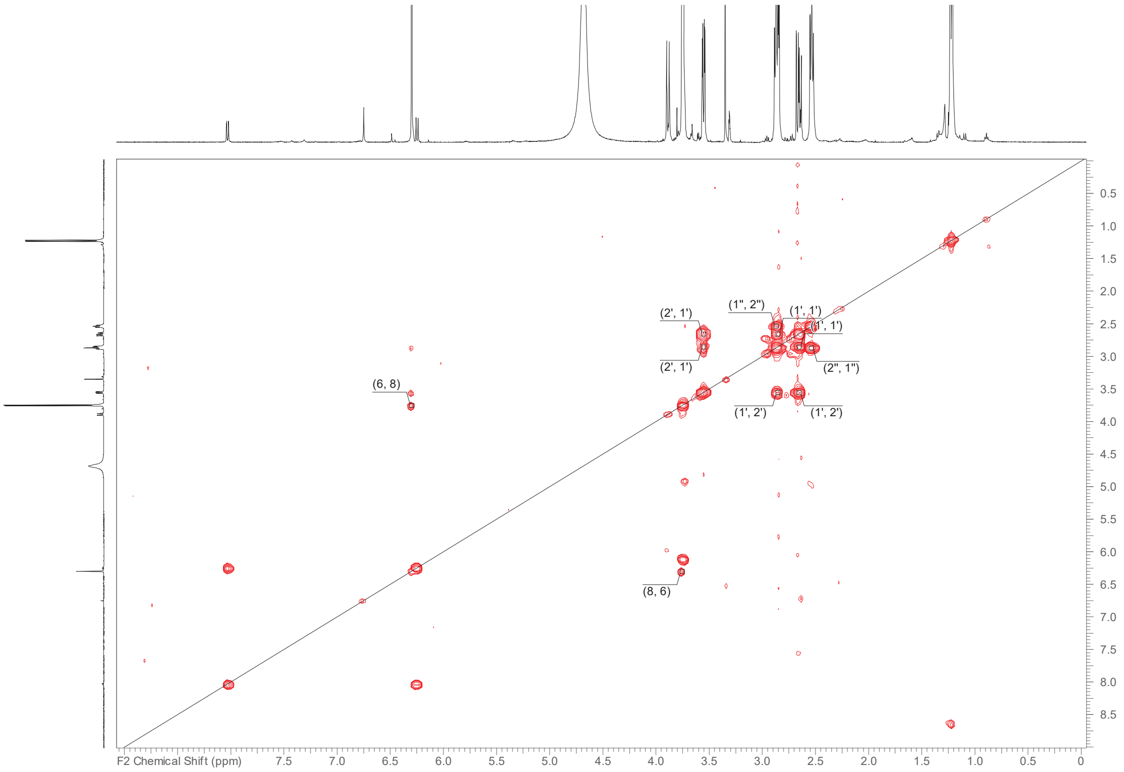

Figure S66. ^{1}H-^{1}H COSY Spectrum of Compound **7** with an impurity (ca. 10%) of **6** (500 MHz, methanol-d_4).

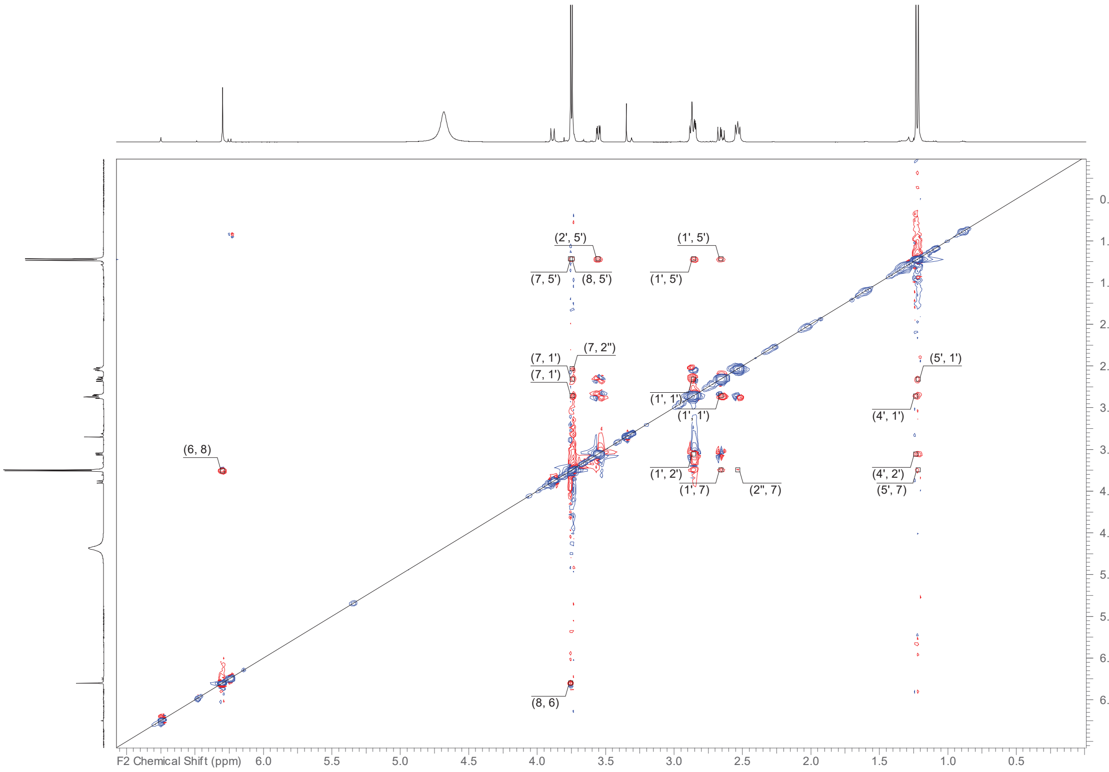

Figure S69. ^{1}H-^{1}H ROESY Spectrum of Compound **7** with an impurity (ca. 10%) of **6** (500 MHz, methanol-d_4).

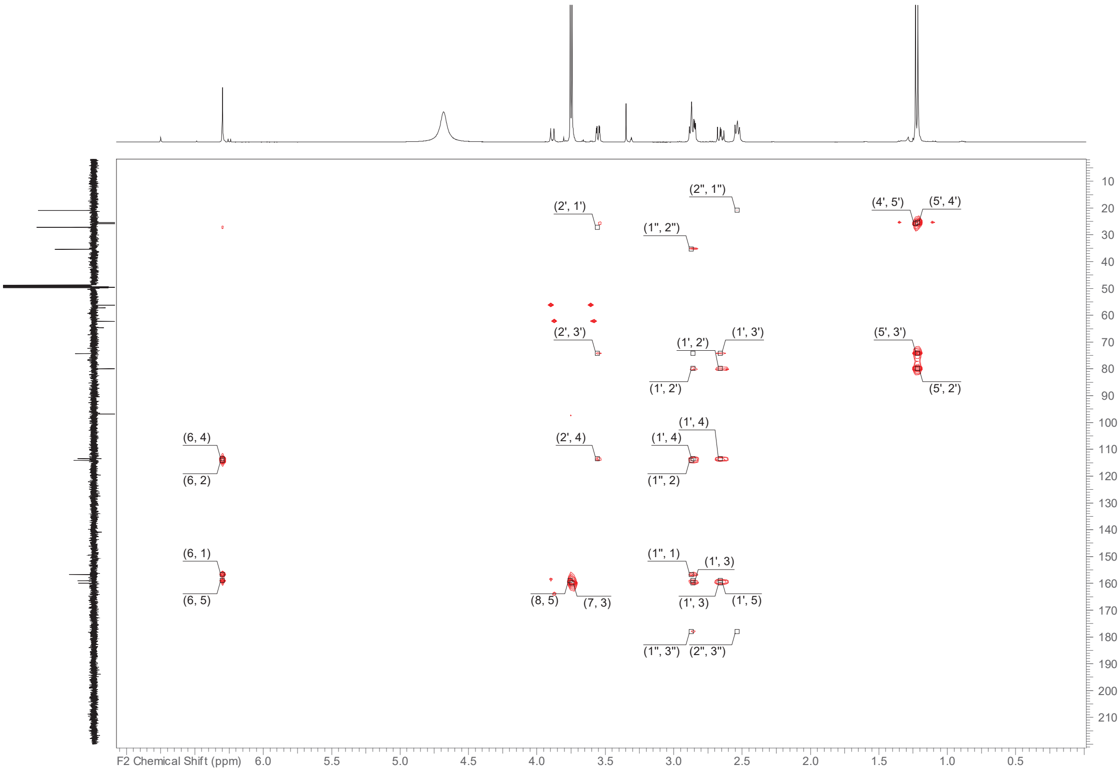

Figure S68. HMBC Spectrum of Compound **7** with an impurity (ca. 10%) of **6** (500 MHz, methanol-d_4).

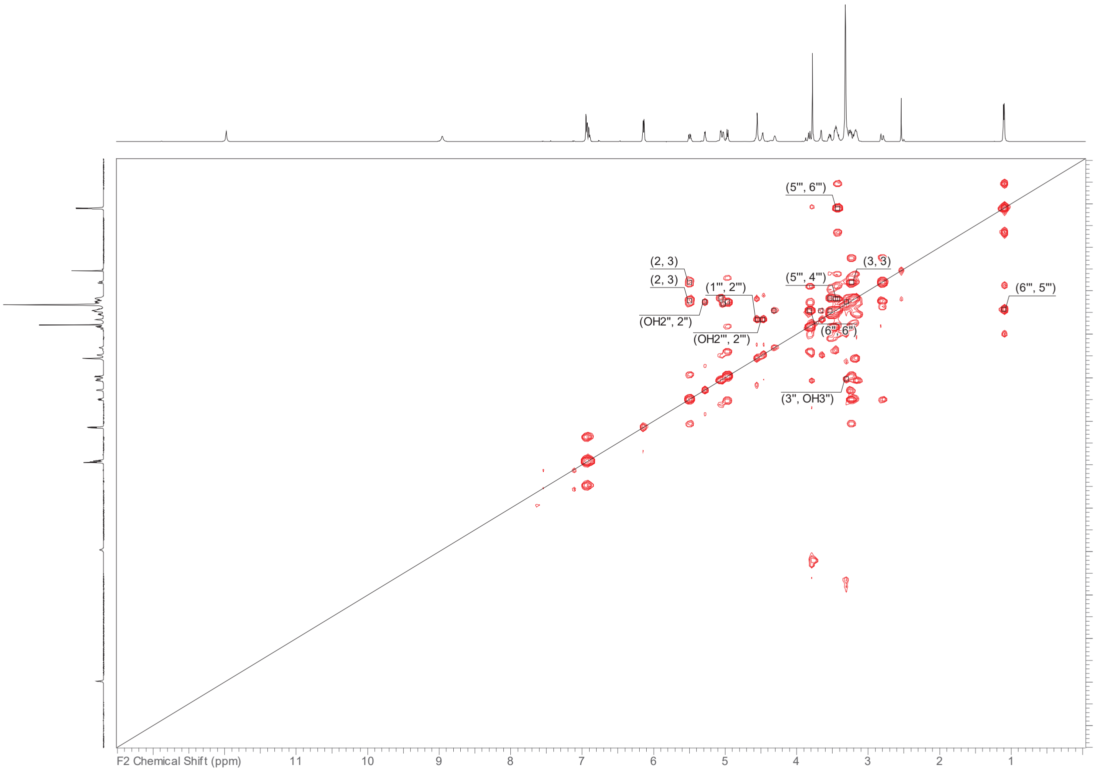

Figure S71. ^{1}H-^{1}H COSY Spectrum of Compound **8** (500 MHz, DMSO-d_6).

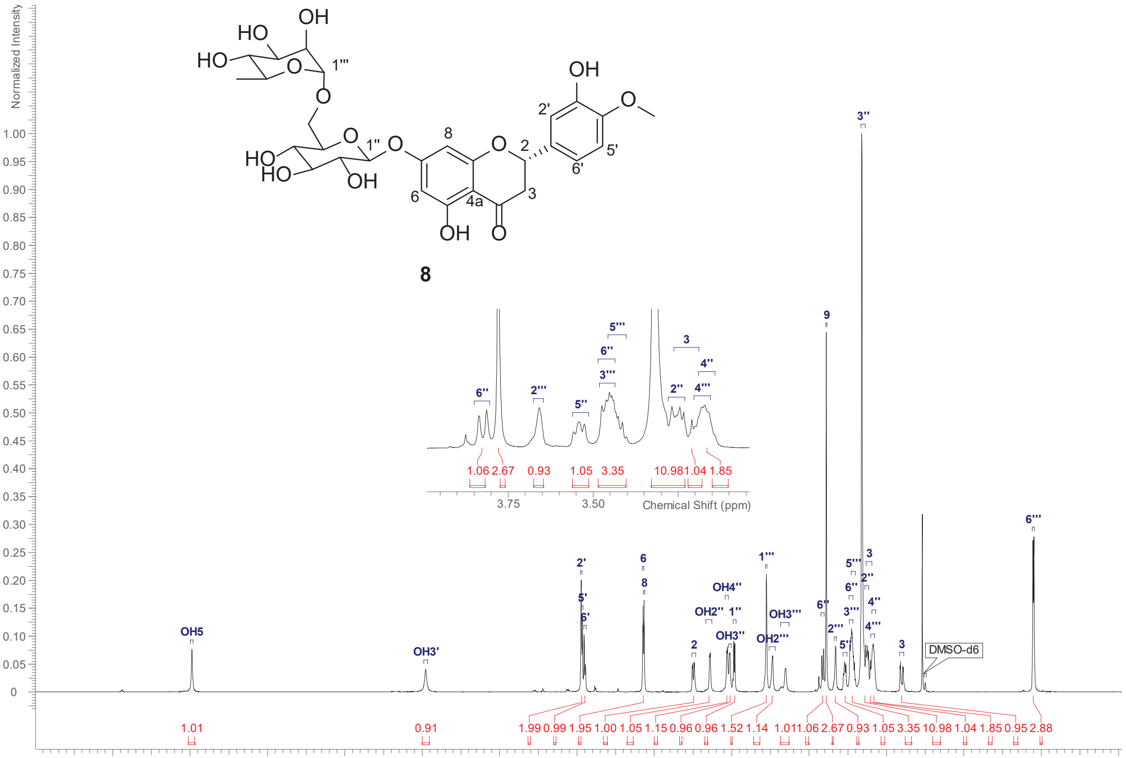

Figure S70. ^{1}H NMR Spectrum of Compound **8** (500 MHz, DMSO-d_6).

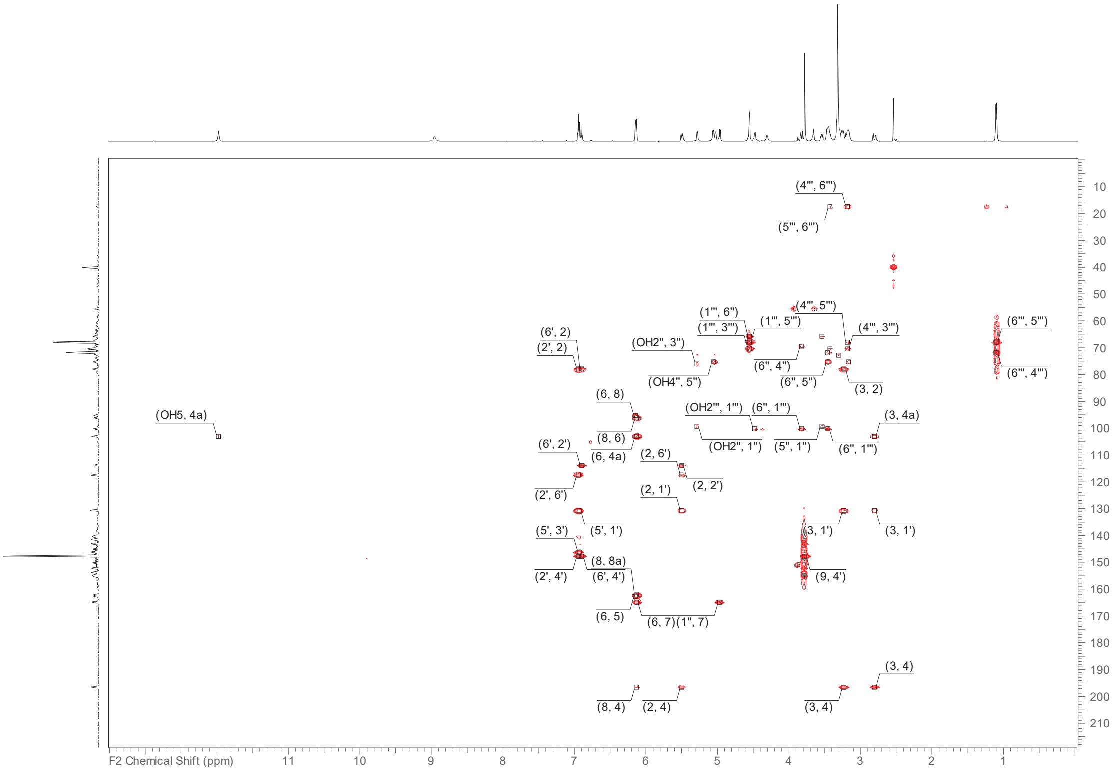

Figure S73. HMBC Spectrum of Compound **8** (500 MHz, DMSO-d_6).

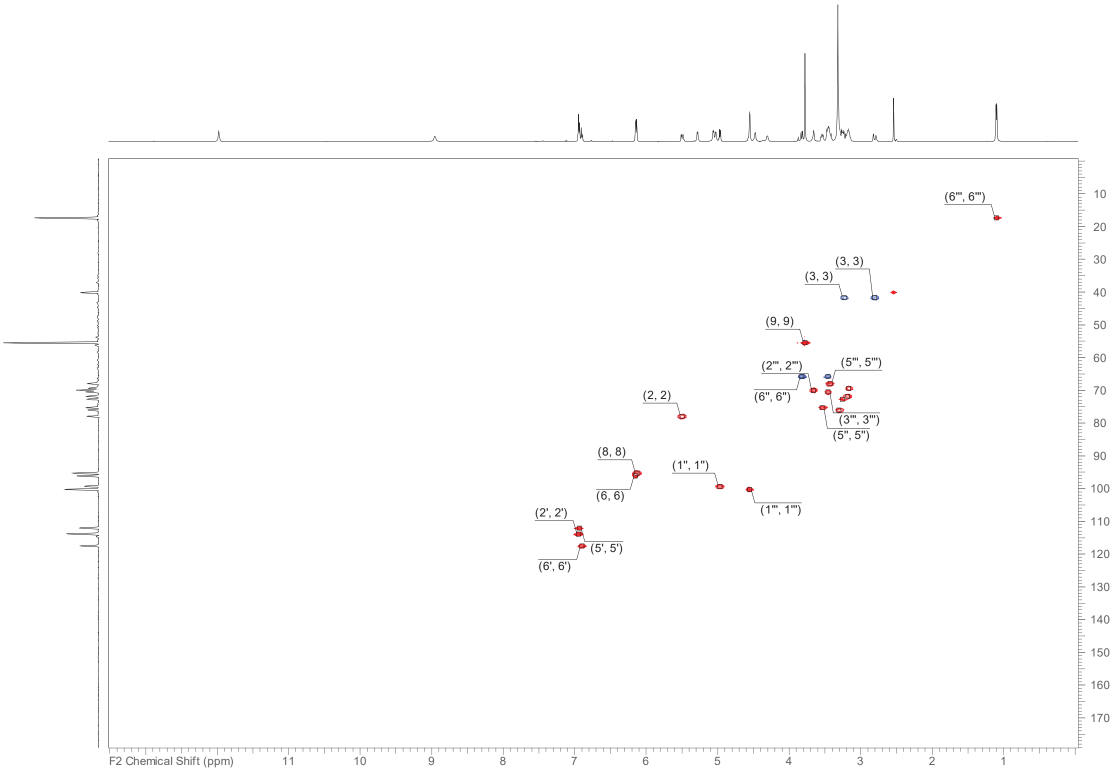

Figure S72. HSQC-DEPT Spectrum of Compound **8** (500 MHz, DMSO-d_6).

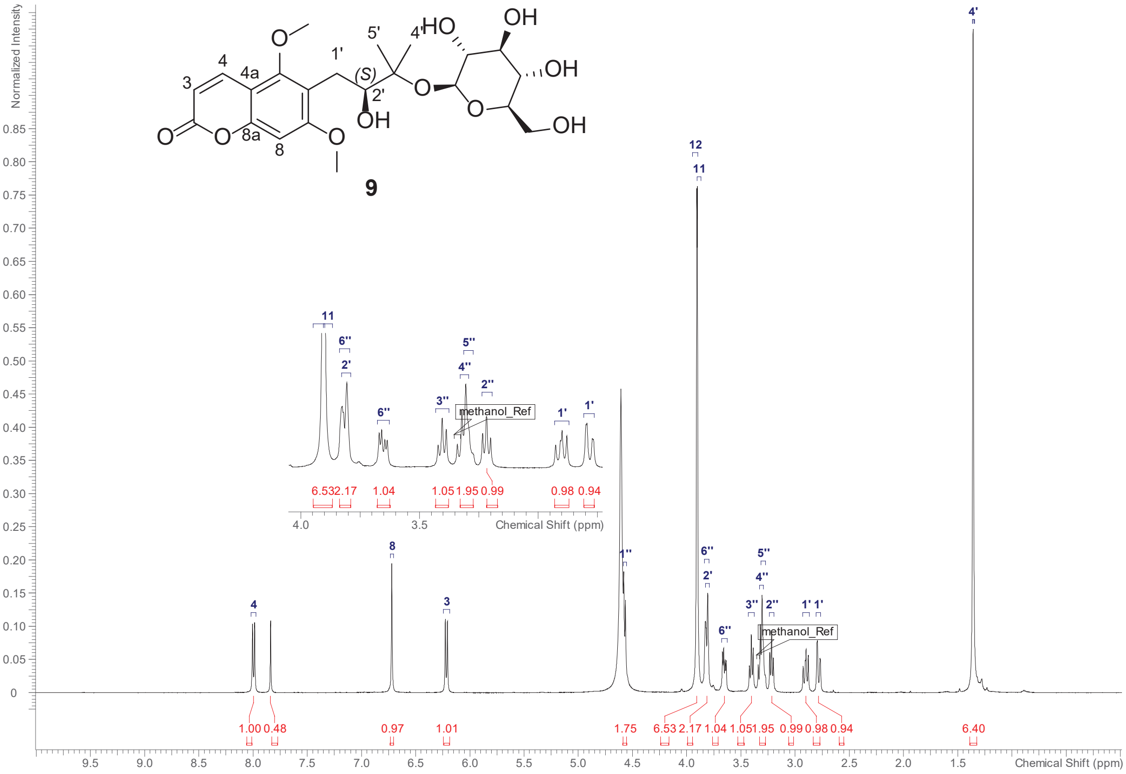

Figure S75. ^{1}H NMR Spectrum of Compound **9** (500 MHz, methanol-d_4).

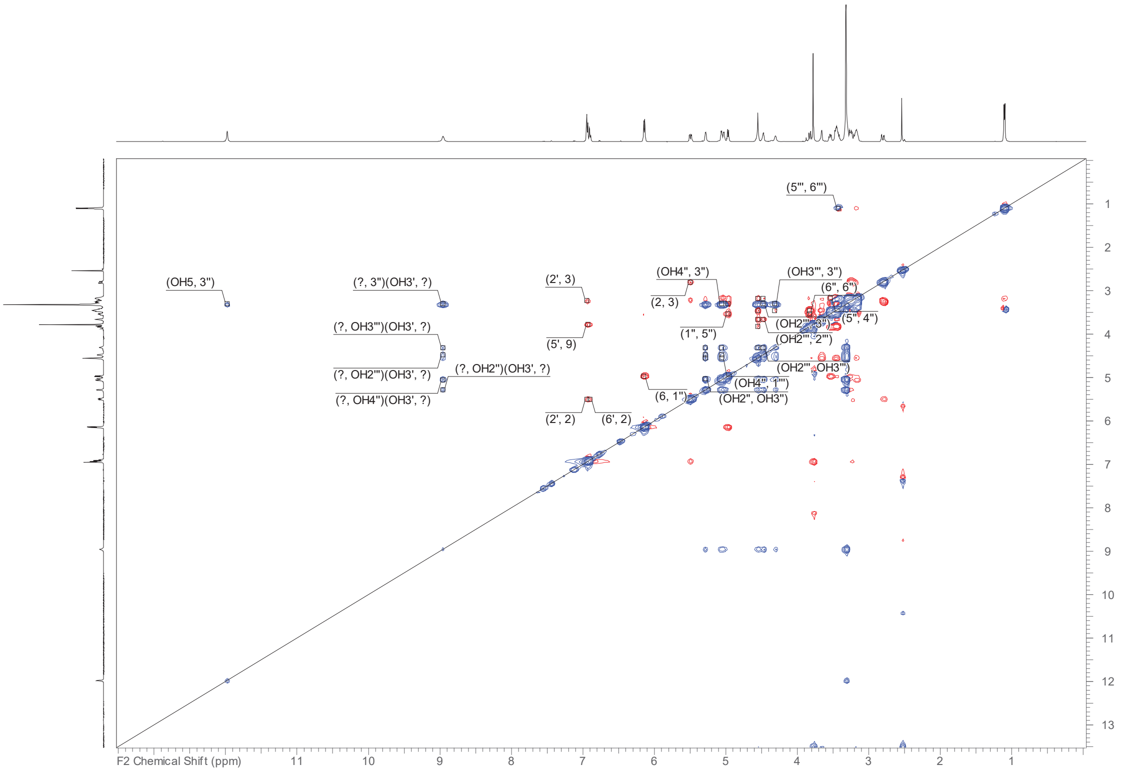

Figure S74. ^{1}H-^{1}H ROESY Spectrum of Compound **8** (500 MHz, DMSO-d_6).

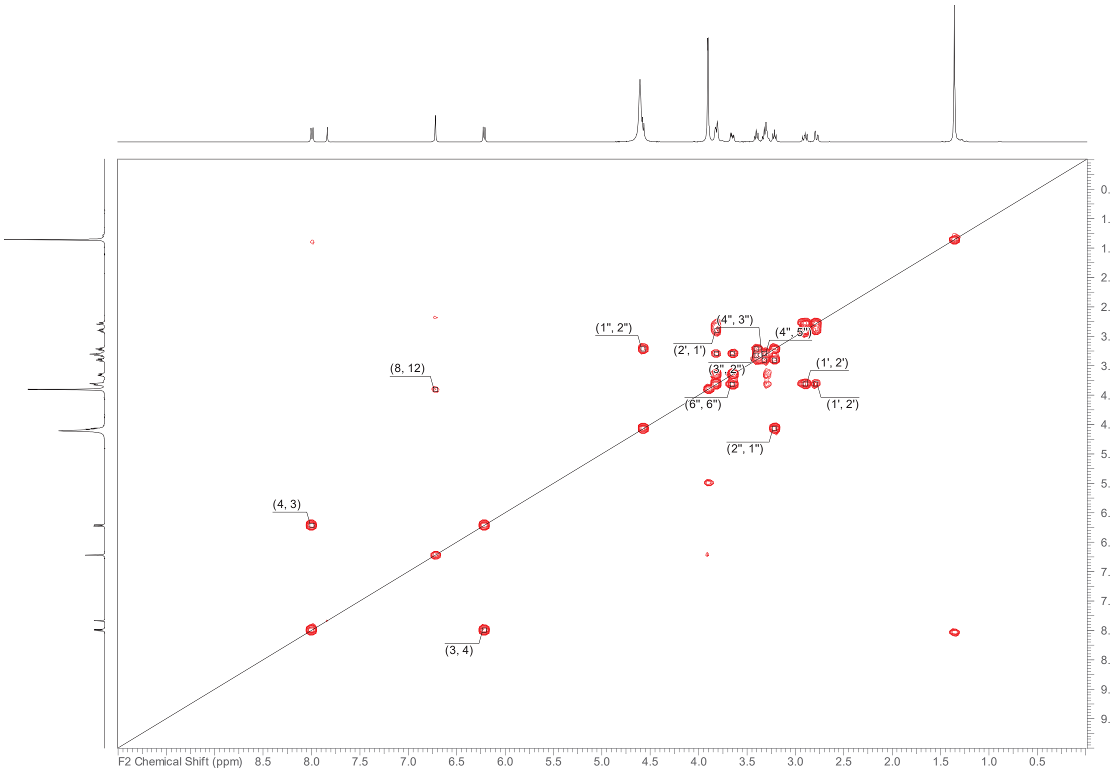

Figure S77. ^{1}H-^{1}H COSY Spectrum of Compound **9** (500 MHz, methanol-d_4).

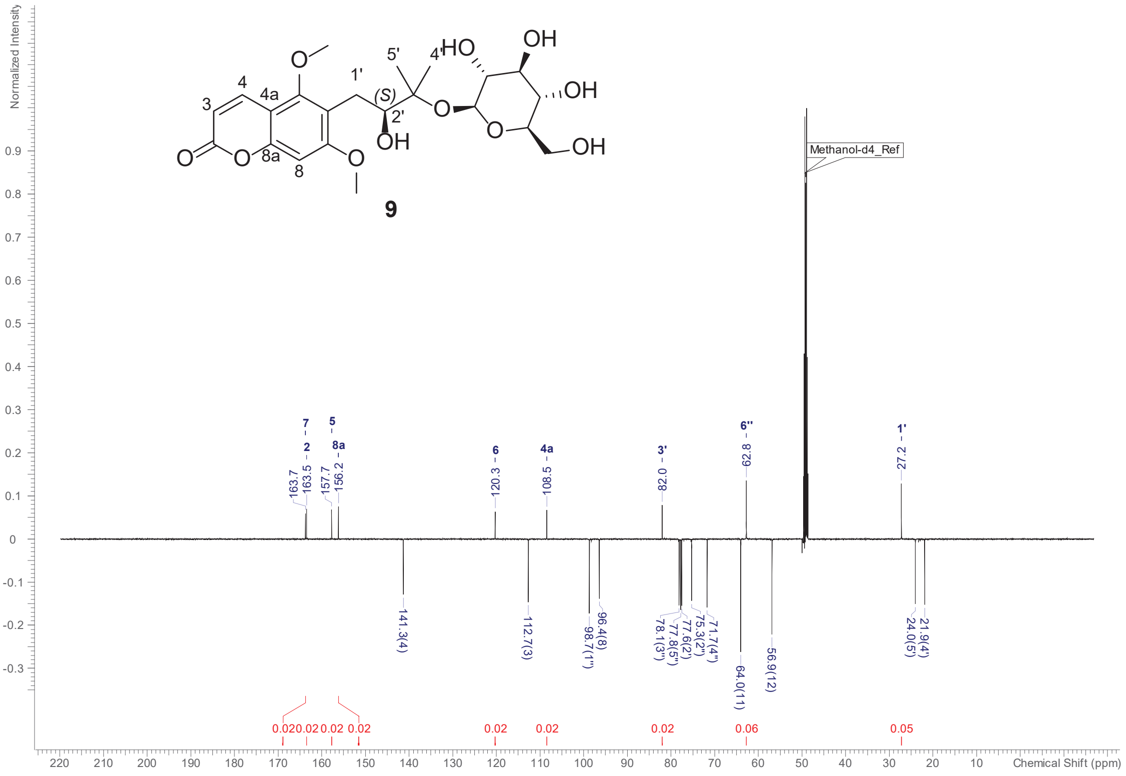

Figure S76. ^{13}C NMR Spectrum of Compound **9** (125 MHz, methanol-d_4).

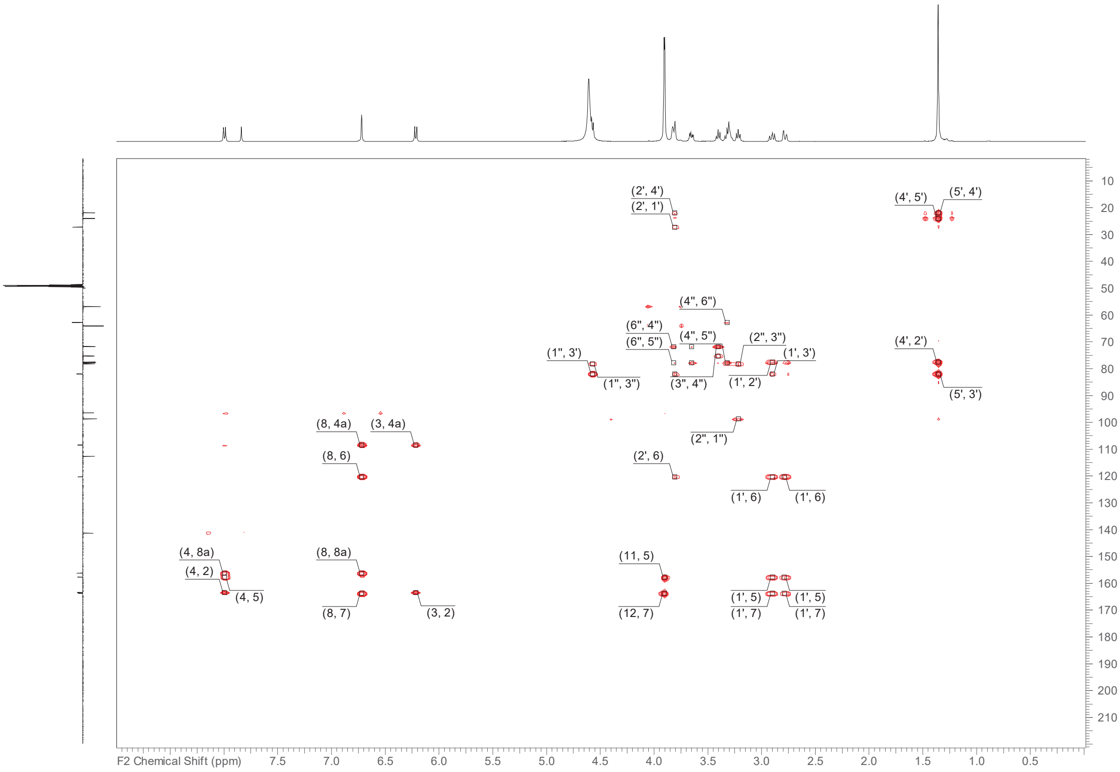

Figure S79. HMBC Spectrum of Compound **9** (500 MHz, methanol-d_4).

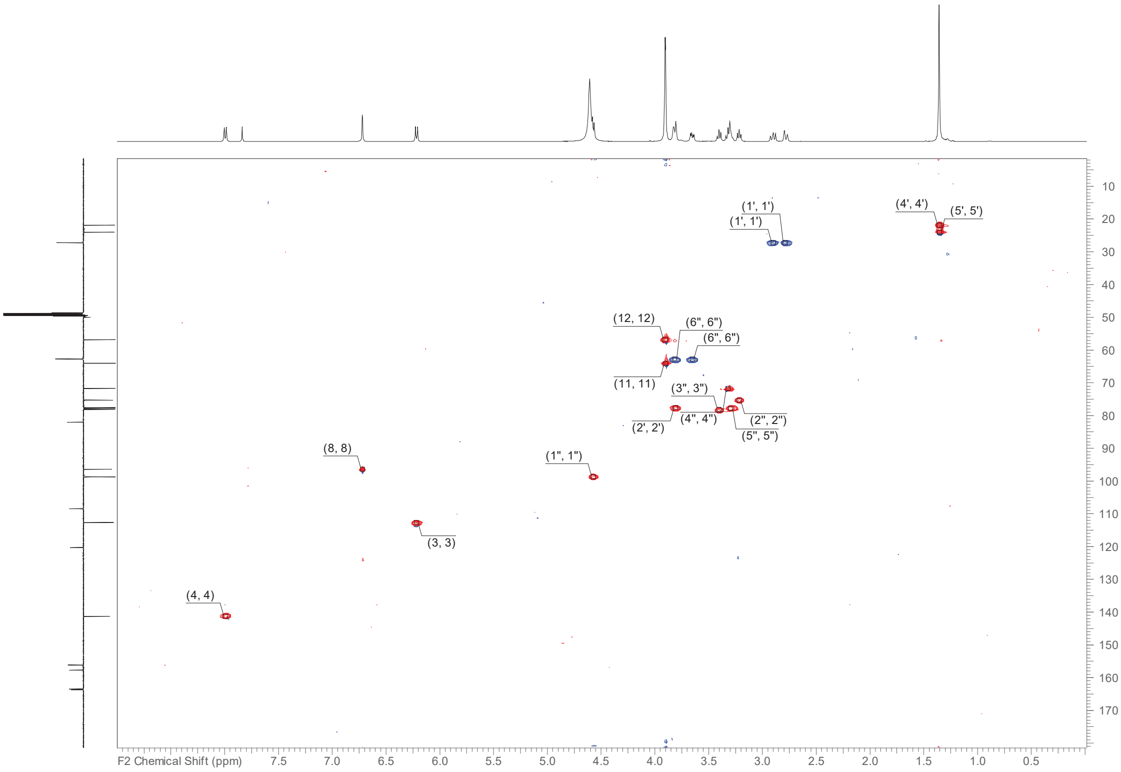

Figure S78. HSQC-DEPT Spectrum of Compound **9** (500 MHz, methanol-d_4).

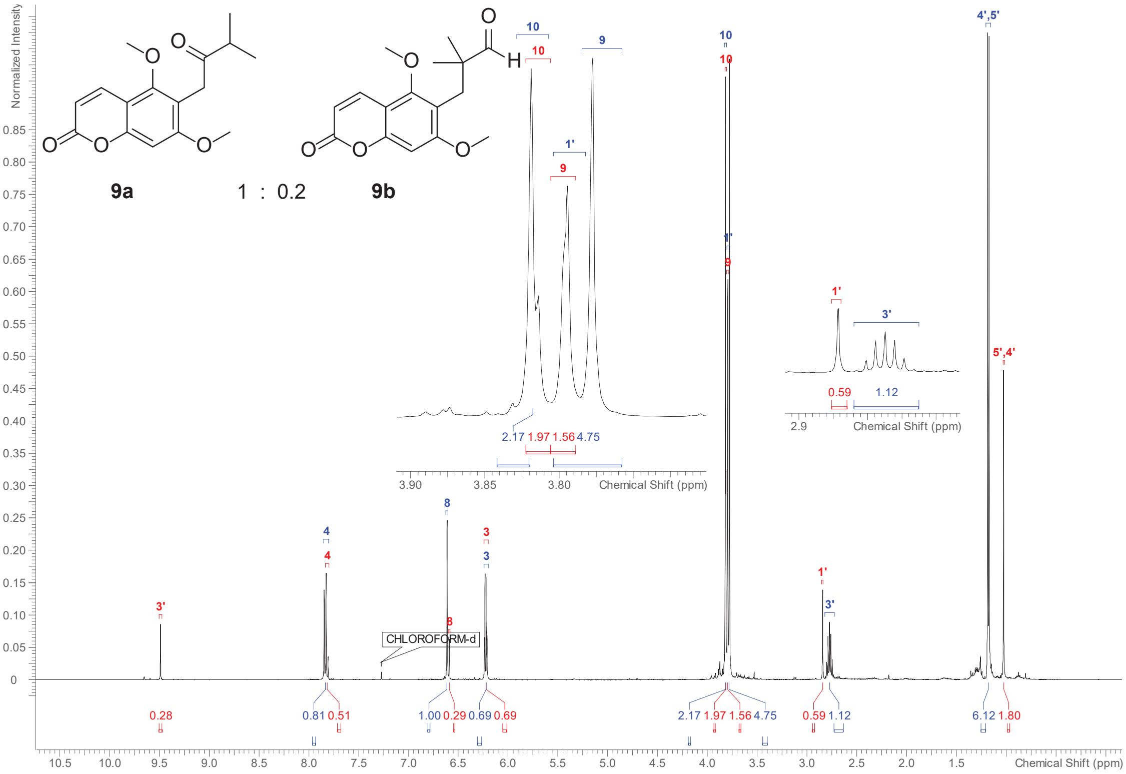

Figure S81. ^{1}H NMR Spectrum of Compounds **9a** (blue) and **9b** (red, molar ratio 3:1) after acid hydrolysis (500 MHz, methanol-d_4).

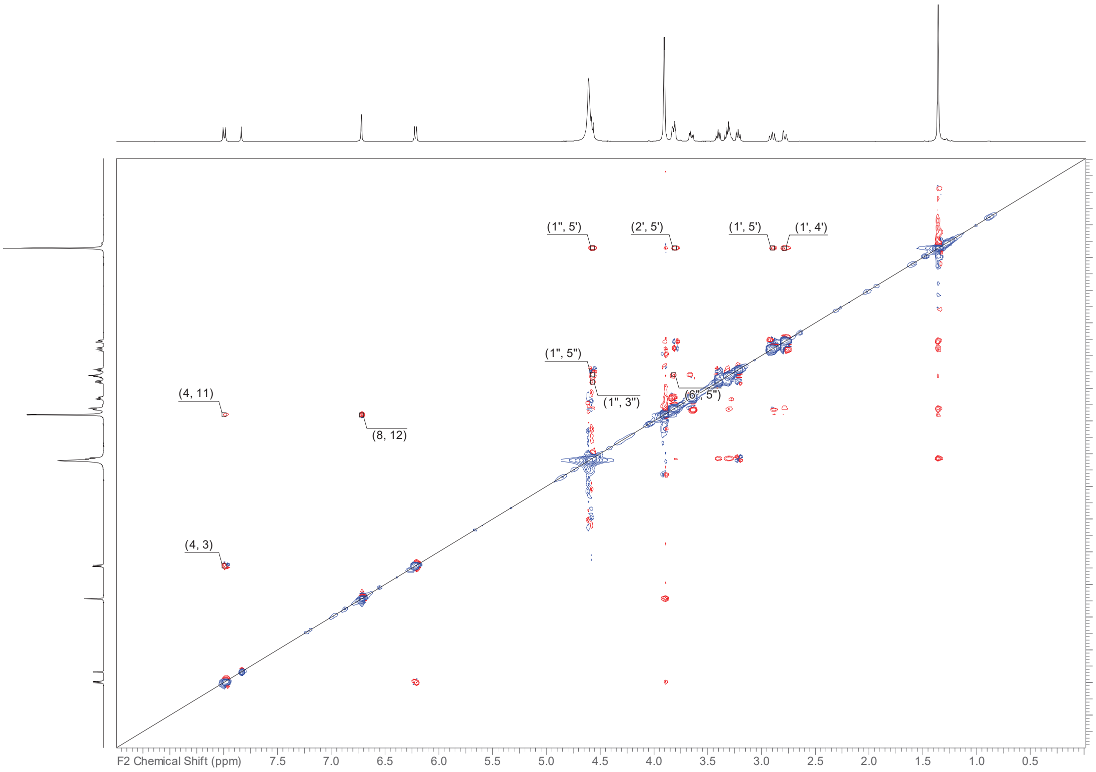

Figure S80. ^{1}H-^{1}H ROESY Spectrum of Compound **9** (500 MHz, methanol-d_4).

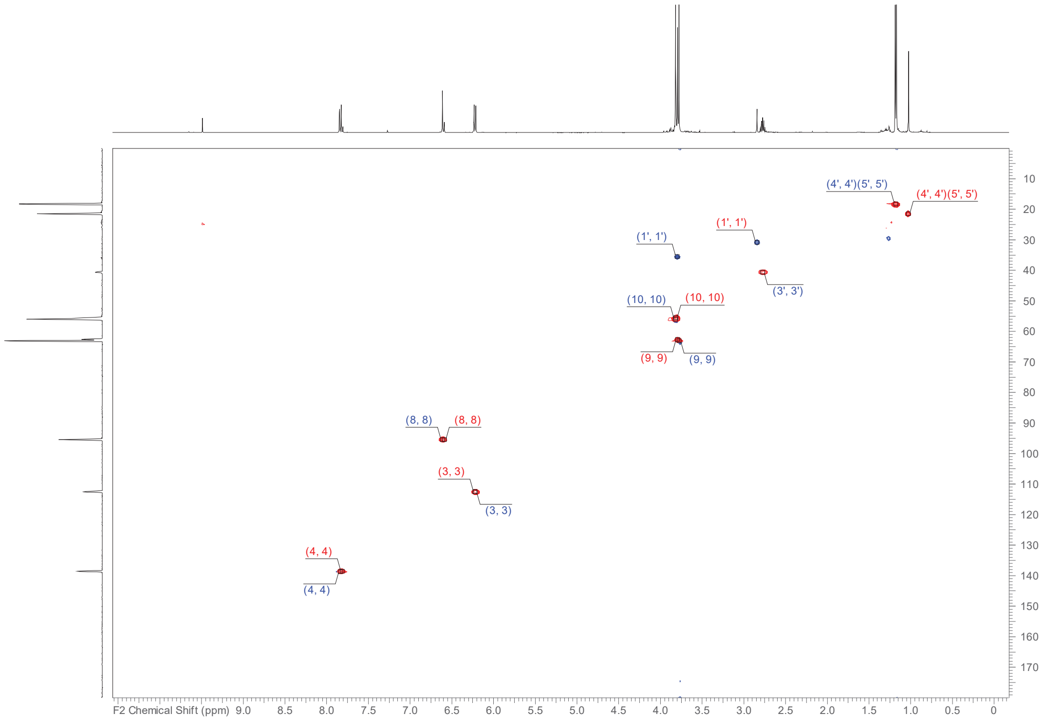

Figure S83. HSQC-DEPT spectrum of **9a** (blue) and **9b** (red, molar ratio 3:1) after acid hydrolysis (500 MHz, methanol-*d*$_4$). The signal for the aldehyde carbon was "wrapped" and is seen at 24 ppm.

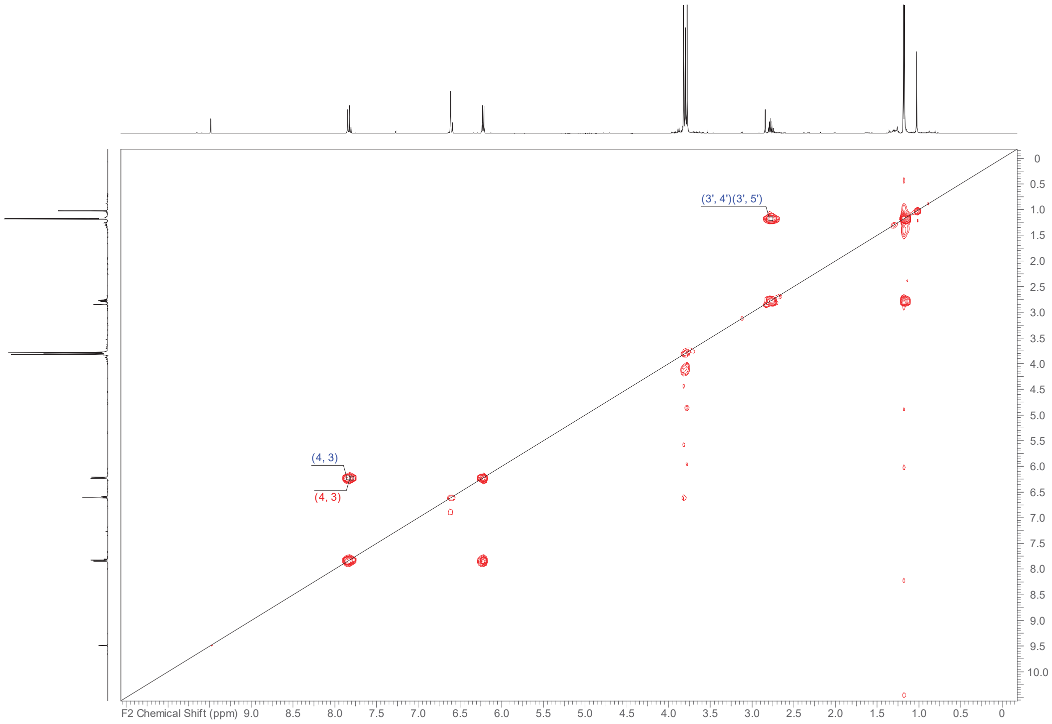

Figure S82. ^{1}H-^{1}H COSY Spectrum of Compounds **9a** (blue) and **9b** (red, molar ratio 3:1) after acid hydrolysis (500 MHz, methanol-*d*$_4$).

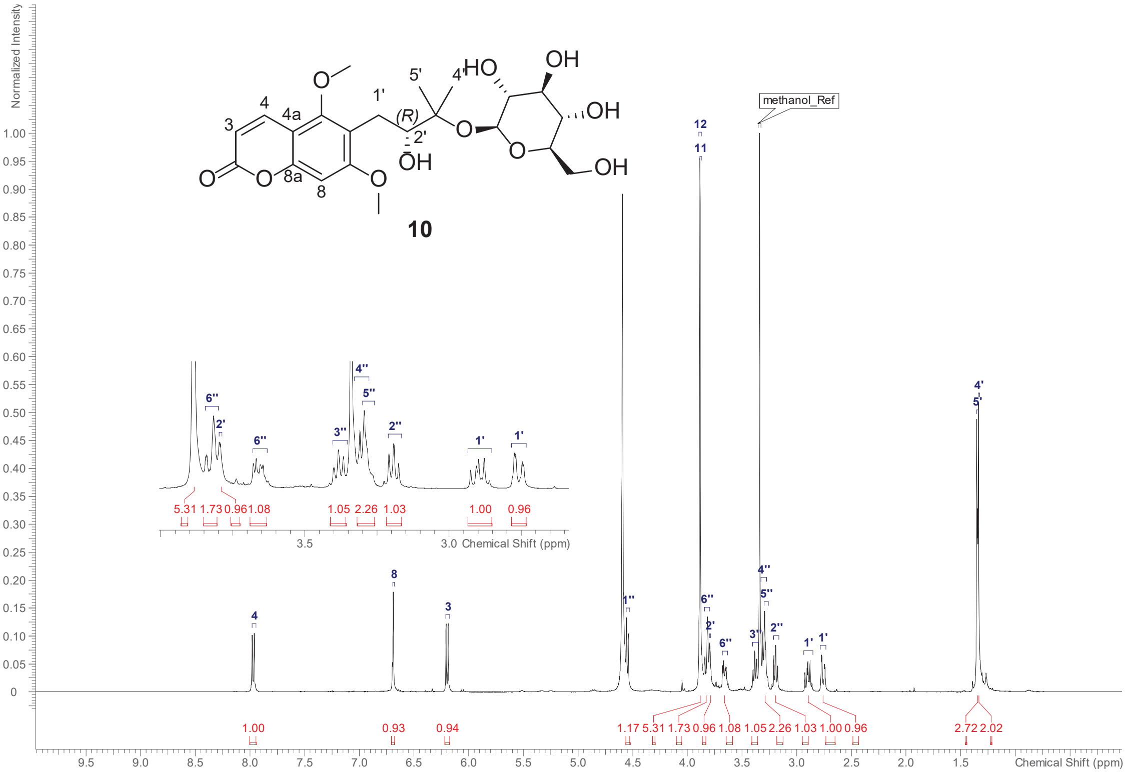

Figure S85. ^{1}H NMR Spectrum of Compound **10** (500 MHz, methanol-d_4).

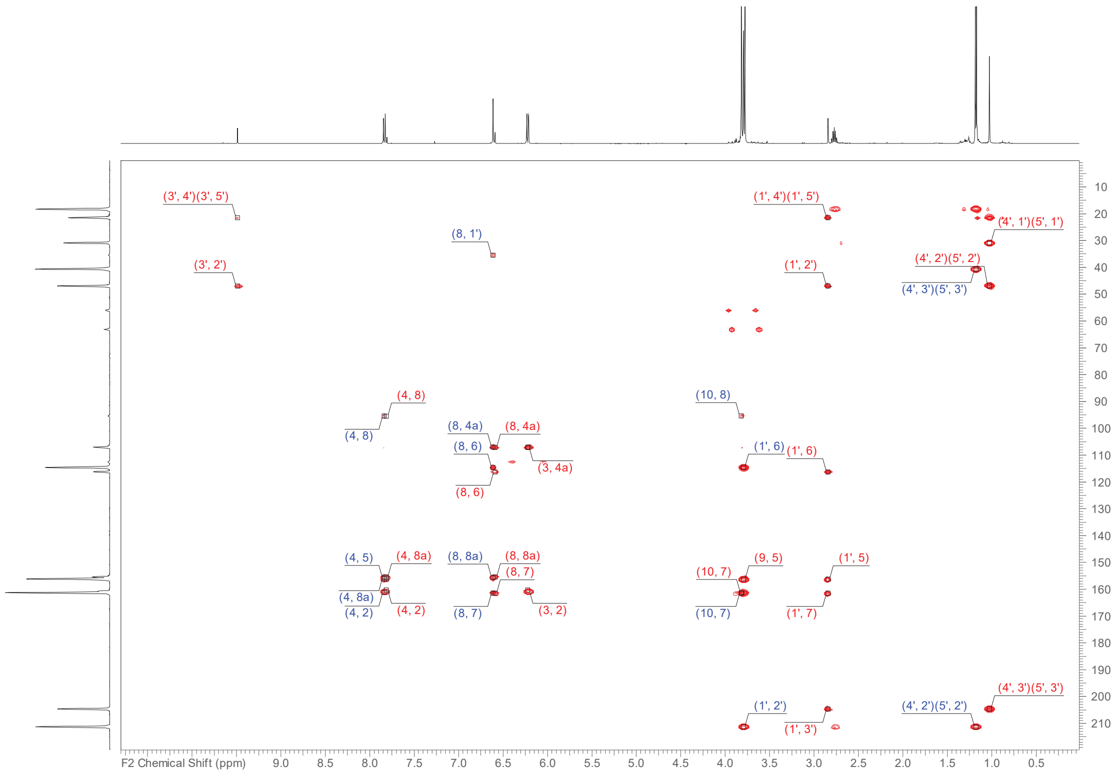

Figure S84. HMBC spectrum of **9a** (blue) and **9b** (red, molar ratio 3:1) after acid hydrolysis (500 MHz, methanol-d_4).

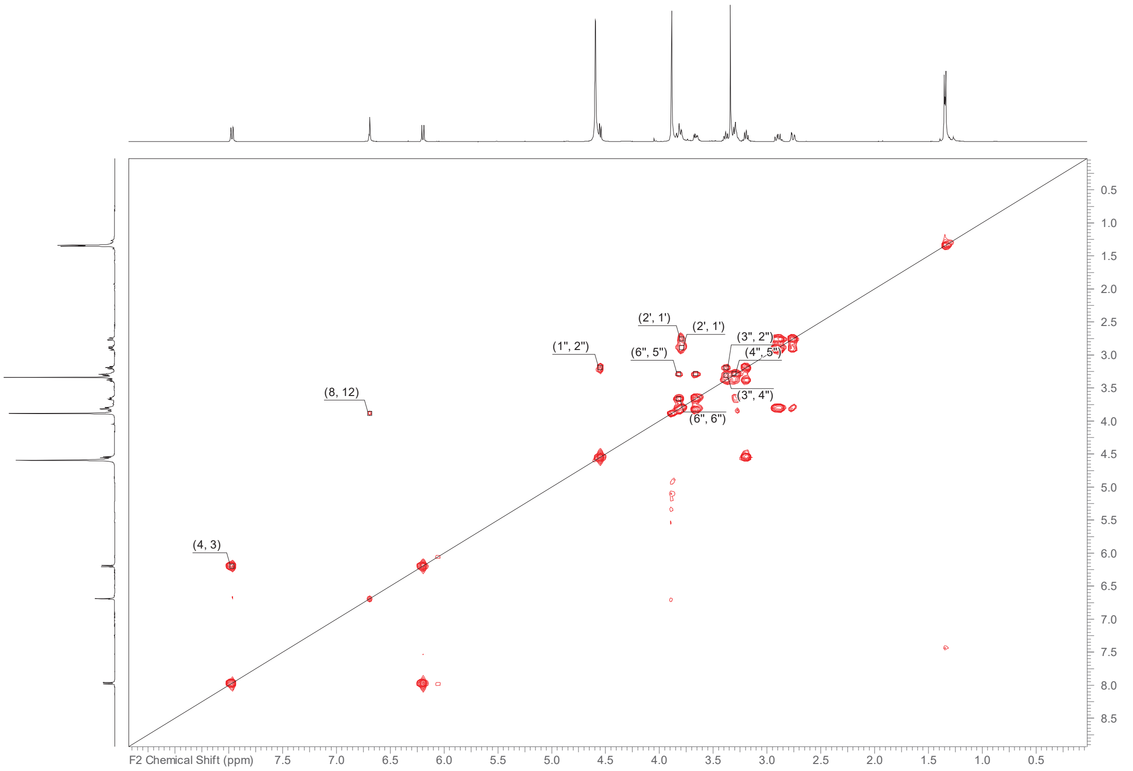

Figure S87. ^{1}H-^{1}H COSY Spectrum of Compound **10** (500 MHz, methanol-d_4).

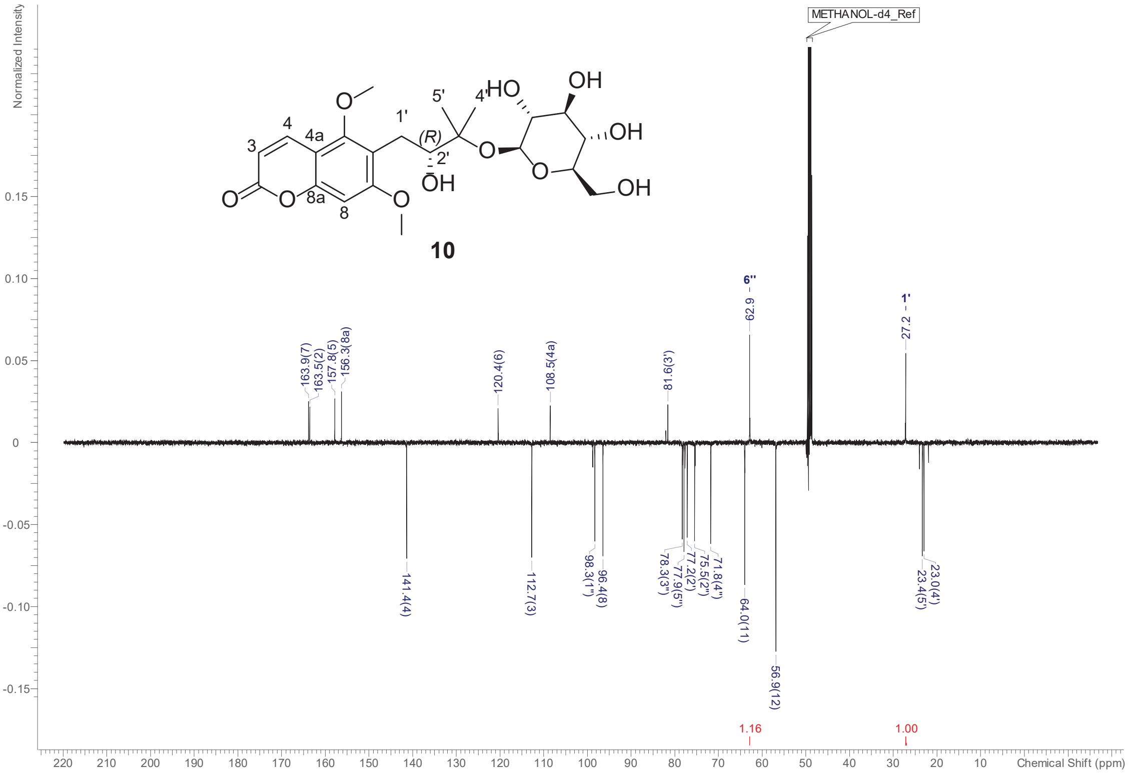

Figure S86. ^{13}C NMR Spectrum of Compound **10** (125 MHz, methanol-d_4).

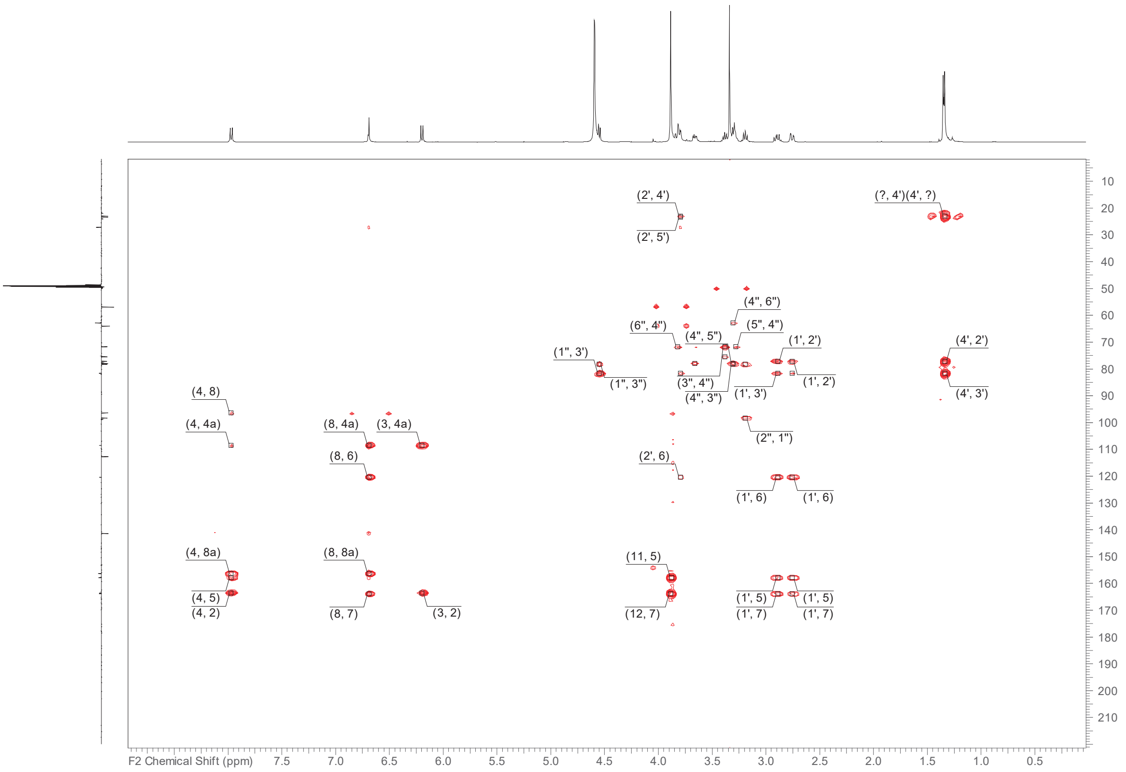

Figure S89. HMBC Spectrum of Compound **10** (500 MHz, methanol-d_4).

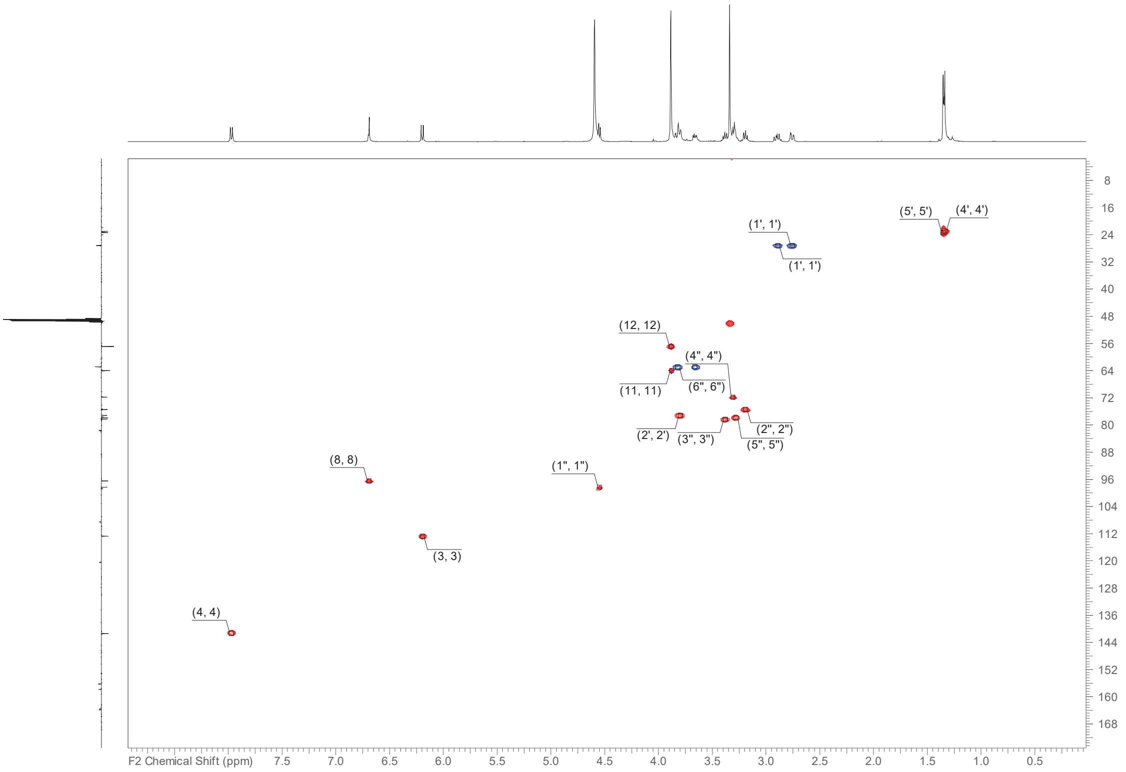

Figure S88 HSQC-DEPT Spectrum of Compound **10** (500 MHz, methanol-d_4).

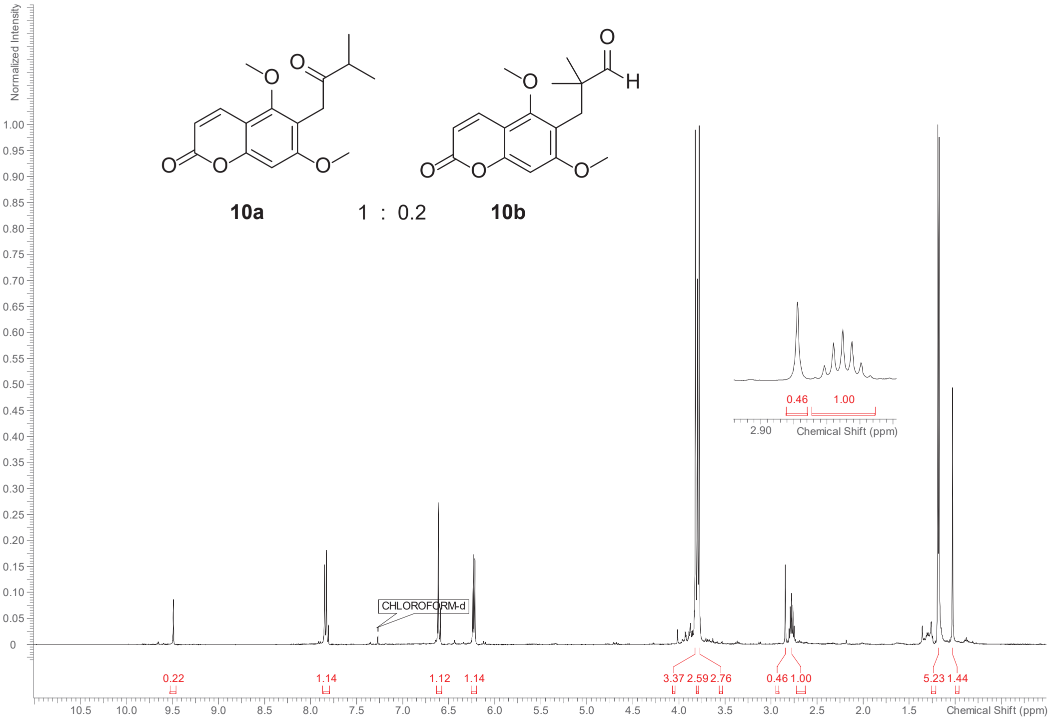

Figure S91. ^{1}H NMR Spectrum of Compounds **10a** and **10b** (molar ratio 1:0.2) after acid hydrolysis (500 MHz, methanol-d_4). Assignment was done analogously to **Figure S76**.

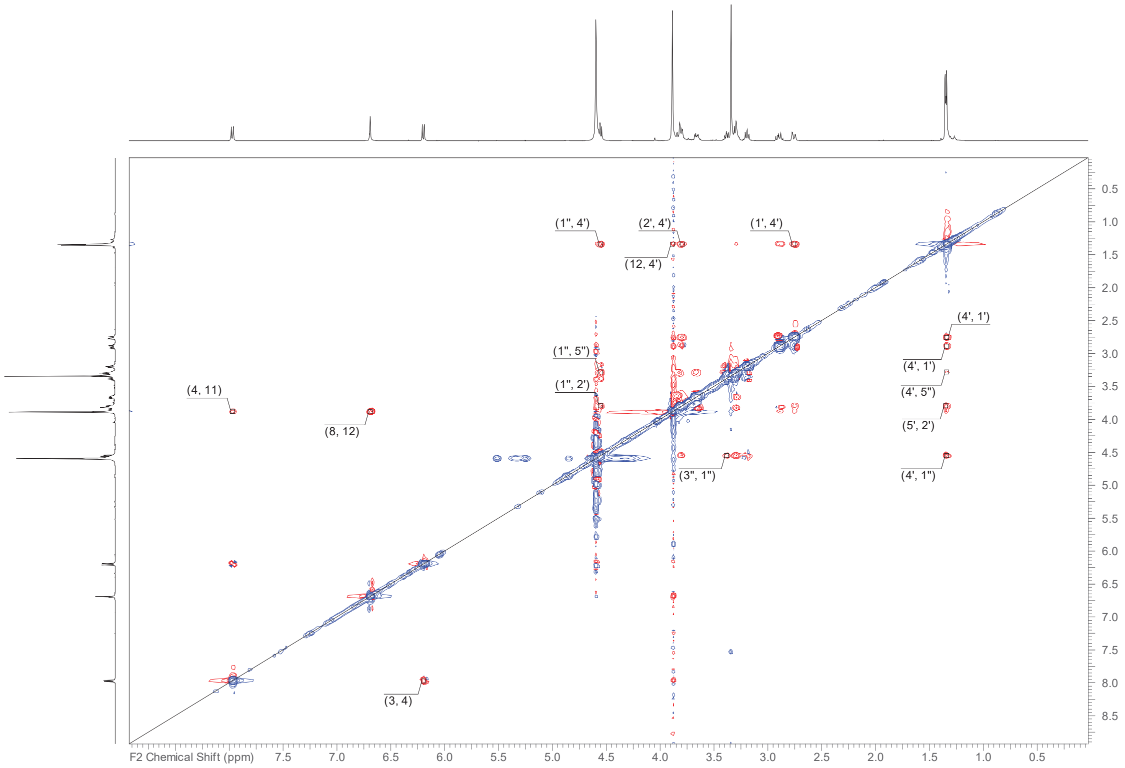

Figure S90. ^{1}H-^{1}H ROESY Spectrum of Compound **10** (500 MHz, methanol-d_4).

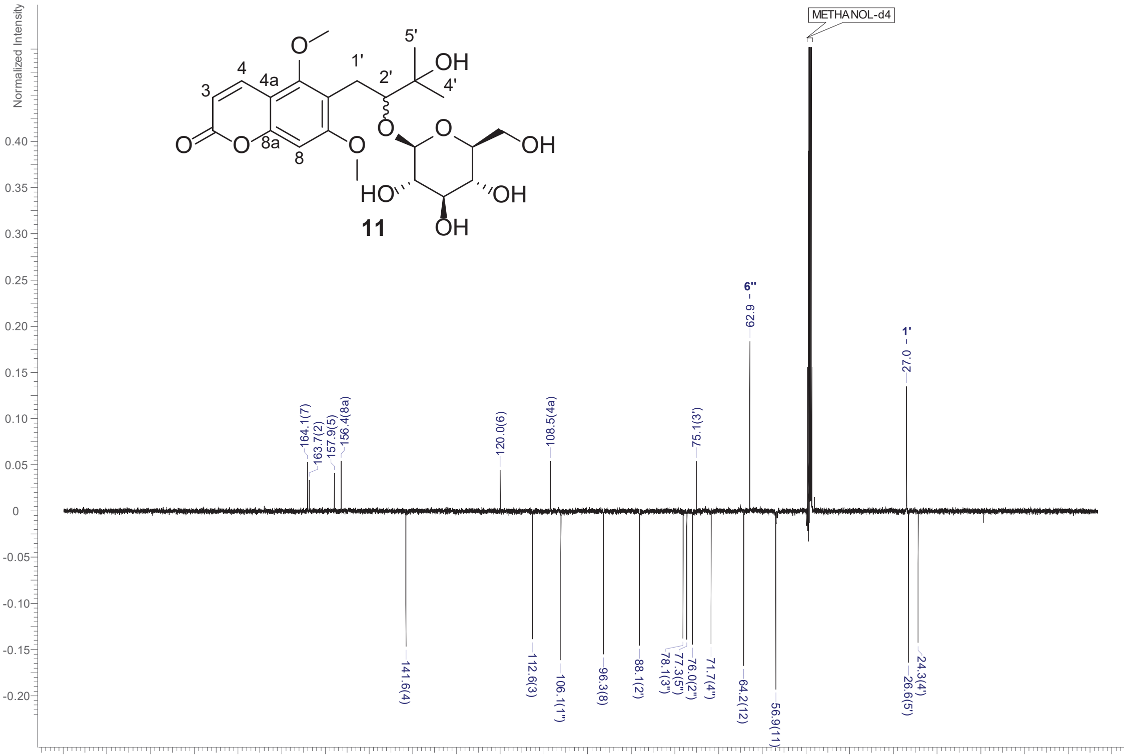

Figure S93. ^{13}C NMR Spectrum of Compound **11** (125 MHz, methanol-d_4).

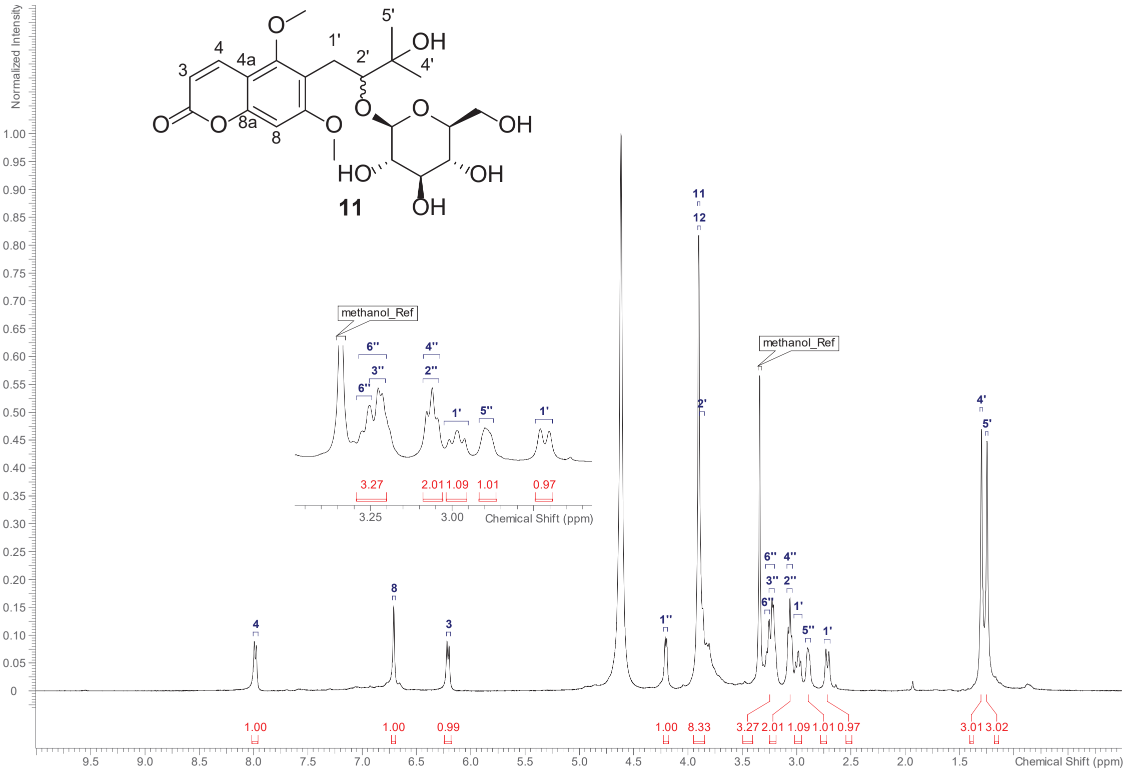

Figure S92. ^{1}H NMR Spectrum of Compound **11** (500 MHz, methanol-d_4).

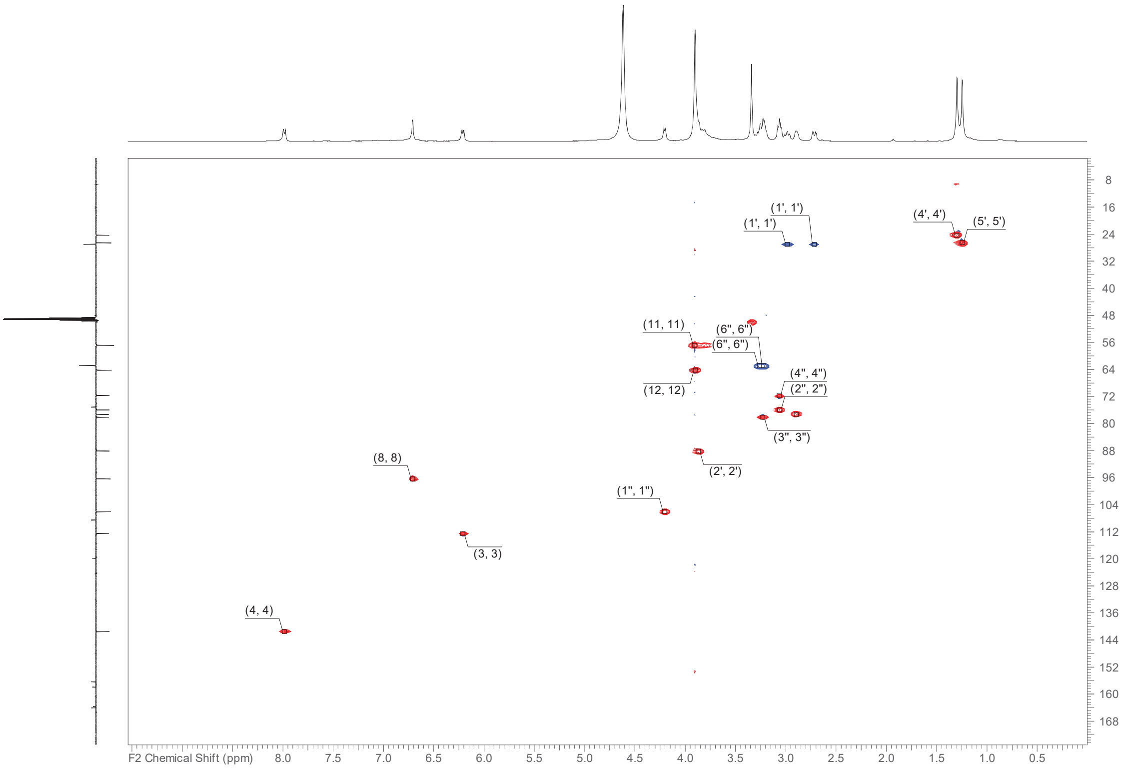

Figure S95. HSQC-DEPT Spectrum of Compound **11** (500 MHz, methanol-*d*$_4$).

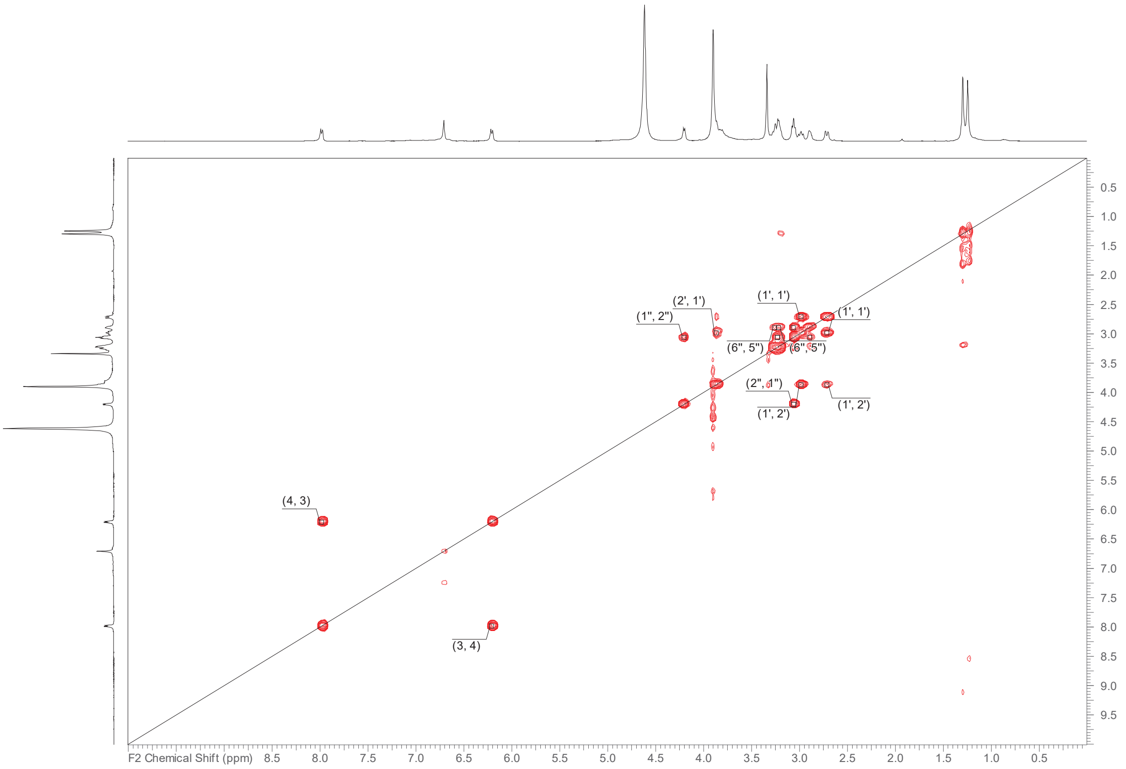

Figure S94. ^{1}H-^{1}H COSY Spectrum of Compound **11** (500 MHz, methanol-*d*$_4$).

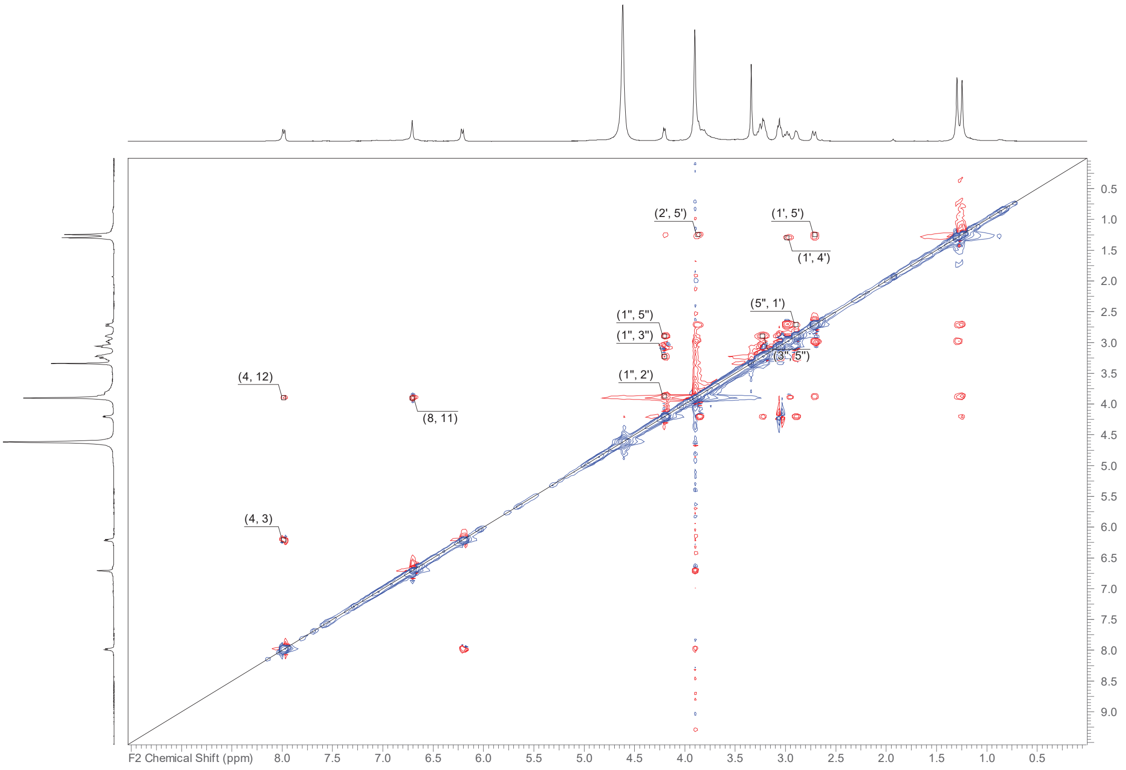

Figure S97. ^{1}H-^{1}H ROESY Spectrum of Compound **11** (500 MHz, methanol-d_4).

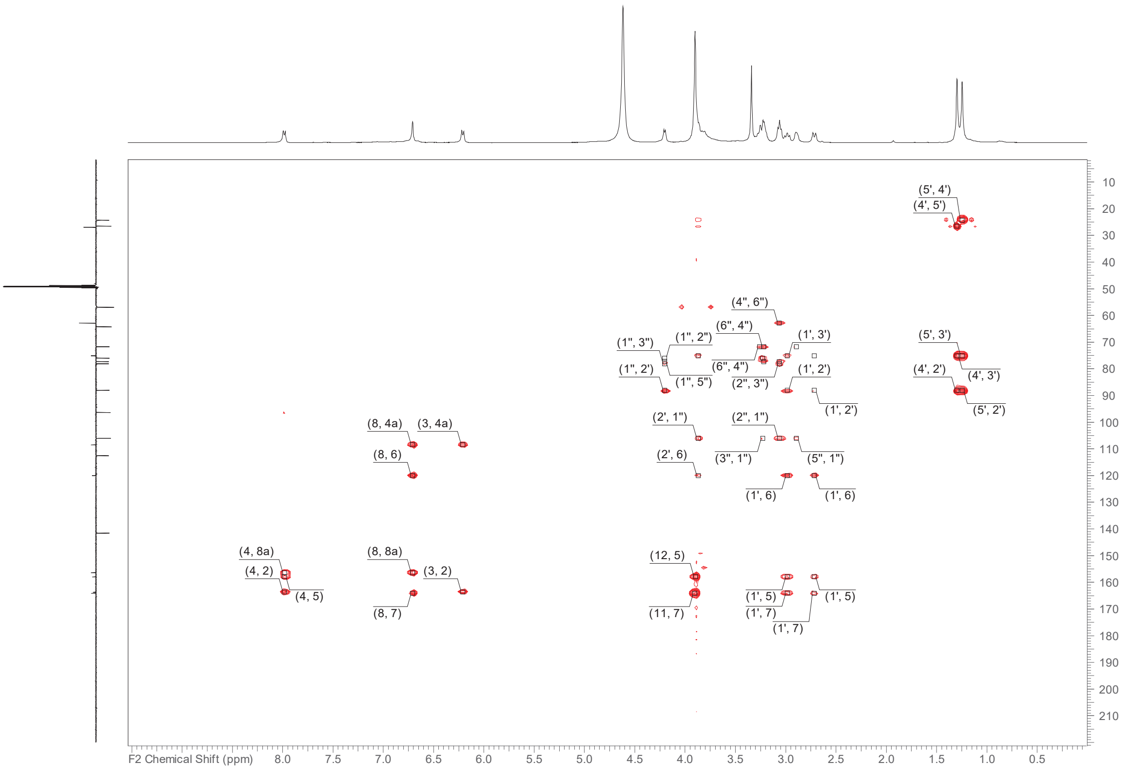

Figure S96. HMBC Spectrum of Compound **11** (500 MHz, methanol-d_4).

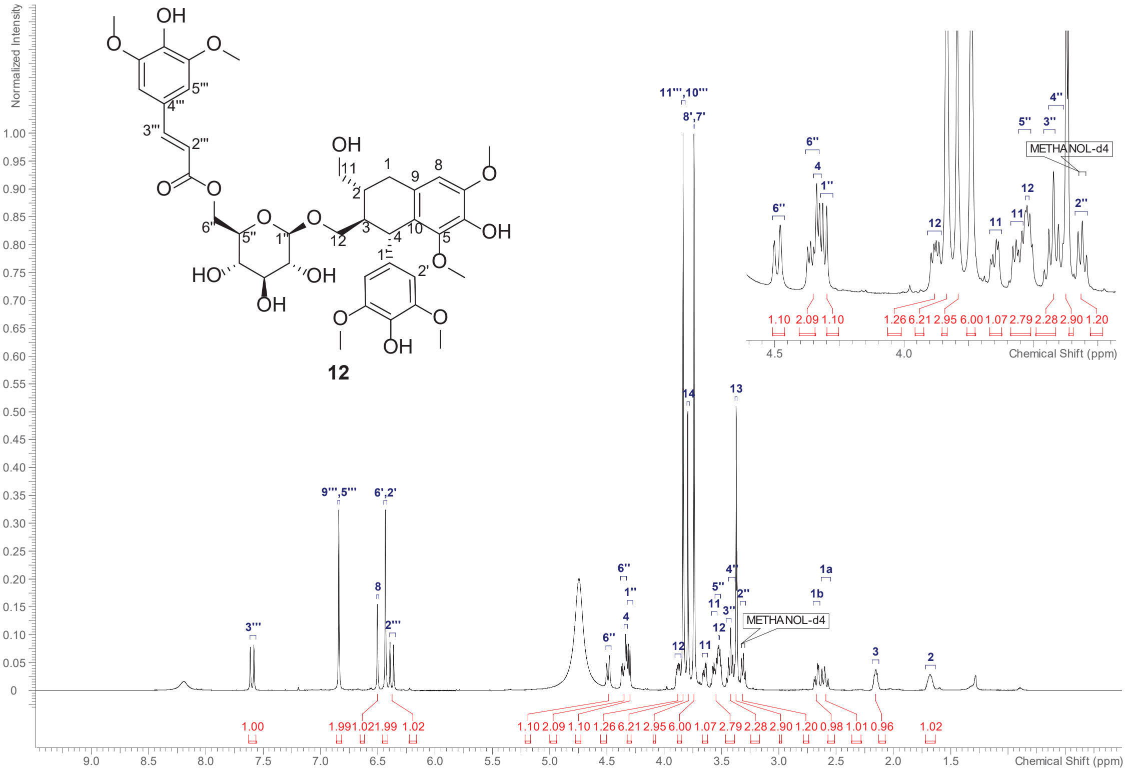

Figure S99. ^{1}H NMR Spectrum of Compound **12** (500 MHz, methanol-d_4).

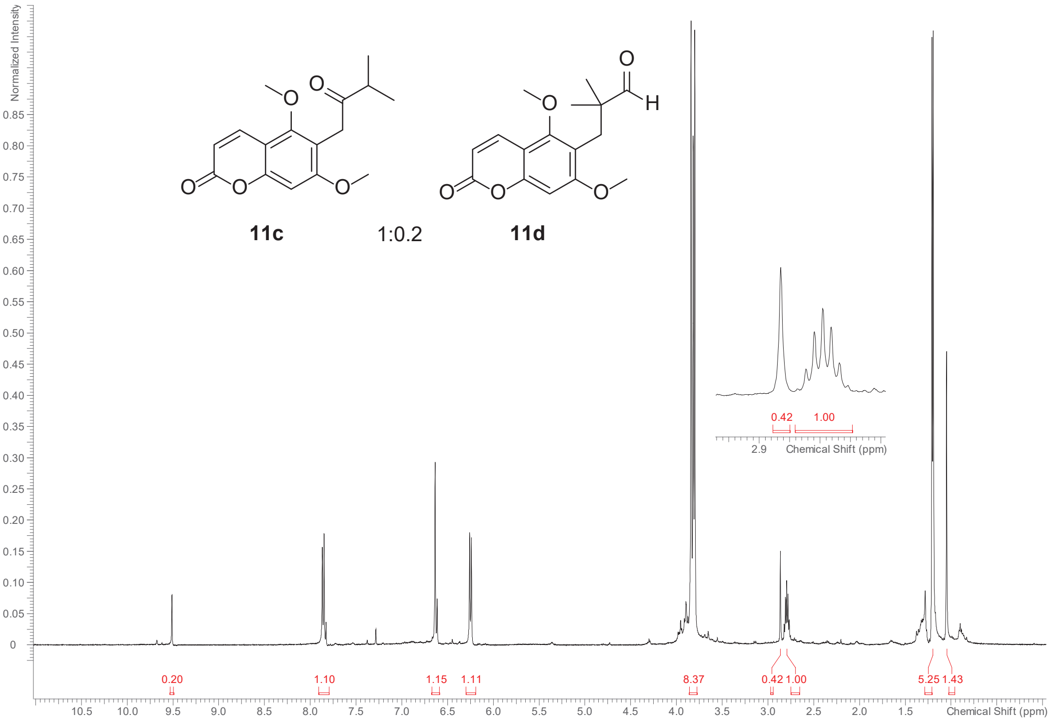

Figure S98. ^{1}H NMR Spectrum of Compounds **11c** and **11d** (molar ratio 1:0.2) after acid hydrolysis (500 MHz, methanol-d_4). Assignment was done analogously to **Figure S76**.

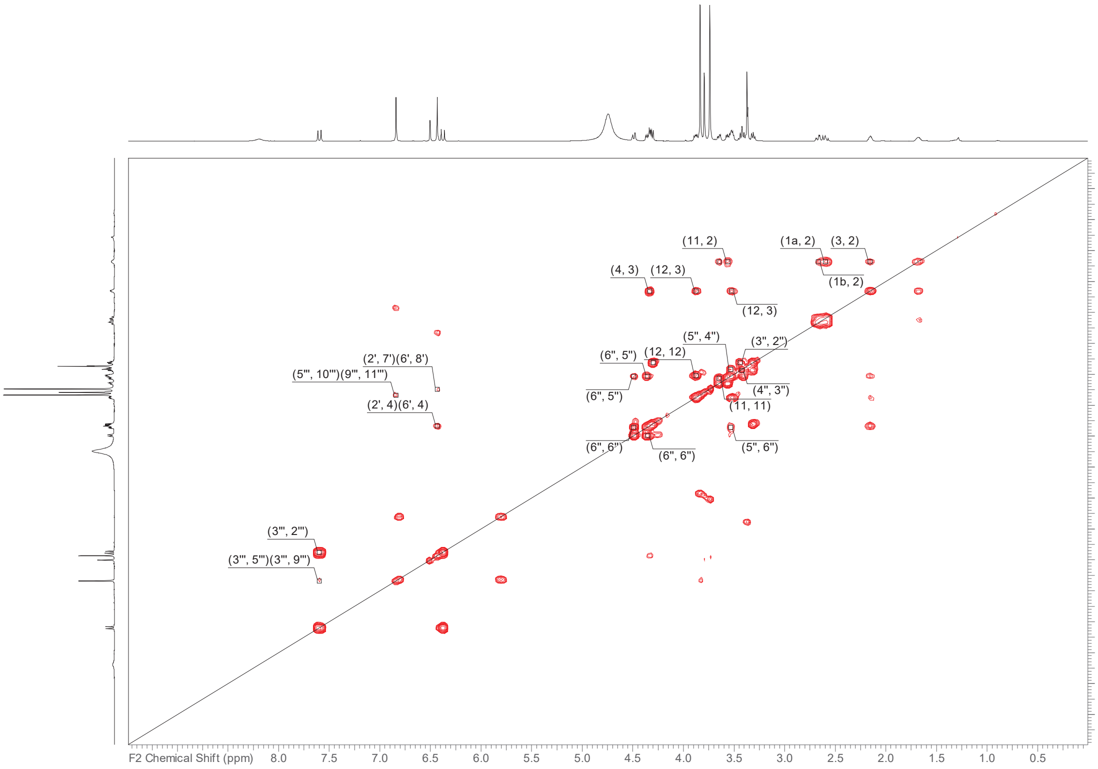

Figure S101. ^{1}H-^{1}H COSY Spectrum of Compound **12** (500 MHz, methanol-d_4).

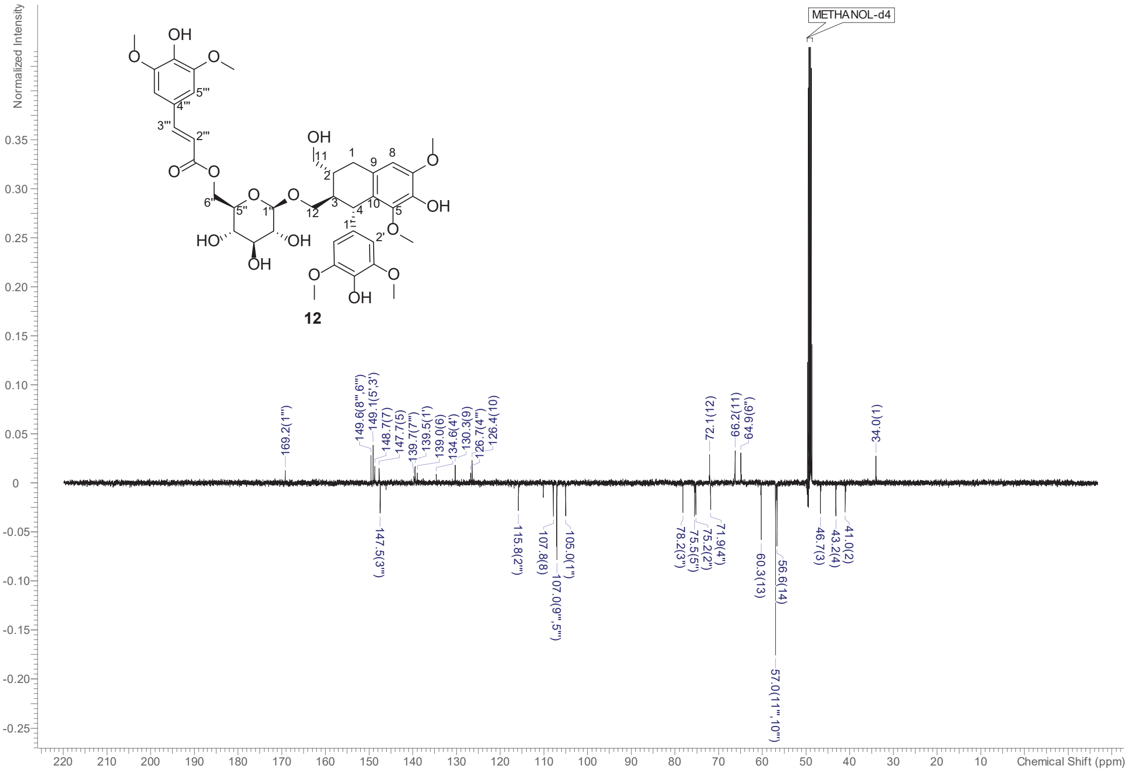

Figure S100. ^{13}C NMR Spectrum of Compound **12** (125 MHz, methanol-d_4).

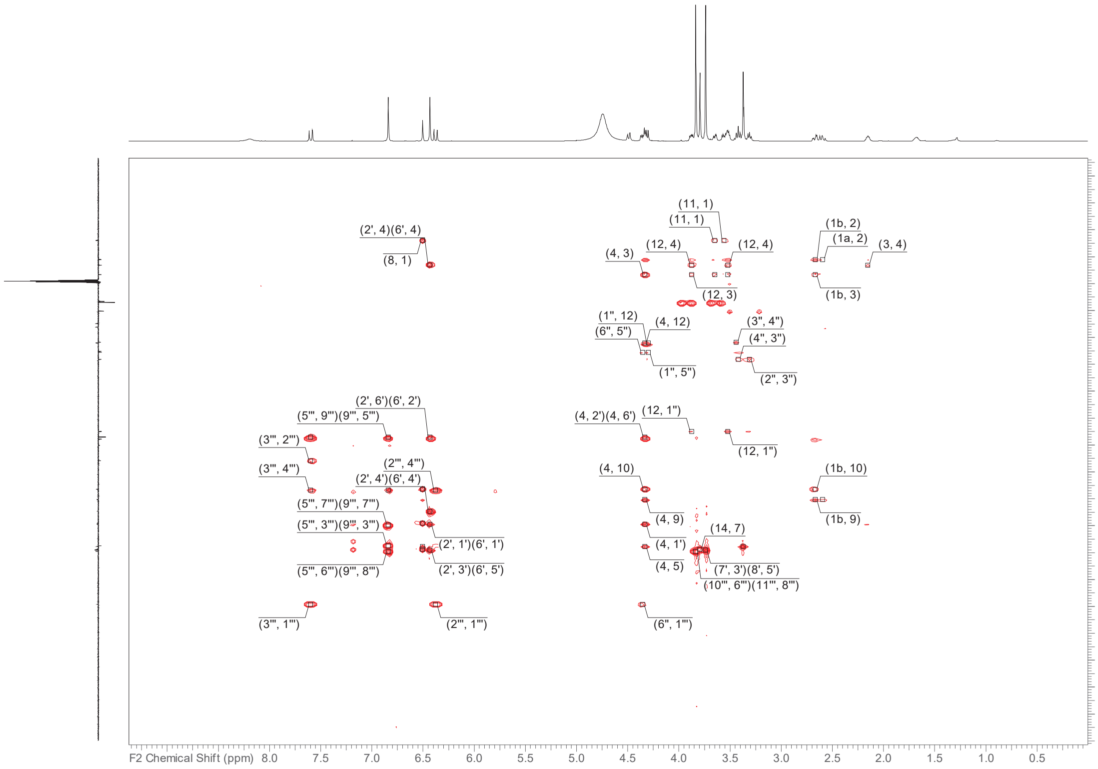

Figure S103. HMBC Spectrum of Compound **12** (500 MHz, methanol-*d₄*).

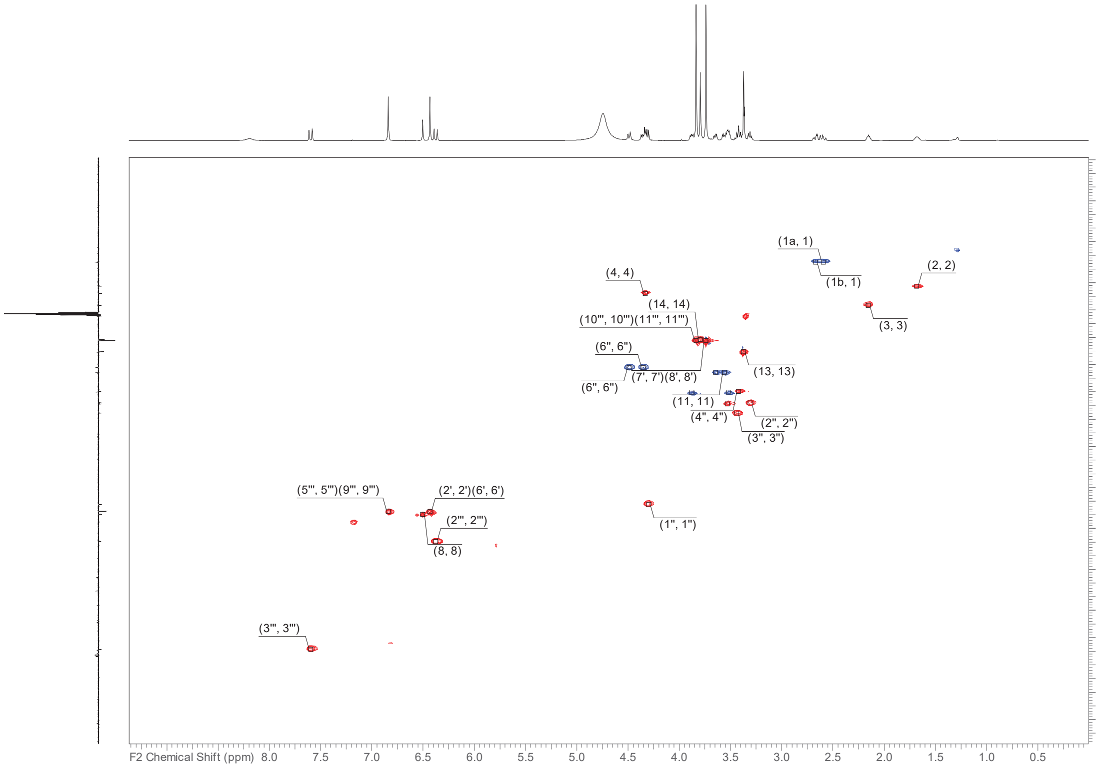

Figure S102. HSQC-DEPT Spectrum of Compound **12** (500 MHz, methanol-*d₄*).

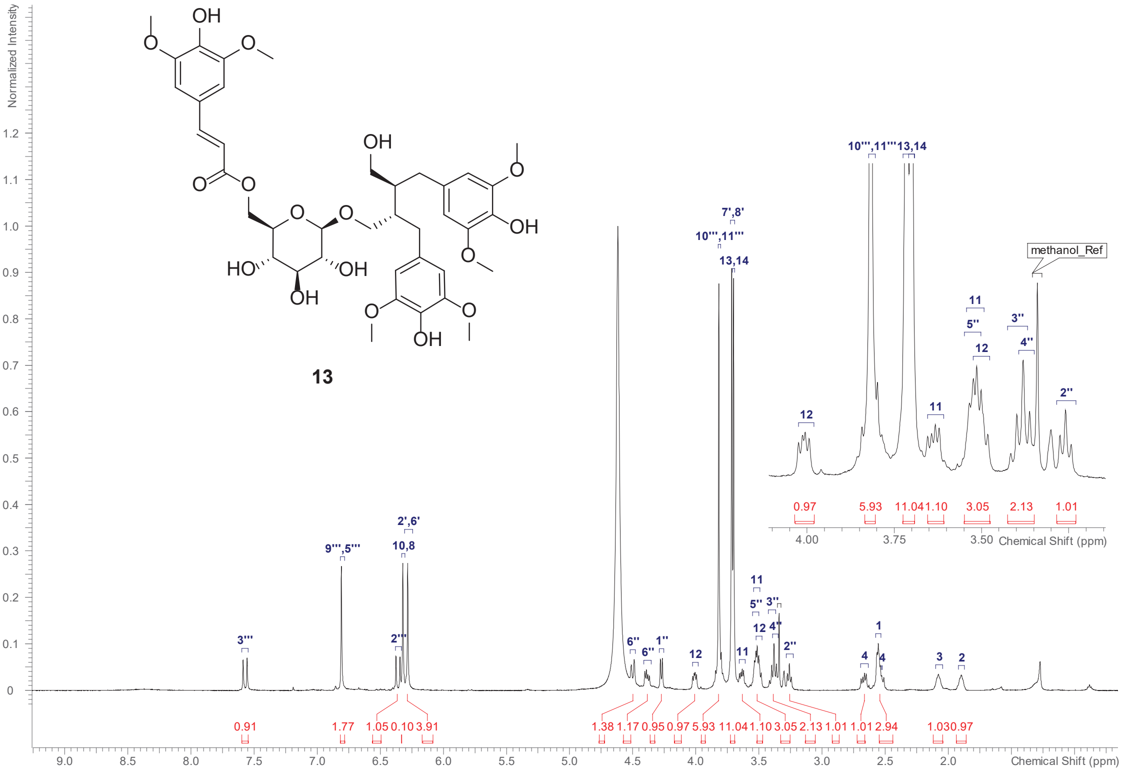

Figure S105. ^{1}H NMR Spectrum of Compound **13** (500 MHz, methanol-d_4).

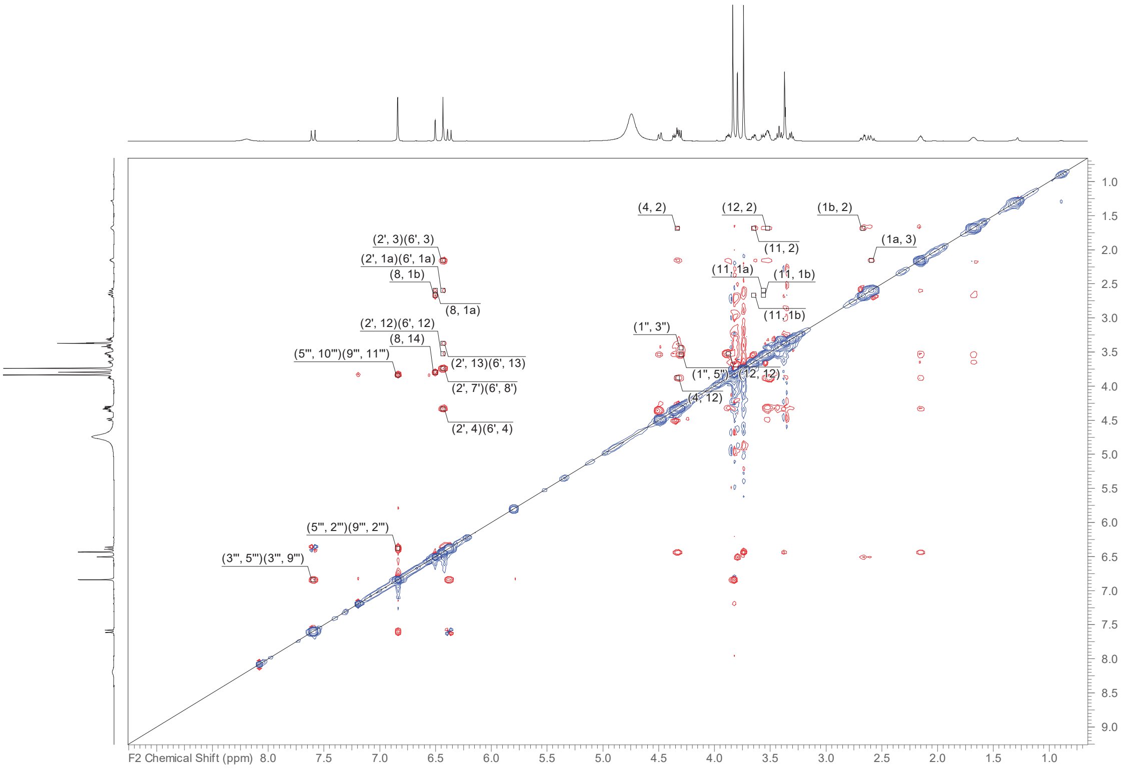

Figure S104. ^{1}H-^{1}H ROESY Spectrum of Compound **12** (500 MHz, methanol-d_4).

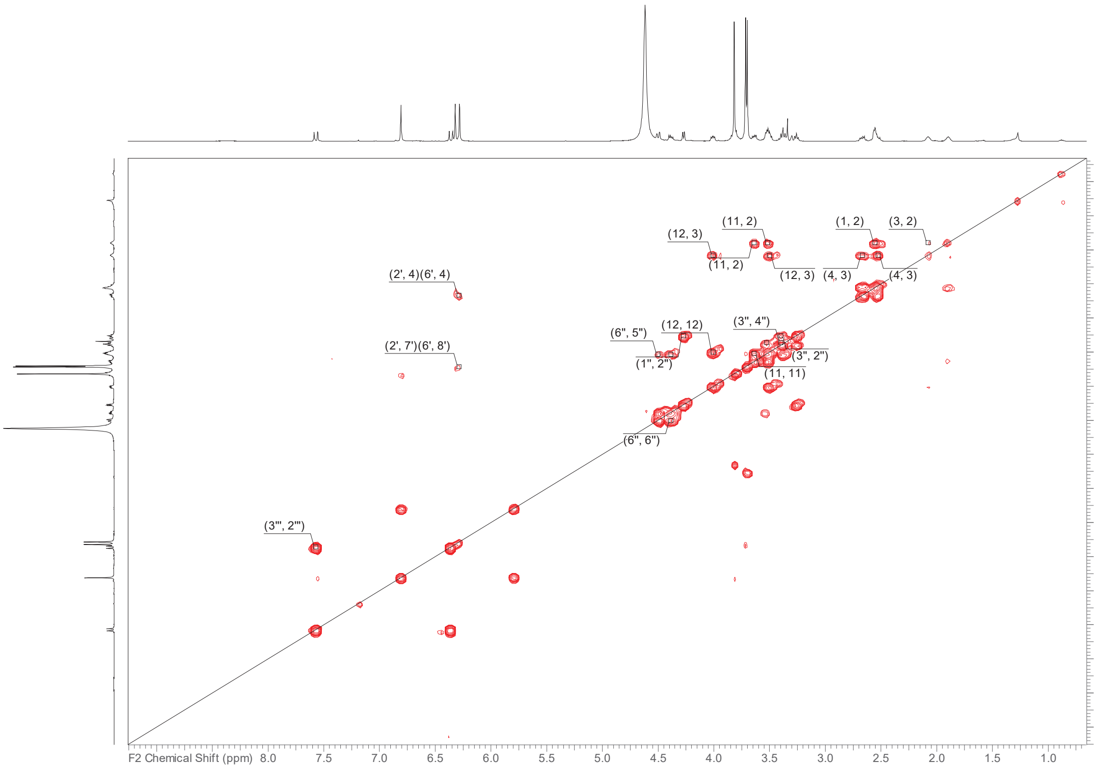

Figure S107. ^{1}H-^{1}H COSY Spectrum of Compound **13** (500 MHz, methanol-d_4).

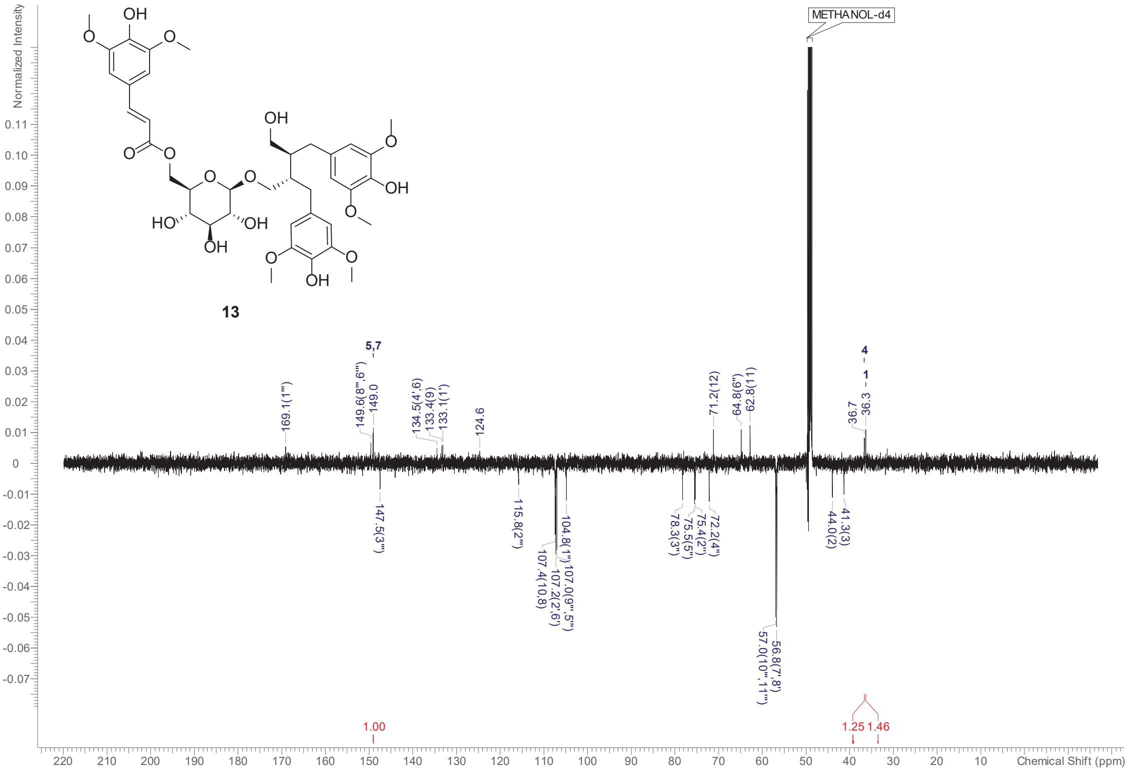

Figure S106. ^{13}C NMR Spectrum of Compound **13** (125 MHz, methanol-d_4).

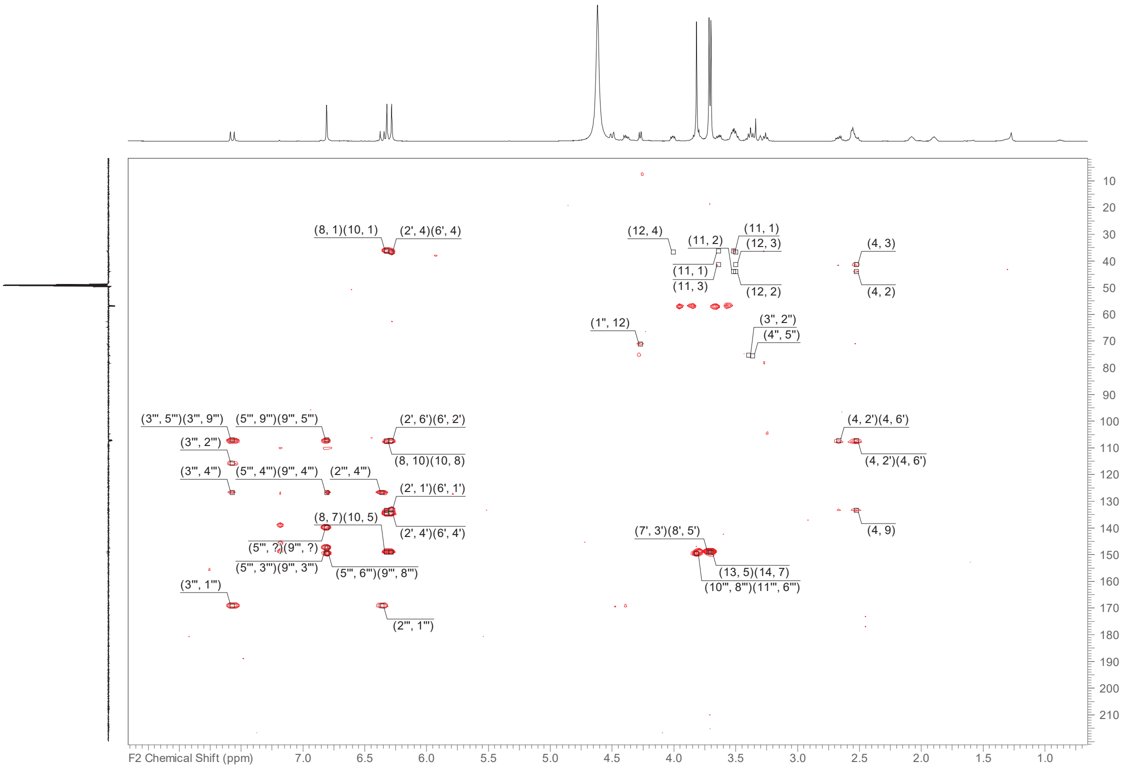

Figure S109. HMBC Spectrum of Compound **13** (500 MHz, CD$_3$OD).

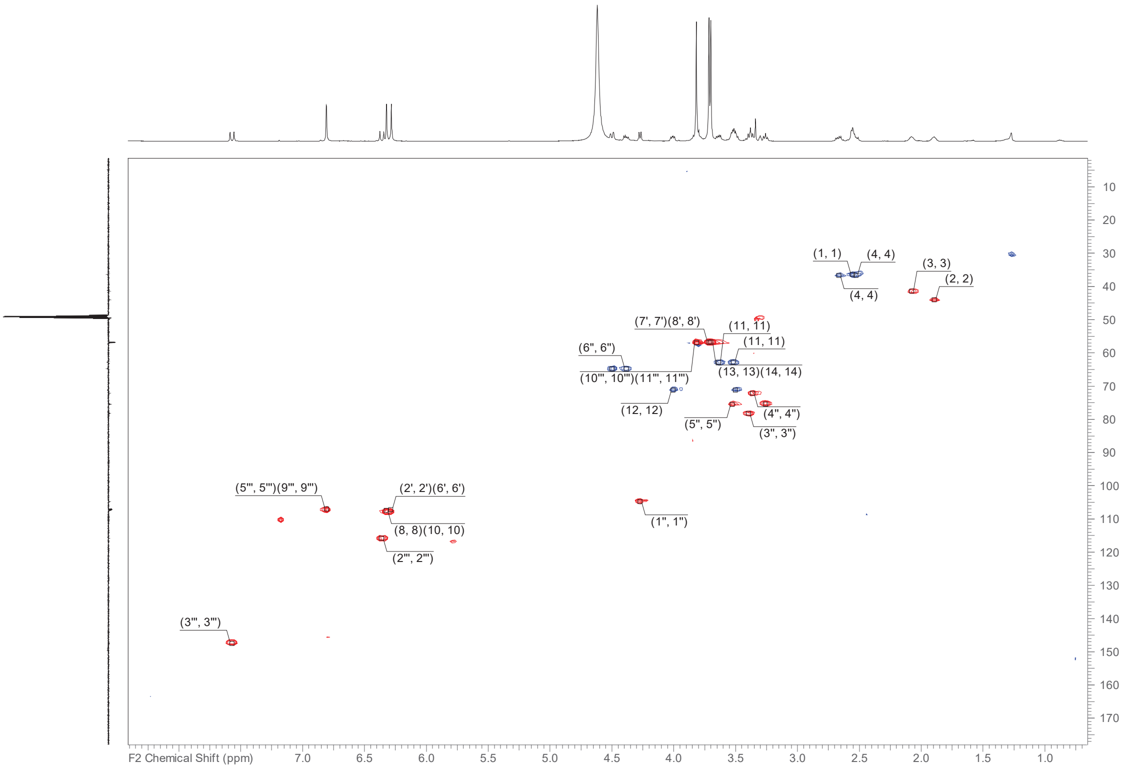

Figure S108. HSQC-DEPT Spectrum of Compound **13** (500 MHz, methanol-*d$_4$*).

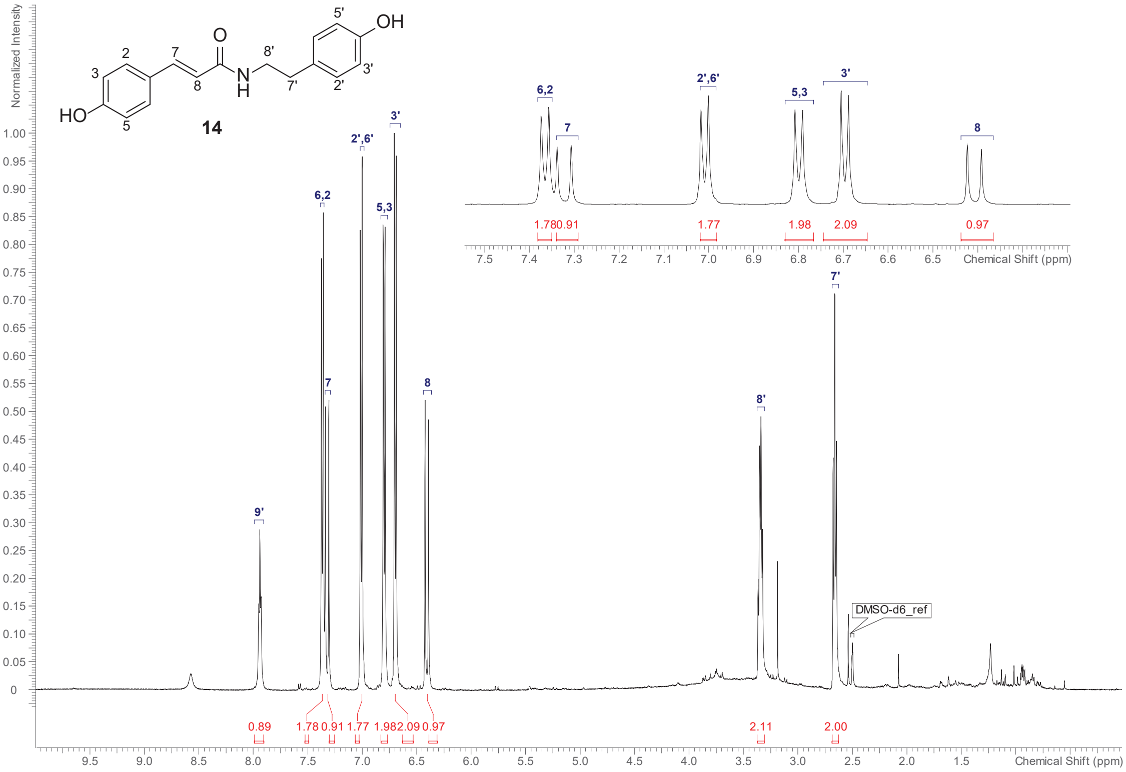

Figure S111. ^{1}H NMR Spectrum of Compound **14** (500 MHz, DMSO-d_6).

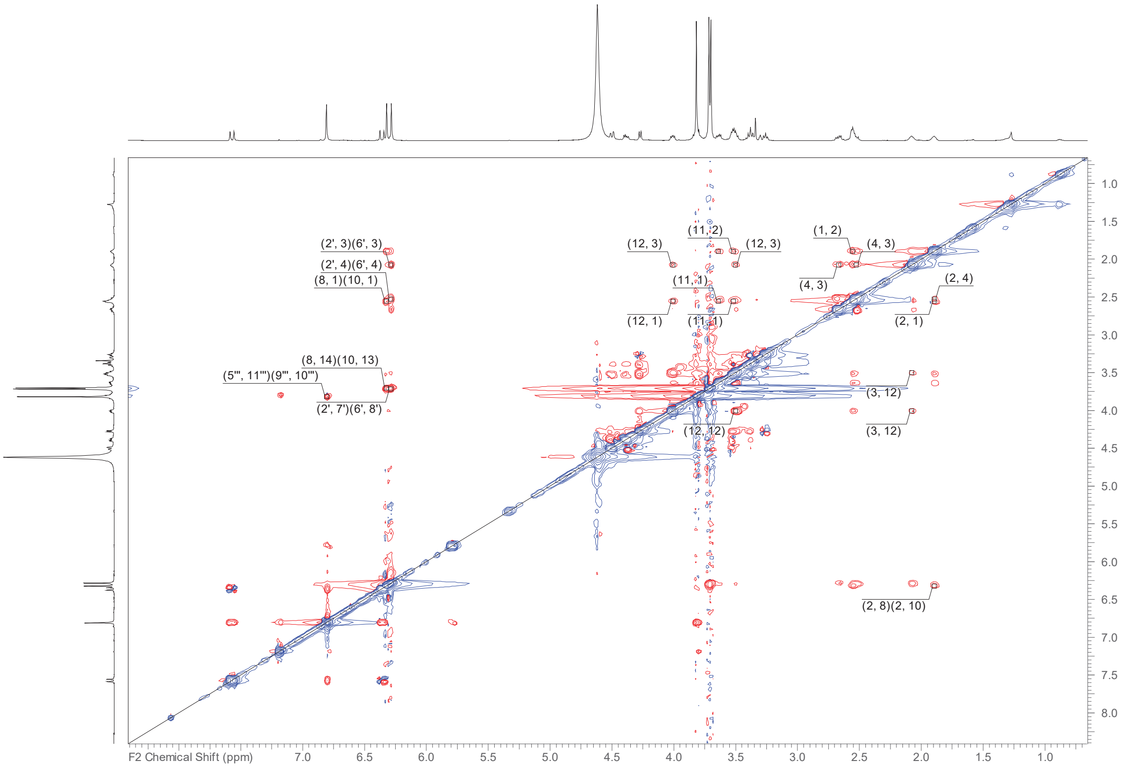

Figure S110. ^{1}H-^{1}H ROESY Spectrum of Compound **13** (500 MHz, methanol-d_4).

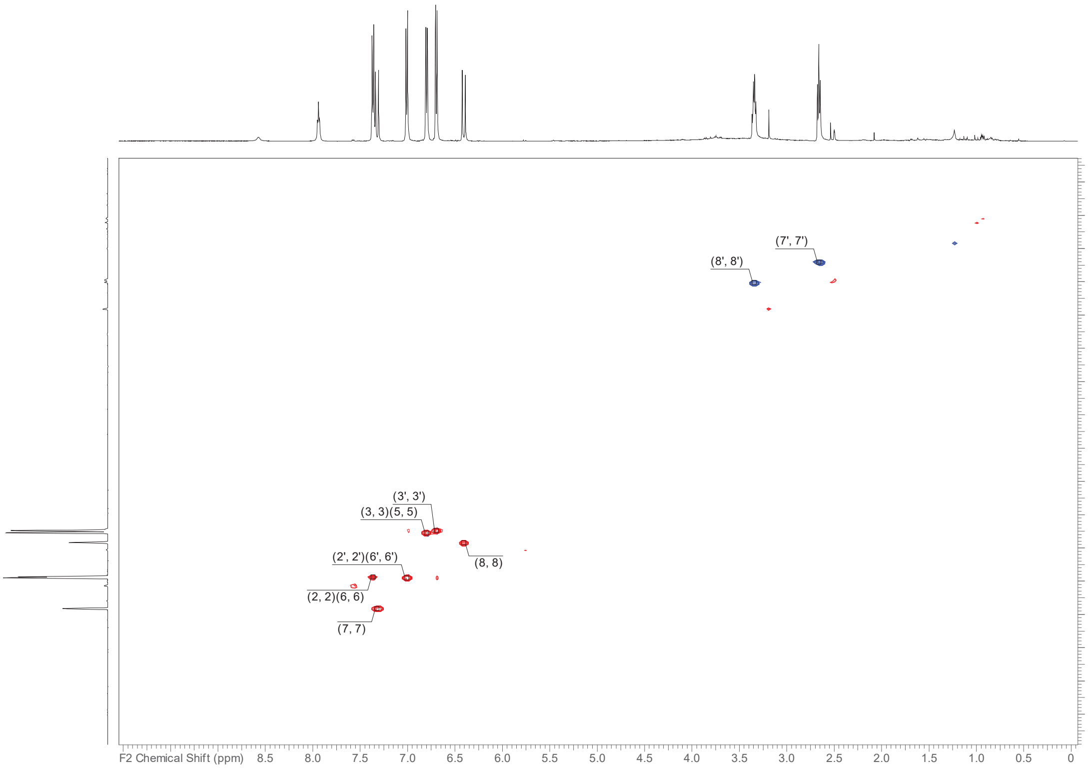

Figure S113. HSQC-DEPT Spectrum of Compound **14** (500 MHz, DMSO-*d*$_6$).

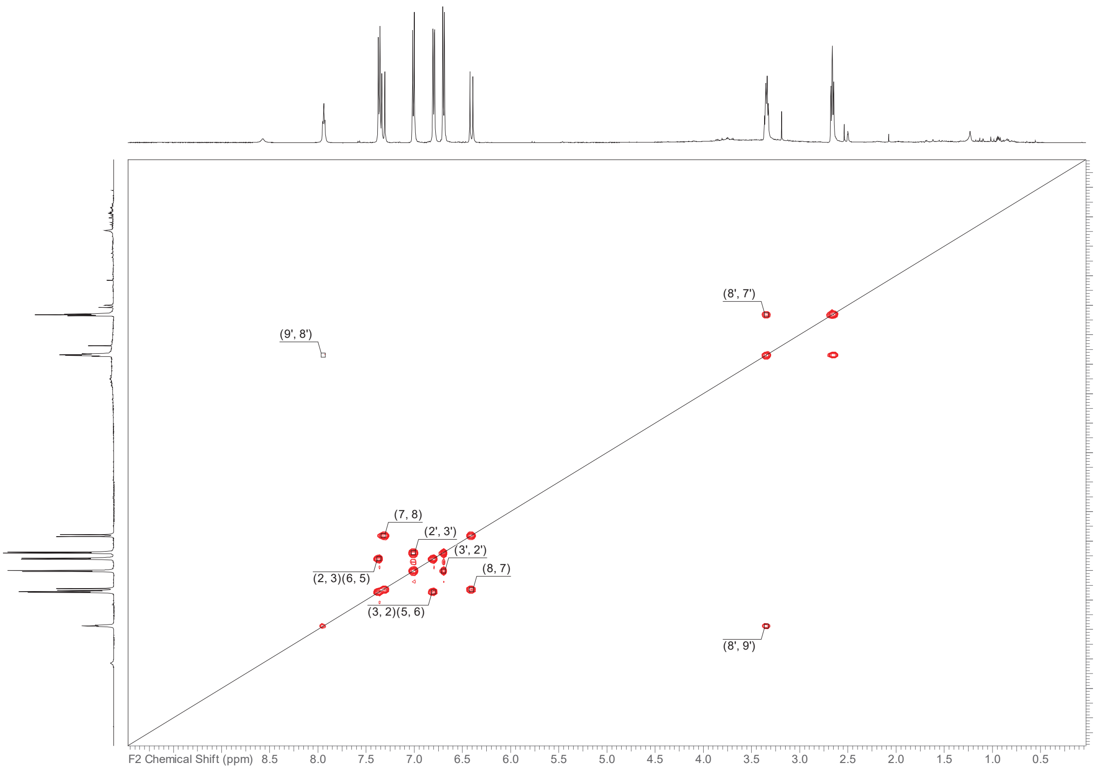

Figure S112. ^{1}H-^{1}H COSY Spectrum of Compound **14** (500 MHz, DMSO-*d*$_6$).

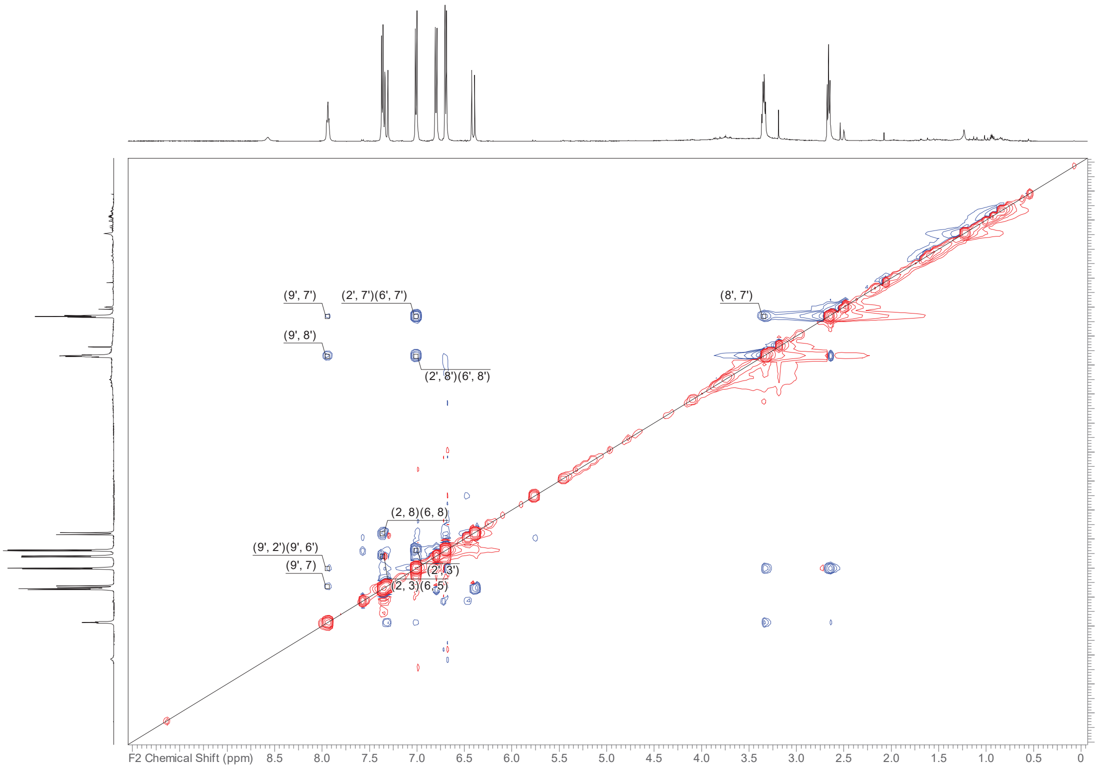

Figure S115. ^{1}H-^{1}H NOESY Spectrum of Compound **14** (500 MHz, DMSO-d_6).

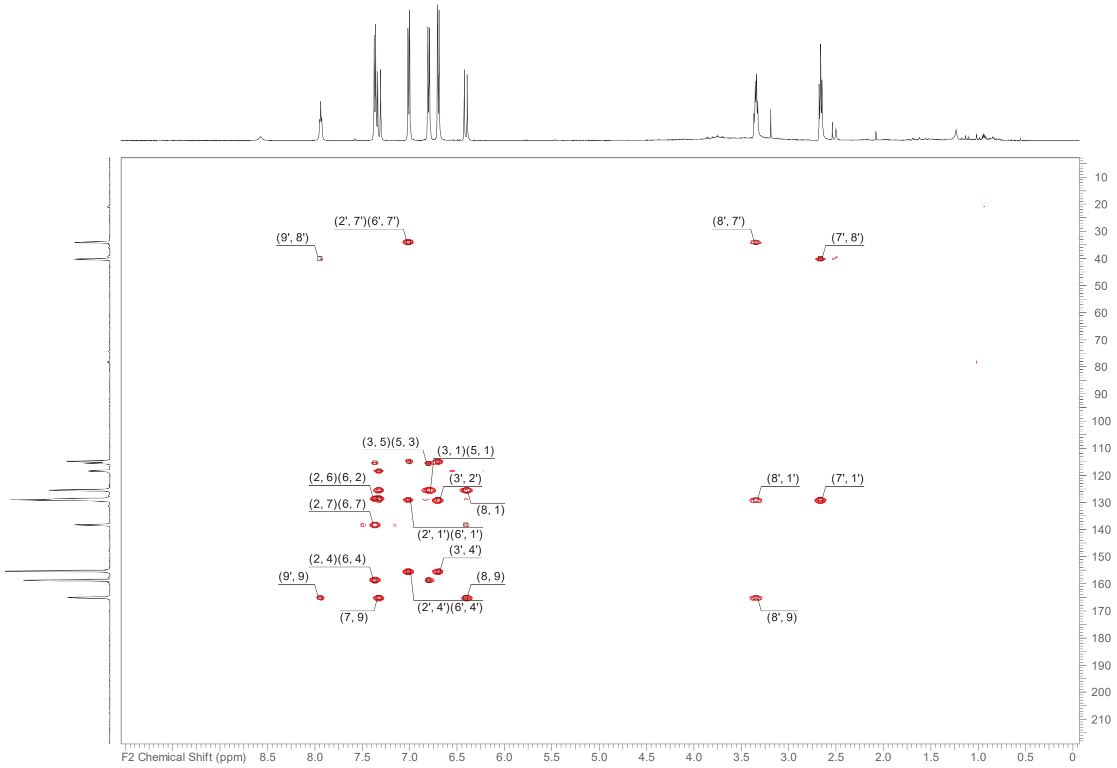

Figure S114. HMBC Spectrum of Compound **14** (500 MHz, DMSO-d_6).

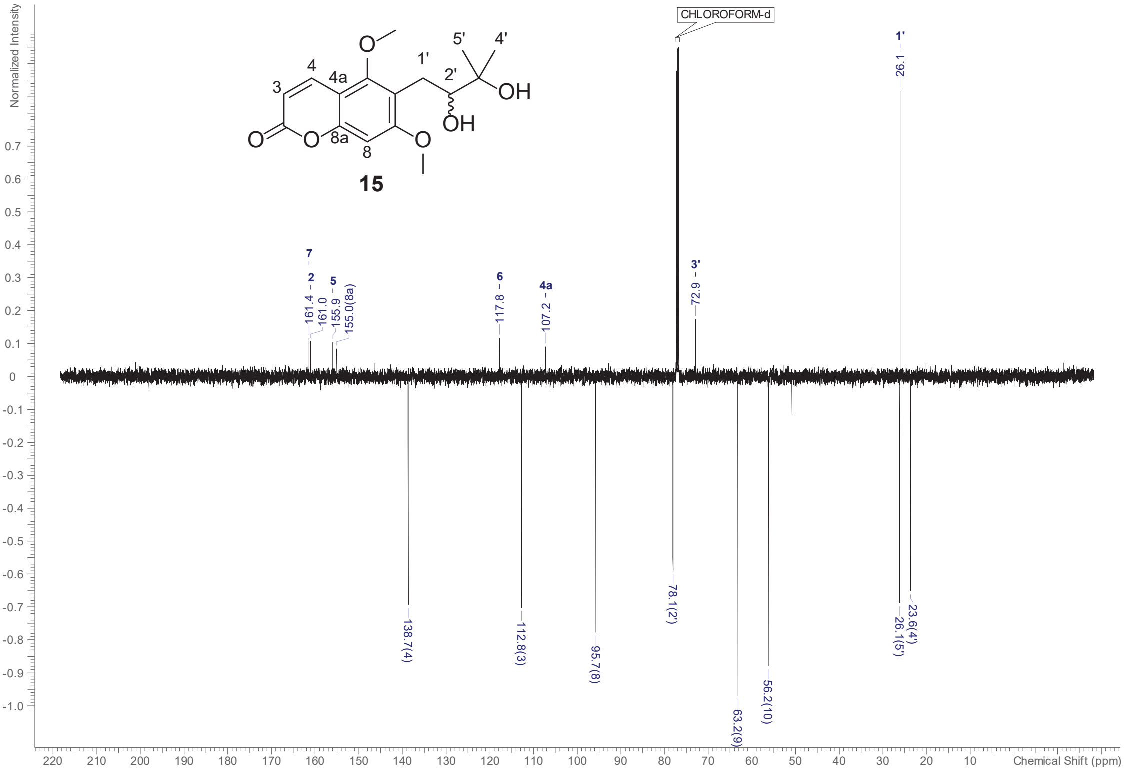

Figure S117. ^{13}C NMR Spectrum of Compound **15** (125 MHz, CDCl$_3$).

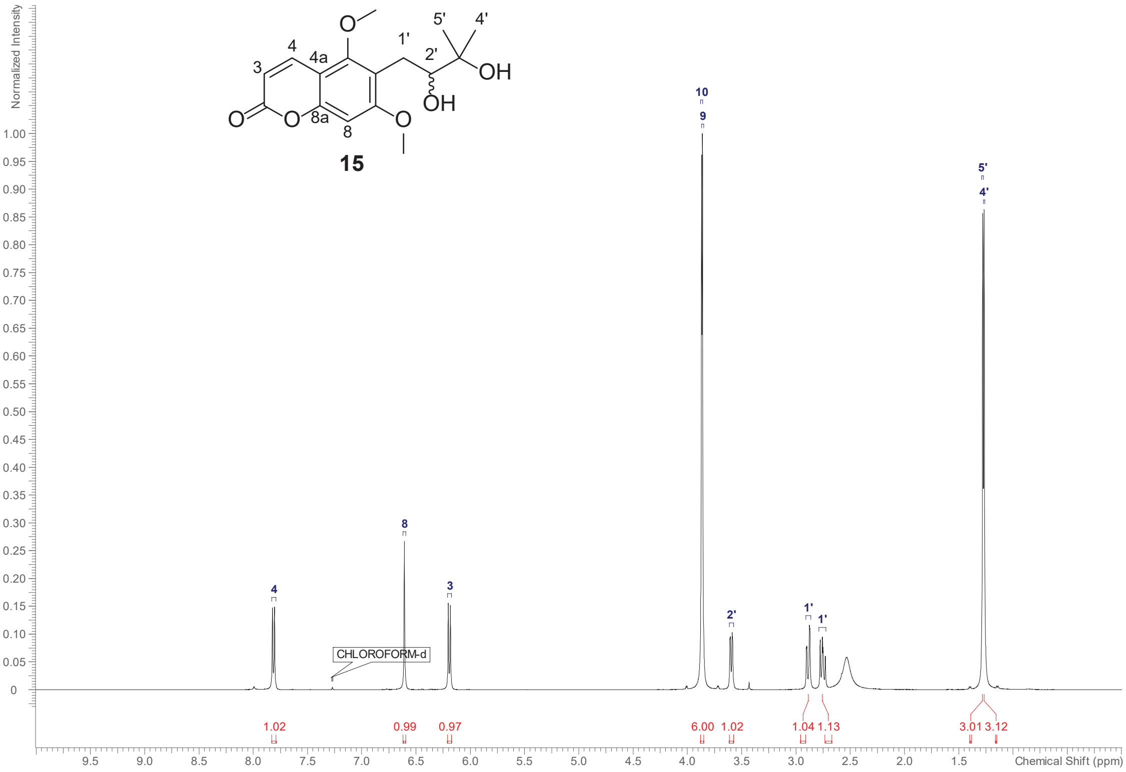

Figure S116. ^{1}H NMR Spectrum of Compound **15** (500 MHz, CDCl$_3$).

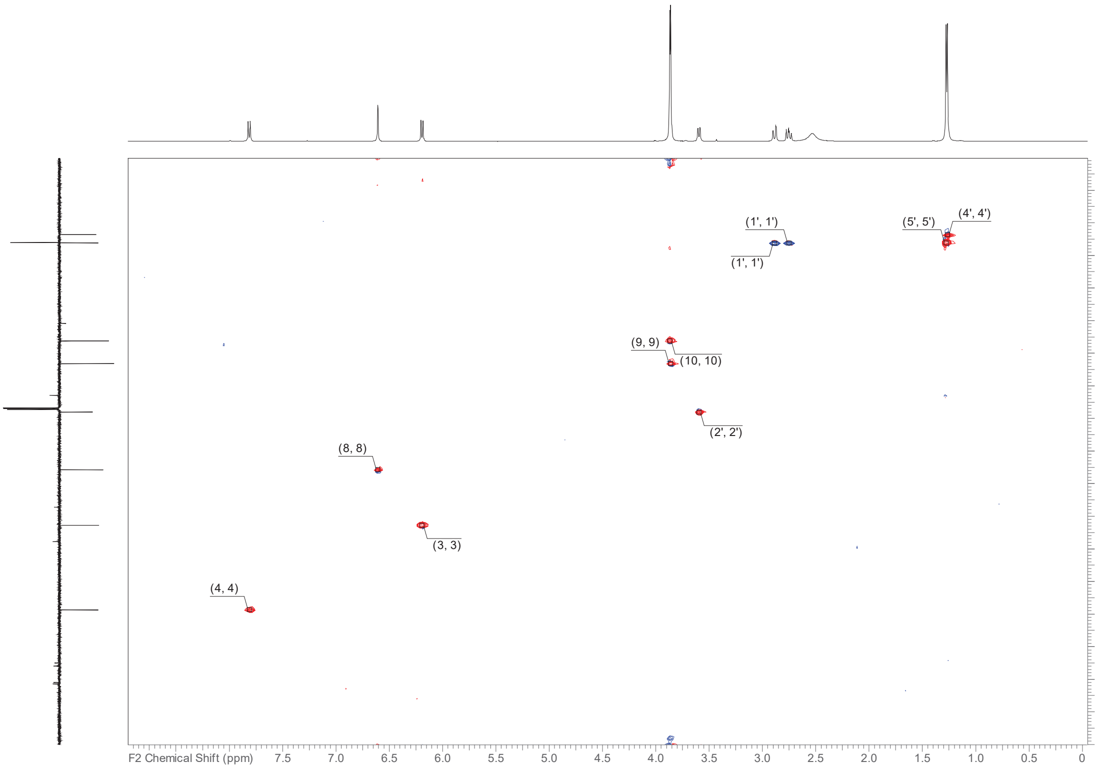

Figure S119. HSQC-DEPT Spectrum of Compound **15** (500 MHz, CDCl₃).

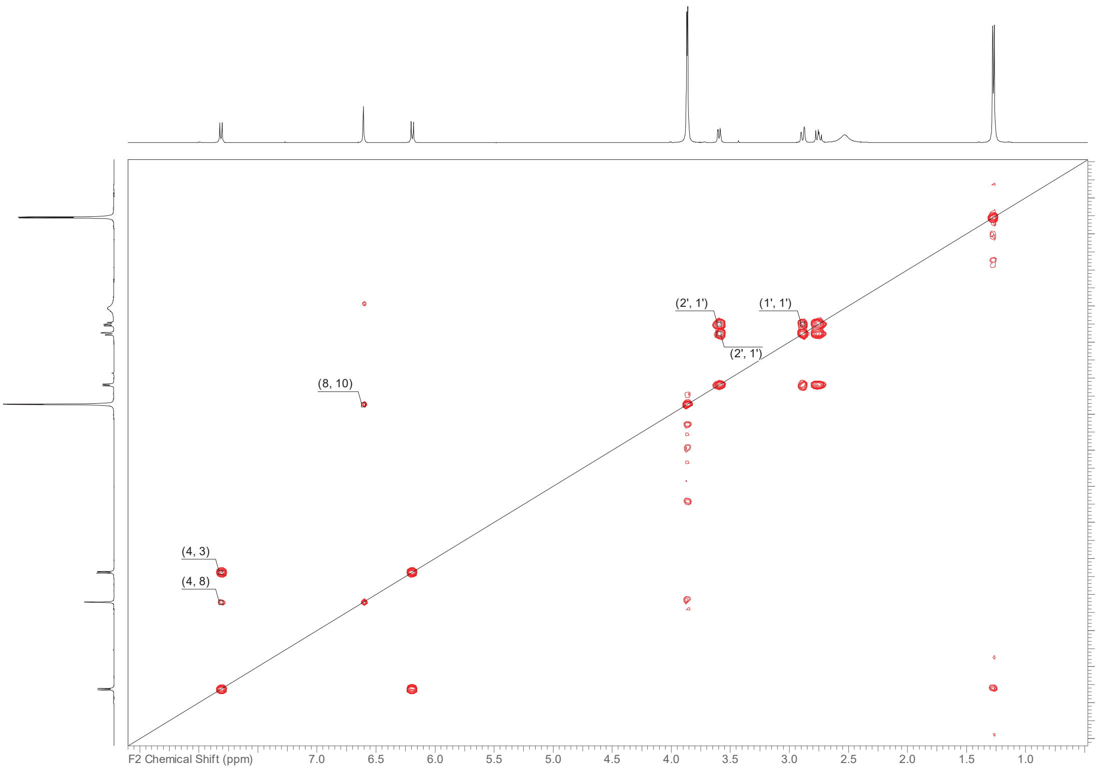

Figure S118. ^{1}H-^{1}H COSY Spectrum of Compound **15** (500 MHz, CDCl₃).

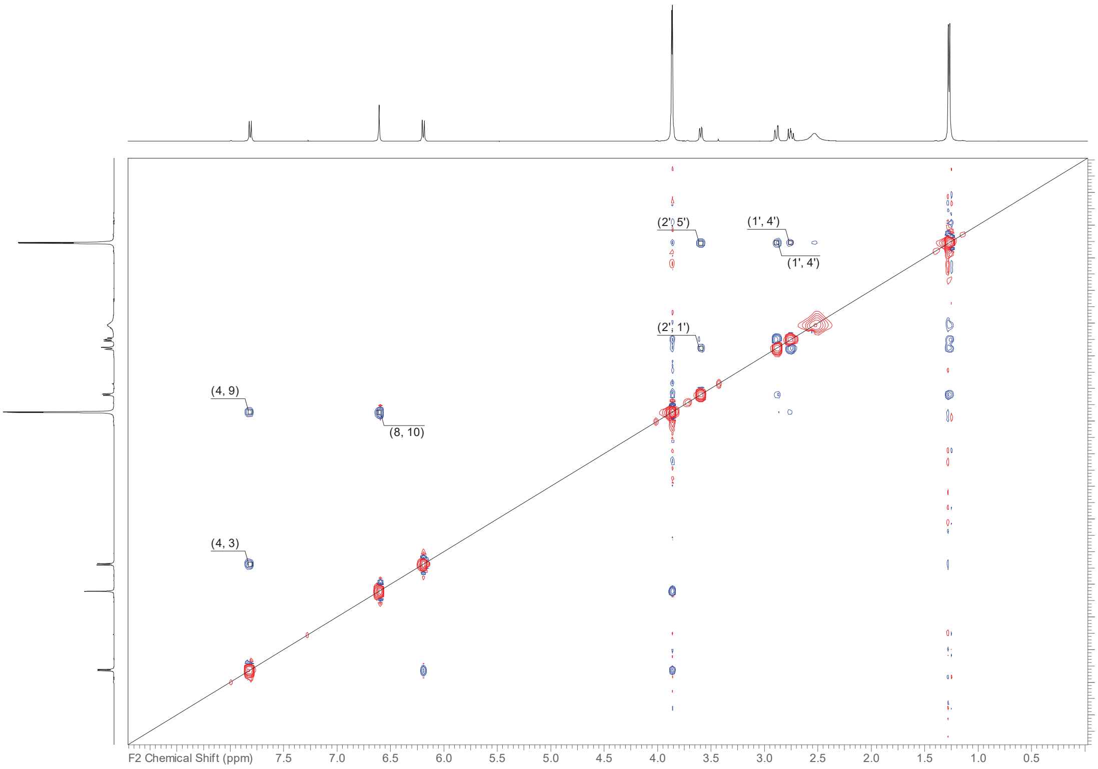

Figure S121. ^{1}H-^{1}H NOESY Spectrum of Compound **15** (500 MHz, CDCl$_3$).

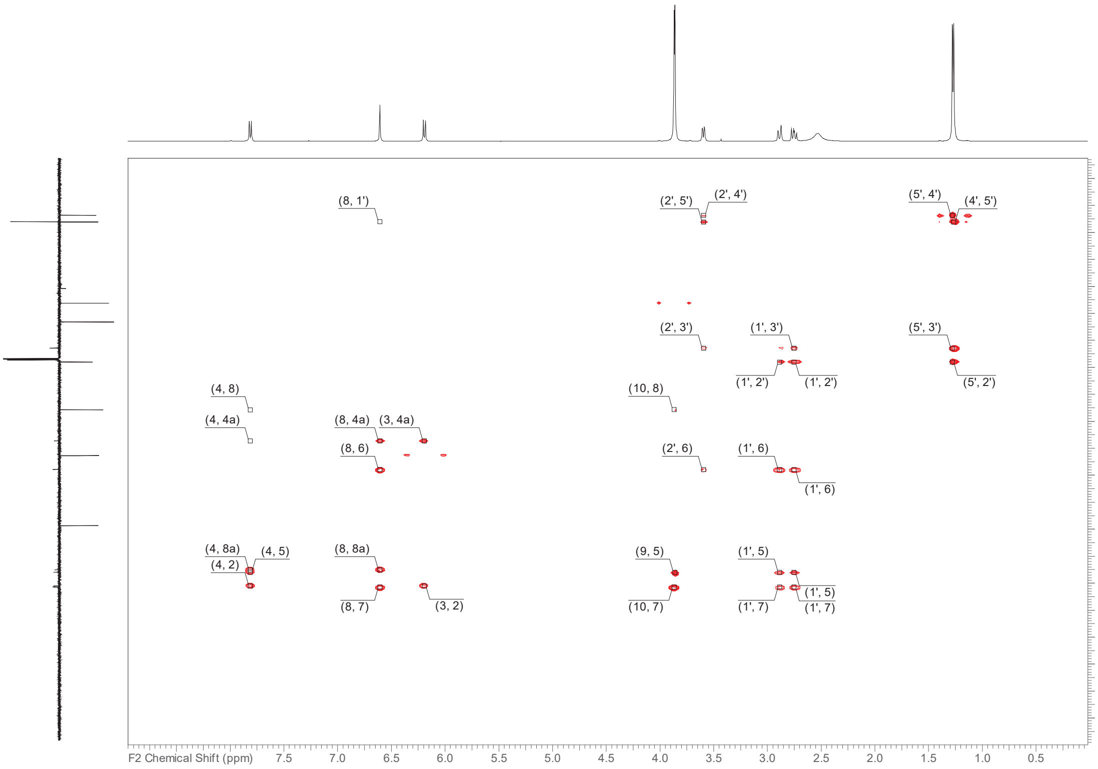

Figure S120. HMBC Spectrum of Compound **15** (500 MHz, CDCl$_3$).

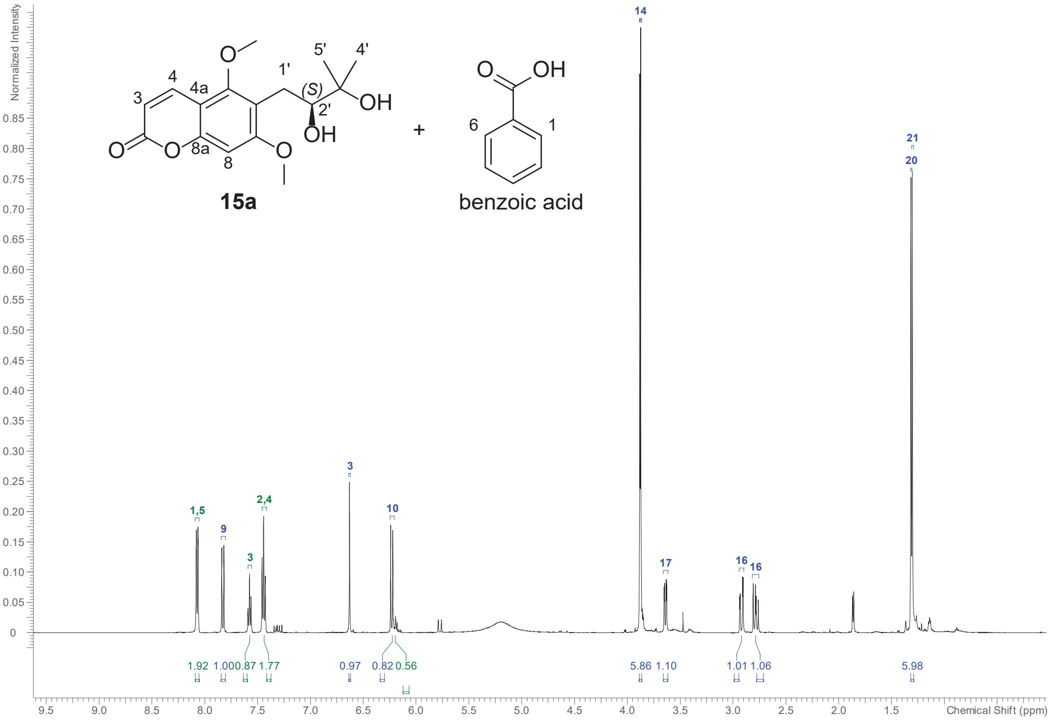

Figure S123. ^{1}H NMR Spectrum of Compound **15a** from enzymatic hydrolysis of **9** with an impurity (molar ratio 1:0.87) of benzoic acid (500 MHz, CDCl$_3$).

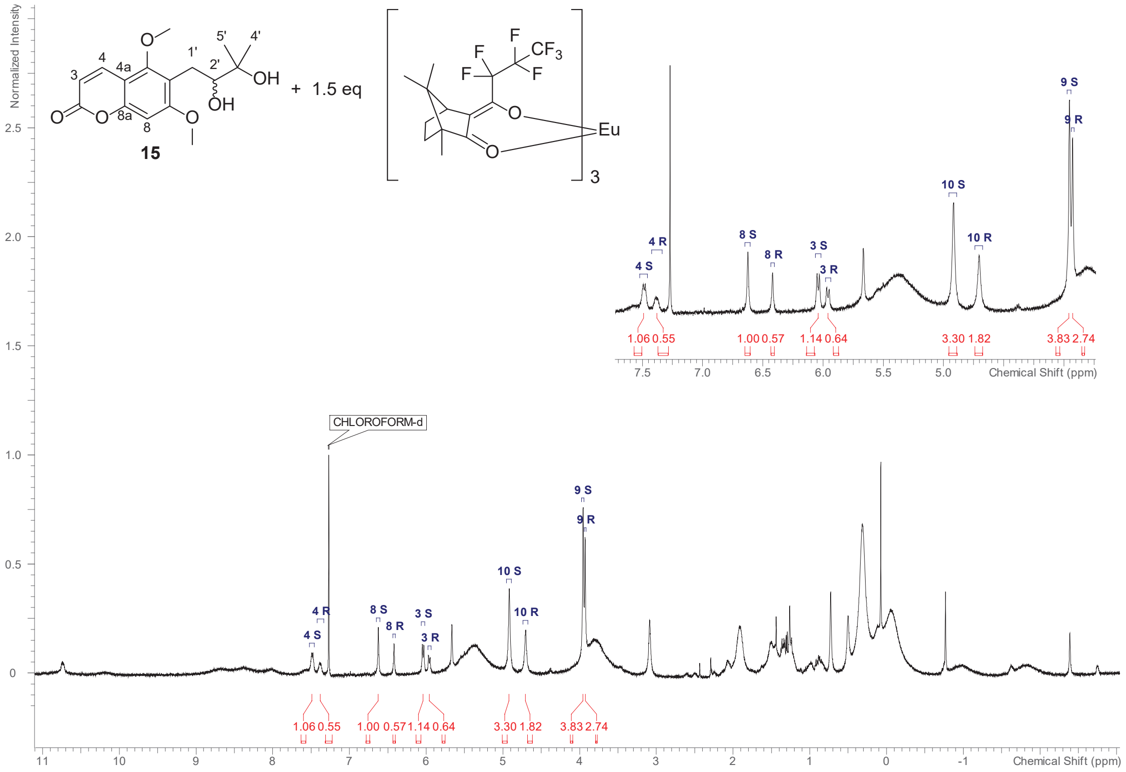

Figure S122. ^{1}H NMR Spectrum of Compound **15** in the presence of 1.5 eq Eu(hfc)$_3$ (500 MHz, CDCl$_3$).

Figure S125. HSQC-DEPT Spectrum of Compound **15a** from enzymatic hydrolysis of **9** with an impurity (molar ratio 1:0.87) of benzoic acid (500 MHz, $CDCl_3$).

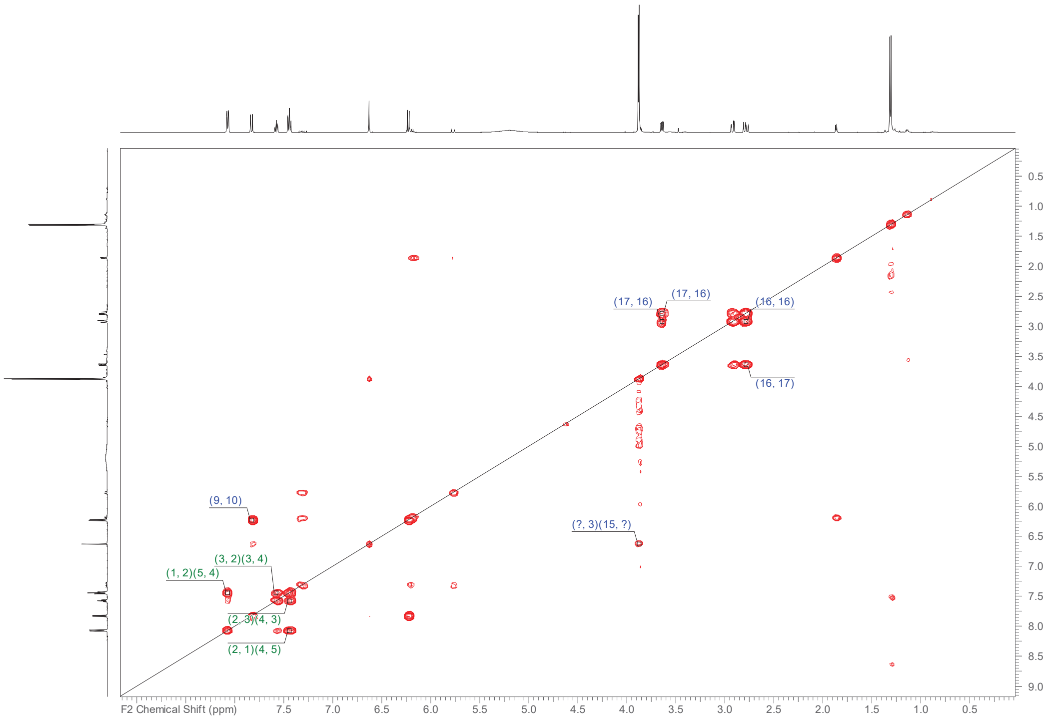

Figure S124. ^1H-^1H COSY Spectrum of Compound **15a** from enzymatic hydrolysis of **9** with an impurity (molar ratio 1:0.87) of benzoic acid (500 MHz, $CDCl_3$).

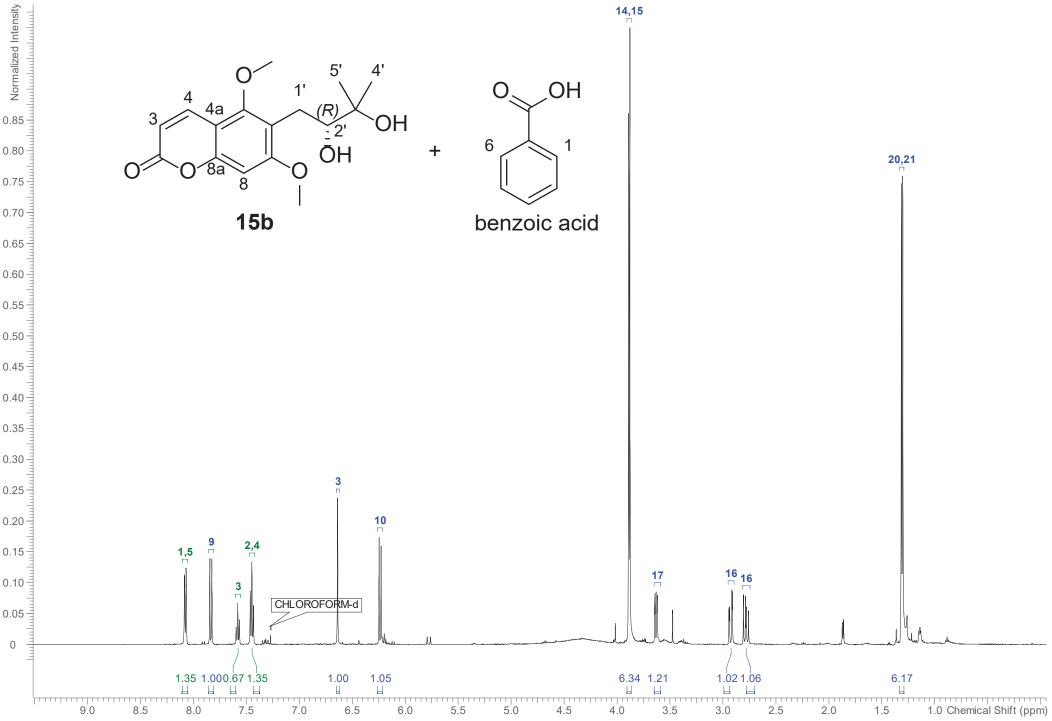

Figure S127. ^{1}H NMR Spectrum of Compound **15b** from enzymatic hydrolysis of **10** with an impurity (molar ratio 1:0.67) of benzoic acid (500 MHz, CDCl$_3$).

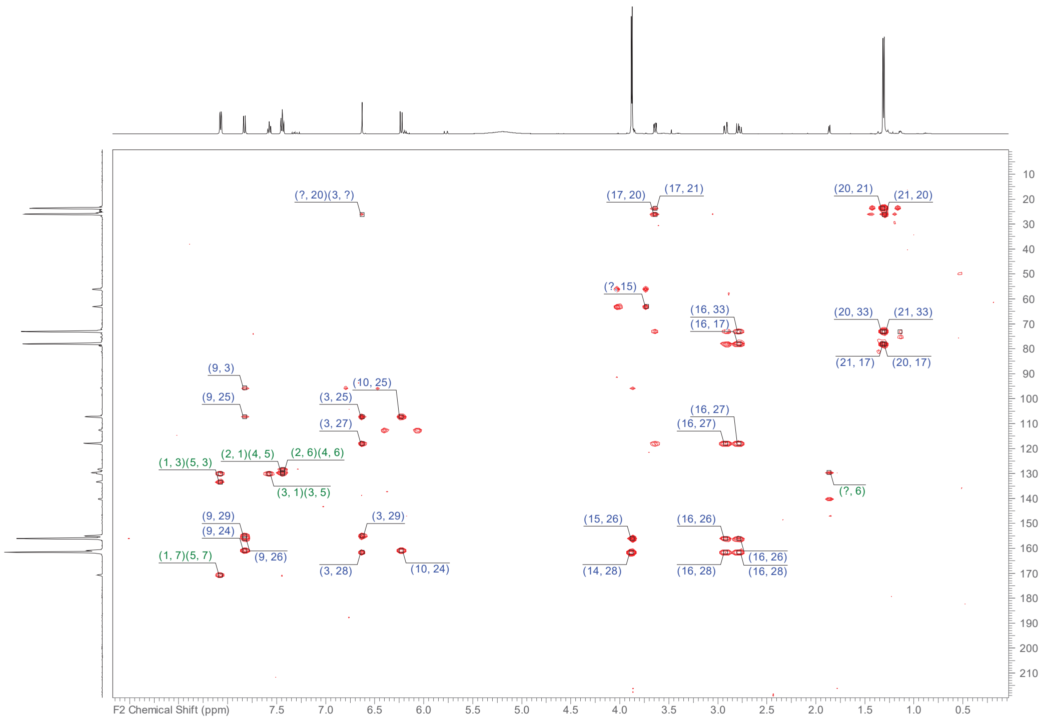

Figure S126. HMBC Spectrum of Compound **15a** from enzymatic hydrolysis of **9** with an impurity (molar ratio 1:0.87) of benzoic acid (500 MHz, CDCl$_3$).

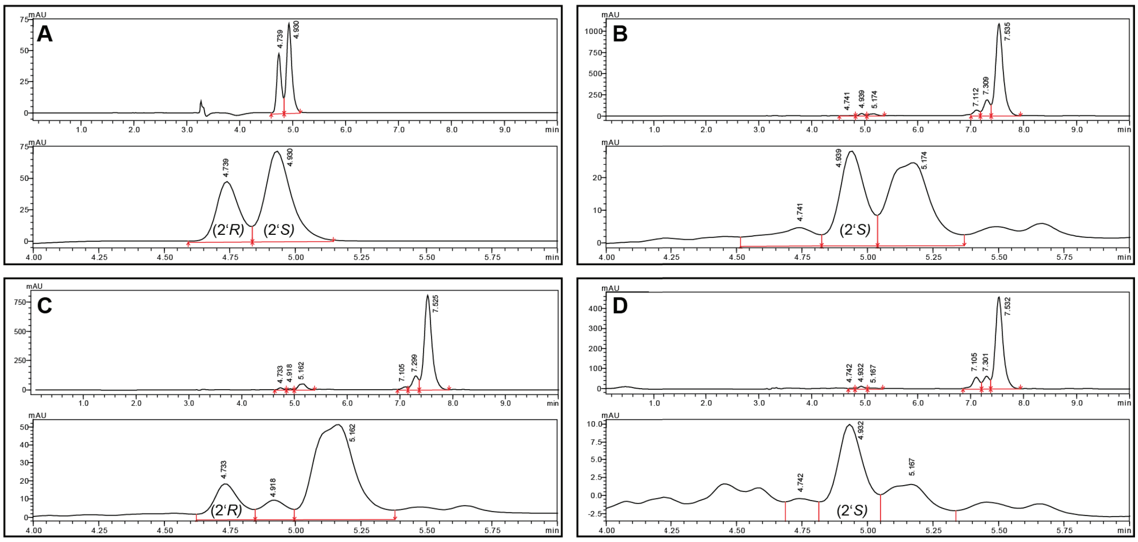

Figure S128. HPLC chromatogram (Daicel Chiralpak IG, 5 µm, 250 x 4.6 mm, 20% CH_3CN in H_2O isocratic flow, detection at 330 nm) for compound **15** (A) and the products from acid hydrolysis of compounds **9** (B), **10** (C), and **11** (D). For each run, the full chromatogram is shown above the focused section between 4 and 6 min.

4. Conclusion and Perspective

Autoimmune diseases are a rising burden in industrialized countries and will continue to affect more and more people as the standard of living keeps increasing throughout the world. In this work, we investigated possible lead compounds from different plant extracts. This contributes to the search for urgently needed small molecule drugs for the treatment of autoimmune diseases.

The initial search among extracts from plants used in Traditional Chinese Medicine led to a number of extracts with significant inhibition of T cell proliferation. From these, the ethyl acetate extract of the herb *Artemisia argyi* and the MeOH extract of the roots of *Toddalia asiatica* were investigated in detail. Compounds from the active regions in the chromatograms were isolated based on the HPLC activity profile. This resulted in the publication of a total of 33 compounds, including flavonoids, sesquiterpene lactones, sesquiterpene lactone dimers, alkaloids, coumarins, lignans, and small phenolics. Of those, seven compounds were new natural products. Significant T cell inhibition *in vitro* was observed for the alkaloid nitidine as well as for several sesquiterpene lactones. Most prominently, *seco*-tanapartholides A and B, and guaianolide sesquiterpene lactones related to canin showed remarkable activity (IC_{50} 1.0-3.7 µM), which could be exploited in the future.

Furthermore, the modes of action of the active constituents isolated from *A. argyi* extract were investigated. An inhibition of the NFAT as well as the NF-κB pathway was observed for both the extract and isolated sesquiterpene lactones. Upon further investigating the NFAT pathway, we observed differential effects on Ca^{2+} signaling from the extract and the sesquiterpene lactones isolated from it. The extract inhibited the ion flux from the ER as well as from the extracellular lumen, while the tested sesquiterpene lactones and a mixture of them only inhibited the Ca^{2+} flux from the extracellular space. This could hint at an inhibition of the CRAC or other Ca^{2+} channels by the tested sesquiterpene lactones. As the extract shows additional inhibition of the ER calcium flux, it likely has an additional mode of action. This could be caused by unidentified compounds, synergies between compounds, effects from identified compounds at the concentrations present in the extract, or a combination of these factors. As the *in vitro* immunosuppressant activity of one extract through at least three different modes of action is a highly unusual finding, further investigation is warranted.

A possible path could be the use of HPLC activity profiling in combination with measuring the intracellular calcium flux. If this would be successful, synergy and concentration effects could be, at least in part, excluded. It would also enable the isolation of compounds responsible for the activity of the *A. argyi* extract. This would give lead structures from *A. argyi* for the targeted inhibition of different points in the NFAT pathway, which could be used to design experiments, but also for the development of new small molecule drugs based on these structures.

Sesquiterpene lactones are a class of highly interesting compounds, particularly through their possible complexity from variable scaffolds, configurations and substitution patterns. The sesquiterpene lactone ring can form covalent bonds with proteins as a kind of “covalent warhead”. As this recognition is dependent on their three-dimensional structure, their exact and reliable stereochemical characterization is strictly necessary for further development. Thus, the absolute configurations reported in this work for the isolated compounds enable the further development of these compounds.

NMR was the primary means to establish the relative configuration. After careful evaluation of NOE information, ^{13}C chemical shifts, and J_{HH} coupling constants, possible relative configurations were compiled. Afterwards, ECD was used as a standard technique for all compounds of which a spectrum could be expected. If a spectrum was obtained, this was compared to *ab initio* calculated spectra of all possible configurations. To overcome limitations in case of more than one possible relative configuration, VCD was used. This proved to be especially helpful in the case of *seco*-tanapartholides A and B, which have almost enantiomeric ECD spectra, but have easily distinguishable VCD spectra. Due to the complexity of the spectra in comparison to ECD, VCD is less straightforward to apply in practice. Thus, its evaluation was aided by computational comparisons. As only the maximal spectrum overlap is considered and no bands are assigned, this can lead to false attributions in some cases. For this reason, the necessity of a visual control cannot be stressed enough in order to avoid false attributions. When this is done, VCD is a very potent technique with respect to assigning absolute configurations absolutely inaccessible by ECD.

An approach combining several methods was used when investigating the compounds isolated from *T. asiatica* root extract. Here, different compounds needed different approaches to determine their configurations. A series of glycosylated coumarins with enantiomeric aglycones and different glycosylation positions was found. After acid hydrolysis, the sugar was determined as D-glucose, but most of the aglycone had lost its chirality due to dehydration of the formed 1,2-diol. The remnants, however, could be analyzed using enantioselective HPLC. Two compounds were confirmed by enzymatic hydrolysis and ECD. These examples show the necessity for the use of a wide variety of methods.

In any case, when assigning absolute configurations, the use of different techniques gives different perspectives on a stereochemical problem, thus contributing significantly to the quality of the work. This also significantly increases the value for any biological testing, as each assay ultimately comes down to the molecular interaction between three-dimensional chiral structures.

5. Curriculum Vitae

Curiculum vitae

October 23, 2020

Name	Jakob Reinhardt
Birth:	23.05.1992 in Fürth (Germany)
Email:	reinhardt.jakob@gmx.de
Nationality:	German

University education

Since 04.2016	PhD Thesis in the Lab of Prof. Dr. Matthias Hamburger in Basel, Switzerland Topic: *“Activity-guided isolation of natural products with immunosuppressive activity”*
03.2016	Master thesis: *„Studies on the biomass-composition of selected microalgae under the influence of exogenous factors“* in the research group of Prof. Dr. Ulrike Lindequist (Pharmaceutical Biology, Greifswald, Germany)
2013 - 2016	“Master of Science” in Biochemistry, University Greifswald, Germany
10.2013	Bachelor thesis: *“Development of a new kind of fluorescence sensors by combining dithiolene ligands with electron deficient fluorophores”* in the research group of Prof. Dr. Carola Schulzke (Bioinorganic chemistry, Greifswald, Germany)
2010 - 2013	“Bachelor of Science” in Biochemistry, University Greifswald, Germany

---

Teaching experience

2020	Supervision of Master students in their practical education for isolation of natural products and structure elucidation
2016 - 2019	Supervision of bachelor students in their practical education in Pharmaceutical Biology and Systematics courses
2014 - 2015	Tutoring of Biochemistry and Environmental studies students in Physical Chemistry

---

Working experience

2009 - 2010	Civil service in patient transportation at the St. Georg Klinikum, Eisenach (Germany)

Publications

08.2020	**Reinhardt JK**, Zimmermann-Klemd AM, Danton O, Smieško M, Huber R, Gründemann C, Hamburger M. *Isolated compounds from Toddalia asiatica: Immunosuppressant activity and absolute configurations.* J. Nat. Prod. **2020**; 83: 3012-3020

07.2020	Zimmermann-Klemd AM*, **Reinhardt JK***, Nilsu T, Morath A, Falanga CM, Schamel WW, Huber R, Hamburger M, Gründemann C. *Boswellia carteri extract and 3-O-acetyl-alpha-boswellic acid suppress T cell function.* Fitoterapia **2020**, DOI: 10.1016/j.fitote.2020.104694: 104694
01.2020	Gründemann C, **Reinhardt JK**, Lindequist U. *European medicinal mushrooms: Do they have potential for modern medicine? – An update.* Phytomedicine **2020**; 66: 153131
04.2020	Zimmermann-Klemd AM*, **Reinhardt JK***, Morath A, Schamel WW, Steinberger P, Leitner J, Huber R, Hamburger M, Gründemann C. *Immunosuppressive Activity of Artemisia argyi Extract and Isolated Compounds*. Front. Pharmacol. **2020**; 11: 402
06.2019	**Reinhardt JK***, Klemd AM*, Danton O, De Mieri M, Smiesko M, Huber R, Burgi T, Grundemann C, Hamburger M. *Sesquiterpene lactones from Artemisia argyi: Absolute configuration and immunosuppressant activity.* J. Nat. Prod. **2019**; 82: 1424-1433
06.2016	Schulze C, **Reinhardt J**, Wurster M, Ortiz-Tena JG, Sieber V, Mundt S. A one-stage cultivation process for lipid- and carbohydrate-rich biomass of *Scenedesmus obtusiusculus* based on artificial and natural water sources. Bioresour. Technol. **2016**; 218: 498-504.
02.2016	Schulze, C., Wetzel, M., **Reinhardt, J.**, Schmidt, M., Felten, L., Mundt, S., **2016**. Screening of microalgae for primary metabolites including β-glucans and the influence of nitrate starvation and irradiance on β-glucan production. J. Appl. Phycol. 28(5), 2719-2725.
07.2014	Ghosh AC, **Reinhardt JK**, Kindermann MK, Schulzke C. The ring opening reaction of 1,3-dithiol-2-one systems is fully reversible. Chem. Commun. (Camb) **2014**; 50: 10102-10104.

*shared first authorship

Conference contributions

09.2019	**Reinhardt JK**, Baburin I, Andranovits S, Hering S, Hamburger M. *High affinity HERG and low affinity Cav1.2 Blockers Dehydroevodiamine and Hortiamine in Decoctions of the TCM drug Evodiae fructus*, **poster presented** at 67th International Congress of the Society for Medicinal Plant and Natural Product Research (GA) 2019 in Innsbruck, Austria.
09.2019	**Reinhardt JK**, Klemd AM, Danton O, De Mieri M, Smieško M, Huber R, Bürgi T, Gründemann C, Hamburger M. *Absolute configuration of sesquiterpene lactones with potent immunosuppressant activity*, **poster presented** at 67th International Congress of the Society for Medicinal Plant and Natural Product Research (GA) 2019 in Innsbruck, Austria.
02.2019	**Reinhardt JK**, Klemd AM, Danton O, De Mieri M, Smieško M, Huber R, Bürgi T, Gründemann C, Hamburger M. *Activity-guided isolation of natural products with immunosuppressive activity*, **oral presentation** at Annual Research Meeting 2019 in Basel, Switzerland.

06.2018	**Reinhardt JK**, Klemd AM, Danton O, De Mieri M, Smieško M, Huber R, Bürgi T, Gründemann C, Hamburger M. *Sesquiterpene lactones from Artemisia argyi - determination of absolute configurations and immunosuppressive activity*, **oral presentation** at Phytopharm 2018 in Horgen, Switzerland.
09.2017	**Reinhardt JK**, Klemd AM, De Mieri M, Smieško M, Bürgi T, Gründemann C, Hamburger M. *Absolute configuration of sesquiterpene lactones with potent immunosuppressive activity*, **Poster presented** at 65th International Congress of the Society for Medicinal Plant and Natural Product Research (GA) 2017 in Basel, Switzerland.

Awards

2019	Travel Grant for the 67th International Congress of the Society for Medicinal Plant and Natural Product Research (GA) 2019 in Innsbruck, Austria

Language proficiency

English	Good knowledge
German	Native proficiency
Spanish	Basic knowledge

Leisure activities

I spend most of my free time with different sport activities. To move on water, I am in a dragon boat team, paddling in sync to keep the flow. On land, I can free my mind when riding my bike, be it a short trip to work or a longer one to Venice. Moving vertically, I enjoy the mental and physical challenges of bouldering and climbing. And to inspire the movement of the mind, I read books, always in pursuit of new ideas and knowledge.

Basel, October 23, 2020